Universitat Politècnica de Catalunya

Departament de Teoria del Senyal i Comunicacions

Tesis Doctoral

Application of Interferometric Radiometry to Earth Observation

Adriano José Camps Carmona

Barcelona, Noviembre 1996 **Directores: Dr. Ignasi Corbella i Sanahuja**

Dr. Javier Bará Temes

Application of Interferometric Radiometry to Earth Observation
Adriano J. Camps Carmona, Ph.D. Dissertation, Universitat Politècnica de Catalunya, 1996.
This Ph. D. has been awarded with the INDRA award of the Spanish Association of Telecommunication Engineers to the best Ph. D. in remote sensing, February 1998, and the Ph.D. Extraordinary award of the Universitat Politècnica de Catalunya, September 1999.

A mi familia

Acknowledgements

I would like to express my gratitude to *Dr. Ignasi Corbella* and *Dr. Javier Bará*, my thesis directors, for their support and suggestions during these years. I would like to express my gratitude in a special manner to *Dr. Francesc Torres* with whom I have discussed most of the daily difficulties, and with whom I have co-directed many student projects. Thank you. Thanks to *Dr. Manuel Martín-Neira* for the deep review of the reports sent to ESA and his comments and suggestions.

Thank you to all the people in the Antennas, Microwave Radar and Photonics group of the Department, specially to *Dr. Jordi Romeu* and *Dr. Sebastián Blanch* for their help in the design of the cup-dipole antennas, their measurement and graphical representation, to *Dr. Albert Aguasca* for his ideas about the circuitry and to *Joaquim Giner*, laboratory technician, *Alfredo Cano*, workshop technician, and *Josep Mª Haro*, system manager.

Finally, I would like to thank my office partner *Francesc Rocadenbosch* and the more than fifteen students to whom I have directed or co-directed their final projects related to this work.

Abstract

The submitted thesis is a contribution to the study of a two-dimensional microwave synthetic aperture radiometer devoted to Earth observation for the measurement of the soil moisture and the ocean salinity. The aperture synthesis concept used in radioastronomy for decades is revised in depth and extended to large thermal sources, the situation found in Earth remote sensing. Differences between both fields are so fundamental that require a complete and systematic error analysis, new calibration methods and new inversion algorithms suitable to deal with antenna pattern errors and extended thermal sources which suffer the subsampling effects -aliasing- during the reconstruction process. The overall performance of an Y-shaped space-borne interferometric radiometer, and specially the radiometric accuracy improvement by means of pixel averaging, is then evaluated by implementing a simulator that brings together the preceding studies.

In order to validate, as far as possible, system error analysis, calibration and inversion algorithms, an experimental X-band digital interferometric radiometer has been designed and built. It consists of two antennas that are moved to synthesize a set of baselines. Electronic hardware has been carefully designed, characterized and calibrated. Experimental results are presented and discussed: the radiometric sensitivity, the angular resolution and the overall system error evaluation have been measured under controlled situations proving to be in good agreement with theoretical results. The results of a field measurement campaign with artificial and natural scenes are finally presented.

Resumen

La presente tesis es una contribución al estudio de un radiómetro de apertura sintética bidimensional en la banda de microondas, dedicado a la observación de la Tierra con el fin de medir la humedad del suelo y la salinidad del mar. El concepto de apertura sintética utilizado en radioastronomía durante varias décadas se ha revisado en profundidad y se ha extendido a fuentes de ruido térmico extensas, la situción encontrada en teledetección de la Tierra. Las diferencias entre ambos campos es tan básica que se ha requerido de un completo y sistemático análisis de errores, de nuevos algoritmos de calibración y de nuevos algoritmos de inversión capaces de incorporar los errores de los diagramas de las antennas y de tratar con fuentes extensas que, además, sufren los efectos del submuestreo durante la formación de la imagen ("aliasing"). La implementación de un simulador que engloba los estudios precedentes ha permitido analizar las prestaciones globales de un radiómetro interferométrico en forma de Y embarcado en una plataforma espacial, y en especial, la mejora introducida en la precisión radiométrica mediante el promediado de pixel.

Para validar, en la medida de lo posible, los algoritmos de calibración e inversión, se ha diseñado y construido un prototipo de radiómetro interferométrico digital en banda X. Dicho interferómetro está formado por dos antenas que se mueven para sintetizar un conjunto de baselines. El hardware electrónico se ha diseñado, caracterizado y calibrado meticulosamente. Se presentan una serie de resultados experimentales: la sensibilidad radiométrica, la resolución angular y la evaluación del conjunto de errores del sistema han sido medidos bajo condiciones controladas, mostrando una buena concordancia con los resultados teóricos. Finalmente se presentan los resultados de una campaña de medidas de campo con escenas artificiales y naturales.

CONTENTS

INTRODUCTION

PREVIOUS WORKS AND JUSTIFICATION OF THE THESIS

In Earth observation programs there is an increasing interest in the measurement from the space of some geophysical parameters of crucial importance in climate models, i.e. the ocean salinity and the soil moisture. These measurements should preferably be passive and performed at L-band where there is a preserved band for this purpose (1400- 1427 MHz). However, the spatial resolution requirements needed by the scientific community would force to use radiometers with large antennas, about 20 meters of diameter. At present, these large antennas cannot be boarded in a satellite.

In the last years aperture synthesis interferometric radiometry has received a special attention by some spatial agencies as a possible solution to overcome these problems. In the late '80s, the American hybrid prototype ESTAR (Electronically Steered Thinned Array Radiometer) demonstrated the validity of the *1D aperture synthesis - 1D real aperture* principle in remote sensing applications. At present, the European Space Agency is currently studying a two-dimensional aperture synthesis interferometer radiometer called MIRAS, for Microwave Imaging Radiometer by Aperture Synthesis, with MATRA-MARCONI SPACE (MMS) as the main contractor. A bread-board demonstrator is currently under development.

At the beginning of this thesis the available bibliography is reviewed: that concerning to radioastronomy, mainly [Thompson et al. 86] and [NRAO 89], to the one-dimensional interferometric radiometer ESTAR and a critical review of the basic equations of interferometric radiometry performed by Dr. I. Corbella [Bará et al. 94]. In radioastronomy system errors are analyzed in terms of signal-to-noise degradation, while the influence of antenna radiation voltage pattern errors and coupling effects is negligible due to the reduced field of view and the distance between elements. These errors were first found in the ESTAR prototype which were calibrated and corrected via the G-matrix inversion method. However, it is difficult to apply this approach to large two-dimensional interferometers due to the difficulty to measure the elements of the G-matrix, its size and robustness problems that appear during the inversion process. Consequently, there was a need to analyze the error sources of the instrument, to establish a calibration procedure and to devise an inversion algorithm capable to deal with extended thermal sources and with antenna pattern and receiver mismatches.

OBJECTIVES OF THE THESIS

This thesis is a contribution to the analysis of a two-dimensional microwave synthetic aperture radiometer devoted to Earth observation and has been developed during three contracts with the European Space Agency related to interferometric radiometry: "**Feasibility Study of a Dual Interferometric Radiometer**" (ESTEC Purchase Order 132255, May 1994), "**Bi-dimensional Discrete Formulation for Aperture Synthesis Radiometers**" (Contract Change Notice 2 to Work Order No 10 to ESTEC Contract No 9777/92/NL/PB) and **"mm-Wave Wide Band Focused Interferometry"**, (Contract Change Notice 1 to ESTEC Contract No 10590/93/NL/JV)

The main objectives pursued in those contracts were, given the original bread-board design proposed by MMS for MIRAS:
i) Determination of the angular resolution of an interferometric radiometer, taking into account decorrelation effects and system imperfections.

ii) Determination of the radiometric sensitivity of an interferometric radiometer as a function of the visibility function window, the kind of demodulation, the shape of the receivers' frequency response and the kind of correlator used.

iii) Analysis of system errors and evaluation of the radiometric accuracy sensibility to them.

iv) Review of the calibration procedures proposed for MIRAS and proposal of improved calibration methods.

v) Review of the G-matrix inversion method and its applicability to the MIRAS case, and proposal of new effective inversion methods.

Without contractual obligation, the following objectives have also been pursued in this thesis:
vi) The development of a simulator of a space-borne Y-shaped interferometric radiometer to evaluate the overall performance of such an instrument including system errors, calibration procedures, inversion algorithms, and specially the determination of the radiometric sensitivity and the radiometric accuracy improvement by means of pixel averaging, that is, by averaging a set of consecutive measurements in which a pixel is being imaged.

vii) The design and implementation of an experimental X-band digital interferometric radiometer to validate, whenever possible, the preceding studies.

ORGANIZATION OF THE THESIS

This thesis is composed by three parts:

PART I: BASIC RADIOMETRY CONCEPTS

In part I the basic concepts of radiometry and emission theory (chapter 1), and interferometric radiometry (chapter 2) are revised.

PART II: SYSTEM PERFORMANCE, CALIBRATION AND INVERSION METHODS

In part II, the tools for analyzing the basic performance of an interferometric radiometer: the spatial resolution and the radiometric sensitivity, are reviewed and improved to account for system imperfections (chapter three). They are then applied to the Y-shaped array geometry, which will be demonstrated that it is the optimal one from the point of view of minimizing electronic hardware requirements (chapter six). The trade-off between the spatial resolution and the radiometric sensitivity is stated in the *interferometric radiometer incertitude principle,* an original contribution of this thesis.

System imperfections are classified, analyzed and their contribution to the radiometric accuracy and sensitivity budgets are quantified (chapter four). The application to Y-arrays of the redundant space calibration method used in radioastronomy is studied and its limitations to Earth observation are pointed out. A new hardware calibration approach based on noise-injection to small groups of antennas is proposed (chapter five). Visibility inversion methods are developed in chapter six: a new technique to perform Fourier transforms over hexagonal grids with standard rectangular algorithms is proposed. This technique avoids interpolations and preserves signal-to-noise ratio and is the basic step of a new iterative inversion algorithm that is proposed to account for antenna voltage pattern errors and fringe-wash effects. The development of an space-borne interferometric radiometer simulator to study the overall system's performance is explained in chapter seven. The radiometric improvement by means of pixel averaging is numerically evaluated by following pixels' trace during their pass along the FOV. The simulator includes a module for generating realistic brightness temperature scenes from geophysical parameters observed from the satellite's position, which is propagated with an orbit generator module.

PART III: EXPERIMENTAL RESULTS

Chapter eight is devoted to the description, verification tests and calibration of the electronic hardware developed to experimentally check, whenever possible, the former error analysis and to apply the proposed calibration and inversion methods. Experimental verification of the 2D-passive aperture synthesis concept is presented in chapter nine through several examples of artificial and natural synthetic images.

At the end, chapter ten summarizes the main conclusions, the original contributions of the author and the future research lines.

Chapter 1. Review of basic concepts on radiometry and emission theory

This chapter presents the basic concepts of radiometry: the science devoted to the study of the thermal radiation and its measurement. Brightness, emissivity and brightness temperature are defined and studied for different kinds of materials and surfaces. At the end of this chapter, atmospheric, ionospheric and the space radiation impact on the apparent brightness temperature are reviewed.

1.1.- BRIGHTNESS AND THE POWER COLLECTED BY AN ANTENNA

The power emitted by a body in a solid angle by unit surface is called the *brightness,* units [W sr^{-1} m^{-2}]. If the emitting surface radiates with a pattern $F_t(2,N)$, the brightness $B(2,N)$ is given by:

$$B(2,N) = \frac{F_t(2,N)}{A_t} \qquad \textbf{(1.1)}$$

where A_t is the total area which is radiating. According to figure 1.1, the power collected by an antenna surrounded by a distribution of incident power $B(2,N)$ can be computed as [Ulaby et al. 81]:

$$P = F_t \frac{A_r}{R^2} = B A_t \frac{A_r}{R^2} \qquad \textbf{(1.2)}$$

where A_r is the effective area of the antenna and R is the distance to the radiating surface. By taking into account that the solid angle observed by the receiving antenna can be expressed as:

$$S_t = \frac{A_t}{R^2} \qquad \textbf{(1.3)}$$

the power collected by the antenna can be computed as:

$$P = B A_r S_t \qquad \textbf{(1.4)}$$

If the radiating surface is not observed from the maximum of the antenna radiation pattern, it must be included in equation (1.4):

$$dP = A_r B(2,N) * F_n(2,N) *^2 \qquad \textbf{(1.5)}$$

where $|F_n(2,N)|^2$ is the normalized antenna radiation pattern. In addition, if the brightness is not constant with frequency, a new magnitude must be defined: the spectral brightness

density $B_f(2,N)$, units [W sr^{-1} m^{-2} Hz^{-1}]. The total power collected by the antenna is then obtained by integrating expression (1.5) over the system's bandwidth and over the space:

$$P = \frac{1}{2} A_r \int_{f}^{f+B} \int_{4\pi} B_f(2,N) \cdot F_n(2,N)^2 \, d\Omega \, df \qquad \textbf{(1.6)}$$

where non-italic B is the bandwidth of the receiving system and the term ½ takes into account that the antenna collects only half the thermal power emitted which is randomly polarized.

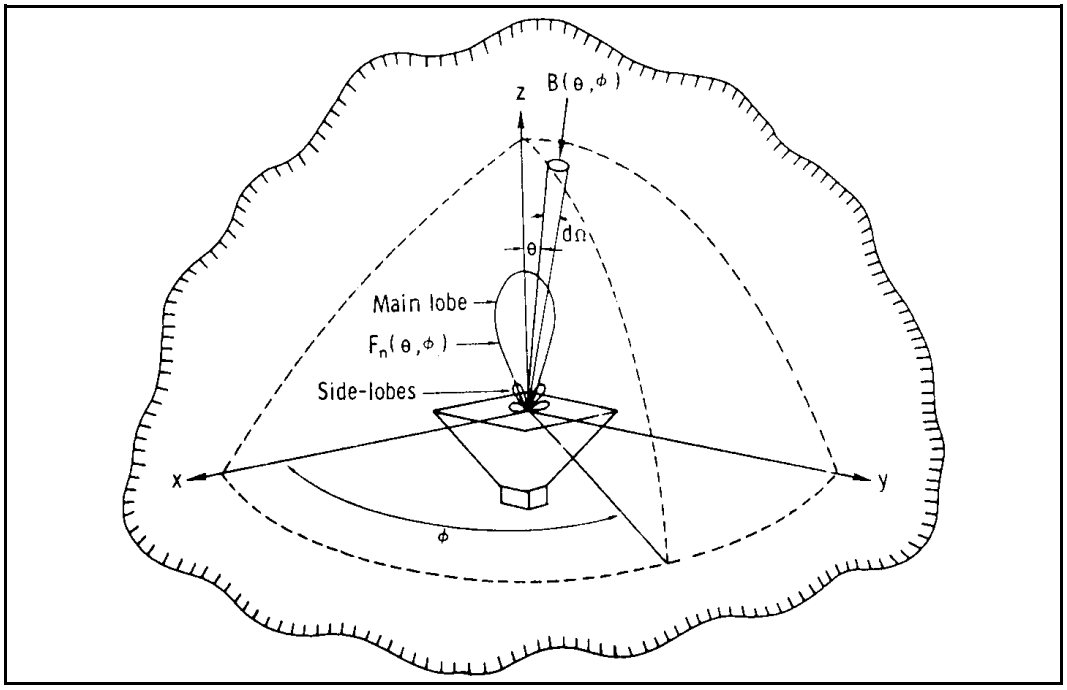

Figure 1.1 .- *Geometry of the radiation incident over the antenna [from Ulaby et al. 81].*

1.2.- THERMAL RADIATION

1.2.1. Planck's blackbody radiation's law

All bodies at a non-zero Kelvin temperature emit electromagnetic radiation. Gases radiate at discrete frequencies. According to quantum theory, each spectral line corresponds to an electron transition from an atomic energy level E_1 to another one E_2. The radiation is produced at a frequency given by Bohr's equation:

$$f = \frac{E_1 - E_2}{h} \qquad \textbf{(1.8)}$$

where h is the Planck's constant, h = 6.63 10^{-34} J.

The atomic emission is originated by a collision with another atom or particle. The probability of emission is greater for larger atomic densities and high kinetic energies. Kirchoff's law states that in thermodynamic equilibria all the absorbed energy is re-radiated. For a perfect absorber body, also called a "black body", the radiated energy follows Plank's law:

$$B_f = \frac{2hf^3}{c^2} \frac{1}{e^{\frac{hf}{k_B T_{ph}}} - 1} \qquad \textbf{(1.9)}$$

where f is the frequency in Hertz, k_B is the Boltzmann's constant $k_B = 1.38\ 10^{-23}$ J K^{-1}, T_{ph} is the absolute temperature in Kelvins and c is the speed of light $c = 3\ 10^8$ m s^{-1}. Natural surfaces absorb a fraction of the incident power, the rest being reflected. A close approximation to the black body are the microwave absorbers used in anechoic chambers. Equation (1.9) depends on the frequency and the absolute temperature. Figure 1.2 shows a set of plots of the spectral brightness density vs. frequency, for different temperatures.

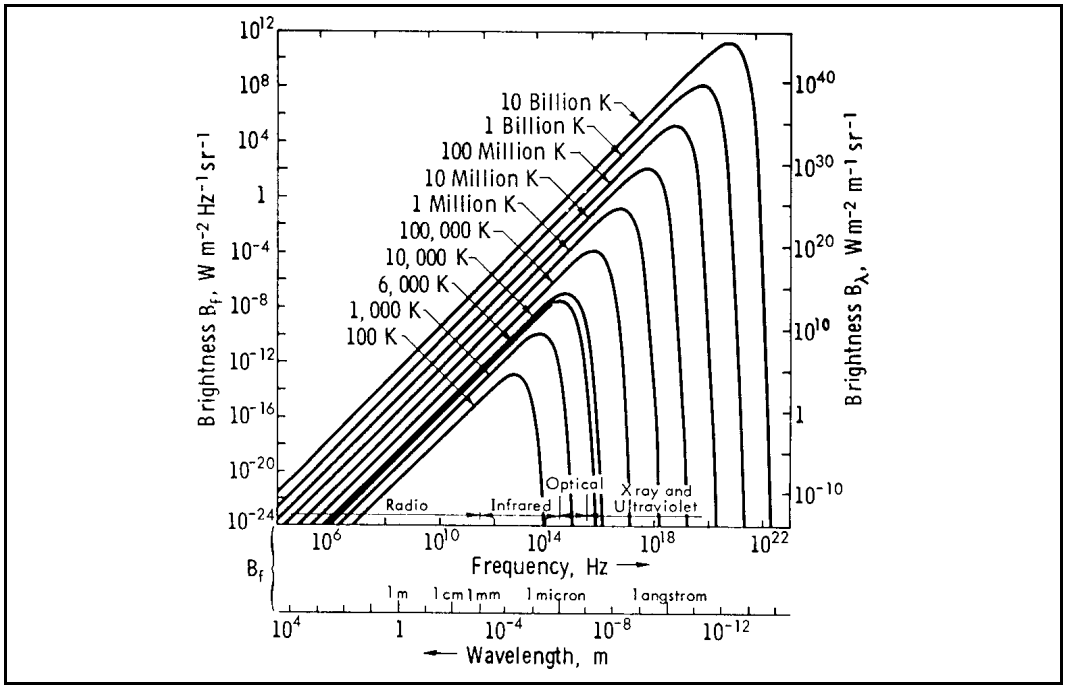

Figure 1.2 .- *Planck's radiation law [from Ulaby et al 81].*

The higher the physical temperature, the higher the brightness and the frequency where the brightness reaches its maximum. The Stefan-Boltzmann law provides an expression for the total brightness and it is obtained by integrating equation (1.9) over all the spectrum:

$$B_{bb} = \int_0^{\infty} B_f \, df = \frac{\sigma T_{ph}^4}{\pi} \qquad \textbf{(1.10)}$$

where σ is the Stefan-Boltzmann constant, $\sigma = 5.673\ 10^{-8}$ [W m^{-2} K^{-4} sr^{-1}] and the subscript *"bb"* stands for the black body radiation.

According to the frequency range two approximations of equation (1.9) can be used. For high frequencies equation (1.9) reduces to Wien's law:

$$B_f = \frac{2h}{c^2} f^3 \, e^{-\frac{hf}{k_B T_{ph}}} \qquad \textbf{(1.11)}$$

Rayleigh-Jeans' law is useful for low frequencies and was obtained by Jeans based in the classic mechanics, prior to Plank's quantum mechanics. Its expression is given by:

$$B_f = \frac{2f^2 k_B T_{ph}}{c^2} = \frac{2k_B T_{ph}}{\lambda^2} \qquad \textbf{(1.12)}$$

Figure 1.3 compares these two approximations with Plank's law. If λ and T satisfy:

$$\lambda T_{ph} > 0.77 \ m\ K \quad or \quad \frac{f}{T_{ph}} < 3.9 10^8 \ Hz\ K^{-1} \qquad \textbf{(1.13)}$$

the error committed by the Rayleigh-Jeans approximation is smaller than 1%, if the physical temperature is 300 K and the frequency is smaller than 117 GHz, which covers a large part of the microwave spectrum. Expression (1.12) will be used from now on. Note that there is linear relation between the spectral brightness density and the physical temperature.

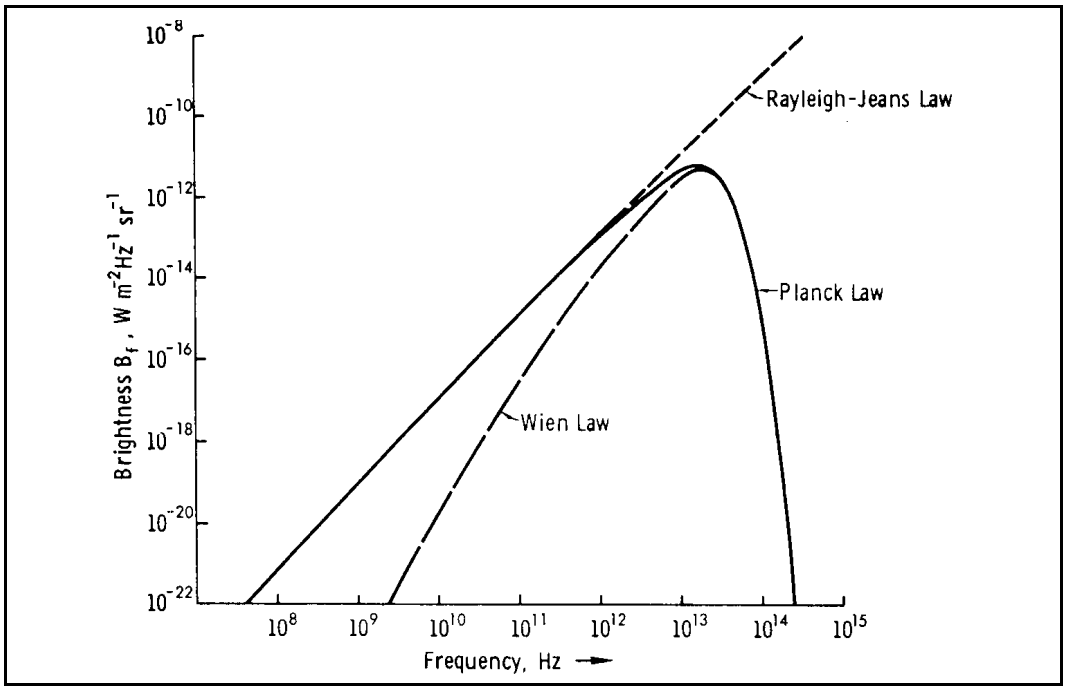

Figure 1.3 .- *Planck's radiation law approximations:*
Rayleigh-Jeans' law (low frequency) and Wien's law (high frequency) [from Ulaby et al 81].

1.2.2.- Relationship between the collected power by an antenna and the temperature

The power collected by a lossless antenna with normalized radiation pattern t(2,N) surrounded by a black body is given by expression (1.6) and the Rayleigh-Jeans' law (1.12):

$$P_{bb} = \frac{1}{2} A_r \int_{f}^{f+B} \int_{4\pi} \frac{2 k_B T_{ph}}{\lambda^2} |F_n(2,N)|^2 \, d\Omega \, df \qquad \textbf{(1.14)}$$

If the bandwidth B is small enough to assume that the spectral brightness density does not change over the frequency range, equation (1.14) reduces to:

$$P_{bb} = k_B T_{ph} B \frac{A_r}{\lambda^2} \int_{4\pi} |F_n(2,N)|^2 \, d\Omega = k_B T_{ph} B \qquad \textbf{(1.15)}$$

where the antenna solid angle has been expressed as a function of its effective area:

$$\Omega_p = \int_{4\pi} |F_n(2,N)|^2 \, d\Omega = \frac{\lambda^2}{A_r} \qquad \textbf{(1.16)}$$

Equation (1.15) establishes a linear relation between physical temperature and the collected power. In 1928, Nyquist found the same expression for the available power at the terminals of a resistance at a physical temperature T_{ph}. This means that for an ideal receiver of bandwidth B, the antenna delivers to the load the same power as a resistance at a temperature T_A: the antenna temperature.

1.2.3.- Gray body radiation

1.2.3.1.- Brightness temperature and emissivity

A blackbody is an idealized body which is a perfect absorber and a perfect radiator. Real bodies, however, radiate less power than the blackbody and do not absorb all the incident power: they are called gray bodies. Figure 1.4 shows a semi-infinite material at a uniform temperature T_{ph}. If the emitted brightness depends on the direction *B(2,N),* a similar equation to that of the black body can be written:

$$B(2,N) = 2\frac{k_B}{8^2} T_B(2,N)B \qquad \textbf{(1.17)}$$

where $I_B(2,N)$ is the equivalent temperature associated to the brightness and it is called the brightness temperature.

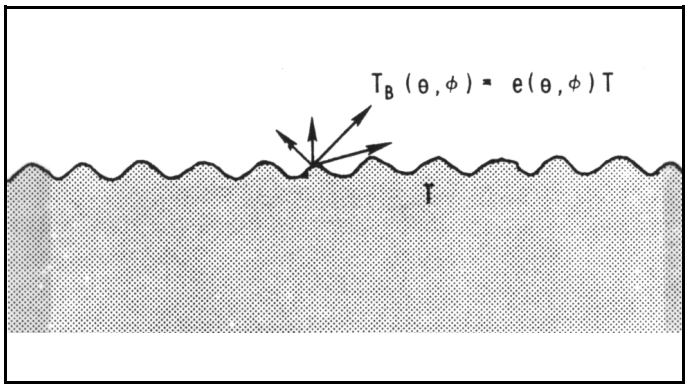

Figure 1.4 .- *Brightness temperature of a semi-infinite medium at a uniform temperature [from Ulaby et al 81].*

Since the brightness temperature of a gray body is smaller than that of a black body, the brightness temperature T_B is smaller than the physical temperature T_{ph}. The parameter relating both magnitudes is called the emissivity *e(2,N)*:

$$e(2,N) = \frac{B(2,N)}{B_{bb}} = \frac{T_B(2,N)}{T_{ph}} \qquad \textbf{(1.18)}$$

Since $B(2,N) \leq B_{bb}$, the emissivity is bounded by $0 \leq e(2, N) \leq 1$. The emissivity is zero for a perfect reflecting material, a lossless metal, and is one for a perfect absorber, the blackbody.

1.2.3.2.- The apparent temperature

The apparent temperature is an equivalent temperature related to the total brightness incident over the antenna, $B_i(2,N)$:

$$B_i(2,N) \; ' \; \frac{2k_B}{8^2} \; T_{AP}(2,N) \; B \qquad \textbf{(1.19)}$$

The apparent temperature depends on several terms related to the different sources radiating over the antenna. Figure 1.5 shows the relationship between them: the radiation emitted by the surface (land or sea) reaches the antenna attenuated by the atmosphere, the radiation emitted downwards by the atmosphere and reflected on the sea/ground in the antenna direction and the upwards radiation emitted by the atmosphere. In the frequency range from 1 GHz to 10 GHz losses for a cloud free atmosphere are very small and can be neglected. Consequently, the apparent brightness temperature T_{AP} can be approximated by the brightness temperature T_B.

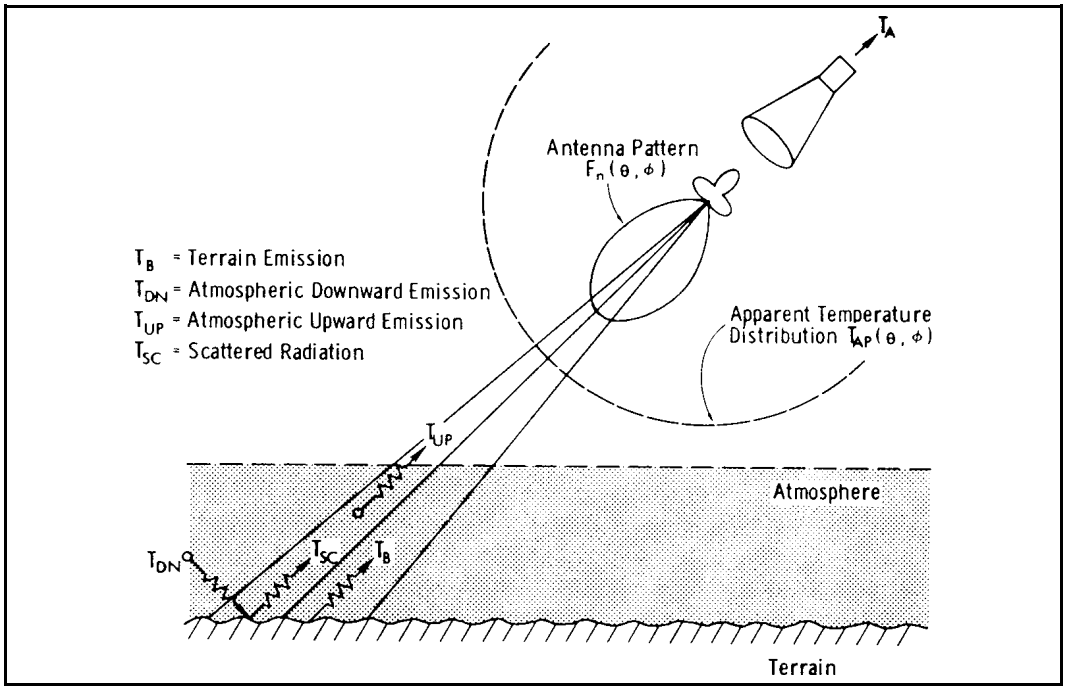

Figure 1.5.- *Relationship between the antenna temperature, the apparent temperature and the brightness temperature [from Ulaby et al 81].*

1.3.- EMISSION THEORY

The reflection of a plane wave over a specular surface produces a plane wave in a single direction as shown in figure 1.6.a. The reflected power P_r is given by:

$$P_r(2_1;p) \; ' \; '(2_1;p)\; P_i(2_1;p) \qquad \textbf{(1.20)}$$

where P_i is the incident power, ' is the specular reflection coefficient and *p* is the polarization: horizontal or vertical. In the case of a specular reflection, by the Kirchhoff 's law, the emissivity can be expressed as a function of the reflection coefficient:

$$e(2_1;p) \; ' \; 1 \; \& \; '(2_1;p) \qquad \textbf{(1.21)}$$

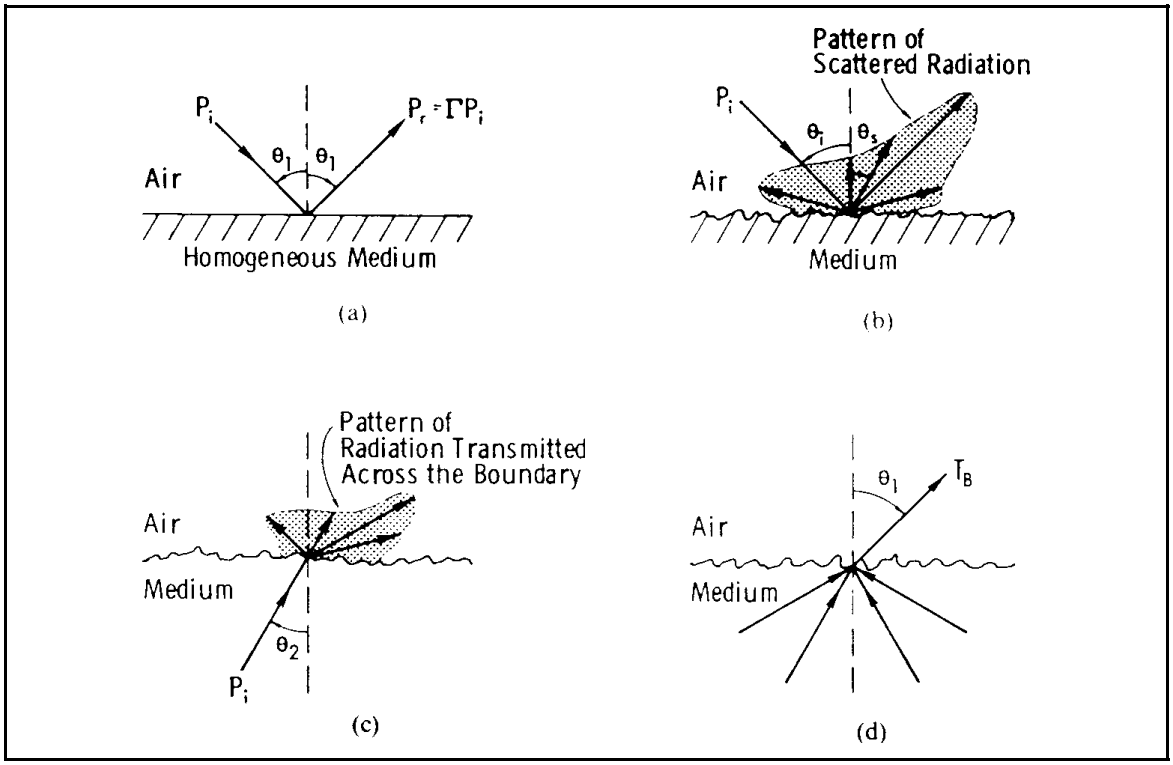

Figure 1.6.- *Specular and rough surface scattering and emission: a) Specular reflection; b) Diffuse scattering; c) Diffuse emission; d) Contributions to $T_B(2)$ come from many directions [from Ulaby et al 81].*

If the reflection is not produced over a plane surface, the incident power will be scattered over the space (figure 1.6.b). Some of the scattered power maintains the phase and is reflected in the specular direction, but the rest of the radiation losses the phase characteristics and it is scattered. In a similar way, the power radiated by the medium to the exterior passes through the surface and it is transmitted over a range of directions (figure 1.6.c). Consequently, T_B (2_1 , p) has contributions coming from several directions of the inner part of the material (figure 1.6.d).

1.3.1.- General expressions for the emissivity

The scattering of a rough surface is characterized by its cross-section by unit area, $F^o(2_o, N_o, 2_s, N_s, p_o, p_s)$. This parameter relates the scattered power in the $(2_s, N_s)$ direction with p_s polarization for an incident plane wave at the $(2_o, N_o)$ direction with polarization p_o. If p_o and p_s are the same, F^o is called the horizontal or vertical scattering coefficient. If p_o and p_s are different, F^o is called the cross-polar scattering coefficient. By applying the Kirchhoff law to the rough surface case, Peake developed in 1959 the expressions for the horizontal and vertical emissivities and reflected temperature T_{SC} $(2_o, N_o, p_o)$ [Peake 59]:

$$e(2_o,N_o;p_o) = 1-\frac{1}{4B\cos 2_o}\int[F^o(2_o,N_o;2_s,N_s;p_o,p_o)+F^0(2_o,N_o;2_s,N_s;p_o,p_s)]dS_s \qquad \textbf{(1.22)}$$

$$T_{SC}(2_o,N_o;p_o) = \frac{1}{4B\cos 2_o}\int[F^o(2_o,N_o;2_s,N_s;p_o,p_o)+F^o(2_o,N_o;2_s,N_s;p_o,p_s)]T_{DN}(2_s,N_s)dS_s \qquad \textbf{(1.23)}$$

1.3.2.- Simple models for the emissivity

Expressions (1.22) and (1.23) can by simplified in two cases of interest: a specular surface and a completely rough surface.

1.3.2.1.- Emission from a specular surface

The scattering produced at a specular surface consists on the coherent reflection of the incident wave. Consequently, the cross-polar scattering coefficient is zero, and the horizontal or vertical polarization scattering coefficients are delta functions:

$$F^o(2_o,N_o;2_s,N_s;p_o,p_o) = 4B\,\Gamma(2_o;p_o)\,\frac{\cos 2_o}{\sin 2_{sp}}\,\delta(2_s-2_{sp})\,\delta(N_s-N_{sp}) \qquad \textbf{(1.24)}$$

where $(2_{sp}, N_{sp})$ is the specular direction:

$$2_{sp} = 2_o \quad and \quad N_{sp} = B+N_o \qquad \textbf{(1.25)}$$

Substituting equations (1.24) and (1.25) in (1.22) and (1.23), the following expressions are obtained:

$$e(2_o,N_o;p_o) = 1 - \Gamma(2_o;p_o) \qquad \textbf{(1.26)}$$

$$T_{SC}(2_o,N_o;p_o) = \Gamma(2_o;p_o)\,T_{DN}(2_o) \qquad \textbf{(1.27)}$$

which are equivalent to (1.20) and (1.21).

1.3.2.2.- Emission from a perfectly rough surface

On the other hand, the scattering coefficient for a perfectly rough surface, also called a *Lambertian surface*, depends only on the product cos θ_o cos θ_s:

$$\gamma^o(\theta_o,N_o;\theta_s,N_s;p_o,p_o) = \gamma^o(\theta_o,N_o;\theta_s,N_s;p_o,p_s) = \gamma^o_o \cos\theta_o\cos\theta_s \qquad \textbf{(1.28)}$$

where γ^o_o is a constant related to the dielectric properties of the scattering surface. The emissivity is obtained by substituting expression (1.28) in (1.22) and (1.23):

$$e(\theta_o,N_o;p) = 1-\frac{1}{4B\cos\theta_o}\int_{N_s=0}^{2B}\int_{\theta_s=0}^{B/2}\gamma^o_o\cos\theta_o\cos\theta_s\sin\theta_s\,d\theta_s dN_s = 1-\frac{\gamma^o_o}{4} \qquad \textbf{(1.29)}$$

which is independent on the polarization and the incident angle.

Sections 1.3.2.1 and 1.3.2.2 have presented the emissivity of two extreme and idealized cases. Natural surfaces do not have neither specular nor Lambertian characteristics. They exhibit a mixed behavior depending on its dielectric properties and the surface roughness compared to the wavelength. Their properties are briefly reviewed in the next section.

1.3.3.- Sea and terrain emissivity properties

Since the purpose of low-frequency interferometric radiometers is the periodic global monitoring of the sea salinity and the soil moisture, in the next paragraphs special attention is paid to the dependence of the emissivity on these parameters and others, such as the wind over the sea or the vegetation cover that may mask the measurements.

1.3.3.1.- Sea emissivity

The penetration depth of electromagnetic waves in sea water is small, 1 cm at 1.4GHz, and, consequently, in depth salinity variations will not be measurable. Sea surface salinity monitoring by radiometric measurements requires low frequencies.

For quiet waters, the brightness temperature of the sea is given by equation (1.26):

$$T_B(\theta;p) = [1-\rho^{SP}(\theta;p)]\,T_o \qquad \textbf{(1.30)}$$

where θ is the incident angle, T_o is sea water physical temperature and $\rho^{sp}(\theta,p)$ is the specular reflectivity of the sea, which depends on the incidence angle θ, the polarization and the relative permitivity of saline water ε_a, which depends at its turn on the frequency, the physical temperature and the salinity S. The measurement of sea salinity to within 1‰ accuracy requires a high radiometric sensitivity, which is specially critical at low temperatures.

In addition, the emissivity is modified by surface roughness, which is mainly governed by wind which induces waves, ripples and foam over the sea surface. To compute the expected emissivity at a given direction, equation (1.22) must be evaluated after the computation of the scattering coefficients for a specified wind velocity and direction [Stogryn 67] [Fung 94]. At 1.4 GHz, the vertical polarization brightness temperature responses ( ) T_{BV}) to salinity changes ( ) S), sea surface temperature changes ( ) SST) and wind speed changes are approximately [Skou 89]:

$$\begin{aligned} &\frac{) T_{BV}}{) S} \;.\; 0.5\, K/{}^{o}\!/_{oo} \\ &\frac{) T_{BV}}{) SST} \;.\; 0.5\, K/{}^{o}C \\ &\frac{) T_{BV}}{) WS} \;.\; 0.4\, K/\ m/s \end{aligned} \qquad \textbf{(1.31)}$$

Salinity measurements require corrections for wind and sea temperature. The horizontally polarized brightness temperature sensitivity is smaller to sea surface temperature and greater to wind speed. To obtain the sea surface temperature and wind speed information the next protected band, 2.7 GHz, can be used. At this band Faraday rotation effects are negligible and the vertical sensitivity to sea salinity is much more reduced and is very independent on wind speed while the response to sea surface temperature is good ( ) T_{BV}/) SST = 0.6 K/ºC). The horizontal polarization response to salinity and temperature is lower, but the response to wind speed is rather large ( ) T_{BH}/) WS = 1.4 K/ m/s). To achieve a 0.25 K radiometric sensitivity, the sea surface temperature must be known within 0.5 ºC and the wind speed within 0.5 m/s [Skou 95].

Sea salinity has small spatial variations, which allows to average measurements over large areas to improve the instrument's radiometric sensitivity at the expense of spatial resolution. This solution does not satisfy the spatial resolution required for river mouths monitoring. However, in this particular situation, buoys can be placed or airborne campaigns can be carried out.

1.3.3.2.- Terrain emissivity and soil moisture dependence

Soil moisture global monitoring is another parameter needed in present climate models. In the following paragraphs simple models showing the relations between soil moisture, soil composition and roughness will be reviewed. The effect of the vegetation cover will be included at the end.

Experimental observations in the microwave spectrum have shown that the brightness temperature for a vegetation free terrain decreases linearly with the soil moisture contents, so frequency must be as low as possible to avoid vegetation and roughness effects [Ulaby et al. 81]. At 1.4 GHz the majority of the brightness power is emitted from the 2-5 cm soil layer on beneath the surface. On the other hand, since the physical temperature of this layer is not easily measured by remote sensing, it must be taken from climatological models or its dependence eliminated by using a dual polarization instrument and taking the ratio between the horizontal and the vertical brightness temperatures [Skou 89].

The slope of the line:

$$S_s = \frac{\delta e_s}{\delta m_v}, \tag{1.32}$$

is called the radiometric sensitivity to soil moisture and decreases with increasing frequency and soil roughness. The sensitivity to soil moisture also changes with soil texture. Schmugge in 1980 noted that the brightness temperature T_{Bs} is more sensitive to the gravimetric soil moisture, m_g, in light soils small clay content.

Vegetation cover attenuates soil emission and emits by itself. If the spacing between leaves, branches... is comparable to the wavelength in the vertical and horizontal directions, the vegetation cover can be assumed to be homogeneous and its effects can be modelled as shown in equation (1.33):

$$T_{B,veg} = \left(1 + \frac{\Gamma_s}{L}\right)\left(1 - \frac{1}{L}\right)(1-a)\,T_v + \frac{1-\Gamma_s}{L}\,T_s \tag{1.33}$$

where *a* is the albedo, the relation between the scattered and the incident power, and T_v and T_s are the physical temperatures of the vegetation cover and the terrain. The 1/L term accounts for the attenuation in the vegetation cover and can be computed as:

$$\frac{1}{L} = e^{-K_e h_v \sec\theta} \tag{1.34}$$

where K_e is the extinction coefficient of the vegetation cover, h_v is its height and θ is the refraction angle in the vegetation medium. This model can be applied if the albedo is smaller than 0.2, scattering inside the vegetation cover is negligible, the reflectivity of the air-vegetation union is negligible and the refraction index of the vegetation is similar to that of the air. The dispersive characteristics of the vegetation depend on its structure, leaves, branches... and are very difficult to be modelled. Typically, the emissivity ranges from 0.36 for humid soils to 0.99 to dry soils, and the brightness temperature from 105 K to 270 K. These large variations allow to recover easily the soil moisture content from radiometric measurements, with a modest 1 K radiometric resolution.

1.4.- THE APPARENT BRIGHTNESS TEMPERATURE FROM SPACE

In a remote sensing mission, in addition to instrumental errors, other phenomena can degrade the radiometric resolution and must be accounted to calibrate them. These phenomena are the Faraday rotation, atmospheric perturbations and cosmic radiation.

1.4.1. Faraday rotation

At microwave frequencies ionosphere effects are negligible. However, in the low range, at 1.4 GHz, its effects must be accounted for. The plane of polarization of the electromagnetic fields propagating from the Earth's surface to the satellite antenna suffers a rotation while passing the ionosphere. The angle of rotation can be computed from [Skou 89]:

$$\Omega \propto \frac{17}{f^2_{[GHz]}} \qquad \textbf{(1.35)}$$

At 1.4 GHz the average rotation angle is $\Omega = 8.7^{o}$. During the day, the maximum angle can be as high as 28º, while during the night decreases down to the 10%. Day to day variations within +100% and -50% of the mean values can be expected. The apparent brightness temperatures measured by the radiometer T'_{BH} and T'_{BV} are mixed values of the true ones T_{BH} and T_{BV} [Skou 89]:

$$\begin{aligned} T'_{BV} &= \sqrt{T^2_{BV}\cos^2\Omega + T^2_{BH}\sin^2\Omega} \\ T'_{BH} &= \sqrt{T^2_{BV}\sin^2\Omega + T^2_{BH}\cos^2\Omega} \end{aligned} \qquad \textbf{(1.36)}$$

Typical T_{BV}=135 K and T_{BH}=70 K values, with a Faraday rotation of 10º lead to T'_{BV}=133.5 K and T'_{BH}=72.8 K. The 1.5 K error in T_{BV} induces an error in the sea salinity of 3‰, which is an unacceptable figure. The system of equations (1.36) can be solved with respect to T_{BV} allowing to solve for it provided the Faraday rotation angle is known. In fact, the polarization angle can be obtained from:

$$\sin^2\Omega = \frac{R^2-(R')^2}{(R^2-1)((R')^2-1)} \qquad \textbf{(1.37)}$$

where R and R' are the true and the measured polarization coefficients, defined as:

$$R = \frac{T_{BV}}{T_{BH}} \qquad R' = \frac{T'_{BV}}{T'_{BH}} \qquad \textbf{(1.38)}$$

According to studies performed by the Technical University of Denmark, the true polarization coefficient of the sea has a marginal dependence on sea salinity and sea temperature, being mainly governed by wind speed. When the wind speed has been measured by a 2.7 GHz channel, the true polarization ratio can be precisely estimated (equation 1.38), the angle θ computed (equation 1.37) and the Faraday rotation effect corrected (equation 1.36).

1.4.2.- Space radiation

Microwave radiation emitted from the space reflects over the sea/soil surface and is collected by the main beam of the antenna. **Cosmic radiation** level is constant, about 2.7 K, and does not affect the quality of the measurement. However, **galactic noise** presents large variations, from 0.8 K to 16 K at 1.4 GHz, depending if the pole or the center of the galaxy is reflected over the Earth's surface. This effect must be avoided by selecting an orbit so that the reflected antenna beam does not intercept the galaxy center. If not, a correction can be performed on measured data since galactic noise is well mapped. **Sun glitter** can affect seriously the measurements, since its high brightness temperature, about 10000 K or more, can be reflected over the sea surface and collected by the antenna. Direct reflections must be avoided, for example by choosing a morning sun-synchronous orbit.

1.4.3.- Atmospheric perturbations

The absorption produced by the atmospheric water vapor is usually of great importance. However, at 1.4 GHz its contribution is negligible. Oxygen absorption is also important, but in the frequency range from 1 GHz to 10 GHz, the zenith brightness temperature due to oxygen has a constant value of about 2 K that can be easily corrected.

1.5.- CONCLUSIONS

At this point, keeping in mind the main conclusions of each section, it is interesting to reproduce some of the SMOS conclusions (Consultative Meeting on Soil Moisture and Ocean Salinity Measurement Requirements and Radiometer Techniques, April 21-22, 1995, ESA-ESTEC, Noordwijk, The Netherlands):

"1.- Mission Objectives.
Soil Moisture and ocean salinity are important parameters for modeling the hydrological cycle in global climate models. They can be measured from space on a global scale using passive microwave radiometry at 1.4 GHz. No practical alternatives for the measurement of these parameters exists.

2.- Instrument Requirements.
A single frequency (1.4 GHz), dual polarization (H and V) instrument in a sun-synchronous dawn-dusk orbit giving 0.5 K radiometric resolution, 1 K radiometric accuracy, 10 Km spatial resolution and 1-3 days revisit time would satisfy most user requirements.

3.- Instrument Technology.
Aperture Synthesis is the preferred option over push-broom and scanning techniques. In-orbit calibration methods need to be developed."

In the next chapters, the basic principles of Aperture Synthesis Radiometry are reviewed and the basic performance of an Interferometric Radiometer in terms of the spatial resolution and the radiometric resolution and sensitivity are computed. Instrumental errors, calibration procedures and inversion algorithms are then studied. Finally these studies are corroborated by the development of an experimental Aperture Synthesis Interferometric Radiometer and the field measurements campaign performed.

Chapter 2. Introduction to Interferometric Radiometry

A passive radiometer is an instrument that measures the spontaneous electromagnetic emission. This radiation is normally associated to a thermal effect: the brightness temperature. As it was shown in chapter one, due to atmospheric effects and reflection from external sources, i.e. the sun, the measured incident power, although being related to the physical temperature, it is different and it is called the "apparent brightness temperature". The spatial resolution achievable by a radiometer is limited by its antenna size. Total power radiometers have large antennas with a narrow beam which is scanned along the field of view. However, the measurement of some physical parameters such as the soil moisture or the sea surface salinity require passive measurements at low frequencies with high spatial resolution (10-20 Km) requiring large antennas, about 20 m of diameter, at present technologically unfeasible. For this reason, bi-dimensional interferometric radiometry is configuring as a preferred option over total power radiometry in view of its lighter structure, although at the cost of more complex electronic hardware, data processing and calibration procedures. This chapter is devoted to review the principles of interferometric radiometry. The relationships between the measurements, also called "visibilities", the antenna positions and their radiation voltage patterns, as well as the receiver's frequency responses are shown. These relations are used in the following chapters when studying instrument errors, calibration procedures and inversion algorithms. Classical total power radiometers will be treated as a particular case of interferometric radiometers.

2.1.- RADIATION PRODUCED BY THE EARTH

From a radiometer point of view, the Earth is an extended source of electromagnetic random emission, having equal probability for horizontal and vertical polarization. Since the antennas are sensitive only to one polarization, this electromagnetic wave can be considered as polarized. As discussed in [Goodman 68] and [Goodman 85] it can be accurately modelled by a *scalar* field $b(x,y,z,t)$ satisfying, thus, the scalar wave equation:

$$\nabla^2 b - \frac{1}{c^2}\frac{\partial^2 b}{\partial t^2} = 0 \qquad \textbf{(2.1)}$$

where c is the velocity of propagation of light $3\ 10^8$ m/s and ∇ the Laplacian operator.

The time and space dependent function $b(x,y,z,t)$ may be viewed as the value of the component of the electric field parallel to the antenna polarization direction. For a given point in space, it is a stationary, ergodic, zero-mean and Gaussian random process. It also

may be described in the frequency domain as β (x,y,z,f) with the aid of the Fourier Transform:

$$\beta(x,y,z,f) = \mathcal{F}\left[b(x,y,z,t)\right] = \int_{-\infty}^{\infty} b(x,y,z,t)\, e^{-j2\pi ft} dt$$
$$b(x,y,z,t) = \mathcal{F}^{-1}\left[\beta(x,y,z,f)\right] = \int_{-\infty}^{\infty} \beta(x,y,z,f) e^{j2\pi ft} dt \qquad \textbf{(2.2)}$$

By introducing (2.2) in (2.1), the frequency domain wave equation is obtained:

$$\nabla^2\beta(x,y,z,f) + k^2\ \beta(x,y,z,f) = 0 \qquad \textbf{(2.3)}$$

being k the wave number k = ω /c and $\omega = 2\pi f$ the angular frequency.

2.2.- PRINCIPLE OF OPERATION OF AN INTERFEROMETER

2.2.1.- Stochastic point source: decorrelation effects

Consider a point source located at given coordinates (X_0,Y_0,Z_0) radiating a random scalar field *b*(x,y,z,t) as shown in figures 2.1 and 2.2.

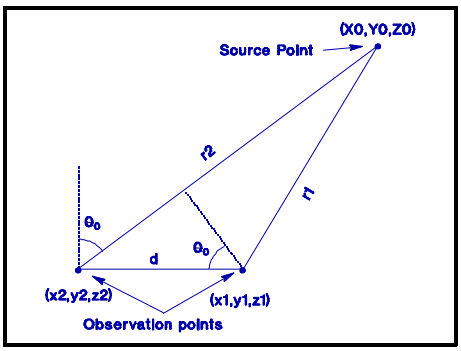

Figure 2.1.- *A point source and two observation points*

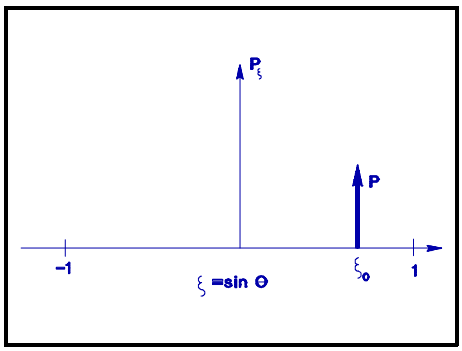

Figure 2.2.- *Angular power distribution of a point source*

If the signal in point (x_1,y_1,z_1) is $b_1(t) = b(x_1,y_1,z_1,t)$, assuming that the process is stationary and ergodic, its mean power (power density of the electromagnetic wave) is:

$$P_1 = \lim_{T\to\infty} \frac{1}{T} \int_{-T/2}^{T/2} [b_1(t)]^2 dt = R_{b_1}(0) \qquad \textbf{(2.4)}$$

$R_{b1}(\tau)$ is the self-correlation function of the real process $b_1(t)$. Using the properties of the analytic signal, this power can be expressed as:

$$P_1 = \frac{1}{2}R_{b_1}(0) = \frac{1}{2}E\left[b_1 b_1^{*}\right] = \frac{1}{2}\lim_{T\to\infty}\int_{-T/2}^{T/2}\frac{1}{T}b_1^{2}dt \qquad \textbf{(2.5)}$$

where R_{b1} (non-italic b) is the self-correlation function of $b_1(t)$, the analytic signal of $b_1(t)$. In optics the intensity of the source is defined directly as $R_b(0)$, which is twice the mean power of the real signal.

The function $b(x,y,z,t)$ is expressed in the frequency domain as $\Psi(x,y,z,f)$ (equation (2.2)). Solving (2.3) for a point source, the signal at point (x_1,y_1,z_1) is expressed as:

$$\Psi(x_1,y_1,z_1,f) = \frac{A(f)}{r_1}e^{-jkr_1} \qquad \textbf{(2.6)}$$

where $A(f)$ is now a complex function of frequency and $k = 2\pi f/c$. Alternatively, in the time domain one has:

$$b_1(t) = b(x_1,y_1,z_1,t) = \int_{-\infty}^{\infty}\frac{A(f)}{r_1}e^{-j\frac{2\pi f}{c}r_1}e^{j2\pi ft}df = \frac{a\left(t-\frac{r_1}{c}\right)}{r_1} \qquad \textbf{(2.7)}$$

where $a(t)$ is the inverse Fourier transform of $A(f)$. The analytic signal of $b_1(t)$ is obtained easily from the analytic signal of $a(t)$:

$$b_1(t) = \frac{a\left(t-\frac{r_1}{c}\right)}{r_1} \qquad \textbf{(2.8)}$$

From (2.5) the mean power density of the wave at the observation point can be obtained:

$$P_1 = \frac{1}{2}\frac{R_a(0)}{r_1^2} \qquad \textbf{(2.9)}$$

where R_a is the self-correlation function of the analytic signal of $a(t)$, that is $a(t)$. The term $\frac{1}{2}R_a(0)$ is defined as the radiation intensity of the source, and will be denoted by P_a:

$$P_a \equiv \frac{1}{2}R_a(0) \qquad \textbf{(2.10)}$$

Let's now consider two points (x_1,y_1,z_1) and (x_2,y_2,z_2), as in figure 2.1, in which the sources produce signals with associated analytic signals $b_1(t)$ and $b_2(t)$ respectively. The visibility function is defined as:

$$V = \frac{1}{2}E\left[b_1(t)b_2^{*}(t)\right] = \frac{1}{2}R_{b_1b_2}(0) \qquad \textbf{(2.11)}$$

Using now the expression (2.8) for $b_1(t)$ and a similar one for $b_2(t)$, it can be concluded that :

$$V = \frac{1}{2}\frac{1}{r_1 r_2} E\left[a\left(t-\frac{r_1}{c}\right) a^{*}\left(t-\frac{r_2}{c}\right)\right] = \frac{1}{2}\frac{1}{r_1 r_2} R_a\left(\frac{\Delta r}{c}\right) \qquad \textbf{(2.12)}$$

being $\Delta r = r_2 - r_1$. It can be expressed in terms of the self-correlation function of the complex envelope of $a(t)$ yielding [Goodman 85]:

$$V(\Delta r) = \frac{1}{r_1 r_2}\tilde{R}_A\left(\frac{\Delta r}{c}\right) e^{j\omega_0\frac{\Delta r}{c}} = \frac{1}{r_1 r_2}\tilde{R}_A\left(\frac{\Delta r}{c}\right) e^{jk_0\Delta r} \qquad \textbf{(2.13)}$$

where $\tilde{R}_A(\omega)$ is the self-correlation function of the complex envelope of $a(t)$, $k_0=\omega_0/c$ and ω_0 is an arbitrary frequency, which, for narrow band signals is usually chosen as the mid-band frequency. The function $\tilde{R}_A(\omega)$ is the inverse Fourier transform of the power spectral density of the complex envelope, which, in turn, is proportional to the power spectral density of the real signal shifted to DC:

$$R_A(\tau) = \Im^{-1}\left[S_A(f)\right] = 4\,\Im^{-1}\left[S_a(f-f_o)\,u(f-f_o)\right] \qquad \textbf{(2.14)}$$

where $S_a(f)$ is the power spectral density of the process $a(t)$ and $u(f)$ is the unit step function:

$$u(f) = \begin{matrix} 1 & f>0 \\ 0 & f<0 \end{matrix} \qquad \textbf{(2.15)}$$

Alternatively, expressing equation (2.13) as a function of the complex degree of coherence of the analytic signal and the complex envelope:

$$V(\Delta r) = \frac{1}{r_1 r_2} P_a\, r_a\left(\frac{\Delta r}{c}\right) = \frac{1}{r_1 r_2} P_a\, \tilde{r}_A\left(\frac{\Delta r}{c}\right)\, e^{jk_0\Delta r} \qquad \textbf{(2.16)}$$

The term $\tilde{r}_A\left(\frac{\Delta r}{c}\right)$ is often called the "fringe-washing function" in interferometry textbooks. Note that if the signal's bandwidth is reduced to zero, the stochastic noise source becomes a sinusoidal source, the amplitude of the fringe-washing function is constant and the visibility function depends only on the pathlength difference Δr:

$$V(\Delta r) = \frac{1}{r_1 r_2} P_a e^{jk_0\Delta r} \qquad \textbf{(2.17)}$$

For the observation point located at $(x_1,y_1,0)$, the distance to the source can be written as:

$$r_1 = \sqrt{(X_0-x_1)^2+(Y_0-y_1)^2+Z_0^2} = \sqrt{R_0^2+d_1^2-2(X_0\,x_1+Y_0\,y_1)} \qquad \textbf{(2.18)}$$

where R_0 and d_1 are respectively the distances of the source and the observation points to an arbitrary origin of coordinates. If we locate this origin of coordinates close to the observation point then R_0 is much greater than the two other terms in and a linear Taylor

approximation may be done, yielding:

$$r_1 \approx R_0 + \frac{d_1^2 - 2(X_0 x_1 + Y_0 y_1)}{2 R_0} = R_0 + \frac{d_1^2}{2 R_0} - x_0 x_1 - h_0 y_1 \qquad \textbf{(2.19)}$$

where:

$$x_0 = \frac{X_0}{R_0} \quad h_0 = \frac{Y_0}{R_0} \qquad \textbf{(2.20)}$$

Using the same equations for r_2 the path difference Δr can be computed as:

$$\Delta r = r_2 - r_1 = \frac{d_2^2 - d_1^2}{2 R_0} - \left[(x_2 - x_1) x_0 + (y_2 - y_1) h_0 \right] \qquad \textbf{(2.21)}$$

Approximating $r_1 r_2 \approx r^2$ and defining $P = P_a / r^2$, equation (2.17) simplifies to:

$$V(u,v) = P\, e^{j\Psi}\, e^{-j\,2p\,[x_0\,u + h_0\,v]} \qquad \textbf{(2.22)}$$

where the phase factor Ψ is given by:

$$\Psi = \frac{p}{l\,R_0}(d_2^2 - d_1^2) \approx 0 \qquad \textbf{(2.23)}$$

and the variables u, v are called the baseline and are defined as the projections over the (x,y) axes of the distance between the antennas normalized to the wavelength:

$$u = \frac{x_2 - x_1}{l} = \frac{D_x}{l}\,; \quad v = \frac{y_2 - y_1}{l} = \frac{D_y}{l} \qquad \textbf{(2.24)}$$

That is, without decorrelation effects equation (2.22) is the Fourier Transform between the apparent brightness temperature distribution and the visibility function:

$$V(u,v) = \mathcal{F}[P\,\delta(\xi - \xi_0, \eta - \eta_0)] \qquad \textbf{(2.25)}$$

Analysis of a non-sinusoidal signal has a non-desired effect in the amplitude of the visibility function. An example will clarify the ideas. Suppose that *a*(t) is a bandlimited point thermal source located at the (ξ_0,η_0) direction. It has a power spectrum centered on a frequency f_0 and constant for a frequency interval lying inside a bandwidth B and zero outside. Then it is easily found that:

$$S_A(f) = 2\,k_B\,T\,\Pi\left(\frac{f - f_0}{B}\right) <> \tilde{R}_A(t) = 2\,k_B\,T\,B\,\mathrm{sinc}(B\,t) \qquad \textbf{(2.26)}$$

being k_B the Boltzmann constant and T the apparent brightness temperature. From (2.13) and (2.21) the visibility function becomes:

$$V(\Delta r) = \frac{k_B T}{r_1 r_2} B\,\mathrm{sinc}\left(B\,\frac{\Delta r}{c}\right) e^{jk_0 \Delta r} = \frac{k_B T}{r_1 r_2} B\,\mathrm{sinc}\left(\frac{u x_0 + v h_0}{W^{-1}}\right) e^{-j\,2p\,[u x_0 + v h_0]} \qquad \textbf{(2.27)}$$

if $\Delta r/c$ is much less that 1/B, the "sinc" function is approximately unity and the result is the

same as for a sinusoidal function. If not, the amplitude of the visibility function decreases and vanishes for $\Delta r = c/B$. The time 1/B is called the *coherence time* of the signal, and this time multiplied by c is the *coherence length.* So for an interferometer to perform well, it must satisfy:

$$\Delta r \gg coherence\ length = \frac{c}{B} \qquad \textbf{(2.28)}$$

For a radioastronomy interferometer this effect supposes no limitation since a time delay is added to the receivers so as to have an effective Δr close to 0. This can be done only if the approximate location of a quasi point source is known a priori. For a wide field of view radiometer this is not possible in general, since the source is extended. This is the main difference between radiometry and other applications of interferometry.

The computed angular power distribution of the source is the inverse Fourier transform of the visibility function in the variables (u,v) < > (ξ,η):

$$\hat{T}(x,h) = \frac{k_B T_0 B}{r^2} \int_{-\infty}^{+\infty}\int_{-\infty}^{+\infty} sinc\left(\frac{u x_0 + v h_0}{W^{-1}}\right) e^{j 2p [u(x-x_0)+v(h-h_0)]}\, du\, dv \qquad \textbf{(2.29)}$$

Equation (2.29) can be integrated by making the change of variables:

$$x = \frac{u x_0 + v h_0}{f_0}$$

$$y = \frac{u x_0 - v h_0}{f_0} \qquad \textbf{(2.30)}$$

leading to:

$$\hat{T}(x,h) = \frac{k_B T_0 f_0^{\,2}}{2 x_0 h_0} \Pi\left[\frac{\frac{x-x_0}{x_0} + \frac{h-h_0}{h_0}}{2B/f_0}\right] d\left[\frac{f_o}{2}\left(\frac{x-x_0}{x_0} - \frac{h-h_0}{h_0}\right)\right] =$$

$$= k_B T_0 \ f_0 \Pi\left[\frac{\frac{x-x_0}{x_0} + \frac{h-h_0}{h_0}}{2W}\right] d\left(x_0 h - h_0 x\right) \qquad \textbf{(2.31)}$$

Note that the amplitude of the recovered brightness temperature of the point source decreases when it is located out of boresight $(\xi,\eta) = (0,0)$. Note also that the recovered brightness temperature distribution suffers from a radial broadening along the line $\eta=\eta_0/\xi_0\xi$, that is, the original point source located at (ξ_0,η_0) appears as a segment $W z_0 = W\sqrt{x_o^2 + h_0^2}$ long as it is shown in figure 2.3.

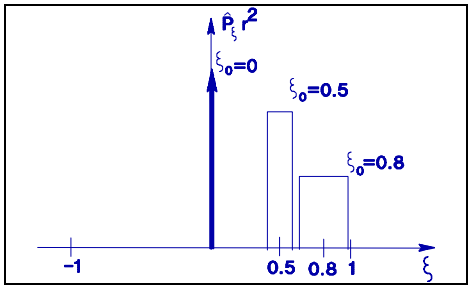

Figure 2.3.- *Angular Power Distribution for a point source with apparent temperature T_0 at z_0=0, 0.5 and 0.8.*

Spatial decorrelation degrades spatial resolution out of boresight and is studied in detail in chapter three.

2.2.2.- Extended stochastic source. The Van Cittert-Zernike Theorem

As stated in the introduction, the Earth must be modelled as an extended source of thermal radiation. In this section previous results are extended by assuming this type of source. Following the same procedure, the wave equation must be first solved in the frequency domain (2.3) and then the analytic signal of the field at two given observation points $(x_1,y_1,0)$ and $(x_2,y_2,0)$ are computed yielding to $b_1(t)$ and $b_2(t)$. The visibility function is then defined as the mean cross-power of these two signals, or their cross-correlation function at the origin ($\tau = 0$), as in equation (2.16). This function depends on the distance between the antennas normalized to the wavelength (u,v)), and the angular power distribution is then computed by a Fourier transform in the plane (u,v) < > (ξ, η).

The solution of (2.3) for an extended source follows from the Huygens-Fresnel principle and can be found for example in [Goodman 68]. Using the same notation as in the previous sections it can be expressed as:

$$b\ (x_1, y_1, 0, f\ ) = -\frac{1}{jl} \iint_{source} A(\ x, y, z, f\ ) \frac{e^{-jkr_1}}{r_1} \cos q_1\ dS \qquad \textbf{(2.32)}$$

where the integral is extended over the source surface, A(x,y,z,f) is the frequency domain value of the field at the source, and the geometric terms are defined in figure 2.4. Equation (2.32) is only valid if the distance from the source to the observation point is much greater than the wavelength, situation which is almost always met.

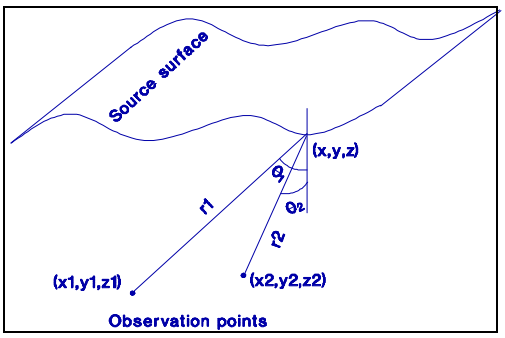

Figure 2.4.- *Definition of geometric terms*

The analytic signal of the field at point $(x_1,y_1,0)$, namely $b_1(t)$ can be readily found from the above equation. The procedure is described

[Goodman 85] and yields the following general result:

$$b_1(t) = \iint_{source} \frac{\cos\theta_1}{2\pi r_1 c} \frac{d}{dt} a\left(x,y,z,t-\frac{r_1}{c}\right) dS \qquad \textbf{(2.33)}$$

where a (x,y,z,t) is the analytic signal of the field at the source point. The time derivative of an analytic signal can readily be found:

$$\frac{da(t)}{dt} = j\omega_0 a(t)\left(1+j\frac{A'}{A\omega_0}\right) \qquad \textbf{(2.34)}$$

where A is the complex envelope of a(t) and A´ its time derivate. For a narrow-band signal this time derivate is small and (2.34) becomes:

$$\frac{da(t)}{dt} \approx j\omega_0 a(t) \qquad \textbf{(2.35)}$$

then (2.33) reduces to:

$$b_1(t) = \iint_{source} \frac{j\cos\theta_1}{r_1 c} f_0\, a\left(x,y,z,t-\frac{r_1}{c}\right) dS \qquad \textbf{(2.36)}$$

The mean power at point $(x_1,y_1,0)$ can be computed as in (2.5) from the self--correlation function of b_1 at $\tau = 0$, $R_{b1}(0)$. At this point we must make the assumption that the source field is spatially uncorrelated, so that [Goodman 85]:

$$E[a(x,y,z,t)\, a^*(x',y',z',t')] = R_a(x,y,z,t-t')\,\delta[(x-x'),(y-y'),(z-z')] \qquad \textbf{(2.37)}$$

note that (x,y,z) and (x',y',z') are points on the source surface. Then the power at point $(x_1,y_1,0)$, P_1 is easily obtained from equation (2.36):

$$P_1 = \frac{1}{2}R_{b_1}(0) = \frac{1}{2}\iint_{source} \frac{\cos\theta_1}{r_1^2\lambda_0^2} R_a(\bar{r},0)\, dS \qquad \textbf{(2.38)}$$

where we have make use that the emitted power depends on the surface's projection in the direction of the observation point, that is:

$$R_a(\bar{r},0)\,\delta_{\theta_1=0} = \cos\theta_1\; R_a(\bar{r},0)\,\delta_{\theta_1=0} \qquad \textbf{(2.39)}$$

and $R_a(\bar{r},0)$ is the power emitted in the surface's normal direction $\theta_1 = 0$.

Using now the complex degree of coherence, and the radiation intensity of the source P_a, from equation (2.38):

$$P_1 = \iint_{source} \frac{\cos\theta_1}{r_1^2\lambda_0^2} P_a(\bar{r})\, dS \qquad \textbf{(2.40)}$$

where it has been used that $r_a(0)=1$.

Considering now two observation points, the visibility function is defined as in equation (2.11) as the cross-correlation function of $b_1(t)$ and $b_2(t)$ at $J = 0$. Assuming that the field is spatially incoherent (equation 2.37) and that it has narrow bandwidth (equation 2.35), the following expression can be obtained:

$$V(\,)r) \;'\; \frac{1}{2}\,E\Big[\mathrm{b}_1(t)\,\mathrm{b}_2^{(}(t)\Big] \;'\; \mathop{\mathrm{mm}}_{source} \frac{\sqrt{\cos 2_1 \cos 2_2}}{r_1 r_2 8_0^2}\; P_a(x,y,z)\; r_a\!\left(\frac{\,)r}{c}\right)\; dS \qquad \textbf{(2.41)}$$

or, in terms of the complex degree of coherence of the complex envelope A(t):

$$V(\,)r) \;'\; \mathop{\mathrm{mm}}_{source} \frac{\sqrt{\cos 2_1 \cos 2_2}}{r_1 r_2 8_0^2}\; P_a(x,y,z)\; \tilde{r}_A\!\left(\frac{\,)r}{c}\right)\; e^{jk_0)r}\; dS \qquad \textbf{(2.42)}$$

The above general expression has only three assumptions:

a) The source is spatially incoherent

b) The source is narrow band

c) The distance of the source to the observation point is much larger than the wavelength.

If the distance between the observation points is much smaller than the distance from any of them to all points in the source, the paraxial approximation holds:

$r_1 \,.\, r_2 \,.\, r$ radial coordinate of the source point

$2_1 .\, 2_2 \,.\, 2$ elevation coordinate of the source point

and equation (2.42) can be expressed in the directing cosines coordinates:

$$\begin{aligned} > \;'\; \frac{x}{r} \;'\; \sin 2 \cos \mathrm{N} \\ 0 \;'\; \frac{y}{r} \;'\; \sin 2 \sin \mathrm{N} \\ \sqrt{1 \,\&\, >^2 \,\&\, 0^2} \;'\; \frac{z}{r} \;'\; \cos 2 \\ dS \;'\; \frac{r^2}{\cos^2 2}\, d> d0 \end{aligned} \qquad \textbf{(2.43)}$$

where formally r and 2 should be expressed as a function of the respective coordinates, but are kept in this manner for convenience.

Finally, by making use of equation (2.21), the phase $k_0\,)\,r = k_0\,(\,r_2 - r_1\,)$, can be expressed as a function of the coordinates using the equations for r_1 and r_2 :

$$k_0) r \bullet Q \,\&2B(u>\%v0) \tag{2.44}$$

where $Q . 0$ is defined in equation (2.23), and (u,v) are the (x,y) projections of the antenna separation normalized to the wavelength and were defined in equation (2.24).

Now equation (2.42) can be expressed in the directing cosines coordinate as:

$$V(u,v) \; ' \; \frac{e^{jQ}}{8_0^2} \int_{\&1}^{1} \int_{\&\sqrt{1\&0^2}}^{\sqrt{1\&0^2}} \frac{P_a(>,0)}{\sqrt{1\&>^2\&0^2}} \; \tilde{r}_A\left(\frac{)r}{c}\right) e^{\&j2B(u>\%v0)} d> d0 \tag{2.45}$$

where the argument of $\tilde{r}_A$ has been maintained as)r/c for simplicity.

To summarize, the above expressions are true if one considers the previous approximations named a), b) and c) and the following:

d) The distance between the observation points is much smaller that the distance from them to any source point

e) The two observation points lay in a plane z=0.

Equation (2.45) states that the visibility function is essentially the two-dimensional Fourier transform of the radiation intensity of the source, which is the result known as the Van Cittert-Zernike theorem [Goodman 85].

The power at an observation point is given in equation (2.40), which can be expressed using the directing cosines coordinates and the above approximations:

$$P_1 \; ' \; \frac{1}{8_0^2} \int_{\&1}^{1} \int_{\&\sqrt{1\&0^2}}^{\sqrt{1\&0^2}} \frac{P_a(>,0)}{\sqrt{1\&>^2\&0^2}} \; d> d0 \tag{2.46}$$

2.3.- RADIOMETER OPERATION

In the preceding paragraphs, the theoretical basis of interferometry have been discussed. The analysis of the operation of a radiometer has to take into account some additional considerations not considered so far. In particular the field at an observation point is not narrow band noise, but white thermal noise generated by a hot body (the Earth). It is measured by locating at that point an antenna with a given power pattern, connected to a band limited receiver and further processed. In this section the previous results are modified in order to take into account those particularities of radiometry.

The output voltage of an antenna is assumed to be proportional to the value of the scalar field *b* in the point where the antenna is located. To take into account the directional properties of the antenna and the frequency response of the receiver, equation (2.32) has to be modified, and is now:

$$\$(f) = -\frac{1}{j8}\iint_{source} A(x,y,z,f)\ F(2,N)\ H(f)\ \frac{e^{-jkr_1}}{r_1}\ \cos 2_1\ dS \qquad \textbf{(2.47)}$$

where the antenna is supposed to be located at the origin of coordinates. F(2,N) is the voltage pattern of the antenna and H(f) the frequency response of the receiver, including the antenna. Equation (2.47) is formally the same as equation (2.32) if one considers that now the value of the field in the frequency domain, is given by:

$$A'(\bar{r},f) = A(\bar{r},f)F(2,N)H(f) \qquad \textbf{(2.48)}$$

2.3.1.- Total Power Radiometer

The output power of the receiver at point $(x_1,y_1,0)$ can be computed from (2.38):

$$P_1 = \frac{1}{2}\iint_{source} \frac{\cos 2_1}{r_1^2 8_0^2}\ R_{a'}(\bar{r},0)\ dS \qquad \textbf{(2.49)}$$

but, using (2.48), $R_{a'}$ is easily found from the properties of the analytic signal:

$$R_{a'}(\bar{r},J) = *F(2,N)*^2\ ö^{-1}\left[*H(f)*^2\ S_a(\bar{r},f)\right] \qquad \textbf{(2.50)}$$

and taking into account that the source is thermal noise with temperature distribution $I(\bar{r})$, the power spectral density of the analytic signal a(x,y,z,t) is:

$$S_a(\bar{r},f) = 2\,k_B\,T(\bar{r})\,u(f) \qquad \textbf{(2.51)}$$

and (2.50) can be expressed in the following way:

$$R_{a'}(\bar{r},J) = *F(2,N)*^2\,2\,k_B\,T(\bar{r})\ ö^{-1}\left[*H(f)*^2\ u(f)\right] \qquad \textbf{(2.52)}$$

By making use of the complex degree of coherence:

$$R(J) = ö^{-1}\left[*H(f)*^2 u(f)\right] = "^2 B\,r(J); \quad r(0) = 1 \qquad \textbf{(2.53)}$$

where " is the voltage gain of the receiving chain. By introducing (2.52) into (2.49):

$$P_1 = "^2\ \frac{k_B B}{8_0^2}\iint_{source} \frac{\cos 2_1}{r_1^2} *F(2,N)*^2\,T(\bar{r})\,dS \qquad \textbf{(2.54)}$$

If the antenna has a narrow beam pointing to a given point in the source in the $(2_0, N_0)$ direction then it can be assumed that the temperature of the source is constant over the subtended area of the antenna:

$$P_1 = \frac{k_B B}{\lambda_0^2} \iint_{source} |F(\theta,\phi)|^2 T(\theta,\phi)\, d\Omega = \frac{k_B B}{\lambda_0^2} T(\theta_0,\phi_0) \iint_{source} |F(\theta,\phi)|^2 d\Omega \qquad \textbf{(2.55)}$$

where $d\Omega = \sin\theta\, d\theta\, d\phi$ is the differential solid angle. By definition, the antenna effective area is related to the antenna radiation voltage pattern and the normalized one by:

$$|F(\theta,\phi)|^2 = A_e F_n(\theta,\phi); \quad A_e = \frac{\lambda_0^2}{\iint_{4\pi} |F_n(\theta,\phi)|^2 \, d\Omega} \qquad \textbf{(2.56)}$$

Then:

$$P_1 = k_B B T(\theta_0,\phi_0) \qquad \textbf{(2.57)}$$

That is, the output power of a receiver having a highly directive antenna is proportional to the apparent brightness temperature of the point of the scene to which it is pointing.

2.3.2.- Interferometric Radiometer

An interferometric radiometer uses a receiver consisting of a number of antennas having each a wide beamwidth. The output voltages of different pairs of antennas are correlated and the visibility function obtained. Using inversion algorithms, the map of temperatures of the scene is then reconstructed (see chapter 6).

From (2.41), and using (2.48) the visibility function for a pair of antennas is given by:

$$V(\vec{r}) = \frac{1}{2} \iint_{source} \frac{\sqrt{\cos\theta_1 \cos\theta_2}}{r_1 r_2 \lambda_0^2} R_{a)}\left(\vec{r}, \frac{\vec{r}}{c}\right) dS \qquad \textbf{(2.58)}$$

where the self-correlation function has been used instead of the complex degree of coherence. Using now (2.52):

$$V(\Delta r) = a_1 a_2 \frac{k_B}{l_0^2} \iint_{source} \frac{\sqrt{\cos q_1 \cos q_2}}{r_1 r_2} F_{n_1}(q_1, f_1) F_{n_2}^{*}(q_2, f_2) T(\bar{r}) R_{12}\left(\frac{\Delta r}{c}\right) dS =$$

$$= a_1 a_2 \frac{k_B \sqrt{B_1 B_2} \sqrt{A_1 A_2}}{l_0^2} \iint_{source} \frac{\sqrt{\cos q_1 \cos q_2}}{r_1 r_2} F_{n_1}(q_1, f_1) F_{n_2}^{*}(q_2, f_2) T(\bar{r}) \tilde{r}_{12}\left(\frac{\Delta r}{c}\right) e^{j k_{12} \Delta r} dS \quad \textbf{(2.59)}$$

where the antennas are supposed to be different, and from equations (A1.2) and (A1.3):

$$R_{12}(t) \triangleq F^{-1}\left[H_1(f) H_2^{*}(f) u(f)\right] a_1 a_2 \sqrt{B_1 B_2}\, r_{12}(t) \quad \textbf{(2.60)}$$

$$R_{12}(t) = \tilde{R}_{12}(t)\, e^{j 2\pi f_{12} t}; \qquad r_{12}(t) = \tilde{r}_{12}(t)\, e^{j 2\pi f_{12} t};\ f_{12} \approx f_o$$

being H_1 and H_2 the frequency responses of the two receivers.

This is the general equation for an interferometer radiometer, and corresponds to equation (2.42) with the characteristics of the receivers taken into account. The only assumption for it to be true are the named a), b) and c) in section 2.2.2, understanding b) as referred to the bandwidth of the receiver.

Finally, if the distance between antennas is much smaller than the distance from satellite to the earth, and the two antennas are located in the plane z=0, the geometric approximations made before hold and equation (2.59) can be expressed in the directing cosines coordinates as:

$$V_{12}(u,v) = a_1 a_2 \frac{k_B e^{jy} \sqrt{B_1 B_2} \sqrt{A_{e1} A_{e2}}}{l_0^2} \iint_{x^2+h^2 \le 1} \frac{T(x,h)}{\sqrt{1-x^2-h^2}} F_{n1}(x,h) F_{n2}^{*}(x,h)$$
$$\tilde{r}_{12}\left(-\frac{ux+vh}{f_0}\right) e^{-j 2\pi (ux+vh)\frac{f_{12}}{f_0}} dx\, dh \quad \textbf{(2.61)}$$

2.4.- CONCLUSIONS

In this chapter the principles of the aperture synthesis radiometry have been briefly reviewed. The final equation (2.61) relates the measured correlation from the outputs of two antennas, V(u,v), with the antennas' and receivers' parameters.

From now on, the constant term outside the integral:

$$a_1 a_2 \frac{k_B e^{j\Psi} \sqrt{B_1 B_2} \sqrt{A_{e1} A_{e2}}}{l_0^2} \qquad \textbf{(2.62)}$$

will be omitted by simplicity, wherever its influence does not need to be explicitly show. The units of the visibility function will no longer be Watt but Kelvin.

Chapter 3. BASIC INTERFEROMETRIC RADIOMETER PERFORMANCE: SPATIAL RESOLUTION AND RADIOMETRIC SENSITIVITY

This chapter addresses the basic performance of an interferometric radiometer in terms of its spatial resolution and radiometric sensitivity. The analysis is focused on Y-shaped arrays, the optimal configuration, as it is shown in chapter 6.

System limitations (finite array size and decorrelation effects) and hardware errors (antenna position errors, antenna radiation patterns and receiver transfer functions: filter responses, phase and group delay errors) are modelled and analyzed for different windows commonly used in signal processing. Spatial resolution is analyzed though the Array Factor first defined in [Ruf et al 88] and it is generalized to account for system errors. Results are particularized for MIRAS, an Y-shaped array with 43 antennas per arm spaced 0.89λ, at 1.4 GHz. Results show the signal decorrelation induced for long baselines as the main perturbing effect, while the incidence on spatial resolution of the remaining errors is negligible if they are kept within achievable hardware requirements or basic calibration procedures.

The second part of this chapter is devoted to the computation of the radiometric sensitivity of an arbitrary shaped Aperture Synthesis Interferometric Radiometer. The study is done by assuming that correlations of the signals coming from the antennas are performed at baseband after I/Q demodulation, as it is usual when the number of correlations is large. The use of double side band or single side band receivers for the same pre-detection RF bandwidth is investigated and some design considerations are extracted. The impact of filters' frequency response on radiometric sensitivity and the kind of correlator (digital/analog) are also studied. Redundancy between simultaneous measurements is studied and its use to improve radiometric sensitivity analyzed, pointing out the main differences with radioastronomy. Results are particularized for MIRAS and the improvement on radiometric sensitivity by means of pixel averaging for the proposed platform orbit are quantified.

Finally, the new *"Interferometric Radiometer Uncertainty Equation"* is obtained. It states the relationship between spatial resolution and radiometric sensitivity and the tradeoff between both parameters.

3.1.- SPATIAL RESOLUTION COMPUTATION

The angular resolution is defined as the width of the impulse response for a point source in the directing cosines domain. The spatial resolution is computed from the angular resolution by projecting the synthesized beamwidth over the Earth's surface.

Let's rewrite equation (2.61) in a simplified form as:

$$V_{12}(u,v) = K_{12} \iint_{x^2+h^2 \le 1} T_{12}(x,h)\, \tilde{r}_{12}\left(-\frac{ux+vh}{f_o}\right) e^{-j2\pi(ux+vh)\frac{f_{12}}{f_o}}\, dx\,dh \qquad \textbf{(3.1)}$$

with the following definitions for:

$$K_{12} = a_1 a_2 \frac{k_B \sqrt{B_1 B_2}\, \sqrt{A_{e1} A_{e2}}\, e^{j\Psi}}{l_0^2} \qquad \textbf{(3.2)}$$

and:

$$T_{12}(x,h) = \frac{T_B(x,h)}{\sqrt{1-x^2-h^2}}\, F_{n1}(x,h)\, F_{n2}^{*}(x,h) \qquad \textbf{(3.3)}$$

with dimensions of Kelvin, is referred to as the *modified temperature*. This latter, which is the actual apparent brightness temperature modified by the obliquity factor $(1-\xi^2-\eta^2)^{-1/2}$ and the antenna normalized radiation pattern, is mathematically a very convenient magnitude and is used throughout as the basic unknown instead of the apparent brightness temperature.

In chapter 2 the effect of system's bandwidth was analyzed resulting in a radial broadening of the system's impulse response. In this chapter the "Equivalent Array Factor" is introduced as the system's impulse response in the modified temperature. The spatial resolution is analyzed by means of the AF for an ideal system in two steps: the coherent case, when there is not spatial decorrelation due to finite transit time, and the main beam broadening due to fringe-washing effects.

3.1.1.- IDEAL SITUATIONS

3.1.1.1.- LIMITING NARROW-BAND SYSTEM

An ideal system is the one having all the antennas, amplifiers, filters and correlators identical and ideal, and whose bandwidth is narrow enough to consider the fringe-wash term unity for all the baselines: B <<)r$_{max}$/c. This situation is denoted by a "º" superscript, ( )º. In this case (3.1) becomes:

$$V^{o}(u,v) \,'\, K \iint_{>^2\%0^2\#1} I(>,0)\, e^{\&j2B(u>\%v0)}\, d> d0 \qquad \textbf{(3.4)}$$

which is inverted to yield:

$$I(>,0) \,'\, \frac{1}{K} \int_{\&4}^{4} \int_{\&4}^{4} V^{o}(u,v)\; e^{j2B(u>\%v0)}\, du\, dv \qquad \textbf{(3.5)}$$

As it was done in chapter two. When there is only a knowledge of the visibility function in a set of points (u_i, v_j) forming a regular grid in the (u,v) space, an estimation of the modified temperature, denoted as "^", can be computed as:

$$\begin{aligned} \hat{I}(>,0) \,'\, \frac{1}{K})s \sum_i \sum_j W(u_i,v_j)\, V^{o}(u_i,v_j)\, e^{j2B(u_i>\%v_j0)} \,, \\ '\, \iint_{>)^2\%0)^2\#1} I(>),0))\; AF^{o}(>\&>),0\&0))\, d>)\; d0) \end{aligned} \qquad \textbf{(3.6)}$$

where)s is the area of the grid's elementary cell.)s = %3/2 d^2 for an hexagonal (u,v) sampling grid such as those given by Y-shaped and triangular shaped interferometers with an spacing between adjacent antennas of d wavelengths. For U-, T-, or L-shaped interferometers, the (u,v) sampling is rectangular and)s=)u)v. In a 1D interferometer, as ESTAR,)s must be replaced by)u [Ruf et al. 88]. If a weighing function W(u, v) (not to be confused with the relative bandwidth W) is used to window the visibility samples prior to inverse Fourier transform to reduce ringing at discontinuities, the *array factor* AF^o is now defined by:

$$AF^{o}(>\&>),0\&0)) \,'\,)s \sum_i \sum_j W(u_i,v_j)\; e^{j2B[u_i(>\&>))\%v_j(0\&0))]} \qquad \textbf{(3.7)}$$

This array factor is obviously the system's impulse response, that is, the system's response to a modified temperature consisting in a delta function. It is also called the system's point spread function (PSF), referred to the modified temperature. The shape of this array factor has been computed for an Y-array with 43-antennas per arm spaced 0.89 8, as MIRAS, with different windows commonly used in signal processing extended to the bi-dimensional case through the definitions given in table 3.1 below. Here the windows have been ordered according to their ability to reduce side lobe levels.

Rectangular	$W(u_{mn},\ v_{mn}) = 1$
Barlett (Triangular)	$W(u_{mn},\ v_{mn}) = 1 - \frac{\rho_{mn}}{\rho_{max}}$
Hamming	$W(u_{mn},\ v_{mn}) = 0.54 + 0.46\cos\left(\pi\frac{\rho_{mn}}{\rho_{max}}\right)$
Hanning	$W(u_{mn},\ v_{mn}) = \frac{1}{2} + \frac{1}{2}\cos\left(\pi\frac{\rho_{mn}}{\rho_{max}}\right)$
Blackmann	$W(u_{mn},\ v_{mn}) = 0.42 + 0.5\cos\left(\pi\frac{\rho_{mn}}{\rho_{max}}\right) + 0.08\cos\left(2\pi\frac{\rho_{mn}}{\rho_{max}}\right)$

Table 3.1.-. *Windows used in this text.* $\rho_{mn}^2 = u_{mn}^2 + v_{mn}^2$, $\rho_{max} = \sqrt{3}\ N_{EL}\ d$

Figure 3.1 shows the Y-array with 3 antennas per arm and figure 3.2 shows its corresponding (u,v) coverage.

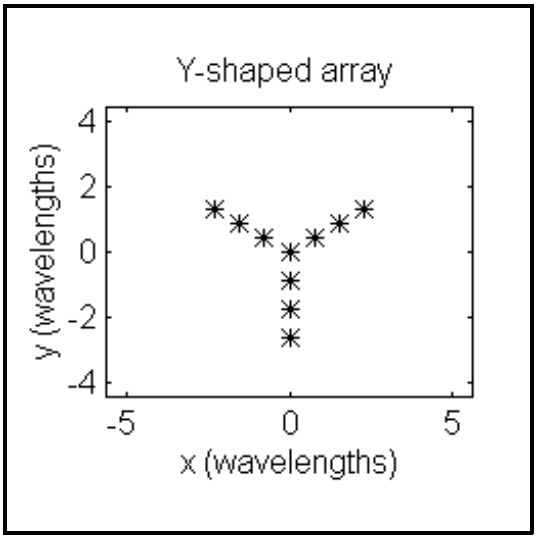

Figure 3.1.- *Structure of a Y-array with 3 antennas per arm spaced 0.89 wavelengths.*

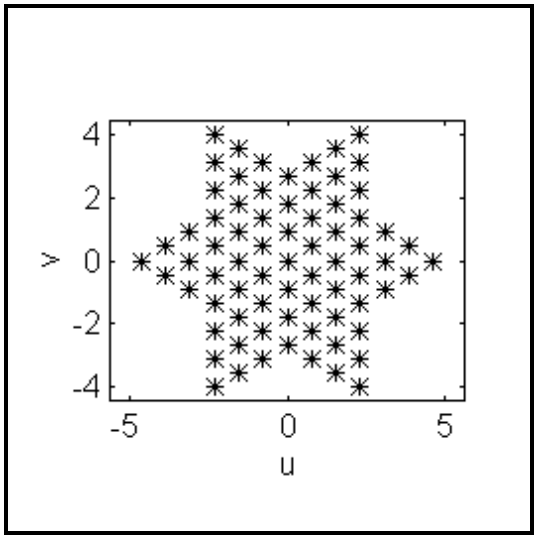

Figure 3.2.- *Spatial frequencies (u,v) coverage for the Y-array shown in figure 3.1.*

Results for the rectangular, Barlett, Hamming and Blackmann windows are plotted in figures 3.3 to 3.6, where the hexagonal shape of the PSF, the progressive reduction of the side lobes and the widening of the main lobe by the window can be clearly observed. Level curves are drawn for -0.04, -3.0, -5.0, -10.0, -15.0 and -20.0 dB.

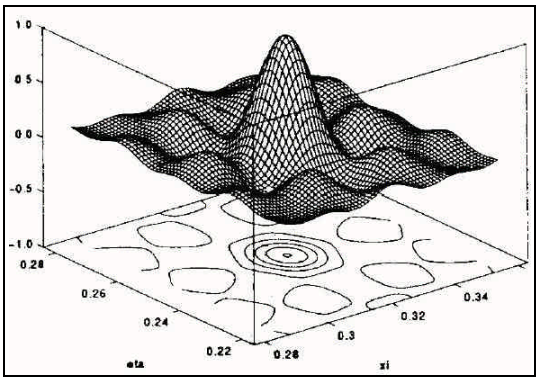

Figure 3.3.- *AF for a Y-array, 43 antennas per arm, d=0.89l Rectangular window, W=0*

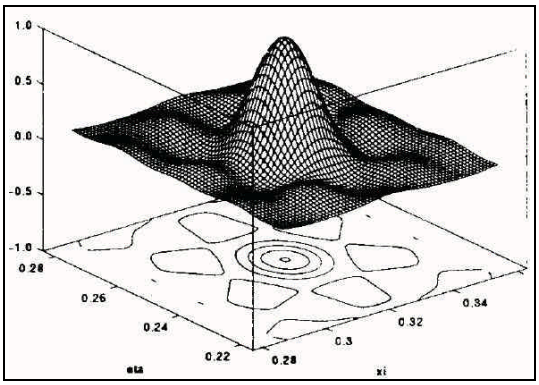

Figure 3.4.- *AF for a Y-array, 43 antennas per arm, d=0.89l Barlett window, W=0*

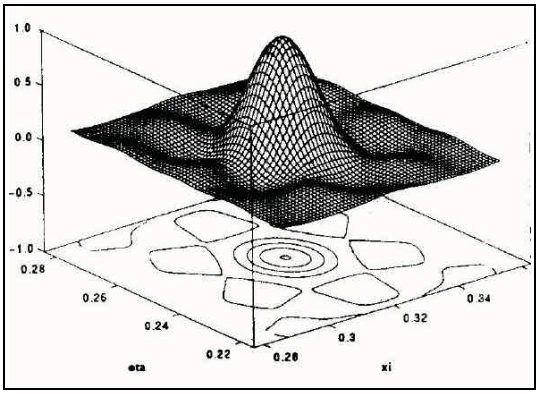

Figure 3.5.- *AF for a Y-array, 43 antennas per arm, d=0.89l Hamming window, W=0*

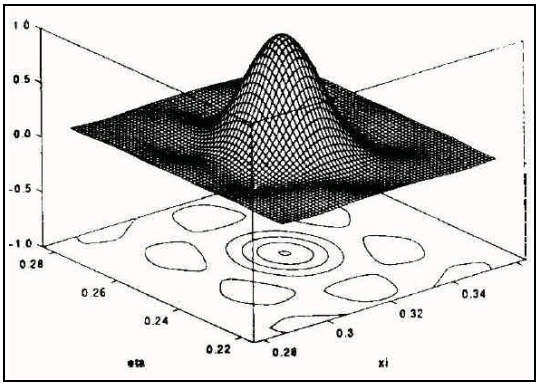

Figure 3.6.- *AF for a Y-array, 43 antennas per arm, d=0.89l Blackmann window, W=0*

Table 3.2 summarizes the PSF's main properties: 3 and 10 dB main beam width, nearest lobe level and main beam efficiency.

Window	**Relative Maximum**	**Side Lobe Level [dB]**	**$\Delta\xi_{rad}$ at -3dB**	**$\Delta\xi_{per}$ at -3dB**	**$\Delta\xi_{rad}$ at -10dB**	**$\Delta\xi_{per}$ at -10dB**	**MBE at -3dB**	**MBE at -10dB**	**MBE at SLL**
Rectangular	100%	8.4	0.77^{o}	0.77^{o}	1.26^{o}	1.21^{o}	27.0%	not defined	42.3%
Barlett	100%	11.3	0.93^{o}	0.93^{o}	1.54^{o}	1.49^{o}	42.4%	68.2%	69.3%
Hamming	100%	12.9	0.96^{o}	0.96^{o}	1.60^{o}	1.55^{o}	45.0%	72.6%	74.5%
Hanning	100%	13.8	1.01^{o}	1.01^{o}	1.66^{o}	1.62^{o}	47.4^{o}	76.1^{o}	78.3%
Blackmann	100%	16.2	1.10^{o}	1.10^{o}	1.86^{o}	1.81^{o}	52.9%	85.7%	89.6%

Table 3.2.- *MIRAS' PSF properties for N_{EL} = 43, d = 0.89 l. Identical receiver delays, pre-detection filters' bandwidth 20 MHz, central frequency 1.400 MHz and beam maximum at (x,h)=(0,0).*

By **spatial resolution** of an imaging or optical system it is usually understood its ability to separate two closely spaced identical point sources. Since this ability depends somewhat on the observer criteria, there is some ambiguity in the definition. In optics the Rayleigh's criterium is frequently used: it states that two point sources are resolved if the valley to peak ratio is 0.80 or less [Born and Wolf 86]. If we apply this criterium to the Blackmann window, figure 3.7, the spatial resolution turns out to be 1.25º, while its main beam 3 dB width is 1.10º. Since this latter concept is widely used in antenna theory, it is taken as the system's spatial resolution. The computation of the fringe-wash free half-power synthesized beam can be performed with the aid of the approximate formulas given below. For a rectangular window (no tapper) the main beamwidth can be approximately computed from:

$$)>^{rect}_{\&3dB} \cdot \frac{B/2}{)u_{max}} ; \quad , < 10\ \%\ if\ )u_{max}>15 \qquad \textbf{(3.8)}$$

where $)\mathbf{u_{max}} = 2\%3\mathbf{N_{EL}d}$ is the maximum dimension of the synthetic aperture: the distance between the two most distant (u,v) points considering the hermitian ones, N_{EL} is the number of antennas per arm, without the central one and d is the spacing between adjacent antennas in wavelengths. The use of tapered weighing functions reduces the side lobe levels at a expense of a broadening of the main beam by a factor:

$$\begin{aligned})>^{triang}_{\&3dB} &' 1.24)>^{rect}_{\&3db} \\ )>^{Hamming}_{\&3dB} &' 1.26)>^{rect}_{\&3db} \\ )>^{Hanning}_{\&3dB} &' 1.33)>^{rect}_{\&3db} \\ )>^{Blackmann}_{\&3dB} &' 1.48)>^{rect}_{\&3db} \end{aligned} \qquad \textbf{(3.9)}$$

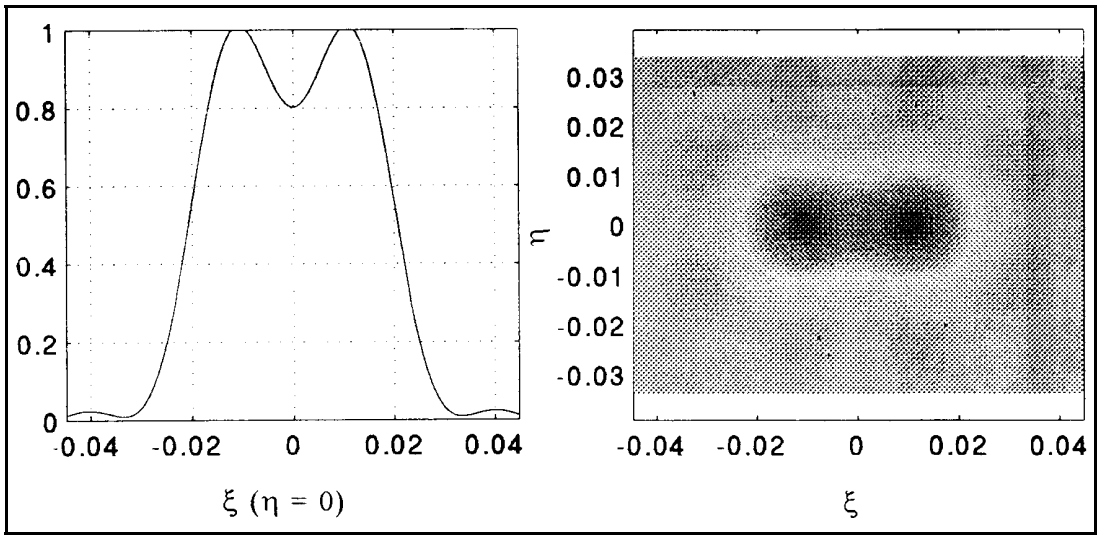

Figure 3.7.- *Spatial resolution definition by the Rayleigh's criterium (Blackmann window).*

3.1.1.2.- SPATIAL DECORRELATION EFFECTS (FRINGE-WASH)

The fringe-wash term is now taken into account, by inserting $\tilde{r}\left(\&(u>\%v0)/f_o\right)$ into the integrand of (3.4). If this equation is now Fourier-transformed and this situation is denoted by a superscript 'f':

$$I^f(>,0) \,'\, \ddot{o}^{\&1}[V^f](>,0) \,'\, \int_{\&4}^{4}\int_{\&4}^{4} V^f(u,v)\, e^{\,j2B(u>\%v0)}\, du\, dv \,'$$

$$'\, K \int_{>'^2\%0'^2\#1}\int I(>),0)\,)\; d>)d0) \int_{\&4}^{4}\int_{\&4}^{4} \tilde{r}\left(\&\frac{u>)\%v0)}{f_o}\right)\, e^{\,j2B[u(>\&>)\%v(0\&0))]}\, du\, dv \qquad \textbf{(3.10)}$$

As in chapter 2, equations (2.32) and (2.33), the rightmost integral can be evaluated through the change of variables:

$$x) \,'\, \frac{u>)\%v0)}{f_o}, \qquad y) \,'\, \frac{u>)\&v0)}{f_o} \qquad \textbf{(3.11)}$$

which reduces to [Bará et al 96A]:

$$I^f(>,0) \,'\, K\, f_o \int_{\&4}^{4} I(F>,F0)\; p\left[f_o\left(1\&\frac{1}{F}\right)\right] dF \qquad \textbf{(3.12)}$$

where p(f) is the Fourier transform of $\tilde{r}(J)$:

$$p(f) \,'\, \int_{\&4}^{4} \tilde{r}(t)\, e^{\,\&j2Bft}\, dt \qquad \textbf{(3.13)}$$

For instance, for an ideal narrow rectangular band-pass filter:

$$\tilde{r}(t) \,'\, sinc(Bt), \qquad p(f) \,'\, \frac{1}{B}\,\Lambda\left(\frac{f}{B}\right) \qquad \textbf{(3.14)}$$

then:

$$I^f(>,0) \,'\, \frac{1}{W} \int_{1\&W/2}^{1\%W/2} I(F>,F0)\, dF \times \bar{I}(>,0) \qquad \textbf{(3.15)}$$

where $\bar{T}(>,0)$ is a weighted averaged version of the modified temperature T along the diagonal of a cell of dimensions:

$$(\,)>,)\,0) \,'\, (>W,0W) \qquad \textbf{(3.16)}$$

centered around each point (>, 0). As in (2.31) the length of the diagonal is:

$$L \,'\, W\sqrt{>^2\%0^2} \,'\, W. \qquad \textbf{(3.17)}$$

where W is the relative bandwidth and the diagonal is oriented along the line joining the point (>,0) with the origin (figure 3.8). That is, the temperature averaging depends on the distance to the origin of the plane (>,0) and it is performed in the radial direction. Since all the information obtained by the radiometer resides on the visibility function V(u,v), or equivalently, on its Fourier transform, from (3.15) it is evident that the decorrelation effects produce an irrecoverable loss of information of the brightness temperature for directions off-boresight even in the ideal, continuous equation case (delta function PSF). In other words, the basic equation (3.1) cannot be inverted, that is, there is no operator that allows the recovery of T from the visibility function.

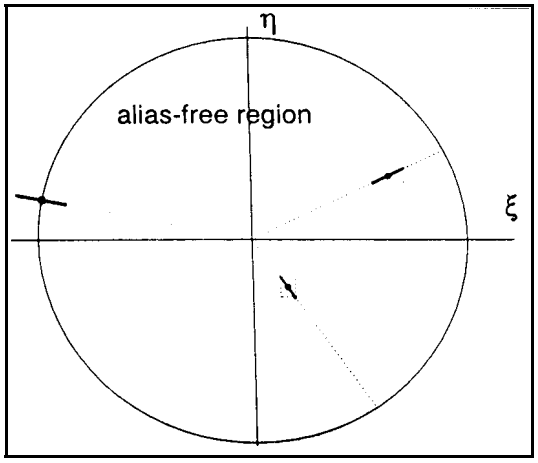

Figure 3.8.- *Examples of segments along which the fringe-wash free array factor is averaged by the fringe-wash effect.*

Anyway, this loss of information on a radiometer like MIRAS is very small (B=20 MHz, W=1.4%) even at the edge of the alias-free region. At this point .=0.4 (see chapter 6), L amounts 0.35º, while the system resolution (Blackmann window) is 1.10º, as shown before. When the discrete case is considered, from (3.15) an estimation of $\bar{T}$ which is again an estimation of T and will be still denoted $\hat{T}$. Now, equation (3.6) is still valid with the new definition for the array factor:

$$AF^{f}(\xi,\xi_0;0,0_0) = \sum_i \sum_j W(u_i,v_j)\tilde{r}\left(-\frac{u_i\xi + v_j 0}{f_o}\right) e^{j2\pi[u_i(\xi-\xi_0)+v_j(0-0_0)]} \qquad \textbf{(3.18)}$$

That is, in the discrete case, the decorrelation can be interpreted as affecting the array factor in such a way that the contributions from baselines non-orthogonal to an off-boresight direction being observed are reduced, and therefore system's resolution is also reduced on those directions. The effect of the decorrelation on the array factor can be accounted for in another way. Let's start from the equations (3.6) and (3.8):

$$\begin{aligned}\hat{I}(\xi,0) &= \iint_{\xi_0^2+0_0^2\le 1} AF^{o}(\xi-\xi_0,0-0_0)\,\bar{I}(\xi_0,0_0)\,d\xi_0\,d0_0 \\ &= \frac{1}{W}\iint_{\xi_0^2+0_0^2\le 1}\ \int_{1-\frac{W}{2}}^{1} AF^{o}(\xi-\xi_0,0-0_0)\,I(F\xi_0,F0_0)\,d\xi_0\,d0_0\,dF\end{aligned} \qquad \textbf{(3.19)}$$

This integration can also be performed by the change of variables x=F>' and y=F0' obtaining:

$$\hat{I}(>,0) = \iint \overline{AF^o}(>,>';0,0')\; I(>',0')\; d>'\, d0' \qquad \textbf{(3.20)}$$

where the averaged array factor has been defined for W<<1 as :

$$\overline{AF^o} = AF^f = \frac{1}{W}\int_{1-\frac{W}{2}}^{1+\frac{W}{2}} AF^o(>-F>', 0-F0')\, dF \qquad \textbf{(3.21)}$$

This array factor is, of course, the same as (3.18) computed from a different point of view. But this form has some advantages; for instance, it can be used to show that the areas under AF^o and AF^f are the same:

$$\begin{aligned}
&\iint_{>'^2+0'^2\le 1} AF^f(>,>';0,0')\, d>'\, d0' = \\
&= \frac{1}{W}\int_{1-W/2}^{1+W/2} dD \iint_{>'^2+0'^2\le 1} AF^o(>-D>',0-D0')\, d>'\, d0' = \\
&= \frac{1}{W}\int_{1-W/2}^{1+W/2} \frac{1}{D^2}\, dD \iint_{>'^2+0'^2\le 1} AF^o(>-\tfrac{>'}{D},0-\tfrac{0'}{D})\, d>'\, d0' = \\
&= \iint_{>''^2+0''^2\le 1} AF^o(>->'',0-0'')\, d>''\, d0''
\end{aligned} \qquad \textbf{(3.22)}$$

In the last step it is assumed that the observed point (>',0') is well within the unit circle so that most of the synthesized beam also falls within it. In practice it means a distance of at least two beamwidths between zeroes, 2 x 1.4º = 2.8º for MIRAS.

That is, the effect of the decorrelation (fringe-wash term) can be accounted for by either:

- Assuming that the array factor remains unchanged, AF^o, and the actual temperature distribution is replaced by the averaged temperature given by (3.15) (effect on the temperature resolution).
- Assuming the actual temperature distribution but replacing the decorrelation free array factor AF^o by its averaged version as given by (3.19) (effect on the spatial resolution).

For a working frequency of 1.400 MHz, even if in the use of all the protected bandwidth 1.400-1.427 MHz, W=0.02, and the integration variable F remains always very close to unity, a fact that was used to perform some simplifications in the derivation of (3.19). The array factor for MIRAS has been computed at the most distant

(from boresight) direction in the field of view, $(\xi,\eta) = (0.32, 0.25)$, for a bandwidth of 20 MHz and for all the windows shown in table 3.1, and the results are summarized in table 3.3, where slight degradations can be observed as compared with the fringe-wash free beam.

Window	Relative Maximum	Side Lobe Level [dB]	$\Delta\xi_{rad}$ at -3dB	$\Delta\xi_{per}$ at -3dB	$\Delta\xi_{rad}$ at -10dB	$\Delta\xi_{per}$at -10dB	MBE at -3dB	MBE at -10dB	MBE at SLL
Rectangular	93.45.%	8.6	0.82º	0.76º	1.35º	1.21º	28.8%	not defined	45.1%
Barlett	95.22%	11.6	0.98º	0.93º	1.63º	1.50º	43.7%	70.2%	71.5%
Hamming	95.46%	13.2	1.01º	0.99º	1.70º	1.57º	46.0%	74.4%	76.6%
Hanning	95.83%	14.0	1.04º	0.99º	1.70º	1.57º	46.0%	74.4%	76.6%
Blackmann	96.44%	16.5	1.14º	1.10º	1.95º	1.82º	52.2%	86.5%	90.6%

Table 3.3.- *MIRAS' PSF properties for N_{EL} = 43, d = 0.89 λ. Identical receiver delays, pre-detection filters' bandwidth 20 MHz, central frequency 1.400 MHz and beam maximum at (x,h)=(0.32, 0.25).*

These degradations progressively decrease with the window side-lobe quality, being minimum for Blackmann's, for which:

- The main beam maximum is reduced by 0.16 dB.
- The nearest lobe level is improved by 0.3 dB.
- Spatial resolution in the radial direction (relative to boresight) is degraded by a 3.6 %.

Figures 3.9 to 3.12 show the windowed array factor for four windows. The elongation of its whole shape along the radial direction can be clearly observed in the level curves.

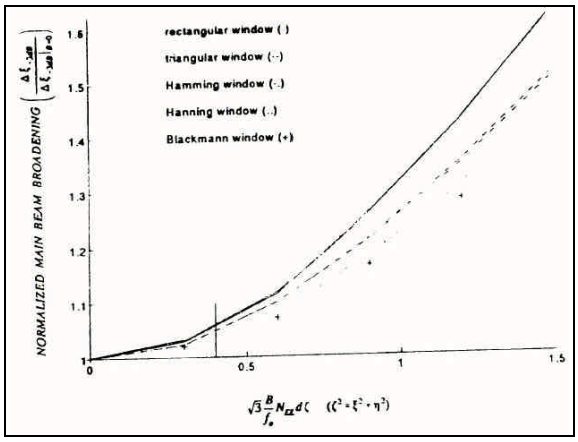

Figure 3.13.- *Half power synthesized beam broadening due to spatial decorrelation vs. z.*

The expansion of the fringe-washed main lobe for the different windows under consideration as a function of its radial distance is shown in figure 3.13.

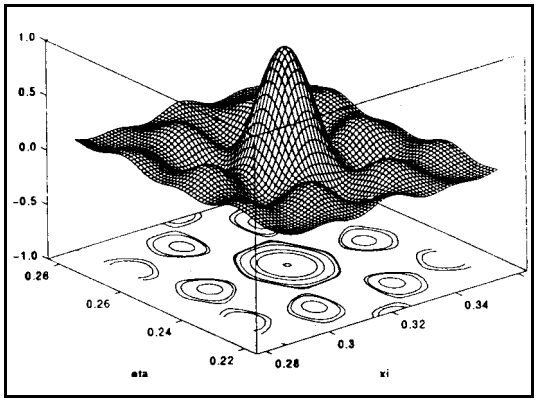

Figure 3.9.- *AF for a Y-array, 43 antennas per arm, d=0.898 Rectangular window, W=0.02*

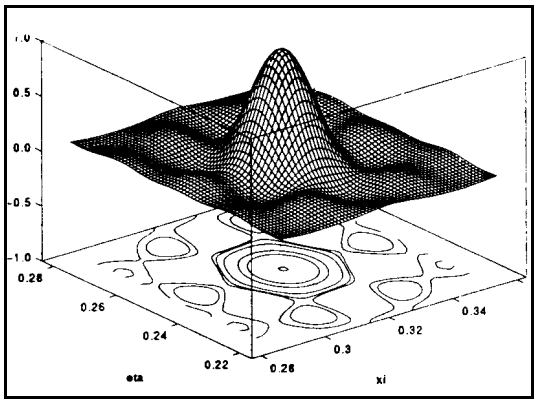

Figure 3.10.- *AFeq for an Y-array, 43 antennas per arm, d=0.898 Barlett window, W=0.02*

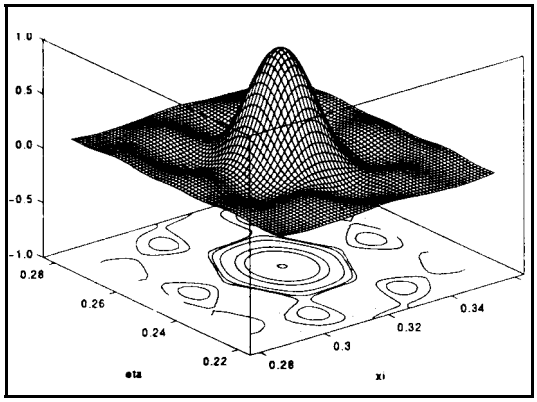

Figure 3.11.- *AFeq for an Y-array, 43 antennas per arm, d=0.898 Hamming window, W=0.02*

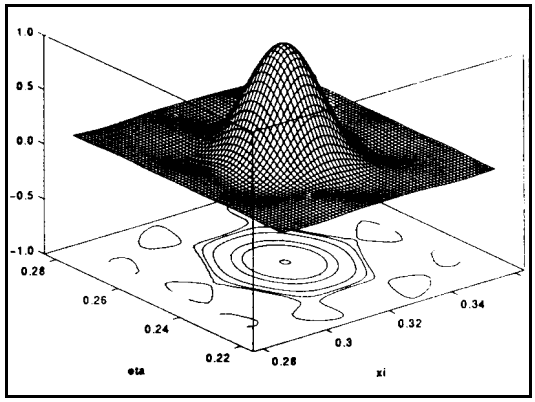

Figure 3.12.- *AFeq for an Y-array, 43 antennas per arm, d=0.898 Blackmann window, W=0.02*

When translated to the Earth's surface, the spatial resolution in the FOV is found to range from:

- Minimum value at (>,0)=(0, 0.26), angle of incidence on the Earth's surface of 55º:

Rectangular window, radial direction:	18.0 km
Rectangular window, perpendicular direction:	17.7 km
Blackmann window, radial direction:	25.6 km
Blackmann window, perpendicular direction:	25.2 km

- Maximum value at (>,0)=(0.40, 0.05), angle of incidence on the Earth's surface of 40º:

Rectangular window, radial direction:	30.0 km
Rectangular window, perpendicular direction:	27.8 km
Blackmann window, radial direction:	41.8 km
Blackmann window, perpendicular direction:	40.3 km

As it is shown in the second part of this chapter, the loss of spatial resolution introduced by windows other than rectangular is accompanied by an increase in the radiometric sensitivity and the choice of the window is a question of trade-off between them. It should be emphasized that the values quoted above are for an ideal, imperfection free system, and as such are limiting values.

3.1.2.- EFFECT OF SYSTEM IMPERFECTIONS

"System imperfections" refer to hardware imperfections or deviations from the assumed model. These affect the following elements:

- Antennas' positions, due mainly to antenna deployment, mechanical modes of oscillation, thermoelastic effects and long term changes [MMS 95].
- The channels from the antennas to the correlators: amplifiers, filters and down converters.
- Antennas' properties: namely, its voltage radiation pattern (amplitude and phase) and pointing errors (which can be reduced to the former). Mutual coupling among different antennas and coupling between H and V polarizations in the same antennas which will not be considered.
- The complex correlators, which are actually implemented by two real correlators. Therefore the actual output of the theoretical complex correlator is affected, among others, by in-phase and quadrature phase errors.

It is assumed that both hardware and software calibration processes are available to partially correct these errors. It is therefore understood that these errors are the residual ones after calibration. The effects of amplitude errors are not considered since they are known to be much smaller than phase errors as far as the array factor is concerned. An exhaustive and systematic analysis of error sources is performed in chapter 4, when computing their impact on the radiometric accuracy.

3.1.2.1.- ERRORS IN THE ANTENNA POSITIONS

In-plane errors in the antenna positions translate into errors in the (u,v) plane points where the visibility function is measured:

$$(u)_i, v)_j) \text{ ' } (u_i, v_j)\%(*u_{ij}, *v_{ij}) \qquad \textbf{(3.23)}$$

and the fringe-wash free array factor AF^o becomes $AF^{o,}$:

$$AF^{o\prime}(\rho,\rho';0,0') = \sum_i \sum_j W(u_i,v_j)\, e^{j2\pi[u_i(\rho-\rho')+v_j(0-0')]}\, e^{-j2\pi(\Delta u_{ij}\rho'+\Delta v_{ij}0')} \tag{3.24}$$

which, for small errors, can be approximated to first order by:

$$AF^{o\prime}(\rho,\rho';0,0') \approx AF^{o}(\rho-\rho',0-0')+\Delta AF(\rho,\rho';0,0')$$
$$\Delta AF(\rho,\rho';0,0') = -j2\pi \sum_i \sum_j W_{ij}\left[\rho'\Delta u_{ij}+0'\Delta v_{ij}\right] e^{j2\pi[u_i(\rho-\rho')+v_j(0-0')]} \tag{3.25}$$

Note that, since only half the baselines are measured (hermitian property of the visibility function):

$$(\Delta u_{-i,-j},\Delta v_{-i,-j}) = -(\Delta u_{ij},\Delta v_{ij}) \tag{3.26}$$

and therefore ΔAF is a real function. Note also that ΔAF=0 for $(\rho',0')=(0,0)$.

ΔAF is computed for a worst-case example of one fourth 0º - 90º sinusoidal in-plane arm bending with a maximum deviation at their ends of 10 cm, such that two of the arms bend towards each other and the third one is fixed. It should be noted that with these errors the first order approximation (3.25) is not longer valid and (3.24) is directly used. Results show that the maximum value of $|\Delta AF|$ remain always below 0.5% of the main beam maximum, and are therefore negligible for spatial resolution considerations. These figures agree with the theoretical considerations to be given in section 3.1.2.2.3 below.

3.1.2.2.- ERRORS IN THE CHANNELS

In this paragraph the effect of slight differences among the transmission channels from the antennas to the correlators will be studied, with all the remaining subsystems free of errors. First, note that since the signals will be down-converted coherently with a master oscillator to an intermediate frequency f_{IF}, there will be filtering both before and after down conversion, like in the general diagram of figure 3.14.

Here the inputs to the correlators are at intermediate frequency assuming $f_{ol} < f_o$:

$$f_i' = f_i - f_{ol}, \quad f_i < f_o, \quad f_i' < f_{IF} = f_o - f_{ol} \tag{3.27}$$

and the fringe-wash term given by (3.14) has to be modified according to:

$$H_i(f) = H_{i1}(f-f_{ol})\, e^{-j\Phi_{oi}} H_{i2}(f),$$
$$\tilde{r}_{ij}(t) = r_{ij}(t) e^{-j2\pi f_{ij}' t} \tag{3.28}$$

where $f_{ij}' < f_{IF}$.

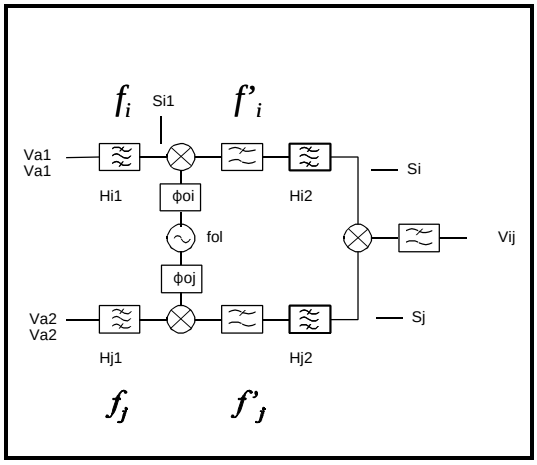

Figure 3.14.- *Block diagram of a baseline with coherent downconversion.*

In an actual system, the pre-multiplication band-pass filter is probably wider than the post-detection one so as to yield this latter full control of the filtering process, but note from (3.28) that the situation is formally identical with that without frequency conversion. Therefore, without loss of generality, equations (2.2) and (3.1) will be used. For the sake of mathematical simplicity, each channel will be modelled by a Gaussian band-pass filter centered around $f_i \approx f_o$, with group delay τ_i and phase lag ϕ_i:

$$H_i(f) = \alpha_i e^{-\frac{\pi}{2}\left(\frac{f-f_i}{B_i}\right)^2} e^{-j2\pi(f-f_i)\tau_i} e^{j\phi_i},$$

$$h_i(t) = \sqrt{2}\alpha_i B_i e^{-2\pi B_i^2 (t-\tau_i)^2} e^{j2\pi f_i t} e^{j\phi_i} \qquad \textbf{(3.29)}$$

recall that the study is performed by using analytic signals of bandwidth B_i defined as in appendix 1. From the definition of the complex degree of coherence (see "Nomenclature and Basic Conventions") and (3.29) it is found that (i=1, j=2):

$$r_{12}(t) = A_{12} e^{-\pi B_{12}^2 (t-\tau_1+\tau_2)^2} e^{j2\pi f_{12} t} e^{j\phi_{12}},$$

$$B_{12}^2 = 2\frac{B_1^2 B_2^2}{B_1^2 + B_2^2}, \qquad f_{12} = \frac{f_1 B_2^2 + f_2 B_1^2}{B_1^2 + B_2^2},$$

$$\phi_{12} = \phi_1 - \phi_2 - 2\pi(f_2 - f_1)\frac{B_1^2\tau_1 + B_2^2\tau_2}{B_1^2 + B_2^2}, \qquad \textbf{(3.30)}$$

$$A_{12} = \sqrt{\frac{2B_1 B_2}{B_1^2 + B_2^2}}\, e^{-\frac{\pi}{2}\frac{(f_1-f_2)^2}{B_1^2+B_2^2}}$$

Before going further, it is convenient to make estimations of the magnitudes involved. First, note that the master local oscillator is assumed to be very stable (quartz controlled), and that the band-pass filtering is effectively performed at the intermediate frequency: for instance, in the margin 1-27 MHz. From commercial catalogues, with standard, non-matched components (a really worst case) the following error bounds can be estimated for the magnitudes involved:

$$|\Delta f| < 0.5 \text{ MHz}, \quad |\Delta B| < 1 \text{ MHz}, \quad \tau_i \approx 80 \text{ ns}, \quad |\Delta\tau_i| < 2 \text{ ns}$$

With these orders of magnitude it turns out that:

$$f_{12} \cdot \frac{f_1 \% f_2}{2} \, ' \, f_{IF} \% \frac{) f_1 \%) f_2}{2} \, ' \, f_{IF} \%) f_{f_{12}}, \quad B_{12} \cdot \frac{B_1 \% B_2}{2} \, '$$

$$B\left(1 \% \frac{) B_1 \%) B_2}{2B} \right) \, ' \, B\,[\,1 \%) B_{12}\,], \quad \mathsf{N}_{12} \cdot \mathsf{N}_1 \& \mathsf{N}_2 \& \mathsf{B}(f_2 \& f_1)(\mathsf{J}_1 \% \mathsf{J}_2), \tag{3.31}$$

$$A_{12} \cdot 1 \& \frac{\mathsf{B}(f_1 \& f_2)^2 \% (B_1 \& B_2)^2}{4B^2} \, ' \, 1 \&) A_{12}$$

$$*) f_{12} * < 0.5 \ MHz, \quad *) B_{12} * < 4 . 10^{\&2}, \quad *) A_{12} * \# 3 . 10^{\&3}$$

For the values assumed above, it can also be found that [Bará et al 96A]:

$$*\mathsf{N}_{12} \& * \mathsf{N}_1 \& \mathsf{N}_2 ** \# 30^o \tag{3.32}$$

which is a very large bound indeed. But since phase errors can in principle be corrected by phase restoration procedures based on the phase closure condition [Lannes 90] [Torres et al. 96A] or by noise injection procedures [Torres et al. 96B], let's see how this is affected:

$$) \mathsf{N}_{closure} \, ' \, \mathsf{N}_{12} \% \mathsf{N}_{23} \% \mathsf{N}_{31} \, ' \, \mathsf{B} \sum_{i}^{3} \,) f_i \, (\,) \mathsf{J}_{i \% 1} \&) \mathsf{J}_{i \% 2}), \ modulo \ 3 \tag{3.33}$$

For the same values assumed before, $) \mathsf{N}_{\text{closure}} \# 1.08^o$, which takes the phase residual errors to the order of magnitude of 1^o or less.

Equation (3.30) can now be written as:

$$r(t;u,v) \, ' \, \left[1 \&) A(u,v) \right] e^{\,\&\mathsf{B} B^2 [1 \%) B(u,v)]^2 [t \&) \mathsf{J}(u,v)]^2} \, e^{\,j 2 \mathsf{B} [f_{IF} \%) f(u,v)] t} \, e^{\,j \mathsf{N}(u,v)} \tag{3.34}$$

This expression can be reasonably extrapolated to filters with a response other than Gaussian:

$$r(t;u,v) \, ' \, \left[1 \&) A(u,v) \right] \tilde{r} \left\{ \left[1 \%) B(u,v) \right] \left[t \&) \mathsf{J}(u,v) \right] \right\} e^{\,j 2 \mathsf{B} [f_{IF} \%) f(u,v)]} \, e^{\,j \mathsf{N}(u,v)} \tag{3.35}$$

where r(t) refers to the correlation function in the absence of errors. But it has to be admitted that the expressions given by (3.31) in terms of center frequencies and band-widths for the parameters appearing in (3.35) may not be useful when the filter shape deviates significantly from an ideal model. Finally, the visibility function can be written as:

$$V_{ij}(u,v) =$$

(3.36)

$$= K\, e^{j f_{ij}} (1 - \Delta A_{ij}) \iint_{x^2+h^2 \le 1} T(x,h)\, \tilde{r} \left\{ (1 + \Delta B_{ij}) \left(- \frac{ux + vh}{f_o} - t_i + t_j \right) \right\} e^{-j 2\pi (ux+vh)\left(1+\Delta \frac{f_{ij}}{f_o}\right)} dx\, dh$$

3.1.2.2.1.- GROUP DELAY ERRORS

Group delay errors affect both the visibility function phase factor ϕ_{ij} in (3.36) through equation (3.31) and the fringe-wash term. Note first the changes appearing in the fringe-wash term. In the absence of channel errors the geometrical time delay at the edge of the IFOV (ζ = 0.4) is 19 ns, and this resulted in a widening of 3.6% of the synthesized main beam (Blackmann window). With the errors assumed for the channels: $|\tau_i - \tau_j| < 4$ns and $\Delta B/B < 4\%$. Besides, these delays are random, while the original fringe-wash delays are strongly correlated, and randomness tends to smooth the changes produced.

Therefore, it can be said a priori that the beam distortion at boresight will be negligible, while at the edge of the IFOV, at worst, the equivalent geometrical time delay is 23 ns. That is, with the assumed channel errors the main beam distortion will be probably much less than that existing in the ideal system for ζ= 0.5.

Results of computations performed at (ξ,η) = (0.32, 0.25) for random delay errors with a normal distribution and standard deviation of 2 ns are shown in table 3.4. It can be seen that the changes brought about by these errors are practically negligible, as expected.

Window	Relative Maximum	$\Delta\xi_{radial}^{-3dB}$	$\Delta\xi_{perp.}^{-3dB}$	$\Delta\xi_{radial}^{-10dB}$	$\Delta\xi_{perp.}^{-10dB}$
Rectang.	92.89%	0.82º	0.77º	1.32º	1.22º
Barlett	94.63%	0.96º	0.93º	1.63º	1.50º
Hamming	94.86%	1.00º	0.94º	1.70º	1.55º
Hanning	95.22%	1.04º	1.01º	1.73	1.62º
Blackmann	95.79%	1.13º	1.10º	1.95º	1.82º

Table 3.4.- *MIRAS' PSF properties for N_{EL} = 43, d = 0.89 l. Different receiver delays with standard deviation s_{tg} = 2 ns. Predeteccion filters' bandwidth 20 MHz, central frequency 1.400 MHz and beam maximum at swath edge: (x,h)=(0.32, 0.25)*

3.1.2.2.2.- FREQUENCY ERRORS

Frequency errors are produced by differences in the channel filters appearing in the exponent of (3.36) are equivalent to errors in the baseline coordinates given by:

$$*u_{ij} ' u_i \frac{)f_{ij}}{f_o}, \quad *v_{ij} ' v_j \frac{)f_{ij}}{f_o} \tag{3.37}$$

For a given frequency error, these equivalent errors increase with the baseline coordinates, as in the case of position errors produced by an incorrect alignment of the arms of the interferometer. Its maximum value is attained for |(u,v)| maximum, $|(u,v)|_{max}$ = 38.8, and for the frequency errors quoted above, this maximum is equivalent to a position displacement of 2.9 mm. Therefore, the effect of frequency errors on the spatial resolution is smaller than the effect of antenna position errors, which are themselves negligible.

3.1.2.2.3.- PHASE ERRORS

Let's turn next to the phase errors N_{ij} appearing in the visibility expression (3.36). From their value given by (3.31) it is seen that they have contributions from the channel phase errors N_i and from frequency differences and group delays. The array factor now takes the form:

$$AF^{o'}(>,>);0,0)) ') s \sum_i \sum_j W_{ij} e^{j2B[u_i(>\&>))\%v_j(0\&0))]} e^{jN_{ij}} \tag{3.38}$$

which has the same form of the array factor in presence of errors in the antenna positions (3.24). In fact, it can be seen, for instance, that for (>',0')=(0.4,0.0) a position error of 10 mm is equivalent to a phase error of 6.72º.

Computation of the array factors for normally distributed random channel phase errors with a standard deviation of F_{Ni}=1º show a negligible effect down to values -16, -20 dB below the main beam's maximum and do not affect spatial resolution. It is important to note here that the same errors have a strong impact on temperature resolution: 1 K or more [Bará et al. 95B] [Bará et al. 96B]. This is clearly understood if is realized that a small degradation of the array factor shape far off its main maximum, in regions where it should be zero, allows a small but spatially large leakage of temperatures from the whole scene into the pixel under consideration. The same is true, of course, for the remaining errors under study as long as they also increase values close to zero above its unperturbed value.

In order to analyze later the effects of antenna radiation pattern errors it is convenient at this point to perform some theoretical considerations. Again, as in (3.25) it can be written:

$$AF^{oe}(x,x';h,h') = AF^{o}(x-x',h-h') + dAF(x,x';h,h')$$

$$dAF(x,x';h,h') = j\,\Delta s \sum_i \sum_j W_{ij} f_{ij} e^{j2p[u_i(x-x')+v_j(h-h')]} \quad \textbf{(3.39)}$$

Changing to a continuous formulation and assuming, for the sake of simplicity, a rectangular window, (3.39) can be written as:

$$dAF(s,t) = j \int_{-\infty}^{\infty}\int_{-\infty}^{\infty} W(u,v)\, f(u,v)\, e^{j2p(us+vt)}\, du\, dv, s = x-x', t = h-h' \quad \textbf{(3.40)}$$

$$E[|dAF(s,t)|^2]_e = \int\int_{S_{uv}} \left[\int\int_{S_{uv}} E[f(u'-u,v'-v) f(u',v')]_e \; d'u\, d'v \right] e^{j(us+vt)}\, du\, dv$$

where S_{uv} is the domain in the (u,v) plane covered by the visibility samples (see figure 3.2). At this point it is expedient to assume that the baseline phase errors are not correlated; in fact this is true only for baselines which do not share a receiving channels since it is the phase errors of these latter which are uncorrelated. With this simplifying assumption:

$$E[f(u'-u,v'-v) f(u',v')]_e = d(u)\,d(v)\,E[f^2(u',v')]_e = d(u)\,d(v)\,s_{fc}^2 \quad \textbf{(3.41)}$$

and (3.40) becomes:

$$E[|dAF(s,t)|^2]_e = s_{fc}^2 \int\int_{S_{uv}} du\,dv \quad \textbf{(3.42)}$$

Noting that:

$$|AF(s,t)|_{\max} = \int\int_{S_{uv}} du\,dv \quad \textbf{(3.43)}$$

it can be written for the MIRAS case that:

$$\frac{E[|dAF(s,t)|^2]^{1/2}}{|AF(s,t)|_{\max}} = \frac{|d\overline{AF}|}{|AF|_{\max}} = 1.13\,10^{-2}\, s_{fc} \quad \textbf{(3.44)}$$

If the validity of this expression is extrapolated to the large value $\sigma_{\phi c}=67.2^o=1.17$rad, which, as seen before, is equivalent to a spatial displacement of 10 mm, the obtained value agrees in order of magnitude (around 1%) with the simulations performed in section 3.1.2.1 (around 0.5%).

3.1.2.3.- ANTENNA PATTERN PHASE ERRORS

If once again the fringe-wash effect is ignored and phase errors in the antenna radiation patterns are considered:

$$F_{ni}(\gamma,0) = F_n(\gamma,0)e^{j\Psi_i}$$

$$F_{ni}F_{nj}^{*} = F_n(\gamma,0)^2 \; e^{j[\Psi_i(\gamma,0)-j\Psi_j(\gamma,0)]} = F_n^2 \; e^{j\Psi_{ij}(\gamma,0)} \tag{3.45}$$

$$with \quad \Psi_{ii} = 0$$

Note that this formulation allows inclusion of channel phase offsets as a constant term independent of $(\gamma,0)$ in Ψ_i. The array factor is now:

$$AF(\gamma,\gamma';0,0') = \sum_i \sum_j W_{ij} \; e^{j2\pi[u_i(\gamma-\gamma')+v_j(0-0')]} \; e^{j\Psi_{ij}(\gamma',0')} \tag{3.46}$$

Proceeding as in the previous paragraph it can be obtained:

$$AF(\gamma,\gamma';0,0') = \int_{-1}^{1}\int_{-1}^{1} W(u,v) \; N(u,v;\gamma',0') \; e^{j2\pi[u(\gamma-\gamma')+v(0-0')]}\,du\,dv \tag{3.47}$$

and, for W(u,v)=1:

$$E\left[|AF(\gamma,\gamma';0,0')|^2\right] =$$

$$= \iint_{S_{uv}} E\left[N(u,v;\gamma',0')N(u',v';\gamma',0')\right]_e e^{j2\pi[(u-u')(\gamma-\gamma')+(v-v')(0-0')]}du\,dv\,du'\,dv' \tag{3.48}$$

The simplifying hypothesis, as before, is that the baseline phases are uncorrelated:

$$\langle N(u,v;\gamma',0')N(u',v';\gamma',0')\rangle_e = \delta(u-u')\delta(v-v')\langle N^2(u,v;\gamma',0')\rangle_e \tag{3.49}$$

Finally, it can reasonably be assumed that there are not preferred directions for the errors to happen:

$$E\left[N^2(u,v;\gamma',0')\right]_e = F_{N_a}^2 \tag{3.50}$$

and:

$$E\left[|AF(u,v;\gamma',0')|^2\right]_e = F_{N_a}^2 \iint_{S_{uv}} du\,dv \tag{3.51}$$

a result similar to (3.42). In fact, as pointed out above, (3.42) is a particular case of (3.51). Therefore, with a proper definition for the phase variance including averaging for both, the baselines and the directing cosines, the effects of phase errors in spatial resolution are equivalent to those of channel phase errors.

The effects of these errors have not been simulated, but from (3.51) and what has been said for channel errors it can be affirmed that, if they are kept to a level such that their effect on radiometric accuracy is acceptable (chapter 4), the effect on spatial resolution is completely negligible.

3.1.3.- CONCLUSIONS ABOUT SYSTEM'S SPATIAL RESOLUTION

The angular and spatial resolutions are computed by means of the equivalent array factor, which is originally formulated in [Ruf et al. 88] for a linear ideal interferometer. The array factor formulation has been extended to the two-dimensional case and to deal with system imperfections. It has been shown that the ideal array factor AF^o, which sets the theoretical limit to the spatial resolution, is mostly affected by the spatial decorrelation produced for off-boresight directions by the receivers' bandwidth B, while it is very tolerant to system's imperfections: antennas' positions, receivers and antennas' radiation pattern. Actually, an aperture synthesis interferometric radiometer like MIRAS designed to meet a requirement of 1-2 K radiometric resolution would show a negligible spatial resolution degradation beyond decorrelation effects, because small imperfections affect more the synthesized beam shape in the large area where it should be negligible allowing pixel contamination from the whole scene.

In the case of MIRAS, which operates in the band 1.400-1.427 MHz, bandwidth is actually limited by the band itself, and use of a maximum value of about 27 MHz (W=2%) which results in very limited spatial resolution degradation at the edge of a useful field of view of $\pm 23.6^o$: 5% for a Blackmann window. With the 20 MHz bandwidth actually under consideration this degradation is only 3.6%. Upon the Earth's surface, for a 31.2^o tilt angle with reference to nadir, resolution values range, depending on the window used to process the images, and on the observed direction within the FOV, from 18 to 40 km. Reaching the objective of 10 Km for the same tilt angle would require an instrument twice as large, with 17 m long arms and a largest dimension of 25 m.

3.2.- RADIOMETRIC SENSITIVITY COMPUTATION:

Radiometric sensitivity is computed as the minimum change at the input that can be detected at the output. There are two phenomena that limit the radiometric sensitivity: the discretization and finite coverage of the spatial frequencies plane (u,v), and the signal to noise ratio. As it is shown, signal to noise ratio can be basically improved by increasing the integration time and/or the pre-detection bandwidth, which is limited by decorrelation effects and by the allocated spectrum for passive observations. However, for high signal to noise ratios a saturation limit is reached due to the finite (u,v) coverage and the ringing (Gibbs phenomenon) introduced in the recovered modified temperature by the Fourier inversion process.

3.2.1.- Discretization and finite (u,v) coverage.

The antenna temperature measured by a total power radiometer is given by [Ulaby et al. 81]:

$$T'_A = \eta_l \eta_M \overline{T}_{ML} + \eta_l (1-\eta_M) \overline{T}_{SL} + (1-\eta_l) T_0 \qquad \textbf{(3.52)}$$

where η_l is the antenna efficiency, η_M is the main beam efficiency, defined as:

$$\eta_M = \frac{\iint_{main\ lobe} |F_n(\ell,m)|^2 \, d\Omega}{\iint_{4\pi} |F_n(\ell,m)|^2 \, d\Omega} \qquad \textbf{(3.53)}$$

T_{ML} is the average brightness temperature in the main beam, T_{SL} is the average brightness temperature in the secondary lobes and T_0 is the physical temperature of the antenna.

The antenna temperature measured by a lossless antenna, $\eta_l = 1$, is given by:

$$T'_A = \eta_M \overline{T}_{ML} + (1-\eta_M) \overline{T}_{SL} \qquad \textbf{(3.54)}$$

instead of the ideal one $T'_{A\ ideal} = T_{ML}$. In fact, the error in the antenna temperature measurement depends on the brightness temperature distribution of the scene. In either case, it can be minimized by maximizing the antenna main-beam efficiency by using antennas with a tapered current distribution, which in turn reduces the achievable spatial resolution.

An ideal aperture synthesis interferometer radiometer forms the brightness temperature map by an Inverse Discrete Inverse Fourier Transform of the visibilities sampled by the array. According to equation (3.18) the impulse response of the interferometer in the direction (ℓ_o, η_o) can be interpreted as the beam synthesized by the

array and its called the equivalent array factor (AF) [Ruf et al. 88],[Camps et al 95A]:

$$AF^{f}(\gamma,\gamma_o,0,0_o) = \sum_n W(u_n,v_n)\tilde{r}_n\left(-\frac{u\gamma - v0}{f_o}\right) e^{-j2\pi(u(\gamma-\gamma_o)-v(0-0_o))} \qquad \textbf{(3.55)}$$

According to equations (3.63) and (3.65) an equivalent antenna main-beam efficiency can be defined for the synthesized beam as:

$$0_M = \frac{\int\int_{main\ lobe} |AF^{f}(\xi,\eta)|^2\, d\Omega}{\int\int_{4\pi} |AF^{f}(\xi,\eta)|^2\, d\Omega} \qquad \textbf{(3.56)}$$

Note that in equation (3.56) the equivalent array factor is not squared since it is related directly to the modified temperature, which is a power measurement. 0_M can be maximized by windowing the visibility samples, as it is usual in Fourier techniques. Table 3.2 shows the side lobe level (SLL) and the main-beam efficiency (MBE) at the different power levels for the windows defined in table 3.1. These values have been computed for the MIRAS space borne instrument: an Y-array with 43 antennas per arm spaced 0.89 wavelengths and neglecting decorrelation effects.

Since the error induced by the secondary lobes depends on the brightness temperature scene, a number of simulations have been done to estimate more precisely its impact on the final radiometric sensitivity for a space borne interferometer. The modified temperature scene used in the simulations is shown in figure 3.15. The unit circle represents the visible space ($\gamma^2+0^2=\sin^2\theta$, $0\le\theta\le B/2$, $0\le N<2B$). The ellipsoidal contour represents the Earth-sky border as seen from a satellite 800 Km height with a tilt angle of 31.2º with respect to nadir.

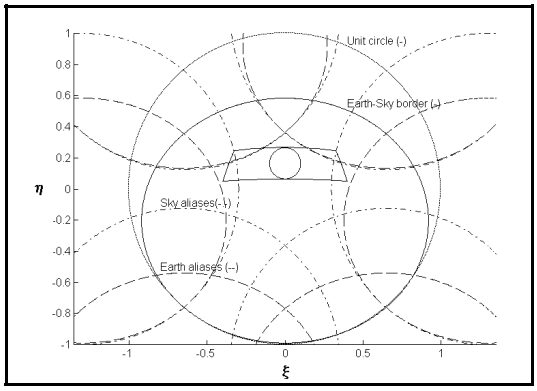

Figure 3.15.- *Unit circle, Earth-sky border and aliases.*

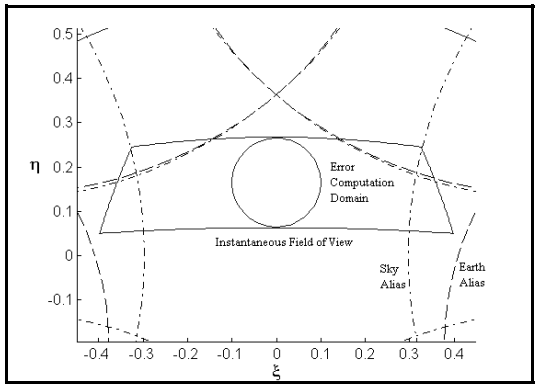

Figure 3.16.- *Earth-sky border and aliases. FOV of interest and error computation domain (zoom)*

The modified temperature of the Earth has been assumed to be constant and equal to 200 K. It should be noted that, since the spacing between the antennas does not satisfy the Nyquist criterion for the hexagonal (u,v) sampling, d > 1/%3 wavelengths (see chapter 6), Earth and sky aliases (dashed lines) are overlapped in the recovered brightness temperature distribution (see figure 3.16). Sky aliases can be removed by making use of "a priori" information: an approximately constant value of about 2-3 K at 1.4 GHz. However, Earth aliases can not be removed and significantly reduce the alias free field of view (FOV). The trapezoidal contour represents the region over the Earth with ground incidence angles ranging from 40º to 55º with respect to the surface's normal, for a 890 Km swath. The circle inside is the region where errors are computed. This circle was chosen because its distance to the swath extremes avoids the presence of the ringings (Gibbs phenomenon) induced by the overlapping aliases.

Discretization and finite (u,v) coverage errors have been computed as the average, for all the pixels lying in the circular region defined above, of the root mean squared error between the inverse Fourier Transform of the scene's visibilities and T_o. The advantage of this scene is that it has an analytical Fourier Transform. Consequently there are no numerical errors involved in the computation of the visibilities. Results are shown in table 3.5. Since signal to noise ratio is infinite, discretization errors can be viewed as the best radiometric sensitivity achievable by the interferometer.

N_{EL}	10	15	20	25	30	35	40
Rectangular	0.87	0.64	0.33	0.27	0.21	0.09	0.08
Barlett	2.94	1.96	1.45	1.16	0.97	0.83	0.73
Hamming	0.26	0.25	0.12	0.10	0.08	0.03	0.03
Hanning	0.23	0.22	0.11	0.09	0.07	0.03	0.03
Blackmann	0.13	0.12	0.07	0.05	0.04	0.02	0.01

Table 3.5.- *Discretization and finite coverage: Impact in radiometric sensitivity. (in K over a 200 K constant scene). N_{EL} is the number of antennas per arm of a Y-shaped array. Total number of antennas $N_T = 3.N_{EL} + 1$*

For a large array, such as MIRAS space borne instrument, with 43 antennas per arm, these errors are well below the typical radiometric sensitivity given by finite bandwidth and finite integration time and can be neglected. For a small array, as the MIRAS demonstrator with 3 antennas per arm, discretization errors can be much higher than finite integration time error and must be included in the radiometric sensitivity budget. Performing a power fitting of the data given in table 3.5, the following expressions can be obtained for the windows being studied:

$$\frac{\Delta T_{rect}}{T_0} \cdot \frac{0.294}{N_{EL}^{1.7}} \qquad \textbf{(3.57)}$$

$$\frac{\Delta T_{triang}}{T_0} \cdot \frac{0.149}{N_{EL}^{1.0}} \qquad \textbf{(3.58)}$$

$$\frac{\Delta T_{Hamming}}{T_0} \cdot \frac{0.115}{N_{EL}^{1.7}} \qquad \textbf{(3.59)}$$

$$\frac{\Delta T_{Hanning}}{T_0} \cdot \frac{0.105}{N_{EL}^{1.7}} \qquad \textbf{(3.60)}$$

$$\frac{\Delta T_{Blackmann}}{T_0} \cdot \frac{0.055}{N_{EL}^{1.7}} \qquad \textbf{(3.61)}$$

which are represented in figure 3.17 as a function of the number of antennas per arm, N_{EL}, for T_o = 200 K, a worst case situation.

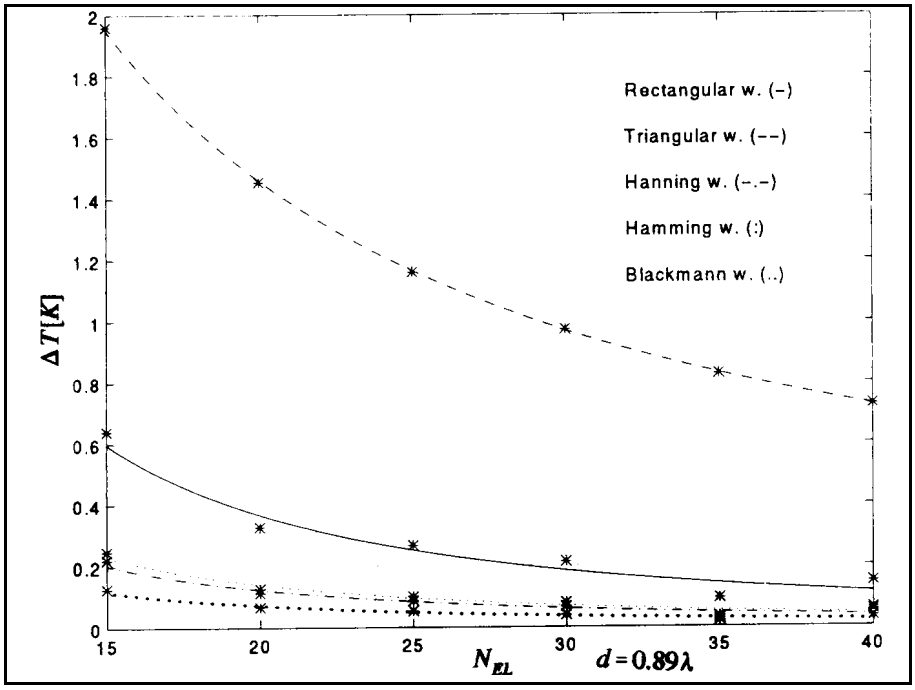

Figure 3.17.- *Discretization error vs.the number of antennas per arm of an Y-array.*

3.2.2.- Radiometric sensitivity computation

3.2.2.1.- Standard deviation in the visibility samples due to finite integration time

In our model of a coherent receiver real and imaginary parts of the visibility function are obtained by correlating the in-phase and quadrature components previously digitized with a 1 bit / 2 level quantization scheme:

$$V_{12}(u,v) = E\left[i_1(t)\, i_2(t)\right] + jE\left[q_1(t)\, i_2(t)\right] \qquad \textbf{(3.62)}$$

Radiometric sensitivity computation with this configuration leads to slightly different results from those presented in [Ruf et al. 88] for the one dimensional interferometer ESTAR, or in [Thompson et al. 86] [Tiuri 64] in radioastronomy. In our computations three effects not considered in [Ruf et al. 88] have been taken into account: pre-detection filters' shape: rectangular or gaussian, difference between the central filters' frequency (f_o) and the oscillator's frequency (f_{lo}) for the same pre-detection bandwidth and the use of analog or digital correlators.

Figure 3.18 shows the fringe-wash function for three kinds of filters: the equivalent low-pass filter for the 4 filters of MIRAS receivers explained above, a gaussian filter with the same noise bandwidth B:

$$H(f) = e^{-\frac{B}{2}\left(\frac{f}{B}\right)^2} \qquad \textbf{(3.63)}$$

and a rectangular filter with the same noise bandwidth B:

$$H(f) = \Lambda\left(\frac{f}{B}\right) \qquad \textbf{(3.64)}$$

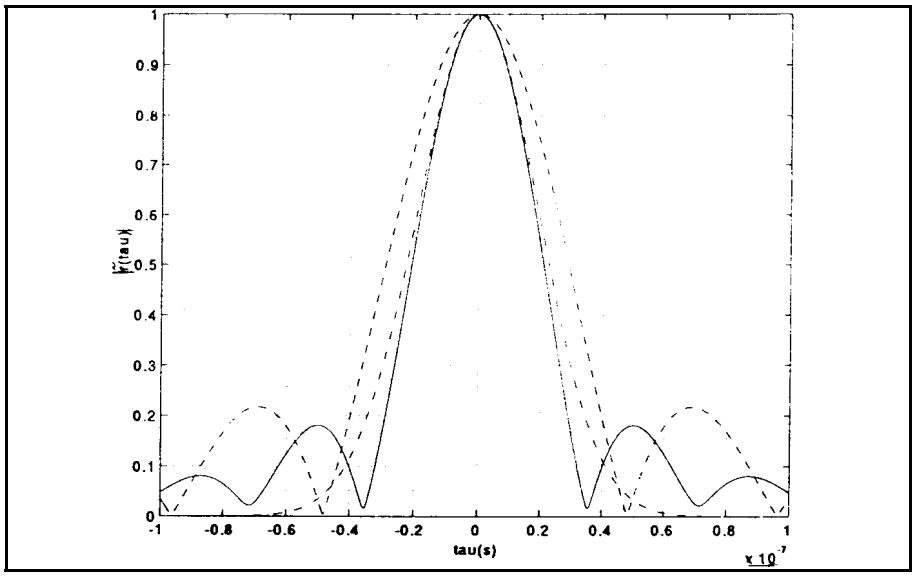

Figure 3.18.- *Fringe-washing functions for MIRAS bread-board filters (-), equivalent gaussian filter (-.-) and equivalent rectangular filter (--).*

For the decorrelation levels involved ($|J| \# 20$ ns) the gaussian filter fits very well the global response of the MIRAS receivers filters. Consequently, the radiometric sensitivity computation with gaussian filters is more accurate than with rectangular filters. Standard deviation in the real and imaginary parts of the visibility function are computed in Appendix 1. The steps are similar to those presented in [Ruf et al. 88] but

the analysis is performed for the in-phase and quadrature components. Results obtained for gaussian pre-detection filters are:

$$\sigma^2_{r,i} = \frac{1}{2\sqrt{2}B\tau_{eff}}\{(T_B + T_R)^2[1 + e^{-\left(\frac{2\pi f}{\sqrt{2}B}\right)^2}] + V^2_{r,i}(u,v)[1 + e^{-\left(\frac{2\pi f}{\sqrt{2}B}\right)^2}] - V^2_{i,r}(u,v)[1 - e^{-\left(\frac{2\pi f}{\sqrt{2}B}\right)^2}]\} \quad \textbf{(3.65)}$$

and for rectangular pre-detection filters:

$$\sigma^2_{r,i} = \frac{1}{2B\tau_{eff}}\{(T_A + T_R)^2\left[1 + \Lambda\left(\frac{2\pi f}{B}\right)\right] + V^2_{r,i}(u,v)\left[1 + \Lambda\left(\frac{2\pi f}{B}\right)\right] - V^2_{i,r}(u,v)\left[1 - \Lambda\left(\frac{2\pi f}{B}\right)\right]\} \quad \textbf{(3.66)}$$

where $2\pi f = \omega_o - \omega_{lo}$ and τ_{eff} is the effective integration time that depends on the kind of correlator (table 3.6):

Effective integration time	Correlator type
$\tau_{eff} = \tau$	analog or digital multibit
$\tau_{eff} = \tau / 2.46$	1 bit x 1 bit Sampling frequency = 2B
$\tau_{eff} = \tau / 1.82$	1 bit x 1 bit Sampling frequency = 4B
$\tau_{eff} = \tau / 1.57$	1 bit x multibit Sampling frequency = 2B
$\tau_{eff} = \tau / 1.32$	1 bit x multibit Sampling frequency = 4B
$\tau_{eff} = \tau / 1.29$	2 bit x 2 bit Sampling frequency = 2B
$\tau_{eff} = \tau / 1.14$	2 bit x 2 bit Sampling frequency = 4B

Table 3.6.- *Effective integration times for different correlator's type [Hagen and Farley 73].*

Examining equations (3.65) and (3.66) it can be seen that for the same RF bandwidth:

- Standard deviation with rectangular pre-detection filters is $\sqrt{2}$=1.41 times higher than with gaussian filters. Noise is more compacted in frequency for rectangular filters,

consequently it suffers less from decorrelation effects and produces a greater output for the same "signal" input power.

-For single side band (SSB) receivers (figure 3.19a) the standard deviation is about half its value for double side band (DSB) receivers (figure 3.19b), even though correlators with double bandwidth and power consumption will be needed. In practice the use of DSB receivers requires a careful design of the receiver in order to guarantee that radiation from local oscillator to the antenna is kept below the threshold of the signals received in the 1.400-1.427 MHz band, preserved for radio-astronomy uses.

- The use of digital correlators reduces the integration time (J) by a factor that depends on quantization levels and sampling frequency. Table 3.6 summarizes some of the properties of commonly used digital correlators [Hagen and Farley 73].

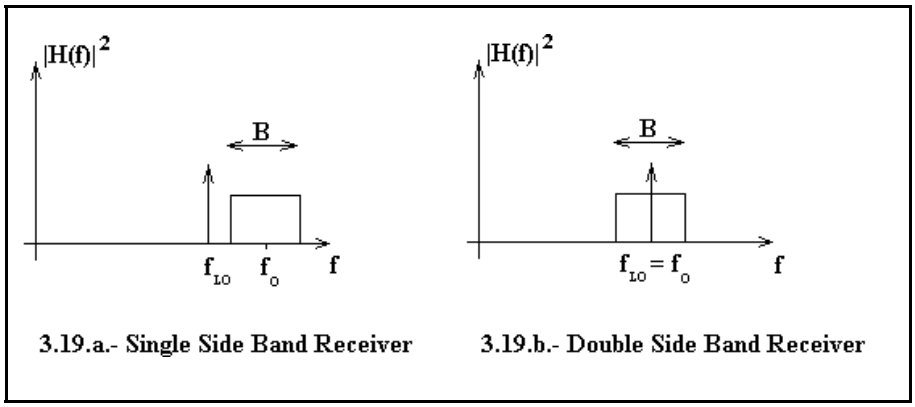

Figure 3.19.- *a) Single Side Band Receiver and b) Double Side Band Receiver*

For an ideal system, the modified temperature distribution can be obtained directly by an inverse Fourier transform of visibility samples. Errors in visibility values are translated into errors in the temperature distribution and, since the Fourier transform is unitary, the error norm is preserved.

$$\tilde{T}(\bar{>}) \text{ ' }) s \sum_{m} \sum_{n} W_{mn}\left[V(\bar{u}_{mn}) \% e_{V_r}(\bar{u}_{mn}) \% j e_{V_i}(\bar{u}_{mn})\right] e^{j2B(\bar{u}_{mn}\bar{>})} \qquad \textbf{(3.67)}$$

$$\bar{>} \text{ ' } (>,0); \quad \bar{u} \text{ ' } (u,v)$$

where (e_{Vr}, e_{Vi}) are the errors in the real and imaginary parts of the visibility function.

Prior to computation of radiometric sensitivity some considerations about *hermiticity* and *redundancy and correlation between errors* are made:

3.2.2.2.- Hermiticity of the visibility samples

Since the visibility function is hermitian, only half of the baselines must be measured (u$0, v$0 and u<0, v>0) :

$$V'(u,v) = \left\{\frac{1}{2} E\left[b_1(t)\ b_2'(t)\right]\right\}' = \frac{1}{2} E\left[b_2(t)\ b_1'(t)\right] = V(-u,-v) \qquad \textbf{(3.68)}$$

Consequently, the noise is hermitian too.

3.2.2.3.- Redundancy and correlation between errors

The cross-correlation of the errors of two identical baselines 1-2 and 3-4 with the same integration time T_{int}, one of them delayed J, is (appendix 2):

$$E\left[\Delta V_{12}(t-\mathrm{J})\ \Delta V_{34}'(t)\right] = R_{\hat{V}_{12}\hat{V}_{34}}(\mathrm{J}) \approx V_{12}V_{34}' = \frac{V_{13}V_{24}'}{BT_{int}}\ sinc\left(\frac{\mathrm{J}}{T_{int}}\right) \qquad \textbf{(3.69)}$$

This expression is still valid if the two baselines share an antenna, or even both of them. In this latter case the expression for the baseline noise is recovered. Note that in an actual on-board interferometer like MIRAS all baselines are measured in the same time interval and J = 0. Given its importance, let's explicitly show that the noise of a visibility sample can be obtained from (3.69):

$$E\left[\left|\Delta V_{12}\right|^2\right] = R_{\Delta V_{12}\ \Delta V_{12}}(0) = \frac{V_{11}V_{22}'}{BT_{int}} + \frac{\left|V(0,0)\right|^2}{BT_{int}} + \frac{(T_A+T_R)^2}{BT_{int}} \qquad \textbf{(3.70)}$$

From (3.69), it can be seen that with ideal noise-free receivers, errors between simultaneous measurements (J = 0) of different visibility samples are strongly correlated if the spacing between antenna pairs 1-2 and 3-4 is much smaller than the downfall of the module of the visibility function. This happens for scenes consisting on point sources [Bará et al. 95B]. In this situation averaging simultaneous measurements does not improve signal to noise ratio.

On the contrary, for a smooth temperature distribution, as in the case of remote sensing of the Earth, the visibility function decays rapidly and errors are only partially correlated (depending on the temperature distribution and its frequency contents) and averaging reduces significantly the noise power.

On the other hand, if there is a mixer as the first stage of the receiver's chain, receiver's noise temperature is usually much higher than the brightness temperature to

be measured. Therefore, the averaging of simultaneous measurements improves the signal to noise ratio, even for scenes consisting of point sources, due to the reduction of receiver's noise. However, in Earth observation at low microwave frequencies, receiver's noise temperature (T_R . 80 K) can be much less than the average brightness temperature (T_A . 250 K) and the benefits of averaging simultaneous measurements are only reduced receiver's noise. A detailed analysis of redundancy and its improvement on radiometric sensitivity requires a specific array configuration and scene under observation, but noise reduction will never be as high as predicted in [Ruf et al. 88]:

$$) T_{no\ \ redundancy} ' \frac{T_B \% T_R}{\sqrt{BJ}} \sqrt{N_V} 6 \;) T_{\substack{redundancy \\ uncorr\ \ errors}} ' \frac{T_B \% T_R}{\sqrt{BJ}} \sqrt{c \% \ln N_V} \qquad \textbf{(3.71)}$$

where: N_V stands for the total number of visibilities.

3.2.2.4.- Redundancy in Y-arrays and its impact on the radiometric sensitivity

Y-shaped arrays provide a very low degree of redundancy [MMS 95], [Bará et. al 95B] [Bará et al. 96A]. If the three central elements introduced in MIRAS for the purpose of phase calibration are disregarded, only baselines between antennas on the same arm can be redundant. By the zero baseline it is understood that corresponding to u=v=0, which in MIRAS is non-redundant, because it is measured by a dedicated total power radiometer. For the Y-shaped array with 3 arms, each with N_{EL}=43 elements, plus a central element, there are:

-Total number of baselines: $3N_{EL}(3N_{EL}+1)/2+1 = 8386$ (the extra one corresponding to V(0,0))

-Non-redundant baselines = non-redundant (u,v)-points: $3N_{EL}^2+3N_{EL}+1 = 5551$ (three are formed by the central antenna and those at the ends of the arms and one is the zero baseline)

-Redundant (u,v)-points: $3(N_{EL}-1) = 126$, with different degrees of redundancy.

-Total number of (u,v)-points: $3N_{EL}^2+4+3(N_{EL}-1) = 3N_{EL}^2+3N_{EL}+1 = 5677$

Recall that when the Hermitian property is considered every (u,v)-point is actually duplicated.

It means that 8386 - 5551 = 2709 correlations (visibilities) lead to 126 (u,v) points. Assuming uncorrelated errors between these visibility samples, the use of the available redundant visibility samples in a Y-array has a negligible impact over the radiometric sensitivity, less than 1% for a 43 antennas per arm Y-array (appendix 3). Consequently, for computational purposes, it is assumed that the visibility errors are uncorrelated from sample to sample:

$$E\ [(e_{v_{r\,m\,n}} \% j e_{v_{i\,m\,n}})\ (e_{v_{r\,p\,q}} \% j e_{v_{i\,p\,q}})^{(}] \bullet 0; \quad m \ldots p,\ n \ldots q \qquad \textbf{(3.72)}$$

The snap-shot radiometric sensitivity can be computed as:

$$\Delta T(\bar{x}) = \Omega_{ant} \Delta s \sum_m \sum_n W_{mn} [\, e_{V_r}(\bar{u}_{mn}) + j\, e_{V_i}(\bar{u}_{mn}) \,] e^{j\,2p\,(\bar{u}_{mn}\bar{x})} \tag{3.73}$$

$$\Delta T^2(x,h) = E[\Delta T(x,h)\Delta T(x,h)^*] =$$

$$= \Omega_{ant}^2 \Delta s^2 [\, \sum_m \sum_n W_{mn}^2 (\, s_{r\,mn}^2 + s_{i\,mn}^2 \,) +$$

$$+ 2 \sum_{\substack{u_m>0,\, v_n\geq 0 \\ u_m\leq 0,\, v_n>0}} \sum W_{mn}^2 (\, s_{r\,mn}^2 - s_{i\,mn}^2 \,) \cos(\, 4p\, (\, u_{mn} x + v_{mn} h \,) \,] \tag{3.74}$$

which can be approximated by:

$$\Delta T(x,h) \approx \Omega_{\text{ant}}\; A \frac{T_A + T_R}{\sqrt{B\, t_{eff}}}\, a_w \frac{a_{OL}}{a_F} \sqrt{N_V} \tag{3.75}$$

where the LO factor is given by ($\Delta f=0$ for DSB or $\Delta f \geq B/2$ for SSB in (3.65) or (3.66)):

$$\begin{aligned} a_F &= 2^{\frac{1}{4}} = 1.19;\ \textit{for gaussian predetection filters} \\ a_F &= 1;\ \textit{for rectangular predetection filters} \end{aligned} \tag{3.76}$$

the filter factor is given by ((3.65) or (3.66)):

$$\begin{aligned} a_F &= \sqrt{2} = 1.41;\ \textit{for DSB receivers} \\ a_F &= 1;\ \textit{for SSB receivers} \end{aligned} \tag{3.77}$$

and the windowing factor is defined as:

$$a_w = \sqrt{\frac{\sum_m \sum_n W_{mn}^2}{N_V}} \tag{3.78}$$

In the MIRAS case:

$$\Delta s = \frac{\sqrt{3}}{2} d^2;\ N_V = 6\ N_{EL}^2 + 6\ N_{EL} + 1 \tag{3.79}$$

Table 3.7 gives the values of the α_w factor for the 5 windows used and a Y-shaped array.

Window	η_w
Rectangular	1
Triangular	0.5212
Hamming	0.5717
Hanning	0.5446
Blackmann	0.4517

Table 3.7.- *Window factors for a Y-shaped array with 43 antennas per arm.*

Note that the weighting function attenuates visibility samples between distant antennas, where signal-to-noise ratio is worse. Radiometric sensitivity is improved at expenses of a loss in the spatial resolution. It should be pointed out that when obtaining the brightness temperature map, the antenna pattern amplifies the error for pixels off the radiation's pattern maximum:

$$T(\ell,m) = \frac{I(\ell,m)}{|F_n(\ell,m)|^2} \sqrt{1-\ell^2-m^2} \qquad \textbf{(3.80)}$$

MIRAS space borne snap-shot radiometric sensitivity can then be computed using equations (3.74-3.79) with the following parameters [MMS 95]:

. Y-array with 43 antennas per arm, generating 11.353 non-redundant visibility samples
. Antenna spacing d=0.89 wavelengths
. Bandwidth: 20 MHz
. Pre-detection filters' central frequency: 1.410 MHz
. Oscillator frequency: 1.395 MHz
. Snap-shot integration time: 0.3 seconds
. Effective integration time: 0.122 seconds (1 bit x 1 bit digital correlators)
. Receivers' noise temperature: 80 K
. Antenna temperature: 100 K $\leq T_A \leq$ 300 K

With these figures the radiometric sensitivity is bounded by:

$$\begin{aligned} 7.08\,K \leq \Delta I^{Interf\ Radiom}_{Rectangular} \leq 14.98\,K \\ 3.20\,K \leq \Delta I^{Interf\ Radiom}_{Blackmann} \leq 6.77\,K \end{aligned} \qquad \textbf{(3.81)}$$

Figure 3.21 shows the snap-shot radiometric sensibility in decibels ($10\log(\Delta T)$ [dBK]) as a function of the signal-to-noise ratio defined as:

$$\frac{S}{N} = 10\log\frac{V(0,0)}{F_V} = 10\log\frac{T_A}{F_V} \qquad \textbf{(3.82)}$$

for parameters given above.

$$31.6\ dB\ \#\ \frac{S}{N}^{*}_{MIRAS}\ \#\ 33.2\ dB \qquad \textbf{(3.83)}$$

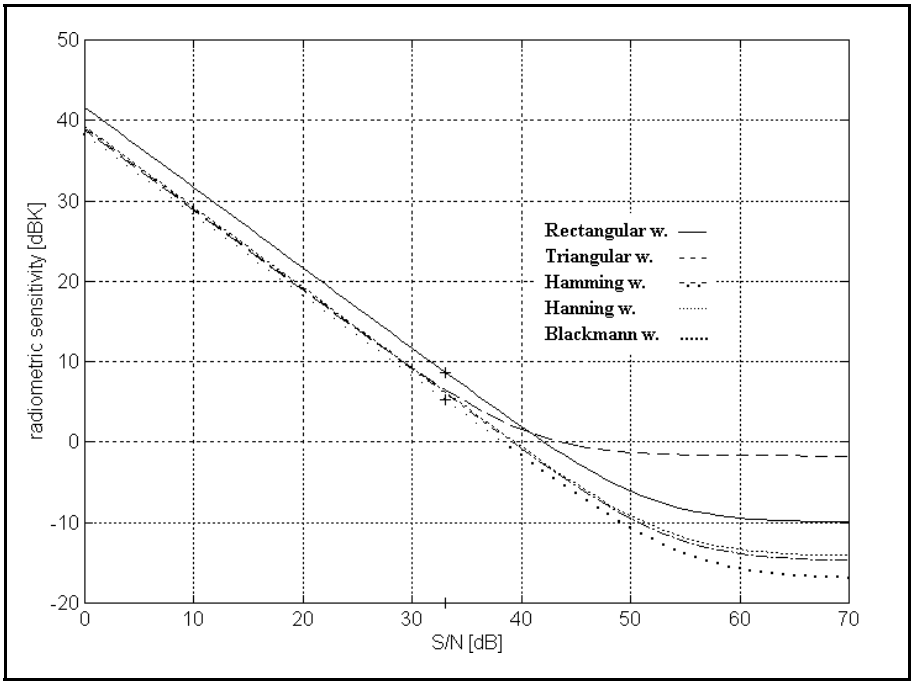

Figure 3.21.- *Radiometric sensitivity in dBK vs. signal-to-noise ratio for MIRAS space borne instrument and* T_{Earth} *= 200 K*

3.2.3.- Radiometric sensitivity improvement by pixel averaging.

In a 2-D interferometric radiometer, radiometric sensitivity can be improved by means of "pixel averaging". "Pixel averaging" means that, since a pixel remains in the Field Of View (FOV) for a long time, the recovered brightness temperature values can be averaged after proper correction of the incidence angle dependence.

In the MIRAS case, a pixel remains in the FOV for about:

$$J \cdot \frac{FOV\ width}{platform\ velocity} \cdot \frac{165\,Km}{7\,Km/s} \cdot 22\,s \qquad \textbf{(3.84)}$$

from which 11 seconds correspond to each polarization. The improvement on the radiometric sensitivity in each polarization is:

$$\frac{)T_{pixel\ avg}}{)T_{snap\&shot}} \cdot \sqrt{\frac{11\,s}{0.3\,s}} \cdot 6 \qquad \textbf{(3.85)}$$

In a single polarization instrument the improvement is 6%2. These

improvements can be achieved because *non-simultaneous measurements are independent* and the error is reduced by the square root of the number of measurements. Equivalently the integration time has been increased by the same factor.

The final expected worst case radiometric sensitivity values for an space borne interferometric radiometer as MIRAS are (dual polarization instrument):

$$\Delta T^{Interf\ Radiom}_{Rectangular} \approx 2.50\,K \quad after\ pixel\ averaging$$

$$\Delta T^{Interf\ Radiom}_{Blackmann} \approx 1.13\,K \quad after\ pixel\ averaging$$

which are close to the values obtained by total power or Dicke radiometers.

3.3.- SPATIAL RESOLUTION VS. RADIOMETRIC SENSITIVITY: THE INTERFEROMETRIC RADIOMETER UNCERTAINTY EQUATION.

The comparison between the radiometric sensitivity of the interferometer radiometer and that of a total power radiometer must be performed in homogeneous terms since their underlying principles are different: 2-D interferometer radiometers image all the FOV simultaneously, while total power radiometers image only the pixel pointed by the antenna.

In order to fix the ideas MIRAS parameters are used. For proposed orbit for MIRAS platform there are $N^2_{ant}=130^2=16.900$ pixels [Camps et al. 95A] [Camps et al. 96A], 8.689 of them in the alias free FOV. An ideal total power radiometer imaging only the alias free FOV pixels with the same spatial resolution and null steering delays would have a maximum integration time of:

$$\tau_{pixel} = \frac{\tau}{8689} = 34.5\mu s \qquad \textbf{(3.86)}$$

leading to a worst case radiometric sensitivity of :

$$\Delta T^{TPRad}_{pixel} = \frac{T_{sys}}{\sqrt{B\tau_{pixel}}} = \frac{T_A + T_R}{\sqrt{B\tau_{pixel}}} = 14.5K \approx \Delta T^{IntRad}_{rectangular} = 14.98\,K \qquad \textbf{(3.87)}$$

which is very close to the snap-shot radiometric sensitivity of the interferometer radiometer when the rectangular window (no windowing) is used. In fact, the slight difference is due to the fact that the pixels are not 100% independent. The basic hexagonal period defined by the 6 points of the star (u,v) domain (figure 3.2) is not complete and has missing visibility samples that enlarge a little the synthesized beam.

The improvement on the radiometric sensitivity given by windowing can be also

understood as a spatial averaging with neighbor pixels. In fact, the sensitivity improvement by windowing is approximately related to the half-power beamwidths given in [Camps et al. 95B] by:

$$\frac{\Delta T_{rectangular}^{Int\ Rad}}{\Delta T_{W}^{Int\ Rad}} = \frac{1}{\alpha_W} \approx \frac{\Delta x_{W}^{-3dB}}{\Delta x_{rectangular}^{-3dB}} \tag{3.88}$$

Consequently, *the product* $\Delta T.\Delta x_{-3dB,W}$ *is a constant.* Let us compute its value for an Y-shaped array. The half-power beam width without weighing function is approximately (equation 3.8):

$$\Delta x_{rectangular}^{-3\ dB} \approx \frac{\pi}{4\sqrt{3}\ N_{EL} d} \tag{3.89}$$

the product $\Delta T.\Delta\xi_{-3dB,\,W}$ is then:

$$\begin{aligned} \Delta T\,\Delta x_{-3dB,W} &\approx \Omega_{ant}\,\frac{\sqrt{3}}{2} d^2\,\frac{T_A + T_R}{\sqrt{B\,\tau_{eff}}}\,\alpha_w \frac{\alpha_{ol}}{\alpha_F}\sqrt{N_V}\,\frac{1}{\alpha_w}\,\frac{\pi}{4\sqrt{3}\,N_{EL} d} \\ &\approx \Omega_{ant}\,\frac{\sqrt{3}\,\pi}{\sqrt{2}\,4}\,\frac{T_A + T_R}{\sqrt{B\,\tau_{eff}}}\,\frac{\alpha_{ol}}{\alpha_F} \quad \left(N_{EL} << 1\right) \end{aligned} \tag{3.90}$$

which can be approximated by:

$$\Delta T\,\Delta x_{-3\ dB,W} \approx \Omega_{ant}\,\frac{T_A + T_R}{\sqrt{B\,\tau_{eff}}}\,\frac{\alpha_{ol}}{\alpha_F}\,d \tag{3.91}$$

Equation (3.91) is the *Interferometric Radiometer Uncertainty Equation*. It states that the product of the radiometric sensitivity ΔT by the 2D angular resolution $\Delta\xi_{-3dB}$ is a constant that depends only on receivers and correlators parameters. It is the interferometric radiometer version of the total power radiometer uncertainty equation given in (6.149) of [Ulaby et al. 81].

3.4.-CONCLUSIONS

In this chapter the concept of the Array Factor -the impulse response of the synthetic aperture interferometric radiometer- has been generalized from its original form [Ruf et al. 88], to two-dimensional arrays and to deal with spatial decorrelation effects, system imperfections and the effect of windowing. The spatial resolution has been evaluated as the half-power synthesized beam-width of the equivalent array factor. It is found that the ideal array factor AF^o sets the theoretical limit to spatial resolution which is mainly degraded by the decorrelation produced for off-boresight directions by the receivers' bandwidth B (AF^f) and it is very tolerant to system imperfections: antennas' positions, receivers and antennas' radiation pattern.

In the case of a Y-array with 43 antennas per arm spaced 0.89 λ, with Blackmann windowing, the half-power beamwidth of the AF^f is 1.14º in the radial direction and 1.10º in the azimutal direction. The projection of the AF^f beamwidth over the Earth's surface produces a spot ranging from 25.6 x 25.2 Km^2 to 41.8 x 40.3 Km^2, for on-ground incidence angles of 55º and 40º respectively, and from a 800 Km height orbit.

The radiometric sensitivity analysis presented in [Ruf et al. 88] has been revised and extended to a 2-D interferometric radiometer. New parameters have been included: i) the impact of the filters' shape has been analyzed in two ideal situations, rectangular and gaussian filters, ii) the use of SSB/DSB receivers and iii) the kind of correlator used. Numerical simulations have shown that the fringe-washing function of real filters is better fitted by equivalent gaussian filters than by rectangular ones. The snap-shot, $\tau = 0.3$ s, radiometric sensitivity is found to be about 3.2 K - 6.8 K in the MIRAS case for the Blackmann windowing. Its improvement by means of pixel averaging has been also analyzed and particularized for the MIRAS instrument and the proposed orbit. An improvement by a factor of 6 is found if all the available time is shared between V and H polarizations.

Finally, the *new Interferometric Radiometer Uncertainty Equation* has been derived. It states that the product of the radiometric sensitivity by the spatial resolution is a constant that depends only on the kind of receivers and correlators and can be interpreted as an improvement on the radiometric sensitivity by windowing the visibility samples at the expense of an spatial averaging of the recovered modified temperature pixels.

Chapter 4. Impact of System Imperfections on the Radiometric Accuracy

This chapter presents a detailed analysis of system imperfections in a two-dimensional aperture synthesis radiometer and their impact on the radiometric accuracy defined as the radiometric error obtained when the radiometric sensitivity is zero (infinite integration time). Their impact on the spatial resolution has shown to be negligible (chapter 3). This new analysis is required since the available literature about the performance of interferometric radiometers is scarce and reduces to radioastronomy [Thompson and D'addario 82] [Thompson et al. 86], the 1-D ESTAR experiment [Ruf et al. 88], [LeVine et al. 89], [LeVine 90], [Ruf 1991], [Tanner and Swift 93] and the MIRAS prototype [Goutoule et al. 94], [Martín-Neira et al. 94].

In radioastronomy, the scenes observed are very small portions of the sky, most of them consisting on point sources with a nearly constant module spatial Fourier transforms, or visibilities. These features allow to use highly directive antennas whose pattern can be precisely known in the Field Of View (FOV). In addition, antennas can be spaced many wavelengths without aliasing problems in the image reconstruction process, with negligible antenna coupling. In addition, many baselines can be generated with a single pair of antennas by using the Earth rotation synthesis which leads to systematic errors that can be accounted for.

On the other hand, from a low orbit, the Earth appears as a wide thermal source filling almost completely the FOV. To cope with it and to avoid image blurring due to satellite motion a complete set of measurements must be obtained in a small fraction of time, by a large number of small antennas whose pattern must be completely known in all the FOV [Bará et al. 96A], [Camps et al. 96B]. In addition, to avoid aliasing these antennas must be closely spaced, increasing the coupling between adjacent antennas and the number of antennas and receivers needed to satisfy the spatial resolution requirements. All these features complicate the analysis of the global performance of this instrument, as well as the calibration procedures [Torres et al. 96B] and the reconstruction algorithms [Camps et al. 95A], [Bará et al. 96A], [Camps et al. 96B].

4.1.- RECEIVER DESCRIPTION

In an amplitude interferometer, measurements are obtained by correlating a number of voltage signal pairs coming from different antennas. Each complex correlation provides a sample of the visibility function. Consequently, the basic receiver requires two channels and a complex correlator to compute each visibility sample, as the one shown in figure 4.1. The receiver is modelled as a system with only an equivalent filter at its input, which sets the receiver noise bandwidth. In our experimental interferometer there are a band-pass and a low-pass filters and a DC block placed before the digital correlators. In the MIRAS bread-board design there are three filters: the spurious band-pass filter, the image band-pass filter, the low-pass filter and the DC-block before the digital correlators (not shown in figure 4.1).

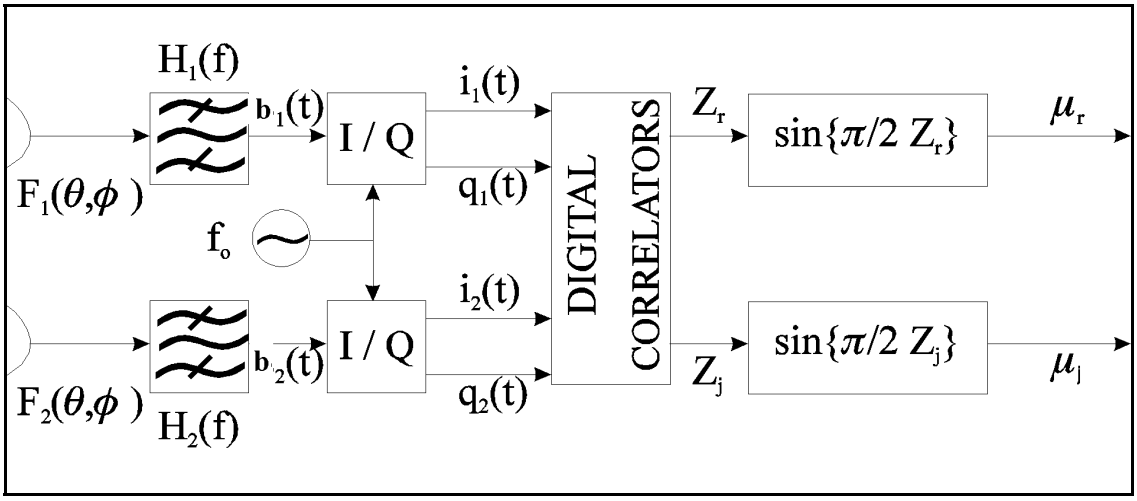

Figure 4.1.- *Interferometric radiometer error model.*

The signal at the output of the antennas is a narrow-band gaussian noise. It can be written as:

$$b_1(t) = S_1(t)\cos(\omega_0 t + \phi_1(t)) \qquad \textbf{(4.1)}$$

where $S_1(t)$ is its amplitude and $\phi_1(t)$ its phase. This form is very useful to model receiver non-idealities.

At the output of the I/Q demodulator the RF signal $b_1(t)$ is down-converted and its baseband components can be written as (figure 4.2):

$$\begin{aligned} i_1(t) &= S_1(t)\cos(\phi_1(t)) \\ q_1(t) &= S_1(t)\sin(\phi_1(t)) \end{aligned} \qquad \textbf{(4.2)}$$

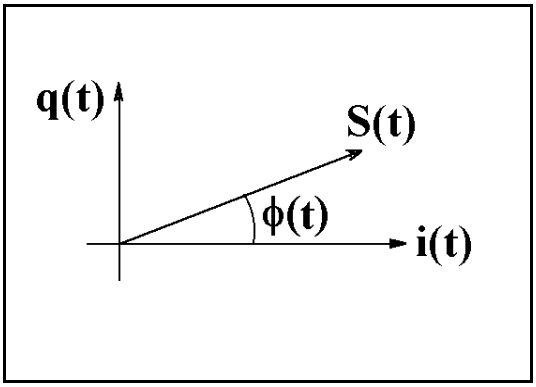

Figure 4.2.- *I/Q vector diagram.*

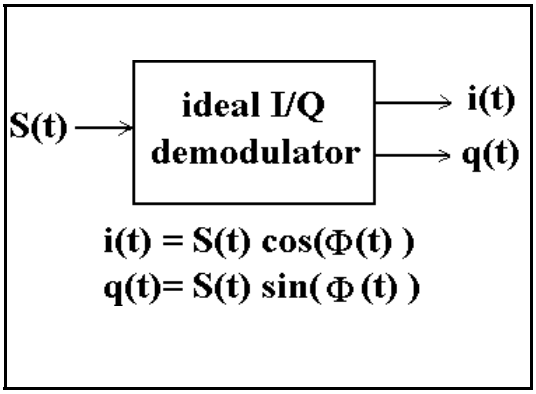

Figure 4.3.- *Ideal I/Q demodulator.*

This demodulation is made for each channel (antenna + receiver) in the system. So, in the basic two-channel receiver model, there are four signals: two in-phase and two quadrature baseband real signals. In MIRAS the in-phase and quadrature components of the channels are the input for a matrix of 1 bit/2 levels (1B/2L) digital correlators, which can assume the required bandwidth and can be packed with a high degree of integration and low power consumption. The proper correlation of these signals leads to a sample of the complex visibility function. Nevertheless, as the correlations are made by an 1B/2L digital correlator, the outputs Z_r and Z_i are not yet the actual correlation between the two signals, but an intermediate magnitude from which the desired correlations can be obtained [Hagen and Farley 73]:

$$\mu_r = \sin\left(\frac{\pi}{2} Z_r\right) \qquad \mu_i = \sin\left(\frac{\pi}{2} Z_i\right) \tag{4.3}$$

Note that 1B/2L correlators measure the normalized visibility function, as:

$$\mu_r = \frac{E\left[i_1(t)\, i_2(t)\right]}{\sqrt{E\left[i_1(t)\, i_1(t)\right] E\left[i_2(t)\, i_2(t)\right]}} = \frac{V_r(u,v)}{\sqrt{T_A T_R}}$$
$$\mu_i = \frac{E\left[i_1(t)\, q_2(t)\right]}{\sqrt{E\left[i_1(t)\, i_1(t)\right] E\left[q_2(t)\, q_2(t)\right]}} = \frac{V_i(u,v)}{\sqrt{T_A T_R}} \tag{4.4}$$

Where the following relationships between the visibility function V_{12}, the analytic signals $b_{1,2}$ (t), the complex envelope $e_{1,2}$ (t), the signals' amplitude $S_{1,2}$ (t) and phase $N_{1,2}$ (t) have been used:

$$V_{12} = \frac{1}{2} E\left[b_1(t)\, b_2^{*}(t) \right]$$

$$V_{12} = \frac{1}{2}\left[R_{i_1 i_2}(0) + R_{q_1 q_2}(0) \right] + j\,\frac{1}{2}\left[R_{q_1 i_2}(0) - R_{i_1 q_2}(0) \right] \quad \textbf{(4.5)}$$

$$b_{1,2}(t) = S_{1,2}(t) e^{j f_{1,2}(t)} e^{j w_0 t} = e_{1,2}(t) e^{j w_0 t}; \qquad e_{1,2}(t) = i_{1,2}(t) + j\, q_{1,2}(t) \quad \textbf{(4.6)}$$

$$S_{1,2}(t) = \sqrt{i_{1,2}^2(t) + q_{1,2}^2(t)} \qquad f_{1,2}(t) = \operatorname{arctg}\left(\frac{q_{1,2}(t)}{i_{1,2}(t)} \right) \quad \textbf{(4.7)}$$

as shown in the figure 4.2.

In addition, since zero mean, gaussian band-pass symmetric random signals satisfy that:

$$R_{i_1 i_2}(0) = R_{q_1 q_2}(0) \quad R_{i_1 q_2}(0) = -R_{q_1 i_2}(0) \quad \textbf{(4.8)}$$

a reduction by a factor of two in the number of real correlators is obtained. By inserting equation (4.9) in (4.6):

$$V_{12} = R_{i_1 i_2}(0) + j\, R_{q_1 i_2}(0) \quad \textbf{(4.9)}$$

which can also be written in terms of separate amplitude and phase terms as:

$$V_{12} = E[S_1(t)\, S_2(t)]\, E[\cos f_1(t) \cos f_2(t)] + j\, E[S_1(t)\, S_2(t)]\, E[\sin f_1(t) \cos f_2(t)] \quad \textbf{(4.10)}$$

Where $S_{1,2}$ and $\phi_{1,2}$ are uncorrelated random variables. Equation (4.10) is very useful when studying amplitude and phase errors. The baseline zero V(0,0) = T_A is assumed to be the same for all the antennas and it is measured by an extra antenna connected to a total power radiometer.

4.2.- ERROR CLASSIFICATION AND STRATEGY TO COMPUTE THE RADIOMETRIC ACCURACY.

The assessment of the performance of an Earth observation interferometric radiometer instrumental errors, related to non-idealities of system components, can be grouped in: i) antenna errors, ii) receiver channel errors, iii) and baseline errors. All the errors appear in the samples of the measured visibility function, which will be called $\mathbf{V}^{\mathbf{raw}}$. However, each error is produced at different position in the receiving chain: antennas, receivers, I/Q demodulators and correlators (figure 4.1), and, accordingly, they can be classified in different groups. This classification is very important when establishing a calibration procedure because it determines which errors can be corrected with a particular calibration procedure and the order in which these errors must be

removed (chapter 5). Errors that can not be calibrated at all or cannot be perfectly calibrated by a specific method remain as residual errors and reflect the upper bounds allowed at each part, in order to satisfy the specified performance. These bounds are the basis to elaborate the system's specifications table at the end of this chapter.

i) Antenna errors affect the exploration of the scene and require *perfectly* known scenes to be calibrated, otherwise, some of them can be on ground measured and included in the inversion algorithm. Antenna imperfections are the antenna pattern phase and gain ripples, the antenna coupling, antenna pattern pointing errors, position errors and the cross-polarization. Some of these errors can be grouped together into antenna voltage pattern errors, but they are treated separately to study their different impact on the radiometric accuracy.

ii) Channel errors appear as *separate factors or addends* at the visibility samples and require antenna-based calibration procedures. These errors are due to in-phase channel errors - filters' phase, time delays... -, I/Q demodulators quadrature errors, and channel gain errors.

iii) Baseline errors *cannot be separated into gain factors or phase addends* related to antenna channel parameters and require baseline-based calibration procedures requiring the injection of correlated noise to all the antennas simultaneously. These kind of errors are due to phase errors -filters response mismatches-, gain errors -filters response mismatches-, offset errors -correlation of common unwanted signals... -, channel delay errors appearing inside the fringe-wash factor, channel frequency responses.

The calibration of the system must be periodically performed on flight when drifts exceed these pre-established upper bounds. The computation of the calibration period is out of the scope of this study and would require a detailed knowledge of the temperature control in orbit and circuit temperature and aging drifts. Errors that are not going to be calibrated on flight must be minimized by: i) an accurate system implementation (accurate manufacturing process and use of accurate components) and ii) on ground calibration and drift minimization.

The general equation relating the visibility function and the modified brightness temperature and the characteristics of the receivers and the antennas:

$$V_{12}(u,v) \text{ ' } K_{12} \text{ mm} \frac{T(>,0)}{\sqrt{1\&>^2\&0^2}} F_{n_1}(>,0) F_{n_2}{}^{(}(>,0) \tilde{r}_{12}\left(\&\frac{u>\%v0}{f_o}\right) e^{\&j2B(u>\%v0)\frac{f_{12}}{f_o}} d>d0$$

(4.11)

reduces to a Fourier Transform (u,v) < > (>, 0):

$$V(u,v) \text{ ' } F\left[\text{I}(>,0)\right]; \qquad \text{I}(>,0) \text{ ' } \frac{T(>,0)}{\sqrt{1\&>^2\&0^2}} *F_n(>,0)*^2 \qquad \textbf{(4.12)}$$

in the ideal case (no decorrelation effects $\tilde{r}_{12}(J) \text{ ' } 1$, identical receivers $f_{12}=f_0$, $K_{12}=K$, and identical antenna patterns $F_{ni} = F_{nj} = F_n$).

The study of all the errors is performed by computing their separate impact on the radiometric accuracy for a reference scene consisting of a modified brightness temperature distribution inside the Earth-sky border of 200 K (figure 4.4) and 0 K outside it:

$$\text{I}(>,0) \text{ ' } \frac{T_B(>,0)}{\sqrt{1\&>^2\&0^2}} \text{ '} 200K; \quad (>,0) \text{ d } earth(>,0)$$

$$earth(>,0): \left(\frac{>}{a}\right)^2 \%\left(\frac{0\%0_0}{b}\right)^2 \# 1 \qquad \textbf{(4.13)}$$

$$a \text{ ' } 0.888, \; b \text{ ' } 0.760, \; 0_0 \text{ ' } 0.234$$

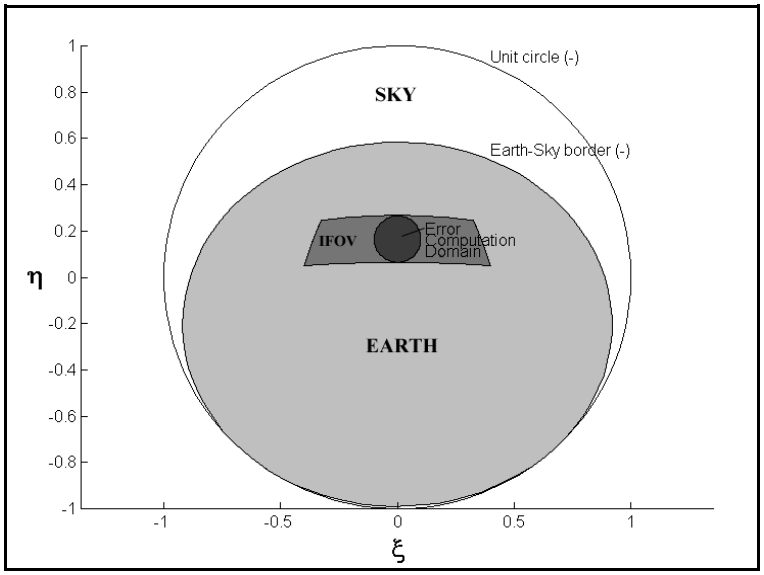

Figure 4.4.- *Error computation cicle, Instantaneous FOV and Earth-sky border for the Y-shaped configuration and d=0.89* 8 antenna spacing.

The recovered temperature distribution is given by the inverse Fourier Transform:

$$\hat{I}(\gamma,0) \;=\; F_H^{-1}\left\{ W(u,v)\; V^{raw}(u,v) \right\} \qquad \textbf{(4.14)}$$

where W(u,v) is a 2D-window (table 3.1) and the inverse Fourier Transform of the contaminated visibilities is performed over the (u,v) hexagonal grid given by the Y-array and its reciprocal $(\gamma,0)$ reciprocal basis as explained in chapter 6 [Camps et al. 95A], [Camps et al. 96A]. Fringe-wash effects are neglected since its main effect is a small broadening of the synthesized beam in the radial direction. The error is computed as the root mean squared value of the difference between the recovered modified temperature and (4.13) for all the pixels lying inside the small circle in the FOV:

$$\Delta I \;=\; \sqrt{\frac{1}{M-1}\sum_{l=1}^{M}\left[\hat{I}(\gamma_l,0_l)-I(\gamma_l,0_l)\right]^2} \qquad \textbf{(4.15)}$$

It should be pointed out that the radiometric accuracy for the modified temperatures obtained from the ideal visibility samples are not zero, but they are the discretization error already studied in chapter 3. The impact over the radiometric accuracy of the aliasing due to subsampling, $d>1/2$ for Y-arrays, is treated in chapter 6, as well as a technique to minimize its impact over the alias-free FOV.

4.3.- ANTENNA ERRORS

The study of the impact of antenna errors over the radiometric accuracy requires a complete set of raw visibility samples to be computed and Fourier inverted. According to the present MIRAS space borne design each Y-arm has 43 antennas, plus a central one and three extra antennas for calibration purposes. In this case, the number of visibility samples to be computed is $3N_{EL}^2+3N_{EL}+1=5.677$, because the visibility function is an hermitian function. Each visibility sample must be obtained by means of a two-dimensional numerical integration of equation (4.11) and it supposes a serious obstacle due to the excessive computing time. However, these errors are multiplicative errors and, as it is shown hereafter, simulation results for a reduced number of antennas per arm can be extrapolated for a larger array. This statement is supported by the fact that the instrument is observing an extended thermal source, the Earth, whose visibility function has an important decline when extending over the (u,v) plane and an increase in the number of antennas adds visibility samples with very small values. Since multiplicative errors are proportional to the visibilities values, the error committed in the recovered brightness temperature distribution does not differ noticeably when the (u,v) coverage is large enough. For the reference modified temperature distribution of (4.13), the following numbers corroborate this assumption:

i) Y-array with 43 antennas per arm plus the central one:

$$\sum_{n}\sum_{m} \# V(u_n,v_m)\#^2 \; ' \; 2.0670\cdot 10^5 \qquad \textbf{(4.16)}$$

ii) Y-array with 15 antennas per arm plus the central one:

$$\sum_{n}\sum_{m} \#V(u_n,v_m)\#^2 \; ' \; 2.0666\cdot 10^5 \qquad \textbf{(4.17)}$$

Visibility samples in equations (4.16) and (4.17) have been computed directly from the Fourier Transform of (4.13). Computing time and memory requirements are strongly reduced down to 12.7 %, while the extrapolation error is about 0.7 %. Numerical evaluations for 20 antennas per arm have also been performed, and confirm this assumption.

4.3.1.- Antenna Pattern Errors

The correct measurement of all the visibility samples requires that all the antennas have the same radiation pattern, which is technologically unfeasible due to mechanical tolerances. These differences affect the amplitude and the phase of the antenna voltage patterns:

$$F_{n_k}(>,0) \; ' \; F_n(>,0)[1\%) F_{n_k}(>,0)] \; e^{j) N_{n_k}(>,0)} \qquad \textbf{(4.18)}$$

$F_{nk}(>,0)$ is the radiation voltage pattern of antenna k, $F_n(>,0)$ is the average radiation voltage pattern of all the antennas, $) F_n(>,0)$ and $N_{nk}(>,0)$ are the voltage amplitude and phase errors.

4.3.1.1.- Theoretical analysis

The impact of antenna amplitude and phase errors over the visibility samples is derived in appendix 1 and the main result is reproduced here:

$$\begin{aligned} &) V_{kl} \; . \;) S_{\&3dB} \; E_{kl}(u_{kl},v_{kl}) \; T_A \\ & E_{kl}(u,v) \; ' \; \mathop{mm}_{>^2\%0^2\#1} \; ,_{kl}(>,0) \; e^{\&j2B(u>\%v0)} \; du \; dv \\ & ,_{kl}(>,0) \; ' \;) F_{n_k}(>,0)\%) F_{n_l}(>,0)\% j( ) N_k(>,0)\&) N_l(>,0)) \end{aligned} \qquad \textbf{(4.19)}$$

Equation (4.19) states that, provided the visibility function has a rapid decline, *the error induced in the visibility sample (u_{kl}, v_{kl}) by the antenna voltage patterns is proportional to the antenna temperature and the sample (u_{kl}, v_{kl}) of the Fourier transform*

of the antenna pattern cross-error $,_{kl}(>,0)$ (equation 4.19).

At this point, the temperature error and the radiometric accuracy can be computed from the visibility error by assuming that visibility errors are uncorrelated except for a sample and its complex conjugate:

$$)I(>,0) \;'\; A \sum_m \sum_n W_{mn})V_{mn}e^{j2B(u_{mn}>\%v_{mn}0)}$$
$$F^2_{)I} \;'\; <*)I*^2> \;.\; A^2 \sum_m \sum_n W^2_{mn}<*)V_{mn}*^2> \qquad \textbf{(4.20)}$$

where $<>$ is the expectation operator and A is the (u,v) pixel area: $\%3d^2/2$ for hexagonal sampling,Y-arrays and triangular arrays, and d^2 for rectangular sampling (T-arrays). In the following sections each antenna error is analyzed separately.

4.3.1.2.- Antenna pattern phase and amplitude ripple: numerical analysis

In this section antenna pattern phase error are first analyzed: $)N_k \neq 0$, $)F_k=0$. The simulations performed make use of an expression for $)N_{nk}(>,0)$ which approximates the experimental measurements made for three X-band cup-dipole antennas (figure 4.5):

$$)N_k(>,0) \;'\; A_k \cos\,(16\;B\;\sqrt{>^2\%0^2}\;\%\;N_k) \qquad \textbf{(4.21)}$$

which represents a phase ripple along the radial direction in the (>,0) plane, A_k is the amplitude ripple and N_k is an aleatory displacement in (>,0) in order to randomize the phase ripple origin. The number of ripple periods has been chosen to meet the measured phase patterns (figure 4.5). It should be pointed out that these antennas have been manufactured at 10.8 GHz, while MIRAS cup-dipoles operate at 1.4 GHz and mechanical tolerances less critical. Consequently, the curves shown in figure 4.5 must be considered a really worst case for 1.4 GHz cup-dipoles.

The radiometric accuracy sensitivity to antenna phase error is shown in table 4.1 as a function of the window used: the rectangular, the triangular or Barlett, the Hanning, the Hamming and the Blackmann one with rotational symmetry and extended up to the maximum (u,v) sample being measured. Parallel studies concerning inversion algorithms have shown the superior performance of the Blackmann window in terms of robustness and noise reduction. *The numerical results presented make use of the* ***Blackmann window*** *unless specified*. Series of simulations for Y-arrays with 20 antennas per arm have also been performed confirming the multiplicative nature of the errors and their impact over the radiometric accuracy allowing to extend these results to larger arrays. According to the

sensitivity shown in table 4.1, the maximum antenna phase error allowed to obtain a 0.5K radiometric accuracy is about $F_{Ak} = 0.34º$ for an average brightness temperature of 200K.

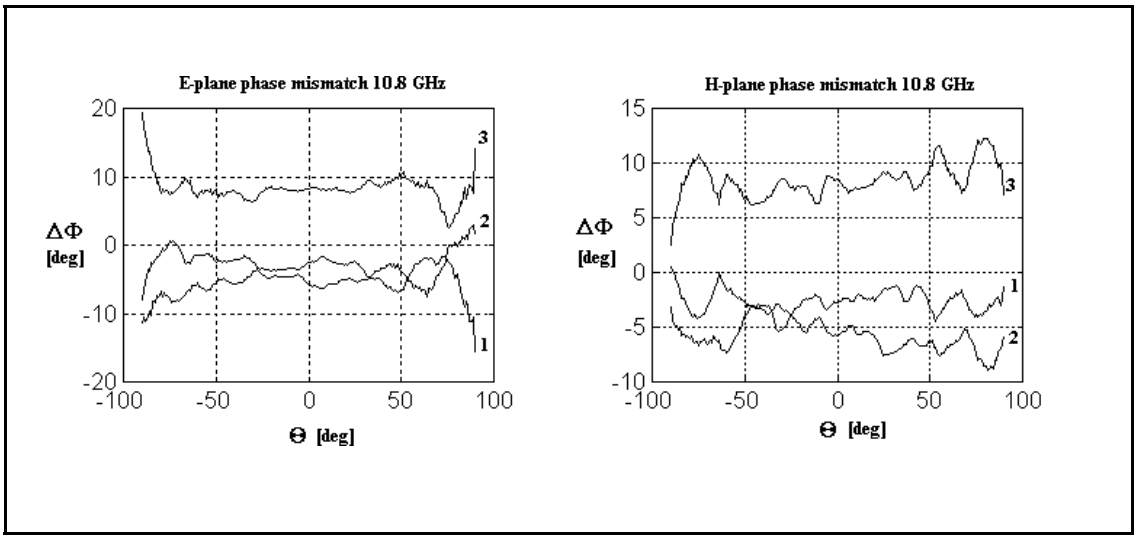

Figure 4.5.- *X-band cup-dipole antenna voltage pattern phase ripples (cup-dipoles # 1, 2 and 3)*

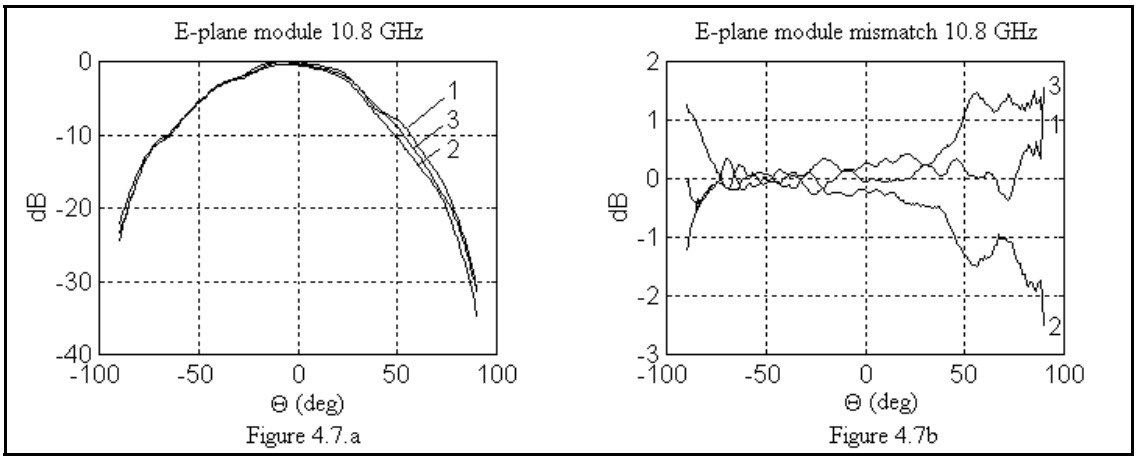

Figure 4.6.- *a) X-band cup-dipoles E-place module, b) X-band cup-dipoles E-place module mismatch*

In a similar way, different antenna pattern gains are modelled as (figure 4.6):

$$F_{n_k}(\theta,0) = A_k \cos(16 \cdot \sqrt{\theta^2 + 0^2} + N_k) \qquad \textbf{(4.22)}$$

where A_k and N_k have the same meaning than for the phase ripple error.
According to the computed sensibility to antenna pattern amplitude errors (table 4.1), the maximum antenna amplitude ripple that can be allowed is about $F_{Ak} = 0.005 = 0.5\%$ in order to obtain a 0.5 K radiometric resolution for an average scene of 200 K.

4.3.1.3.- Antenna pointing errors

Pointing errors are the third source of antenna radiation voltage pattern errors and they can be generated by a mechanical misalignment or by an electrical phase error, such as that produced by the mechanical construction of the cup-dipoles which forces a dipole arm to be slightly higher than the one connected to the shielding (appendix 10).

Cup-dipoles antenna gain pattern that can be fitted very well by the following expression:

$$*F_n(2)*^2 \ ' \ \cos^3(2) \qquad \textbf{(4.23)}$$

where 2 is the angle with respect the Z axis. This antenna pattern has a directivity of 9dB such as that of the cup-dipoles. With pointing errors, expression (4.23) becomes:

$$F_n(>,0) \ ' \ \left[>\sin(2_o)\cos(\mathsf{N}_o)\%0\sin(2_o)\sin(\mathsf{N}_o)\%\sqrt{1\&>^2\&0^2}\cos(2_o)\right]^{\frac{3}{2}} \qquad \textbf{(4.24)}$$

where $(2_o,\mathsf{N}_o)$ represents the direction of the antenna radiation pattern maximum's.

Computed sensitivities are summarized in table 1 for the different windows, as a function of the standard deviation of the angle 2_o, the angle N_o being uniformly distributed over [0, 2B]. According to the 0.15º antenna pointing accuracy that can be attained [MMS 1995], the radiometric accuracy is 0.2 K for an average scene of 200 K.

4.3.2.- Antenna position errors.

The mechanical structure of the Y-array consists of 3 arms joined at one extreme (figure 3.1). The cross-section of the arms is rectangular and the resonant frequencies in the plane of the array (X,Y) and in the perpendicular direction (Z) are not necessary equal. Accelerations/decelerations of the platform during its orbit, as well as thermal effects (dilations/contractions) produce oscillations of the arms around their balance points. The amplitude of these vibrations are kept low enough to guarantee the correct performance of the instrument. The study can then be simplified to the first resonant mode:

$$\begin{aligned} d\bar{r}(s,t) \ ' \ & A_{ip_{\max}}\sin\left(\frac{\mathsf{B}}{2l}s\right)\sin(")\sin(\mathsf{T}_{rip}t\%\mathsf{N}_{ip})\ \hat{x}\ \% \\ & \%A_{ip_{\max}}\sin\left(\frac{\mathsf{B}}{2l}s\right)\cos(")\sin(\mathsf{T}_{rip}t\%\mathsf{N}_{ip})\ \hat{y}\ \% \\ & \%A_{op_{\max}}\sin\left(\frac{\mathsf{B}}{2l}s\right)\ \sin(\mathsf{T}_{rop}t\%\mathsf{N}_{op})\ \hat{z} \end{aligned} \qquad \textbf{(4.25)}$$

where $A_{ip\ max}$ and $A_{op\ max}$ are the maximum in-plane and off-plane amplitudes of the oscillations in each arm, s is the radial distance to the joining point of the arms, " is the angle of the arm with the X axis, $T_{r,ip}$ and $T_{r,op}$ are the in-plane and off-plane resonant frequencies of the arm, and $N_{ip}$and N_{op} are their corresponding the phases.

These oscillations induce a phase modulation in the measured voltage that produces an uncertainty in the position of the antennas and in the baseline being measured (appendix 5):

$$
\begin{aligned}
) u \ ' \ )_x \sin\left(\frac{T_{rip} J}{2} \% 2_x\right) sinc(f_{rip} J) \\
) v \ ' \ )_y \sin\left(\frac{T_{rip} J}{2} \% 2_y\right) sinc(f_{rip} J) \\
) w \ ' \ )_z \sin\left(\frac{T_{rop} J}{2} \% 2_z\right) sinc(f_{rop} J)
\end{aligned}
\qquad \textbf{(4.26)}
$$

where the formulas relating $)_x$, $)_y$, $)_z$, 2_x, 2_y, 2_z to the mechanical parameters $"_{1,2}$, $N_{ip1,2}$, $N_{op\ 1,2}$, $A_{ip\ 1,\ 2}$ and $A_{op\ 1,2}$ are developed in appendix 5. This uncertainty can be canceled if the integration time is a multiple of the least common multiple of the in-plane and off-plane resonant periods, which is not possible because in the initial design the resonant frequencies are f_{rip}= f_{rop}= 0.4 Hz and the integration time is limited to J = 0.30s to avoid image blurring. However, baseline uncertainty can be reduced by averaging consecutive measurements during the time the pixel remains in the FOV: 22 seconds, 11 seconds at each polarization.

The computed radiometric accuracy sensibility to off-plane position errors is given in table 4.1 for different windows. Since the maximum amplitude of the oscillation is guaranteed to be 5 mm for the space-borne instrument [MATRA 1995] the expected radiometric accuracy is $)T$=0.0006 cm^{-1} . 0.5 cm . 200 K = 0.06 K for a 200 K constant test scene. The analysis for in-plane position errors is performed in a similar way. The corresponding radiometric accuracy sensibilities are shown in table 1 for different windows. The expected radiometric accuracy is $)T$=0.0010 cm^{-1} . 0.5 cm . 200 K = 0.10 K for a 200K constant test scene.

4.3.3.- Antenna V/H cross-polarization

In the present design [MATRA 1995] only one set of visibilities at horizontal or vertical polarization is computed at each time interval by switching the V/H antennas preventing from calibration of V/H cross-polarization errors. These errors must then be upper bounded by a proper design:

$$\hat{T}_H = (1-\varepsilon_{HV})T_H + \varepsilon_{HV}T_V$$
$$\hat{T}_V = (1-\varepsilon_{HV})T_V + \varepsilon_{HV}T_H \qquad \textbf{(4.27)}$$

The cross-polarization factor ε_{HV} is contributed by: i) the antenna cross-polarization ratio, which is the dominant term for the cup-dipoles proposed for MIRAS [MATRA 1995] ε_{HV}=25 dB = 3.10^{-3} and ii) the error induced by the antenna pointing accuracy ε_{HV}=$\sin^2(0.15^o)$. 7.10^{-6} [MATRA 1995]. Accuracy errors can be upper bounded by ΔT_H=0.16 K and ΔT_V=0.63 K, assuming T_{Hmax} = 300 K and T_{Vmax} = 200 K.

Sensitivity $\frac{\partial T/T}{\partial F_{error}}$	**Rectangular**	**Triangular**	**Hamming**	**Hanning**	**Blackmann**
Ant. pattern phase ripple	0.0120 /º	0.0065 /º	0.0092 /º	0.0089 /º	**0.0074 /º**
Ant. pattern amplit. ripple	0.84	0.52	0.65	0.63	**0.53**
Ant. pattern pointing error	0.0085 /º	0.0054 /º	0.0068 /º	0.0067 /º	**0.0064 /º**
Off-plane position error	0.0046 /cm	0.0037 /cm	0.0049 /cm	0.0049 /cm	**0.0046 /cm**
In-plane position error	0.0019 /cm	0.0013 /cm	0.0010 /cm	0.0010 /cm	**0.0010 /cm**

Table 4.1.- *Radiometric accuracy sensibility to antenna errors*

4.3.4.- Antenna coupling

In some interferometric radiometry fields, i.e. radio-astronomy, the effect of antenna coupling is usually negligible due to several reasons: the antennas are usually very directive and, because of the small angular extension of the scenes being imaged, the distance between the antennas is usually large. On the other hand, interferometric radiometers devoted to Earth observation require closely spaced antennas with a large half-power

beamwidth to cope with the large FOV without aliasing problems in the image formation process. In [Ruf 1991] it is stated that the interference pattern in the ESTAR unidimensional interferometric radiometer is not sinusoidal because of antenna coupling and multiple reflections in the array structure. Errors are analyzed through the distorted interference patterns and the G matrix inversion method. However, the Fourier-based inversion techniques envisaged for large two-dimensional arrays as MIRAS [Camps et al. 1995][Martín-Neira et al. 1996] require further analysis in order to analyze antenna coupling errors and possible calibration methods.

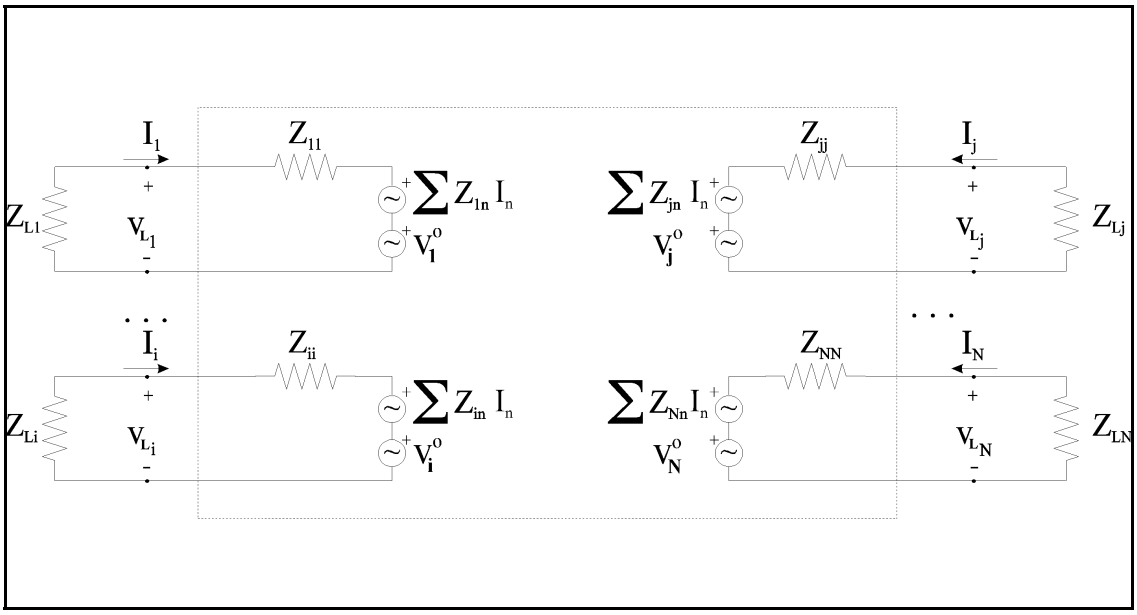

Figure 4.7.- *Circuit model for analyzing antenna coupling effects.*

Figure 4.7 shows the circuit model of the antenna array. The array is treated as a multiport where each port corresponds to an antenna. The particular values of Z_{mm} *and* Z_{mn} depend on the geometry, as well as on the antenna distance and their relative orientation and *must be measured when all the antennas are mounted in the array:*

$$Z_{mm} = \frac{v_m}{i_m}\Big|_{i_p = 0 \text{ } \forall p \neq m} \quad ; \quad Z_{mn} = \frac{v_m}{i_n}\Big|_{i_p = 0 \text{ } \forall p \neq n} \qquad \textbf{(4.28)}$$

In this way, measured input and mutual impedances take into account the effect of the mechanical structure and their coupling. The voltage $v_{L\,m}$ is the voltage measured at the load connected to port "m" affected by load mismatches and coupling, while v^{o}_{m} is the voltage that would be measured at the "m" port when all the antennas where open-circuited, the assumption underlying the derivation of equation (2.61) [Thompson et al. 1986]. The visibilities corresponding to (2.61) are named $V^{(1)}$, while those that are measured with

antenna coupling errors are named $V^{(2)}$. The voltage generators lump together the effect coupling over a particular antenna. The relationship between the "load" and ideal "°" voltages can be derived from:

$$\begin{bmatrix} v_{L_1} \\ v_{L_2} \\ \vdots \\ v_{L_N} \end{bmatrix} = \begin{bmatrix} Z_{11} & Z_{12} & \cdots & Z_{1N} \\ Z_{21} & Z_{22} & \cdots & Z_{2N} \\ Z_{N1} & Z_{N2} & \cdots & Z_{NN} \end{bmatrix} \begin{bmatrix} i_1 \\ i_2 \\ \vdots \\ i_N \end{bmatrix} + \begin{bmatrix} v_1^o \\ v_2^o \\ \vdots \\ v_N^o \end{bmatrix}; \qquad \textbf{(4.29)}$$

$$\overline{v_L} = \overline{\overline{Z}}\,\bar{i} + \bar{v}^o$$

$$\begin{bmatrix} i_1 \\ i_2 \\ \vdots \\ i_N \end{bmatrix} = \begin{bmatrix} v_{L_1}/Z_{L_1} \\ v_{L_2}/Z_{L_2} \\ \vdots \\ v_{L_N}/Z_{L_N} \end{bmatrix} \qquad \textbf{(4.30)}$$

by substituting (4.30) in (4.29) and isolating for the load voltages:

$$\begin{bmatrix} v_1^o \\ v_2^o \\ \vdots \\ v_N^o \end{bmatrix} = \begin{bmatrix} 1+\frac{Z_{11}}{Z_{L_1}} & \frac{Z_{12}}{Z_{L_2}} & \cdots & \frac{Z_{1N}}{Z_{L_N}} \\ \frac{Z_{21}}{Z_{L_1}} & 1+\frac{Z_{22}}{Z_{L_2}} & \cdots & \frac{Z_{2N}}{Z_{L_N}} \\ \cdots & \cdots & \cdots & \cdots \\ \frac{Z_{N1}}{Z_{L_1}} & \frac{Z_{N2}}{Z_{L_2}} & \cdots & 1+\frac{Z_{NN}}{Z_{L_N}} \end{bmatrix} \begin{bmatrix} v_{L_1} \\ v_{L_2} \\ \vdots \\ v_{L_N} \end{bmatrix}; \qquad \textbf{(4.31)}$$

$$\bar{v}^o = \overline{\overline{C}}\,\overline{v_L}$$

$$\overline{v_L} = \overline{\overline{C}}^{-1}\,\bar{v}^o$$

which states that the measured voltage is a linear combination of the open-circuit voltages. Consequently, the ideal and the measured visibilities are related by the $\overline{\overline{C}}$ matrix according to:

$$\overline{\overline{V}}^{(2)} = \frac{1}{2Z_o} E\left[\overline{v_L}\ \overline{v_L}^H\right] = \overline{\overline{C}}^{-1} \frac{1}{2Z_o} E\left[\bar{v}^o\ \bar{v}^{oH}\right] \left(\overline{\overline{C}}^{-1}\right)^H = \overline{\overline{C}}^{-1}\,\overline{\overline{V}}^{(1)} \left(\overline{\overline{C}}^{-1}\right)^H \qquad \textbf{(4.32)}$$

where $b_i(t)$ in (4.1) is by definition: $b_i(t) \bullet v_{Li}(t) / \sqrt{Z_o}$ (not to be confused with a travelling voltage wave).

In order to point out the significance of equation (4.32), let us assume that we have an array formed by two equal antennas satisfying $Z_{11} = Z_{22}$, $Z_{12} = Z_{21}$ and $Z_{L1} = Z_{L2}$. With these assumptions, the visibility sample that would be measured between antennas 1-1, $V_{11}^{(2)}$, and between antennas 1-2, $V_{12}^{(2)}$, can be computed from (4.32) as:

$$V_{11}^{(2)} = \frac{1}{\left| \left(1 + \frac{Z_{11}}{Z_L}\right)^2 - \frac{Z_{12}}{Z_L^2} \right|^2} \left\{ -2\Re\left[\left(1 + \frac{Z_{11}}{Z_L}\right) \frac{Z_{12}^*}{Z_L^*} V_{12}^{(1)} \right] + \left[\left| 1 + \frac{Z_{11}}{Z_L} \right|^2 + \left| \frac{Z_{12}}{Z_L} \right|^2 \right] T_A \right\} \quad \textbf{(4.33)}$$

$$V_{12}^{(2)} = \frac{1}{\left| \left(1 + \frac{Z_{11}}{Z_{L1}}\right)^2 - \frac{Z_{12}}{Z_L^2} \right|^2} \left\{ -2\Re\left[\left(1 + \frac{Z_{11}}{Z_L}\right) \frac{Z_{12}^*}{Z_L^*} \right] T_A + \left| \frac{Z_{12}}{Z_L} \right|^2 V_{12}^{(1)*} \left| 1 + \frac{Z_{11}}{Z_L} \right|^2 V_{12}^{(1)} \right\} \quad \textbf{(4.34)}$$

where we have make use of $V_{11}^{(1)} = V_{22}^{(1)} = T_A$. Equation (4.33) reveals that zero-spacing visibility sample $V_{11}^{(2)}$, which should be constant, contains the spatial frequency $V_{12}^{(1)}$. On the other hand, equation (4.34) reveals that the spatial frequency sample $V_{12}^{(2)}$ is contaminated with an offset term proportional to the antenna temperature $T_A = V_{11}^{(1)}$. While the visibility sample $V_{12}^{(1)}$ of an extended thermal source decreases at least at a $1/\rho = \lambda/r$ rate, due to the abrupt contrast between the sky and the Earth, this offset term decreases with the inverse of the antenna spacing as 1/r, because of the factor Z_{12}, and may be an important error source. These analytical results justify the shape of the interference patterns shown in [Ruf 1991]. In a more general situation, equation (4.32) reveals that the measured visibilities are a linear combination of all the visibilities that can be synthesized by the array, enlarging the spatial frequency bandwidth, by transferring power from the smallest baselines to the larger ones, and inducing high frequency artifacts in the recovered brightness temperature distribution [Bará et al. 1996]. At the same time the decoupled visibility samples can be obtained from the coupled ones if we manage to compute or measure the $\overline{C}$ matrix. The number of antennas in the array has an obvious influence on the coupling effect: the more antennas, the greater the coupling, but extra antennas added at the end of the Y-arms have an almost negligible effect due to the smaller coupling.

In the preceding analysis sinusoidal signals have been assumed instead of band-limited thermal noise, because of the low coupling and the small transit time between coupled antennas (J # 3 ns, $d_{1\text{-}2}$ # 0.9 m, B = 20 MHz, f_o = 1.4 GHz), with a negligible impact over decorrelation effects (0.99#*r̃(J)*#1). For high coupling antennas, such as parallel half wavelength dipoles, an exact analysis including decorrelation effects in the transit time between far antennas can be carried out by including the transit delay between antennas in the currents (equation (4.29)).

In order to evaluate the impact of antenna coupling and residual calibration errors on the radiometric accuracy two series of numerical simulations have been carried out. Simulation parameters are: 15 antennas per arm, X-band cup-dipoles measured mutual and self-impedances data and Blackmann windowing. The radiometric accuracy sensibility to coupling errors has been computed for two cases: i) antenna coupling is not calibrated at all ( ) T_1/T), and ii) antenna coupling is calibrated assuming that all the parameters have their nominal values ( ) T_2/T).

The first series of simulations assumes that: i) the load impedances are random gaussian variables with Z_L = 50S mean and $F_{)Z^L}$ = 2S standard deviation, and ii) the parameters of the $\overline{\overline{Z}}$ matrix are random gaussian variables with mean their corresponding measured value, and a variable standard deviation which is a percentage of the mean value $F_{)Zmn}$ = " Z_{mn}. Numerical simulations have been performed varying the parameter " in the range [0, 0.3]:

$$\frac{)T_1}{T} \;.\; 0.058; \qquad)T_1 \;.\; 11.6K^*_{T_o'200K}$$

$$\frac{)T_2}{T} \;.\; 0.0034\%0.041"; \qquad)T_2 \;.\; 0.7K^*_{T_o'200,"'0} \qquad \textbf{(4.35)}$$

$$)T_2 \;.\; 1K^*_{T_o'200,"'4\%}$$

That is, even for low coupling antennas such as these cup-dipoles, $|S_{12}|$ # -30 dB for d=0.98 (appendix 11), uncalibrated antenna coupling errors degrade significantly the radiometric accuracy which exhibits a negligible dependence on the variation of the input and self-impedances. On the other hand, the calibration of antenna coupling errors reduces the residual radiometric accuracy by a factor of 10 even the parameters have drifted: $F_{)Z^L}$ = 2S and "=4%.

The second series of simulations assumes that the load impedances have their nominal value Z_L=50S, and the parameters of the $\overline{\overline{Z}}$ matrix vary as above:

$$\frac{)T_1}{T} \;.\; 0.056; \qquad)T_1 \;.\; 11.2K^*_{T_o\,'\,200K}$$

$$\frac{)T_2}{T} \;.\; 0.0004\%0.069\,"; \qquad)T_2 \;.\; 0.08K^*_{T_o\,'\,200,"\,'\,0} \qquad \textbf{(4.36)}$$

$$)T_2 \;.\; 1K^*_{T_o\,'\,200,"\,'\,7\,\%}$$

That is, the effect of uncalibrated antenna coupling errors over the radiometric accuracy is: similar and an ideal calibration may reduce the error down to the discretization threshold [Bará et al. 1996], or a larger incertitude in the measurement of the input and mutual impedances is allowed (7%) for a 1 K radiometric accuracy .

4.3.5.- Summary of antenna errors

In this section a general procedure to analyze the major problems associated with the antenna subsystem in a synthetic aperture interferometric radiometer has been presented. It has been found that most of the requirements can be satisfied with the available technology: i) positioning ( ) T < 0.16 K), ii) pointing accuracy ( ) T = 0.19 K) and iii) cross-polarization ratios ( ) T_H . 0.16 K and) T_V . 0.63 K). However, antenna voltage patterns and coupling effects are critical and require a calibration procedure or their correction during the inversion algorithm.

It has been demonstrated that mismatches between a pair of antenna voltage patterns "k"-"l" produce an error in the visibility sample $V(u_{kl}, v_{kl})$ being measured which is approximately proportional to the antenna temperature and to the (u_{kl}, v_{kl}) spectral component of the error of the product of the two antenna voltage patterns. Closely matched antenna radiation voltage patterns (0.5 % in amplitude and 0.34º in phase) are required for a 0.5 K radiometric accuracy. However, antenna patterns can be measured with this precision to be included in a suitable inversion algorithm that takes into account their effects [Camps et al. 1995][Martín-Neira et al. 1996].

Since Fourier based inversion techniques are envisaged for large two-dimensional interferometric arrays, a technique has been proposed to quantify the impact of antenna coupling errors and calibrate them during the antenna design stage. This new method is based in the measurement of the antenna load impedances and the impedance parameters of the array over its mechanical structure with a moderate precision: 7% for 1 K radiometric accuracy. This study shows that each visibility sample being measured is a linear combination of all the visibility samples that can be synthesized by the array, providing an analytical explanation of the non-sinusoidal behavior of the interference patterns found in ESTAR [Ruf 1991].

4.4.- CHANNEL ERRORS

Channel errors appear as separate amplitude factors or phase addends at the visibility samples and are mainly due to filter's phase errors, different channel gains and noise temperatures and quadrature errors at I/Q demodulators.

Figure 4.1 shows the model of a baseline formed by two channels and a complex correlator which is reproduced here for convenience with the definitions of the different visibilities involved in the analysis (figure 4.8).

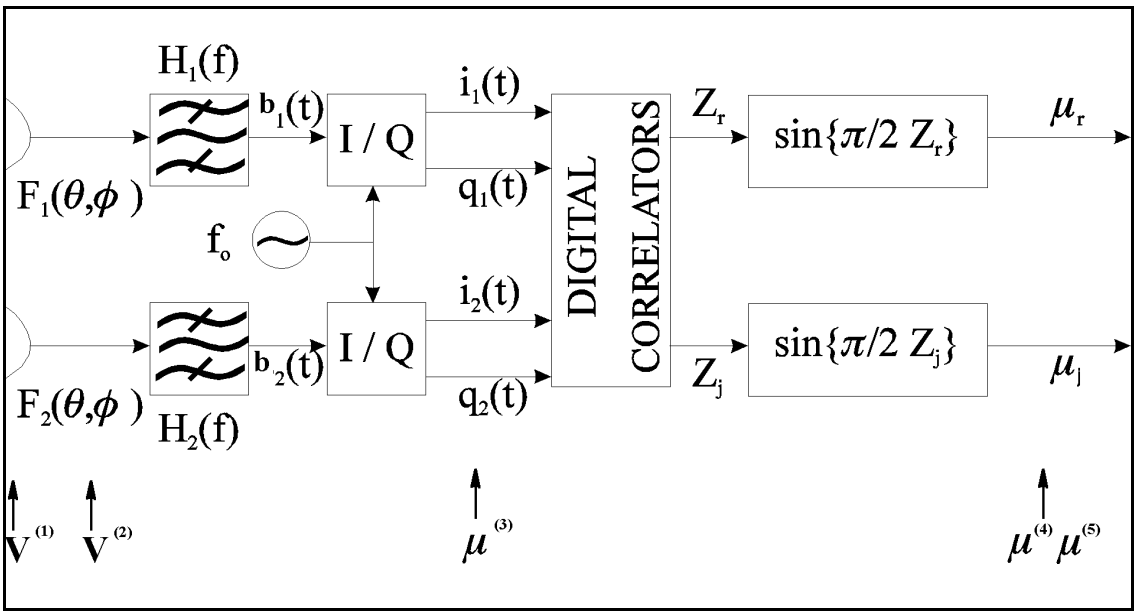

Figure 4.8.- *Receiver phase error model and visibilities definition.*

Assuming Gaussian filters, the equivalent band-pass voltage transfer function takes the form:

$$H(f) = \alpha_n e^{-\frac{1}{2}\frac{(f-f_n)^2}{B_n^2}} e^{-j2\pi(f-f_n)J_g} e^{-j\phi_n}; \quad f \geq 0 \qquad \textbf{(4.37)}$$

where α_n is the voltage gain, f_{ol} is the local oscillator frequency, $f_n = f_{ol} + f_n$ is the filter's central frequency, $B_n = B + B_n$ is the filters noise bandwidth, J_g is the group-delay at the local oscillator frequency, ϕ_n is the filters' phase and the phase of the local oscillator arriving at the I/Q demodulators.

Under this assumption, the fringe-wash function takes the form:

$$\tilde{R}\left(\tau'-\frac{\Delta r}{c}\right) = F^{-1}\left[H_1(f-f_o)H_2^{*}(f-f_o)\,u(f-f_o)\right] = \Lambda_1\Lambda_2 B\, e^{-\frac{\pi}{2}\frac{(\Delta f_1-\Delta f_2)^2}{B_1^2+B_2^2}} e^{-j\pi N_V} e^{-\pi B(\tau-\tau_g)^2 B'^2} e^{j2\pi\Delta f'\tau}$$

$$\tilde{r}\left(\tau'-\frac{\Delta r}{c}\right) = \frac{B}{\sqrt{B_1 B_2}} e^{-\frac{\pi}{2}\frac{(\Delta f_1-\Delta f_2)^2}{B_1^2+B_2^2}} e^{-j\pi N_V} e^{-\pi B(\tau-\tau_g)^2 B'^2} e^{j2\pi\Delta f'\tau} \tag{4.38}$$

where $\Delta f'$ is the equivalent central frequency deviation of the fringe-wash function:

$$\Delta f = \frac{\Delta f_1 B_2^2 + \Delta f_2 B_1^2}{B_1^2+B_2^2} \cdot \frac{\Delta f_1 + \Delta f_2}{2} - \frac{\Delta B_1 - \Delta B_2}{2B}(\Delta f_1 - \Delta f_2) \tag{4.39}$$

B' is its equivalent noise bandwidth:

$$B' = \frac{\sqrt{2}\,B_1 B_2}{\sqrt{B_1^2+B_2^2}}$$

$$\frac{B'}{\sqrt{B_1 B_2}} = \sqrt{2}\sqrt{\frac{B_1 B_2}{B_1^2+B_2^2}} \cdot 1+\frac{1}{4}\left(\frac{\Delta B_1}{B}-\frac{\Delta B_2}{B}\right)^2 \tag{4.40}$$

$\Delta\tau_g = \tau_{g1} - \tau_{g2}$ is the group-delay mismatch,
and N_V is the phase mismatch:

$$\begin{aligned} M_V = {} & M_1-2\pi f_{ol}\tau_{g1}-M_2+2\pi f_{ol}\tau_{g_2}+2\pi\Delta f\Delta\tau_g \cdot \\ & \cdot\left[M_1-2\pi f_{ol}\tau_{g1}+2\pi\frac{\Delta f_1}{2}\left(1-\frac{\Delta B_1}{B}\right)\Delta\tau_{g1}\right]+ \\ & -\left[M_2-2\pi f_{ol}\tau_{g2}+2\pi\frac{\Delta f_2}{2}\left(1-\frac{\Delta B_2}{B}\right)\Delta\tau_{g2}\right]+ \\ & +(\Delta f_1-\Delta f_2)\left(\frac{\Delta B_1}{B}\Delta\tau_{g2}+\frac{\Delta B_2}{B}\tau_{g1}\right)+\frac{\Delta f_2}{2}\Delta\tau_{g1}\left(1+\frac{\Delta B_1}{B}\right)-\frac{\Delta f_1}{2}\Delta\tau_{g2}\left(1+\frac{\Delta B_2}{B}\right) \div \\ & \div 2\theta_{1}-2\theta_{2}+N_{12} \end{aligned} \tag{4.41}$$

Let's examine equations (4.37)-(4.41) in some detail:

i) The amplitude term:

$$A = \frac{B'}{\sqrt{B_1 B_2}} e^{-\frac{B}{2}\frac{(\tau_1-\tau_2)^2}{B_1^2+B_2^2}} \cdot \left[1+\frac{1}{4}\left(\frac{\Delta B_1}{B}-\frac{\Delta B_2}{B}\right)^2\right]\left\{1+\frac{B}{4}\left[\left(\frac{\Delta f_1}{B}\right)^2-\left(\frac{\Delta f_2}{B}\right)^2\right]\right\} \qquad \textbf{(4.42)}$$

$$= 1+\Delta A$$

represents a non-separable amplitude gain factor: a baseline error that is studied in section 4.5.1.

ii) The visibility phase error Φ_V is composed by two error terms due to parameters of each channel:

$$\Phi_{V_n} = \Phi_n - 2\pi f_{ol}\Delta\tau_{gn} + 2\pi\frac{\Delta f_n}{2}\left(1-\frac{\Delta B_n}{B}\right)\Delta\tau_{g_n} \qquad \textbf{(4.43)}$$

and a non-separable one:

$$\Phi_{12} = (\tau_1-\tau_2)\left(\frac{\Delta B_1}{B}\Delta\tau_{g2}+\frac{\Delta B_2}{B}\Delta\tau_{g1}\right)+$$
$$+\frac{\Delta f_2}{2}\Delta\tau_{g1}\left(1+\frac{\Delta B_1}{B}\right)-\frac{\Delta f_1}{2}\Delta\tau_{g2}\left(1+\frac{\Delta B_2}{B}\right) \qquad \textbf{(4.44)}$$

in which the parameters of both filters are mixed together. The separable one can be calibrated by the procedures explained in chapter 5, but the non-separable one remains as a baseline phase error that, to be calibrated, requires the injection of correlated noise to all the receivers simultaneously.

iii) The group delay mismatch, $\Delta\tau_g$, appears inside the fringe-wash function and must be minimized. Note that if there are group delay mismatches in the filters, calibration by correlated noise injection, even with a perfectly equalized distribution network, would lead to a wrong amplitude value since the fringe-wash function decreases.

iv) The equivalent frequency deviation $\Delta f'$ appears as a frequency modulation that is translated into a baseline position error, as well as the antenna arm oscillations. $\Delta f'$ and $\Delta\tau_g$ should be minimized by using closely matched filters (see section 4.10).

Before going further, let us make an estimation of the magnitudes involved. The local oscillator is very stable, and the band-pass filtering is effectively performed at IF and at base-band. With standard, non-matched commercial components and filters, the following error bounds for the magnitudes involved can be estimated:

$|\Delta f_m - \Delta f_n| < 1$ MHz, B = 25 MHz, $|\Delta B| < 1$ MHz, $\Delta\tau_n < 80$ ns, $|\Delta\tau_n| < 2$ ns.

$|\Delta f'| < 0.52$ MHz, $|\Phi_{12}| < 0.43^\circ$, $\Delta A < 2.10^{-3}$

Receiver amplitude errors are mainly due to receivers' different gain, when using analog or multibit digital correlators, or due to receiver's noise temperature when using 1 bit/2 level digital correlators.

The signal at the input of the I/Q demodulator can be written as:

$$b_1^{raw}(t) = b_1(t) + n_1(t)$$
$$b_2^{raw}(t) = b_2(t) + n_2(t) \qquad \textbf{(4.45)}$$

for the signals at the input of the demodulators 1 and 2. In the last expressions, $\boldsymbol{b_1^{raw}(t)}$ and $\boldsymbol{b_2^{raw}(t)}$ are the signals at the input of the demodulators and may suffer from the antenna coupling effects explained in section 4.3.4, whereas $\mathbf{n_1(t)}$ and $\mathbf{n_2(t)}$ are the zero mean narrow band gaussian noise introduced by the receiver, whose average power is:

$$N_i(t) = k_B T_{R_i} B \qquad \textbf{(4.46)}$$

where k_B is the Boltzmann constant, T_{Ri} the i^{th} receiver's noise temperature and B the receiver's noise bandwidth defined in the section "Nomenclature and basic conventions". Since $n_1(t)$ and $n_2(t)$ are uncorrelated signals, the measured normalized visibility function can be written as:

$$\mu_{12}^{(3)} = \frac{E\left[b_1^{raw}(t)\ b_2^{raw}(t)\right]}{\sqrt{E\left[b_1^{raw}(t)\ b_1^{raw}(t)\right]\ E\left[b_2^{raw}(t)\ b_2^{raw}(t)\right]}} =$$
$$= \frac{E\left[b_1(t)\ b_2(t)\right]}{\sqrt{\left(E\left[b_1(t)\ b_1(t)\right]+E\left[n_1^2(t)\right]\right)\ \left(E\left[b_2(t)\ b_2(t)\right]+E\left[n_2^2(t)\right]\right)}} =$$
$$= \frac{E\left[b_1(t)\ b_2(t)\right]}{\sqrt{\left(k_B T_{A1} B + k_B T_{R1} B\right)\ \left(k_B T_{A2} B + k_B T_{R2} B\right)}} = \qquad \textbf{(4.47)}$$
$$= \frac{E\left[b_1(t)\ b_2(t)\right]}{k_B B \sqrt{\left(T_{A1}+T_{R1}\right)\ \left(T_{A2}+T_{R2}\right)}} =$$
$$= \frac{E\left[b_1(t) b_2(t)\right]}{k_B B T_A \sqrt{\left(1+\frac{T_{R1}}{T_{A1}}\right)\left(1+\frac{T_{R2}}{T_{A2}}\right)}} =$$

$$' \frac{1}{\sqrt{1\%\frac{T_{R1}}{T_{A1}}}} \frac{1}{\sqrt{1\%\frac{T_{R2}}{T_{A2}}}} \mu_{12}^{(2)}$$

$$\times g_1 g_2 \mu_{12}^{(2)}$$

Consequently, the factor K_{12} of equations (3.1) and (3.2), contains an additional term: the correlator gain c_{12} defined as $g_1 g_2$:

$$\mu_{12}^{(3)} ' c_{12} \mu_{12}^{(2)} ' g_1 g_2 \mu_{12}^{(2)} \quad \textbf{(4.48)}$$

The above equation show that the measured normalized visibility function is always the ideal one multiplied by two factors depending on the two channels involved in the given baseline. Note that, since the channel has a non-zero receiver temperature similar or even greater than the incoming brightness temperature c_{12} is small and must be taken into account.

Moreover, the in-phase and quadrature errors must be taken into account.

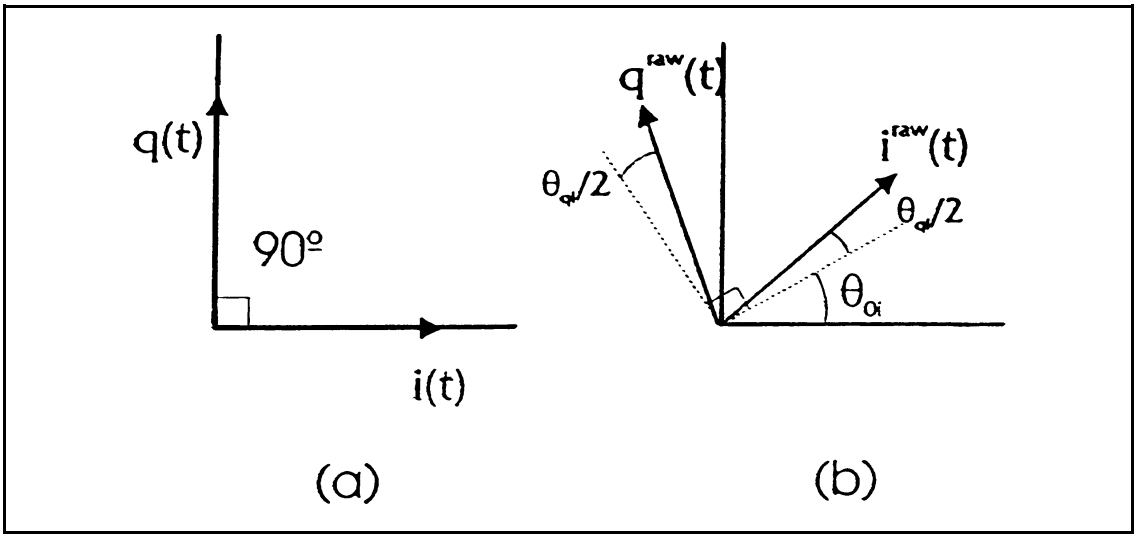

Figure 4.9.- *In-phase and quadrature components. (a) No error, (b) phase channel and quadrature error.*

The signal at the input of the block diagram of figure 4.8 can be expressed as:

$$b_1(t) ' S_1(t) \cos(\omega_0 t \% \Phi_1(t)) \quad \textbf{(4.49)}$$

where $\Phi_1(t)$ is the phase of a given channel, that is, the phase due to the path that the signal has to undergo to reach the antenna in concern. Note that the information lies mainly in the phase difference between these two signals. At the output of the I/Q demodulators there are

two signals: the in-phase $i_1^{raw}(t)$ and the quadrature $q_1^{raw}(t)$ signals which differ from (4.2) if phase errors θ_{o1} and quadrature θ_{q1} errors are not zero (figure 4.9):

$$\begin{aligned} i_1^{raw}(t) &= S_1(t)\cos\left(f_1(t)+q_o 1+q_q\frac{1}{2}\right) \\ q_1^{raw}(t) &= S_1(t)\sin\left(f_1(t)+q_o 1-q_q\frac{1}{2}\right) \end{aligned} \qquad \textbf{(4.50)}$$

θ_{q1} has been splitted into the I and Q demodulator outputs to ease the calibration procedures presented in chapter 5 since each phase unknown appears as many times as the others.

By defining the normalized visibility samples as:

$$m_r = \overline{R_{i_1 i_2}^{raw}(0)} \quad m_i = \overline{R_{q_1 i_2}^{raw}(0)} \qquad \textbf{(4.51)}$$

both amplitude and phase errors can be taken into account:

$$\begin{bmatrix} m_{r_{12}}^{(3)} \\ m_{i_{12}}^{(3)} \end{bmatrix} = \begin{bmatrix} \cos\left(q_o 2-q_o 1+q_q\frac{2}{2}-q_q\frac{1}{2}\right) & \sin\left(q_o 2-q_o 1+q_q\frac{2}{2}-q_q\frac{1}{2}\right) \\ -\sin\left(q_o 2-q_o 1+q_q\frac{2}{2}+q_q\frac{1}{2}\right) & \cos\left(q_o 2-q_o 1+q_q\frac{2}{2}+q_q\frac{1}{2}\right) \end{bmatrix} \begin{bmatrix} m_{r_{12}}^{(2)} \\ m_{i_{12}}^{(2)} \end{bmatrix} \qquad \textbf{(4.52)}$$

$$m_{12}^{(4)} = g_1 g_2 m_{12}^{(3)}$$

or, in a compact notation:

$$\overline{m_{12}^{(4)}} = g_1 g_2 \overline{P_{12}} \quad \overline{m_{12}^{(2)}} \qquad \textbf{(4.53)}$$

The extension for the whole system produces a sparse system of linear equations:

$$\begin{bmatrix} m_{r1} \\ m_{i1} \\ m_{r2} \\ m_{i2} \\ \vdots \\ m_{rM} \\ m_{iM} \end{bmatrix}^{(4)} = \begin{bmatrix} g_{11}g_{21}\overline{P}_1 & 0 & 0 & \dots & 0 \\ 0 & g_{11}g_{21}\overline{P}_1 & 0 & \dots & 0 \\ \vdots & \vdots & \ddots & \vdots & \vdots \\ \vdots & \vdots & \vdots & \ddots & \vdots \\ 0 & \dots & \dots & 0 & g_{11}g_{21}\overline{P}_1 \end{bmatrix} \begin{bmatrix} m_{r1} \\ m_{i1} \\ m_{r2} \\ m_{i2} \\ \vdots \\ m_{rM} \\ m_{iM} \end{bmatrix}^{(2)} \qquad \textbf{(4.54)}$$

where the vector $\boldsymbol{\mu}^{(2)}$ is the vector of normalized visibility samples at the outputs of the antennas, including mutual coupling effects (equation (4.32)), $\boldsymbol{\mu}^{(4)}$ is the vector containing the measured normalized visibilities, the $\mathbf{P}_i$ matrices are defined in equations (4.52) and (4.53) and the gain factor $c^i_{12}=g_{1i}g_{2i}$ is the i^{th} correlators' gain defined in (4.47). Equations (4.52)-(4.54) allow to simulate the impact of separable amplitude, in-phase quadrature errors on the radiometric accuracy.

4.4.1.- Receiver phase errors

To study the impact of receiver phase errors a series of numerical simulations have been performed for an Y-array with 15 antennas per arm and Blackmann windowing, Simulations have been performed for in-phase and quadrature errors added directly to the receiver's channel: $\overline{\mu_{ij}^{(4)}} \;'\; \overline{\overline{P_{ij}}\;\overline{\mu_{ij}^{(2)}}}$; $g_i \,' g_j \,' 1$. Figure 4.10 shows their impact on the radiometric accuracy, which is very similar.

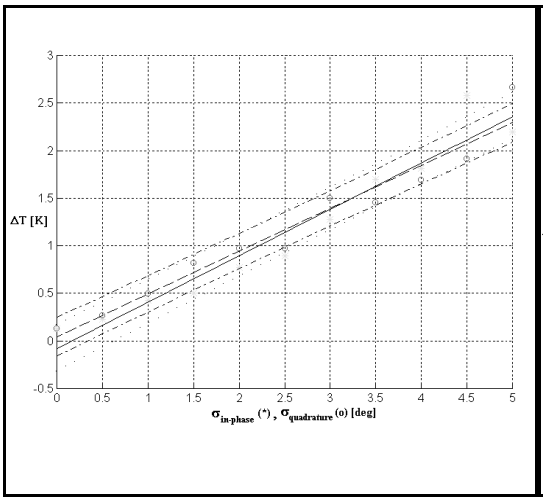

Figure 4.10.- *Radiometric accuracy vs. in-phase and quadrature errors (-----) and 50 % confidence limits*

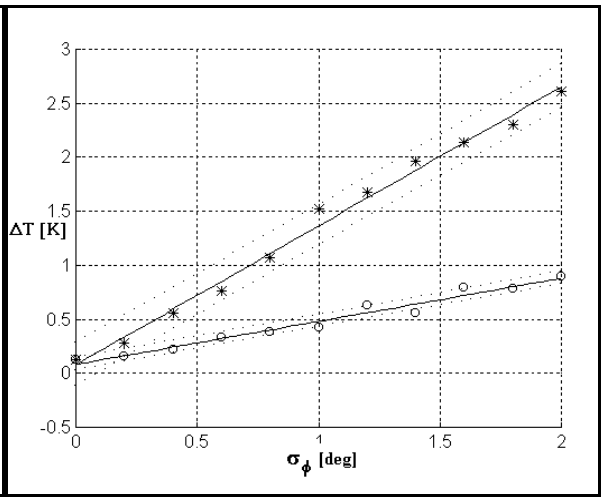

Figure 4.11.- *Radiometric accuracy vs. uncorrelated (S)Q)phase errors (*), channel phase errors(o) and 50% confidence limits*

Assuming that in-phase and quadrature errors are uncorrelated, the variance of phase errors is $F^2_2 = F^2_{2o}+F^2_{qo}$. Each curve has been computed by assuming only one of the two phase errors, the other one being set to zero. From figure 4.10 it can be noted that both in-phase and quadrature errors impact on radiometric accuracy is very similar.

Simulation results are also compared with the analytical results developed in Appendix 6. All simulations have been performed with 15 antennas per arm and the Blackmann window. Observe that the *results are better when the phases are added to the*

channels (correlated phase errors) than when they are added to the visibility samples (uncorrelated phase errors), which is due to image's symmetry [Bará et al 96, WP-10].

The average error decreases for modified temperature distributions where the even component is greater than the odd one, as it is the case for the test scene. As it will be shown in chapter 5, residual receiver phase errors after calibration can be as low as 0.1º, leading to a radiometric accuracy of 0.04 K for a 200 K constant scene.

4.4.2- Receiver amplitude errors

Errors treated in the previous section stand for phase differences between the channels. In this section errors in the module of the visibility samples are taken into account. These errors are modeled as:

$$m_{12}^{(3)} = g_1 g_2 m_{12}^{(2)}$$

$$V_{12}^{(3)} = \hat{T}_A m_{12}^{(3)} \approx V_{12}^{(2)} \left(1 + \frac{\Delta T_A}{T_A} + \Delta g_1 + \Delta g_2 \right) - V_{12}^{(2)} (1 + \Delta V_{12}) \qquad \textbf{(4.55)}$$

where ΔV_{12} is a zero mean error of deviation $\sigma_{\Delta V}$:

$$\Delta V_{12} = \Delta V_{21} \qquad \textbf{(4.56)}$$

Equation (4.55) holds only for small separable amplitude errors due to: i) errors in the measurement of the receivers' noise temperatures (equation 4.47), ii) the errors induced by the assumption that all the antenna temperatures are the same $T_A = T_{A1} = T_{A2}$, when in fact, they depend on the antenna pattern shape, and iii) the error induced in the measurement of the antenna temperature T_A by means of a total power radiometer ($\Delta T_A / T_A$).

The signal-to-noise ratio can be defined as:

$$\left(\frac{S}{N} \right) = -10 \log s_{\Delta V} = -10 \log \left(\sqrt{2}\ s_{\Delta g_i} \right) \qquad \textbf{(4.57)}$$

Typical uncertainty of a total power radiometer is $\sigma_{\Delta T} = 0.015$ K, resulting in an uncertainty of the visibility $\sigma_{\Delta Vo} = 5\ 10^{-5}$. The high S/N = 43 dB has a negligible impact over the radiometric accuracy, as shown in figure 4.12. In fact, for this signal to noise ratio, the radiometric accuracy has reached its saturation value: the discretization error. Then, amplitude error is mainly given by the remainder calibration amplitude error:

$$s_{\Delta V}^2 = s_{\Delta V_O}^2 + s_{\Delta m}^2 \approx s_{\Delta m}^2 \qquad \textbf{(4.58)}$$

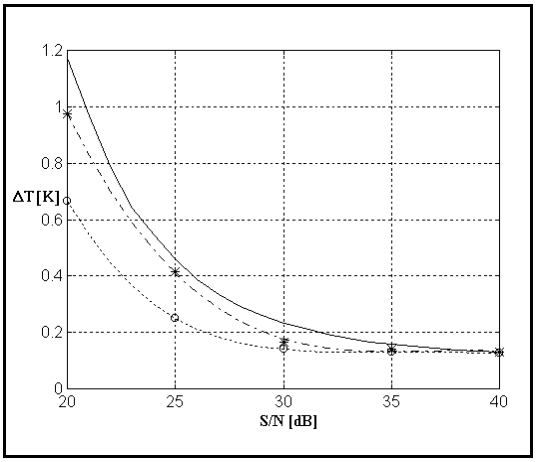

Figure 4.12.- *Radiometric accuracy vs. residual amplitude errors: (-) theoretical, (*) uncorrelated and (o) correlated*

Figure 4.12 shows the results when simulating amplitude calibration residual errors, $F_{)V}$, for the constant 200 K test scene and an Y-array tilted $=31.2º with respect to nadir, with N_{EL} = 15 antennas per arm spaced d = 0.898. The simulations have considered: (*) uncorrelated error in the visibilities corresponding to the theoretical analysis developed in appendix 6 and (o) uncorrelated errors in the channels, $g_{i,}$ leading to correlated gain errors in the visibilities.

The following table summarizes this last case:

S/N [dB]	**20**	**25**	**30**	**35**	**40**
) T (K)	0.67	0.25	0.14	0.13	0.13

Table 4.2.- *Radiometric accuracy vs. signal-to-noise ratio in channel amplitude calibration residual errors.*

The amplitude error is very dependent on the error in estimating the gain factors $g_{i,}$ which depend on the knowledge of the receiver noise temperature T_R. Let's compute the precision when estimating receiver's noise temperature. From (4.50) the calibration gain factors are:

$$\hat{g}_i = \left(1 + \frac{\hat{T}_{R_i}}{T_A}\right)^{-\frac{1}{2}} \qquad \textbf{(4.59)}$$

where all the antenna temperatures have been assumed to be the same $T_{A1}=T_{A2}=T_A$. Then, writing the receiver's noise temperature as:

$$T_{Ri} = \hat{T}_{Ri} +)T_{Ri} \qquad \textbf{(4.60)}$$

The calibrated normalized visibility sample is:

$$\hat{\mu}_{12}^{(2)} = \hat{g}_1^{-1}\,\hat{g}_2^{-1}\mu_{12}^{(3)} = \frac{g_1\,g_2}{\hat{g}_1\,\hat{g}_2}\,\mu_{12} = \mu_{12} + ()\mu_{12}) \qquad \textbf{(4.61)}$$

where $)\mu_{12}$ is the amplitude error, given by:

$$\Delta m = \frac{g_1 g_2}{\hat{g}_1 \hat{g}_2} - 1 = \left[\frac{\left(1 + \frac{\hat{T}_{R_1}}{T_A}\right)\left(1 + \frac{\hat{T}_{R_2}}{T_A}\right)}{\left(1 + \frac{\hat{T}_{R_1} + \Delta T_{R_1}}{T_A}\right)\left(1 + \frac{\hat{T}_{R_2} + \Delta T_{R_2}}{T_A}\right)} \right]^{\frac{1}{2}} - 1 \qquad \textbf{(4.62)}$$

If the residual calibration errors are small $\Delta T_R \ll T_R + T_A$ and $T_{R1} \approx T_{R2}$ then, the above expression can be approximated by:

$$\Delta m = \left(1 + \frac{\Delta T_{R_1}}{\hat{T}_{R_1} + T_A}\right)^{-\frac{1}{2}} \left(1 + \frac{\Delta T_{R_2}}{\hat{T}_{R_2} + T_A}\right)^{-\frac{1}{2}} - 1 \approx \frac{1}{2} \frac{\Delta T_{R_1} + \Delta T_{R_2}}{\hat{T}_R + T_A} \qquad \textbf{(4.63)}$$

hence, the receiver's noise temperature residual error is related to the amplitude error by:

$$\sigma_{\Delta m} = \frac{1}{\sqrt{2}} \frac{\sigma_{\Delta T_R}}{\hat{T}_R + T_A} \qquad \textbf{(4.64)}$$

A good L-band receiver can have a noise temperature as low as T_R=80 K, while the antenna temperature for a wide pattern antenna from a low orbit is about T_A=200 K. Receiver noise temperature errors ΔT_R can be now related to the radiometric accuracy through equation (4.63) and table 4.2. Results are shown is table 4.3.

S/N dB	20	25	30	35	40
ΔT (K)	0.67	0.25	0.14	0.13	0.13
ΔT_R (K)	3.96	1.25	0.39	0.12	0.12

Table 4.3.- *Radiometric accuracy vs. error in receiver noise temperature.*

Note that the receiver's noise temperature must be estimated with a very small error. A ΔT_R = 4 K gives a radiometric accuracy ΔT = 0.7 K which is very "close" to the technological limit.

4.5.- BASELINE ERRORS

Baseline errors appear as amplitude and phase error terms that can not be split into two terms associated to the channels being correlated. They are due to different receivers' filter shape, but also to local oscillator's amplitude, phase and thermal noise as well as errors in the correlators themselves.

4.5.1.- Baseline receiver errors

In section 4.4, when presenting receiver errors, a number of errors were found to depend not only on the parameters of a single channel, but on the parameters of both channels: they are called *baseline errors*.

4.5.1.1.- Baseline receiver phase errors

Assuming that the complete receiver voltage transfer function can be approximated by a gaussian function, the non-separable phase error term can be expressed by (equation 4.47):

$$M_{12} \approx (\Delta f_1 - \Delta f_2)\left(\frac{\Delta B_1}{B}\Delta J_{g2} + \frac{\Delta B_2}{B}J_{g1}\right) + \frac{\Delta f_2}{2}\Delta J_{g1}\left(1 + \frac{\Delta B_1}{B}\right) - \frac{\Delta f_1}{2}\Delta J_{g2}\left(1 + \frac{\Delta B_2}{B}\right) \quad \textbf{(4.65)}$$

which, for typical commercial values: $|\Delta f_m - \Delta f_n| < 1$ MHz, B = 20 MHz, $|\Delta B_m| < 1$ MHz, $J_m \approx 80$ ns and $|\Delta J_m| < 2$ ns, is bounded by:

$$M_{12} < 0.43^\circ$$
$$M_{12_{rms}} < 0.30^\circ \quad \textbf{(4.66)}$$

This non-separable phase error can not be calibrated by correlated noise injection to groups of antennas nor by "phase closure" relationships (see chapter 5), where its impact is critical because each phase closure equation is contaminated by an error on the order of 1.3º and it propagates along the antennas when establishing new "phase closure" relations:

$$|M_{12} + M_{23} + M_{31}| < 1.3^\circ \quad \textbf{(4.67)}$$

According to figure 4.15, the impact over the radiometric accuracy of a uniformly distributed non-separable phase error lies in the range 0.13 K - 0.18 K for a constant test scene of 200 K.

Typical filters, however are of Chebyschew type, allowing high frequency selectivity at a expense of amplitude attenuation ripples in the pass-band and high phase and group delay distorsion. As explained above, MIRAS bread-board filters in 4 steps. There are two band-pass filters at 1.410 MHz of Chebyschew type designed from low-pass prototypes of orders 3 and 4 with bandwidths 30 MHz and 35 MHz respectively, and in-band attenuation ripples of 0.05 dB and 0.075 dB. The low-pass filtering is performed by a Chebyschew filter of order 7, bandwidth 20.75 MHz and in-band attenuation ripple of 0.06 dB. Finally a RC network eliminates the components below 1 MHz. An analytical study of the non-separable phase error introduced by these four filters in cascade can not be performed. However, for long integration times, the noise injection calibration procedure described in chapter 5 has proved to recover very accurately the separable phase terms in the absence of other errors. When baseline phase errors are introduced, channel phases are recovered with an error very close to the non-separable one. With this technique, the baseline receiver phase term can be estimated for the real filters in order to bound its tolerances. Results are shown in table 4.4 in order to have a baseline error of 0.43º for the constant test scene of 200 K.

Parameter	**Sensitivity to parameter's variations**	**Filters' tolerances for baseline rms phase error of º**
Bandwidth of 1st band-pass filter (BBP_1)	$\delta\phi_{12}/\delta BBP_1 = 1.86^{\circ}$/MHz	120 KHz
Bandwidth of 2nd band-pass filter (BBP_2)	$\delta\phi_{12}/\delta BBP_2 = 2.52^{\circ}$/MHz	85 KHz
Bandwidth of the low-pass filter (BLP)	$\delta\phi_{12}/\delta BLP = 12.54^{\circ}$/MHz	18 KHz
Bandwidth of the RC network (BHP)	$\delta\phi_{12}/\delta BHP = 3.04^{\circ}$/MHz	72 KHz
Central frequency of 1st band-pass filter (fc_1)	$\delta\phi_{12}/\delta fc_1 = 8.42^{\circ}$/MHz	26 KHz
Central frequency of 2nd band-pass filter (fc_2)	$\delta\phi_{12}/\delta fc_2 = 12.19^{\circ}$/MHz	18 KHz
Attenuation ripple of 1st band-pass filter (RBP_1)	$\delta\phi_{12}/\delta RBP_1 = 2.20^{\circ}$/dB	0.98 dB
Attenuation ripple of 2st band-pass filter (RBP_2)	$\delta\phi_{12}/\delta RBP_2 = 2.30^{\circ}$/dB	0.92 dB
Attenuation ripple of low-pass filter (RLP)	$\delta\phi_{12}/\delta RLP = 3.97^{\circ}$/dB	0.06 dB

Table 4.4.- *Baseline error sensitivity to MIRAS BB filters and tolerances for 0.43º baseline phase error*

The severe filter's tolerances are due to the high phase and group delay distorsions. If they can not be met, other filters must be used, which is currently under study in MIRAS/LICEF activities.

4.5.1.2.- Baseline receiver amplitude errors

Assuming that the complete receiver voltage transfer function can be approximated by a gaussian function, the non-separable amplitude error term can be expressed by (equation 4.42):

$$A = \frac{B'}{\sqrt{B_1 B_2}} e^{-\frac{B}{2}\frac{(\Delta f_1 - \Delta f_2)^2}{B_1^2 + B_2^2}} \cdot \left[1 + \frac{1}{4}\left(\frac{\Delta B_1}{B} - \frac{\Delta B_2}{B}\right)^2\right] \left\{1 + \frac{B}{4}\left[\left(\frac{\Delta f_1}{B}\right)^2 + \left(\frac{\Delta f_2}{B}\right)^2\right]\right\} \qquad \textbf{(4.68)}$$

$$= 1 + \Delta A$$

which, for typical commercial values: $|\Delta f_m - \Delta f_n| < 1$ MHz, B = 20 MHz ,$|\Delta B_m| < 1$ MHz, J_m . 80 ns and $|\Delta J_m| < 2$ ns, is bound by:

$$\Delta A = 0.002; \qquad \frac{S}{N} = 27\,dB \qquad \textbf{(4.69)}$$

which accounts for a radiometric accuracy of 0.2 K (table 4.8, figure 4.17) for the 200 K constant scene.

4.5.1.3.- Baseline fringe-wash errors

Differential delays introduced by filter responses and transmission lines causes a decorrelation of the signals and hence an amplitude error. This amplitude error can not be calibrated with a delay line, as it is performed in radioastronomy, since it depends on the direction (>,0) of the incoming radiation and the FOV is very wide:

$$\tilde{r}\left(\frac{\Delta r(>,0)}{c} + \Delta J_{g_{mn}}\right) = e^{-B\left(\frac{u>+v0}{f_o} + \Delta J_{g_{mn}}\right)^2} \qquad \textbf{(4.70)}$$

To have a negligible impact on the radiometric accuracy, the differential group delay must satisfy that:

$$\Delta J_{g_{mn}} \ll \left.\frac{u>+v0}{f_o}\right|_{\max,\ swath\ limit} < 4\,ns \qquad \textbf{(4.71)}$$

but ΔJ_{gm} is about 2 ns. However, the visibilities affected by high decorrelation levels, far (u,v) points, are very small and its impact over the global radiometric accuracy is completely negligible.

4.5.2.- Errors generated by the local oscillator

Each visibility sample is obtained from the complex correlation of the signals received by each pair of antennas. The complex correlation is obtained as the product of these two signals followed by a low-pass filter. To simplify the distribution network and the correlation circuitry the multiplication process is usually performed at baseband and the frequency translation is achieved by mixing all the signals with a common oscillator to preserve their phase as shown in figure 4.13.

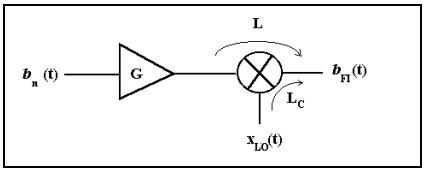

Figure 4.13.- *Frequency conversion, signals. Parameters: G preamplifier's gain, L* conversion loss

The local oscillator signal can be expressed as:

$$x_{lo}(t) = A(1 + m_n(t))\, e^{j(w_{lo}t + f_n(t))} + n(t) \qquad \textbf{(4.72)}$$

where $m_n(t)$ is the local oscillator's amplitude noise, $\phi_n(t)$ its phase noise and n(t) is wide-band thermal noise.

4.5.2.1.- Local oscillator's amplitude noise

Local oscillator's amplitude noise is translated to the IF signal through the mixer conversion losses, which depend on the local oscillator level:

$$x_{lo}(t) = A(1 + m_{lo}(t))\, e^{j w_{lo} t}$$

$$b(t) = S(t)\, e^{j(w_o t + f(t))} \qquad \textbf{(4.73)}$$

$$b_{FI}(t) = \sqrt{G}\sqrt{\frac{L(t)}{L_c}}\, S(t)\, e^{j(w_{FI} t + f(t))};\; w_{FI} = w_0 - w_{lo}$$

When analog or multibit digital correlators are used, if the time constant of the low-pass filter which sets the integration time is much smaller than the LO amplitude fluctuations, mixer conversion losses are constant and represent an amplitude gain factor. On the contrary, if the integration time is greater than the LO amplitude fluctuations, they are averaged an its effect is negligible. In either case, the correlation gain factor:

$$g = E_t\,[\,L(t)\,] \qquad \textbf{(4.74)}$$

can be minimized by driving the mixers to saturation as is done in the interferometer that has been developed (chapter 8). When 1 bit/2 level digital correlators are used, the gain factor (4.74) has a negligible impact on the measured correlation, provided that the signals' amplitude is much greater than the errors in the comparators' threshold .

4.5.2.2.- Local oscillator's phase noise

Local oscillator's phase noise $N_n(t)$ is also translated into the IF signal though the mixer:

$$\begin{aligned} x_{ol}(t) &= A\, e^{j(\omega_{lo} t + N_n(t))} \\ b(t) &= S(t)\, e^{j(\omega_o t + N(t))} \\ b_{FI}(t) &= \sqrt{G}\sqrt{\frac{L}{L_c}}\, S(t)\, e^{j(\omega_{FI} t + N(t) + N_n(t))} \end{aligned} \tag{4.75}$$

Where L is the mixer's conversion loss, L_C is the mixer's conversion loss of the RF and image bands at the LO input and G is the preamplifier's gain. However, it does not have any effect over the computed visibility since it cancels with itself when the signals are correlated:

$$V_{12} = \frac{1}{2} E_J\left[b_1(t) b_2^*(t)\right] = \frac{1}{2}\frac{G\,L}{L_c} E_J\left[S_1(t) S_2(t) e^{j(N_1(t) - N_2(t))}\right] \tag{4.76}$$

4.5.2.3.- Local oscillator's thermal noise

The impact of LO thermal noise over the RF bandwidth:

$$x_{ol}(t) = A e^{j\omega_{ol} t} + S_{n_{th}}(t) e^{j(\omega_0 t + N_{n_{th}}(t))} \tag{4.77}$$

can be studied by applying the superposition principle at IF, since the amplitude of the collected signal and the thermal noise are much smaller than that of the LO.

$$|S(t)|,\ |S_{n_{th}}(t)| \ll A \tag{4.78}$$

$$b_{FI}(t) = \sqrt{\frac{G}{L}}\, S(t)\, e^{j(\omega_{FI} t + N(t))} + \frac{1}{\sqrt{L_c}}\, S_{n_{th}}(t) e^{j(\omega_{FI}(t) + N_{n_{th}}(t))} \tag{4.79}$$

The second term in equation (4.79) is equivalent to a correlated noise term added to the incoming signal:

$$b(t) = S(t)\, e^{j(\omega_{FI} t + N(t))} + \sqrt{\frac{L}{G\,L_c}}\, S_{n_{th}}(t) e^{j(\omega_{FI}(t) + N_{n_{th}}(t))} \tag{4.80}$$

When correlating two signals $b_1(t)$ and $b_2(t)$, the correlated noise term produces an offset in the measured visibility:

$$V_{12}^{(5)} = \frac{1}{2} E\left[b_1(t)\, b_2^*(t)\right] = V_{12}^{(4)} + \frac{L}{L_c\, G}\, k_B\, T_{lo}\, B \tag{4.81}$$

where T_{lo} is the physical temperature of the LO. Let's have a cavity oscillator directly feeding the mixer at T_{lo} = 300 K with the following parameters L = 7dB, L_c=25dB and a three stage low-noise preamplifier with G = 25dB. This gives a temperature offset of:

$$T_{off} = \frac{L}{L_c G} T_{lo} = 0.015\ K \qquad \textbf{(4.82)}$$

which increases to 0.15 K, 1.5 K or 15 K if the LO is buffered through a 10 dB, 20 dB or a 30 dB amplifier. In those cases the offset level can be reduced by inserting a selective filter at LO output to attenuate properly the LO noise at the RF band.

4.5.3.- Errors generated by the correlators

In this section the baseline errors induced by 1B/2L correlators are studied. The study is focused only in 1B/2L digital correlators since they have been chosen for MIRAS and for the experimental interferometer radiometer explained in chapter 8. The selection is based on their simplicity, the ability to cope with large bandwidth signals, their insensitivity to gain fluctuations and their low power consumption when integrated in a chip.

The principles of digital correlation techniques can be found in [Hagen and Farley 73]. In this paper the relationships between the measured correlation and the true correlation are derived for different kinds of digital correlators. For 1 bit/2 level digital correlators the distortion introduced by the comparator in the signal to be correlated is permissible since for gaussian signals, the true normalized correlation function can be inferred from the correlation of the distorted one:

$$m_{12}(\tau) = \frac{E\left[b_1(t)\, b_2(t-\tau)\right]}{\sqrt{E\left[|b_1(t)+n_1(t)|^2\right] E\left[|b_2(t)+n_2(t)|^2\right]}}$$

$$Z_{12}(\tau) = E\left[\, sign(b_1(t))\, sign(b_2(t-\tau))\,\right] \qquad \textbf{(4.83)}$$

$$m_{12}(\tau) = \sin\left(\frac{\pi}{2} Z_{12}(\tau)\right)$$

which is denormalized through:

$$V_{12}(\tau) = \frac{1}{2} E\left[b_1(t)\, b_2^*(t-\tau)\right] = \sqrt{(T_A + T_{R_1})(T_A + T_{R_2})}\, m_{12}(\tau) \qquad \textbf{(4.84)}$$

where $T_A = E[|b_1(t)|^2] = E[|b_2(t)|^2]$ is the antenna temperature, and T_{R1} and T_{R2} are the receivers' noise temperatures of channels 1 and 2:

$$T_{R1} = E[|n_1(t)|^2], \qquad T_{R2} = E[|n_2(t)|^2].$$

Remember that the Boltzmann constant and the wavelength, as well as the receivers' gain and bandwidth have been omitted for simplicity (equations (2.61) and (2.62)).

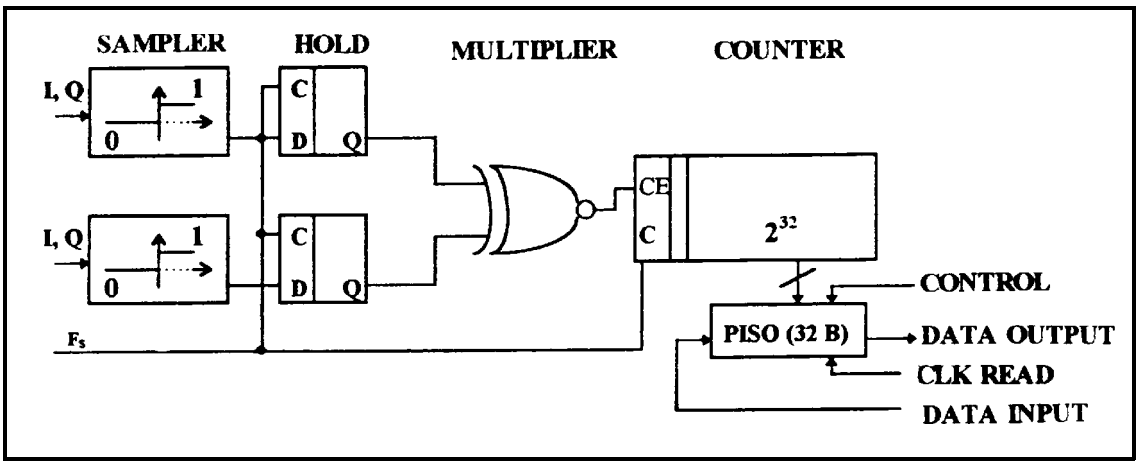

Figure 4.14.- 1 bit/2 level digital correlator scheme.

In fact, the digital correlator computes Z_{12} (J) from:

$$Z_{12}(J) = \frac{1}{N} \sum_{n=0}^{N-1} b_1(n.T_s)\ b_2(n.T_s - J) \qquad \textbf{(4.85)}$$

where T_s is the sampling period and N is the total number of counts.

Errors in the computation of Z_{12} come mainly from two sources: i) errors in the threshold of the comparators that perform the "sign(x)" function and, ii) skew and jitter in the sampling instants of the comparators. They are studied in the following sections.

4.5.3.1.- Threshold errors

When the comparator's threshold is not zero, the relationship between the distorted correlation, Z_{12}, and the normalized one, μ_{12}, can be computed by Price's Theorem:

$$\begin{aligned} \mu_{12}(0) &= E[b_1(t)\ b_2(t)] \\ Z_{12}(0) &= E[g_1(b_1(t))\ g_2(b_2(t))] \\ \frac{\partial^m Z_{12}(\mu_{12})}{\partial \mu_{12}^m} &= F^{2m} E\left[\frac{\partial^m g_1}{\partial b_1^m} \cdot \frac{\partial^m g_2}{\partial b_2^m}\right] \end{aligned} \qquad \textbf{(4.86)}$$

where $g_n(x) = \text{sign}(x)$ for ideal comparators and $g_n(x) = \text{sign}(x - \delta x_n)$ when there are threshold errors. For two joint gaussian functions $b_1(t)$ and $b_2(t)$ with joint probability density function:

$$f(b_1,b_2) = \frac{1}{2\pi F^2\sqrt{1-\mu_{12}^2}}\, e^{-\frac{b_1^2+b_2^2-2b_1b_2\mu_{12}}{2F^2(1-\mu_{12}^2)}} \tag{4.87}$$

and for m=1, the distorted correlation can be computed from (4.85):

$$\frac{\partial \hat{Z}_{12}(\mu_{12})}{\partial \mu_{12}} = F^2 E\left[\frac{\partial g_1}{\partial b_1}\cdot\frac{\partial g_2}{\partial b_2}\right] =$$

$$= 4F^2\, E\left[\partial(b_1(t)-x_1)\,\partial(b_2(t)-x_2)\right] =$$

$$= \frac{2}{\pi}\int_{-\infty}^{+\infty}\int_{-\infty}^{+\infty}\partial(b_1-x_1)\,\partial(b_2-x_2)\frac{1}{\sqrt{1-\mu_{12}^2}}e^{-\frac{b_1^2+b_2^2-2b_1b_2\mu_{12}}{2F^2(1-\mu_{12}^2)}}\,db_1\,db_2 = \tag{4.88}$$

$$= \frac{2}{\pi}\,\frac{1}{\sqrt{1-\mu_{12}^2}}e^{-\frac{x_1^2+x_2^2-2x_1x_2\mu_{12}}{2F^2(1-\mu_{12}^2)}}$$

Integration of expression (4.88) does not have a closed form. However, if the threshold errors x_n are much smaller than the signal's input power F^2, it can be developed in a Taylor series and then integrated:

$$\hat{Z}_{12}(\mu_{12}) = \frac{2}{\pi}\int_0^{\mu_{12}}\frac{1}{\sqrt{1-y^2}}\left\{1-\frac{x_1^2+x_2^2-2x_1x_2y}{2F^2(1-y^2)}\right\}dy =$$

$$= \frac{2}{\pi}\left[\arcsin(\mu_{12}) + \frac{2x_1x_2-(x_1^2+x_2^2)\mu_{12}}{2F^2\sqrt{1-\mu_{12}^2}}-\frac{2x_1x_2}{2F^2}\right]\times \tag{4.89}$$

$$\times\frac{2}{\pi}\left[\arcsin(\mu_{12}) + \frac{a\mu_{12}+b}{\sqrt{1-\mu_{12}^2}}-b\right]$$

where:

$$\begin{aligned} a &= -\frac{(x_1^2+x_2^2)}{2F^2} \\ b &= +\frac{2\,x_1\,x_2}{2F^2} \end{aligned} \qquad \textbf{(4.90)}$$

Let's quantify the error committed in the normalized visibility function when equation (4.89) is inverted as if the comparators were ideal a=b=0:

$$\begin{aligned} \hat{\mu}_{12} &= \sin\left(\frac{B}{2}\hat{Z}_{12}\right) = \sin\left(\arcsin(\mu_{12}) - \frac{a\mu_{12}+b}{\sqrt{1-\mu_{12}^2}}+b\right) = \\ &= \mu_{12}\cos\left(\frac{a\mu_{12}+b}{\sqrt{1-\mu_{12}^2}}-b\right)-\cos(\arcsin(\mu_{12}))\,\sin\left(\frac{a\mu_{12}+b}{\sqrt{1-\mu_{12}^2}}-b\right) = \\ &= \mu_{12}\cos\left(\frac{a\mu_{12}+b}{\sqrt{1-\mu_{12}^2}}-b\right)-\sqrt{1-\mu_{12}^2}\,\sin\left(\frac{a\mu_{12}+b}{\sqrt{1-\mu_{12}^2}}-b\right) \end{aligned} \qquad \textbf{(4.91)}$$

which can be approximated for $\mu_{12}\to 1$ by:

$$\hat{\mu}_{12} \approx \mu_{12}\left[\cos(a\mu_{12}) - a\right] \approx \mu_{12}\left[1-a-\frac{a^2}{2}\mu_{12}^2\right];\quad \mu_{12} \ll 1 \qquad \textbf{(4.92)}$$

Results are presented in figure 4.15 and have been computed by averaging the amplitude and phase errors over [0, 2 B]:

$$\begin{aligned} \mu_{12} &= \mu_{12_0}\, e^{j\Delta\phi_0} \\ \hat{\mu}_{12} &= \mu_{12}(\nu)\, e^{j\Delta\phi(\nu)} \\ E[\Delta\mu^2] &= \frac{1}{2B}\int_0^{2B} |\mu_{12}(\nu)-\hat{\mu}_{12}(\nu)|^2 d\nu \\ E[\Delta M^2] &= \frac{1}{2B}\int_0^{2B} (\nu_0-\Delta\phi(\nu))^2 d\nu \end{aligned} \qquad \textbf{(4.93)}$$

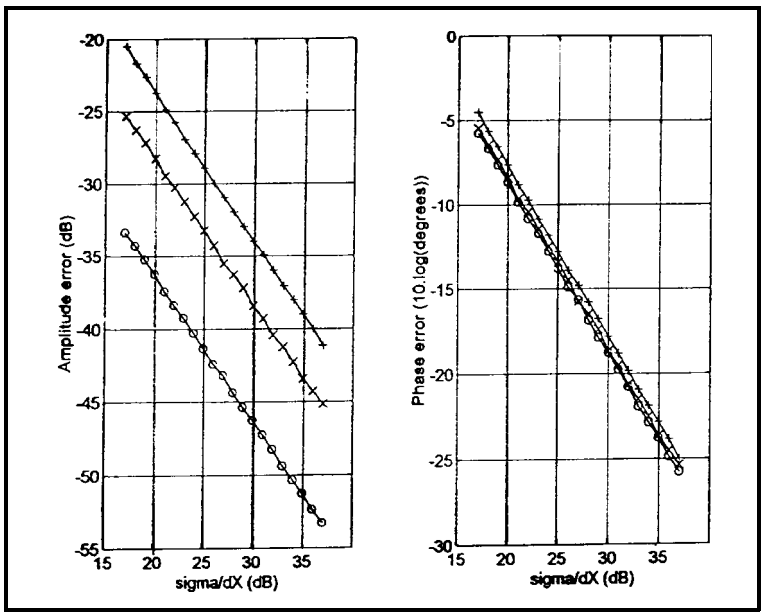

Figure 4.15.- Amplitude and phase baseline errors due to comparators' threshold errors.

For a typical high speed comparator as the MAX 915, the maximum offset voltage at the input is 1.4 mV. For an input power of 0 dBm, F/) x = 44 dB, the amplitude error is negligible even for high correlations: $\mu_0 = 0.9$,) μ_{12} . 1.6 10^{-5}. Phase errors are even less important 4 10^{-5} º.

However, correlator's performance degrades quickly if the input noise has a small DC component or the comparator's offset is high compared to the effective signal's amplitude. Graphical results are shown in figure 4.16 for a 50 mV DC and an input power of 0 dBm. In this case, amplitude errors can be as high as 17% and phase errors up to 2º can be expected. The non-separable amplitude and phase errors invalidate channel-based calibration procedures based on phase closure relationships and those based on noise injection to groups of receivers. Consequently, it is critical to guarantee that the input signals being correlated are zero mean.

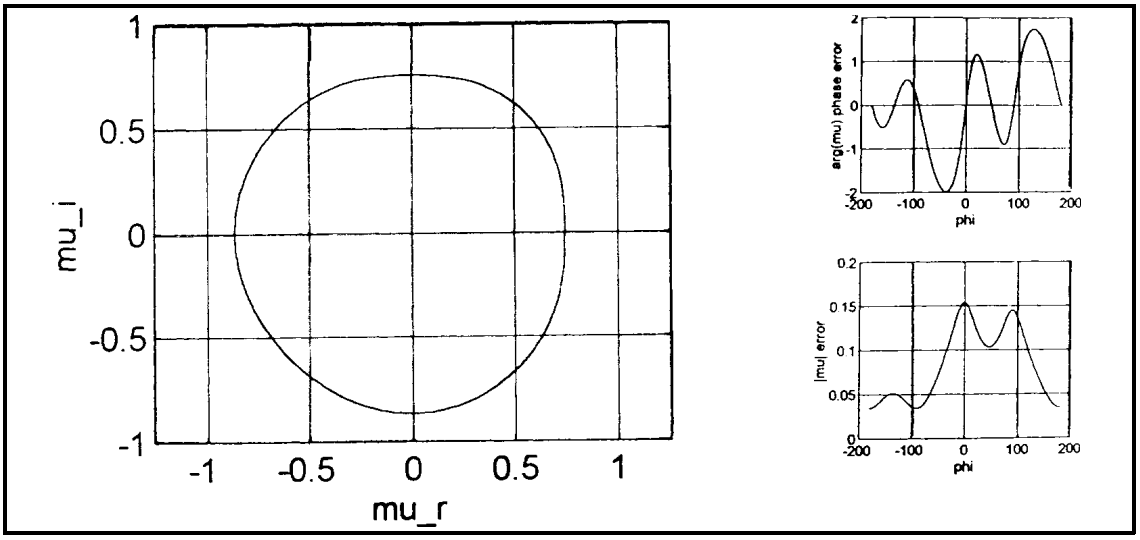

Figure 4.16.- Amplitude and phase baseline errors due to comparators' threshold errors for Pin = 0 dBm and V_T = 50 mV.

4.5.3.2.- Delay errors

Visibility samples are usually computed with real correlators from the in-phase and quadrature components of both signals:

$$\mu_{12_r} = E[i_1(t)\ i_2(t-\tau)]|_{\tau=0}\ ;$$
$$\mu_{12_i} = E[-i_1(t)\ q_2(t-\tau)]|_{\tau=0}\ ; \qquad \textbf{(4.94)}$$

When there is a time delay τ in one channel with respect to the other one, the measured correlations are no longer $\mu_{12\,r}$ and $\mu_{12\,i}$, but:

$$\hat{\mu}_{12_r} = e^{-\pi B'^2_{i_1 i_2}\tau^2}\left[\mu_{12_r}\cos(2\pi)f'_{i_1 i_2}\tau)-\mu_{12_i}\sin(2\pi)f'_{i_1 i_2}\tau)\right];$$
$$\hat{\mu}_{12_i} = e^{-\pi B'^2_{i_1 q_2}\tau^2}\left[\mu_{12_i}\cos(2\pi)f'_{i_1 q_2}\tau)+\mu_{12_r}\sin(2\pi)f'_{i_1 q_2}\tau)\right]; \qquad \textbf{(4.95)}$$

where the exponential term is the fringe-washing function, and the cos( ) and sin ( ) functions account for the rotation of the I/Q components when the demodulation has not translated the signals' components down to baseband. Note also that since the low-pass filters placed after the I/Q demodulators outputs can be different, B'_{i1i2} and B'_{i1q2}, $)f'_{i1i2}$ and $)f'_{i1q2}$ can also be different.

Let us compute the expected value for the real component μ_{12r} when the time delay τ is a gaussian random variable with mean t_d, sampling skew, and standard deviation F_τ, sampling jitter.

$$E[\hat{m}_{12_r}] = \frac{m_{12_r}}{\sqrt{2p}\,s_t}\int_{-\infty}^{+\infty}\cos(2p\,\Delta f'_{i1i2}(t_d+\Delta t))\,e^{-p(t_d+\Delta t)^2 B'^2_{i1i2}}e^{-\frac{\Delta t^2}{2s_t^2}}\,d\,\Delta t + \quad \textbf{(4.96)}$$

$$+\frac{m_{12_i}}{\sqrt{2p}\,s_t}\int_{-\infty}^{+\infty}\sin(2p\,\Delta f'_{i1i2}(t_d+\Delta t))\,e^{-p(t_d+\Delta t)^2 B'^2_{i1i2}}e^{-\frac{\Delta t^2}{2s_t^2}}\,d\,\Delta t$$

Defining:

$$k = 2s_t^2 B'^2_{i1i2}p;\quad a = \frac{p\,B'^2_{i1i2}t_d^2}{1+k};\quad b = 1+\frac{1}{k}; \qquad \textbf{(4.97)}$$

expression (4.96) can be computed as:

$$E[\hat{m}_{12_r}] = \frac{m_{12_r}}{\sqrt{2p}\,s}e^{-a}\int_{-\infty}^{+\infty}\cos(2p\,\Delta f'_{i1i2}(t_d+\Delta t))\,e^{-p(t_d+\Delta t)^2 B'^2_{i1i2}b}\,d\,\Delta t +$$

$$+\frac{m_{12_i}}{\sqrt{2p}\,s}e^{-a}\int_{-\infty}^{+\infty}\sin(2p\,\Delta f'_{i1i2}(t_d+\Delta t))\,e^{-p(t_d+\Delta t)^2 B'^2_{i1i2}b}\,d\,\Delta t = \qquad \textbf{(4.98)}$$

$$= \frac{e^{-\left(\frac{p\,\Delta f'_{i1i2}}{B'_{i1i2}b}+a\right)}}{\sqrt{2p\,b}\,s_t\,B'_{i1i2}}\left[m_{12_r}\cos\left(2p\,\Delta f'_{i1i2}\frac{t_d}{1+k}\right)+\,m_{12_i}\sin\left(2p\,\Delta f'_{i1i2}\frac{t_d}{1+k}\right)\right]$$

The expected value for the imaginary component μ_{12i} can be computed in a similar way:

$$E[\hat{m}_{12_i}] = \frac{e^{-\left(\frac{p\,\Delta f'_{i1q2}}{B'_{i1q2}b}+a\right)}}{\sqrt{2p\,b}\,s_t\,B'_{i1q2}}\left[m_{12_i}\cos\left(2p\,\Delta f'_{i1q2}\frac{t_d}{1+k}\right)-\,m_{12_r}\sin\left(2p\,\Delta f'_{i1q2}\frac{t_d}{1+k}\right)\right] \textbf{(4.99)}$$

To get an idea of the magnitudes involved, equations (4.98) and (4.99) will be simplified for the typical values of the parameters involved: for the MAX-915 high speed comparator $\sigma_\tau < 3$ ns and the propagation delay lies between 6 ns and 8 ns, $t_d < 2$ ns. The maximum equivalent noise bandwidth is about 30 MHz for the protected radioastronomy band 1,400-1,427 MHz and in the MIRAS case, with the LO at 1,395 MHz, $\Delta f' \approx 15\text{MHz} \pm 0.2$ MHz:

$$k = 0.051 \gg 1;\quad a = 0.011 \gg 1;\quad b = 20.65 \qquad \textbf{(4.100)}$$

Equations (4.98) and (4.99) reduce now to:

$$E[\hat{\mu}_{12_r}] = e^{-\pi\left[2\pi(\tau_{i_1 i_2}-\tau_{i_1 i_2}^{J})^2+(\pi\Delta f_{i_1 i_2}\Delta t_{i_1 i_2})^2\right]} \cdot \left[(\mu_{12_r}+j\mu_{12_i})e^{j2\pi\tau_{i_1 i_2}}\right] \qquad \textbf{(4.101)}$$

and:

$$E[\hat{\mu}_{12_i}] = e^{-\pi\left[2\pi(\tau_{i_1 q_2}-\tau_{i_1 q_2}^{J})^2+(\pi\Delta f_{i_1 q_2}\Delta t_{i_1 q_2})^2\right]} \cdot \left[(\mu_{12_r}+j\mu_{12_i})e^{j2\pi\tau_{i_1 q_2}}\right] \qquad \textbf{(4.102)}$$

The first term in equations (4.101) and (4.102) is a fringe-wash gain factor, about 0.95 for the above values, that affects each baseline separately and it is different for the real and the imaginary parts of the measured correlation. To allow baseline based calibration procedures this term must be very close to unity, and requires closely matched filters. The phase term inside the brackets is a different phase error in each component of the measured visibility sample. It can be decomposed in a baseline phase error and a quadrature baseline error:

$$M_{12}^{in\ phase} = \frac{M_{12_r}+M_{12_i}}{2} = \pi(\tau_{i_1 i_2}+\Delta t_{d_{i_1 i_2}}+\tau_{i_1 q_2}+\Delta t_{d_{i_1 q_2}}) < 10.8^{o}$$

$$M_{12}^{quadrature} = M_{12_r}-M_{12_i} = 2\pi(\tau_{i_1 i_2}+\Delta t_{d_{i_1 i_2}}-\tau_{i_1 q_2}-\Delta t_{d_{i_1 q_2}}) < 0.14^{o}$$

which are comparable to those introduced by the filters. Again, these values must be minimized by using closely matched filters and samplers. Since noise injection techniques to all the receivers are not technologically feasible for large arrays, the baseline phase error must be corrected i.e. by measuring a polarimetric hot point. The quadrature phase error can not be corrected, but has a small impact over the radiometric accuracy 0.18 K (figure 4.11, uncorrelated phase errors curve).

4.6.- RADIOMETRIC ACCURACY IMPROVEMENT BY PIXEL AVERAGING

In chapter 3 it was shown that a radiometric sensitivity improvement factor as high as six can be achieved by means of the pixel averaging technique, because for the selected MIRAS orbit, the error due to finite integration time is independent in each of the 36 available measurements per polarization, 11 seconds and 0.3 seconds/measurement. On the other hand, amplitude and phase errors are systematic or vary very slowly and can be considered constant over the averaging interval. The pixel averaging improvement is not easy to quantify and depends on the modified temperature distribution being imaged. However, an analytical study can be performed by assuming that the modified brightness temperature distribution is a constant 200 K scene inside the Earth, and the brightness temperature of the sky is zero.

When the visibility samples are corrupted with residual amplitude errors after calibration, the recovered modified brightness temperature can be computed from:

$$\hat{T}(x,h) = \frac{\sqrt{3}}{2} d^2 \sum_m \sum_n W(u_{mn},v_{mn}) V(u_{mn},v_{mn}) (1+\Delta V(u_{mn},v_{mn})) e^{j2p(u_{mn}x+v_{mn}h)} \quad \textbf{(4.103)}$$

where the visibility amplitude error satisfies that:

$$\Delta V(u_{mn},v_{mn}) = \Delta V(u_{-m-n},v_{-m-n}) \quad \textbf{(4.104)}$$

Similarly, when the visibility samples are corrup(ted with small phase errors, the recovered modified brightness temperature can be computed from:

$$\hat{T}(x,h) = \frac{\sqrt{3}}{2} d^2 \sum_m \sum_n W(u_{mn},v_{mn}) V(u_{mn},v_{mn}) e^{j\Phi_V(u_{mn},v_{mn})} e^{j2p(u_{mn}x+v_{mn}h)} \approx \quad \textbf{(4.105)}$$

$$\approx \frac{\sqrt{3}}{2} d^2 \sum_m \sum_n W(u_{mn},v_{mn}) V(u_{mn},v_{mn}) (1 + j\Phi_V(u_{mn},v_{mn})) e^{j2p(u_{mn}x+v_{mn}h)}$$

and, since the visibility function is a Hermitian function:

$$\Phi_V(u_{mn},v_{mn}) = -\Phi_V(u_{-m-n},v_{-m-n}) \quad \textbf{(4.106)}$$

Note that expressions (4.103) and (4.105) are formally identical. Defining:

$$e_{mn} = \Delta V(u_{mn},v_{mn}) \text{ or } j\Phi_V(u_{mn},v_{mn}) \quad \textbf{(4.107)}$$

Assuming that the errors are uncorrelated, except for a (u,v) point and its hermitian one, the average root mean squared error can be computed as (appendix 6):

$$\sigma_T^2 = E[\Delta T^2(x,h)] =$$

$$= E\left[\left(\frac{\sqrt{3}\,d^2}{2}\right)^2 \sum_m \sum_n \sum_r \sum_s W_{mn} W_{rs} V(u_{mn},v_{mn}) V^*(u_{rs},v_{rs}) e_{mn} e_{rs}^* e^{j2p[(u_{mn}-u_{rs})x+(v_{mn}-v_{rs})h]}\right] =$$

$$= \left(\frac{\sqrt{3}\,d^2}{2}\right)^2 \sigma_e^2 \sum_m \sum_n W_{mn}^2 |V(u_{mn},v_{mn})|^2 \pm \left(\frac{\sqrt{3}\,d^2}{2}\right)^2 \sigma_e^2 \sum_m \sum_n W_{mn}^2 \Re[V(u_{mn},v_{mn})^2 e^{-j4p(u_{mn}x+v_{mn}h)}] \quad \textbf{(4.108)}$$

where $\Re$ stands for the "real part" operator, the "+" sign applies to amplitude errors and the "-" sign applies to phase errors. Equation (4.108) can be approximated, leading to:

$$\sigma_T \approx \frac{\sqrt{3}\,d^2}{2} \sqrt{\sum_m \sum_n W_{mn}^2 |V(u_{mn},v_{mn})|^2}\, \sigma_e \quad \textbf{(4.109)}$$

which is independent of the pixel's location.

When the satellite is moving, each pixel follows a trace over the Earth's surface represented by the series of positions shown in figure 4.17 (appendix 8). Snap-shot pixels follow approximately a line:

$$(>(p),0(p)) \;'\; (>_0,0_0) \;\%\; (\,)>,\,)0)p; \quad p\;'\;0\ldots P\&1$$

$$)> \;'\; \frac{>_f\&>_0}{P\&1}; \qquad)0 \;'\; \frac{0_f\&0_0}{P\&1} \tag{4.110}$$

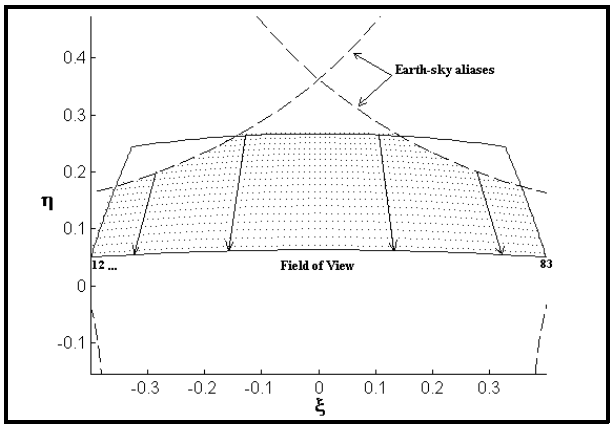

Figure 4.17.- Pixel's trace over the Earth limited to alias free FOV

The error after averaging all the (>,0) points over each line can be computed from:

$$\overline{)\,I\,(>,0)} \;'\; \frac{1}{P}\frac{\sqrt{3}}{2}d^2 \sum_{p}^{P\&1}{}_0 \;\sum_m \sum_n W_{mn}V(u_{mn},v_{mn}),_{mn} e^{j2B(u_{mn}>_0\%v_{mn}0_0)} e^{j2B(u_{mn})>\%v_{mn})0)p},$$

$$\times \frac{\sqrt{3}}{2}d^2 \sum_m \sum_n W_{mn}V(u_{mn},v_{mn}),_{mn} e^{\,j\mathsf{M}_{0_{mn}}} \left[\frac{1}{P}\sum_p^{P\&1}{}_0\, e^{\,j)\mathsf{M}_{mn}p}\right] ,$$

$$' \;\frac{\sqrt{3}}{2}d^2 \sum_m \sum_n W_{mn}V(u_{mn},v_{mn}),_{mn} e^{\,j\mathsf{M}_{0_{mn}}}\, e^{\,j\frac{)\mathsf{M}_{mn}}{2}(P\&1)} \;\frac{\sin\left(\,)\,\mathsf{M}_{mn}\,\frac{P}{2}\right)}{P\,\sin\left(\frac{)\mathsf{M}_{mn}}{2}\right)}$$

(4.111)

Remember that in a real situation the averaging must be done over the recovered parameter, i.e. soil moisture or ocean salinity, in order to avoid the dependence of the brightness temperature with the angle. The root mean squared error can be computed now, as in (4.108), assuming independent errors:

$$\sigma_T^2 = E[\Delta T^2] =$$

$$= E\left\{ \left[\frac{\sqrt{3}}{2} d^2 \sum_m \sum_n W_{mn} V(u_{mn}, v_{mn}) \cdot n_{mn} e^{j\Phi_{0_{mn}}} e^{j\frac{\Delta\Phi_{mn}}{2}(P-1)} \frac{\sin\left(\frac{\Delta\Phi_{mn}}{2}\right)}{P \sin\left(\frac{\Delta\Phi_{mn}}{2}\right)}\right]\right.$$

$$\left. \left[\frac{\sqrt{3}}{2} d^2 \sum_r \sum_s W_{rs} V^*(u_{rs}, v_{rs}) \cdot n_{rs} e^{-j\Phi_{0_{rs}}} e^{-j\frac{\Delta\Phi_{rs}}{2}(P-1)} \frac{\sin\left(\frac{\Delta\Phi_{rs}}{2}\right)}{P \sin\left(\frac{\Delta\Phi_{rs}}{2}\right)}\right]\right\} =$$

$$= \left(\frac{\sqrt{3}}{2} d^2\right)^2 \sigma_n^2 \sum_m \sum_n W_{mn}^2 |V(u_{mn}, v_{mn})|^2 \left[\frac{\sin\left(\frac{\Delta\Phi_m}{2}\right)}{P \sin\left(\frac{\Delta\Phi_m}{2}\right)}\right]^2 +$$

$$+ \left(\frac{\sqrt{3}}{2} d^2\right)^2 \sigma_n^2 \sum_m \sum_n W_{mn}^2 \Re\left[V^2(u_{mn}, v_{mn}) e^{-j4\pi(u_{mn}x_0 + v_{mn}y_0)}\right] \cdot$$

$$\cdot \left(\frac{\sqrt{3}}{2} d^2\right)^2 \sigma_n^2 \sum_m \sum_n W_{mn}^2 |V(u_{mn}, v_{mn})|^2 \left[\frac{\sin\left(\frac{\Delta\Phi_m}{2}\right)}{P \sin\left(\frac{\Delta\Phi_m}{2}\right)}\right]^2 \quad \textbf{(4.112)}$$

which can be approximated by:

$$\sigma_T = \frac{\sqrt{3}}{2} d^2 \sqrt{\sum_m \sum_n W_{mn}^2 |V(u_{mn}, v_{mn})|^2 \, sinc^2[u_{mn}(x_f - x_0) + v_{mn}(y_f - y_0)]}\ \sigma_n \quad \textbf{(4.113)}$$

Compared to equation (4.109) the "sinc^2 "function acts as a weighing function tapering long baselines for (>,0) pixels out of boresight. The pixel averaging gain can now be defined as the quotient of the root mean squared error without and with averaging:

$$G_{avg} \; ' \; \frac{F_I}{F_T} \qquad \textbf{(4.114)}$$

Figure 4.18 shows the averaging gain for the (>,0) points shown in figure 4.17, the visibility samples corresponding to the constant 200 K scene inside the Earth-sky border and the five windows under study: rectangular, triangular, Hamming, Hanning and Blackmann. Note that the gain factor is greater for pixels far from boresight because of the faster variations of the "sinc" function due to the higher ($>_f$->$_0$) and (0_f-0_0) terms.

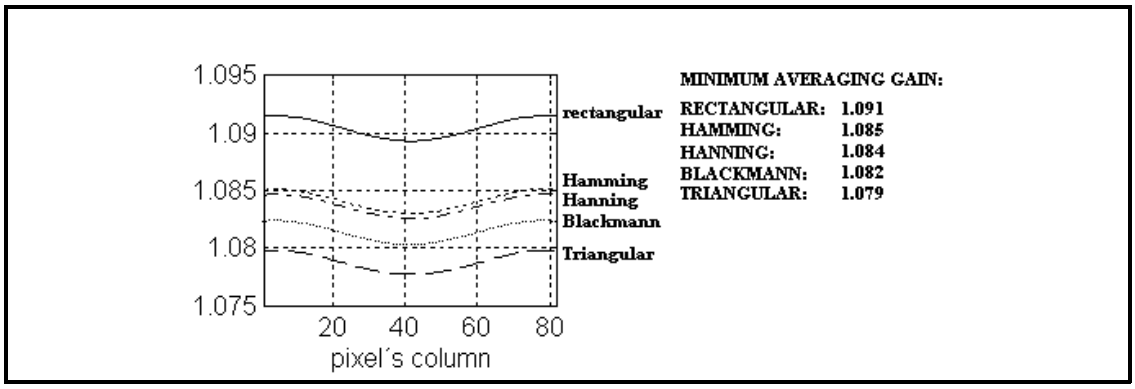

Figure 4.18.- Pixel averaging gain for an Y-array with 43 antennas per arm spaced 0.89 8

Pixel averaging improves the radiometric accuracy by a modest 8%, while radiometric sensitivity is improved by a 600%. This is due to the nature of the errors: phase and amplitude errors are multiplicative, while thermal noise due to finite integration time is additive.

Numerical simulations of this technique have been performed for the same test scene, in order to verify the analytical study for uncorrelated visibility amplitude and phase errors, but also to analyze the situation in which errors are correlated, because many baselines share a common antenna and receiver. Correlated/uncorrelated phase errors have been studied in the range from 0.2º to 4º. Correlated/uncorrelated amplitude errors have been studied in the range from 10 dB to 40 dB. The mean averaging gain for all the pixels is quite constant, and results for uncorrelated amplitude and phase errors are in agreement with the predicted results. However, the mean averaging gain for correlated errors is two times larger for phase errors and three times larger for amplitude errors. Tables 4.5 and 4.6 show the mean averaging gain for phase and amplitude correlated/uncorrelated errors with the Blackmann and the rectangular windows.

	Rectangular window	Blackmann window
Receiver phase error (correlated)	14.8 % ± 0.9 %	**12.4 % ± 1.1 %**
Baseline phase error (uncorrelated)	9.9 % ± 1.1 %	8.5 % ± 1.5 %

Table 4.5.- *Mean averaging gain for receiver and baseline phase errors*

	Rectangular window	Blackmann window
Receiver amplitude error (correlated)	25.8 % ± 3.6 %	**21.8 % ± 2.8 %**
Baseline amplitude error (uncorrelated)	12.4 % ± 1.0 %	9.9 % ± 1.5 %

Table 4.6.- *Mean averaging gain for receiver and baseline amplitude errors*

4.7.- SUMMARY OF SYSTEM ERRORS AND CONCLUSIONS.

In this chapter system errors have been systematically investigated and classified attending to their form in the visibility function: antenna errors, receiver or channel errors and baseline errors. Results are summarized in table 4.7 Their impact on the radiometric accuracy or sensitivity for the MIRAS space-borne instrument is given, as well as the tolerances of system parameters to achieve a performance close to SMOS recommendations (see section 1.5).

ERROR SOURCE	$(\delta T/T)/\delta\sigma_\Delta$	ACCURACY BUDGET	SENSITIVITY BUDGET	AFTER PIXEL AVERAGING
CONCEPT LIMITATIONS				
- discretization & windowing	-	0.02 K		0.00 K
- thermal noise τ=0.3s (mean value)	-		5.14 K (snap-shot)	0.86 K
SYSTEM IMPERFECTIONS				
***ANTENNA ERRORS**				
- Phase ripple (σ_ϕ=0.34º)	0.0074/º	0.50 K		0.44 K
- Amplitude rip. (σ_A=0.5%)	0.0053/%	0.53 K		0.44 K
- Coupling (σ_{Zij}= 7%)	0.0007/%	1.0 K		0.91 K
- Pointing (σ_θ=0.15º)	0.0064/º	0.20 K		0.16 K
- In-plane osc. (5mm)	0.0010/cm		0.10 K	0.02 K
- Off-plane osc. (5mm)	0.0046/cm		0.06 K	0.01 K
- V/H cross-talk (X-Polar:25dB)	-	0.16K (H-POL) 0.63K (V-POL)		0.15K(H-POL) 0.58K(V-POL)
***RECEIVER ERRORS**				
- In-phase & I/Q (σ_ϕ=0.1º)	0.0018/º	0.04 K		0.04 K
- Amplitude errors (TPRad)	-	0.02 K		0.02 K
- Amplitude errors ($\Delta\mu_{ij}$) ($\sigma_{\Delta TR}$ = 1.25 K)	0.001 /K	0.25 K		0.20 K

***BASELINE ERRORS**				
- Resid. Offset (OL) (F_{offset}=1.5.10^{-6})	-	0.07 K		0.06 K
- Filter's Phase errors (N_{12} = 0.43º)	-	0.18 K		0.17 K
- Filter's Amplit. errors ( ) μ_{ii}=0.002)	-	0.20 K		0.18 K
- Digital Correlators threshold errors	**-**	**-**		**-**
- Digital correlators delay errors:)f' . 15MHz±0.2MHz B'=30MHz, t_d = 2ns Phase error: 5.4º pre-cal, 0.1º cal	*0.0058 /º*	*0.03 K*		*0.03 K*
Quadrature error: 0.7º pre-cal	*0.0058/º*	*0.18 K*		*0.17 K*
TOTAL (quadratic summation)		***0.99K (H-POL) 1.17K (V-POL) (SNAP-SHOT)***	***5.14 K (SNAP-SHOT)***	***1.46K(H-POL) 1.57K(V-POL) (PIXEL AVG.)***

Table 4.7.- *System requirements and system radiometric resolution and sensitivity performances*

As it can be seen, one of the most important error sources are the antennas, which must have very well matched radiation voltage patterns in amplitude and phase and very low coupling. Anyway, if antenna pattern tolerances cannot be satisfied, they can be measured within this precision in order to be included in a suitable inversion algorithm (see chapter 6). A new approach to the antenna coupling impact over the visibilities has been developed from the impedance matrix of the array. Analytical results explain the shape of the interference patterns found in ESTAR [Ruf 91], showing the critical factors.

The second major problem comes from the filters, specially the narrow ones which determine the effective noise bandwidth, but introduce large non-separable amplitude and phase errors terms that hinder phase restoration and channel based noise injection calibration procedures (chapter 5). Digital correlators sampling delay errors introduce a non-separable phase error term that must be minimized by using high speed comparators with low skew delays and low jitter.

If the parameters' tolerances cannot be satisfied the required radiometric accuracy, 1 K, can be achieved by selecting a baseline based calibration procedure and by measuring the antennas' radiation voltage patterns to be included in an inversion algorithm.

Chapter 5. Calibration Procedures

As it has been shown in chapter four, amplitude and phase errors must be calibrated to achieve the required radiometric accuracy,) I < 1 K [SMOS 95]. The use of natural scenes as calibrators is not clear at present due to several factors: Earth and sky aliasing, natural calibrator models, scene temperature uncertainty.... In addition the use of *calibrating polarimetric warm points* over the Earth's surface is not feasible. At this point it must be pointed out recommendation g) from the SMOS Consultative Meeting [SMOS 95]:

> g) The group recommends to consider the importance of the integrity of the 1.400-1,427 MHz with respect to in-band interferors, as expressed in radio regulation RR8-92/721: "All emissions in the band 1,400 - 1,427 MHz are prohibited", and with respect to spurious signals of interferors from services in the adjacent bands.

In the absence of external calibrating signals, antenna imperfections can not be on-board calibrated (OB) and require an accurate on-ground characterization (OG) to be accounted for in the inversion algorithm (chapter six).

This chapter is devoted to investigate two calibration procedures: i) the application of the redundant space calibration method from radioastronomy to Earth observation and ii) a new method based on the injection of correlated noise to overlapped groups of antennas instead of the injection of the same correlated noise to all the antennas simultaneously. Both methods are based on the assumption that all amplitude and phase errors are separable. Consequently, baseline errors are disturbing factors that must be minimized by using closely matched receivers, filters and correlators. These errors can not be calibrated unless correlated noise is injected to all the channels simultaneously, which requires a large phase stable noise distribution network, at present technologically unfeasible.

5.1.- REDUNDANT SPACE CALIBRATION

5.1.1.- Introduction

The redundant space calibration method comes from radio-astronomy and it is based in the measurement of redundant baselines. A brief introduction of radio-astronomy precedents is presented and then the redundant space method is applied to the calibration of amplitude and phase of Y-arrays, by studying its geometry and the available redundancy. Finally, its robustness in front of error sources is studied: signal to noise ratio, non-separable phase and amplitude errors, quadrature errors, filter's and antenna mismatches.

5.1.2.- Radioastronomy precedents

Calibration techniques in radioastronomy benefit from the fact that most of the scenes being observed are known from prior measurements, mostly in the optical spectrum. These observations provide valid data which do not vary noticeably with time. A calibration is performed by measuring the complex gain factors for each baseline when pointing to a calibrating source close to the region to be observed and then pointing to the scene to be measured.

In radioastronomy, there are hundreds of very bright radio sources of small diameter isolated from other sources which are ideal for calibrating purposes. This calibration technique is specially useful because it allows to measure the impulse response of the system, calibrating the changes induced by the atmosphere, the antennas and the electronic systems, without any additional hardware.

However, this method can not be applied in all the situations. Rarely the complex gain factors affecting the calibrator are the same than those affecting the scene to be measured because they do not share the same atmospheric irregularities. This problem specially affects the phases of the measured visibilities. In fact, during some time, in the VLBI (Very Long Baseline Interferometer) only the amplitudes were used because the phase information was masked by clock instability and atmospheric fluctuations.

5.1.2.1.- Phase and amplitude closures

The "phase closure" is a relationship between the phases of each baseline for each set of three elements of the interferometer, which is independent of clock and atmospheric fluctuations [Jennison 58]. The relationship between the measured visibility phase and the ideal one takes the form:

$$N_{ij}^{raw} = f_i - f_j + N_{ij}^{id} \qquad (5.1)$$

where N^{raw}_{ij} is the phase of the measured visibility sample between antennas "i" and "j", f_i and f_j are the phase errors associated with each element (antenna + receiver) or "instrumental errors" and N^{id}_{ij} is the phase of the ideal visibility sample. Let's assume a closed loop between three baselines formed by three elements "i", "j" and "k". If N_{ij}, N_{jk} and N_{ki} are the phases associated to the visibilities corresponding to the spaces "ij", "jk" and "ki", then:

$$N_{ij}^{raw} + N_{jk}^{raw} + N_{ki}^{raw} = N_{ij}^{id} + N_{jk}^{id} + N_{ki}^{id} \qquad (5.2)$$

which is independent of the phase errors and depends only on the structure of the scene being observed.

The total number of phase closures can be computed graphically for a N- element array in the following way: with an antenna fixed all the triangles with two other antennas are formed. Any other combination between antennas can be written as a linear combination of the former phase closure relations. Consequently, the number of independent "phase closures" can be computed as [Rogstad 68]:

$$Number\ of\ phase\ closures = \binom{N-1}{2} = \frac{1}{2}(N-1)(N-2) \tag{5.3}$$

which agrees with the number of correlations minus the number of instrumental phase unknowns, taking an instrumental reference phase as zero.

Applying this method to the amplitudes, it can be found that each amplitude is affected by two gain factors (only receiver amplitude error terms):

$$|V_{ij}^{raw}| = |g_i|\,|g_j|\,|V_{ij}^{id}| \tag{5.4}$$

where $|V_{ij}^{raw}|$ is the amplitude of the measured visibility sample between the elements "i" and "j", $|g_i|$ and $|g_j|$ are the amplitude gain factors associated with each element and $|V_{ij}^{id}|$ is the amplitude of the ideal visibility sample. In order to form an "amplitude closure" and to cancel amplitude errors, four elements measuring four baselines are needed.

$$\frac{|V_{ij}^{raw}|\,|V_{kl}^{raw}|}{|V_{ik}^{raw}|\,|V_{jl}^{raw}|} = \frac{|V_{ij}^{id}|\,|V_{kl}^{id}|}{|V_{ik}^{id}|\,|V_{jl}^{id}|} \tag{5.5}$$

The number of amplitude closures can be computed for a 2D N-element array in a recursive way. For a 4-element array there are 2 amplitude closures, for a 5-element array there are 3 more closures, for a 6-element one there are 4 more closures. For a N-element 2D array there are:

$$Number\ of\ amplitude\ closures = \frac{1}{2}N(N-1)-N \tag{5.6}$$

which agrees with the total number of correlations (redundant or not) except the gain unknowns [Rogstad 68].

5.1.2.2.- "Self-calibration" and "redundant space calibration"

In radio-astronomy there are two basic methods to calibrate the measured visibilities based on the phase and amplitude closures. The "self-calibration" method is based on an "a priori" knowledge of the scene to be observed. The "redundant space calibration" is based on the use of the available redundancies present in the array.

The "self-calibration" method obtains the necessary data to solve the system of unknowns from the incomplete "a priori" knowledge of the scene. The initial model of the radio-sources is improved with the phase closures by an iterative method working in the space domain and its transformed one. The basic requirement of this method is that the total number of unknowns, complex gain unknowns plus number of parameters in the brightness temperature distribution model, is smaller than the total number of independent visibility samples. To perform well, this method requires a high signal-to-noise ratio and simple radio-sources structures [Thompson et al. 86], [NRAO 89]. Since polarimetric warm points are forbidden in the 1,400 MHz - 1,427 MHz band, "self-calibration" has little chances to be useful for space-borne Earth remote sensing sensors such as MIRAS.

On the other hand , the "redundant space calibration method" obtains the complex gain factors from different correlations measuring the same baseline. This method is very suitable to T- or Y-arrays because of the great number of redundant measurements along the arms where the antennas are placed. It is studied in the next section.

5.1.3.- Redundant space calibration applied to Y-shaped arrays

In an ideal system redundant baselines must produce the same visibilities. Deviations from this condition are due to instrumental gain and phase errors and their propagation during the inversion process [Hamaker 77]. If the number of redundant measurements leads to a determined/overdetermined system of equations the ideal visibility samples can be estimated from the separable error terms. However, as it is shown later, the absolute value of the brightness temperature distribution is lost as well as its exact position.

5.1.3.1. - Interferometer's geometry and available redundancies

Figure 5.1.a shows the geometry of an Y-array with 4 antennas per arm. An extra antenna (numbered 0) is located at the end of one arm for calibration purposes as will be shown later.

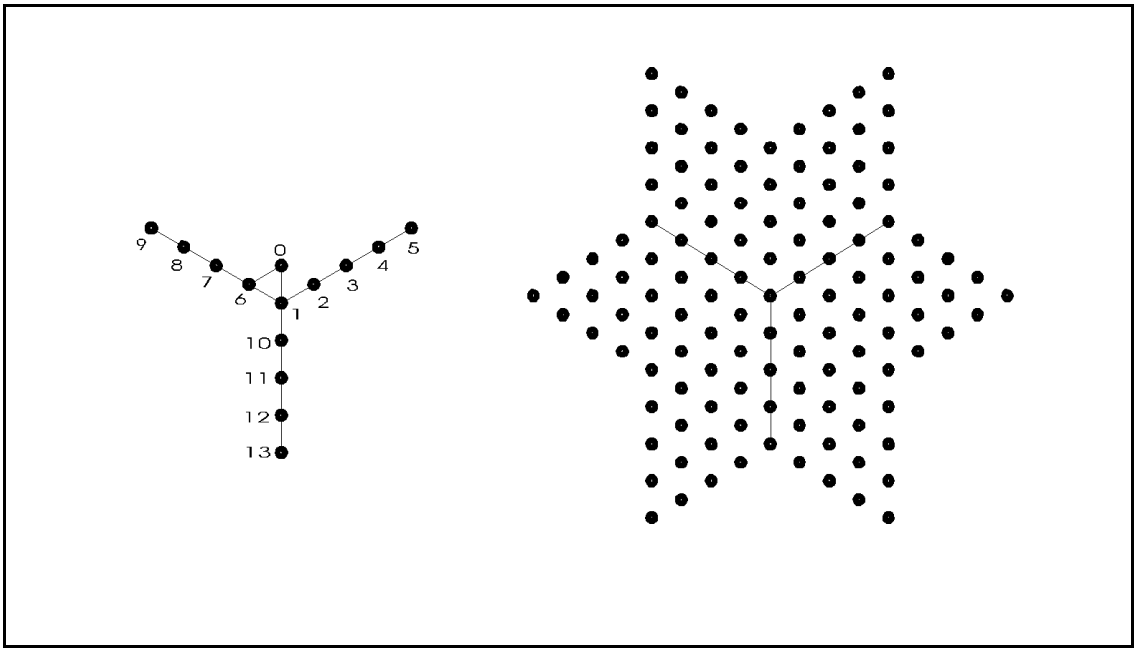

Figure 5.1.- *a) Y-array structure for 4 antennas per arm and b) its (u,v) coverage*

When all the correlations between the signals collected by all the antennas are measured, the set of visibility samples evaluated at the (u,v) points shown in figure 5.1.b is obtained. For an Y-array with N_{EL} antennas per arm there are $6N^2_{EL}+6N_{EL}+1$ (u,v) points, from which the sample at the origin is obtained by means of a total power radiometer and only half of the samples, $3N^2_{EL}+3N_{EL}$, have to be measured because the visibility function is hermitian.

Consequently, there are only $3N^2_{EL}+3N_{EL}$ independent correlations from a total number of ½ $(3N_{EL}+1)$ $(3N_{EL})$ = $4.5N^2_{EL}+1.5N_{EL}$. All the correlations between antennas placed in the same arm lead to ½ $(N_{EL}+1)$ N_{EL} redundant correlations. The 3/2 $(N_{EL}+1)$ N_{EL} redundant correlations are used by the "redundant space calibration method" to evaluate the gain and amplitude instrumental errors. In the next section the redundancy required to apply this method is studied.

5.1.3.2.- Phase closures

As it has been shown, phase closures are formed by the phases of the correlations measured between three antennas forming a loop:

$$N_{ij}^{raw} \cdot N_{jk}^{raw} \cdot N_{ki}^{raw} - N_{ij}^{id} \cdot N_{jk}^{id} \cdot N_{ki}^{id} \qquad \textbf{(5.7)}$$

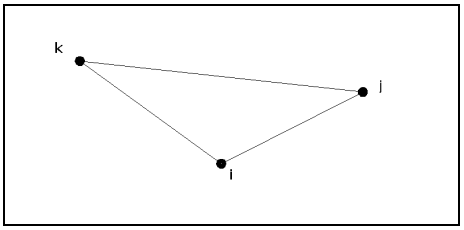

Figure 5.2.- *Baselines forming a phase closure*

The number of independent non-redundant phase closures is $3N^2_{EL} = 2N_{EL}.N_{EL}+N_{EL}.N_{EL}$, which is obtained from the baselines between an arm and the other two and the baselines between these two last arms. The number of visibility phases is then $N_V=3N^2_{EL}+ 3N_{EL}$.

Let see the general form of each of those closures using some redundant correlations. Assuming that antennas 2 and 3 are measuring the same baseline than antennas 1 and 2:

$$f^{raw}_{12} + f^{raw}_{23} - f^{raw}_{13} = f^{id}_{12} + f^{id}_{23} - f^{id}_{13} \qquad \textbf{(5.8)}$$

Since $f^{id}_{12} = f^{id}_{23}$:

$$f^{raw}_{12} + f^{raw}_{23} - f^{raw}_{13} = 2 f^{id}_{12} - f^{id}_{13} \qquad \textbf{(5.9)}$$

By performing all the possible correlations between the elements of an arm $\frac{1}{2}N_{EL}(N_{EL}-1)$ closures are obtained, a new equation for each new redundance. All those equations are not independent, since there are N_{EL} phases corresponding to the correlations between the central antenna and the other ones and only N_{EL}-1 independent linear equations, all visibility phases being referenced to one of them. For the whole array the total number of independent linear equations is 3 (N_{EL}-1) and the total number of unknowns is 3 N_{EL}, consequently a phase must be known in each arm to solve for the other phases. At this point the extra antenna, numbered 0 in figure 5.1.a, introduces new redundant correlations between antennas belonging to different arms, allowing to relate the reference phases of the three arms between them without introducing new unknowns.

$$f^{raw}_{01} + f^{raw}_{16} + f^{raw}_{60} = f^{id}_{01} + f^{id}_{16} + f^{id}_{60} \qquad \textbf{(5.10)}$$

but $f^{id}_{01} = f^{id}_{1,10}$ and $f^{id}_{60} = f^{id}_{12}$:

$$f^{raw}_{01} + f^{raw}_{16} + f^{raw}_{60} = f^{id}_{1,10} + f^{id}_{16} + f^{id}_{12} \qquad \textbf{(5.11)}$$

Finally, a system with two more unknowns than equations is obtained: two reference phases are needed, whose physical interpretation is commented in section 5.1.3.4.2.

Note that the planned MIRAS space-borne instrument has three extra antennas for calibration purposes. The two new extra antennas do not add new linear independent equations, but add robustness to the calibration procedure in the case of malfunctioning of one of them.

Table 5.1 summarizes the number of available equations and unknowns for the phase closures:

	N_{EL}	N_{EL}=43 (MIRAS SPACE BORNE)
number of phases	$3\ N_{EL}^2+3\ N_{EL}$	5676
number of non-redundant closures	$3\ N_{EL}^2$	5547
total number of closures	$4.5\ N_{EL}^2 - 1.5\ N_{EL}$	8256
number of independent closures	$3\ N_{EL}^2 + 3\ N_{EL} - 2$	5674
minimum number of redundancies	$3\ (N_{EL}-1)$ (+2 extra antenna)	126 (128)

Table 5.1.- *Number of phase closure equations, unknowns and redundancies for an Y-array*

5.1.3.3.- Amplitude closures

Amplitude closures are formed from the amplitudes of four correlations between four antennas whose baselines form a closed loop.

$$\frac{|V_{12}^{raw}||V_{34}^{raw}|}{|V_{13}^{raw}||V_{24}^{raw}|} = \frac{|V_{12}^{id}||V_{34}^{id}|}{|V_{13}^{id}||V_{24}^{id}|} \qquad \textbf{(5.12)}$$

or:

$$\frac{|V_{12}^{raw}||V_{34}^{raw}|}{|V_{14}^{raw}||V_{23}^{raw}|} = \frac{|V_{12}^{id}||V_{34}^{id}|}{|V_{14}^{id}||V_{23}^{id}|} \qquad \textbf{(5.13)}$$

Amplitude closures are multiplicative relationships between amplitudes which can be linearized by taking logarithms.

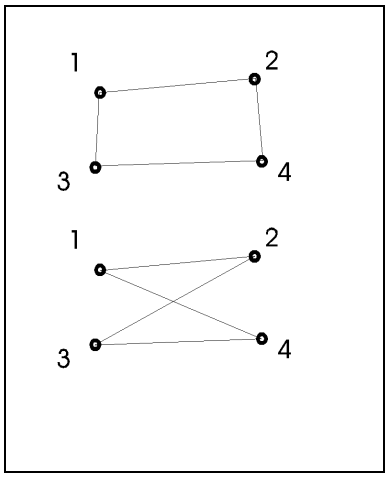

Figure 5.3.- *Possible amplitude closures*

The computation of the available number of amplitude closures was done in section 5.1.2.1, obtaining: ½ N_T (N_T - 3) = 4.5 N^2_{EL}- 1.5 N_{EL} - 1, N_T= 3 N_{EL} + 1, which agrees with the total number of correlations minus the number of instrumental errors: ½N_T (N_T-1) -N_T. Each redundant correlation that is eliminated, reduces one closure, if all the antennas appear correlated with two other antennas at least once. Since there are 3/2 N_{EL} (N_{EL}-1) redundant baselines in an Y-shaped array, the number on non-redundant amplitude closures is:

$$\textit{Number of independent amplitude closures} = 3N_{EL}^2 - 1 \qquad \textbf{(5.14)}$$

Table 5.2 summarizes the number of available equations and unknowns for the amplitude closures:

	N_{EL}	N_{EL}=43 (MIRAS SPACE-BORNE)
number of amplitudes	$3\,N_{EL}^2 + 3\,N_{EL}$	5676
number of non-redundant closures	$3\,N_{EL}^2 - 1$	5546
total number of closures	$4.5\,N_{EL}^2 - 1.5\,N_{EL} - 1$	8255
number of independent closures	$3\,N_{EL}^2 + 3\,N_{EL} - 1$	5675
minimum number of redundancies	$3\,N_{EL}$	129

Table 5.2.- *Number of amplitude closure equations, unknowns and redundancies for an Y-array*

5.1.3.4.- Solution of the system of equations

Once the general form of the equations for the phase and amplitude closures has been shown, the whole system of equations can be set and then solved. Matrix $\overline{\overline{A}}$ relates the ideal visibility phases in the phase closures relations and matrix $\overline{\overline{B}}$ relates the measured visibility phases, including the redundant ones.

$$\begin{bmatrix} 2 & -1 & 0 & 0 & \cdots & 0 & 0 & \cdots \\ 1 & 0 & -1 & 0 & \cdots & 1 & 0 & \cdots \\ 1 & 0 & 0 & -1 & \cdots & 0 & 1 & \cdots \\ 1 & 0 & 0 & 0 & \cdots & \cdots & \cdots & \cdots \\ \cdots & \cdots & \cdots & \cdots & \cdots & \cdots & \cdots & \cdots \\ \cdots & \cdots & \cdots & \cdots & \cdots & \cdots & \cdots & \cdots \end{bmatrix} \begin{bmatrix} N_{12}^{id} \\ N_{13}^{id} \\ N_{14}^{id} \\ \cdots \\ \cdots \\ \cdots \end{bmatrix} = \begin{bmatrix} 1 & -1 & 0 & 0 & \cdots & 1 & 0 & 0 & \cdots \\ 1 & 0 & -1 & 0 & \cdots & 0 & 1 & 0 & \cdots \\ 1 & 0 & 0 & -1 & \cdots & 0 & 0 & 1 & \cdots \\ 1 & 0 & 0 & 0 & \cdots & \cdots & \cdots & \cdots & \cdots \\ \cdots & \cdots & \cdots & \cdots & \cdots & \cdots & \cdots & \cdots & \cdots \\ \cdots & \cdots & \cdots & \cdots & \cdots & \cdots & \cdots & \cdots & \cdots \end{bmatrix} \begin{bmatrix} N_{12}^{raw} \\ N_{13}^{raw} \\ N_{14}^{raw} \\ \cdots \\ \cdots \\ \cdots \\ N_{23}^{raw} \\ \cdots \end{bmatrix} \qquad \textbf{(5.15)}$$

$$\overline{\overline{A}}\,\overline{N}^{id} = \overline{\overline{B}}\,\overline{N}^{raw}$$

For a 43-antennas per arm, such as MIRAS space-borne, matrix **A** is 5.804 x 5.676

and matrix $\overline{\overline{B}}$ is 5.804 x 5.804, including the equations that relate the reference phases and using only the minimum number of redundant correlations. The solution of this system of equations requires a high computational capability that can be minimized by noticing that it is equivalent to know only the visibility phases, $3\,N^2_{EL} + 3\,N_{EL}$, or the instrumental phase errors, $3\,N_{EL}$. If the smallest baselines are taken as the redundant ones, the phase closure equations can be written as:

$$\begin{aligned} N_{12}^{raw} &= 0 - f_2 + N_{12}^{id} \\ N_{23}^{raw} &= f_2 - f_3 + N_{12}^{id} \\ N_{34}^{raw} &= f_3 - f_4 + N_{12}^{id} \\ &\ldots \end{aligned} \qquad \textbf{(5.16)}$$

where f_i is the instrumental error of the element "i" (antenna + receiver), not to be confused with receiver's central frequency, and N are the phases of the correlations. Note that the first element phase is taken as the reference one, and its phase is assigned to 0.

Equation (5.16) can be written matricially as:

$$\begin{bmatrix} 1 & -1 & 0 & 0 & 0 & 0 & \cdots \\ 1 & 1 & -1 & 0 & 0 & 0 & \cdots \\ 1 & 0 & 1 & -1 & 0 & 0 & \cdots \\ 1 & 0 & 0 & 1 & -1 & 0 & \cdots \\ \cdots & \cdots & \cdots & \cdots & \cdots & \cdots & \cdots \\ \cdots & \cdots & \cdots & \cdots & \cdots & \cdots & \cdots \end{bmatrix} \begin{bmatrix} N_{12} \\ \cdot \\ f_2 \\ f_3 \\ f_4 \\ \cdot \end{bmatrix} = \begin{bmatrix} N_{12}^{raw} \\ N_{23}^{raw} \\ N_{34}^{raw} \\ \cdot \\ \cdot \\ \cdot \end{bmatrix} \qquad \textbf{(5.17)}$$

$$\overline{\overline{C}}\,\overline{f_i} = \overline{N}^{raw}$$

For a 43-antennas per arm, such as MIRAS space-borne, matrix $\overline{\overline{C}}$ is 132 x 132, using the minimum number of correlations: 43 in each arm and other two generated by the extra antenna relating the reference phases. Once the instrumental channel phases, f_i, are known, the calibrated visibility phases N_{ij} can be derived from the measured ones N_{ij}^{raw} and the f_i's:

$$N_{ij}^{id} = N_{ij}^{raw} - f_i + f_j \qquad \textbf{(5.18)}$$

For the amplitude closures a similar system of equations can be derived:

$$\begin{bmatrix} 1 & . & 1 & 1 & 0 & 0 & 0 & 0 & . \\ 1 & . & 0 & 1 & 1 & 0 & 0 & 0 & . \\ 1 & . & 0 & 0 & 1 & 1 & 0 & 0 & . \\ 1 & . & 0 & 0 & 0 & 1 & 1 & 0 & . \\ . & . & . & . & . & . & . & . & . \\ . & . & . & . & . & . & . & . & . \\ . & . & . & . & . & . & . & . & . \end{bmatrix} \begin{bmatrix} \log|V_{12}| \\ . \\ \log(g_1) \\ \log(g_2) \\ \log(g_3) \\ \log(g_4) \\ . \end{bmatrix} = \begin{bmatrix} \log|V_{12}^{raw}| \\ \log|V_{23}^{raw}| \\ \log|V_{34}^{raw}| \\ \log|V_{45}^{raw}| \\ . \\ . \\ . \end{bmatrix} \qquad \textbf{(5.19)}$$

$$\overline{\overline{D}}\ \overline{\log(g_i)} = \overline{\log|V_{ij}|}^{raw}$$

where matrix $\overline{\overline{D}}$ is 136 x 136, including the equation that forces the amplitude reference.

Once the instrumental channel gains g_i, are known, the calibrated visibility amplitudes $|V_{ij}^{id}|$ can be derived from the measured ones $|V_{ij}^{raw}|$ and the g_i's:

$$|V_{ij}^{id}| = \frac{|V_{ij}^{raw}|}{|g_i|\,|g_j|} \qquad \textbf{(5.20)}$$

5.1.3.4.1.- Reference phases

In this section the impact of an error in the reference phases required by the redundant space calibration method is studied. Considering only the correlations between antennas along an arm and that the phase reference is taken between the first and the second element, the phase closure relationships can be written as:

$$\Phi_{12}^{raw} + \Phi_{23}^{raw} - \Phi_{13}^{raw} = 2\Phi_{12}^{id} - \Phi_{13}^{id} \qquad \textbf{(5.21)}$$

equivalently:

$$\Phi_{13}^{id} = 2\,\Phi_{12}^{id} + \textit{linear combination of measured phases} \qquad \textbf{(5.22)}$$

In general:

$$\Phi_{1n}^{id} = (n-1)\,\Phi_{12}^{id} + \textit{linear combination of measured phases} \qquad \textbf{(5.23)}$$

and for the correlations between two different arms:

$$\Phi_{ij}^{id} = m\,\Phi_{1a}^{id} + n\,\Phi_{1b}^{id} + \textit{linear combination of measured phases} \qquad \textbf{(5.24)}$$

where Φ^{id}_{1a} and Φ^{id}_{1b} are the reference phases corresponding to the arms containing antennas "i" and "j" respectively, and "m" and "n" are factors that grow linearly with the

distance from antennas "i" and "j" to the central one. This linear dependence has two important consequences:
i) Errors in the reference phases propagate along the elements growing linearly with the distance to the central antenna, translating into a linear displacement of the recovered modified temperature distribution. In radio-astronomy this information can be recovered by an accurate knowledge of the position of some radio-sources. In an Earth remote sensor such as MIRAS this information may be recovered by looking at the shape of the Earth aliases in the recovered modified temperature distribution, as it is shown in figure 5.4.

ii) Errors induced in a baseline by noise, antenna mutual coupling, non-separable error terms... accumulate along the arm and long baselines suffer from larger phase errors.

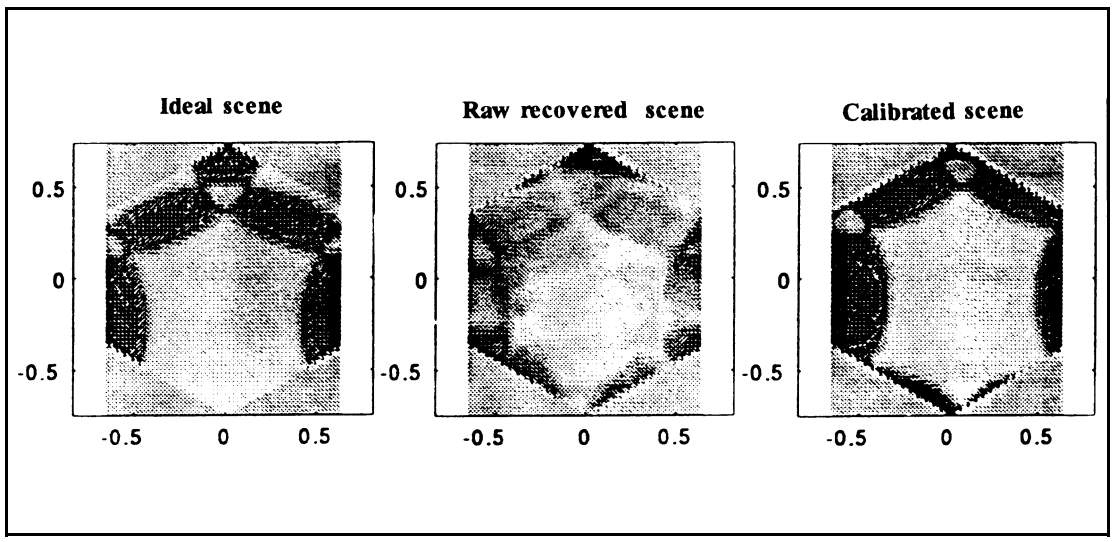

Figure 5.4.- *Calibrated test scene with a phase reference error of 45º. Test scene consisting of a 200K constant modified temperature inside the Earth border.*

To avoid this problem correlated noise can be injected to a reduced set of antennas at the center of the array (e.g. 1, 2, or 3 antennas per arm plus the central one) allowing to compute the complex gain g_m of each receiver. In this case, the shortest baselines, the most significant ones, and the reference phases are computed with high accuracy by the noise injection method (see section 5.2). The redundant space method is then used to calculate the remaining g_m complex factors for longer baselines. Note that this mixed method has the advantage that does not require a large and heavy power distribution network to drive correlated noise to all the receivers.

5.1.3.4.2.- The role of the extra antenna

A phase error in an arm forces a translation of the recovered modified temperature distribution in the direction of this arm. The extra antenna, numbered as "zero", relates the phases in the three arms which are no longer independent:

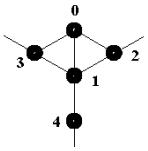

$$N_{01}^{raw} + N_{13}^{raw} + N_{30}^{raw} = N_{14}^{id} + N_{13}^{id} + N_{12}^{id} \qquad \textbf{(5.25)}$$

$$\Delta N_{12} + \Delta N_{13} + \Delta N_{14} = 0$$

However, non-separable phase terms in the baselines forming the loop are not included in equation (5.25) and, in general:

$$\Delta N_{12} + \Delta N_{13} + \Delta N_{14} \neq 0 \qquad \textbf{(5.26)}$$

which translates in a phase aberration in the recovered modified temperature distribution.

5.1.3.4.3.- Selection of the redundant baselines.

From a low-orbit remote sensor the Earth appears as an extended thermal source. This means that its associated visibility function, spatial Fourier Transform, has a rapid decline with the baseline distance. On the other hand, the baseline noise is constant and does not depend on the amplitude of the measured correlation (equation (3.65) with $\Delta f > B/2$):

$$\sigma_V^2 = \sigma_r^2 + \sigma_i^2 = \frac{1}{\sqrt{2}\, B\, J_{eff}} (T_B + T_{R_1})(T_B + T_{R_2}) \qquad \textbf{(5.27)}$$

Consequently, the redundant space calibration is more robust if the smallest baselines are used as the redundant ones.

5.1.3.4.4. - Raw measurements pre-processing.

$\mu^{(5)}$, the normalized raw visibilities at the output of the 1 bit/ two level digital correlators include all the errors studied in chapter four: antenna errors, receiver's and correlator's phase/quadrature and amplitude errors, separable or not, and offset errors induced by local oscillator's leakage. The redundant space calibration method does not deal with all of them and some must be pre-calibrated (see figure 5.5):

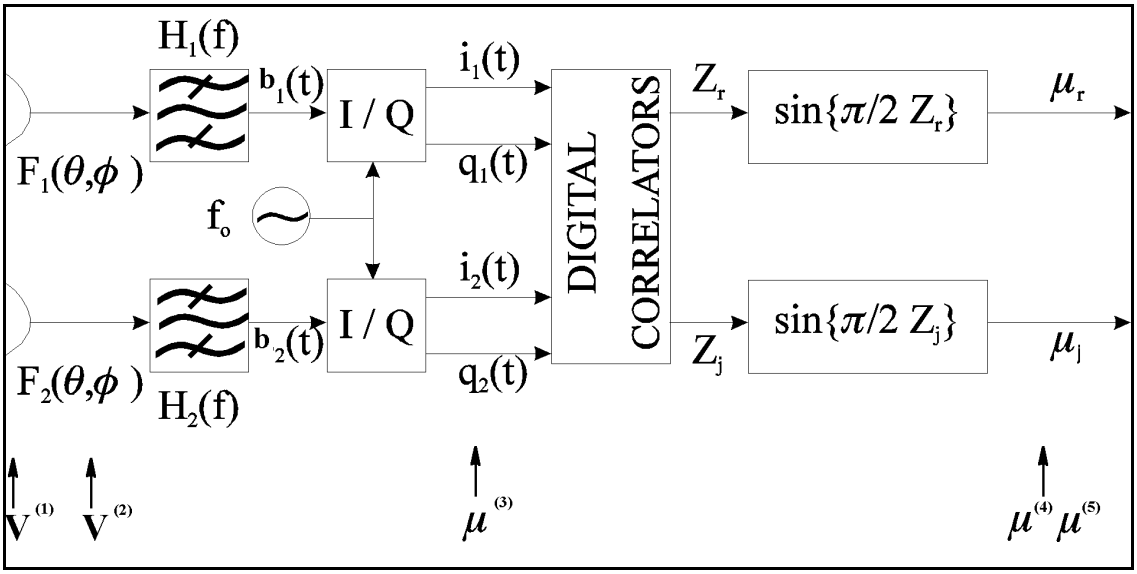

Figure 5.5.- *Visibilities definition.*

i) $\mathbf{Z}^{(4)}$ is computed by extracting the offset in $\mathbf{Z}^{(5)}$. This is done as:

$$Z_{raw}^{(4)} \leftarrow Z_{raw}^{(5)} * _{corr} \& Z_{raw}^{(5)} * _{uncorr} \qquad \textbf{(5.28)}$$

Note that the offset is measured by injecting uncorrelated noise to all the receivers, which is done by switching each antenna to a matched load.

ii) $\boldsymbol{\mu}^{(4)}$ is computed taking into account the non-linear relationship between the measured correlation given by 1B/2L correlators and the ideal normalized correlation:

$$\mu_{raw}^{(4)} \leftarrow sin\left(\frac{B}{2} Z_{raw}^{(4)}\right) \qquad \textbf{(5.29)}$$

iii) $\boldsymbol{\mu}^{(\text{red sp cal})}$ is computed by removing the quadrature phase errors:

$$\overline{\mu^{(3)}} \leftarrow \frac{1}{g_1} \frac{1}{g_2} \overline{\mu^{(4)}}$$

$$\begin{bmatrix} \mu_r^{(3)} \\ \mu_i^{(3)} \end{bmatrix} \leftarrow \begin{bmatrix} 1 & 0 \\ \sin(2_{qi}) & \cos(2_{qi}) \end{bmatrix} \begin{bmatrix} \cos(2_{oj} \& 2_{oi}) & \sin(2_{oj} \& 2_{oi}) \\ \& \sin(2_{oj} \& 2_{oi}) & \cos(2_{oj} \& 2_{oi}) \end{bmatrix} \begin{bmatrix} \mu_r^{(2)} \\ \mu_i^{(2)} \end{bmatrix} \qquad \textbf{(5.30)}$$

$$\overline{\mu}^{(3)} \leftarrow \overline{\overline{P_k}}\, \overline{\mu}^{(2)} \leftarrow \overline{\overline{P_q}}\, \overline{\overline{P_2}}\, \overline{\mu}^{(2)}$$

$$\overline{\mu}^{(red\ sp\ cal)} \leftarrow \overline{\overline{P_q}}^{\&1}\, \overline{\mu}^{(3)} \leftarrow \overline{\overline{P_2}}\, \overline{\mu}^{(2)}$$

iv) Compute $\mathbf{V}^{(1)}$ by applying the redundant space calibration method to $\mathbf{V(0,0)}$ $\boldsymbol{\mu}^{(\text{red sp cal})}$ and estimating the receiver gain and phase factors.

v) Apply a suitable inversion algorithm to the calibrated visibility samples $V^{(1)}$ (see chapter six).

Note that antenna coupling errors are still present in $\mu^{(red\ sp\ cal)}$ and degrade the performance of the calibration method as shown later.

5.1.4.- Robustness of the method

In order to test the method, the raw visibilities V^{raw} of the modified temperature distribution $T(\xi,\eta)$ defined in equation (4.13) have been computed by introducing antenna and receiver imperfections to each channel:

$$V_{mn}^{raw}(u,v) = \iint_{x^2+h^2\le 1} T(x,h)\, F_{n_m}(x,h)\, F^{*}_{n_n}(x,h)\, \tilde{r}_{mn}(-t)\, e^{-j2p(ux+vh)}\, dx\, dh + \Delta V_{nm} \qquad \textbf{(5.31)}$$

where ΔV_{nm} is complex noise due to the finite integration time and $\tilde{r}_{mn}(-t)$ is the fringe-wash term includes receiver phase and amplitude error terms. Note that in the case of antenna pattern imperfections the double integral must be computed for each visibility sample V^{raw}_{mn}. However, in the case that antenna errors are not taken into account and the spatial delay is negligible, $\tau \approx 0$, equation (5.31) can be simplified to:

$$V_{mn}^{raw}(u,v) = G_{mn} V^{id}(u,v) + \Delta V_{mn} \qquad \textbf{(5.32)}$$

where $V^{id}(u,v)$ is the ideal visibility sample computed as the Fourier transform of the test scene and G_{mn} is the baseline complex gain between antennas "m" and "n". Once V^{raw} is computed by one of the two methods, the redundant space calibration procedure is applied to estimate the baseline complex gains G_{mn} and to calibrate the raw visibilities:

$$V_{mn}^{cal}(u,v) = \hat{g}_m^{-1}\, \hat{g}_n^{-1}\, V_{mn}^{raw}(u,v) \qquad \textbf{(5.33)}$$

To test the calibration robustness the temperature distribution is recovered from an hexagonal inverse discrete Fourier Transform (see chapter six) when there are only residual errors:

$$\hat{T}(x,h) = F_H^{-1}\left[W(u,v) V^{cal}(u,v)\right] \qquad \textbf{(5.34)}$$

and by means of a suitable inversion algorithm (chapter 6), in the case that antenna errors are considered. The radiometric root mean squared error has been computed from (4.15) inside the circle shown in figure 4.4 .

In the following paragraphs the redundant space calibration procedure is tested to assess its robustness when dealing with different kinds of errors. Simulations are performed for an Y-array with 43 antennas per arm, such as the MIRAS space-borne case, when computation time

and memory allocation are not limited, and for an Y-array with 15 antennas per arm otherwise. Radiometric accuracy due to discretization and finite coverage of the (u,v) plane relating this two case of interest are $\Delta T = 0.13$ K for $N_{EL}=15$, and $\Delta T=0.03$ K for $N_{EL}= 43$, which are the absolute lower bound for radiometric error.

5.1.4.1.- Effect of signal-to-noise ratio

In this case only a random complex noise term is added to the raw visibility samples in order to simulate the effect of the finite integration time. The reference amplitude and phases are supposed to be perfectly known. To asses the impact at each signal-to-noise ratio 50 simulations have been performed. In each one both the receiver parameters g_m and the complex random term ΔV_{mn} have been changed. To compute the error introduced by the calibration method, the degradation in the radiometric accuracy has been computed as:

$$\Delta T^2 = s^2_{T_{calibrated}} - s^2_{T_{noise}} \qquad \textbf{(5.35)}$$

In this case σ_{Tnoise} is the radiometric error when the calibration is not required, there are not phase and amplitude errors and the temperature distribution is recovered by a direct inverse Fourier transform of the visibility samples contaminated with noise. $\sigma_{Tcalibrated}$ is the radiometric error when the calibration has to be performed previously to the inverse Fourier transform. In this way *DT represents the degradation of radiometric resolution at each S/N due to the calibration.* Simulations have been performed for $N_{EL}=15$. Results are summarized in table 5.3. The error recovering the channel phases ϕ_m and the channel gains $|g_m|$ is included.

S/N	$\sigma_{\phi m}$	$\sigma_{\|gm\|}$	ΔT	σ_{Tnoise}
30 dB	1.8628	3.6547 %	3.0 K	8.91 K
35 dB	0.5906	1.0779 %	0.73 K	2.82 K
40 dB	0.2024	0.3437 %	0.20 K	0.90 K
45 dB	0.0602	0.1047 %	0.12 K	0.31 K

Table 5.3.- *Radiometric accuracy degradation due to calibration affected by noise*

The snap-shot degradation for an Y-shaped array of 43 antennas per arm is about 0.73 K. However it should be pointed out that the instrument does not change during adjacent measurements and averaging of the recovered amplitude and phase parameters can be perfomed. If each image is corrected from the output of the last 100 measurements, then the equivalent S/N when calibrating is 45 dB and the degradation falls down to 0.12 K. Of course, it assumes that the reference phase and amplitude do not change during averaging.

Figure 5.6 shows the rms error on phase and amplitude for each antenna when the signal-to-noise ratio is 45 dB. Note that error increases linearly as the antennas are more distant to the center of the array due to error propagation.

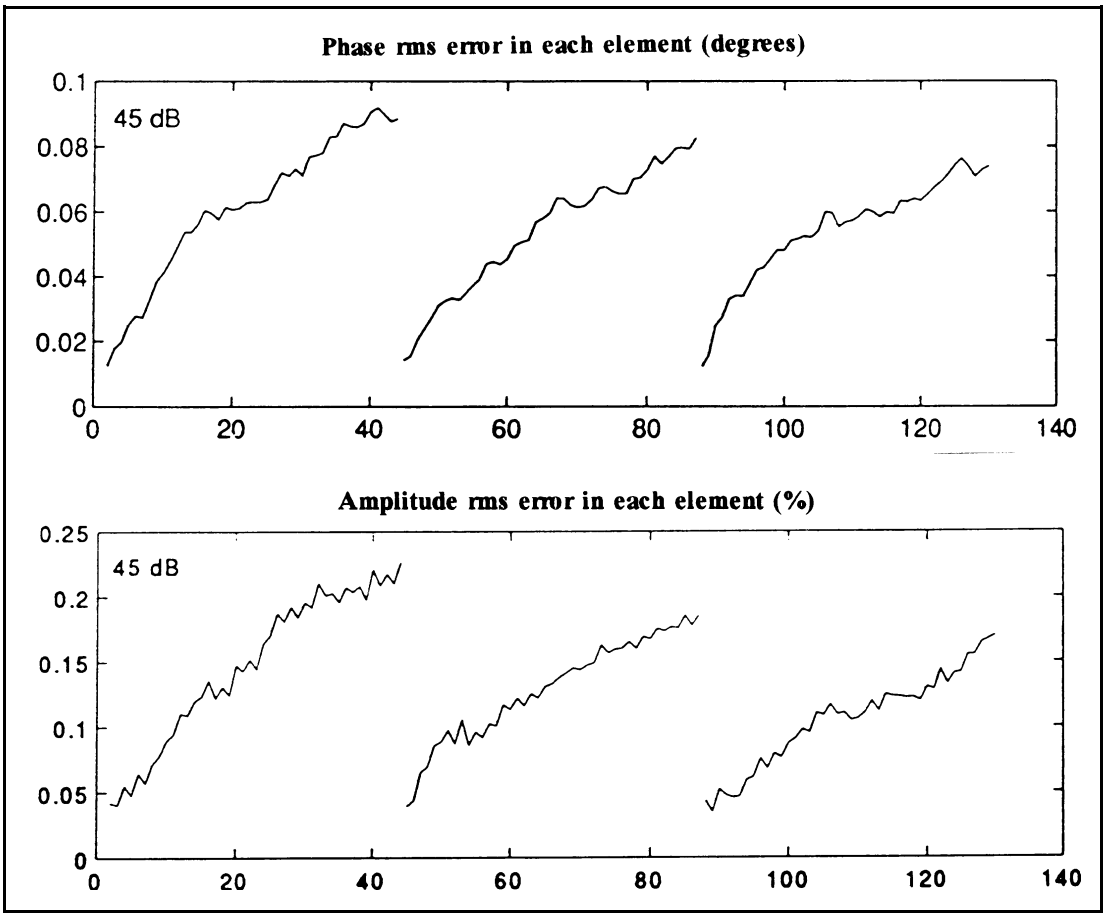

Figure 5.6.- *RMS error on phase and amplitude vs. antenna number, S/N = 45 dB.*

5.1.4.2.- Effect of non-separable error terms

As seen previously, the baseline complex gain G_{mn} was factorized into single channel complex gains $g_m g_n$. However, in a real case there is a non-separable part g_{mn} that cannot be split into isolated complex factors. In this case, the measured visibility is expressed as:

$$V_{mn}^{raw} = G_{mn} V_{mn}^{id} \qquad V_{mn}^{raw} = g_m g_n g_{mn} V_{mn}^{id} \qquad \textbf{(5.36)}$$

Such non-separable complex factors are due filter misalignments in each receiver channels and to sampling errors in the correlators. The calibration process cannot estimate this factor, which contaminates the calibration procedure and remains as a residual error. This residual error can be expressed as $g_{mn}=(1+\varepsilon_{mn})e^{j\phi_{Nmn}}$. To assess the impact of non-separable phase errors on the radiometric resolution, V^{raw} has been calculated adding non-separable phase errors. Simulations have been performed for $N_{EL}=15$ and the degradation of radiometric resolution ΔT has been calculated with respect to the ideal case (only discretization and finite coverage errors, but without noise) for a constant temperature distribution at T=200 K (figure 4.4). Results are summarized in table 5.4.

$\Delta\phi_{mn}$	$F_{\Delta\phi m}$	ΔT
0.1 E	1.3695 E	0.17 K
0.3 E	4.1753 E	0.7 K
1 E	16.5411 E	1.86 K

Table 5.4.- *Radiometric accuracy degradation vs. non-separable phase error.*

Note that the calibration algorithm amplifies the rms phase error. The non-separable phase error $\Delta\phi_{mn}$ must be kept below 0.3° which imposes serious restrictions on filters tolerances (see table 4.4) and correlator's samplers. In the case of amplitude errors we have:

$\Delta\varepsilon_{mn}$	$F_{\Delta\varepsilon m}$	ΔT
0.1 %	0.5235 %	0.3 K
0.5 %	2.3550 %	0.9 K

Table 5.5.- *Radiometric accuracy degradation vs. non-separable amplitude error.*

Amplitude errors are also amplified by the calibration procedure. The non-separable amplitude error $\Delta\varepsilon_{mn}$ must be kept about 0.2% to get an acceptable residual error, leading to very restrictive filter tolerances. For an equivalent gaussian filter parameters' deviations must be bound by (see section 4.5.1.2): f_o = 1.4 GHz, B = 25 MHz, J_o= 80 ns, $\Delta f_i^* < 0.5$ MHz, $\Delta B_i^* < 1$ MHz, $\Delta J_i^* < 2$ ns. Sampling tolerances in the correlator's samplers are also very restrictive, and sampling errors must be also smaller than 2 ns (see section 4.5.3.2).

Non-separable amplitude and phase terms are introduced mainly by filter mismatches and timing errors in the comparator's samplers. Since the redundant space method requires very low non-separable terms, this gives very stringent filter specifications that are very difficult to achieve. If filter parameters have low drift due to aging and

temperature, their specifications can be greatly relaxed by non-separable error pre-processing. If the receiver voltage response $H_m(f)$ is ground tested for all the channels, the filter contribution can be computed for each baseline as:

$$\tilde{r}(0) = F^{-1}[H_m(f)\ H_n^*(f)]e^{-jw_0 t} \qquad \textbf{(5.37)}$$

and , the raw visibilities can be pre-processed as:

$$V_{mn}^{pre\text{-}proc} = \frac{V_{mn}^{raw}}{\tilde{r}(0)} \qquad \textbf{(5.38)}$$

the redundant space calibration procedure is applyied to $V^{pre\text{-}proc}$, in which the non-separable terms have been significantly reduced.

5.1.4.3.- Effect of quadrature errors

As it has been shown quadrature errors must be removed prior to applying the redundant space method since they do not allow the complex notation of the baseline gain G_{mn}. Instead, a matricial relationship is required:

$$\begin{bmatrix} m_r^{(4)} \\ m_i^{(4)} \end{bmatrix} = g_i g_j \begin{bmatrix} 1 & 0 \\ \sin(q_{qi}) & \cos(q_{qi}) \end{bmatrix} \begin{bmatrix} \cos(q_{oj} - q_{oi}) & \sin(q_{oj} - q_{oi}) \\ -\sin(q_{oj} - q_{oi}) & \cos(q_{oj} - q_{oi}) \end{bmatrix} \begin{bmatrix} m_r^{(2)} \\ m_i^{(2)} \end{bmatrix} \qquad \textbf{(5.39)}$$

Quadrature errors can be tested on-ground and assumed not to drift or can be estimated by placing additional correlators to correlate the in-phase I_m and the quadrature signal Q_m at each receiver output as:

$$q_{qm} = \arcsin\left[E[I_m, Q_m] \right] \qquad \textbf{(5.40)}$$

This solution requires $3N_{EL}$ extra correlators, which is not a significant increase considering the total number of correlators [Laursen 95]. Now, quadrature errors can be removed by left multiplication of $\boldsymbol{\mu}^{(4)}$ by the inverse of the quadrature matrix $\overline{P}_q^{-1}$

$$\overline{m}^{(4)} = g_1 g_2 \overline{P_k}\, \overline{m}^{(2)} = g_1 g_2 \overline{P_q}\, \overline{P_q}\, \overline{m}^{(2)} \qquad \textbf{(5.41)}$$

$$\overline{m}^{(red\ sp\ cal)} = \overline{P_q}^{-1}\, \overline{m}^{(4)}$$

The impact over the radiometric accuracy of residual quadrature errors is summarized in table 5.6.

$\sigma_{\theta q}$	$\sigma_{\phi m}$	$\sigma_{\Delta m}$	ΔT
0.1°	0.8554°	0.1557 %	0.07 K
0.3°	2.0723°	0.4250 %	0.16 K
1°	6.0507°	1.2645 %	1.09 K
2°	13.9492°	2.3833 %	1.57 K

Table 5.6.- *Radiometric accuracy degradation vs. residual quadrature error.*

In this case residual quadrature errors $\sigma_{\theta q}$ must be kept around 0.3° or below.

5.1.4.4.- Effect of antenna imperfections

Antenna imperfections are an important source of errors which can be classified in two groups: errors due to antenna pattern errors (amplitude and phase ripple, position errors, and pointing errors) and mutual coupling between antennas.

Antennas used by interferometer radiometers observing punctual radio-sources can be modeled by a constant phase and gain antenna pattern. However, the Earth, seen from a low orbit satellite with low directive antennas, occupies a large part of the antenna main beam. Hence, antenna pattern imperfections must be taken into account by the calibration and inversion algorithms to minimize image aberration. Once the receiver phase and amplitude are calibrated, the inversion algorithm can remove the effect of antenna imperfection [Camps et. al 96B]. However, those antenna imperfections contaminate the redundant space calibration method and degrade receiver phase and amplitude estimation. As seen previously, this gives stringent specifications to antenna parameters (phase and amplitude ripple, pointing errors, antenna position and antenna coupling) in high resolution interferometer radiometers, with a large number of antennas.

In order to assess the impact of antenna imperfections on radiometric resolution simulations have been performed as follows: $\mu^{(2)}$ has been computed for the test scene consisting in a constant temperature distribution at 200 K, assuming a determined phase, amplitude and antenna pattern for each receiver. Then, phase and amplitude errors have been estimated by the redundant space method. Once phase and amplitude errors have been removed from $\mu^{(2)}$ as:

$$m_{mn}^{(1)}(u,v) = \hat{g}_m^{-1}\,\hat{g}_n^{-1}\,m_{mn}^{(2)}(u,v) \qquad \textbf{(5.42)}$$

the inversion algorithm recovered the temperature distribution making use of the known antenna patterns. Standard deviation of antenna imperfections used to perform the simulations are obtained from chapter 4: 0.15° pointing error, 0.5% amplitude ripple and 0.34° of phase ripple.

In the case of N_{EL}=15 antennas per arm, the radiometric degradation with respect to the case without receiver phase and amplitude errors (no need to calibrate the receiver) is about ΔT=0.2 K.

Note that antenna coupling impact on the calibration method can be highly reduced by selecting as redundant baseline antennas spaced some basic units (e.g. four or five would suffice). This also gives a decrease in the baseline signal-to-noise ratio that can be compensated by averaging consecutive measurements.

5.1.5.- Conclusions

The redundant space method, as used in radio-astronomy, can be applied to the calibration of an interferometer radiometer devoted to Earth observation provided that some especial considerations are taken into account.

It has been shown that receiver phase and amplitude errors increase along the arms which makes the calibration procedure very weak in front of errors not contemplated by the calibration procedure: quadrature errors, phase and amplitude non-separable errors, antenna pattern imperfections, etc. if the number of antennas per arm is high. However, since the Earth appears as an extended thermal source with relatively smooth transitions, its visibility function, or spatial Fourier transform, has a rapid decline that attenuates the effect of error propagation along the arms. The shorter baselines, which have the lowest errors, concentrate the largest percentage of the information collected by the interferometer.

Errors not taken into account by the redundant space calibration procedure have been classified and studied, obtaining a set of hardware specifications if the calibration procedure is to be successful. These specifications are basically the same that those obtained in chapter four, when studying the system errors.

5.2.- CALIBRATION BY CORRELATED/UNCORRELATED NOISE INJECTION

5.2.1.- Introduction

The correlated noise injection method has some advantages over methods based on phase and module closure relationships [Thompson et al. 86] [MMS 95]. Noise injection allows calibration of the receiver parameters, independently of antenna imperfections such as coupling effects, pointing errors, amplitude and phase errors... Once the receiver parameters are determined, antenna imperfections can be calibrated out of the measurement of a known scene, other external signal sources or by antenna ground testing. Moreover, correlated/uncorrelated noise injection allows calibration of errors that cannot be taken into account by phase and module relationships, such as receiver quadrature phase errors or offsets. On the other hand, noise injection implies increased hardware requirements and should be used only if errors not corrected by phase and module closure relationships have critical impact on system performance.

Simultaneous correlated noise injection to all the antennas in large arrays is technologically very critical because of the stringent requirements on mass, volume and phase equalization of the noise distribution network. In this section an approach that makes use of a set of uncorrelated noise sources uniformly distributed in the array is proposed. The calibration procedure is optimized in the sense of minimization of hardware requirements and the number of measurements. Each noise source drives correlated noise only to a small set of adjacent antennas. These sets of antennas are overlapped in order to maintain phase and module track along the array.

This approach reduces drastically mass and volume requirements of the noise distribution network compared to the standard method, which uses a single correlated noise source distributed to all the antennas. Moreover, the phase matching requirements of the distribution network are strongly relaxed because noise sources are driven to small sets of adjacent antennas. Power stability of the uncorrelated noise sources is also not a stringent requirement, because noise source temperatures are also estimated during the calibration process. This procedure allows independent phase and module calibration by making use of a reduced number of redundant correlations. It shoul be pointed out that the standard correlated noise injection determines the baseline complex gain factors as (figure 5.5):

$$V_{mn}^{(4)} \text{ ' } g_{mn}\, V_{mn}^{(2)} \qquad \textbf{(5.43)}$$

while the reduced set noise injection method estimates channel gain factor g_m, g_n and g_{mn} . g_m g_n, therefore non-separable amplitude and phase errors remain as residual errors that must be minimized and bind by the error in estimating the visibility amplitude and phase terms.

5.2.2.- The c/u noise injection method

5.2.2.1.- Uncorrelated noise injection

If zero-mean, narrow band Gaussian uncorrelated noise is injected at the receiver inputs, the real and the imaginary outputs of the 1B/2L digital correlators should be $\mathbf{Z_r}$=0, $\mathbf{Z_i}$=0. Moreover, as explained in chapter four, the measured correlations are not zero $\mathbf{Z^{(5)}_{uncorr}}$...0, $\mathbf{Z_i^{(5)}}_{\mathbf{uncorr}}$... 0, due to the leakage from the common local oscillator's thermal noise. From now on the measured complex visibility $\boldsymbol{\mu}^{(4)}$ to be calibrated is given by:

$$Z^{(4)} = Z^{(5)*}_{corr} - Z^{(5)*}_{uncorr}$$

$$\mu^{(4)} = \sin\left(\frac{B}{2}Z^{(4)}\right) \cdot \frac{1}{\sqrt{1+\frac{T_{R_1}}{T_{A_1}}}} \cdot \frac{1}{\sqrt{1+\frac{T_{R_2}}{T_{A_2}}}} \cdot \mu^{(3)} \times g_1\, g_2\, \mu^{(3)} \qquad \textbf{(5.44)}$$

$$\mu^{(3)} \times \frac{V^{(3)}}{\sqrt{T_{A_1}\, T_{A_2}}}$$

Where $\mu^{(4)}$ contains amplitude and phase errors and $\mu^{(3)}$ is free from amplitude errors.

5.2.2.2.- Correlated noise injection

If zero-mean, narrow band Gaussian correlated noise is injected at the receiver inputs, the real and imaginary parts of the ideal normalized visibility are μ_r=1, μ_i=0, and the unknowns 2_{oi}, 2_{oj} , 2_{qi}, 2_{qj}, T_{Ri} and T_{Rj} can be derived out of the measured visibilities μ_r^{raw} and μ_i^{raw}.

$$\begin{bmatrix}\mu_r^{(4)}\\ \mu_i^{(4)}\end{bmatrix} = g_i g_j \begin{bmatrix}\cos\left(2_{oj}-2_{oi}+\frac{2_{qj}}{2}-\frac{2_{qi}}{2}\right) & \sin\left(2_{oj}-2_{oi}+\frac{2_{qj}}{2}-\frac{2_{qi}}{2}\right)\\ -\sin\left(2_{oj}-2_{oi}+\frac{2_{qj}}{2}+\frac{2_{qi}}{2}\right) & \cos\left(2_{oj}-2_{oi}+\frac{2_{qj}}{2}+\frac{2_{qi}}{2}\right)\end{bmatrix}\begin{bmatrix}\mu_r^{(2)}\\ \mu_i^{(2)}\end{bmatrix} \times g_i g_j \overline{\overline{P_{ij}}}\,\overline{\mu}^{(2)}$$

(5.45)

However, it must be guaranteed that correlated noise is distributed correctly to all the antennas. The standard method makes use of a single noise source. However, in a large array, it is very difficult to maintain phase equalization of the noise distribution network

through the whole operating temperature range. Moreover the mass and volume requirement of a phase matched on-board distribution network 1-to-131, such as it would be required in MIRAS, can not be handled. The proposed solution reduces drastically these hardware requirements.

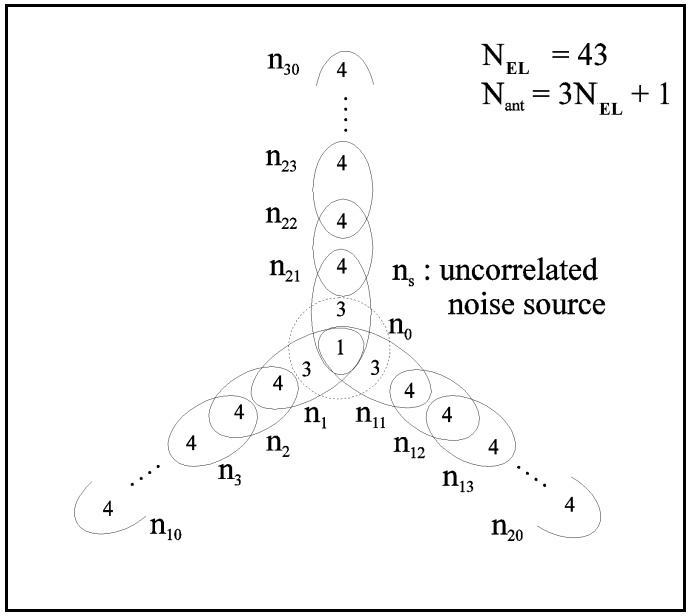

Figure 5.7.- *Noise distribution scheme. Each source drives correlated noise to a set of eight adjacent antennas*

Figure 5.7 shows the proposed noise distribution network. Antennas are grouped in sets of 4 to keep the groups specified in [MMS 95] and allows the use of 2^n power divider networks. Therefore, in order to have overlapped sets of antennas each noise source must drive noise to a set of eight consecutive antennas. As seen in figure 5.7, 31 uncorrelated noise sources are required and each antenna is driven by two adjacent noise sources allowing phase and amplitude calibration of the array. The source n_0 must deliver power to the remaining 10 central antennas in order to keep phase and module track between the three arms of the Y-array. This noise source must be monitored with good accuracy so as to perform amplitude calibration of the whole set of visibility samples.

Figure 5.8 gives a detail of noise distribution along a single arm. Antennas a_0 .. a_7 receive correlated noise only from source n_1. Therefore the largest baseline that can be computed is d = 7 (d = 1 is the basic 0.89 8 baseline). Antennas a_4 .. a_{11} receive correlated noise only from source n_2. And, finally, antennas a_4 .. a_7 are common to both groups allowing phase and module tracking along the arms. As it is shown later, errors do not propagate significantly along the arms when applying this calibration procedure.

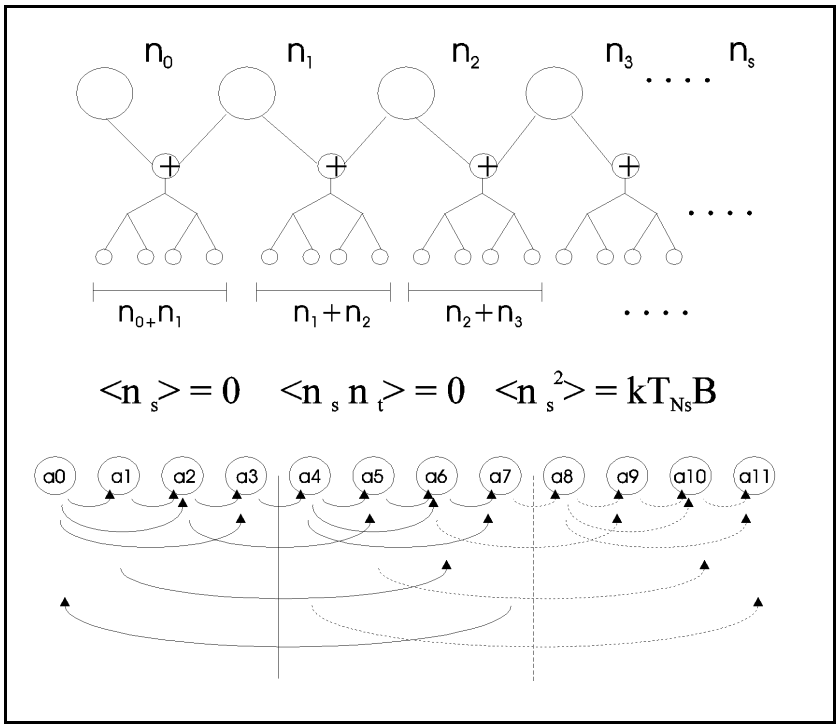

Figure 5.8.- *Noise distribution scheme. Each source drives correlated noise to a set of eight adjacent antennas*

Since only short length matched coaxial lines are required mass and volume of the noise distribution network are greatly reduced. Moreover, its phase matching requirements are strongly relaxed because it is only necessary within small sets of adjacent antennas. Only unbalanced phase drifts due to temperature variations must be minimized. The calibration procedure determines noise source temperatures out of the knowledge of n_0. Hence, simple non-stabilized diodes can be used as noise sources. In addition, as shown hereafter, it is possible to calibrate phase and amplitude independently with reduced hardware requirements.

5.2.2.3.- Calibration equations and redundancy

Once the correlated noise is injected the normalized visibilities should be $\mu^{(2)}_{r\,ij}=1$ and $\mu^{(2)}_{i\,ij}=0$. Hence, each correlation gives the two following equations:

$$\mu_{r_{ij}}^{(4)} = g_i g_j \cos\left(2_{oj} - 2_{oi} - \frac{2_{qj}}{2} - \frac{2_{qi}}{2}\right) \qquad \textbf{(5.46a)}$$

$$\mu_{i_{ij}}^{(4)} = -g_i g_j \sin\left(2_{oj} - 2_{oi} - \frac{2_{qj}}{2} - \frac{2_{qi}}{2}\right) \qquad \textbf{(5.46b)}$$

where 2_{oi}, 2_{oj}, 2_{qi}, 2_{qj} and the gain factors g_i,g_j are the unknowns. The gain factors can be eliminated by dividing the measured real and imaginary parts of the visibilities. Hence, an equation relating the phases out of each correlation is obtained:

$$\&\mu_{r_{ij}}^{(4)} \sin\left(2_{oj} \& 2_{oi} \% \frac{2_{qj}}{2} \% \frac{2_{qi}}{2}\right) ' \mu_{i_{ij}}^{(4)} \cos\left(2_{oj} \& 2_{oi} \% \frac{2_{qj}}{2} \& \frac{2_{qi}}{2}\right) \quad \textbf{(5.47)}$$

Once the phases are recovered an estimation of the gain factors g_i, g_j can be computed from (5.46a) or (5.46b).

Now the number of available correlations can be computed. There are two possibilities:

i) Use a minimum set of redundant correlations: figure 5.8 shows a close to the minimum set of redundant correlations which enables calibration of the phase terms. As it can be seen, a set of 8 antennas leads to 14 correlations (solid arrows). By adding 4 antennas the number of correlations (dashed arrows) increases by 9. Therefore, there are 95 correlations, 5 non-redundant and 90 redundant relating each arm of 44 antennas.

ii) Use all possible correlations: there are 28 correlations within a set of 8 antennas. By adding 4 antennas, the number of correlations increases by 22. Therefore, there are 226 correlations, 7 non-redundant and 219 redundant, relating each arm of 44 antennas.

The following table relates the number of available equations to the number of unknowns:

case	Number of antennas	Number of correlations	Number equation phases	Number equation gains	Unknown phases	Unknown gains
(i)	44	95	95	95	88	44
(ii)	44	226	226	226	88	44

Table 5.7.- *Number of equations and unknowns for a close-to-the minimum redundant correlation noise injection calibration and for a full-redundant noise injection calibration.*

As it is seen in this table, case (a) makes use of a system of equations with very little overdetermination while in case (b) it is highly overdetermined. In a Y-array with 43 antennas per arm the following values hold: 8385 complex correlations, 5676 non-redundant correlations and 2709 redundant correlations. In relation with the calibration procedure:

case (a) 3 x 90=270 redundant
case (b) 3 x 219=657 redundant

That is, even when all possible correlations within each set of 8 antennas are used only a small fraction of MIRAS redundant samples are required, which implies great hardware and power supply savings.

5.2.2.4.- Phase Calibration

Once all the measurements are performed, equation (5.47) turns into a system of 226 equations (44 antennas per arm, 226 correlations):

$$f(\hat{2}_{oi}, \hat{2}_{oj}, \hat{2}_{qi}, \hat{2}_{qj}) \text{ ' } 0 \qquad \textbf{(5.48)}$$

that is solved by a least-squares minimization to recover the phases.

5.2.2.5.- Amplitude calibration

Once the phase terms are known, the gain factor $g_i\, g_j$ can be estimated out of equations (5.46). From the two equations where each product $g_i\, g_j$ appears, only the value given by the equation less sensitive to phase estimation errors is used, the one having the greatest term: $\cos(2_{oj}-2_{oi}+2_{qj}/2-2_{qj}/2)$ or $\sin(2_{oj}-2_{oi}+2_{qj}/2+2_{qj}/2)$.

Note that these gain factors are not those that are required because during the measurement of a scene:

$$g_i^{meas} \text{ ' } \left(1 \% \frac{T_{R_i}}{T_{A_i}}\right)^{\&\frac{1}{2}} \qquad g_j^{meas} \text{ ' } \left(1 \% \frac{T_{R_j}}{T_{A_j}}\right)^{\&\frac{1}{2}} \qquad \textbf{(5.49)}$$

since during the calibration they are given by:

$$g_i^{cal} \text{ ' } \left(1 \% \frac{T_{Ri}}{T_{ni}}\right)^{\&\frac{1}{2}} \qquad g_j^{cal} \text{ ' } \left(1 \% \frac{T_{Rj}}{T_{nj}}\right)^{\&\frac{1}{2}} \qquad \textbf{(5.50)}$$

Therefore, *it is not enough to estimate the factors g_i and g_j during calibration, but it is also required to estimate the receiver noise temperatures T_{Ri} and T_{Rj}.* Once they are known, the desired calibration factors are computed out of the scene average temperature T_A given by the total power radiometer.

At this point it should be noted that, in order to estimate the receiver noise temperatures, it is necessary that only one noise source is driving each set of eight antennas that are simultaneously under calibration. Hence, calibration is performed by measuring the visibilities, first with the even noise sources ON and the odd sources OFF, and, afterwards, with the even noise sources OFF and the odd sources ON. From figure 5.8 it is seen that proceeding in this way, receivers are always driven by a single noise source.

Now, taking into account the first set of eight antennas -($a_0..a_7$) in figure 5.7-, which are driven by the odd noise source T_{n1} (T_{n2} OFF), the odd coefficient is given by:

$$K_{ij}^{1} = \frac{1}{g_i^2 g_j^2} \left(1 + \frac{T_{Ri}}{T_{n1}}\right)\left(1 + \frac{T_{Rj}}{T_{n1}}\right) \qquad \textbf{(5.51)}$$

out of the correlations performed between antennas "i" and "j". T_{Ri} and T_{Rj} are the noise temperatures of receivers "i" and "j". The system of equations is linearized by taking logarithms:

$$\log K_{ij}^{1} = \log\left(1 + \frac{T_{Ri}}{T_{n1}}\right) + \log\left(1 + \frac{T_{Rj}}{T_{n1}}\right) \qquad \textbf{(5.52)}$$

$$a_{ij}^{1} = x_{1i} + x_{1j}$$

where x_{1i} stands for a linear coefficient related to antenna "i" when driven by the noise source T_{n1}. For the 44 antennas, there are 226 equations leading to a linear system:

$$\overline{\overline{A}}\ \bar{x} = \bar{a} \qquad \textbf{(5.53)}$$

Where $\overline{\overline{A}}$ is a 226 x 44 matrix. $\overline{\overline{A}}$ is a sparse matrix whose rows contain all zeros except for two ones relating the position of the receivers in each correlation. The linear coefficients are determined as $x_0 = \overline{\overline{A}}^{-1}\ a^0$, where $\overline{\overline{A}}^{-1}$ is the pseudo-inverse of $\overline{\overline{A}}$.

Once the linear coefficients x_0 are known, the receiver temperatures can be recovered by means of a recursive process. The only requirement is the first noise source T_{n1} to be known. Relating the first set of antennas ($a_0..a_7$), the receiver noise temperatures are directly:

$$T_{Ri} = T_{n1}\left(10^{x_{1i}} - 1\right) \qquad \textbf{(5.44)}$$

where only the odd correlations have been used. Once the receiver's noise temperatures of a_0 .. a_7 are determined, the even noise source T_{n2} can be extracted out of the even correlations performed within $a_4..a_7$ as the mean value:

$$T_{n2} = \overline{T_{Ri}\left(10^{x_{2i}} - 1\right)^{-1}} \qquad \textbf{(5.55)}$$

Now x_{2i} is the linear coefficient of antenna "i" when driven by the even noise source T_{n2}. Once T_{n2} is determined this procedure is repeated with the second set of antennas $a_7..a_{11}$ and the unknown odd noise source T_{n3}. This recursive procedure ends with all the receiver noise temperatures T_{Ri} and noise source temperatures T_{ni} are determined.

The above procedure is based on the knowledge of the first noise source of each arm (T_{n1} in our example). In fact it is only necessary to know T_{no}, which is placed at the center of the array and delivers correlated noise to the 10 central antennas. T_{n1}, T_{n11} and T_{n21} (see figure 5.7) are recovered from T_{no} by a procedure similar to the one explained above, relating the correlations performed within the set of the 10 central antennas. In conclusion, the accuracy of module calibration is highly dependent on the accuracy of T_{n0} which can be determined either by switching during calibration the total power radiometer to this noise source, or by dedicating a special power measurement unit.

5.2.3.- Method robustness

To test the proposed calibration procedure a set of measured visibilities is required. These visibilities must be corrupted with generated receiver phase and module errors, as well as additive noise to take into account the finite integration time. First of all, the error coefficients of a real receiver will be defined and the measured visibilities will be generated and corrupted by noise. After calibration, it allows a comparison between real and recovered the receiver error coefficients.

A real receiver can be modelled with a matrix **C** of error coefficients:

$$\overline{\overline{C}} = \begin{bmatrix} 0 & \varepsilon_{q0} & T_{R0} & T_{n0} \\ \varepsilon_{o1} & \varepsilon_{q1} & T_{R1} & \vdots \\ \vdots & \vdots & \vdots & T_{ns} \\ \vdots & \vdots & \vdots & 0 \\ \varepsilon_{oN_T} & \varepsilon_{qN_T} & T_{RN_T} & \vdots \end{bmatrix} \qquad \textbf{(5.56)}$$

where $N_T = 3\ N_{EL} + 1$ is the number of antennas in the array and s the number of noise sources. Note that the central antenna sets the phase reference $\varepsilon_{o0} = 0$. Receiver phases have a zero mean Gaussian distribution with standard deviation $\sigma_{\varepsilon o}$ and $\sigma_{\varepsilon q}$. Noise temperatures have also a Gaussian distribution of mean T_R = 80 K and T_n = 200 K, and standard

deviation F_{TR} and F_{Tn}. For calibration purposes, T_{no} is considered to be known with enough accuracy. Once the receiver coefficients are generated the matrix $\overline{\overline{P}}(\overline{\overline{C}})$ that simulates the real receiver is computed as:

$$\overline{\overline{P}}\left(\overline{\overline{C}}\right) = \begin{bmatrix} \overline{\overline{P_1}} & 0 & \cdots & 0 \\ 0 & \overline{\overline{P_2}} & \cdots & 0 \\ \vdots & \vdots & \ddots & \vdots \\ 0 & 0 & \cdots & \overline{\overline{P_M}} \end{bmatrix} \tag{5.57}$$

$\overline{\overline{P}}(\overline{\overline{C}})$ is a sparse matrix composed by 2 x 2 matrices $\overline{\overline{P_k}}$ in its diagonal. $\overline{\overline{P_k}}$ (equation (5.45)) relates the ideal normalized visibilities with their measured counterparts. M is the number of visibility samples, redundant or not, that are measured during the calibration process.

$$\begin{bmatrix} \mu_{r_1} \\ \mu_{i_1} \\ \vdots \\ \mu_{r_M} \\ \mu_{i_M} \end{bmatrix}^{(4)} = \overline{\overline{P}}\left(\overline{\overline{C}}\right) \begin{bmatrix} \mu_{r_1}^{(2)} \% n_{r_1} \\ \mu_{i_1}^{(2)} \% n_{i_1} \\ \vdots \\ \mu_{r_M}^{(2)} \% n_{r_M} \\ \mu_{i_M}^{(2)} \% n_{i_M} \end{bmatrix} \tag{5.58}$$

The ideal visibilities μ_k when measuring correlated noise are $\mu_{rk}=1$ and $\mu_{ik}=0$. However, zero mean Gaussian noise $n_k = n_{rk} + j\, n_{ik}$ is added to account for the finite integration time. The noise is specified out of the signal to noise ratios which is equivalent to specifying different integration times:

$$\left(\frac{S}{N}\right) = \frac{1}{F_v}; \quad F_v^2 = 2E[n_{rk}^2] = 2[n_{ik}^2] \tag{5.59}$$

where F_v is the standard deviation of the visibilities. F_v in MIRAS it is about 35 dB due to the 0.3 s finite integration time. Note that during the calibration process the integration time is not limited by the platform's movement and signal-to-noise ratio can be increased by averaging consecutive calibrations. The effective standard deviation during calibration, F', is then given by:

$$F' = \frac{F}{\sqrt{N_{avg}}} \tag{5.60}$$

It is, averaging N_{avg} = 100 measurements (30 s integration time) gives an increase in signal-to-noise ratio of 10 dB and averaging N_{avg} = 1.000 measurements (300 s integration time) the increase is of 15 dB.

Note that two simulations have to be performed in order to account for the following measurements:

i) Even T_{ni} ON, odd T_{ni} OFF. Measure of μ_r and μ_i .

ii) Even T_{ni} OFF, odd T_{ni} ON. Measure of μ_r and μ_i .

where the correlations are changed. Of course, this implies new values for T_{ni} and the noise terms $n_k = n_{rk} + j\, n_{ik}$.

In order to check the consistency of the method, receiver errors have been modelled with the following parameters: $\Phi_{2o} = 20^o$, $\Phi_{2q} = 5^o$, T_R = 80 K, Φ_{TR} = 10 K, T_n=300 K and Φ_{Tn} = 25 K. Simulations proved not to be very sensitive to this data. Then, a set of measured normalized visibilities μ^{raw} are simulated and the coefficients recovered using the calibration procedure explained previously. In the following sections the effect of different errors is analized. Errors are computed as:

$$\begin{aligned} \Delta 2_{oi} &= \hat{2}_{oi} - 2_{oi} \\ \Delta 2_{qi} &= \hat{2}_{qi} - 2_{qi} \\ \Delta T_{Ri} &= \hat{T}_{Ri} - T_{Ri} \end{aligned} \qquad \textbf{(5.61)}$$

5.2.3.1.- Effect of signal-to-noise ratio: averaging adjacent measurements

Figure 5.9 shows the rms error in each receiver along an arm in terms of the S/N. The estimated coefficient rms errors are summarized below.

S/N	$\Phi_{\Delta 2o}$	$\Phi_{\Delta 2q}$	$\Phi_{\Delta TR}$
35 dB	0.018º	0.009º	0.124 K
40 dB	0.006º	0.003º	0.041 K
45 dB	0.002º	0.001º	0.015 K

Table 5.8.- *Residual in-phase, quadrature and noise temperature errors vs. signal-to-noise ratio*

Note that, when measurements are only corrupted by Gaussian additive noise, errors in the estimated parameters are negligible and do not increase significantly along the arms.

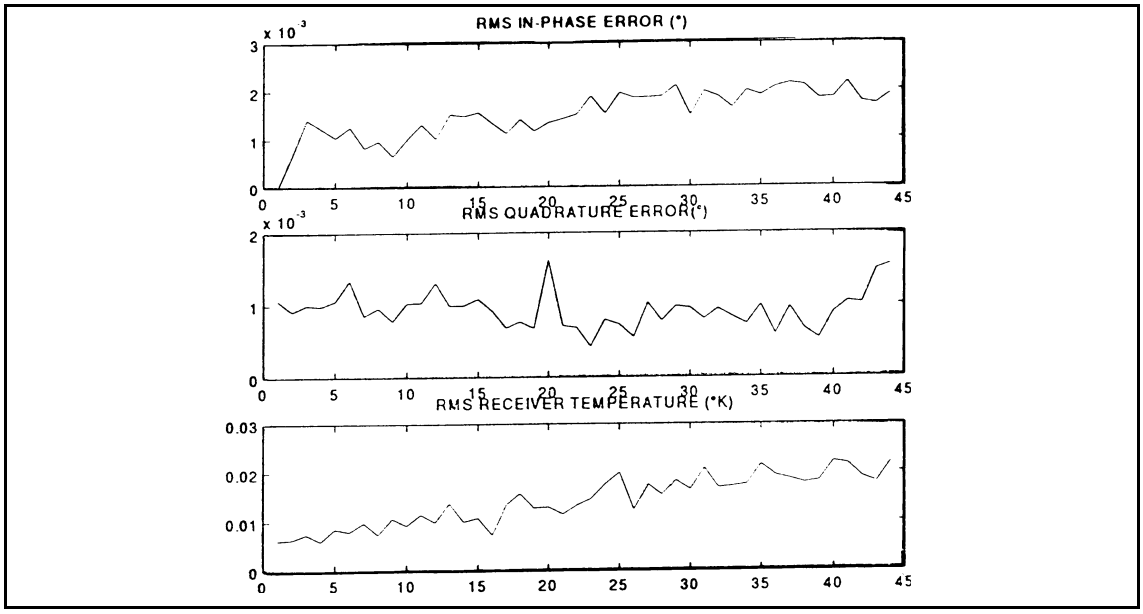

Figure 5.9.- *Element errors vs S/N.* F_{2o}*=20º,*F_{2q}*=5º,*T_R*=80 K,*F_{TR}*=10 K,*T_n*=300K,* F_{Tn}*=25K, S/N=45dB.*

5.2.3.2.- Effect of the uncertainty in the central noise source.

Figure 5.10 shows the rms error in each receiver along an arm in terms of the uncertainty in $T_{no.}$ Signal-to-noise ratio is fixed to 45 dB to make results independent of noise. The estimated coefficient errors are summarized below:

$)T_{no}$	$F_{)TR}$
0.1% (0.3 K)	0.04 K
0.5% (1.5 K)	0.27 K
1.0% (3 K)	0.47 K
2.0% (6 K)	1.09 K

Table 5.8.- *Residual noise temperature errors vs.* $)T_{no}$

$)T_{no}$ has negligible error on the phases, as expected. Error in the expected receiver noise temperatures is about $)T_R$. $)T_{no}/4$, which is consistent with T_{no}/T_R =300K/80K . 4.

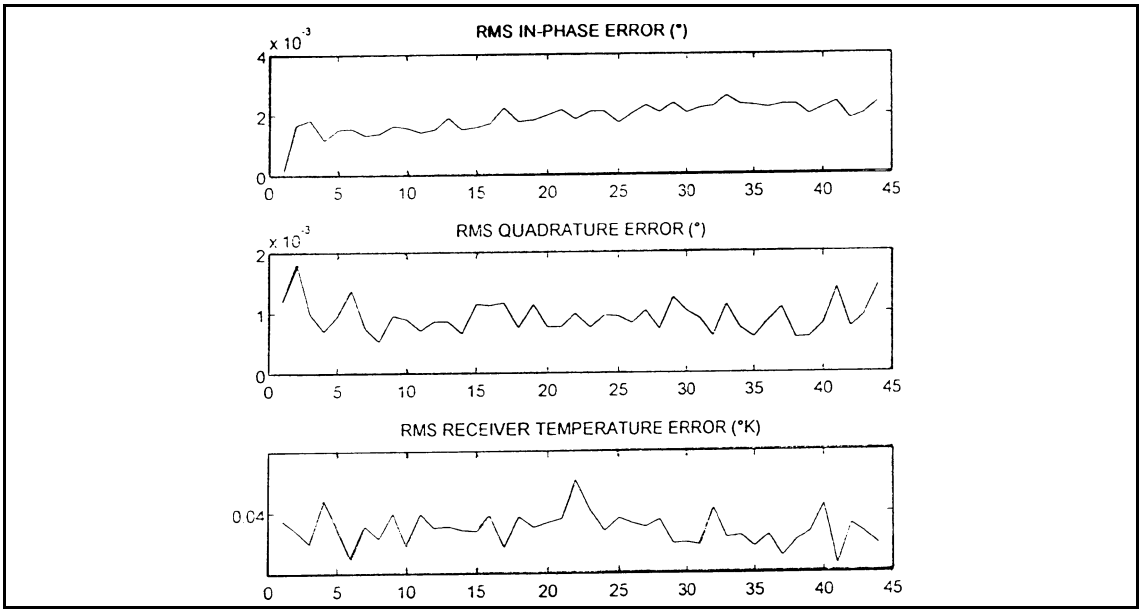

Figure 5.10.- *Element errors vs ΔT_{no}. $F_{2o}=20^o, F_{2q}=5^o, T_R=80$ K, $F_{TR}=10$ K, $T_n=300$K, $F_{Tn}=25$K, ΔT_{no}=0.3K.*

5.2.3.3.- Effect of non-separable phase terms

Figure 5.11 shows the rms error in each antenna along an arm in terms of the uncertainty in ΔN_{mn}. Signal-to-noise ratio is fixed to 45 dB to avoid noise errors and ΔT_{no} to 0.1% (0.3K), therefore results depend only on ΔN_{mn}. The estimated coefficient errors are summarized below.

$F_{\Delta Nmn}$	$F_{\Delta 2o}$	$F_{\Delta 2q}$	$F_{\Delta TR}$
0.1 º	0.110º	0.081º	0.222 K
0.3 º	0.665º	0.270º	0.579 K
1.0 º	1.523º	0.838º	1.822 K

Table 5.10.- *Residual in-phase, quadrature and noise temperature errors vs. non-separable phase error*

Note that errors in the phases are about $F_{\Delta N mn}$ as expected. However, the error on the receiver temperatures is increased. Note that if ΔT_R = 1.25 K, the radiometric accuracy is ΔT = 0.25 K. This fixes the maximum $F_{\Delta N mn}$ = 0.7º, which is lower than the bound obtained for the maximum non-separable phase error (see table 4.11).

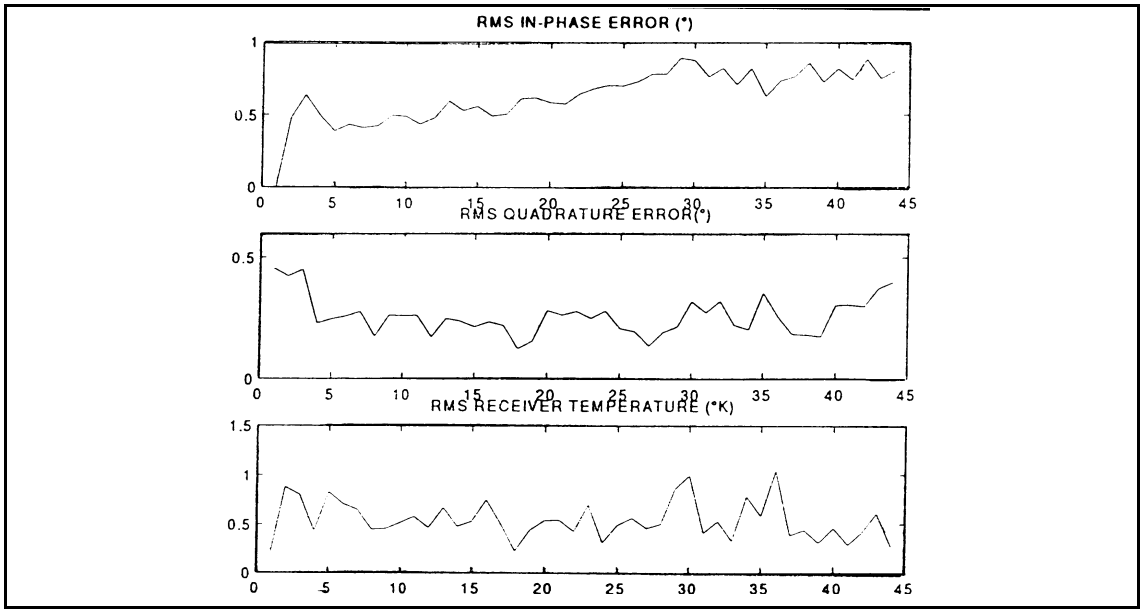

Figure 5.11.- *Element errors.F_{2o}=20º,F_{2q}=5º,T_R=80 K,F_{TR}=10 K,T_n=300K,F_{Tn}=25K,) T_{no}=0.3K,) N_{mn}=0.3º*

5.2.3.4.- Effect of antenna losses on the receiver noise temperature estimation

As seen in figure 5.12, the receiver noise temperature estimated when injecting correlated noise does not include the effect of antenna losses, which must be included when computing the calibration gain factors g_i. Let consider an antenna of efficiency 0, at physical temperature T_{ph} . The noise figure of the receiver after the antenna is T_R. The equivalent receiver noise temperature T_e is given by:

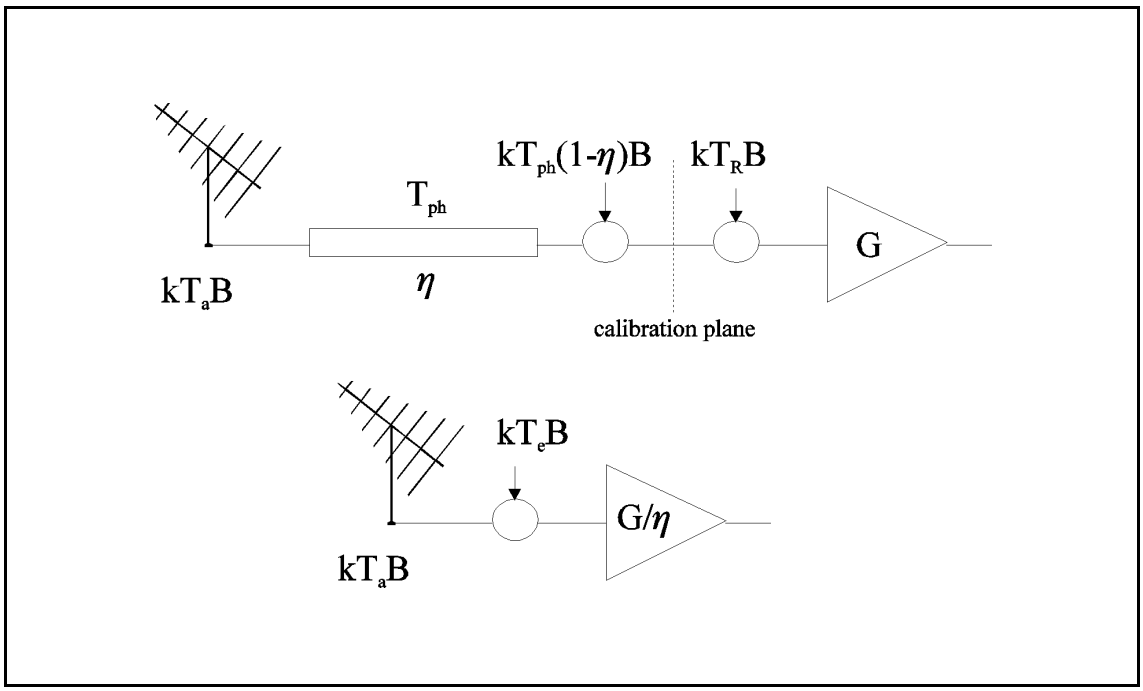

Figure 5.12- *Model of the noise contribution of an antenna of efficiency 0 at physical temperature T_{ph}.*

$$T_e = \frac{T_R}{\eta} + T_{ph}\left(\frac{1}{\eta} - 1\right) \tag{5.62}$$

The determination of the parameters T_R, T_{ph} and η:

$$\begin{aligned} \hat{T}_e &= T_e + \Delta T_e \\ \hat{T}_{ph} &= T_{ph} + \Delta T_{ph} \\ \hat{\eta} &= \eta + \Delta\eta \end{aligned} \tag{5.63}$$

induces an error in the receiver noise temperature:

$$\hat{T}_e = \frac{\hat{T}_R + \Delta\hat{T}_R}{\eta + \Delta\eta} + (\hat{T}_{ph} + \Delta\hat{T}_{ph})\left[\frac{1}{\eta + \Delta\eta} - 1\right] \tag{5.64}$$

which can be simplified to:

$$\hat{T}_e = \frac{\hat{T}_R}{\eta} + \hat{T}_{ph}\left[\frac{1}{\eta} - 1\right] + \Delta\hat{T}_e \tag{5.65}$$

where:

$$\Delta\hat{T}_e = \frac{\Delta\hat{T}_R}{\eta} + \Delta\hat{T}_{ph}\left[\frac{1}{\eta} - 1\right] + \frac{\hat{T}_R + \hat{T}_{ph}}{\eta}\,\Delta\eta \tag{5.66}$$

The following table relates the error in the receiver noise temperature with the radiometric accuracy ΔT.

S/N	$F_{\Delta V}$	ΔT	ΔT_e
20 dB	0.010	0.67 K	3.95 K
25 dB	0.003	0.25 K	1.19 K
30 dB	0.001	0.14 K	0.40 K

Table 5.11.- *Radiometric accuracy impact of receiver noise temperature error.*

Where it is assumed that module error is only due to the error in the receiver's noise temperature estimation ΔT_e:

$$F_{\Delta V} = \frac{1}{\sqrt{2}}\frac{F_{\Delta T_e}}{T_e + T_a} \tag{5.67}$$

Taking an antenna temperature T_a=200 K, a receiver noise temperature T_e=80 K and an antenna efficiency η = 0.9 (0.5 dB) the following table gives the accuracies for the receiver's noise temperature estimation, the antenna physical temperature measurement and the antenna efficiency measurement assuming that the three contributions to ΔT_e are

equivalent (equation 5.66).

) T	) T_e	) T_R	) T_{ph}	) 0/0
0.67 K	3.95 K	2.03 K	18.7 K	1.26% (0.05 dB)
0.25 K	1.19 K	0.61 K	5.6 K	0.38% (0.02 dB)
0.14 K	0.40 K	0.20 K	1.9 K	0.13%(0.006dB)

Table 5.12.- *Accuracies for the receiver's noise temperature estimation, the antenna physical temperature measurement and the antenna efficiency measurement.*

Note that the error in the antenna efficiency is the most critical parameter since it is very difficult to characterize with high accuracy. If the efficiency approaches to unity, 0 dB, the error) T_e simplifies to:

$$0 \bullet 1 \&) 0 \qquad \textbf{(5.68)}$$
$$) T_e \bullet) T_R \% (\hat{T}_R \% \hat{T}_{ph})) 0$$

As a conclusion, the antenna temperature must be measured with an accuracy better than 0.38 % to achieve a radiometric resolution of 0.25 K. This precision can be achieved by the cryoload technique which attains the 0.1% [Hardy et al. 74] or 0.7 K [Blume 77].

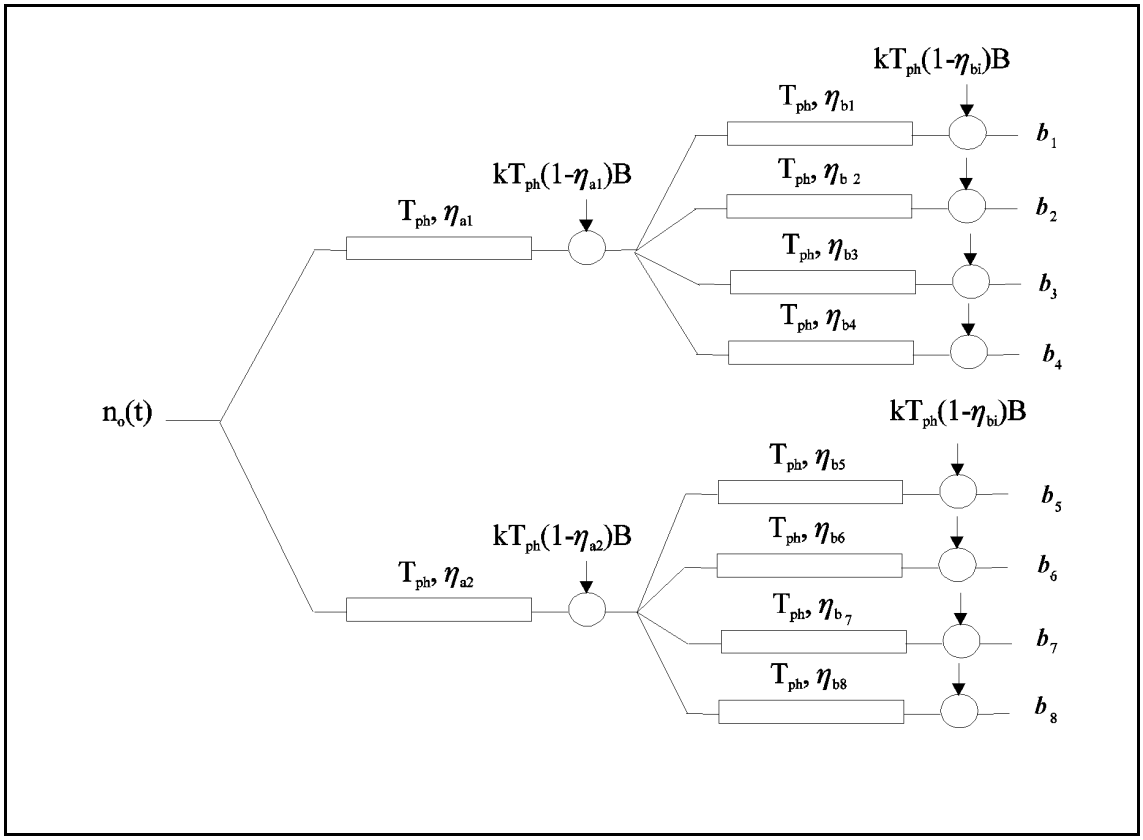

Figure 5.13.- *Noise model of the correlated noise distribution network.*

5.2.3.5.- Effect of the noise distribution losses on the receiver noise temperature estimation

Figure 5.13 presents a model of the noise contribution of the power divider network which introduces correlated and uncorrelated noise into the measurement.

Note that noise caused by the loss in the first section, $\eta_{a\,1,2}$, is correlated noise when measuring, for instance μ_{12}, and it is uncorrelated noise when measuring, for instance μ_{15}. It is, the correlations performed within the first set of 4 adjacent antennas give

$$\frac{1}{2}E\left[b_1 b_2^*\right] = k_B B\left[\frac{T_{no}}{8}h_{a_1}\sqrt{h_{b_1}h_{b_2}} + \frac{T_{ph}}{4}(1-h_{a_1})\sqrt{h_{b_1}h_{b_2}}\right]$$

$$\frac{1}{2}E\left[b_1 b_1^*\right] = k_B B\left[\frac{T_{no}}{8}h_{a_1}h_{b_1} + \frac{T_{ph}}{4}(1-h_{a_1})h_{b_1} + T_{ph}(1-h_{b_1}) + T_{R_1}\right] \qquad \textbf{(5.69)}$$

$$\frac{1}{2}E\left[b_2 b_2^*\right] = k_B B\left[\frac{T_{no}}{8}h_{a_1}h_{b_2} + \frac{T_{ph}}{4}(1-h_{a_1})h_{b_2} + T_{ph}(1-h_{b_2}) + T_{R_2}\right]$$

Note that noise generated between the 1-to-2 and the 1-to-4 dividers has dramatic impact in the calibration procedure, that is, it cannot be assigned either to the noise source or to η_{bi}. This cannot be taken into account by the calibration procedure, and cannot be processed efficiently to derive the receiver temperatures T_{Ri}. However, the correlations performed within the two adjacent sets of 4 antennas (e.g. μ_{15}) give:

$$\frac{1}{2}E\left[b_1 b_5^*\right] = k_B B\left[\frac{T_{no}}{8}\sqrt{h_{a_1}h_{a_2}h_{b_1}h_{b_5}}\right]$$

$$\frac{1}{2}E\left[b_1 b_1^*\right] = k_B B\left[\frac{T_{no}}{8}h_{a_1}h_{b_1} + \frac{T_{ph}}{4}(1-h_{a_1})h_{b_1} + T_{ph}(1-h_{b_1}) + T_{R_1}\right] \qquad \textbf{(5.70)}$$

$$\frac{1}{2}E\left[b_5 b_5^*\right] = k_B B\left[\frac{T_{no}}{8}h_{a_2}h_{b_5} + \frac{T_{ph}}{4}(1-h_{a_2})h_{b_5} + T_{ph}(1-h_{b_5}) + T_{R_5}\right]$$

Neglecting phase errors, μ_{15} can be written as:

$$m_{15}^{raw} = \frac{\frac{1}{2}E\left[b_1\ b_5^*\right]}{\sqrt{\frac{1}{2}E\left[b_1\ b_1^*\right]\frac{1}{2}E\left[b_5\ b_5^*\right]}} = g_1 g_5 \qquad \textbf{(5.71)}$$

where:

$$g_1 = \left[1 + \frac{T_{R_1} + T_{ph}(1+\eta_{b_1}) + \frac{T_{ph}}{4}(1+\eta_{a_1})\eta_{b_1}}{\frac{T_{no}}{8}\eta_{a_1}\eta_{b_1}} \right]^{-\frac{1}{2}}$$

$$g_5 = \left[1 + \frac{T_{R_5} + T_{ph}(1+\eta_{b_5}) + \frac{T_{ph}}{4}(1+\eta_{a_2})\eta_{b_5}}{\frac{T_{no}}{8}\eta_{a_2}\eta_{b_5}} \right]^{-\frac{1}{2}} \quad \textbf{(5.72)}$$

Hence, the calibration algorithm recovers:

$$T_{R_1}^{cal} = \frac{T_{R_1} + T_{ph}(1+\eta_{b_1}) + \frac{T_{ph}}{4}(1+\eta_{a_1})\eta_{b_1}}{\eta_{a_1}\eta_{b_1}} \quad \textbf{(5.73)}$$

and the noise contribution of the power divider network can be removed from the estimated receiver noise temperature as:

$$\hat{T}_{R_1} = T_{R_1}^{cal}\,\eta_{a_1}\eta_{b_1} - \hat{T}_{ph}(1+\eta_{b_1}) - \frac{\hat{T}_{ph}}{4}(1+\eta_{a_1})\eta_{b_1} \quad \textbf{(5.74)}$$

The error in estimating T_{Ri} due to the power divider is mainly contributed by η, whose effect over T_R is exactly the same as the antenna efficiency. Note, however that divider losses can be characterized with an accuracy higher than the antenna efficiency.

In order to compute the gain coefficients g_i only the correlations between sets of four antennas should be used. That is, 4 # d # 7. This minimizes the noise contribution of the distribution network. An arm of 44 antennas has 160 of these correlations to solve for the 44 g_i unknowns.

5.2.3.6.- Phase errors due to the power divider network

The calibration process injects noise to the receiver at the antenna output. Hence, the phase estimated by the algorithm, ϕ_{oi}^{cal}, does not include the phase contribution of the antenna ϕ_{oa}. Moreover, the phase contribution of the power distribution network ϕ_{on} is added. Therefore, the desired phase ϕ_{oi} is:

$$\hat{\phi}_{oi} = \hat{\phi}_{oi}^{cal} + \hat{\phi}_{oa} - \hat{\phi}_{on} = \phi_{oi} + \Delta\phi_{oi} \quad \textbf{(5.75)}$$

where the phase error $\Delta\phi_{oi}$ is given by:

$$F^2_{)2_{oi}} \text{ ' } F^2_{)2^{cal}_{oi}} \% F^2_{)2_{on}} \% F^2_{)2_{oa}} \quad \textbf{(5.76)}$$

Note that the antenna and the power divider phases must be ground calibrated. The quadrature error 2_{qi} is not affected by this correction and does not require any further processing after the calibration algorithm.

5.2.4.- Calibration implementation

The calibration procedures can be summarized as follows:

i) Switch the correlated noise sources OFF and the uncorrelated noise sources ON. Measure the offset coefficients.

ii) Switch EVEN noise sources ON and ODD noise sources OFF. Measure the correlations within each set of eight antennas which are driven by the same EVEN noise source. Remove the offset. Average, i.e. 100 measurements of 0.3 s to have a high signal-to-noise ratio (MIRAS case).

iii) Switch EVEN noise sources OFF and ODD noise sources ON. Measure correlations within each set of eight antennas which are driven by the same ODD noise source. Remove the offset. Average, i.e. 100 measurements.

iv) Set in-phase error of the antenna 0 (at the center of the array) to $2_{o0} = 0$. Solve the set of equations relating antenna phases to estimate the 2_{oi} and 2_{qi}.

v) Compute the gain factors g_i g_j using the less sensitive equation. Solve the linear coefficients x_i using correlations 4 # d # 7 to minimize effect of the distribution network.

vi) Measure the noise source temperature T_{n0} and apply the recursive method to determine the receiver noise temperatures and the noise source temperatures from the x_i coefficients.

vii) Remove the phase contribution of the power distribution network and add the phase contribution of the antenna.

viii) Remove the noise contribution of the power distribution network and add the contribution of the antenna losses.

ix) Measure the scene average power T_A to compute the receiver gain factors as

$$g_i = \left(1 + \frac{T_{Ri}}{T_A} \right)^{-\frac{1}{2}} \quad \textbf{(5.77)}$$

x) Compute the calibration matrices $\overline{\overline{P}}_k^{-1}$ out of the error coefficients of each receiver. Note that $\overline{\overline{P}}_k^{-1}$ must be computed for all the baselines -redundant or not- that are measured during scene exploration.

$$\mu^{(2)} = \frac{1}{g_1} \frac{1}{g_2} \overline{\overline{P}}_k^{-1} \mu^{(4)} \quad \textbf{(5.78)}$$

5.2.5.- Hardware requirements

The hardware requirements required by the proposed calibration method can be summarized as follows:

i) Correlated noise sources: 31 as seen in figure 5.7. They can be implemented by means of noise diodes operated in the avalanche mode (as Alpha DNA 6337). They have low power consumption (< 50 mW) and high noise output ENR = 30 dB).

ii) Uncorrelated noise sources (matched loads): 131. Each receiver requires an uncorrelated noise source.

iii) Switches: Switches can be avoided if the noise sources are coupled to the antenna path by 10-15 dB couplers. The noise sources can be switched ON/OFF by means of TTL signals.

iv) Coaxial cables:

131 ant x 1 cab/ant x 0.4 m/cab x 40 gr/m = 2096 gr
31 nse_sour x 2 cab/nse_sour x 0.4 m/cab x 40 gr/m = 992 gr
total weight =3088 gr = 1029 gr/arm

v) Correlators: The proposed method makes use of all the correlations d#7. It makes 657 redundant correlations. Two measurements are needed to account for the ODD/EVEN noise sources.

vi) Antenna efficiency. It is a key point since it must be measured with extreme accuracy if module calibration is to be performed. 1.26 % error in 0 (0.05 dB) already gives a radiometric resolution) T = 0.7 K.

vii) Power distribution network. Its contribution to module and phase errors can be extracted from the calibrated values. Accuracy of its characterization seems to be within technological limits.

5.2.6.- Conclusions

In these section a new calibration approach has been proposed for large synthetic aperture interferometric radiometers. It makes use of a set of uncorrelated noise sources uniformly distributed in the array. Each noise source drives correlated noise only to a small set of adjacent antennas. These sets of antennas are overlapped in order to maintain phase and module track along the array. This approach reduces dramatically mass and volume of the noise distribution network, thus being very suitable to space-borne interferometric radiometers.

5.3.- COMPARISON OF THE TWO CALIBRATION METHODS

The redundant space calibration method and the noise injection to sets of antennas are both channel based calibration methods. This means that complex baseline gains are not recovered, but only gain factors and phases associated to the channels from which baseline gains and phase can be derived, neglecting non-separable error terms.

In addition, the noise injection method provides information about quadrature errors and errors remain bounded along the Y-arms. On the other hand, in order to position the image correctly, the redundant space method requires two reference phases to be known very accurately, as well as the absolute amplitude of the measured brightness temperature.

To compare the performance of both methods an image must be selected, the corresponding raw visibilities must be calibrated by both methods, and the modified brightness temperatures, with both calibrations, recovered with a suitable inversion algorithm (see chapter six).

Two images have been selected: i) the first one is the reference scene used when computing the impact of system errors over the radiometric accuracy (equation (4.14)), and ii) an image of Cape Cod (scales not preserved) modified properly to give realistic modified temperature values: 100 K over the sea and between 200 K and 300 K over the land, inside an ellipse defining the Earth-sky border as in (4.13), see figure 5.14.

Non-separable phase and amplitude terms have been modelled by equivalent gaussian filters with 1 MHz noise bandwidth standard deviation, 1 MHz central frequency standard deviation and 1 ns group delay standard deviation.

Table 5.13 summarizes the impact of residual calibration errors over the 200 K constant test scene.

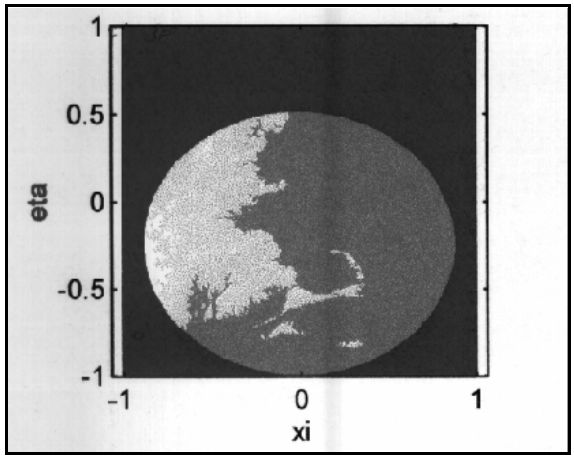

Figure 5.14.- *Pseudo-modified temperature image of Cape Cod*

	Redundant Space Calibration	**Noise Injection Method**
S/N = 45 dB	0.11 K	0.003 K
Quadrature error (0.3º)	0.16 K	-
Filter errors ($F_{)B}$=1MHz, $F_{)fc}$=1MHz, $F_{),J}$=1ns)	0.71 K	0.36 K
Antenna coupling (X-band cup-dipoles 30dB)	0.53 K	-

Table 5.13.- *Test scene radiometric accuracy calibrated with the redundant space calibration method and the noise injection method.*

For the noise injection method quadrature errors are not shown since they are recovered by the method, as well as antenna coupling errors that do not affect the calibration procedure and are calibrated afterwards.

Table 5.14 summarizes the average root mean squared calibration error for the Cape Cod test scene. Error images will be presented in the next chapter.

	Redundant Space Calibration	Noise Injection Method
S/N = 35 dB (MIRAS case)	3.3 K	2.38 K
Quadrature Error (0.5^o)	0.77 K	-
Filter errors ($\sigma_{\Delta B}$=1MHz, $\sigma_{\Delta fc}$=1MHz, $\sigma_{\Delta\tau}$=1ns)	2.97 K	1.05 K
Antenna coupling (X-band cup-dipoles 30dB)	1.54 K	-

Table 5.14.- *Cape Cod scene radiometric accuracy calibrated with the redundant space calibration method and the noise injection method.*

From tables 5.13 and 5.14 it is apparent that the noise injection method is somewhat more robust and produces better results because of the constant gain and phase residual errors along the arms. In addition, the redundant space method requires two reference phases to be known very precisely, and the antenna coupling can contaminate them harmfully, while with the noise injection method a single noise source drives correlated noise to the ten closest antennas, allowing a baseline calibration of the most significant visibility samples. However, it requires additional hardware with its mass, volume and power consumption requirements.

The noise injection method can be applied to calibrate the receiver, and then the redundant space method can be applied to the improvement of the calibration of the phase in the path between the antennas to the point where noise is injected.

5.4.- CALIBRATION OF ANTENNA COUPLING

Antenna coupling can be tested on-ground, and calibrated by using the coupling matrix $\overline{C}$ derived in section 4.3.4:

$$\overline{V}^{(1)} = \overline{C}\,\overline{V}^{(2)}\,\overline{C}^{H} \qquad \textbf{(5.79)}$$

As seen in 4.3.4, a radiometric accuracy of 1 K is achieved provided mutual impedances are known with an error smaller than 7 %.

Note that, in order to recover $\mathbf{V^{(1)}}$, all the baselines, redundant or not, must be measured. However, distant antennas within an arm are slightly little coupled and their associated mutual impedance Z_{ij} can be set to zero. In fact, X-band cup-dipoles mutual impedance is too small to be measured for $d > 3$. Hence, redundant baselines along an arm can be constrained to $d \leq 7$, as required to calibrate the receiver by the noise injection method.

5.5.- FULL CALIBRATION PROCEDURE

In this section it is assumed that system imperfections have already been characterized with enough accuracy. As presented in the previous sections, this characterization has been performed either by on-board testing (receivers) or ground measurements (antennas).

i) $\mathbf{Z}^{(5)}$ is the raw output of the 1B/2L digital correlator, which is corrupted by all system imperfections.

ii) $\boldsymbol{\mu}^{(4)}$ is computed by extracting the offset in $\mathbf{Z}^{(5)}$ and using the non-linear function that relates the true correlation and the measured one. This is done as:

$$\begin{aligned} Z^{(4)} &= Z^{(5)*}_{corr} - Z^{(5)*}_{uncorr} \\ \mu^{(4)} &= \sin\left(\frac{\pi}{2} Z^{(4)}\right) \end{aligned} \qquad \textbf{(5.80)}$$

Note that the offset is measured by injecting uncorrelated noise to all receivers, which is done by switching all the antennas to different matched loads.

iii) $\boldsymbol{\mu}^{(3)}$ is computed taking into account the channel gain factors:

$$\mu^{(3)} = \frac{1}{g_1}\frac{1}{g_2}\mu^{(4)} \qquad \textbf{(5.81)}$$

iv) $\mathbf{V}^{(2)}$ is computed by removing the phase and amplitude contribution of the receivers and denormalization:

$$\begin{aligned} \mu^{(2)*}_{corr} &= \overline{\overline{P}}_k^{-1}\mu^{(3)*}_{corr} \\ V^{(2)} &= V(0,0)\overline{\overline{P}}_k^{-1}\mu^{(3)} \end{aligned} \qquad \textbf{(5.82)}$$

Note that the matrix $\overline{\overline{P}}_k$ and the gain factors g_1 and g_2 are computed by injecting correlated noise to groups of receivers.

Since noise is injected just behind the antennas:

$$\mu^{(2)*}_{raw\,corr} = \begin{bmatrix} 1 \\ 0 \end{bmatrix} \qquad \textbf{(5.83)}$$

The phase and amplitude terms which are recovered, $\hat{2}'_{qi}$, $\hat{2}'_{oi}$, $\hat{T}'_{Ri}$, are not those which are required. The contribution of the noise distribution network must be removed, and the contribution of the antenna must be added:

$$\begin{aligned} \hat{q}_{qi} &= \hat{\hat{q}}'_{qi} \\ \hat{q}_{oi} &= \hat{\hat{q}}'_{oi} - \hat{q}^{nse}_{oi} + \hat{q}^{ant}_{oi} \\ \hat{T}_{Ri} &= f\ (\hat{\hat{T}}'_{Ri}, T_{ph}, h_{nse}, h_{ant}) \end{aligned} \qquad \textbf{(5.84)}$$

The average scene temperature V(0,0) = T_A is measured by means of the total power radiometer. Now, the gain coefficients g_i can be computed and the visibility samples denormalized.

$$g_i = \left[1 + \frac{T_{Ri}}{T_A} \right]^{-\frac{1}{2}} \qquad \textbf{(5.85)}$$

$$V^{(2)}u,v) = V(0,0)\, m^{(2)}(u,v)$$

Note that the gain coefficients g_i are computed from T_A and T_{Ri}, because they cannot be derived directly when injecting correlated noise. When calibrating, the antenna temperature T_A is substituted by the noise source temperature T_{no}, and the gain factors are not those which are required during scene exploration.

v) $\mathbf{V}^{(1)}$ is computed by removing the effect of antenna coupling. It is calculated as:

$$\overline{V}^{(1)} = \overline{C}\,\overline{V}^{(2)}\overline{C}^{H} \qquad \textbf{(5.86)}$$

where $\overline{C}$ relates the antenna open circuit voltage v^o with the measured voltages v^{raw} when antenna coupling is present.

vi) $\mathbf{V}^{(0)}$ is the visibility function when system imperfections have already been removed, being only affected by the fringe-wash term, different antenna patterns and small errors in the antenna positions due to Y-arm oscillations. It is computed from $\mathbf{V}^{(1)}$ by removing other antenna imperfections such as antenna phase and amplitude ripple and position errors. This error extraction is performed by a suitable inversion algorithm such as that presented in chapter six. Since MIRAS does not measure both polarizations simultaneously, V/H crosstalk remains as a residual error.

5.6.- CONCLUSIONS

In this chapter two receiver-based calibration methods have been investigated: i) the application of the redundant space method, based on amplitude and phase closures, to Y-arrays and ii) a new method based on the injection of correlated noise to overlapping groups of antennas by means of a set of distributed noise sources. The first one is simpler, while the second one is more robust to system imperfections but requires a specific calibration hardware.

An space-borne interferometric radiometer may take advantage of both methods by:

i) A noise-injection baseline-based calibration of the central baselines, since the central noise source feeds the closests antennas in the three arms. This calibration would greatly improve system's performance since the smallest baselines are the most significant ones.

ii) Since both methods are sensitive to gain factors, a noise-injection channel-based amplitude calibration can be implemented with a power detector in each channel, like those planned to be integrated to test MIRAS/LICEF receivers.

iii) A noise-injection channel-based phase calibration of the rest of the baselines by using the distributed noise-injection method proposed.

iv) A calibration of antenna coupling effects, if necessary (it depends on antenna type and the array's geometry).

v) And a channel-based calibration of the average antenna amplitude and phase errors by means of the redundant space method.

Non-constant antenna pattern amplitude and phase errors can be included in a suitable inversion algorithm if they are accurately measured.

Chapter 6. Inversion Algorithms in Interferometric Radiometry

The need of passive low frequency (L-band) measurements to monitor soil moisture and ocean salinity with high spatial resolution 10-20 Km, a radiometric resolution of 1 K and a revisit time of 1-3 days [SMOS 95] has raised the interest in interferometric radiometers because of their reduced mass and hardware requirements. As explained in the preceding chapters, interferometric radiometers measure the correlation between pairs of nondirective antennas. Each complex correlation is a sample of the "visibility" function which, in the ideal case (identical antenna patterns and negligible fringe-wash effects) is the spatial Fourier transform of the modified brightness temperature distribution. On-board hardware requirements -antennas, receivers and correlators- can be minimized by a proper choice of the interferometer's array shape which determines the (u,v) sampling strategy and the minimum number of visibility samples required for a determined aliasing level (alias-free swath). In this sense, it is demonstrated that Y-shaped and triangular-shaped arrays with equally spaced antennas are optimal.

In the first part of this chapter discrete Fourier transforms over non-rectangular grids are studied and the *hexagonal FFT* is proposed. This technique allows to process the visibility function sampled over the hexagonal sampling grids given by Y- and triangular-arrays with *standard rectangular FFT routines*, preserving signal to noise ratio, avoiding interpolation processes and minimizing the risk of induced artifacts in the recovered brightness temperature over the wide Field Of View required in Earth observation missions.

In the second part, some inversion techniques found in the radioastronomy and remote sensing literature are briefly reviewed, as well as some image processing techniques. Since most receiver phase and amplitude errors can be hardware calibrated, antenna pattern errors and mutual coupling must be small, Fourier-based inversion algorithms can be applied. In this line, a new Fourier-based iterative inversion algorithm to recover the modified brightness temperature distribution out of the set of visibility samples is proposed. Its properties, the acceleration of the convergence and its robustness are studied and presented through several examples.

6.1.- INVERSION ALGORITHMS IN APERTURE SYNTHESIS INTERFEROMETRIC RADIOMETRY: IDEAL CASE

After proper calibration of system errors, the equation (3.1) must be solved for $I(\xi,\eta)$. It should be noted that the whole physical space, $0 \le \xi \le B$ and $0 \le \eta \le B$, is mapped into the (ξ,η) unit the circle and, therefore, any modified brightness temperature distribution $I(\xi,\eta)$ is supported by the unit circle:

$$\xi^2 + \eta^2 = \sin^2(\theta)\cos^2(\phi) + \sin^2(\theta)\sin^2(\phi) = \sin^2(\theta) \le 1 \qquad \textbf{(6.1)}$$

From signal theory it is known that this class of signals are optimally sampled by using an hexagonal grid, in the sense that this grid requires the minimum density of (u,v) samples to recover it with a specified aliasing level (13.4% less samples than rectangular sampling) [Mersereau 79] [Dudgeon and Mersereau 84]. Y-shaped and triangular-shaped arrays (figures 6.1a and 6.1b) produce visibility samples over an hexagonal grid in the spatial frequencies domain (u,v) (figures 6.2a and 6.2b). Figure 6.2a shows the (u,v) coverage in the case of MIRAS breadboard, a simpler Y-shaped interferometer radiometer with only 3 antennas per arm spaced 0.89 wavelengths. As it can be seen in figures 6.2a and 6.2b, for the same hardware complexity, similar number of antennas, receivers and correlators, the spatial resolution obtained for a Y-shaped array is better than that for a triangular-shaped array, since the spatial frequency coverage is larger in the first case. On the other hand, triangular-shaped arrays cover a complete hexagonal period, while Y-shaped arrays have missing (u,v) samples between the star points (figure 6.1a). These missing values must be extrapolated in some way [Bará et al. 96A] [Camps et al. 96B] in order to prevent the artifacts induced by the (u,v) star-shaped low-pass window. However, this is an important effect only in small arrays where the star-shaped window effectively low-pass filters the visibility function. For large arrays, such as the planned MIRAS space borne instrument, with 43 antennas per arm, less than 0.7 % visibility power is not collected by the array and this effect is negligible [Bará et al. 96A].

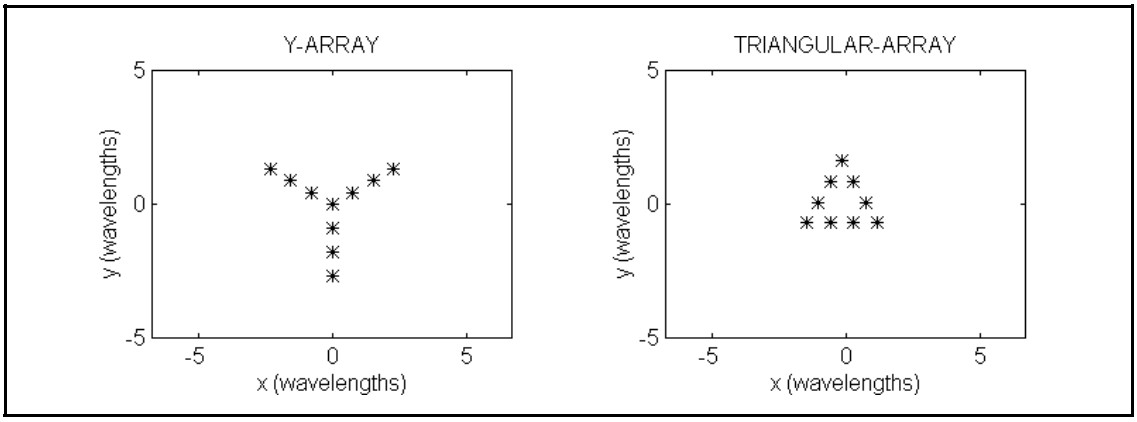

Figure 6.1.- *a) Y-shaped array and b) Triangular-shaped array*

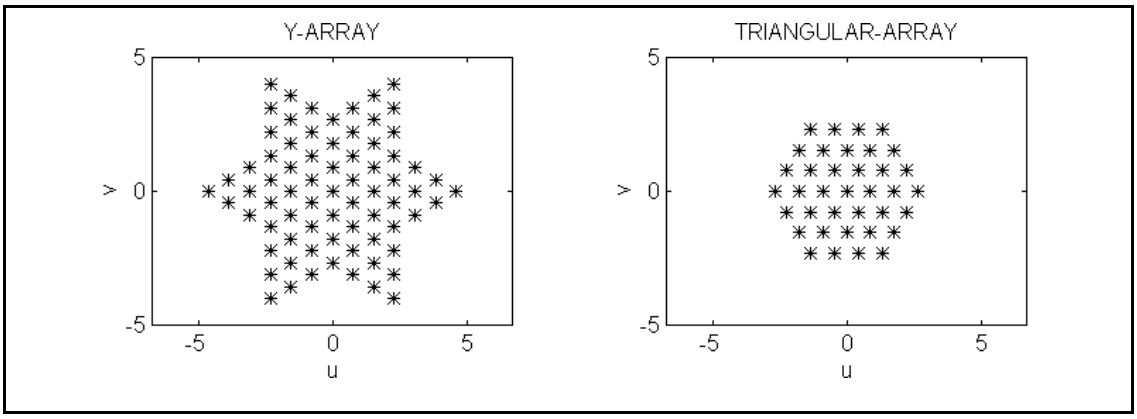

Figure 6.2.- *(u,v) Spatial frequency coverage for a) Y-shaped array and b) Triangular-shaped array* **.**

From now on, the study will only be focused on Y-shaped arrays where the visibility function is sampled over the grid:

$$u = \frac{\sqrt{3}}{2}\, d\, k_1; \qquad k_1,\ k_2 : 0 \ldots N_T$$

$$v = \frac{d}{2}\,(\&k_1 \% 2k_2) \qquad \textbf{(6.2)}$$

$$V(u,v) \div V(\bar{k}); \qquad \bar{k} = (k_1, k_2)$$

where $N_T = 3\,N_{EL} + 1$ is the total number of antennas, N_{EL} is the number of antennas in each arm of the Y array and d is the spacing in wavelengths between adjacent antennas. It should be pointed out that since the brightness temperature distribution is obtained by an inverse discrete Fourier transform, it can suffer from aliasing, which is determined by the spacing between adjacent antennas "d". This effect is studied in detail in section 6.1.2. In the next section a new procedure devised to apply standard rectangular FFT routines to the hexagonal (u,v) coverage given by Y-shaped arrays, avoiding the need of interpolations, preserving signal to noise ratio and retaining the benefits of the hexagonal sampling grid is presented.

6.1.1.- Hexagonal FFT, Smith-normal decomposition and reciprocal basis

Let's first recall some concepts about 1D Fourier Transforms. The DFT of a band limited 1D sequence x(n) of length N obtained by sampling the signal x(t) each T_s seconds, gives N samples of the spectrum of the signal $\tilde{x}(t)$, the periodic extension of x(t) in time interval [0, $N.T_s$]. These N frequency samples are a single period of the periodic spectrum. As they come out of the FFT these samples appear swapped, this means that the samples

corresponding to negative frequencies appear right after the positive ones. On the other hand, by padding the sequence x(n) with zeros a smoother spectrum's shape can be obtained without adding new information.

In band-limited 2D sequences, in addition to the number of zero padded samples that can be put, the periodic extension of the spectrum itself can be chosen (figures 6.3 and 6.4). This means that the known spectrum samples do not need to be necessarily periodically repeated along the "u" and "v" axes. The way the spectrum is repeated is characterized by its periodicity matrix $\overline{\overline{N}}$:

$$\tilde{V}(\bar{k}) = \tilde{V}(\bar{k} \% \overline{\overline{N}}.\bar{r}) \qquad \textbf{(6.3)}$$

where $\tilde{V}(\bar{k})$ is the periodic extension of $\overline{\overline{V}}(\bar{k})$, $\overline{\overline{N}}$ is a non-singular integer matrix called the periodicity matrix and $\bar{r}$ is an integer vector.

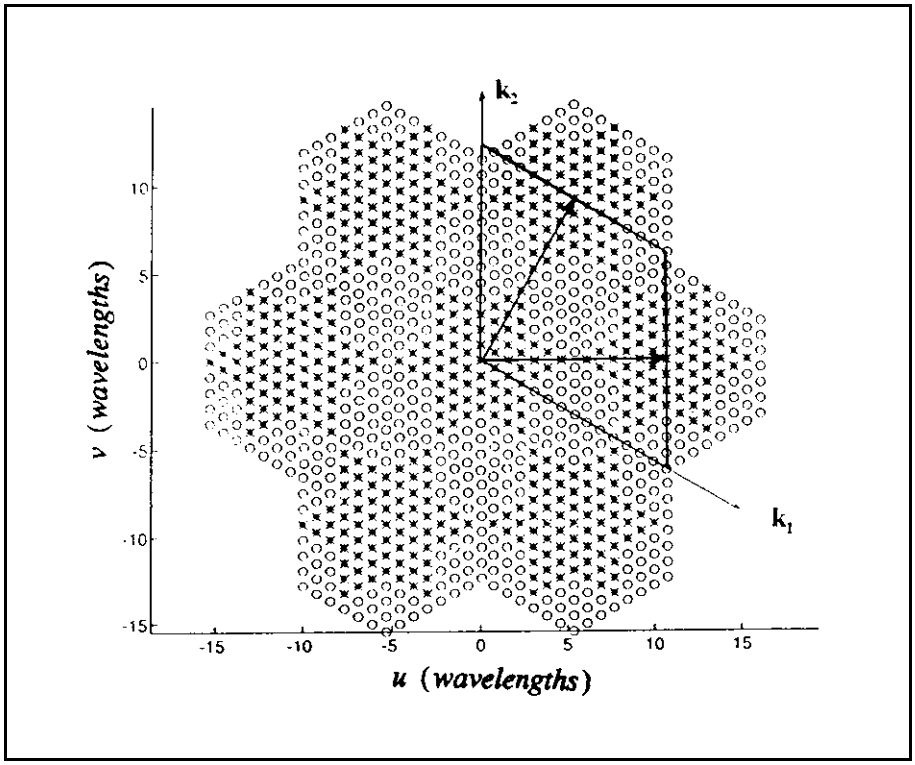

Figure 6.3.- *Periodic extension of the (u,v) coverage given in figure 6.2.a. Mersereau's HFFT required [Mersereau 79]*

The number of samples, zero or not, in one period is given by $\det(\overline{\overline{N}})$, for a given periodicity matrix $\overline{\overline{N}}$ [Dudgeon and Mersereau 84]. For an Y-array, the number of non-

redundant visibility samples is given by:

$$N_V \text{ ' } 6\ N_{EL}^2 \text{ \% } 6\ N_{EL} \text{ \% } 1 \qquad \textbf{(6.4)}$$

and the number of missing samples to be initially padded with zeros is:

$$N_{V\&} \text{ ' } \det(\overline{\overline{N}}) \text{ \& } N_V \qquad \textbf{(6.5)}$$

which should be minimized by properly choosing the periodicity matrix $\overline{\overline{N}}$. The choice of $\overline{\overline{N}}$ is not unique. A possible choice is presented in figure 6.3 for N_{EL} = 3. For this periodic extension, $\overline{\overline{N}}$ is given by:

$$\overline{\overline{N}} \text{ ' } \begin{bmatrix} N_T & 2N_T \\ 2N_T & N_T \end{bmatrix}; \quad \det(\overline{\overline{N}}) \text{ ' } 3N_T^2 \qquad \textbf{(6.6)}$$

which leads to Mersereau's hexagonal FFT algorithm [Mersereau 79] and [Dudgeon and Mersereau 84].

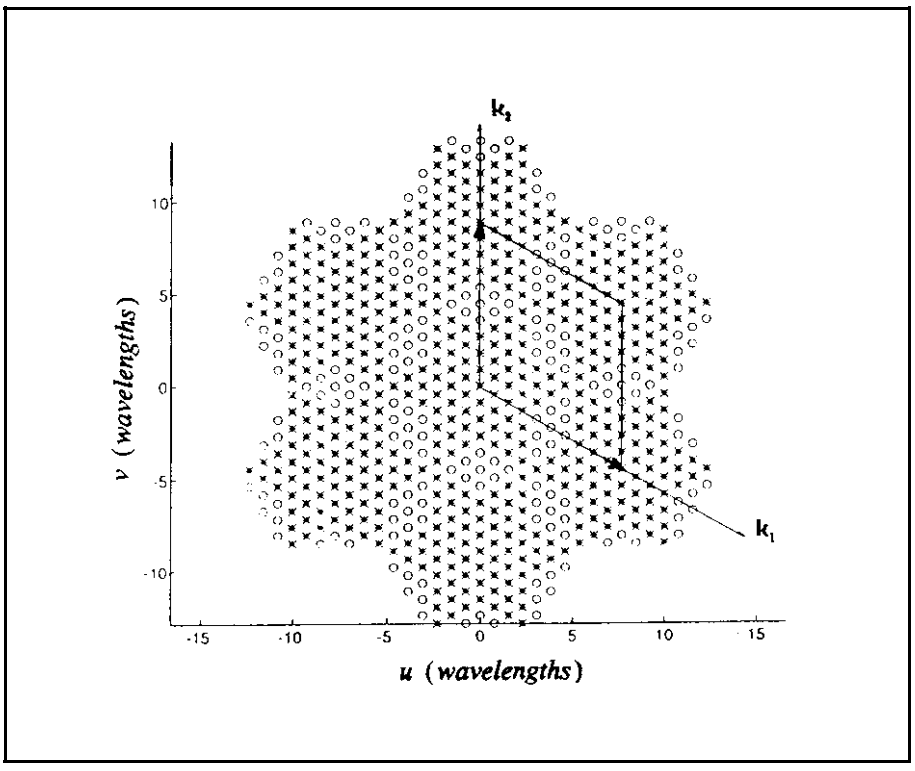

Figure 6.4.- *Periodic extension of the (u,v) coverage given in figure 6.2.a. Standard rectangular FFT can be applied.*

A more general approach can be used with the help of the Smith Normal decomposition [Gündüzhan et al. 94] [Bernardini and Manduchi 94], which states that any non-singular integer matrix $\overline{\overline{N}}$ can be diagonalized by pre- and post-multiplication by unimodular integer matrices $\overline{\overline{E}}$ and $\overline{\overline{F}}$:

$$\overline{\overline{N}} = \overline{\overline{E}} \cdot \overline{\overline{\gamma}} \cdot \overline{\overline{F}} \tag{6.7}$$

$$\det(\overline{\overline{E}}) = \det(\overline{\overline{F}}) = 1 \tag{6.8}$$

$\overline{\overline{\gamma}}$ is a diagonal matrix, thus any arbitrary fundamental period, not only that presented in figure 6.3, and over any arbitrary sampling grid, not only an hexagonal one, can be mapped into a rectangular one allowing rectangular FFT routines to be used in the reordered indexes $\overline{k'}$ and $\overline{n'}$:

$$\begin{aligned} I(\overline{n}) &= I\left(>(n_1, n_2), 0(n_1, n_2)\right) = \\ &= \frac{1}{|\det(\overline{\overline{N}})|} \sum_{\overline{k}} \tilde{V}(\overline{k}) e^{j 2\pi (\overline{k}^T \overline{\overline{N}}^{-1} \overline{n})} = \\ &= \frac{1}{|\det(\overline{\overline{N}})|} \sum_{\overline{k}} \tilde{V}(\overline{k}) e^{j 2\pi ((\overline{k}^T \overline{\overline{F}}^{-1}) \overline{\overline{\gamma}}^{-1} (\overline{\overline{E}}^{-1} \overline{n}))} = \\ &= \frac{1}{|\det(\overline{\overline{N}})|} \sum_{\overline{k}} \tilde{V}(\overline{k}) e^{j 2\pi (\overline{k'}^T \overline{\overline{\gamma}}^{-1} \overline{n'})} \end{aligned} \tag{6.9}$$

where:

$$\overline{k'} = (\overline{\overline{F}}^{-1})^T \overline{k} \tag{6.10}$$

and:

$$\overline{n'} = \overline{\overline{E}}^{-1} \overline{n} \tag{6.11}$$

The method proposed in this thesis is based in the choice of an appropriate diagonal matrix $\overline{\overline{N}}$ that minimizes the number of samples in the periodic cell, $3N_T^2$, and the number of non-measured visibilities which must be initially padded with zeros, $3N_T^2 - N_V$, allowing to use standard rectangular FFT routines and avoiding the permutation of indexes required by the Smith-Normal decomposition (equations (6.10) and (6.11)). Let's periodically extend the (u,v) fundamental period as in figure 6.4. In this scheme measured visibility samples are repeated following the relation given below:

$$\tilde{V}(u',v') = V(u,v)$$

$$\begin{bmatrix} u' \\ v' \end{bmatrix} = \begin{bmatrix} u \\ v \end{bmatrix} \% \overline{\overline{U}} \begin{bmatrix} k_1 \\ k_2 \end{bmatrix} \qquad \textbf{(6.12)}$$

where:

$$\overline{\overline{U}} = N_T\, d \begin{bmatrix} 0 & \frac{\sqrt{3}}{2} \\ 1 & -\frac{1}{2} \end{bmatrix}; \quad \overline{u_1} = N_T\, d\, [0,\ 1]^T \quad \overline{u_2} = N_T\, d \left[\frac{\sqrt{3}}{2},\ -\frac{1}{2}\right]^T \qquad \textbf{(6.13)}$$

is a sampling matrix in the (u,v) domain. The $\overline{\overline{U}}$ matrix is not unique, since all the sampling matrices given by:

$$\begin{aligned} \overline{\overline{U_1}} &= [\ -\overline{u_1},\ \overline{u_2}] \\ \overline{\overline{U_2}} &= [\ \overline{u_1},\ -\overline{u_2}] \\ \overline{\overline{U_3}} &= [\ -\overline{u_1},\ -\overline{u_2}] \end{aligned} \qquad \textbf{(6.14)}$$

reproduce the same periodic extension in the (u,v) plane. This choice, however, determines the numbering of the (u,v) and (>,0) samples to process them properly. The associated periodicity matrix in the (k_1, k_2) axes is:

$$\overline{\overline{N}} = \begin{bmatrix} N_T & 0 \\ 0 & N_T \end{bmatrix}; \quad \det\left(\overline{\overline{N}}\right) = N_T^2 \qquad \textbf{(6.15)}$$

If the sampling points in the (>,0) directing cosines are forced to satisfy the following relation:

$$\overline{\overline{U^T}} \cdot \overline{\overline{\Xi}} = \overline{\overline{I}} \qquad \textbf{(6.16)}$$

then:

$$\overline{\overline{\Xi}} = \left(\overline{\overline{U^T}}\right)^{-1} = \frac{1}{N_T\, d} \begin{bmatrix} \frac{1}{\sqrt{3}} & \frac{2}{\sqrt{3}} \\ 1 & 0 \end{bmatrix} \div \left[\overline{>_1},\ \overline{>_2}\right] \qquad \textbf{(6.17)}$$

and the Fourier transform kernel becomes separable, even if the (u,v) and (>,0) sampling points are not chosen over a rectangular grid. $\left[\overline{>_1},\ \overline{>_2}\right]$ form the so called *reciprocal basis* of $\left[\overline{u_1},\ \overline{u_2}\right]$ in the (>,0) domain (figures 6.4 and 6.5). With this concept, the sampled (u,v) and (>,0) points are given by:

$$(u,v)=\left(\frac{\sqrt{3}}{2}d\,k_1,\frac{d}{2}(-k_1+2k_2)\right);\ k_1,k_2:0\ldots N_T-1 \qquad \textbf{(6.18a)}$$

$$(\xi,\eta)=\left(\frac{1}{\sqrt{3}\,N_T\,d}(n_1+2n_2),\frac{1}{N_T\,d}n_1\right);\ n_1,n_2:0\ldots N_T-1 \qquad \textbf{(6.18b)}$$

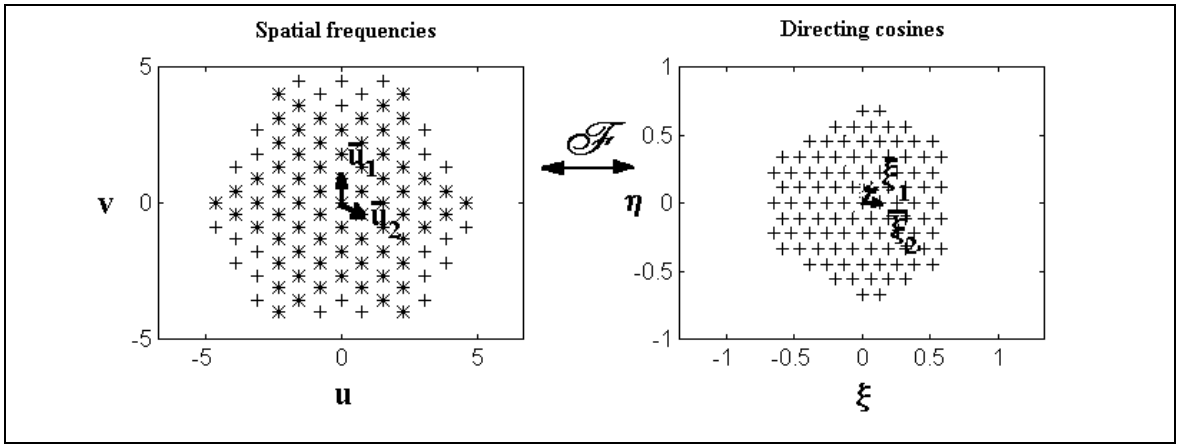

Figure 6.5.- *Sampled points in the directing cosines domain and the reciprocal basis* $[\xi_1,\xi_2]$ *of figure 6.4* $[u_1,u_2]$ *basis*

And the Inverse Fourier Transform of the hexagonally sampled V(u(k1,k2),v(k1,k2)) is given by:

$$T(n_1,n_2)\triangleq T(\xi(n_1,n_2),\eta(n_1,n_2))=$$

$$=\frac{\sqrt{3}\,d^2}{2}\sum_{n_1=0}^{N_T-1}\sum_{n_2=0}^{N_T-1}V(k_1,k_2)\,e^{j2\pi[u(k_1,k_2)\xi(n_1,n_2)+v(k_1,k_2)\eta(n_1,n_2)]}= \qquad \textbf{(6.19)}$$

$$=\frac{\sqrt{3}\,d^2}{2}\sum_{n_1=0}^{N_T-1}\sum_{n_2=0}^{N_T-1}V(k_1,k_2)\,e^{j\frac{2\pi}{N_T}(k_1n_2+k_2n_1)}$$

Expression (6.19) can be recognized as a standard rectangular FFT with n_1 and n_2 interchanged. The factor $3d^2/2$ is the hexagonal-shape pixel's area in the (u,v) domain. The recovered modified brightness temperature distribution given by equation (6.19) is repeated periodically over the (ξ,η) domain. The centers of periodic cells can be found by applying the periodicity condition to the argument in the Fourier kernel:

$$\frac{2\pi}{N_T}\left[\vec{u}_1^{\,T}(\xi_n,\eta_n)+\vec{u}_2^{\,T}(\xi_n,\eta_n)\right]=2\pi\left[(0,d)(\xi,\eta)+\left(\frac{\sqrt{3}}{2}d,-\frac{d}{2}\right)(\xi,\eta)\right]=2\pi m; \qquad \textbf{(6.20)}$$

$$m=0,\pm1,\pm2\ldots$$

whose solutions closest to the origin are:

$$(\xi_n, \eta_n) = \frac{2}{\sqrt{3}d}\left(\cos\left(n\frac{\pi}{3}\right), \sin\left(n\frac{\pi}{3}\right)\right); \quad n = 0,1,2...5 \qquad \textbf{(6.21)}$$

If the extension of the modified brightness temperature is the whole unit circle, the (ξ_n,η_n) points must be at a distance of 2 from the origin to completely avoid aliasing. It forces a maximum antenna spacing of $d \leq \lambda/\sqrt{3}$. Compared to rectangular sampling, where the maximum antenna spacing is $d \leq \lambda/2$ to avoid aliasing, a 13.4 % = 1 - (λ/2) / ($\lambda/\sqrt{3}$) hardware savings is provided by the hexagonal sampling. Figures 6.6a and 6.6b show the alias-free FOV for a T-array, rectangular (u,v) sampling, and a Y-array, hexagonal (u,v) sampling, whose adjacent antennas are spaced in both cases $d = 0.89\,\lambda$. It can be observed that the alias free FOV is larger for hexagonal sampling. In the Earth observation situation, the Earth does not occupy the hole unit circle and the antenna spacing condition can be relaxed depending on the required alias-free swath (figure 6.6). The $0.89\,\lambda$ spacing between antennas in MIRAS is a compromise between array thinning and alias free swath, which is about 900 Km for on-ground incidence angles between 40º and 55º [MMS 95]. This swath satisfies the 3 day revisit time necessary to update soil moisture and ocean salinity measurements [SMOS 95].

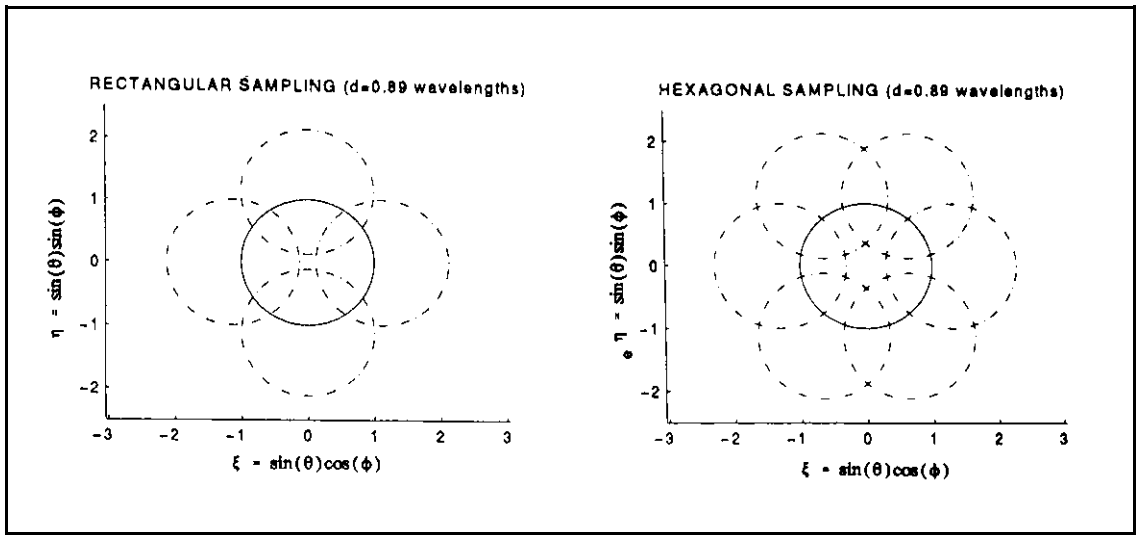

Figure 6.6.- *Alias-free regions for a: a) T-array (rectangular (u,v) sampling) and b) Y-array (hexagonal sampling) with adjacent antennas spaced 0.89λ*

In addition, since there are not interpolations in the inversion process, neither in the (u,v) domain nor in the (ξ,η) domain, artifacts are not induced in the recovered brightness temperature map and signal to noise ratio is preserved. At this point two important relationships between the interferometer's array geometry and the (u,v)-(ξ,η) points should be pointed out:

i) the *total number of correlations, N_T^2, is equal to the number of samples in the fundamental hexagonal* (u,v) *and* (ξ,η) *cells* (equation (6.15)).

ii) the *number of redundant correlations between antenna pairs, including those leading to the zero baseline, is equal to the number of missing* (u,v) *visibility samples which are initially padded with zeros.*

This technique has been applied to the particular sampling grids given by Y-arrays, such as MIRAS, but it can be used with any other sampling strategy with an appropriate $\overline{\overline{\Xi}}$ 31 matrix satisfying equations (6.17), (6.18a) and (6.18b).

6.1.2.- Example of application: aliasing and windowing impacts

Figures 6.7 and 6.8 show the results of the application of this technique to a case similar to the space-borne MIRAS (Y-interferometer with 43 antennas per arm spaced 0.89 wavelengths). The image treated in this example has been taken from MATLAB ((c) The MATH WORKS Inc.) and has been properly modified in order to give realistic brightness temperature values. This image is composed by an ellipsoidal (ξ,η) contour (figure 6.7a, equation (4.13)) representing the Earth-sky border as seen from a platform 800 Km height with the Y-array tilted 31.2° with respect to nadir. The sky occupies the zone in between the ellipsoidal contour and the unit circle and its brightness temperature is assumed to be 3 K. The brightness temperature of the sea has been taken 100 K and that of the coast ranges from 220 K to 300 K.

The original brightness temperature is shown in figure 6.7a, from which the set of visibilities have been computed over the (u,v) hexagonal grid given in equation (6.18a) according to expression (3.1). When computing these values the noise due to finite integration time has been assumed to be negligible ($\tau = \infty$), consequently any error in the recovered images is only due to the Fourier inversion process. Figure 6.7b shows the brightness temperature map restricted to the alias free field of view (FOV). Figures 6.7c and 6.7d show the inverse Fourier Transform of the visibility samples computed according to (6.18a) without weighting function (rectangular window) and with a Blackmann window respectively. Since the spacing between antennas exceeds $1/\sqrt{3}$ wavelengths, the Nyquist criterion for hexagonal sampling is not satisfied and some aliasing exists (see figure 6.6b): results are shown cut to the alias free FOV. Note the absence of artifacts, usually of periodic character, that generally appear when interpolations are performed [Camps et al. 95A]. Note also that the Blackmann windowed image appears more blurred than its rectangular windowed counterpart. Figures 6.8a and 6.8b show the discretization and (u,v) finite coverage errors computed as the difference between the recovered brightness

temperature maps (figures 6.7c and 6.7d) and the original brightness temperature (figure 6.7b). Note the high errors due to Gibbs phenomenon at the coast line due the 120 K step in the brightness temperature. Errors decrease when highly tapered windows are used. The trade-off shown in chapter 3 [Camps et al. 96A] between high spatial resolution, requiring low weighting functions, and high radiometric resolution, requiring highly tapered weighting functions, can be easily appreciated.

Since the (u,v) coverage is finite, its inverse Fourier Transform is not limited and some alias' "tails" partially enter in the nominal alias free FOV. In figures 6.7c and 6.8a one pixel of the border has been removed to minimize this effect. However, it is more apparent in figures 6.7d and 6.8b because of the wider system's impulse response caused by the Blackmann weighting function. However, as it will be shown in section 6.2.3, aliasing impact in the FOV can be minimized by using some "a priori" information such as the sky brightness temperature and the average Earth brightness temperature. Aliasing degrades interferometer's performance at swath edges and presents added difficulties in the inversion process since measured visibilities depend also on the brightness temperature from the aliased regions. These difficulties can be partially alleviated by restricting the inversion region to a smaller area inside the alias free FOV [Bará et al. 96A].

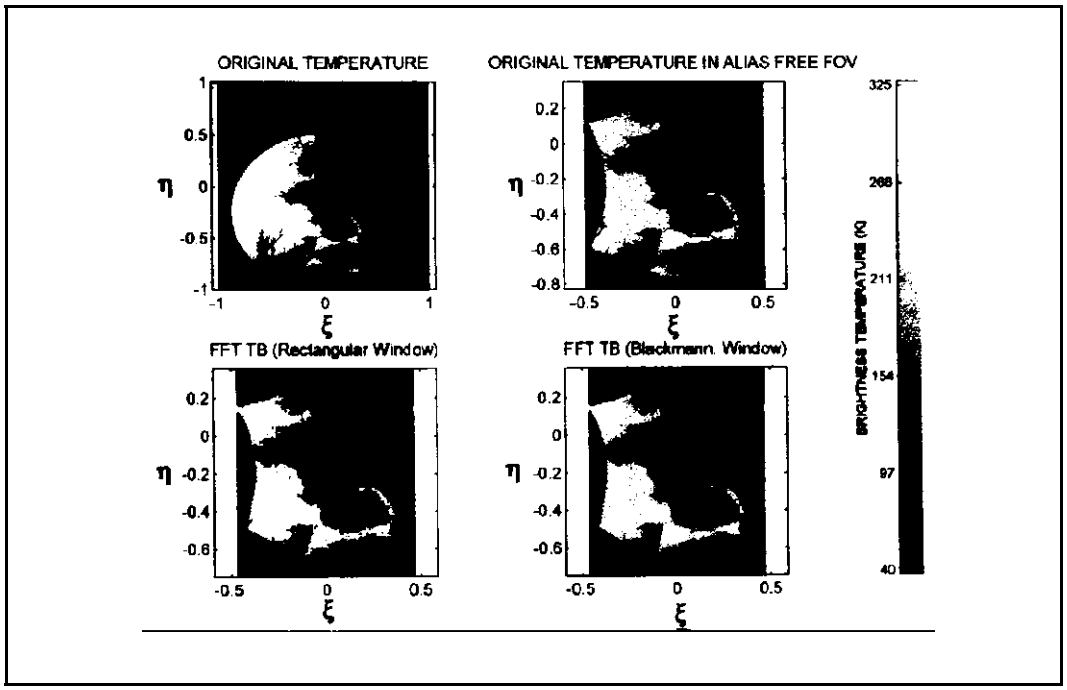

Figure 6.7.- *6.7a 6.7b 6.7c 6.7d*

Figure 6.7a.- *Hypothetical Earth model for hexagonal visibility processing using standard FFT as seen from a 800 Km height, 31.2º tilted platform.*

Figure 6.7b.- *Alias free field of view of figure 6.8.a. Subsampling with 0.898 spacing between antennas reduces alias free swath to 900 Km*

Figure 6.7c.- *Recovered brightness temperature in the alias free field of view by inverse Fourier transform of hexagonally sampled visibilities with rectangular weighting window.*

Figure 6.7d.- *Recovered brightness temperature in the alias free field of view by inverse Fourier transform of hexagonally sampled visibilities with Blackmann weighting window.*

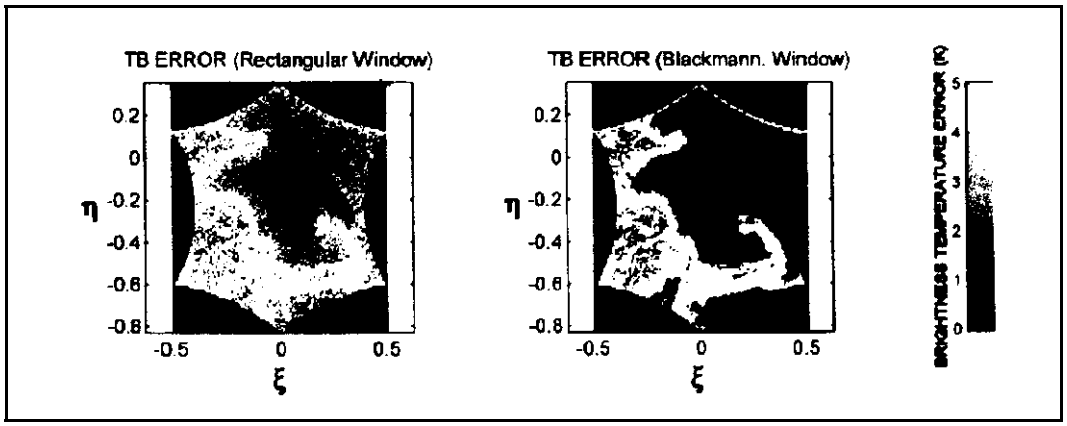

Figure 6.8.- *6.8a 6.8b*

Figure 6.8a- *Error in the recovered brightness temperature with rectangular weighting window (figure 6.8b minus 6.8.c)*

Figure 6.8b- *Error in the recovered brightness temperature with Blackmann weighting window (figure 6.8b minus 6.8d)*

6.1.3.- Conclusions

It has been shown that a proper choice of the interferometer's array configuration allows a substantial reduction of the number of visibility samples and hardware requirements for a determined aliasing level. In this sense Y-shaped and triangular-shaped arrays sample the visibility function over a hexagonal grid which is the optimal one. Compared to rectangular (u,v) sampling a hardware reduction of 13.4 % is obtained. In addition, Y-shaped arrays provide larger (u,v) coverage than triangular-shaped arrays, thus improving the spatial resolution capabilities of the instrument.

This section has presented a simple procedure to fully exploit the benefits of the hexagonal sampling grid given by Y-shaped arrays, as MIRAS: reduction on hardware requirements and the number of visibility samples (13.4 %), increased computational speed (25 %) with standard rectangular row-column routines and avoidance of the drawbacks of hexagonal to rectangular conversion mainly: additional computational load, interpolation induced artifacts and signal to noise degradation. This technique is based on the use of rectangular FFT to process hexagonally sampled signals provided that the (>,0) pixels are properly chosen over the reciprocal grid of the (u,v) hexagonal grid. However, it is not restricted to hexagonal grids and can be used with other sampling strategies, provided that the reciprocal basis is used.

An example of this technique has been presented applied to an Y-array with 43 antennas per arm, as MIRAS. Subsampling problems have been pointed out: mainly aliasing and radiometric resolution degradation at swath edges.

6.2.- INVERSION ALGORITHMS IN APERTURE SYNTHESIS INTERFEROMETRIC RADIOMETRY: GENERAL CASE

At this point it is important to remember that, since most errors can be accurately calibrated, the inversion process should be addressed to recover the brightness temperature distribution from the $\mathbf{V}^{(1)}$ set of visibility samples: that is, the visibility samples affected by the fringe-washing function and by antenna pattern amplitude and phase errors.

6.2.1.- Review of inversion methods

In order to solve equation (3.1) numerically, it can be discretized as follows:

$$V_{kl}(u_{kl},v_{kl}) \mu \; \mathrm{j}_p \; \mathrm{j}_q \; \mathrm{I}(>_{pq},0_{pq})F_{nk}(>_{pq},0_{pq})$$
$$F_{nl}^{(}(>_{pq},0_{pq}) \; \tilde{r}_{kl}\left(\& \frac{u_{kl}>_{pq} \% v_{kl}0_{pq}}{f_o} \right) \; e^{\&j \; 2\mathrm{B} \; (u_{kl}>_{pq} \% v_{kl}0_{pq})} \qquad \textbf{(6.22)}$$

The (u_{kl}, v_{kl}) points are determined by the array shape, in our case the Y-array which is optimal in terms of minimum number of samples required. $(>_{pq},0_{pq})$ are the directing cosines sampling points and can be arbitrary chosen provided the discretization error is low enough so that equation (6.22) holds. *However, since in the ideal case equation (6.22) reduces to an hexagonal DFT, it is interesting to take the* $(>_{pq},0_{pq})$ *pixels over the reciprocal grid previously given by equation (6.18a).* In this case, the brightness temperature pixel area is given by:

$$) \; ' \; \frac{\sqrt{3}d^2}{2} \qquad \textbf{(6.23)}$$

By mapping (k,l) and (p,q) pairs of indexes into single ones "m" and "s", the set of equations (6.22) for all the visibility samples can be written simultaneously in matrix notation:

$$\overline{V}_m \; ' \; \overline{\overline{G}}_{m,s} \; \overline{T}_s \qquad \textbf{(6.24)}$$

where each element of the **G** operator is given by:

$$g_{ms} \; ' \; \frac{\sqrt{3}d^2}{2} F_{nm}(>_s,0_s) F_{nm}^{(}(>_s,0_s) \tilde{r}_m \left(\& \frac{u_m>_s \% v_m 0_s}{f_o} \right) e^{\&j \; 2\mathrm{B} \; (u_m>_s \% v_m 0_s)} \qquad \textbf{(6.25)}$$

It should be noted that the value assigned to the $\overline{\overline{G}}$ elements is not the same of that presented for ESTAR [Ruf et al. 88]. In that case the impulse response of the system ($\overline{\overline{G}}$ matrix elements) was directly measured, including all system imperfections: antenna coupling effects, antenna pattern, receiver errors ... In our approach, antenna coupling and receiver phase/quadrature errors must be previously calibrated.

When solving equation (6.24) there are three possible situations:

i) The number of unknowns (brightness temperature pixels) is the same as the number of available visibility samples. In this case the expected temperature vector will be given by:

$$\overline{T} \;=\; \overline{\overline{G}}^{-1}\;\overline{V} \qquad \textbf{(6.26)}$$

ii) The number of unknowns is smaller than the number of visibility samples. In this case a least squares fitting can be done:

$$\overline{T} \;=\; (\overline{\overline{G}}^{H}\;\overline{\overline{G}})^{-1}\;\overline{\overline{G}}^{H}\;\overline{V} \qquad \textbf{(6.27)}$$

iii) The number of unknowns is greater than the number of visibility samples and there are infinite possible solutions that satisfy equation (6.24). Among all the possible solutions, an analytical solution is obtained by the Moore-Penrose pseudo-inverse given by [Ruf et al. 88][LeVine et al. 89][LeVine et al. 90][LeVine et al 92][Tanner and Swift 93][Jain 89]:

$$\overline{T} \;=\; \overline{\overline{G}}^{H}\;(\overline{\overline{G}}\;\overline{\overline{G}}^{H})^{-1}\;\overline{V} \qquad \textbf{(6.28)}$$

which is used as the basis in the ESTAR inversion process [Ruf et al. 88].

As it has been shown in section 6.1, *the number of redundant correlations corresponds to the number of missing visibility samples required to fill up a fundamental hexagonal period*. Thus the number of unknowns is (basic hexagonal (>,0) cell) is:

$$N_T^2 \;=\; (3N_{EL}-1)^2 \;=\; 9N_{EL}^2-6N_{EL}+1 \qquad \textbf{(6.29)}$$

and the number of data is (number of non-redundant (u,v) samples):

$$N_V \;=\; 6N_{EL}^2-6N_{EL}+1 \qquad \textbf{(6.30)}$$

This problem corresponds to the third situation on above and, since there is no unique solution, there are different techniques to find a reasonably "good" solution, not only the one provided by the pseudo-inverse (equation (6.28)).

In the following paragraphs a quick review to different inversion techniques that have been explored is presented and the relationships between them are pointed out. Special attention is paid to the $\overline{\overline{G}}$ operator and the possibility to be extended to 2-D interferometers. The Maximum Entropy Method and the CLEAN algorithm, currently used in radioastronomy are also reviewed. Other procedures, such as the Krylov method, the conjugate gradient method and the preconditioned conjugate gradient method are briefly revised to show their relationships with the algorithm that is proposed in section 6.2.2.

At this point it should be noted that most of these methods (7 of 10) have been programmed and tested to study their suitability to the problem that concerns us.

6.2.1.1.- The G operator

The inverse $\overline{\overline{G}}$ operator defined in equation (6.28) is also called the Moore-Penrose pseudoinverse. In the ideal case, when the $\overline{\overline{G}}$ operator becomes the 2-D discrete Fourier Transform Operator, it can be easily shown that the solution given by (6.28) corresponds to that obtained by an inverse Fourier Transform with non-measured visibility samples set to zero, since:

$$\overline{\overline{G}}^{H}\ (\overline{\overline{G}}\ \overline{\overline{G}}^{H})^{-1}\ \cdot\ \overline{\overline{F}}^{H}\ (\overline{\overline{F}}\ \overline{\overline{F}}^{H})^{-1}\ \cdot\ \overline{\overline{F}}^{-1}\ (\overline{\overline{F}}\ \overline{\overline{F}}^{-1})^{-1}\ \cdot\ \overline{\overline{F}}^{-1} \qquad \textbf{(6.31)}$$

In this case, since the Fourier transform preserves the norm and non-measured visibilities have been set to zero, *the solution that is obtained is the Minimum Norm Solution.*

The main problems appearing with a 2-D $\overline{\overline{G}}$ operator inversion approach are:

i) Difficulty in measuring the impulse response for a 2-D aperture synthesis radiometer since the number of independent temperature pixels grows with the square of the number of antennas. In addition, as it was done in ESTAR, the number of pixels must be much higher in order to stabilize the inversion process by lowering the condition number of the $\overline{\overline{G}}\ \overline{\overline{G}}^{H}$ matrix. For a space-borne interferometer, drifts in receivers parameters require a periodic calibration which needs to locate over the Earth's surface a large number of polarimetric hot points, which is impractical, and forbidden by frequency regulation boards (RR8-92/721).

ii) Stringent memory requirements: $\overline{\overline{G}}$ operator's size is N_V = 11,353 rows by N_T^2=16,900 columns, that is 1,92 10^8 complex elements requiring 3,07 Gigabytes to be stored. Even though these values can be halved by benefiting from the hermiticity resort, it is a large amount of information to be stored.

iii) Large computational load:

- The evaluation of each term of the $\overline{\overline{G}}$ operator (equation (6.25)) requires 3 complex products and 2 real products. The total number of complex products required raises to N_1=(4 x 3+2) N_V N_T^2 = 2,69 10^9 real products
- The computation of $\overline{\overline{G}}\ \overline{\overline{G}}^{H}$ requires $N_T^2.N_V^2$ complex products or N_2= 4 N_T^2 N_V^2= = 8,71 10^{12} real products.

- The computation of the inverse $\overline{\overline{A}}\ '\ (\overline{\overline{G}}\ \overline{\overline{G}}^{H})^{\&1}$ by the Gauss-Jordan algorithm requires about of 5/6 N_V^3 complex products or $N_3 = 10/3\ N_V^3 = 4{,}88\ 10^{12}$ real products
- And finally, the product $\overline{\overline{G}}^{H}\ \overline{\overline{A}}$ requires $N_4 = 4\ N_T^2\ N_V^2 = 8{,}71\ 10^{12}$ real products

The total number of operations raises up to $N = N_1+N_2+N_3+N_4 = 22{,}3\ 10^{12}$ real products. Considering that the total number of pixels in the FOV of interest is about 2500, at each snap-shot the number of operations to be performed in order to recover the brightness temperature map is: $N' = 4\ 2{,}500\ N_V = 113\ 10^6$ real products.

The amount of operations is quite impressive and would require a considerable amount of time to be performed, even in a super-computer. Memory requirements are also very demanding and would occupy most of the available RAM in today's super-computers.

iv) On the other hand, *this method is not well adapted to describe a dynamic system* that must be periodically re-calibrated.

v) And since the required radiometric resolution is high, the condition number or stability of the inversion process must be studied to asses the impact of noise amplification due to error propagation.

It has been found that the condition number of $\overline{\overline{G}}\ \overline{\overline{G}}^{H}$ increases with: narrower antenna patterns, higher decorrelation effects, increasing number of antennas and smaller spacing between antennas. Due to memory requirements and the large computational load, the study has been carried out with a number of antennas per arm up to 8, this means 25 antennas in total. Depending on the half-power beam-width, from 60º to 90º, and on the ratio $W = B/f_o$, from 0 to 0.2, the condition number ranges from about 25 to more than 1.000. The dependence with the half power beam-width is very strong and can be understood by the mixing effect that is produced in the product $\overline{\overline{G}}\ \overline{\overline{G}}^{H}$, where pixels pointed by the main beam are multiplied by others pointed from a low gain portion of the antenna pattern. In either case these numbers are not acceptable because the recovered brightness temperature values found are too noisy.

Figures 6.9-6.12 show the sparsity graphs for the $\overline{\overline{G}}\ \overline{\overline{G}}^{H}$ product, for a half-power beam-width of 70º, for N_{EL}=3 and 5 and d=1/%3 and 0.89 wavelengths respectively. The mixing effect commented before is apparent. Note that, in the ideal case, the **G** operator tends to the discrete Fourier operator and $\overline{\overline{G}}\ \overline{\overline{G}}^{H}$ tends to the identity matrix,

while in fact the $\overline{\overline{G}}\,\overline{\overline{G}}^{H}$ matrix tends to a band-matrix, as it can be seen in figures 6.9 to 6.12, for different number of antennas per arm and different antenna spacings.

In order to benefit from this configuration some iterative techniques have been studied, such as the Pan-Reif algorithm [Phip 86] [Press 86]. The bands near the corners slow the convergence of these methods and direct algorithms (i.e. Gauss-Jordan) have proven to perform better.

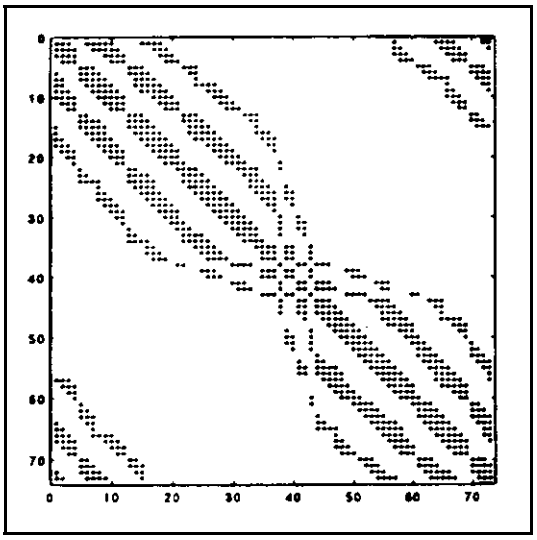

Figure 6.9.- *GG^H sparsity graph: N_{EL}=3, d=1/%38,) 2_{-3dB}=70º*

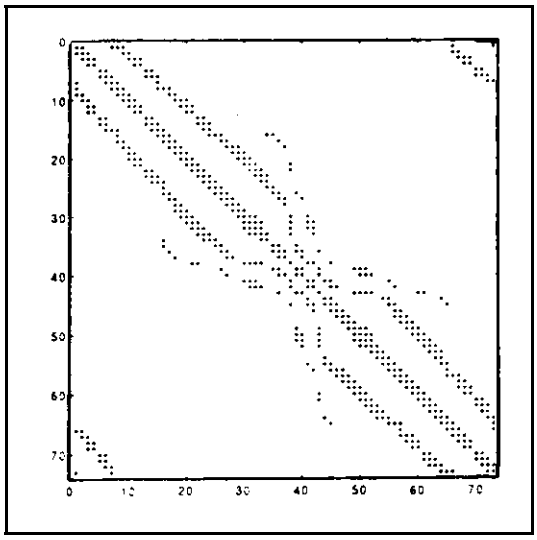

Figure 6.10.- *GG^H sparsity graph: N_{EL}=3, d=0.898,) 2_{-3dB}=70º*

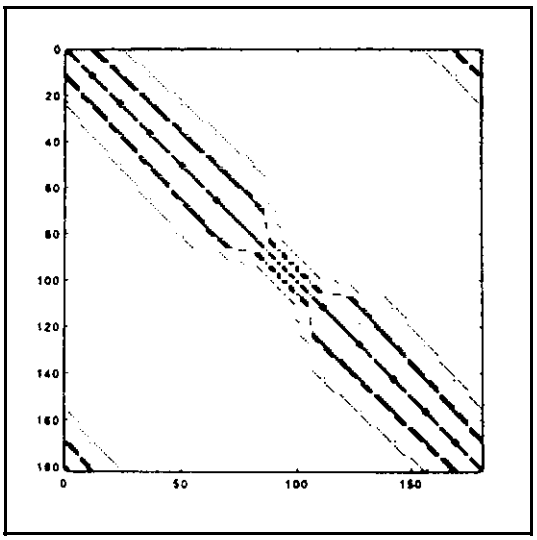

Figure 6.11.- *GG^H sparsity graph: N_{EL}=5, d=1/%38,) 2_{-3dB}=70º*

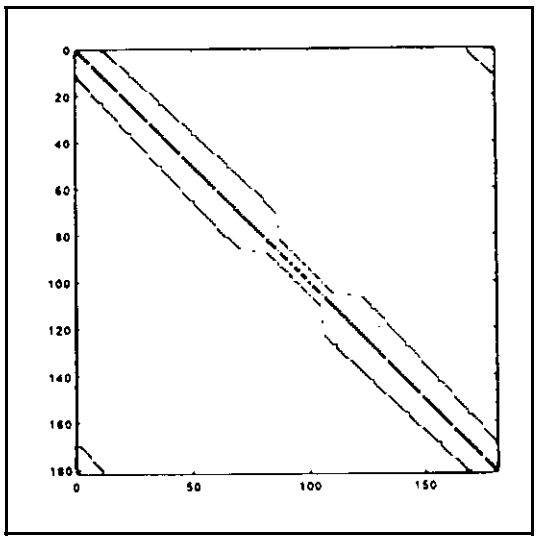

Figure 6.12.- *GG^H sparsity graph: N_{EL}=5, d=0.898,) 2_{-3dB}=70º*

6.2.1.2- Singular Value Decomposition and Generalized Inverse

The vector $\overline{T}^{\%}$ that is a solution of equation (6.24) and has the minimum norm among all the possible solutions is called the minimum norm least squares solution (MNLS):

$$\overline{T}^{\%} = \min \left\{ \|\overline{T}\|^2, \overline{\overline{G}}^H \overline{V} = \overline{\overline{G}}^H \overline{\overline{G}}\ \overline{T} \right\} \qquad \textbf{(6.32)}$$

Using the Singular Value Decomposition of $\overline{\overline{G}}$, it can be shown that the transformation between $\overline{V}$ and $\overline{T}^{\%}$ is linear and unique. It is given by [Jain 89]:

$$\overline{T}^{\%} = \overline{\overline{G}}^{\%} \overline{V} \qquad \textbf{(6.33)}$$

The $\overline{\overline{G}}^{\%}$ matrix is called the generalized inverse of $\overline{\overline{G}}$. If the MxN (N_VxN_T^2) $\overline{\overline{G}}$ matrix has the SVD expansion given by:

$$\overline{\overline{G}} = \sum_{m=1}^{r} \sqrt{\lambda_m}\ \overline{Q}_m\ \overline{M}_m^T \qquad \textbf{(6.34)}$$

where $\overline{M}_m$ are the eigenvectors of $\overline{\overline{G}}^H \overline{\overline{G}}$ and $\overline{Q}_m$ are the eigenvectors of $\overline{\overline{G}}^H \overline{\overline{G}}$, its generalized inverse is a NxM matrix with a SVD decomposition:

$$\overline{\overline{G}}^{\%} = \sum_{m=1}^{r} \lambda_m^{-\frac{1}{2}}\ \overline{M}_m\ \overline{Q}_m^T \qquad \textbf{(6.35)}$$

corresponding to the singular values λ_m.

Note that the rank of $\overline{\overline{G}}$ is M=N_V + N_T^2, since there are N_V independent equations and N_T^2 unknowns. In such a case the SVD decomposition of $\overline{\overline{G}}$ satisfies:

$$\overline{\overline{G}}^{\%} = \overline{\overline{G}}^H (\overline{\overline{G}}\ \overline{\overline{G}}^H)^{-1} \qquad \textbf{(6.36)}$$

which is equivalent to the Moore-Penrose Pseudoinverse (equation (6.28)). With this approach, the main problem is the required computational load to calculate the vectors $\overline{M}_m$ and $\overline{Q}_m$ for large matrices, as the $\overline{\overline{G}}$ operator.

6.2.1.3.- One-step Gradient Methods: the steepest descent method

If there is no interest in the pseudoinverse itself, but only in the recovered vector $\overline{T}$, iterative gradient methods are practical because they avoid the need to store and invert huge matrices.

These methods take the form [Jain 89]:

$$\overline{T}_{n+1} = \overline{T}_n - \alpha_n \overline{g}_n ; \quad \overline{T}_0 = 0 \tag{6.37}$$

where:

$$\overline{g}_n = -\overline{\overline{G}}^H (\overline{V} - \overline{\overline{G}}\,\overline{T}_n) \tag{6.38}$$

In order to improve the speed of convergence the parameter α should be adjusted at each iteration according to:

$$\alpha_n = \frac{\overline{g}_n^H \overline{g}_n}{\overline{g}_n^H \overline{\overline{G}}^H \overline{\overline{G}}\,\overline{g}_n} \tag{6.39}$$

6.2.1.4.- The Van Cittert Filter [Dudgeon and Mersereau 84] [Jain 89]

When the matrix $\overline{\overline{G}}^H \overline{\overline{G}}$ is ill conditioned the speed of convergence of one-step gradient methods is not significant lowered by replacing α_n by a constant α. The optimum value of this constant is given by:

$$\alpha_{opt} = \frac{2}{\lambda_{max}(\overline{\overline{G}}^H \overline{\overline{G}}) + \lambda_{min}(\overline{\overline{G}}^H \overline{\overline{G}})} ; \quad 0 < \alpha < \frac{2}{\lambda_{max}} \tag{6.40}$$

In this case, the solution at the i^{th} iteration can be written as:

$$\overline{T}_{i+1} = \overline{\overline{E}}_i \overline{V} \tag{6.41}$$

where:

$$\overline{\overline{E}}_i = \alpha \sum_{k=0}^{i} (\overline{\overline{I}} - \alpha \overline{\overline{G}}^H \overline{\overline{G}})^k \overline{\overline{G}}^H \tag{6.42}$$

Since this unconstrained iteration converges to the inverse filter solution, it possesses most of the undesirable properties associated with inverse filtering, i.e. noise amplification and convergence problems. However, the imposition of some *restrictions* on the solution such as *positiveness or finite support may alleviate these problems* [Schaffer et al. 81], [Trussell 83], [Jain 89]. The similitudes between the method proposed in sections 6.2.2.2 and 6.2.2.3 and this one, as well as the restrictions imposed to the solution, mainly the finite support, will become more apparent.

6.2.1.5.- The Wiener Filter

Let's consider a zero mean brightness temperature distribution leading to equation (6.24), except for the zero baseline, which accounts for the average value:

$$\overline{)V} = \overline{\overline{G}}\ \overline{)I} + \overline{n} \qquad \textbf{(6.43)}$$

where $\overline{n}$ represents the noise vector present in the measurement of the visibilities. The dimensions of vectors $\overline{)V}$ and $\overline{n}$ are N_Vx1, $\overline{)I}$ is N_T^2x1 and $\overline{\overline{G}}$ is N_VxN_T^2. The true brightness temperature distribution is obtained at the end by adding the average value T_A to $\overline{)I}$. The best linear estimate:

$$)\hat{I} = \overline{\overline{H}}\ \overline{)V} \qquad \textbf{(6.44)}$$

that minimizes the average mean square error:

$$\sigma_e^2 = \frac{1}{N_T^2} E\left[(\overline{)I} -)\hat{I})^T (\overline{)I} -)\hat{I})\right] \qquad \textbf{(6.45)}$$

is obtained by the orthogonal relation:

$$E\left[(\overline{)I} -)\hat{I})\overline{)V}^H\right] = 0 \qquad \textbf{(6.46)}$$

which leads to the Wiener filter as a N_T^2 x N_V matrix [Jain 89]:

$$\overline{\overline{H}} = E\left[\overline{)I})\hat{I}^T\right]\left(E\left[\overline{)V}\ \overline{)V}^H\right]\right)^{-1} = \overline{\overline{R}}_T\ \overline{\overline{G}}^H\left[\overline{\overline{G}}\ \overline{\overline{R}}_T\ \overline{\overline{G}}^H + \overline{\overline{R}}_n\right]^{-1} \qquad \textbf{(6.47)}$$

where $\overline{\overline{R_T}}$ and $\overline{\overline{R_n}}$ are the covariance matrices of $\overline{)I}$ and $\overline{n}$:

$$\overline{\overline{R}}_T = E\left[\overline{)I}\ )\hat{I}^T\right] \qquad \textbf{(6.48)}$$

$$\overline{\overline{R}}_n = E\left[\overline{n}\ \overline{n}^H\right] \qquad \textbf{(6.49)}$$

and:

$$E\left[\overline{)I}\ \overline{n}^H\right] = 0 \qquad \textbf{(6.50)}$$

If noise is uncorrelated from sample to sample, which is approximately true as a result of the redundancy study (section 3.2.2.3), then the covariance matrix $\overline{\overline{R_n}} = \overline{\overline{I}}$, where $\overline{\overline{I}}$ stands for the identity matrix. The $\overline{\overline{R_T}}$ matrix, the brightness temperature covariance matrix, is very difficult to find because it depends on the particular image, but according to the physical phenomenon involved in the thermal radiation process, it can be assumed that pixels are uncorrelated (equation (2.37)) and $\overline{\overline{R_T}} = \overline{\overline{I}}$.

With these two assumptions, the Wiener Filter becomes:

$$\overline{\overline{H}} = \overline{\overline{G}}^H\left[\overline{\overline{G}}\ \overline{\overline{G}}^H + \sigma_n^2\ \overline{\overline{I}}\right]^{-1} \qquad \textbf{(6.51)}$$

which tends to the Moore-Penrose Pseudoinverse in the absence of noise (F_n^2 -> 0). When measurements are noisy, as it is usual, *the pseudoinverse method explained above is not the optimum.*

On the other hand, the method has been tested and for signal-to-noise ratios about S/N . 35 dB (J = 0.3 s, B = 20 MHz) the diagonal term added to the $\overline{\overline{G}}\,\overline{\overline{G}}^H$ matrix (figures 6.9-6.12) does not improve noticeably its condition number, while the memory requirements and computational load is the same.

6.2.1.6.- The Krylov method

The Krylov method is a general iterative procedure to solve systems of equations:

$$\overline{E} = \overline{\overline{L}}\,\overline{J};$$
$$\overline{E} \div \overline{V}\ ; \quad \overline{\overline{L}} \div \overline{\overline{G}}\ ; \quad \overline{J} \div \overline{T} \tag{6.52}$$

The solution is sought as follows [Cátedra et al. 95]:

$$\overline{I}_n = \overline{I}_{n-1} + a_n \overline{P}_n\ ; \quad n \geq 1; \quad \overline{I}_0 \ \textit{arbitrary}$$
$$\overline{r}_n = \overline{r}_{n-1} - a_n \overline{\overline{G}}\,\overline{P}_n\ ; \quad n \geq 1; \quad \overline{P}_1 = \overline{\overline{M}}\,\overline{r}_0 \tag{6.53}$$
$$\overline{P}_n = \overline{\overline{M}}\,\overline{r}_{n-1} + \sum_{m=1}^{n-1} \beta_{nm} \overline{P}_m$$

where $\overline{\overline{M}}$ is an arbitrary linear operator to be chosen. The additional degree of freedom introduced by the parameters β_{nm} allows to find the searching direction in a more sophisticated way, improving the convergence of the method. The functional $\|\overline{I} - \overline{I}_n\|_i$ is minimized at each iteration on the subspace spanned by:

$$\overline{H}_n = \{\overline{P}\}_{j=1}^{n} = \{\overline{\overline{M}}\,(\overline{\overline{G}}\,\overline{\overline{M}})^{-1}\,\overline{r}_0\}_{j=1}^{n} \tag{6.54}$$

with the following parameters:

$$a_n = \frac{\langle \overline{I} - \overline{I}_{n-1}, \overline{P}_n \rangle_i}{\|\overline{P}_n\|_i^2}$$
$$\beta_{nj} = -\frac{\langle \overline{\overline{M}}\,\overline{r}_{n-1}, \overline{P}_j \rangle_i}{\|\overline{P}_j\|_i^2}\ ; \quad j = 1,\ldots,n-1 \tag{6.55}$$

However, the solution being sought, $\overline{I}$, appears in (6.55) for a_n. Consequently a_n can only be explicitly calculated in a few cases. Table 6.1 summarizes some versions of the Krylov method:

i	M	Functional Minimized	a_n	Krylov method: $\alpha_{n,m}$	CG method: $\alpha_{n,m}$
1	L^A	$\|\|T-T_{n_n}\|\|$	$\frac{\|\| r_{n-1} \|\|^2}{\|\| P_n \|\|^2}$	$-\frac{\langle M^A r_{n-1}, P_m \rangle}{\|\| P_m \|\|^2}$	$\frac{\|\| r_{n-1} \|\|^2}{\|\| r_{n-2} \|\|^2}$
2	I	$\|\| r_n \|\|$	$\frac{\langle r_{n-1}, M r_{n-1} \rangle}{\|\| M P_n \|\|^2}$	$-\frac{\langle M r_{n-1}, M P_m \rangle}{\|\| M P_m \|\|^2}$	$\frac{\langle r_{n-1}, M r_{n-1} \rangle}{\langle r_{n-2}, M r_{n-2} \rangle}$
2	L^A	$\|\| r_n \|\|$	$\frac{\|\| M^A r_{n-1} \|\|^2}{\|\| M P_n \|\|^2}$	$-\frac{\langle M M^A r_{n-1}, M P_m \rangle}{\|\| M P_m \|\|^2}$	$\frac{\|\| M^A r_{n-1} \|\|^2}{\|\| M^A r_{n-2} \|\|^2}$
3	I	$\langle T-T_n, M(T-T_n) \rangle$	$\frac{\|\| r_{n-1} \|\|^2}{\langle P_n, M P_n \rangle}$	$-\frac{\langle r_{n-1}, M P_m \rangle}{\langle P_m, M P_m \rangle}$	$\frac{\|\| r_{n-1} \|\|^2}{\|\| r_{n-2} \|\|^2}$

Table 6.1.- *Different versions of the Krylov and CG methods [Kleinmann & Van den Berg 91]*
Note: For i=2, T=I is only valid if L is self-adjoint, for i=3 is valid only if L is self-adjoint and positive.

6.2.1.7.- Conjugate Gradient Method

The versions of the CG method that are most commonly used are obtained as particularizations of the Krylov methods where the $M G$ operator is self-adjoint with respect to some scalar product. In this case [Cátedra et al. 95]:

$$\alpha_{nj} = 0, \quad j = 1,\ldots,n-2$$

$$\alpha_{n,n-1} = -\frac{\langle M r_{n-1}, P_{n-1} \rangle_i}{\|P_{n-1}\|_i^2} \qquad \textbf{(6.56)}$$

and the functions P_n depend only on P_{n-1}, but the error is minimized on the subspace spanned by all the previous functions.

Some versions of the CG method and their relationships with the Krylov method are summarized in table 6.1.

6.2.1.8.- Preconditionned Conjugate Gradient Algorithms

Note that if $\overline{\overline{M}}$ is chosen so that:

$$\overline{\overline{M}} \approx \overline{\overline{G}}^{-1} \tag{6.57}$$

and $\overline{I}_o = \overline{0}$, equation (6.53) reduces to:

$$\begin{aligned} \overline{r}_0 &= \overline{V} - \overline{\overline{G}}\,\overline{I}_0 = \overline{\overline{V}} \\ \overline{P}_1 &= \overline{\overline{M}}\,\overline{r}_0 = \overline{\overline{G}}^{-1}\,\overline{V} \end{aligned} \tag{6.58}$$

and the exact solution is found in only one iteration, which is an obvious result.

In our case, the inverse operator is not known. However, if a preconditioner operator $\overline{\overline{M}} = \overline{\overline{G_{ap}}}$ is chosen such that $\overline{\overline{G}}\,\overline{\overline{G_{ap}}}$ is close to the identity operator, then the CG method would converge much faster than the $\overline{\overline{G}}$ operator itself.

In section 6.2.2.1, the inversion algorithm that is proposed is based on the selection of a simple preconditioner operating over differential visibilities, followed by a simple Neumann iteration. This algorithm has proven to be performant and its convergence is very fast, without computing the a_n and $\zeta_{n,m}$ coefficients.

6.2.1.9.- Maximum Entropy Methods

Maximum Entropy Methods are commented here in order to make the link to deconvolution techniques for radio synthesis images. The method has been tested to verify its performance with subsampled extended thermal sources.

All ME algorithms are based on maximizing [Mersereau and Dudgeon 74] [McDonough 74] [Andrews and Hunt 77] [González and Wintz 77] [Wernecke and d'Addario 77] [Lang and McClellan 80] [Trussell 80] [Lim and Malik 81] [Lang and McClellan 82] [Malik and Lim 82] [Wahl 87] [Jain 89]:

$$\chi(\overline{T}) = -\sum_{n=1}^{N_T^2} T(n)\ln(T(n)) \tag{6.59}$$

or:

$$, (\overline{T}) \; ' \; \& \sum_{n}^{N_T^2} \ln(T(n)) \qquad \textbf{(6.60)}$$

subject to the constrain:

$$\frac{1}{2} \; * \overline{V} \; \& \; \overline{\overline{G}} \; \overline{T} *^{2} \; ' \; \mathsf{F}_n^{2} \qquad \textbf{(6.61)}$$

The "ln" function in (6.59) and (6.60) forces new extrapolated visibility samples and super-resolution on bright, isolated objects. In addition, it has been reported that this method works also for extended sources [Wernecke and d'Addario 77]. In the literature it has been demonstrated that other functions satisfying positive first derivate and negative second derivate provide similar results [Lim 90].

Even though an analytical solution exists for the 1-D problem, the solution of equations (6.59) or (6.60) and (6.61) in the 2-D case must be obtained in an iterative way. Among the different methods proposed in the literature which are very computationally demanding, the method proposed by Lim and Malik [Lim and Malik 81], apparently one of the most efficient, has been tested. As reported in [Lim 90], this algorithm to be performant requires: a small set of data, typically less than [7 x 7], a large domain where visibility samples are to be extrapolated in order to assure no aliasing in the DFT and a low signal-to-noise ratio (S/N < 5 dB).

Even though these conditions are far from those that are found in Earth observation, this method has been tested for the case of the MIRAS bread-board, a small Y-array with 3 antennas per arm providing 73 visibility samples with a signal-to-noise ratio of 35 dB. The domain where visibility samples are to be extrapolated is extended up to [128 x 128] from the minimum coverage required [N_TxN_T] = [10x10] (N_T = 3 N_{EL} + 1= 10 antennas). Results for an extended source, a constant brightness temperature inside the Earth contour as seen from the satellite (equation 4.13), even the case of no aliasing (spacing between antennas d=1/%3 wavelengths) were deceiving and little or null convergence was experimented due the high signal-to-noise ratios involved.

In this method, the nonlinear function 'ln' does not work with zero mean temperatures, and since in the case that d=0.89 wavelengths there is no Earth-sky transition, all the recovered brightness temperatures have positive values and the extrapolation power due to the "ln" function is not apparent.

6.2.1.10.- The CLEAN algorithm

The 'CLEAN' algorithm was devised by J. Högbom in 1974 and provides a solution to the convolution equation given by (3.20) which relates the recovered and the true brightness temperature distributions through the Equivalent Array Factor.

$$\hat{T}(>,0) = \iint_{>^2+0^2\le 1} AF_{eq}(>,>),0,0)\,T(>,0)\,d>\,d0 \qquad \textbf{(6.62)}$$

where the equivalent array factor is given for the hexagonal sampling grid by:

$$AF_{eq}(>,>),0,0) = \frac{\sqrt{3}d^2}{2} \sum_{n_1=1}^{N_T} \sum_{n_2=1}^{N_T} W(u_{n_1,n_2},v_{n_1,n_2}) \; \tilde{r}_{n_1,n_2}\left(-\frac{u_{n_1,n_2}>+v_{n_1,n_2}0}{f_0}\right) e^{j2\pi\left[u_{n_1,n_2}(>->))+v_{n_1,n_2}(0-0))\right]} \qquad \textbf{(6.63)}$$

The convolution of the true brightness temperature distribution with its space-variant impulse response, the equivalent array factor, represents the response of the interferometer.

The 'CLEAN' algorithm represents a radio source by a number of point sources in an empty field of view. An iterative approach is employed to find the positions and strengths of these point sources. The final "cleaned" image is the sum of these point sources convolved with a beam, usually a gaussian beam, with the same half-power beamwidth of the original synthesized beam. This allows a low-pass filtering of the high frequency components which are usually very noisy.

Since this algorithm is fundamental to understand the algorithm that is proposed in section 6.2.2.1, its basic steps are commented without discussing other optimized versions such as the Clark or the Cotton-Schwab algorithms [NRAO 89]:

i) The position and the strength of the most brilliant (absolute value) peak is found in the dirty image. In some cases it is interesting to search only in a restricted area.

ii) The dirty beam (equivalent to the Point Spread Function in Image Processing and to the Equivalent Array Factor defined before) is subtracted from the dirty image multiplied by the peak strength and a damping factor (called loop gain. Current values for (normally lie in the [0.1, 0.25] range.

iii) The process is repeated until any remaining peak is below an specified threshold.

iv) And the map obtained by the point sources is convolved with a gaussian beam with the same half-power beamwidth as the dirty beam.

From its principles it is clear that in this form, this algorithm would have difficulties when applied directly to the Earth observation case because the Earth appears as an extended thermal source almost filling the FOV and not as a set of point sources.

6.2.1.11.- Conclusions

In this section, several inversion algorithms used in Earth observation interferometric radiometry, radioastronomy, and image processing have been presented. Except for the Singular Value Decomposition, the Van Cittert filtert and the general Krylov method, which reduce to other methods, the seven other algorithms have been programmed and tested to analyze their applicability to large two-dimensional interferometric radiometers.

i) The ESTAR's $\overline{\overline{G}}$ operator has been extended to the 2D case and it has been shown to be impractical because of the required computational load and memory requirements, but also because of the intrinsec difficulty in measuring its elements for large 2D arrays.
ii) The SVD and the Generalized Inverse tend to the $\overline{\overline{G}}$ operator because the rank of $\overline{\overline{G}}$ is rank ($\overline{\overline{G}}$) = $N_V \cdot N_T^2$, and the pseudo-inverse satisfies the Moore-Penrose equation (6.36).
iii) Steepest-descent gradient methods are useful when there is no need to compute the whole pseudoinverse and one is only looking for the solution.
iv) However, when the problem is ill conditioned, as it is, convergence is not significantly slowed down if the step size is fixed. In this case, the previous method reduces to the Van Cittert filter, which tends to the inverse filter and has most of its undesirable properties: noise amplification, convergence problems ...
v) The Wiener filter has also been studied. It has shown that, provided certain reasonable hypotheses about the signal's and noise's covariance matrices and the signal-to-noise ratio is high, about 35 dB, as it is in the MIRAS case, it tends to the Moore-Penrose pseudo-inverse.
vi) Maximum Entropy Methods are used satisfactorily in radioastronomy when observing points sources over constant brightness temperatures. However, to perform well they require a small set of visibilities and a low signal-to-noise ratio (S/N < 5 dB), conditions that are not satisfied in the MIRAS bread-board case, and even less, in the space-borne case.

vii) The CLEAN algorithm has been briefly revised, as well as the Krylov method, the CG and the Preconditionned CG methods. As it will become apparent in the next section, when observing extended sources, the Neumann iteration performed pixel by pixel in the CLEAN algorithm, performs much better when dealing with all the pixels simultaneously. The convergence of the Neumann iteration is so accelerated by using differential pre-conditionned visibilities, that the computation of the a_n and $(_{n,m}$ factors in the Krylov and CG methods is not required.

6.2.2.- Proposed inversion method applied to 2D large synthetic aperture radiometers

This section is devoted to the description of an inversion algorithm suitable to large 2D interferometric radiometers. This method takes into account antenna pattern errors and receiver mismatches appearing inside the fringe-washing function. The convergence of the method is accelerated by using some available "a priori" information, the sky brightness temperature and the Earth-sky border, that allows to work over a set of differential visibilities and by restricting the domain of the solution to the alias-free FOV.

6.2.2.1.- The use of "a priori" information: differential visibilities processing

As it was shown in chapter five most errors can be hardware calibrated by noise injection and/or by the redundant space method, and antenna coupling effects can be minimized by a proper design of the antennas, or can be calibrated with on-ground measurements. Consequently, the inversion process is reduced to solve equation (3.1) for T(>,0). In the general case, this equation has not an analytic solution. Only when all the antenna patterns are all equal and the fringe-wash factor is negligible ($\tilde{r}(t) \cdot 1$) for all the baselines, equation (3.1) reduces to a Fourier Transform and can be easily inverted.

$$V(u,v) \quad \dot{E}_{76} \quad I(>,0)*F_n(>,0)*^2 \qquad \textbf{(6.64)}$$

Where $\dot{E}$ stands for the Fourier Transform. From now on, the hexagonal discrete Fourier Transform $\boldsymbol{F_H}$ (equation 6.19) and the available "a priori" information about the scene will be used to simplify and optimize the inversion process.

In order to not force conditions that could not be met in a real situation, the only "a priori" information that will be used is:
i) the knowledge of the average sky temperature, T_{sky} about 2 or 3 K at 1.4 GHz., provided that neither the sun, the moon, the center of the galaxy or any other radiation source enters in the antenna beam directly or by a reflection over the Earth or the sea surfaces.

ii) the function "earth (ξ,η)" that defines the region occupied by Earth over the sky as seen from the satellite, for a given altitude and tilt angle in the directing cosines reference system (equation (4.13)). It equals unity for (ξ,η) pixels over the Earth and zero otherwise.

With this information, calibrated visibility samples $\mathbf{V^{(1)}}$ can be decomposed in three terms:

$$V^{(1)}(u,v) = \Delta V(u,v) + \mathrm{T}_{SKY}\,\gamma_{SKY}(u,v) + \mathrm{T}_{EARTH}\,\gamma_{Earth}(u,v) \qquad \textbf{(6.65)}$$

where:

$$\gamma_{SKY(k,l)}(u_{kl},v_{kl}) \triangleq \iint\limits_{\xi^2+\eta^2\le 1-earth(\xi,\eta)} F_{n_k}(\xi,\eta)\,F^{*}_{n_l}(\xi,\eta)\,\tilde{r}_{kl}\left(-\frac{u_{kl}\xi+v_{kl}\eta}{f_o}\right)e^{-j2\pi(u_{kl}\xi+v_{kl}\eta)}\,d\xi\,d\eta \qquad \textbf{(6.66)}$$

$$\gamma_{EARTH\,(k,l)}(u_{kl},v_{kl}) \triangleq \iint\limits_{earth(\xi,\eta)} F_{nk}(\xi,\eta)\;F^{*}_{nl}(\xi,\eta)\;\tilde{r}_{kl}\left(-\frac{u_{kl}\xi+v_{kl}\eta}{f_o}\right)e^{-j2\pi(u_{kl}\xi+v_{kl}\eta)}\;d\xi\;d\eta \qquad \textbf{(6.67)}$$

$$T_{EARTH} \triangleq \frac{V^{(1)}(0,0) - \mathrm{T}_{SKY}\iint\limits_{\xi^2+\eta^2\le 1-earth(\xi,\eta)} |F_{n_o}(\xi,\eta)|^2\,d\xi d\eta}{\iint\limits_{earth(\xi,\eta)} |F_{n_o}(\xi,\eta)|^2\,d\xi d\eta} \qquad \textbf{(6.68)}$$

$|F_{no}(\xi,\eta)|^2$ is the radiation pattern of the total power radiometer antenna.

Note that $\gamma_{SKY}(u,v)$ and $\gamma_{EARTH}(u,v)$ are normalized unitless visibilities and, according to (6.65) $\Delta V(0,0) = 0$.

Equation (3.1) has now to be solved for $\Delta V(u,v)$ instead of $V(u,v)$. It should be noted that *since the sky brightness temperature has been removed, the alias free Field Of View has expanded and it is now limited by the periodic repetition of the Earth-sky border and not by the periodic repetition of the unit circle (figure 6.13).*

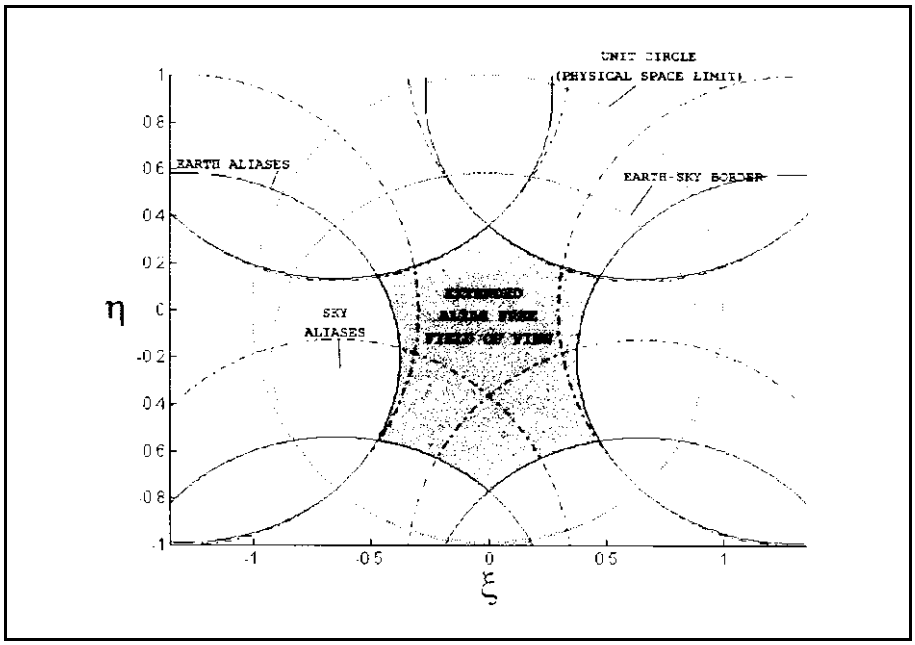

Figure 6.13.- *Extended alias-free FOV by sky brightness temperature substraction.*

6.2.2.2.- Description of the proposed algorithm

The algorithm that is presented proceeds in a similar way as the 'CLEAN' algorithm (section 6.2.1.10) [Thompson et al. 86], [NRAO 89], with the following main differences:

i) The Earth is an extended source that fills almost completely the Field Of View, and it is recovered overlapped with 6 alias of itself (figure 6.13): there are some pixels whose value accounts for the brightness temperature of 2 or even 3 directions of the space. In this situation, the recovery of any aliased value is unfeasible and the reconstruction algorithm should be limited to the alias free FOV. As it has been shown previously, the alias free FOV can be partially extended by subtracting the sky contribution: in this case the AF-FOV is not limited by the periodic repetition of the unit circle, but of the earth-sky border.

ii) The equivalent to the 'CLEAN' dirty map is called the brightness temperature residue ($\mathbf{T}^{res}$), and the 'cleaned' image is the deconvolved brightness temperature ($\mathbf{T}^{dec}$).

iii) In the "CLEAN" algorithm each iteration searches the most brilliant pixel. In the proposed algorithm iterations are performed at each step for *all the pixels* available *in the alias free FOV (AF-FOV) at the same time.* It should be noted that usually *1 guard-pixel* should be left at the border of the AF-FOV, since the equivalent array factor or space variant impulse response (equation 6.63) for pixels lying in the aliased zone extends into the AF-FOV and are truncated and vice versa. When errors are large, mainly due to very

different antenna patterns, the extension of the equivalent array factor is larger and more guard-pixels should be taken.

iv) When the number of visibility samples is low, as it is in the MIRAS bread-board instrument, the number of pixels should be increased in order to assure that the discretization error in equation (6.22) is low. This process is performed by zero padding the fundamental (u,v) hexagonal period. In this way, when the brightness temperature distribution is truncated to the AF-FOV, the high frequency content of the visibility function has been increased, but does not suffer from aliasing of itself. In the case of the MIRAS space-borne instrument, the low-pass shape of visibility function makes discretization errors given by the minimum [N_T x N_T] mesh low compared to the thermal noise (N_T = 130).

The main steps of the algorithm are presented below:

i) Hardware calibration of receiver errors by i.e. correlated/uncorrelated noise injection. Removal of system errors: correlators' offset, phase/gain errors and antenna coupling errors by computing $\mathbf{V}^{(1)}$ out of $\boldsymbol{\mu}^{(5)}$.

ii) Computation of the average Earth modified temperature and the differential visibilities by subtracting the sky and the average brightness temperature of the Earth visibilities (equations (6.65) to (6.68)).

iii) Equation (3.20) can be to discretized and written in the following way:

$$\overline{\Delta T^{raw}} = \overline{\overline{F_H}}^{-1} [\, \overline{\overline{G}} [\, \overline{\Delta T^{dec}} \,]] ./ < | \overline{F_n} |^2 > \triangleq \overline{\overline{H}}\, \overline{\Delta T^{dec}}$$

$$\overline{T^{dec}} = T_{EARTH} + \overline{\Delta T^{dec}} \qquad \textbf{(6.69)}$$

where:

$$\overline{\Delta T^{raw}} = \overline{\overline{F_H}}^{-1} [\, \overline{\overline{W}}\, \overline{\Delta V} \,] ./ < | \overline{F_n} |^2 > \qquad \textbf{(6.70)}$$

$\overline{\overline{F_H}}^{-1}$ stands for the hexagonal inverse Fourier Transform

the "./" operator stands for the division element by element

and:

$\left\langle \left| \overline{F_n} \right|^2 \right\rangle \triangleq \dfrac{1}{N_T} \sum_{k=1}^{N_T} \left| F_{n_k}(\xi_s, \eta_s) \right|^2$ is the **average antenna radiation pattern** of all the antennas.

In fact, the $\overline{\overline{G}}$ operator defined in equations (6.24) and (6.25) applied over a modified temperature $\overline{)T^{dec}}$ returns a set of visibility samples that are weighted with a window $\overline{\overline{W}}$. Of course, these visibilities are affected by fringe-washing effects, antenna pattern errors and antenna position errors. When it is inverted simply by means of a Fourier transform (the hexagonal one if the (u,v) points are placed over a hexagonal grid) and the result is compensated by the average antenna radiation pattern of all the antennas, a good estimate of the modified temperature is obtained. This estimate is the first term of a series in which the solution of (6.69), $\overline{)T^{dec}}$, is expanded (equations (6.74) and (6.76))

It is advantageous to work over the modified temperatures instead of the visibilities because the aliasing can be easily removed in the (>,0) domain, restricting the inversion process only to the alias-free FOV.

Note that the operator:

$$\overline{\overline{F_H}}^{\&1} \left\{ \quad \right\} ./ <*\overline{F_n}*^2> \qquad \textbf{(6.71)}$$

acts as a preconditioner of the $\overline{\overline{G}}$, as in some CG algorithms. In fact, in the ideal case, when all the antenna patterns are the same and fringe-washing effects are negligible:

$$\overline{\overline{G}}^{\&1} ' \overline{\overline{F_H}}^{\&1} \left\{ \quad \right\} ./ <*\overline{F_n}*^2> \qquad \textbf{(6.72)}$$

and $\overline{\overline{H}} ' \overline{\overline{I}}$.

Each row of the $\overline{\overline{H}}$ operator in (6.69) can be understood as the array factor or impulse response to a point source located at (>',0')= ($>_s$,0_s).

The inversion method follows as explained below:

iv) Start the iteration for k=1,2,3...

$$\overline{)T^{res}}^{(k\%1)} ' (\overline{\overline{I}} \& \overline{\overline{H}}) \overline{)T^{res}}^{(k)} ' (\overline{\overline{I}} \& \overline{\overline{H}})^{(k\%1)} \overline{)T^{raw}} 6 \overline{0} \qquad \textbf{(6.73)}$$

$$\overline{)T^{dec}}^{(k\%1)} ' \overline{)T^{dec}}^{(k)} \% \overline{)T^{res}}^{(k)} ' \mathop{\mathrm{j}}_{n}^{k}{}_{0} (\overline{\overline{I}} \& \overline{\overline{H}})^n \overline{)T^{raw}} 6 \overline{\overline{H}}^{\&1} \overline{)T^{raw}} \qquad \textbf{(6.74)}$$

with the initial values:

$$\overline{)T^{res}}^{(1)} ' (\overline{\overline{I}} \& \overline{\overline{H}}) \overline{)T^{raw}} \qquad \textbf{(6.75)}$$

and:

$$\overline{)T^{dec}}^{(1)} ' \overline{)T^{raw}} ' \overline{\overline{F_H}}^{\&1} [\overline{W} \overline{)V}] ./ <*\overline{F_n}*^2> \qquad \textbf{(6.76)}$$

both limited to the alias-free FOV.

v) Repeat step (iv) until the squared Euclidean norm of the residue decreases below a determined threshold:

$$\| <*\overline{F_n}*^2> \overline{T^{res}}^{(k)} \|_2^2 \# T^2 ' T_{noise}^2 \% T_{Gibbs}^2 \qquad \textbf{(6.77)}$$

The first term in the right hand side of equation (6.77) corresponds to the thermal noise and can be computed with the formulas derived in [Thompson et al. 86], [NRAO 89], [LeVine et al. 90], [LeVine 90], [Camps et al. 95B] or [Bará et al. 96A]. The second one corresponds to the oscillations or ringing due to the finite (u,v) coverage which are known as the Gibbs phenomenon and depends basically on T_{Earth} (equation 6.68), the average brightness temperature of the Earth and the window used to taper the visibility samples. It can be computed with the formulas derived in [Camps et al. 95] or in chapter 3.

The main advantage of this approach to the inversion problem is that it avoids large matrix products, which require a high computational capability, nor need to store huge matrices. In fact, the $\overline{\overline{H}}$ operator is easily computed by:

i) calculating the intermediate visibilities multiplying, row by row, the $\overline{\overline{G}}$ operator by the modified temperature distribution,

ii) taking the 2D inverse Fourier Transform over the hexagonal grids defined in (6.18a,b)

iii) and dividing the result by the average antenna radiation pattern.

The $\overline{\overline{G}}$ operator uses the information about the antenna voltage patterns, antenna positions and receivers' frequency responses through equation (6.25). The maximum vector size to be processed at any time is $[N_T^2 \text{ x } 1] = [16.900 \text{ x } 1]$ long and the size of the 2D-FFT is [130 x 130], which can be performed in a PC.

This algorithm is, in fact a simple Neumann iteration, a particular case of the general Krylov method (6.2.1.6) with $\overline{I}_0 ' \overline{0}$, $a_n = 1$ and $(_{n,m} = 0$. The residue in the Krylov formulas (6.58) is computed from the visibility samples, while in the proposed algorithm it is computed equivalently from the modified brightness temperature pixels.

6.2.2.3.- Convergence of the inversion process

The recovered modified temperature distribution is the 2D convolution of the actual brightness temperature with the space variant interferometer impulse response or equivalent array factor (equation 6.63). Using the recursions shown in equations (6.73) to (6.77) the values of the residue and deconvolved temperature at the k^{th} iteration can be expressed as:

$$\overline{\Delta T}^{\,res\,(k)} = (\overline{\overline{I}} - \overline{\overline{H}})^{k} \cdot \overline{\Delta T}^{\,raw} \qquad \textbf{(6.78)}$$

$$\overline{\Delta T}^{\,dec\,(k)} = \sum_{n=0}^{k-1} (\overline{\overline{I}} - \overline{\overline{H}})^{n} \cdot \overline{\Delta T}^{\,raw} \qquad \textbf{(6.79)}$$

The matrix series of equation (6.79), if it converges, tends to:

$$\sum_{n=0}^{k-1} (\overline{\overline{I}} - \overline{\overline{H}})^{n} \rightarrow \overline{\overline{H}}^{-1} \qquad \textbf{(6.80)}$$

provided that:

$$|\lambda' - 1|_{\max} < 1 \qquad \textbf{(6.81)}$$

where λ' are the eigenvalues of $\overline{H}$.

In practice, the residue given by equation (6.78) shows the rms error committed. The eigenvalues of $\overline{H}$ do not need to be computed since, when the process is not convergent, the norm of the residue vector grows at each step. In this case, the procedure can be initialized with a damping factor $\gamma<1$, as it is done in the CLEAN algorithm:

$$\overline{\Delta T}^{\,res\,(k)} = (\overline{\overline{I}} - \gamma\,\overline{\overline{H}})^{k} \cdot \overline{\Delta T}^{\,raw} \qquad \textbf{(6.82)}$$

$$\overline{\Delta T}^{\,dec\,(k)} = \gamma \sum_{n=0}^{k-1} (\overline{\overline{I}} - \gamma\,\overline{\overline{H}})^{n} \cdot \overline{\Delta T}^{\,res\,(0)} \qquad \textbf{(6.83)}$$

This resort is only necessary when very large antenna errors are present, a situation not found in simulations with real antenna patterns.

In the ideal case, when the $\overline{G}$ operator tends to the 2D Fourier operator $\overline{F}$, the $\overline{H}$ operator tends to the identity operator $\overline{I}$, all the eigenvalues of $\overline{H}$ are $\lambda'=1$, the inversion process stops at the first step and reduces to an inverse Fourier Transform followed by antenna pattern compensation. In a non-ideal case two factors accelerate noticeably the convergence process: i) the processing of differential visibilities and ii) the precompensation by the average antenna radiation pattern, which approaches the **G** operator to **F**, the discrete Fourier Operator. Depending on the magnitude of the errors and the number of antennas (affects ΔT for the same S/N), convergence is usually achieved in up to 2-6 iterations for a Y-interferometer of 10-43 antennas per arm with tolerances in the present MIRAS instrument design [MMS 95] and the available SNR=35dB (τ = 0.3 s).

6.2.2.4.- Inversion robustness in front of errors

The image processed in this example is the same of the previous examples (figure 6.7a). In order to have reasonable processing times we have worked with a Y-interferometer with 10 antennas per arm.

System parameters can be adjusted to check system's response in terms of radiometric accuracy and robustness of the inversion algorithm. The parameters that can be adjusted are the following. See [MMS 95] for a detailed description of each one:

- Array parameters:
  - . Number of antennas per arm.
  - . Spacing between antennas in the arm.
  - . Tilt angle of the Y-array with respect to nadir.
  - . In-plane arm deviation amplitude (sinusoidal oscillation)
  - . Out-of-plane arm deviation amplitude (" ")
  - . In-plane arm first resonant frequency.
  - . Off-plane arm first resonant frequency.
  - . Phase of each arm deviation.

- Antenna parameters:
  - . Polarization (V/H) (to compute antenna coupling
    [King 57] [Baker 62], [Richmond and Geary 70].
  - . Selection of wire-dipoles/cup-dipoles for antenna coupling [Appendix 3]

  If wire-dipoles are selected:
  - . Dipole length.
  - . Dipole radius.

  Antenna pattern (equations (6.34) and (6.35)):
  - . Directivity parameter.
  - . θ_o pointing error standard deviation, ϕ uniform in $[0,2\pi]$.
  - . Amplitude error standard deviation.
  - . Phase error standard deviation.

- Receiver parameters:
  - . Total Power Radiometer sensitivity.
  - . Nominal receiver noise temperature & st.dev.
  - . Coaxial characteristic impedance (Z_{L0}).
  - . Antenna matching: antenna charge impedances can be selected between Z_{LO} and the complex conjugate input impedance when the antenna is isolated in free space.
  - . Local oscillator frequency.
  - . Band-pass filters' central frequency & st.dev for spurious and image filters
  - . Spurious filter nominal bandwidth & st. dev.
  - . Image filter nominal bandwidth & st. dev.
  - . Low-pass filter nominal bandwidth & st. dev.
  - . DC-block cut-off frequency & st. dev.
  - . Spurious filter in-band ripple & st. dev.
  - . Image filter in-band ripple & st. dev.
  - . Low-pass filter in-band ripple & st. dev.
  - . Spurious filter low-pass prototype order.
  - . Image filter low-pass prototype order.
  - . Low-pass filter order.

  - . St. deviation of channels time delay.
  - . St. deviation of local oscillator phase at each I/Q demod.
  - . St. deviation of I/Q phase unbalance at each I/Q demod.
  - . St. deviation of correlators' offset.

  - . Correlators' integration time.
  - . Correlator type: 1 bit/Nyquist rate
    1 bit/2 times Nyquist rate
    analog

- Platform parameters:
  - . Earth radius.
  - . Platform altitude.

- Field of View:
  - . Swath.
  - . Minimum incidence angle over the Earth.
  - . Maximum incidence angle over the Earth.

- Processing parameters:
  - . Resolution mode:
    - enhanced (use all the available (u,v) samples)
    - standard (use (u,v) samples in the inner hexagon to the (u,v) coverage: reduced, but complete hexagonal period)
  - . Visibility window (Rectangular, Bartlett, Hamming, Hanning and Blackmann windows with rotational symmetry).
  - . Damping factor (γ).

A series of simulations have been performed for each one of the following error sources. In each series, the error has been increased until the algorithm fails to work. These effects are: i) fringe-wash effects (identical receivers but increasing system bandwidth), ii) fringe-wash and receiver phase errors due to bandwidth, central frequency, time delay and in-phase errors, iii) fringe-wash and receiver quadrature phase errors, iv) antenna-pattern shape, v) antenna pattern mismatches due to pointing errors, vi) antenna pattern mismatches due to amplitude errors, vii) antenna pattern mismatches due to phase errors, viii) in-plane arms oscillations, ix) off-plane arms oscillations, x) finally all errors have been included simultaneously with their maximum allowed values. *From this study it can be concluded that antenna voltage pattern errors, specially phase errors, are critical when receiver phase errors have been calibrated and antenna coupling is negligible or it has been calibrated.*

Table 6.2 summarizes the main results of these simulations. RMS errors have been computed inside a nominal constant brightness temperature square over the sea constant brightness temperature, at the up-right side. The average rms error for the whole map is lower after the inversion process (figure 6.17b with respect 6.17a) even though it is higher inside the constant domain where the standard deviations have been computed (table 6.2).

The ***ideal image*** is obtained by taking the Inverse Fourier Transform of the visibility samples computed for a perfect system. The ***raw image*** is obtained by taking the Inverse Fourier Transform of the visibility samples computed for an interferometer with the antenna pattern imperfections and fringe-wash effects. Finally, the ***deconvolved image*** is the result of the inversion process previously described. The error images are defined as the difference between the ideal image and the raw/deconvolved images.

Figure 6.14a shows the original image from which visibilities will be computed. Figure 6.14b shows the ideal image restricted to the extended alias free FOV (sky information has been removed). Figures 6.14c and 6.14d represent the raw and the deconvolved images for an exaggerated large antenna voltage pattern phase error ($\sigma_{\Delta\phi}$=15º).

This is not a realistic situation but it demonstrates how errors can be incorporated into the inversion algorithm and how image quality can be improved. Even in this case, the coast contour can be recognized because of the high contrast with the Earth's brightness temperature (100 K - 220 K).

The effect of the proposed inversion method is more apparent when comparing the two error images (figures 6.15a and 6.15b). Note that, since the interferometer's size has been reduced by a factor 4.3 with respect to the example in figure 6.7, the synthesized beam broadens by the same factor and the spatial resolution is poorer. *In the raw temperature error image high error bands are present, while in the deconvolved temperature error image errors are distributed more uniformly* over the entire image except at the border. However, antenna pattern phase errors are so large that the algorithm is not able to compensate them perfectly.

The error in the deconvolved image is concentrated in the border due to:
i) the truncation of the impulse responses of the pixels lying inside the alias free FOV and ii) the truncation of the "tails" of the impulse responses of the pixels lying outside the alias free zone that enter in the alias free FOV.

Error source	Min. value	Max. value	$\sigma_{typ}(T_{id}-T_{raw})$ [K] T_{id} = 100K	$\sigma_{typ}(T_{id}-T_{dec})$ [K] T_{id} = 100K
Fringe-wash	B = 20 MHz f_o= 1410 MHz	B = 86 MHz f_o= 1410 MHz	1.02	3.37
Fringe-wash & phase errors	$\sigma_{\Delta f}$ = 0.5 MHz σ_B = 1 MHz $\sigma_{\tau g}$ = 10 ps $\sigma_{\tau ph}$= 10 ps	$\sigma_{\Delta f}$ = 0.5 MHz σ_B = 1 MHz $\sigma_{\tau g}$ = 0.6 ns $\sigma_{\tau ph}$= 50 ps	1.43	3.27
Fringe-wash & I/Q errors	$\sigma_{I/Q}$ = 0.1º	$\sigma_{I/Q}$ = 1º	1.19	3.71
Antenna pattern shape	isotropic antennas	$\lvert F_n(\theta)\rvert^2=\cos^3(\theta)$	-	-
Antenna pointing	σ_θ = 1º	σ_θ =2º	1.55	3.14
Antenna amplitude	σ_{Aa} = 0.05	σ_{Aa} = 0.4	0.95	3.10
Antenna phase	σ_{Aph} = 0.5º	σ_{Aph} = 15º	5.62	7.60
In-plane arm oscillation	A_{ip} = 5mm	-	1.20	3.75
Out-of-plane arm oscillation	A_{op} = 5mm	-	1.40	3.82

Table 6.2.- *Error source range and typical errors (discretization and fringe-wash errors are included in σ's)*

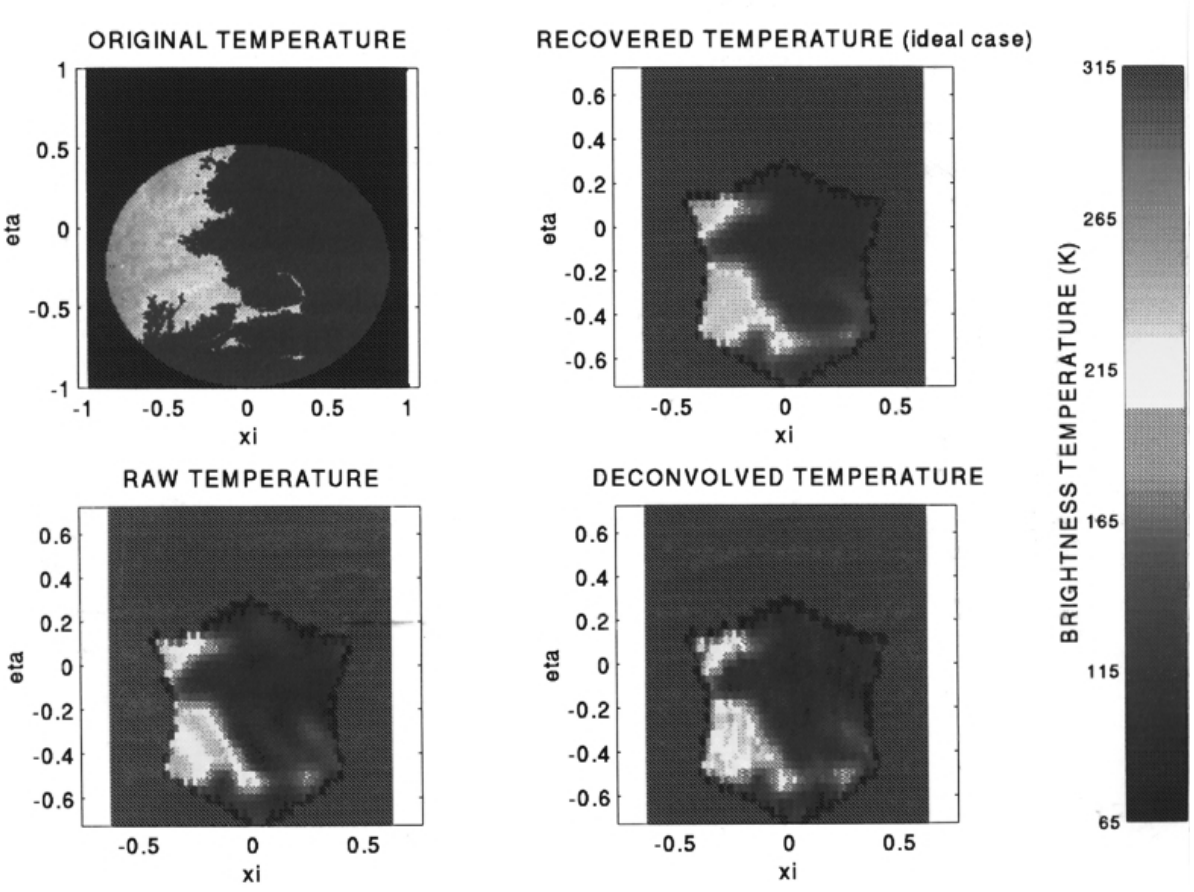

Figure 6.14.- *a) Original brightness temperature distribution b) Extended alias free FOV (pixels available N_{EL} = 10) c) Raw Temperature distribution d) Deconvolved Temperature distribution*

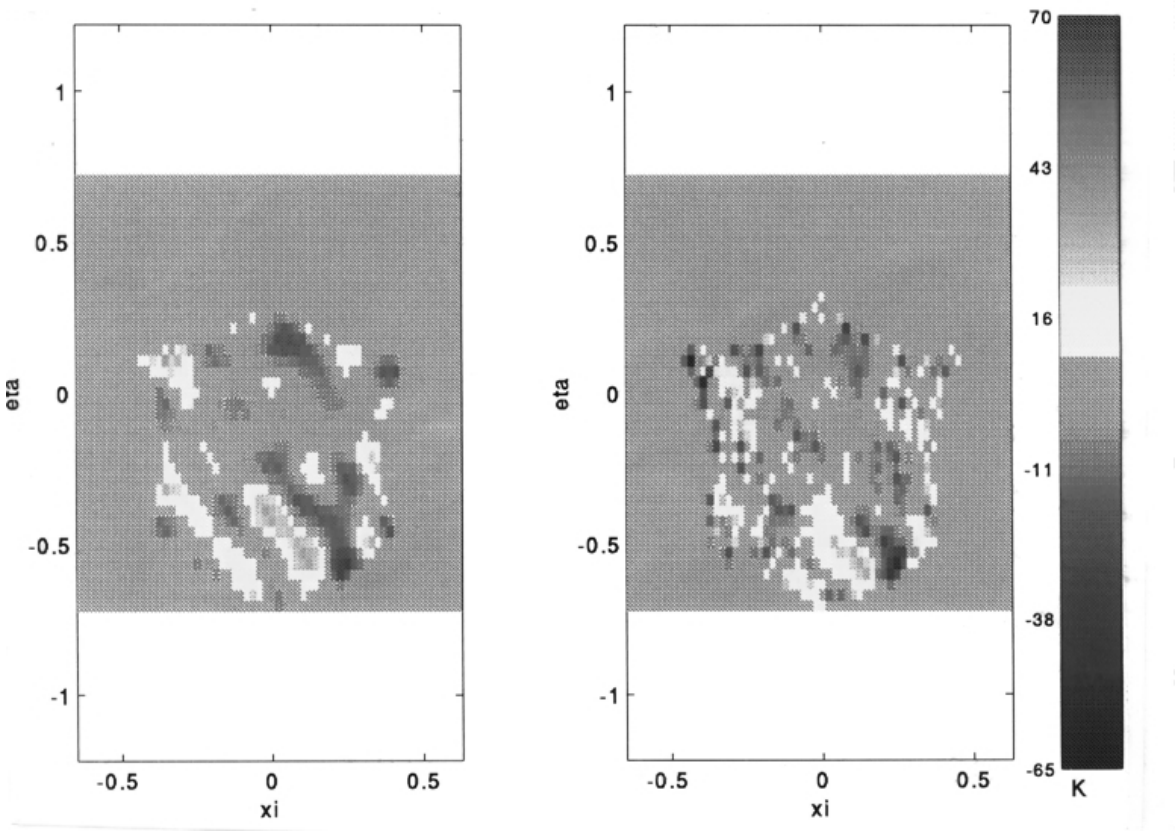

Figure 6.15.- *a) Raw error image* *b) Deconvolved error image*

6.2.2.5.- Snap-shot simulation of a large 2D synthetic aperture interferometric radiometer

These simulations are intended to show how different error sources or remainder calibration errors -see figure 5.5- affect the radiometric accuracy for a 2D large Y-shaped interferometric radiometer with 43 antennas per arm. Figure 6.16a shows the original modified brightness temperature distribution, figure 6.16b its truncation to the extended alias free FOV, figure 6.16c the ideal image and figure 6.16d shows deconvolved image: the final result of the deconvolution algorithm (note that the images are in a different order than in 6.14). Figure 6.16e is the raw image, obtained by direct Inverse Fourier Transform of the $\mathbf{V}^{(1)}$ visibilities (antenna pattern and position errors and fringe-washing effects). In this case only two iterations have been required to reduce the 6.5 K rms error present in figure 6.16e down to 2.5 K (figure 6.16d), below ΔT=4K, the noise threshold for 43 antennas per arm (equation 6.77), Blackmann windowing and T_{Earth}= 145 K. It is difficult to notice visually the differences between both images because of the small rms error compared to the scale (6.5K over 320K). However, it can be appreciated an improvement on the definition of the island (low-right side) and in the constant brightness temperature of the sea (most of the yellow dots in figure 6.16e disappear in figure 6.16d.

Figure 6.16f shows the result of direct inverse Fourier Transformation of $\mathbf{V}^{(2)}$ visibilities (same as $\mathbf{V}^{(1)}$ with antenna coupling errors) and average antenna pattern compensation, antenna coupling not been calibrated. Figure 6.16g shows the result of the direct inverse Fourier Transform of $\mathbf{V}^{(3)}$ (same as $\mathbf{V}^{(2)}$ with receiver phase errors) and average antenna pattern compensation. Finally, figure 6.16h shows the results of $(\overline{T_A}\%\overline{T_R})\mu^{(5)}$ direct inverse Fourier Transform and average antenna pattern compensation (all system errors are included: amplitude and offset errors too).

From this simulations it can be concluded that *channel phase errors are the most important and must be properly hardware calibrated. Time delay mismatches need to be minimized by design, since they appear inside the fringe-wash function.*

Figures 6.16i and 6.16j show similar results obtained by direct Inverse Fourier Transform and average antenna pattern compensation of the $\mathbf{V}^{(1)}$ and $\mathbf{V}^{(2)}$ visibilities. In this case *antenna coupling has been computed with half-wavelength wire dipoles* [King 57] [Baker 62] [Richmond and Geary 70]), *vertical polarization. In this case the modified brightness temperature distribution has been completely blurred.* The high impact of antenna coupling over the visibilities, amplifying high frequency components at a expense of low frequency components, is clear and makes other error sources negligible (figure 6.16h).

These simulations have required the following computational load: 76.1 Gflops to compute system's model and the 8.450 2D numerical integrations for the visibility samples and 52.4 Gflops in the 2 iterations required to reduce the residue below the threshold. However, this algorithm can been run, and in a 486 personal computer with 16 Mbytes of RAM. If required, the inversion time can be reduced in parallel machines by a factor up to 8.450 by computing simultaneously as many visibitities as processors.

6.2.2.6.- Conclusions

A new deconvolution algorithm suitable for 2D large arrays, as MIRAS space borne instrument, has been proposed in this section. It is based on a Neumann iteration on the differential visibilities obtained by substracting from the calibrated visibilities, the contributions coming from the sky and an average modified temperature from the Earth. Iterations are performed in the (>,0) reciprocal grids of the hexagonal (u,v) grid using the Hexagonal Fourier techniques described in the former section. The main advantages of the proposed algorithm are:

i) capability to deal with *instrument imperfections.* Updated parameters can be directly used as inputs in the algorithm to invert a new set of measured visibilities,

ii) *computational speed and low memory requirements* by using FFTs and row-column matrix operations. No large matrices must be stored, nor processed, allowing *MIRAS space borne instrument simulations to be run on a PC, and*

iii) the *algorithm is well adapted to parallel machines*. The speed up factor can be as high as 8.450 for the MIRAS space borne instrument, opening the doors to real time processing.

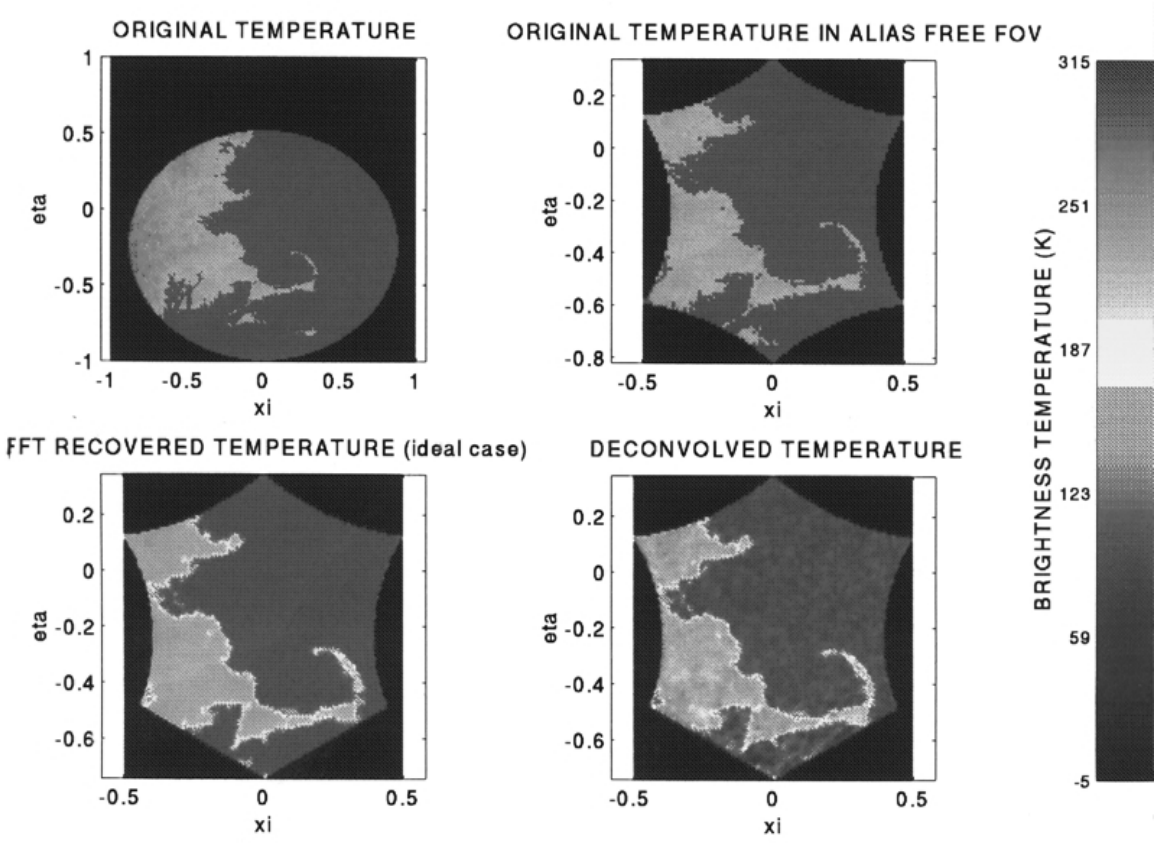

Figure 6.16.- *a) Original brightness temperature distribution* *b) Truncation of 6.16a to the extended alias-free FOV* *c) Ideal temperature* *d) Deconvolved temperature*

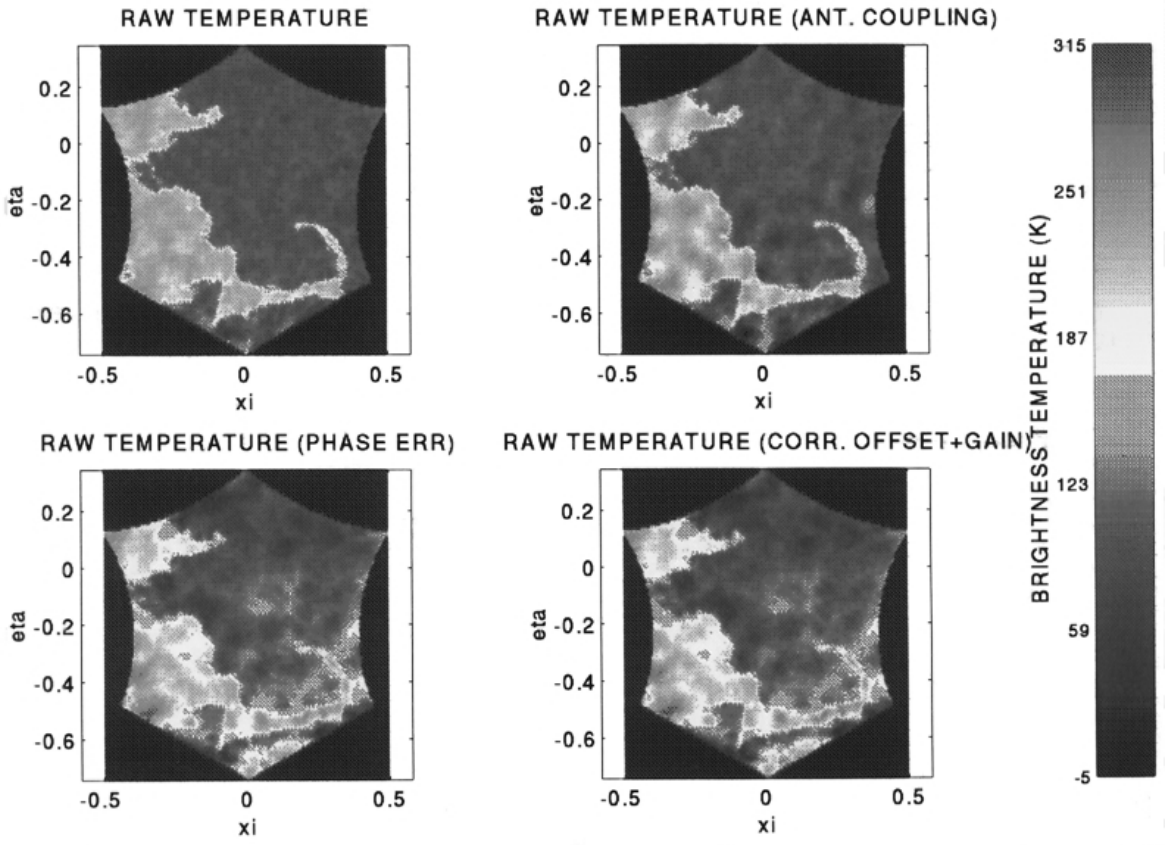

Figure 6.16.- *ANTENNA COUPLING MODELLED WITH MEASURED X-BAND CUP-DIPOLES*

e) Raw temperature ($V^{(1)}$)

f) Brightness temperature distribution with antenna coupling errors ($V^{(2)}$)

g) Brightness temperature distribution with phase errors ($V^{(3)}$)

h) Brightness temperature distribution with all errors ($(T_A+T_R)\mu^{(5)}$)

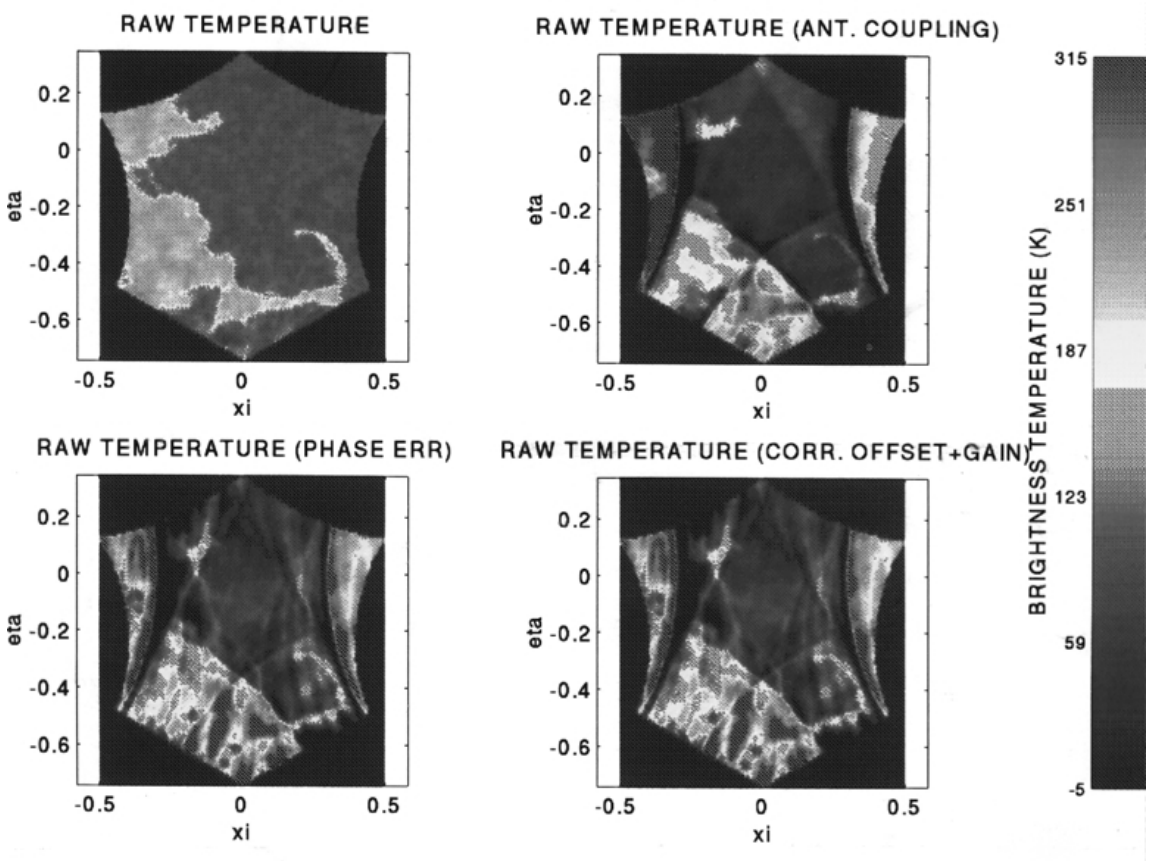

Figure 6.16.- *ANTENNA COUPLING MODELLED WITH VERTICAL HALF-WAVELENGTH WIRE DIPOLES*
i) Raw brightness temperature distribution ($V^{(1)}$) *j) Brightness temperature distribution with antenna coupling errors ($V^{(2)}$)*
k) Brightness temperature distribution with phase errors ($V^{(3)}$) *l) Brightness temperature distribution with all errors ($(T_A+T_R)\mu^{(5)}$)*

6.3.- CONCLUSIONS

In this chapter some configurations for an interferometer array have been studied. Y-shaped and triangular-shaped arrays sample the visibility function over a hexagonal (u,v) grid saving a 13.4% of the required visibility samples and the associated hardware for a determined aliasing level or available swath. In addition, Y-shaped arrays provide larger (u,v) coverage than triangular-shaped arrays, thus improving the spatial resolution capabilities of the instrument.

A new technique based on the use of rectangular FFT to process hexagonally sampled signals has been proposed. It requires that the (>,0) pixels are properly chosen over the reciprocal grid of the (u,v) hexagonal grid. This procedure avoids interpolations and induced artifacts, and preserves signal-to-noise. This technique is general, it is not restricted to hexagonal grids and can be used with other sampling strategies, provided that the reciprocal basis is used.

Several inversion algorithms used in 1D-interferometric radiometry devoted to Earth observation, radioastronomy, and image processing have been revised: the ESTAR's $\overline{\overline{G}}$ operator extended to the 2D MIRAS' case, the SVD and the Generalized Inverse, the steepest-descent gradient method, the Van Cittert and the Wiener filters, and two non-linear methods used in radioastronomy: the Maximum Entropy and the CLEAN algorithms. The Krylov method, the CG and the Preconditioned CG methods have also been briefly presented to show the relationships of the proposed method with other methods found in the literature.

Finally, a deconvolution algorithm suitable for large 2D arrays has been presented. It is based on a Neumann iteration on the differential visibilities obtained by subtracting from the calibrated visibilities the contributions coming from the sky and an average modified temperature from the Earth. Iterations are performed in the (u,v) < > (>,0) reciprocal grids using the proposed Hexagonal Fourier techniques. Its main advantages are: the capability to deal with instrument imperfections, *computational speed and low memory requirements* by using FFTs and row-column matrix operations.

Chapter 7. Implementation of a Y-shaped Space Borne Interferometric Radiometer Simulator

The need of the implementation of a 2D space borne interferometric radiometer simulator appears when system's global performance is to be studied, specially the radiometric accuracy and sensitivity improvement by means of pixel averaging. As explained in chapter four, an analytical study of pixel averaging is only possible with some simplifying considerations: very simple modified brightness temperature distributions and inversion of the set of visibility samples by means of a Fourier transform. It is, for a real system, with residual calibration errors, antenna pattern errors and time varying scenes, the improvement that can be achieved by pixel averaging can only be quantified numerically with the aid of an interferometer simulator.

To represent a real system, the simulator must be able:

i) to propagate platform's orbit to get accurately the rate of variation of the scenes being imaged,

ii) to generate realistic scenes. It is brightness temperature distributions generated from geo-physical parameters, i.e. physical temperature, snow and vegetation cover, soil moisture and sea salinity...

iii) to model the system: antenna radiation patterns and mutual coupling, receivers' frequency response and correlators' response.

iv) to apply a calibration algorithm, as the one presented in chapter five, and a suitable inversion algorithm, as the one presented in chapter six.

v) to represent the results graphically to be easily interpreted.

vi) and, at the end of a sequence of consecutive snap-shot images, to perform an error analysis to assess the pixel averaging improvement.

This chapter is composed of four sections. In the first one the procedure used to compute platform's orbit is briefly discussed. The second one is devoted to the L-band synthetic brightness temperature scene generator, including simple sea and soil models. The third one deals with the system's modelling and the graphical representation of the results. And finally, the fourth one presents some examples of the simulator and the results on radiometric accuracy improvement by means of pixel averaging for a sequence of 25 snap-shots of the Mediterranean coast of Spain.

7.1.- ORBITAL PROPAGATOR

To formulate the mathematics of a satellite navigation problem it is necessary to choose a reference coordinate system, usually a Cartesian one. For the purpose of computing the position of the satellite and the pixels being imaged at each snap-shot it is convenient to use a coordinate system that rotates with the Earth, known as an Earth-centered Earth-fixed (ECEF) system. The ECEF system that will be used is the same as the GPS one. It has the XY plane coincident with the Earth's equatorial plane, the +X-axis points in the direction of 0º longitude, the +Y-axis points in the direction of +90º East longitude and the +Z-axis is chose to be normal to the equatorial plane in the direction of the geographical north pole.

If the Earth were a perfect sphere of uniform density, Earth's gravity would behave as if the Earth were a point mass. Then the gravitational force $\overline{F}$ acting on the object would be given by:

$$\overline{F} = m\,\overline{a} = m\,\frac{d^2\overline{r}}{dt^2} = -G\,\frac{m\,M}{r^3}\,\overline{r} \qquad \textbf{(7.1)}$$

where M is the mass of the Earth, $\overline{a}$ is the acceleration of the object in an inertial system (note that the ECEF system previously defined is not an inertial system), and the distance from the center of the Earth to the object is $r = |\boldsymbol{r}|$. Equation (7.1) can be rewritten as:

$$\frac{d^2\overline{r}}{dt^2} = -\frac{\mu}{r^3}\,\overline{r}\;; \quad \mu \equiv GM \qquad \textbf{(7.2)}$$

which is the expression of the Keplerian satellite motion.

Since the Earth is not spherical and has an uneven distribution of mass, the true acceleration due to Earth's gravity can be modelled by a potential function [Kaplan 95]:

$$U = \frac{\mu}{r}\left\{1 - \sum_{l=2}^{4}\sum_{m=0}^{l}\left(\frac{a}{r}\right)^{l}\left[C_{lm}\cos(m\lambda) + S_{lm}\sin(m\lambda)\right]P_{lm}(\cos\phi)\right\}$$

$$\overline{a} = \frac{d^2\overline{r}}{dt^2} = \nabla U \qquad \textbf{(7.3)}$$

where r is the distance of the point from the origin, $\phi = 90º$ - latitude is the angle measured from the +Z-axis, λ is the right ascension of the point, a is the mean equatorial radius of the Earth (6,378,137 m in WGS-84), P_{lm} is the associated Legendre function and C_{lm} and S_{lm} are the spherical harmonic cosine and sine coefficients of degree l and order m. Note that equation (7.2) is recovered from (7.3) if all the harmonic cosine and sine coefficients are set to zero.

Although many applications require the accuracy provided by the fully perturbed equations of motion, orbital parameters are often defined in terms of the six elements of the Keplerian satellite motion. These Keplerian elements depend on the initial conditions $\mathbf{r}_0$, $\mathbf{v}_0$ and $\mathbf{t}_0$ for which the solution of (7.2) is the section of a conic by a plane. Figure 7.1 shows the first three Keplerian orbital elements that define the shape of the orbit: **a** the semimajor axis of the ellipse, **e** the eccentricity of the ellipse and **J** the time of perigee passage (hyperbolic and parabolic trajectories are not be considered for Earth observation satellites).

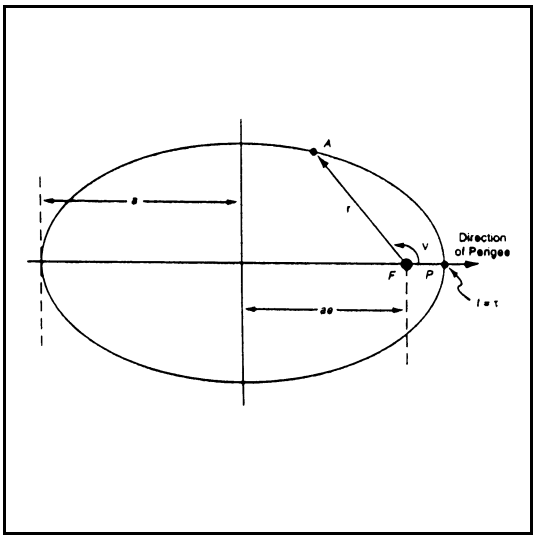

Figure 7.1.- *The three Keplerian orbital elements defining the shape of the orbit [Kaplan 95]*

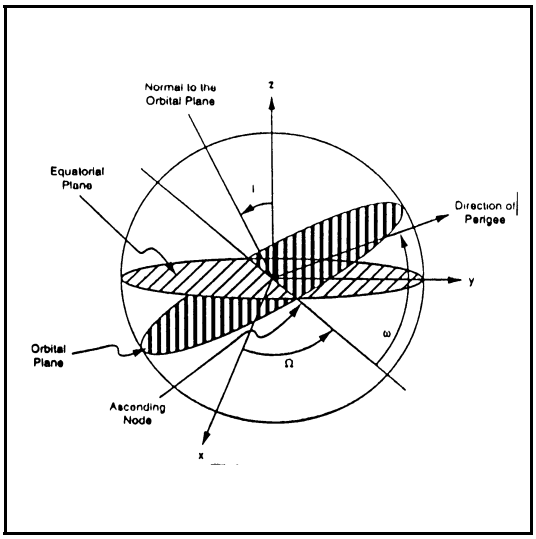

Figure 7.2.- *The three Keplerian orbital elements defining the orientation of the orbit [Kaplan 95]*

Figure 7.2 shows the second three Keplerian orbital elements that define the orientation of the orbit: **i** the inclination of the orbit, **S** the longitude of the ascending node, which is the point in the satellite's orbit where it crosses the equatorial plane with +z component of velocity, and **T** the argument of the perigee, that measures the angle from the ascending node to the direction of the perigee. It should be noted that for a fully perturbed motion the six Keplerian orbital elements are not constant and must be periodically updated.

The impact of other forces acting over the satellites are reviewed in appendix 7, and their impact has been studied with the aid of the "Orbital Workbench v1.1" program [Cygnus 90] by enabling or disabling different forces to act. The orbit parameters of the MIRAS' reference orbit are [MMS 95]:

- Semi-major axis (a): 7159,5 Km
- Inclination (i): 98,549387º
- Eccentricity (e): 0,001165
- Argument of perigee (T): 90º

- Local time descending node (S): 10:00 h
- Nodal crossing time (descending): 10:00 h

and: - Mean altitude: 799,8 Km

Disturbances due to the Moon, the Sun and the solar radiation pressure are found to be approximately of the same order of magnitude, but they are negligible in front of geo-potential harmonics (equation (7.3)). On the other hand, it should be noted that the atmospheric drag is the dominant perturbation factor below 300 Km height and it is important up to 1,000 Km height (planned MIRAS' platform height is 800 Km), but it has not been modelled because of the lack of the knowledge of the platform.

Platform's trajectory is computed by integrating equation (7.3) and taking into account that at each step the platform's longitude has to be decreased according to the Earth rotation rate $\theta(t) = \theta_0 - \dot{\theta}(t - t_0)$, where $\dot{\theta} = 7{,}2921151467\ 10^{-5}$ rad/s [Kaplan 95].

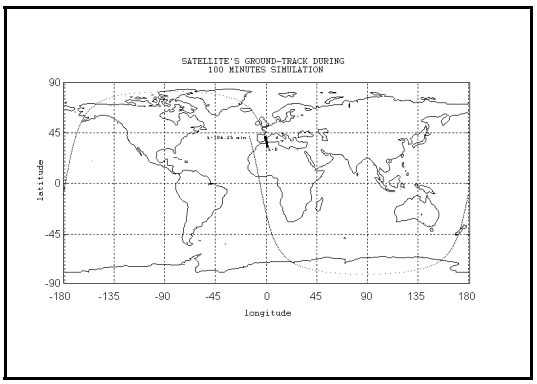

Figure 7.3.- *Ground track for a complete MIRAS orbital period. Thick line: ground track of simulation performed in section 7.4*

Figure 7.3 shows the ground track computed with our orbital propagator for a complete orbit period, about 100 minutes. The darker line represents the 100 seconds simulated in section 7.4

7.2.- L-BAND BRIGHTNESS TEMPERATURE SCENE GENERATOR

The L-band brightness temperature scene generator is the module charged of the computation of a "realistic" brightness temperature distribution for simulation purposes. The brightness temperature distribution map is computed from the satellite position given by the orbital propagator over a thin mesh to guarantee that the errors committed in the numerical two-dimensional integration of the visibility samples are negligible. It requires the distance between the sampling (>,0) points to be much smaller than the synthesized half-power beam-width in the (>,0) coordinates, a kind of Nyquist sampling criterion.

Vertical and horizontal brightness temperatures are computed from the following physical parameters: soil and snow albedos, snow depth, soil roughness, vegetation

albedos, soil moisture, soil surface temperature, ocean salinity, zonal and meridional winds over the oceans, vegetation height, ocean surface temperature and ocean ice cover. These parameters have been extracted from the CD set: "Global Data Sets for Land-Atmosphere Models ISLSCP Initiative 1: 1987-1988 Volumes 1-5" of the NASA Goddard Space Flight Center [NASA 95 A] [NASA 95 B] and the book series "Microwave Remote Sensing: Active and Passive" volumes II and III [Ulaby et al 82][Ulaby et al 86]. The data contained in this CD set has been acquired from a variety of sources, including model outputs, satellite and ground measurements and are mapped in a common spatial resolution: a 1º x 1º grid, with a monthly temporal resolution. However, some parameters have a 6 hour temporal resolution. The data corresponding to December 1988 has been selected, that is why most mountain ranges appear covered by snow, showing a contrast in the brightness temperature.

The 1º x 1º grid corresponds to a pixel's size of 110 Km x 110 Km over the equator, which is larger than the spot over the Earth's surface of the synthesized beam-width of an Y-array with 43 antennas per arm spaced 0.898 as MIRAS (chapter 3). To solve this problem the resulting brightness temperature pixels have been linearly interpolated to a thinner grid. To preserve the high frequency content, the coast line has been computed with high spatial resolution, up to 1/12º x 1/12º = 9.26 Km x 9.26 Km, from the NOAA ETOPO5 5 minutes resolution global digital elevation model.

The sequence used to compute the brightness temperature for each pixel is the following:

i) A (>,0) mesh is created over the interval [-1,1] x [-1 1].
ii) For each (>,0) pixel pointing to the Earth (equation (4.13)), its latitude and altitude are computed for a given orbital position according to the formulas given in the appendix 8.
iii) The angle with respect to the Earth's surface normal is computed according to (figure 4):

$$2_{inc} \text{ ' } \arccos\left(\frac{\overline{PS}.\overline{EP}}{*\overline{PS}*.*\overline{EP}*} \right) \qquad \textbf{(7.4)}$$

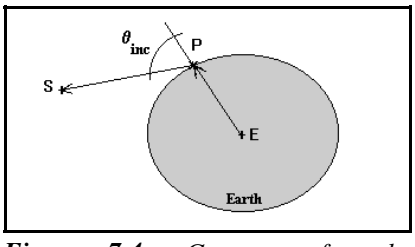

Figure 7.4.- *Geometry for the incidence angle computation.*

iv) If the pixel's coordinates (latitude, longitude)=(2,8) correspond to soil, then two models may apply [Ulaby et al 86, chapter eleven]:

iv.1) If soil is covered by snow, then the brightness temperature is computed from:

$$T_{B,pack}(q,p)=\frac{1-\Gamma_{as}}{1-\Gamma_{as}\Gamma_{sg}/L^2}\left[\left(1+\frac{\Gamma_{sg}}{L}\right)\left(1-\frac{1}{L}\right)(1-a)T_s+\frac{1-\Gamma_{sg}}{L}T_g\right] \qquad \textbf{(7.5)}$$

where a is the snow albedo, Γ is the specular power reflection coefficient at incidence angle θ in "p" polarization, and the subscripts "*as*" denotes air-snow boundary, "*sg*" snow-ground boundary, "*s*" snow and "*g*" ground. By approximating the physical temperatures of soil and snow by $T_s \approx T_g \approx T_o$, and since $G_{as}G_{sg} < 0.01$ and $G_{sg} < 0.05$ for $q \le 70^o$, then substituting $L = e^{k_e\, d\, \sec(q')}$, equation (7.5) reduces to:

$$T_{B,pack}(q,p)\approx(1-\Gamma_{as})\left\{(1-a)+\left[(1-\Gamma_{sg})-(1-a)\right]e^{-k_e\, d\, \sec(q')}\right\}T_0 \qquad \textbf{(7.6)}$$

where d is the snow depth, $k_e=\frac{1}{d_p}\approx\frac{1}{3.25\ m}$. and q' is the angle of refraction in the snow.

iv.2) If the soil is covered by vegetation, the brightness temperature is computed from:

$$T_{B,can}(q,p)=\left(1+\frac{\Gamma_s}{L}\right)\left(1-\frac{1}{L}\right)(1-a)T_v+\frac{1-\Gamma_s}{L}T_s \qquad \textbf{(7.7)}$$

where a is the vegetation albedo, T_v and T_s are the vegetation and soil physical temperatures, $L = e^{k_e\, h\, \sec(q')}$, h is the vegetation height, q' is the angle of refraction in the vegetation, G_s is the reflectivity of the vegetation-soil boundary:

$$\Gamma_s(q,p)=\Gamma^{sp}(q,p)\,e^{-h'\cos^2(q_{inc})} \qquad \textbf{(7.8)}$$

$G^{sp}(q,p)$ is the specular surface power reflection coefficient at "p" polarization, $h' = 4k^2 s^2$, and s is the soil roughness. As it was shown in chapter one, at 1.4 GHz the soil brightness temperature is mainly governed by the soil moisture content though the dependence of the specular reflection coefficient on the dielectric permitivity.

On the other hand, if the pixel's coordinates correspond to the sea, again two models may apply [Ulaby et al 86, chapter eleven]:

iv.3) If the sea is not covered by ice, the brightness temperature is computed from:

$$T_{B,sea}(q,p,u)=T_B(q,p,0)+a(q,p)\,u \qquad \textbf{(7.9)}$$

where:

$$T_B(q,p,0)=\left[1-\Gamma^{sp}(q,p)\right]T_o \qquad \textbf{(7.10)}$$

$G^{sp}(q,p)$ is the specular surface reflectivity, that depends on the surface salinity though the dependence of the water dielectric constant on the salinity contents, T_o is the physical

temperature of the sea, "$a(q, p)$ " is a function that depends on the incidence angle and the polarization and "u" [m/s] is the wind speed at a certain height in the up-wind direction. A linear fit indicates that $a \approx 0$ for vertical polarization and for the horizontal polarization "a" increases from 0.34 K/m at 1.4 GHz to 1.06 K/m at 19.34 GHz at q=55º, provided that neither foam nor whitecaps are present on the water surface, in that case a rapid increase in the brightness temperature is observed. The " $a(q, p)$" function has been obtained empirically from the numerical results of [Brey 91] and those that will be presented in chapter ten.

iv.4) If the sea is partially covered by ice, the brightness temperature are computed as the weighted sum of the brightness temperature due to the sea, equation (7.15), and the brightness temperature due to the ice:

$$T_{B,\ iced\ sea} = (1 - ic)\, T_{B,\ sea} + ic\ \ T_{B,\ ice} \qquad \textbf{(7.11)}$$

where "ic" is the fraction of the sea surface covered by ice. The brightness temperature of the iced sea is computed according to the equation (7.11) with the dielectric constant of the ice computed with the formulas given in the appendix E of [Ulaby et al. 86].

Since the purpose of this simulator is not to include very accurate brightness temperatures models, but to study the radiometric accuracy improvement of the pixel averaging technique and the overall system's response, atmospheric attenuation effects -otherwise negligible at 1.4 GHz- and solar reflections have not been modeled.

Figure 7.5 shows an example of the computed brightness temperatures in vertical and horizontal polarizations for the Mediterranean sea region. It should be noted that most of the models found in the literature are given for incidence angles up to 60º-80º and may lead inaccurate results when extrapolated.

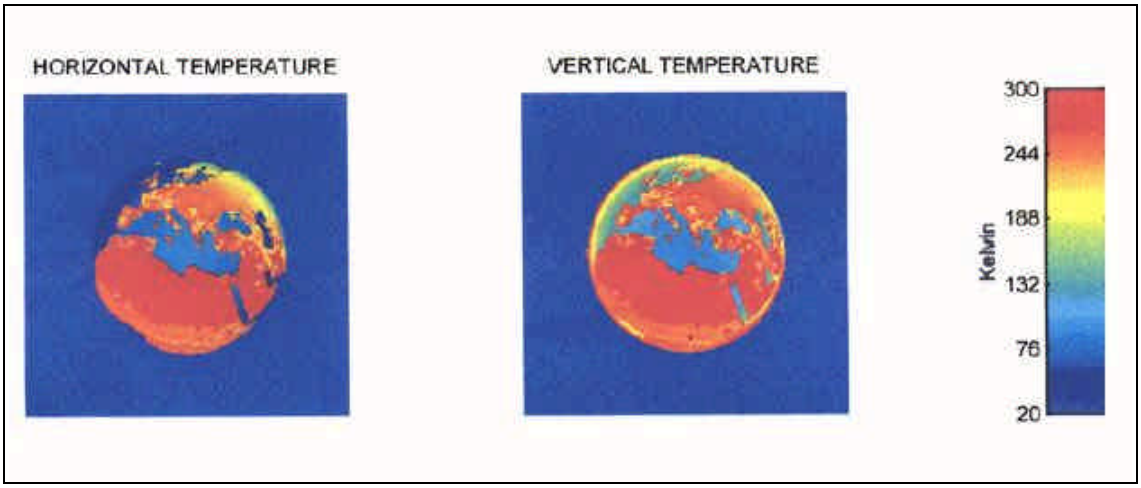

Figure 7.5.- *Computed vertical and horizontal brightness temperatures from 20¹ E, 35¹ N, 4.000 m. Mediterranean sea, December 1998*

7.3.- INSTRUMENT'S MODELING

This section is devoted to the explanation of the modeling of the hardware of the 2D interferometer:

i) the array structure modeling and its mechanics are based on [MMS 95],
ii) antenna patterns have been fitted from MMS measured cup-dipoles, while mutual impedances values have been taken from measurements of frequency scaled X-band cup-dipoles,
iii) receivers' frequency response are computed numerically for the basic scheme and the parameters and standard deviations specified in [MMS 95],
iv) 1B/2L digital correlators are modeled according to the error analysis performed in chapter four, and the experience gained in the design of the digital correlator unit (chapter eight).

The calibration hardware modeling is based on the distributed noise-injection technique described in chapter five and the iterative inversion algorithm is the one proposed in chapter six. In the following sections each subsystem is explained in more detail.

7.3.1.- Array structure

The structure of the interferometer's array is shown in figure 7.10 [MMS 95]. It is composed by three arms forming 120º between them. In the MIRAS space-borne instrument each arm is about 9 m long and has N_{EL}= 43 cup-dipole antennas spaced d=0.89 wavelengths. In the center there are three extra antennas for calibration purposes (phase restoration techniques) [MMS 95]. In fact, as explained in chapter five, two of them are redundant and only one is strictly necessary to relate the phases between the arms when establishing the phase closure relationships.

The oscillations of the arms and their relationships with the integration time and the error committed in the baseline are modeled in section 4.3.2.

7.3.2.- Antenna modeling

In order to improve the antenna voltage pattern model used in the error analysis, the lists of measurements provided by MMS of MIRAS bread-board cup-dipoles have been fitted. Measurements were given for three cuts (ϕ = 0º, 45º and 90º) for which they have been fitted, for other ϕ angles interpolation formulas have been used. Amplitude pattern errors are smaller than 3% and phase pattern errors are smaller than 0.25º, for $|\theta|<60º$. More details can be found in appendix 9.

7.3.3.- Receivers modeling

The basic MIRAS bread-board scheme is the same as used in the error analysis except that instead of a single equivalent filter there are four filters:
i) the spurious filter to prevent signal interferences. It is a Chebyschew band-pass filter obtained from a 3rd order Chebyschew low-pass filter prototype.
ii) the image filter to reject the image band. It is a Chebyschew band-pass filter obtained from a 4th order Chebyschew low-pass filter prototype.
iii) the low-pass filter to set signals' bandwidth after I/Q demodulation. In the MIRAS BB design it is a 7th order Chebyschew low-pass filter, but the simulator allows to analyze the response to a flat delay inverse Chebyschew filter to minimize decorrelation effects due to filters' tolerances.
iv) the DC-block RC high-pass filter at comparators' input to eliminate offset voltages induced in the demodulators.

The nominal frequency response of each filter is set by three parameters:
i) their -3 dB bandwidth: 30 MHz, 35 MHz, 20.75 MHz and 1 MHz respectively.
ii) their in-band ripple: 0.05 dB, 0.075 dB and 0.06 dB for the three Chebyschew-type filters.
iii) and the order of the low-pass prototype: 3, 4 and 7

while the central frequency for the two band-pass filters is common and is set equal to f_0=1.410 MHz. The common local oscillator frequency is equal f_{LO}=1.395 MHz.
Three additional parameters establish filters' tolerances: the -3 dB bandwidth standard deviation, the in-band ripple standard deviation and the central frequency error standard deviation.

Other error sources modelled are: delay errors due to path differences (σ_{td}=50ps, corresponding to a path mismatch of 1 cm with an ε_r = 2.1), errors in the LO phase $\sigma_{\theta LO}=2^{\circ}$ and quadrature errors between the I/Q signals at demodulators' output $\sigma_{\theta IQ} = 2^{\circ}$.

In order to simulate the impact of comparators' offset errors, receivers' gain is assumed to be G = 100 dB $\pm$ 0.2 dB. Receivers' noise temperature is assumed to be T_R=80K $\pm$ 10 K. Antenna coupling errors is modelled with the mutual impedances measured between our X-band cup-dipoles (appendix 11), with a 50 Ω charge load -the LNA input impedance- or the antenna free-space self-impedance: Z_{11} .

With all the information relative to the receiver, the fringe-wash factor is computed as:

$$\tilde{r}_{kl}(t) = r_{kl}(t)\, e^{-j2p\, f_o t}$$

$$r_{kl}(t) = \int_0^\infty H_k(f)\, H_l^*(f)\, e^{j2pft}\, df \qquad \textbf{(7.12)}$$

where: $H_k(f)$ and $H_l(f)$ are the equivalent band-pass responses of the receivers involved in the correlation:

$$H_k(f) = H_{spurious\,k}(f)\, H_{image\,k}(f)\, H_{low\text{-}pass\,k}(f - f_o)\, H_{DC\text{-}block\,k}(f - f_o) \qquad \textbf{(7.13)}$$

Figure 7.6 shows the nominal response of the spurious, the image and the low-pass Chebyschew filters with the group delay response. As it can be appreciated, the most important contribution to decorrelation is due to mismatches in the group delay response of the low-pass filters. However, numerical simulations have shown that contributions from the narrow band-pass filters are not negligible and can degrade system's performance if tolerances are not strictly controlled.

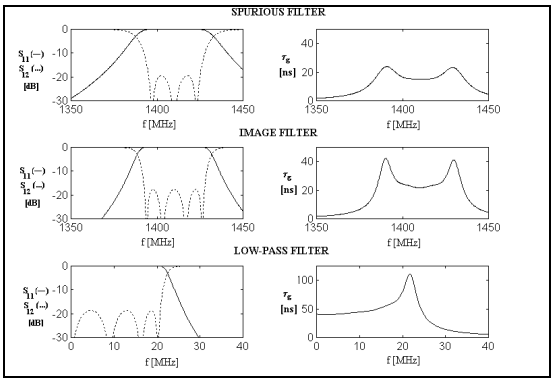

Figure 7.6.- *Nominal frequency response of MIRAS BB spurious, image and low-pass Chebyschew filters*

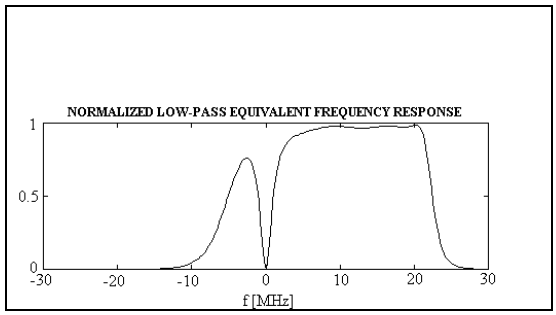

Figure 7.7.- *Equivalent low-pass frequency response of the four filters in cascade.*

Figure 7.7 shows the low-pass equivalent receiver's frequency response from which the fringe-wash response is computed for each baseline:

$$H_{low\text{-}pass\,k}(f) = H_k(f - f_{ol}) \qquad \textbf{(7.14)}$$

For computational purposes, the amplitude of the fringe-wash factor is then adjusted by a gaussian function, and the phase is adjusted by a line:

$$\tilde{r}(t) = A\, e^{-p\, B_{eq}^2 (t - t_0)^2}\, e^{-j\Phi_0}\, e^{j2p\, f_p t} \qquad \textbf{(7.15)}$$

$$A = |\tilde{r}(0)|\, e^{-p\, B_{eq}^2 t_0^2}$$

as it is shown in figure 7.8. B_{eq} is the equivalent noise bandwidth of the baseline, t_0 is the equivalent group delay difference, Φ_0 is the equivalent phase difference and f_p is the equivalent central frequency. For gaussian filters, the analytical formulas of the parameters B, $\Delta\tau_g$, ϕ_V and $\Delta f'$ are found in equations (4.38) to (4.42).

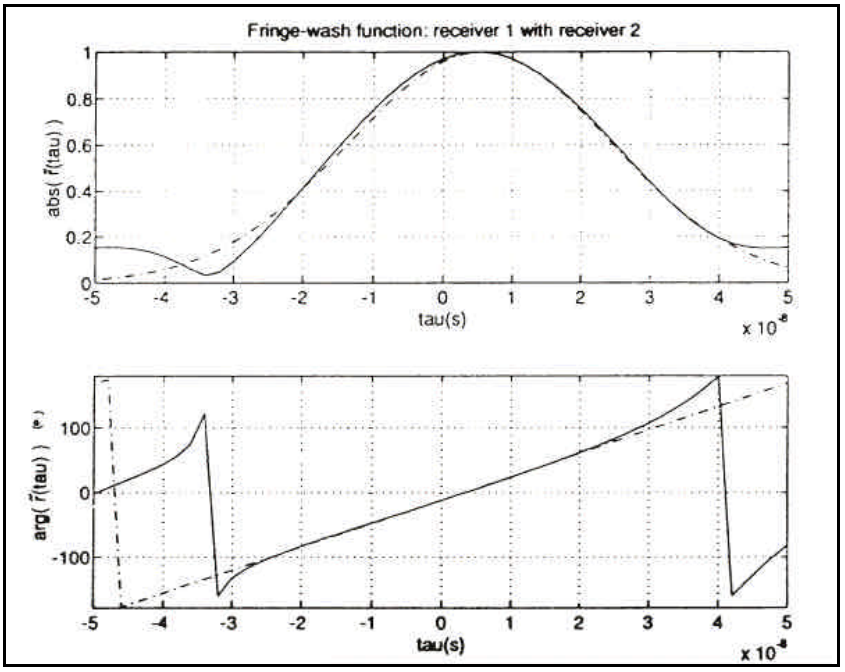

Figure 7.8.- *Fringe-wash function and gaussian fit.*

7.3.4.- Correlators and LO modeling

1 bit/2 level digital correlators have been modeled according to the error analysis performed in chapter four (equations (4.90), (4.91), (4.101) and (4.102)) and the experience gained in the development of the digital correlator unit (chapter 8 and appendix 15). LO thermal noise in the RF band introduces an offset term that is added at the end.

At this point the sequence followed to generate a set of raw visibility samples is complete:

i) Generation of a brightness temperature distribution from a propagated orbital position.
ii) Computation of the $V^{(1)}$ visibilities by a two-dimensional numerical integration of equation (3.1), including the computed brightness temperature distribution, different antenna radiation voltage patterns, errors in the antenna positions and different receivers' frequency response trough the fringe-wash function.
iii) Addition of a zero-mean gaussian random variable to simulate the measurement uncertainty due to finite integration time (equation (3.65)):

$$\hat{V}_{r,i}^{(1)}(u_{kl}, v_{kl}) = V_{r,i}^{(1)}(u_{kl}, v_{kl}) + \Delta V_{r,i} \qquad \textbf{(7.16)}$$

iv) Computation the coupled visibility samples (equation (4.32)):

$$\overline{V}^{(2)} = \overline{C}^{-1}\overline{V}^{(1)}\left(\overline{C}^{-1}\right)^{H} \tag{7.17}$$

v) Addition in-phase and quadrature errors: $\Delta\theta_{OL}$, $\Delta\theta_{IQ}$, and $\Delta\theta_o$ (equation 4.52):

$$\begin{bmatrix} V_r^{(3)} \\ V_i^{(3)} \end{bmatrix} = \overline{P_{kl}} \begin{bmatrix} V_r^{(2)} \\ V_i^{(2)} \end{bmatrix} \tag{7.18}$$

vi) Computation of the normalized visibility samples $\mu_{kl}^{(4)}$ [Hagen and Farley 73]:

$$m_{kl}^{(4)} = \frac{1}{\sqrt{T_{A_k} + T_{R_l}}} \frac{1}{\sqrt{T_{A_k} + T_{R_l}}} V_{kl}^{(3)} \tag{7.19}$$

vii) Introduction of comparators' threshold errors and correlator's gain due to jitter errors in the sampling instant (equations (4.90), (4.91), (4.101) and (4.102)).
viii) And addition of offset errors due to local oscillator leakage:

$$m_{r,i}^{(5)} = m'^{(4)}_{r,i} + m_{r,i\,offset} \tag{7.20}$$

7.3.5.- Calibration hardware modeling

From the two methods proposed in chapter five, the distributed noise injection method has been implemented in the simulator because of its greater robustness. However, it has been found that the large non-separable amplitude errors that are introduced by the filters, with present MIRAS bread-board specifications, may cause errors in the calibration of the receiver gain factors. To avoid this problem, the measurement of each receiver's noise temperature and the antenna's temperatures is modeled with a linear power detector.

The calibration hardware scheme is modeled according to figures 5.7 and 5.8.

Calibration parameters are:
i) the noise temperature at the input of the LNA, $T_{noise} \approx 300$ K, which is different from the noise temperature of the noise source, $T_{diode} \approx 2.400$ K,
ii) the standard deviation of the noise temperatures at the input of the LNAs, $\Delta T_{noise} \approx 10$K,
iii) and the number of 0.3 s integrations that are performed to improve the signal-to-noise ratio.

7.3.6.- Processing parameters

The processing parameters affect the way the inversion process is performed and, consequently, the spatial resolution and the radiometric sensitivity and accuracy. The *resolution-mode parameter* sets the (u,v) set of samples to be used in the inversion process. In the standard resolution mode only the (u,v) samples of the inner hexagon are taken (see figure 7.9), in the enhanced, all the available visibility samples are used. It has been noticed that there is not any problem due to the missing (u,v) samples that have to be extrapolated between the star points, and it is preferable over the standard mode because of its better spatial resolution, even for small arrays.

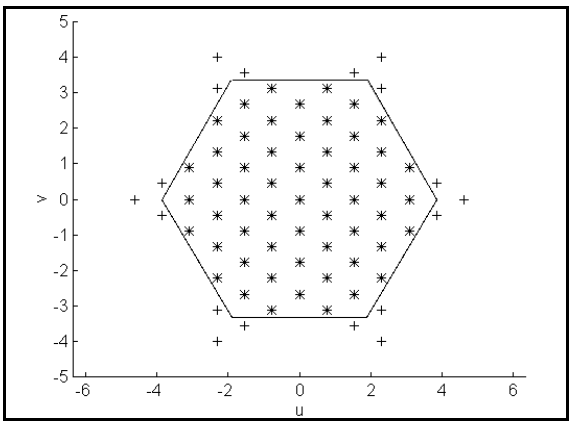

Figure 7.9.- *Definition of the standard resolution mode and the enhanced resolution mode*

The *window* used to tapper the visibility samples can also be selected between the five ones used in this study: the rectangular one, the Barlett one, the Hamming one, the Hanning one and the Blackmann one (table 3.1).

The best performance of the inversion algorithm is obtained with very smooth windows, i.e. the Hamming, the Hanning and the Blackmann windows, and the selection between them is a trade-off between spatial resolution and radiometric sensitivity. In our simulations the Blackmann window is always used. The rectangular and the Barlett windows are not very useful because of the high secondary lobes of the impulse response that make the truncation error to the alias-free FOV very high and slow down the convergence of the inversion process.

The *gain loop factor* (can also be selected to prevent convergence problems. In theory, it should be selected to satisfy:

$$0<*(8_{max}\&1*<1 \qquad \textbf{(7.21)}$$

but in practice, a factor of (=0.5 suffices. Rarely the inversion process is not convergent, in fact, this problem has only been noticed for very large antenna amplitude and phase errors ($F_{)1}$ > 15º) or when the calibration process has provided wrong receivers' noise temperatures and/or receivers' phase error estimates due to large filters' mismatches.

Since the inversion process controls the convergence trough the norm of the residue (equation (6.77)), when convergence is not achieved, the process is re-initialized with a new factor: ('=(/2.

Finally, the *number of guard pixels* in the alias-free FOV border can also be selected. As commented in chapter six, for the errors and tolerances involved one guard pixel is sufficient, but it can be increased if antenna pattern errors are too large to make the tails of the impulse response of outside pixels to enter excessively in the alias-free FOV.

7.3.7.- Graphical representation of results

The original brightness temperature distribution, as well as the simulation results can be displayed in the directing cosines representation as well as in the cartographic projections and expansions [Martín 90], which are just listed below:

i) Directing cosines representation.
ii) Cartographic projections: stereographic projection, gnomonic projection (central, meridian or transverse and horizontal or oblique), stereographic (polar, meridian or transverse and horizontal or oblique) and orthographic (equatorial or direct, meridian or transverse and horizontal or oblique).
iii) Cartographic expansion: Lambert's equivalent cylindrical expansion, equivalent cylindrical expansion with automecoic meridians, Mercator shaped cylindrical expansion, transverse cylindrical expansion, UTM projection, conical expansion and Lambert's shaped conical expansion.

7.4.- Simulation results and radiometric accuracy improvement by means of pixel averaging

In order to analyze the radiometric improvement by means of pixel averaging the first 25 snap-shots, with a 4 seconds interval, of the orbit shown in figure 7.4 have been simulated. The interferometer is an Y-array with 27 antennas per arm, corresponding to two of the three sections that will form each arm of the MIRAS instrument. The array's size reduction translates into shorter execution times, while keeping the main characteristics of MIRAS. Anyway, the simulation of the 25 snap-shots took more than 116 hours in a 100MHz Pentium with 16 Mbytes of RAM.

The imaged FOV passes from the Noth of Africa to the Noth of the Mediterranean coast of Spain. Instrumental parameters and errors are those specified in chapter four to achieve a 1.2 K radiometric accuracy and 0.86 K radiometric sensitivity. Calibration parameters have been obtained with the noise-injection method described in chapter five by averaging 100 measurements of 0.3 seconds. The inversion process is that explained in chapter six with $\epsilon=0$. Simulation results of snap-shots numbers 12 and 25 are shown in

figure 7.10 restricted to the alias-free FOV. In the left side the ideal brightness temperature maps that would be obtained with an ideal Y-shaped interferometer with 43 antennas per arm and an infinite integration time. In the right side, the recovered brightness temperature maps with an instrument modeled with all the errors studied in chapter four, including digital correlator errors ($\sigma_{\Delta x^i}$ = 1 mV, σ_{td} = 0.1 ns), fringe-washing effects, non-separable amplitude and phase errors and thermal noise corresponding to 0.3 seconds integration time.

Figure 7.11 shows the rms error of each pixel followed along the FOV during the different snap-shots according to figure 4.17. The average rms error for all the pixels in the FOV is 4.76 K, which includes 3.42 K corresponding to the 0.3 seconds finite integration time (continuous lines). The average rms error for all the pixels after the averaging of all available measurements in the FOV is reduced down to 2.34 K, from which 0.84 K come from the averaging of the thermal noise (dotted lines). Consequently, the improvement in the radiometric accuracy by means of pixel averaging can be computed approximately as $G_{pix\,avg} \approx 1.54$ from:

$$s_o^2 = s_{noise}^2 + s_{sys\,err}^2 \Rightarrow 22.68\ K^2 = 11.70\ K^2 + 10.98\ K^2$$

$$s_f^2 = \frac{s_{noise}^2}{14} + \frac{s_{sys\,err}^2}{G_{pix\,avg}^2} \Rightarrow 5.46\ K^2 = 0.84^2 + \frac{10.98\ K^2}{G_{pix\,avg}^2}$$

$$G_{pix\,avg} \approx 1.54$$

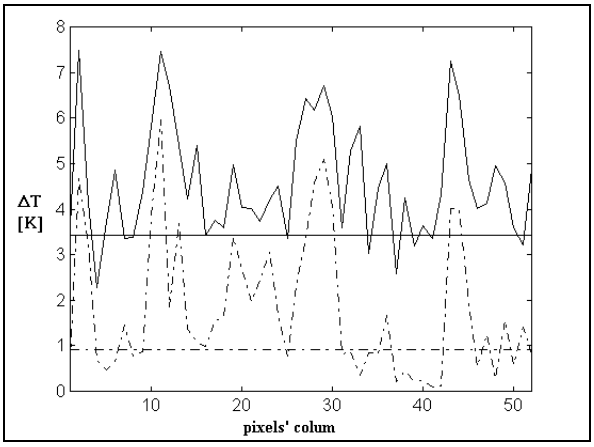

Figure 7.11.- *Radiometric error in the pixels' column with (-.) and without (-) pixel averaging.*

which is is good agreement with the theoretical analysis and the computer simulations performed in chapter four for the 200 K constant brightness temperature scene. However, this gain depends on the scene being imaged and can only be considered as a guide for system's performance prediction.

Present filters tolerances generate non-separable phase terms as high as 6º, that hinder the calibration algorithm, and account for the high radiometric error computed, about 8.25 K. This means that a baseline-based calibration procedure by c/u noise injection is required at least for the shortest baselines, the most significant ones, to improve the instrument's performance.

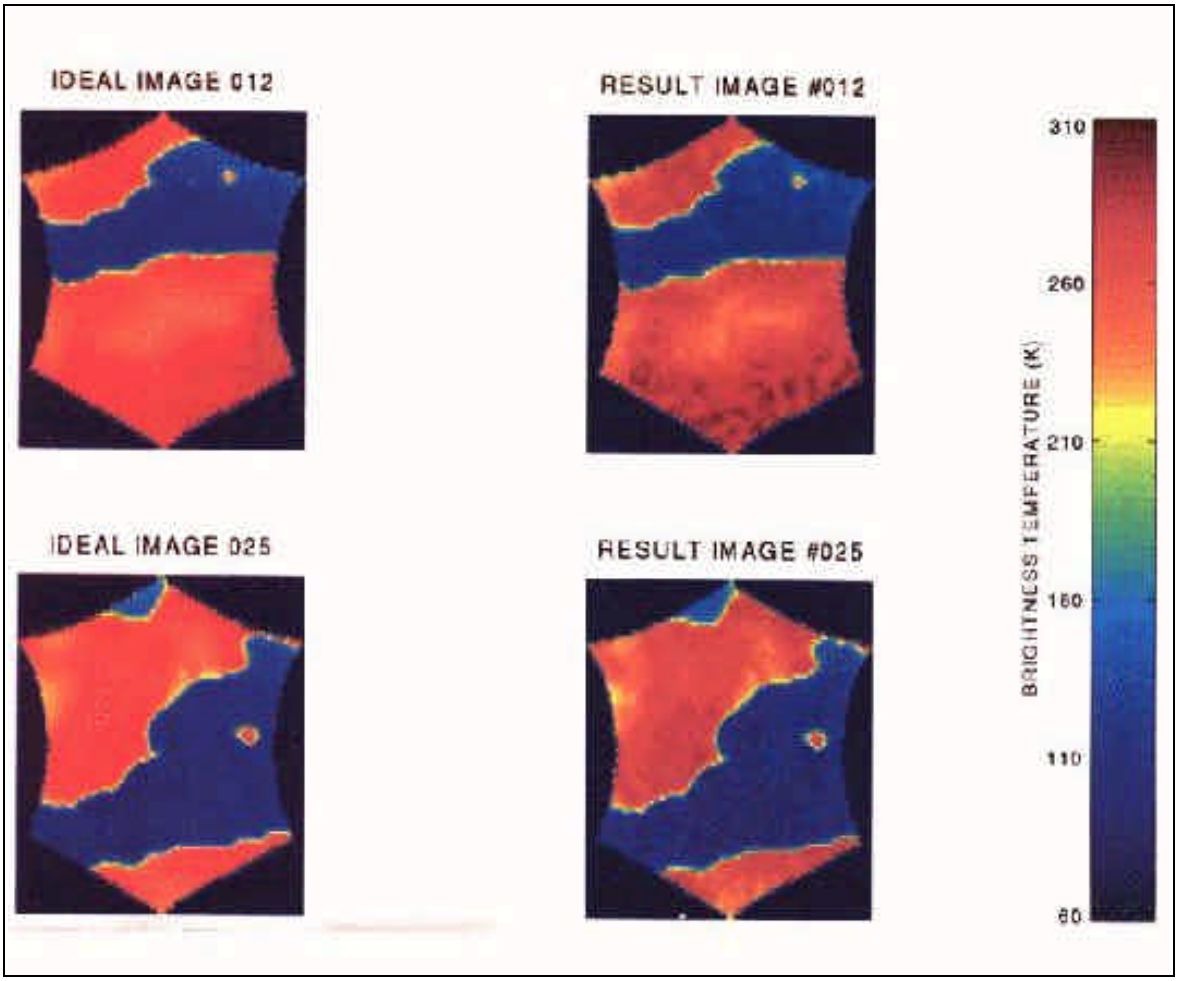

Figure 7.10.- *Ideal and deconvolved images corresponding to snap-shots #12 and #25. Snap-shot rms errors are about 8.25 K*

7.5.- CONCLUSIONS

This chapter has described the simulator implemented to analyze the radiometric improvement by means of pixel averaging: the orbital propagator, the scene generator to obtain realistic brightness temperature distributions, the system modeling: from MMS measured cup-dipoles to the digital correlators developed by us.

The chapter ends with the simulation of a platform carrying a Y-interferometer of 27 antennas per arm (two sections of the three that would form each MIRAS' arm) flying over the Spanish Mediterranean coast. All error sources are modeled and taken into account with the values given in [MMS 95]. The pixel averaging improvement is found to be about 1.54, which is somewhat higher than predicted in the theoretical analysis and the computer simulations performed for a constant temperature scene for correlated or uncorrelated phase and amplitude visibility errors (section 4.6). However, this is not a definitive result since it depends on the test scene.

Chapter 8. Design and characterization of a 2D Experimental Interferometric Radiometer

This chapter presents the characterization of the circuits designed to implement an experimental 2D interferometric radiometer developed to verify, as far as possible, the performance predicted in preceding chapters, as well as the calibration and inversion algorithms. It should be pointed out that, while the purpose of a Space Borne Interferometric Radiometer is to obtain L-band passive measurements, the prototype has been developed at X-band because of the availability of commercial components. In addition, following the technique described in [Laursen & Skou 94] only a baseline formed by two antennas, two receiving chains and a complex digital correlator has been built. The complete set of baselines is synthesized by changing the antenna positions along the array.

First of all system's overall scheme is presented. Then each subsystem is explained and characterized: i) the mechanical design of the array, ii) the antenna design and characterization, iii) the RF front-end and IF section, including TV-DBS external units, custom IF amplifiers and I/Q demodulators, iv) the LF circuit design, including a selection of the filters, video amplifiers and peak detector and v) the 1 bit/2 level digital complex correlator unit.

At the end of the chapter, the whole system is characterized in terms of global offset, amplitude and phase errors and its calibration sequence is presented. The sensitivity of the instrument is checked through several laboratory experiments.

8.1.- INSTRUMENT DESCRIPTION

Figure 8.1 shows the schematic of the interferometric radiometer that has been built. Its main characteristics are: input frequency 10.7 GHz, equivalent noise bandwidth 30MHz, equivalent noise temperature T_{Ri} < 120 K and 93 dB / 107 dB adjustable gain. It is composed of four blocks:

i) The PVC Y-array mounted over a photographic tripod where two cup-dipole antennas are placed. Cup-dipole antennas have been selected because of their small size: 0.89 λ diameter, the low coupling presented: less than 30 dB even when they are touching, and the wide antenna pattern: about 70º half-power beam-width. The *RF band is centered at 10.7 GHz,* occupying a *protected band for passive measurements.*

ii) The RF front-end is formed by two DBS external units, whose local oscillator has been extracted and substituted by a common synthesized one. The external units also perform the first frequency conversion from 10.7 GHz down to 881.5 MHz, where the signal is further amplified and its in-phase and quadrature components are extracted to perform the correlation at baseband by means of real correlators. I/Q demodulators are also driven by a common synthesized local oscillator to preserve the phase information.

iii) The Low Frequency section is formed by a bank of four 7^{th} order, 21.4 MHz half-power bandwidth Chebyschew filters that limit signals' bandwidth to satisfy the Nyquist criterion when sampled at 66 MHz by the digital correlators unit (DCU). An adjustable gain video amplifier amplifies signals' level to drive properly the comparators of the DCU. The DCU computes the real and imaginary parts of the visibility samples from the correlation of the in-phase signals and the mixed correlation of a quadrature signal with and in-phase one:

$$V(u,v) \;\; ' \;\; R_{i_1 i_2}(0) \;\% \; j \; R_{q_1 \; i_2}(0) \qquad \textbf{(8.1)}$$

Since only three of the four available signals are used, $q_2(t)$ signal is driven to a peak detector to monitor signal's power.

iv) The 1B/2L DCU uses high speed comparators and Fast-TTL technology to cope with high clock frequency. The DCU board is controlled by a signal acquisition board and a C++ program. Integration time can be adjusted from 1 ms to 64 s. Correlators' outputs are then software denormalized and pre-calibrated.

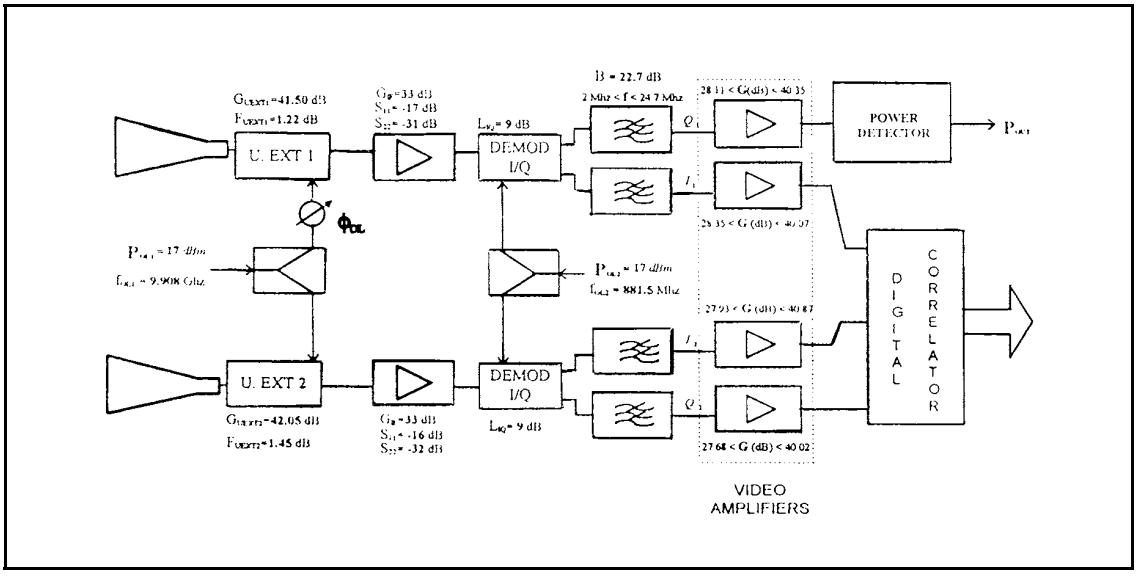

Figure 8.1.- *Experimetal Interferometric Radiometer scheme.*

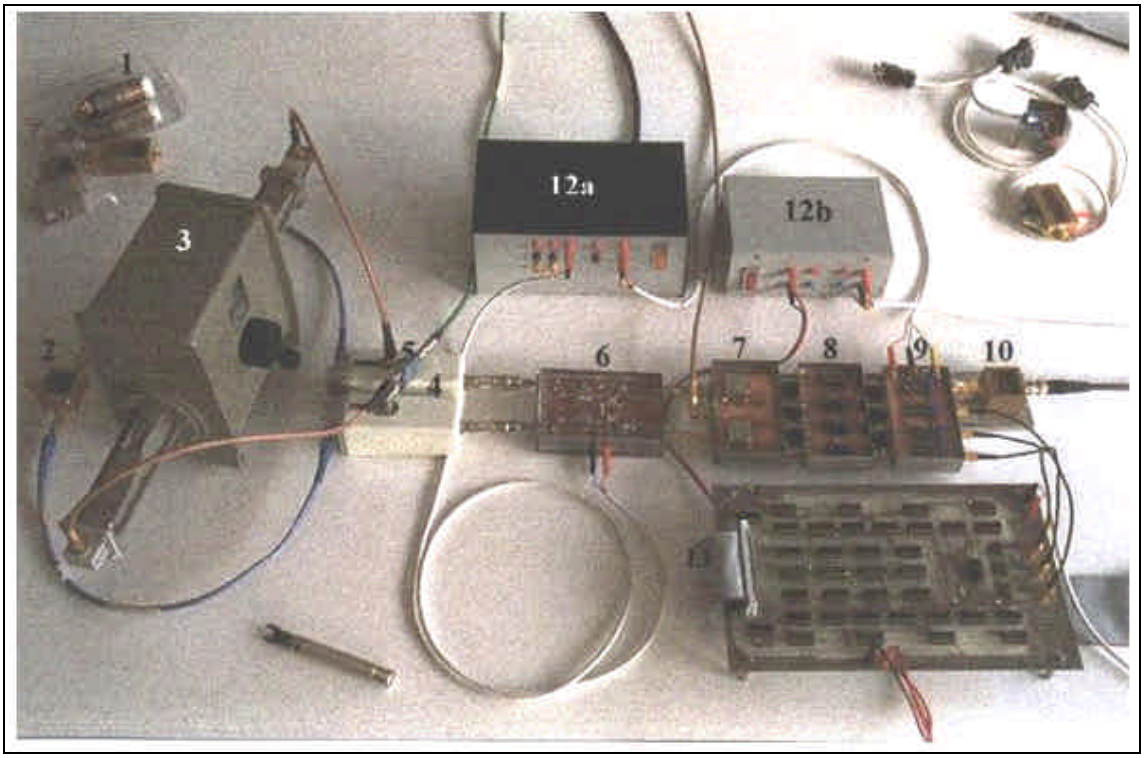

Figure 8.2.- *Experimetal Interferometric Radiometer picture during laboratory tests .*

Figure 8.2 legend*:*

1.- Cup-dipole antennas
2.- Non-resistive power splitter
3.- Phase-shifter
4.- TV external units
5.- Wilkinson power splitter
6.- IF amplifiers
7.- I/Q demodulators
8.- Low-pass filters bank
9.- Video amplifiers bank
10.- Peak detector
11.- 1B/2L digital correlator unit
12a.- Analog circuitry power supply
12b.- Digital circuitry power supply

8.2.- ARRAY AND ANTENNA DESIGN

8.2.1.- Array design

The array is designed according to an Y-shaped geometry, which provides an hexagonal sampling in the spatial frequencies (u,v) plane. In chapter six, it has been shown that this configuration is the optimal one in terms of the required number of visibility samples for an specific aliasing level: minimizing hardware requirements in a complete array and, in our two-antenna interferometer, minimizing the sequence of measurements to be carried out.

The Y-array is built from a PVC board and it is mounted over a photographic tripod that allows some kind of orientation. Three slots have been cut in the arms to let the antennas slide. At 10.7 GHz, cup-dipoles' diameter is 0.89λ and Y-arms' length correspond to up to fifteen different antenna positions. A graduated rule has been marked in each arm to indicate the antenna position along the arm. Since the minimum antenna spacing is greater than $1/\sqrt{3}\,\lambda$, the Nyquist criterion for hexagonal sampling of signals supported by the unit circle is not satisfied and the recovered image suffers from aliasing effects in the reconstruction process, as it is shown in the next chapter.

8.2.2.- Antenna design and characterization

Independently of the particular kind of antenna that is chosen, mechanical aspects are of great importance since they are first required to be light and second to slide along the three Y-arms preserving the polarization when changed from one arm to another one. To satisfy these two requirements the antenna is mounted over an hexagonal bolt, whose sides form a 120º angle. In this way, the antenna slides along each arm guided by two opposite sides of the hexagon and polarization in preserved.

A third key point in the mechanical design of the antenna is the balun (BALanced-to-UNbalanced) which forces symmetric currents over the dipole arms. Since the antenna must work in a narrow band, 30 MHz at 10.7 GHz, a 0.3 % relative bandwidth, a simple Bazooka balun is selected. It consists on a conducting cylinder $\lambda/4$ height short-circuited by the ground plane to the coaxial line driving the dipole (figure 8.3).

Finally to improve antenna coupling, specially when antennas are very close, an external metal cylinder wrapping all the structure has been made (figure 8.3). Since the external cylinder height impact on the antenna matching and the shape of the antenna radiation pattern was not "a priori" known, it was designed to be movable and can be fixed with a screw.

The first, the second and the fourth requirements are satisfied because the mechanical structure of the antenna has been specially designed. The third one depends mostly on the kind of feeder illuminating the aperture of the cup. As indicated in the precedent sections, a dipole is selected because of its simplicity. However, the soldering of dipoles arms to the coaxial line was found to be the most critical part of the construction because of the reduced size of the dipole arms and the small soldering points.

Two kind of dipoles have been tested: triangular dipoles and wire dipoles. Triangular dipoles have a larger bandwidth and are easier to tune. However, the capacitive effect induced by the balun thickness -2 mm- and its proximity -0.5 mm- to the dipole arm distorted the current distribution over the dipole arms and the radiation pattern. This effect is clearly shown in the E-plane cut, while it is not observed in the H-plane, due to the symmetry in the current distribution (figure 8.4). To minimize this effect wire dipoles were tested, showing an improvement in the antenna radiation pattern at a expense of the ease of tuning, because of the resonance peak shown at the frequency where the arm's length is a quarter wavelength. Figures 8.5 and 8.6 show the final voltage radiation pattern of the three cup-dipoles in the E- and H-planes as well as the amplitude and phase errors.

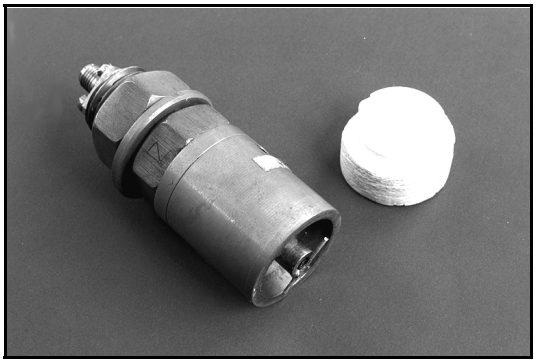

Figure 8.3.- Cup-dipole antenna

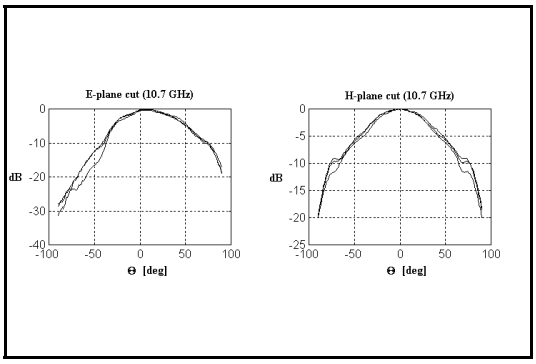

Figure 8.4.- *Triangular cup-dipoles: measured E-plane and H-plane radiation pattern.*

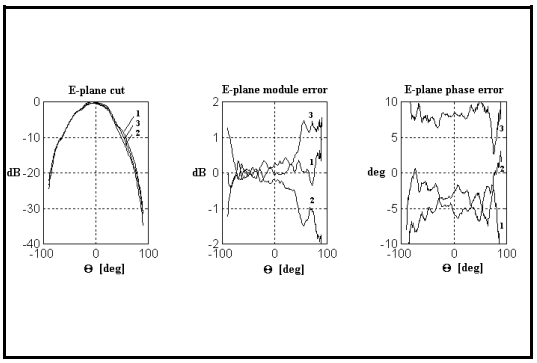

Figure 8.5.- Wire cup-dipoles: meausred E-plane cut, E-plane module and phase errors (10.7GHz)

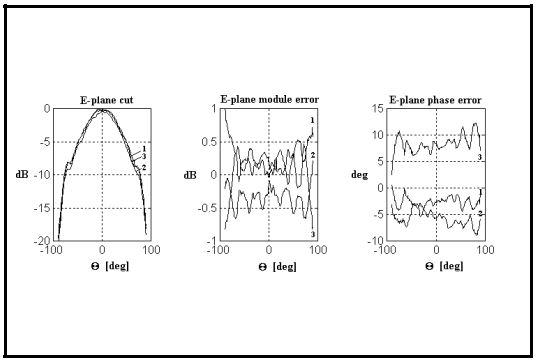

Figure 8.6.- *Wire cup-dipoles: measured H-plane cut, H-plane module and phase error (10.7GHz)*

The directivities are: 8,94 dB, 9.05 dB and 9.00 dB for the cup-dipoles 1, 2 and 3 respectively. Directivities have been computed from the integration of the whole antenna radiation pattern and agree very well with the values predicted in the appendix 10.

Note that the maximum's of the radiation pattern in the E-plane is deviated 4º because a dipole arm is 0.5 mm higher than the other one, inducing an electrical phase shift of "=5º. This deviation can be approximately computed by assuming that the centers of the arms are spaced 8/4 and:

$$"\,\%kd\sin(N|_{max})\,'\,0\;\;'>5^{o}\%\frac{360^{o}}{8}\frac{8}{4}\sin(N|_{max})\,'\,0\;\;'>N|_{max}\,'\,\&3.2^{o} \qquad \textbf{(8.2)}$$

Note also, that the 12º constant phase error between cup-dipole number 3 and the other two corresponds to a 0.9 mm error in the length of the coaxial feeding the dipole. This error does not present any problem during the measurements because it is calibrated with other separable phase errors induced by the receiving chain by means of a "polarimetric hot point" (chapter 9).

Appendix 11 lists the complete set of antenna coupling measurements for different antenna positions in the Y-array, which is always better than 30 dB.

The following table summarizes the main performances of the wire cup-dipole antennas:

Center frequency	10.7 GHz
Directivity	9 dB
Half-power beam-width	71º
Cross-polarization	< -17 dB
Antenna coupling (d = 0.89 8)	< -30 dB
Matching	< -10 dB

Table 8.1.- *Wire cup-dipoles parameters*

8.3.- RF CIRCUIT DESIGN AND CHARACTERIZATION

This section presents the RF section of the interferometer. It consists on a pair of low-cost X-band TV-DBS external units, having a low noise figure and a high gain, that perform the first frequency conversion down to UHF. Their LO were extracted and then substituted by a common synthesized LO to preserve signals' phase. At UHF there is a second custom amplifier followed by an in-phase/quadrature demodulator that splits the IF signals into their I and Q baseband components to be correlated.

8.3.1.- RF front-end

The RF front-end is composed by two X-band TV DBS external units model GSE-303 of TAGRA, for the reception of the ASTRA satellites in the 10.7 GHz - 11.8 GHz band, whose Local Oscillator (LO) has been extracted and replaced by a 50 S line and a SMA connector (appendix 12).

Because of the availability of commercial components at IF (filters and I/Q demodulators), the IF center frequency was fixed at 881.5 MHz, which is out of the specified output frequency band. The LO frequency was changed accordingly resulting in a loss of the overall gain mainly due to an increase in mixer's insertion loss. TV-DBS external units were characterized to check their output bandwidth, their gain and their noise factor. The following table summarizes the main performance of the two TV-DBS external units:

Parameter	DBS external Unit A	DBS External Unit B
Input Frequency	10.6895 GHz	10.6895 GHz
Output frequency	881.5 MHz	881.5 MHz
LO Frequency	9.808 GHz	9.808 GHz
LO power	10 dBm	10 dBm
Gain	41.50 dB	42.05 dB
Noise Factor	1.22 dB	1.5 dB

Table 8.2.- *DBS external units performance for use in the experimental interferometric radiometer.*

8.3.2.- IF section

The IF section satisfies five missions:

i) it provides the power supply to the DBS external unit in the same coaxial cable,
ii) it matches the 75Ω output impedance of the DBS external unit to the 50Ω input impedance of the filters and amplifiers used,
iii) acts as the first stage of the filtering process,
iv) acts as the second stage in the amplifier chain and
v) performs the second frequency conversion and I/Q demodulation

The DBS external unit power supply is driven through the inductance on the left side. The **impedance matching circuit** is formed by the inductance and the capacitor in "L" configuration.

IF filters are KDF-881RY-25A type, of Kyocera. They consist of three capacitive coupled "tuned" high-Q ceramic cavities using coaxial connections. Their center frequency is 881.5 MHz and their half power bandwidth is specified to be larger than 25 MHz.

Since filters' response mismatches are responsible for non-separable errors, a set of six filters were characterized, confirming manufacturers specifications: half-power bandwidth greater than 25 MHz, 3 dB maximum insertion loss, input/output return losses smaller than 13 dB, and, what is even more important from the point of view of the interferometer system, group delay is closely matched with peak differences of only 0.3 ns.

The **IF amplifier** is built with two MAR-8 MINICIRCUITS integrated amplifiers, each one having a nominal gain at 900 MHz of 23 dB. Oscillation problem were solved by connecting a 100 S resistance in parallel with IF filter's output at a expense of a gain loss. The main performance of the two IF amplifiers is shown in table 8.3.

Parameter	**Amplifier 1**	**Amplifier 2**
Half-power bandwidth	40 MHz	46 MHz
Gain	33 dB	36 dB
Input return loss	-17 dB	- 6.4 dB
Output return loss	-16 dB	- 7.8 dB

Table 8.3.- *Performance of IF amplifiers*

The **phase-quadrature demodulators** perfom two basic functions:
i) Split each signal into its in-phase and its quadrature components and
ii) Perform the second frequency conversion to allow a third amplifying stage prior to sampling and correlation.

MINICIRCUITS MIQC-895D I/Q demodulators have been selected because of their commercial availability. The main performance given by the manufacturer are reproduced in the table below. Note the order of the errors involved and the residual errors required (chapter 4).

Parameter	**Value**
RF and OL band	868 - 895 MHz
I/Q band	DC - 5 MHz
Conversion loss	8.7 dB typ.
Amplitude unbalance	0.3 dB max.
Phase unbalance	4º max.
OL level	10 dBm
1 dB compression point	4 dBm at the input
I/Q current	40 mA

Table 8.9.- *I/Q parameters.*

Note that the I/Q band ranges from DC to 5 MHz, while our 2nd IF band ranges up to

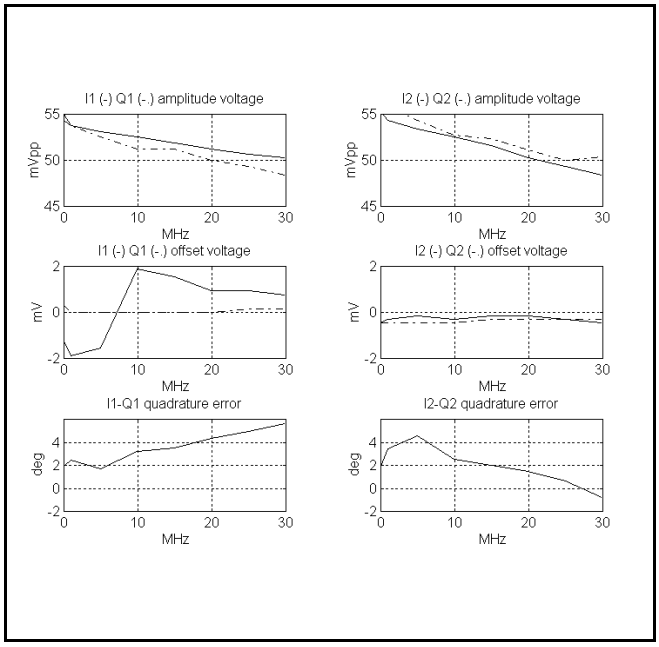

Figure 8.7.- *I/Q demodulators performance.*

25 MHz approximately. Consequently, demodulators were previously tested to verify their performance over the required 25 MHz bandwidth. Results are shown in figure 8.7 and demonstrate that they perform well for larger bandwidths than specified. Note that quadrature phase error is not constant over the whole bandwidth and deviations from a constant differential quadrature error can not be calibrated and remain as a residual error as it is shown later.

8.4.- LF CIRCUIT DESIGN AND CHARACTERIZATION

The low frequency section performs two basic functions:
i) filters the four signals coming from the I/Q demodulators: i_1, i_2, q_1 and q_2, and
ii) amplifies them to a level high enough to make threshold errors in the 1 bit comparators negligible, without saturating neither the last amplifying stage nor the comparators.

In addition, since the computation of the real and the imaginary parts of the visibility function requires only three signals, $V_r = E [i_1 i_2]$ and $V_i = E [q_1 i_2]$, the signal q_2 is connected to a peak detector and a signal conditioning circuit provides an approximate measurement of the input power.

Low-pass filters have the smallest bandwidth and set system's bandwidth. Since the sampling frequency of the 1 bit comparators of the Digital Correlator Unit is 66 MHz, filters must be narrow enough to attenuate properly the higher frequencies and satisfy the Nyquist criterion: B < 33 MHz, but noise bandwidth must be as large as possible in order to improve the radiometric sensitivity. However, if the filter is required to have a sharp transition from the pass-band to the stop-band, it will have high peaks in the group delay frequency response. Differences in the group delay response, about several nanoseconds, are translated into the fringe-washing function, with a rapid decrease, showing the decorrelation suffered by the signals. On other hand, filters having a good group delay performance, have very smooth attenuation characteristics and must have a small bandwidth to properly attenuate frequencies over 33 MHz.

In order to study this trade-off two kind of filters have been tested: the MINICIRCUITS' SCLF-21.4, Chebyschew 7th order, and the flat group delay MINICIRCUITS' PBLP-39 filters. Figure 8.8 shows the frequency responses of the two banks of four filters.

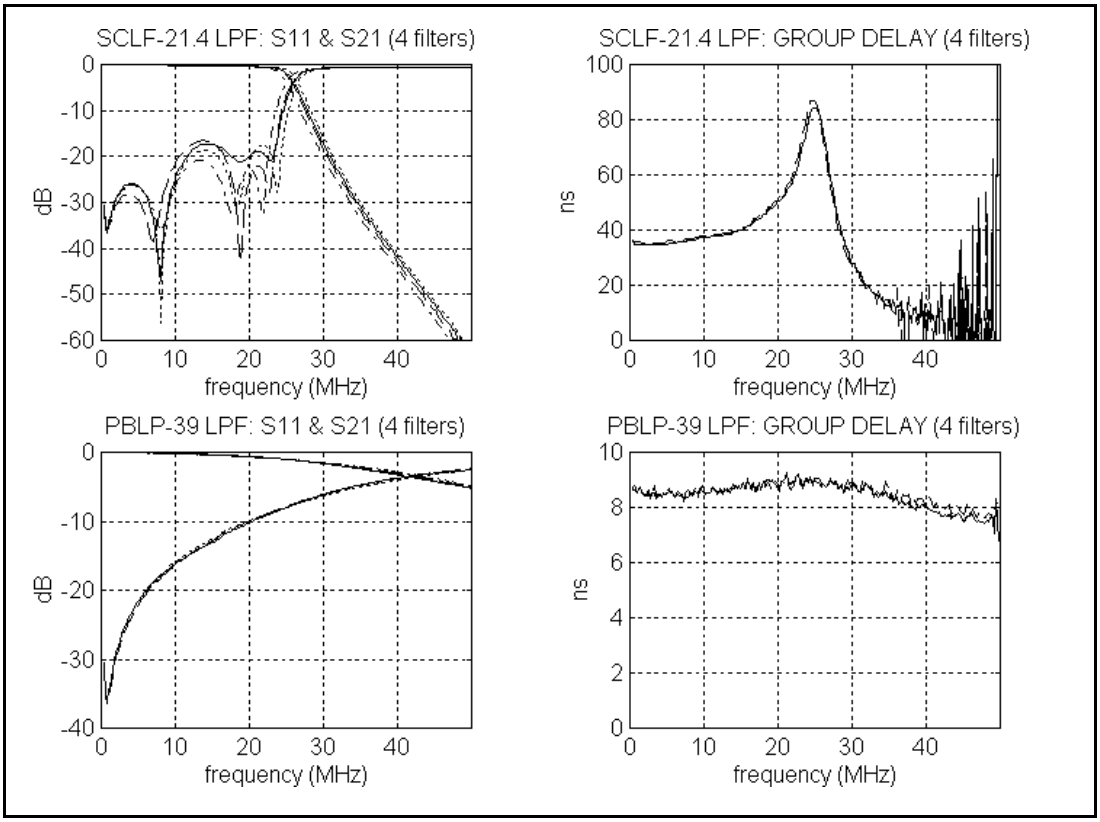

Figure 8.8.- *SCLF-21.4 and PBLP-39 MINICIRCUITS filters frequency and group delay responses.*

As it can be observed, Chebyschew filters are more selective and have a high group delay peak. Filter mismatches are apparent. On the other hand, flat delay filters have a very smooth transition and a nearly constant group delay.

SCLF-21.4 filters were finally selected because of their frequency selectivity. Once the whole system was assembled filter mismatches were minimized by interchanging filters' position in the bank. The final V_r-V_i amplitude mismatch is only 4 % (section 8.6.3).

As commented before, the bank of **video amplifiers** amplifies the four signals coming from the I/Q demodulators to a level where comparators' threshold errors are negligible, about 0 dBm or 220 mV_{ef} over 50 S. The input power is:

$$P_{in} \text{ ' } k_B\, T_A\, B \text{ ' } \&99 \ldots \&104\, dBm \quad T_A \text{ ' } 100\,K \ldots 300\,K \qquad B \text{ ' } 30\,MHz \tag{8.3}$$

and the overall gain of the previous stages is about G . 42 dB + 33 dB - 9 dB = 66 dB, this means that the required gain for the video amplifiers must cover the range from 33 dB to 38 dB. To avoid the offset voltage generated by the I/Q demodulators amplifiers are DC decoupled and matched to 50 S at its input. More details about their design and performance are given in appendix 13.

Finally, the **peak detector** is composed by a 50 S parallel resistor to match input's impedance, followed by a Schottky diode and a parallel capacitor acting as a low pass filter. The peak detector signal conditioning circuit is shown in appendix 14.

8.5.- DIGITAL CORRELATOR UNIT DESIGN AND CHARACTERIZATION

In the original design of the interferometric radiometer analog correlators were selected because of its theoretical better performance in terms of radiometric sensitivity. An analog correlator circuit was implemented with two AD-834-JN analog 500 MHz four quadrant multipliers and two RC low-pass filters. Since the multipliers have differential inputs and outputs the video amplifier section was included in the printed circuit board and was used to perform the conversion from single-ended to differential.

The main problems that were found to be associated with the analog correlator unit are:

i) There is a voltage offset due to a current unbalance at the outputs of the multipliers. This voltage offset is about 20 times smaller than the measured correlations and suffered drifts during the measurement process. It was found that the 13 dB dynamic margin at the output was completely insufficient for this application.

ii) Since the receiving chain has not an automatic gain control and the analog correlator is sensitive to signal's amplitude, variations and drifts in the overall channels' gain were detected at the output, being eventually interpreted as variations of the signal's power.

These reasons lead to us to design a new correlator unit insensitive to signal's amplitude, with very low offsets and small drifts and with an adjustable integration time, between 1 ms to 64 s. From the number of digital correlators described in the literature [Hagen & Farley 73], the most appropriate for our application is the 1 bit/2 level digital correlator because of its simplicity and its insensitivity to signals' amplitude and to threshold errors (see chapter four). 1B/2L digital correlators compute the cross-correlation of two signals by looking at their sign and increasing a counter each time the sign is the same (figure 4.14).

In order to check the performance of the digital correlator unit a series of tests are performed. Even though 1B/2L digital correlators are well suited to compute the correlation of signals with a gaussian statistics, correlator's linearity is tested with a zero mean rectangular wave in the i_2 channel and constant +5V signals in the i_1 and q_1 channels. In this way, correlator's outputs:

$$Z_r = \frac{N_{count\ i_1\text{-}i_2}}{N_{count}}\ ; \qquad Z_r = \frac{N_{count\ q_1\text{-}i_2}}{N_{count}} \tag{8.4}$$

give a measurement of the duty cycle of the input signal. Signal's parameters: amplitude, frequency and duty cycle are varied to test correlator's performance vs. amplitude -threshold errors or saturation of the comparators- and vs frequency -timing errors-.

8.5.1.- Linearity vs. signal's frequency

Figure 8.9 shows the relative error in the measured linearity for a signal with 300mVpp amplitude and a duty cycle of 50 % as a function of frequency. As it can be expected, the higher the frequency, the larger the errors, because the ratio delay error to signal's period increases (equations (4.101) and (4.102)). Linearity tests for other duty cycles have shown the same trend but with decreasing errors as the duty cycle is increased.

8.5.4.2.- Linearity vs. signal's amplitude

Figure 8.10 shows the relative error in the measured linearity for a 15 MHz signal and a duty cycle of 50% vs. signal's amplitude. As expected, due to comparator's threshold errors the error is very high for low amplitudes. For large amplitudes the saturation of the comparators causes an extra delay that increases the correlation error. Consequently, for an optimum operation (error < 0.5%), signals' frequency must be smaller than 15 MHz and signals' amplitude must be in the range 200 to 500 mVpp, which is attained by adjusting video amplifiers' gain.

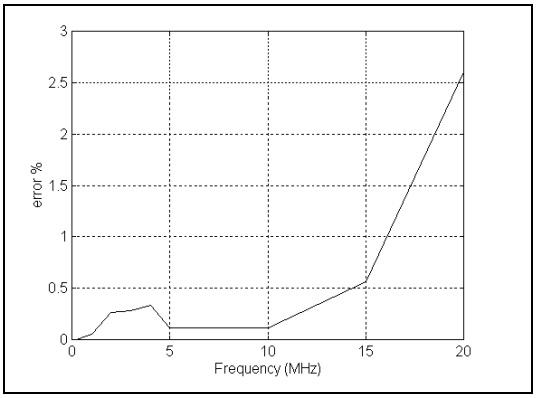

Figure 8.9.- *Digital Correlator Unit linearity error vs. signal's frequency. h = 50 %, A=300mVpp*
(Function generator accuracy "0.5%)

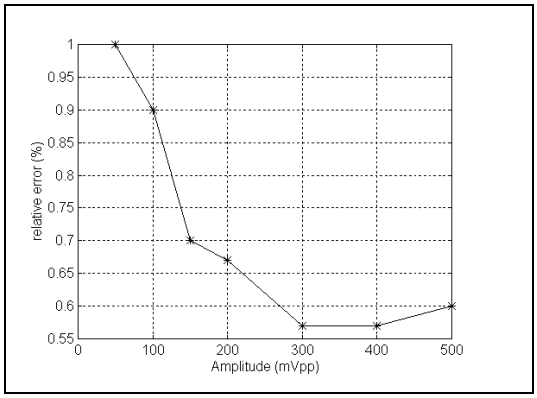

Figure 8.10.- *Digital Correlator Unit linearity error vs. signal's amplitude. h = 50 %, f=15MHz.*
(Function generator accuracy "0.5%)

Overall correlators performance has proven to be excellent, with a near to 35 dB dynamic margin, allowing to achieve a high differential radiometric sensitivity: 0.1 K.

8.6.- INSTRUMENT CHARACTERIZATION

Once all the subsystems are integrated and adjusted for optimum performance, the whole system is characterized in order to verify its global performance and its calibration (see section 5.5). In addition to the basic control routine of the digital correlator unit, a number of routines have been implemented to ease the calibration of offset and in-phase errors, as well as the measurement of the radiometric sensitivity.

8.6.1.- Calibration of offset errors

As explained in chapter 4, offset errors are mainly originated from local oscillator's thermal noise leakage through the mixers. Offset errors are software calibrated by subtracting to the measurement, the correlation that is measured when two different matched loads are connected instead of the antennas.

$$Z_{r,i}^{(4)} = Z_{r,i\ measured}^{(5)} - Z_{r,i\ offset} \qquad \textbf{(8.5)}$$

In order to have a good radiometric accuracy, offset calibration is performed during a long period of time, usually on the order of 20-30 seconds, for which the radiometric sensitivity is about $\sigma_{\mu r,i} = 2\ 10^{-5}$. It has been noticed that the real channel has always a small positive offset, and the imaginary one a small negative one (figure 8.11). Measured offset drifts are very small, even for long measurement periods (figure 8.11). Peak-to-peak offset drifts are as small as $\Delta Z_r = 3\ 10^{-4}$ (ΔV_r=0.18 K) in one hour and a half.

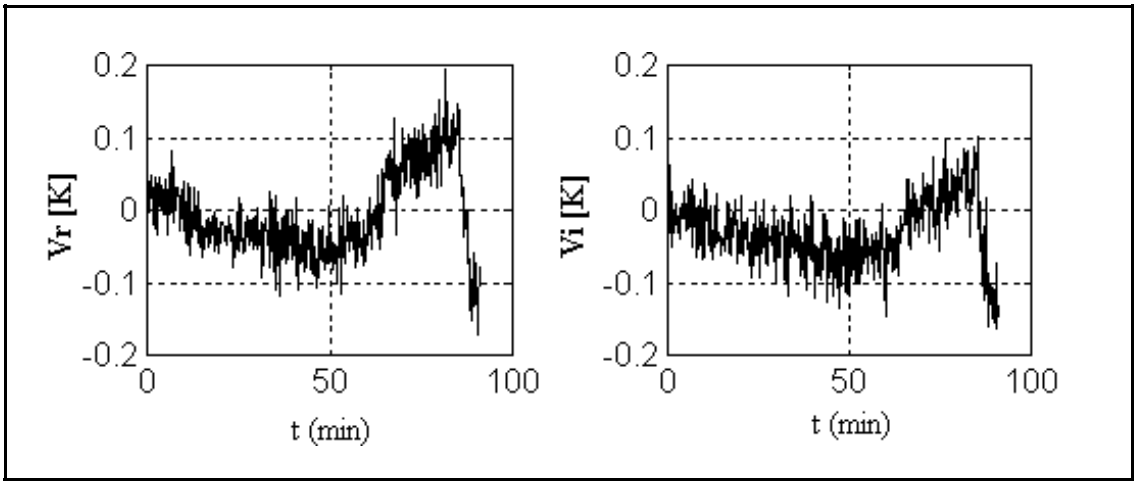

Figure 8.11.- *Real and imaginary offset drifts.*

Once offset errors are calibrated, the normalized correlation is obtained by using the non-linear relationship:

$$\mu_{r,i}^{(4)} \text{ ' } \sin\left(\frac{B}{2} Z_{r,i}^{(4)}\right) \qquad \textbf{(8.6)}$$

8.6.2.- Calibration of in-phase errors

In-phase errors are hardware calibrated by injecting correlated noise to both channels and by adjusting the phase with an X-band phase shifter inserted between the LO and a TV-DBS external unit (figures 8.1 and 8.2).

The injection of correlated noise is a major problem, since any passive power splitter with isolated outputs, i.e. a Wilkinson power divider, contains at least one resistor that also introduces correlated noise. In addition, the noise generated in the Wilkinson's resistance is in 0º-180º phase at its outputs and cancels the noise generated by a matched load connected at the Wilkinson's input. Therefore, it was necessary to built a X-band non-resistive power splitter (figure 8.2). However, since its outputs are not isolated, front-end inputs must be well matched in order to perform properly. In this way, the amount of noise that is reflected and then coupled to the other port through the non-isolated outputs of the power splitter is negligible and phase calibration is not perturbed by new offset terms.

At this point, the phase calibration routine allows the user to introduce the real and imaginary offsets, or to pick up the offset values that were previously measured. The correlation is then measured with typical integration times on the order of 3 seconds, and phase calibration is repeated until the measured imaginary part of the correlation is zero.

Mid-term system's phase stability is shown in figure 8.12. Anyway, during the measurement of a set of baselines system's phase stability is mainly degraded by the movement of the cables connecting the antennas to the front-end. Phase errors must be considered even if a pair of phase stable cables are used. In the next chapter, a procedure is described to track these phase variations, which are very important when forming synthetic images.

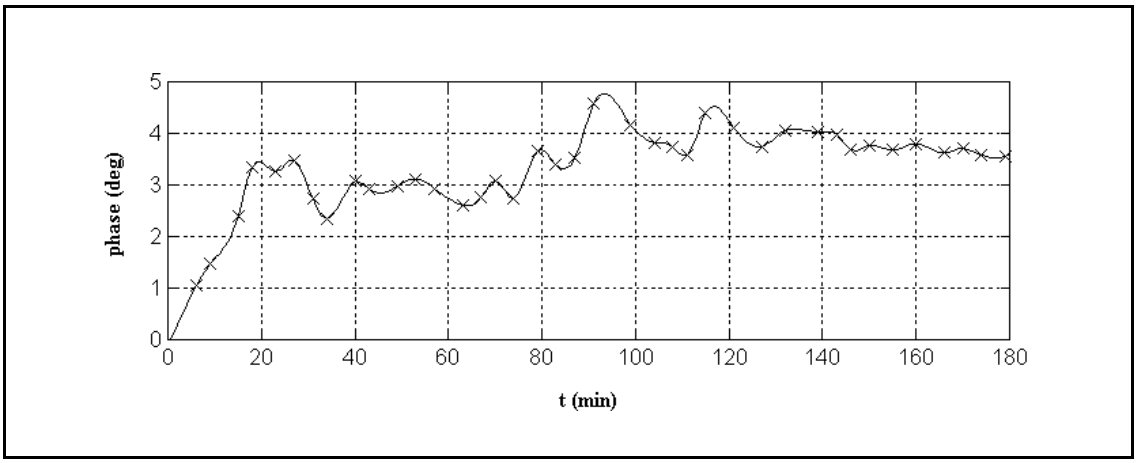

Figure 8.12.-*Measured phase drifts.*

8.6.3.- Calibration of amplitude and quadrature errors

As it is shown in chapter four, amplitude and quadrature errors appear as a consequence of mismatches in the channel's frequency response and differential errors in the sampling times in the comparators of the real and imaginary channels of digital correlators. In this section, *a new procedure is devised to characterize, measure and then calibrate overall system's amplitude and quadrature errors, neglecting their origin:* filters' response, correlators... . This technique consists on the measurement of the response of both real and imaginary channels when the phase of the phase-shifter (figure 8.1) is varied. In this situation, the theoretical real and imaginary correlations, should vary according to:

$$\mu_r^{(4)} \text{ ' } \mu_r^{(2)} \text{ ' } \mu_0 \cos(\ ) \text{N})$$
$$\mu_i^{(4)} \text{ ' } \mu_i^{(2)} \text{ ' } \mu_0 \sin(\ ) \text{N}) \qquad \textbf{(8.7)}$$

However, when amplitude and I/Q errors are present, the measured normalized correlations take the form $\mu_r^{(4)}$, $\mu_i^{(4)}$ (equations (4.52) and (4.53)):

$$\mu_r^{(2)} = \mu_{or}\cos(\theta) + g_r\,\mu_0\cos(\theta)$$

$$\mu_i^{(2)} = \mu_{oi}\sin(\theta) + g_i\,\mu_0\sin(\theta)$$

$$\mu_r^{(4)} = \mu_r^{(2)}; \qquad (\textit{calibrated by the phase shifter}) \tag{8.8}$$

$$\mu_i^{(4)} = g_i\mu_i^{(2)}\cos(2\varphi_q) - \mu_r^{(2)}\sin(2\varphi_q) \Rightarrow \mu_i^{(2)} = \frac{1}{g_i}\frac{\mu_i^{(4)} - \mu_r^{(2)}\sin(2\varphi_q)}{\cos(2\varphi_q)}$$

from which the calibrated correlations can be extracted. Figure 8.13 shows the plot of $(\mu_r^{(4)}, \mu_i^{(4)})$, continuous line, and that of $(\mu_r^{(2)},\mu_i^{(2)})$, dotted line. Unknowns have been found by adjusting the set of measurements to a circle by the least squares method. Prior to the optimization process g_r is set to 1, and μ_o is computed from the knowledge of the physical temperature of the matched load connected to the input of the non-resistive power splitter, and the previous measurements of the front-ends' noise temperature, including cables and connectors' losses. The overall quadrature error is about $2\varphi_q$=-5.55º, which is above the demodulator's quadrature nominal error because they are forced to work in a larger bandwidth, and the overall amplitude error has found to be g_i=0.96, which is within the predictions made in chapter 4 for the filters' and correlators' baseline amplitude error.

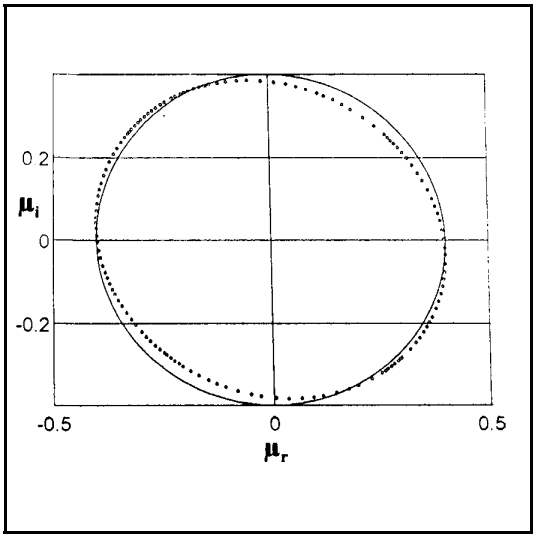

Figure 8.13.- *Graphical calibration of overall amplitude and quadrature errors.*

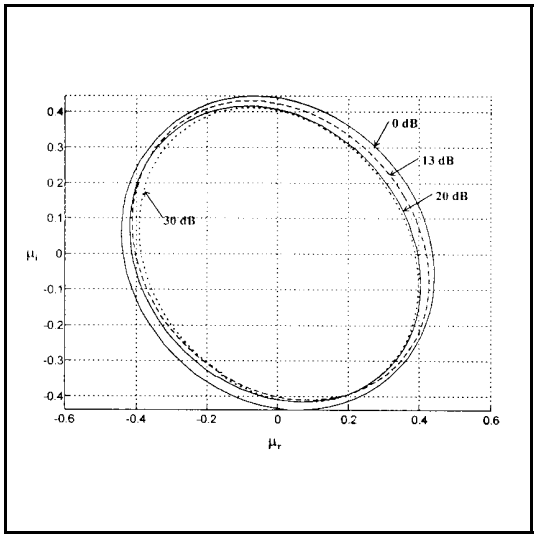

Figure 8.14.- *Uncalibrated $(\mu_r^{(4)}, \mu_i^{(4)})$ plot for different IF attenuations.*

The uncalibrated eccentricity diminishes from 1.13 down to 1.02. At present, it is not well known why it is not possible to calibrate completely the eccentricity, but it can be probably due to the fact that quadrature errors (figure 8.7) are not constant with frequency.

To validate the calibration method, and to test the robustness of the digital correlator unit versus signal's power level, the previous measurement has been repeated by inserting attenuators from 10 dB up to 30 dB at the IF stage. Results are shown in figure 8.14, and demonstrate that even when signals' level is strongly reduced, the correlator unit performs well and the ellipse preserves approximately its shape and orientation. However, ellipse's amplitude has decreased because signal's amplitude is too low to excite the comparators at each sampling time and some counts are missed. The slight deformation suffered by the ellipse, is mainly due to the impact of signal's level and comparators' threshold errors.

8.6.4.- Characterization of system's fringe-wash function

The fringe-wash function is the measurement of the decorrelation suffered from a signal when it is correlated when a delayed version of itself. It is related to the receivers' frequency response trough:

$$r_{12}(t) = \int_0^{\infty} H_1(f)\, H_2^*(f)\, e^{j2\pi f t}\, df$$

$$\tilde{r}_{12}(t) = r_{12}(t)\, e^{-j2\pi f_o t} \qquad \textbf{(8.9)}$$

The measurement of the fringe-wash response is performed by injecting correlated noise to both channels with the non-resistive power splitter. Different delays are generated by inserting different coaxial cables in the path of the i_1 baseband signal. These delays are measured with a reflectometer measuring the two-way delay introduced when a pulse train is injected.

Noise is generated with a Hewlett-Packard wide band noise source with a ENR=15dB [HP A], which is equivalent to a matched load at a physical temperature of:

$$T_{source} = \frac{1}{2} 290 \left(10^{15/10} - 1\right) \approx 4.440\, K \qquad \textbf{(8.10)}$$

The theoretical module of the normalized correlation at τ=0 is given by:

$$m = \frac{T_{source}}{\sqrt{T_{source} + T_{R_1}}\sqrt{T_{source} + T_{R_2}}} \approx 0.977 \qquad \textbf{(8.11)}$$

which is very close to unity.

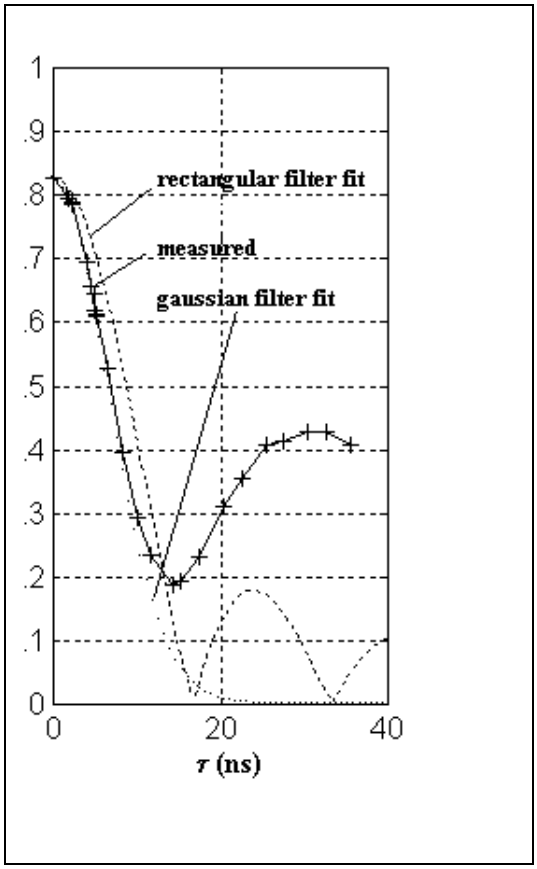

Figure 8.15.- *Measured fringe-wash function: i) measured module and gaussian/rectangular fits and ii) measured phase*

However, the measured correlation at the origin is much smaller, 0.827 (figure 8.15), coming from an absolute gain loss due to differences in the receivers' frequency response between the i_1-i_2 channels: $\mathbf{g_r}$=0.827/0.977=**0.846.** In addition, in section 8.6.3 it is found that the relative loss in the correlation between i_2-q_1 was g_i=1/0.96=1.04 times smaller than that between the i_1-i_2 channels, resulting in an absolute loss due to receivers' frequency response between the i_2-q_1 channels of: $\mathbf{g_i}$=0.846 0.96 = **0.812**. As studied in chapter four, it is found that for the decorrelation levels involved τ < 10 ns, the fringe-wash function is best fitted by a gaussian function (gaussian filters B=30 MHz), while for large delays, the secondary lobes are best fitted by a "sinc" function (rectangular filters B = 30 MHz). At present, the large amplitude of the secondary lobe shown in figure 8.15 is not well understood.

8.6.5.- Radiometric sensitivity characterization

Radiometric sensitivity is characterized with two tests:

i) Two matched loads are connected to front-ends' input the standard deviation is computed from a large set of measurements for different integration times and

ii) A matched load is connected to the input of the non-resistive power splitter producing correlated noise. Two adjustable attenuators are connected to power splitter's outputs producing uncorrelated noise and attenuating the correlated noise generated by the matched load. The complex correlation is then measured for different values of the attenuation and for different phases determined by the phase shifter. Results are checked with theoretical results to be validated.

8.6.5.1.- Radiometric sensitivity dependence on the integration time

Correlator's output when two different matched loads are connected to the inputs of the front-end must be zero except for small offset errors that drift very slowly and can be calibrated and thermal noise due to finite integration time. When the visibility sample is zero: V = 0 + j 0, the radiometric sensitivity is given by (equation (3.65)):

$$s_{V_{r,i}} = \frac{1}{\sqrt{\sqrt{2}\, B\, t_{eff}}} \sqrt{T_A + T_{R_1}} \sqrt{T_A + T_{R_2}} \qquad \textbf{(8.12)}$$

where: T_A = 290 K, T_{R1} = 120 K, T_{R2} = 90 K, B ≈ 30 MHz is obtained by adjusting the fringe-wash function by a gaussian function and for 1B/2L digital correlators the effective integration time is related to the integration time are related by (table 3.6):

$$t_{eff} = \frac{t}{2.46} \qquad \textbf{(8.13)}$$

With these parameters, equation (8.12) reduces to:

$$s_{V_{r,i}} = \frac{0.095\, K}{\sqrt{t}} \quad \text{or} \quad s_{m_{r,i}} = \frac{2.4 10^{-4}}{\sqrt{t}} \qquad \textbf{(8.14)}$$

Figures 8.16 and 8.17 show the normalized radiometric sensitivity of the real and the imaginary channels:

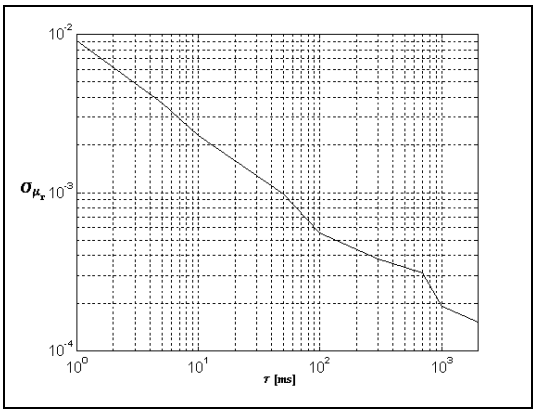

Figure 8.16.- *Radiometric resolution of the real part of the normalized visibility.*

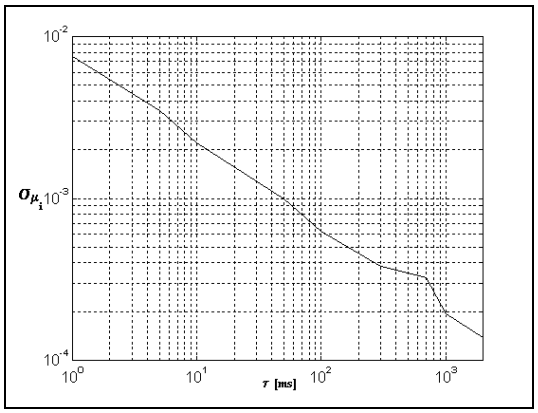

Figure 8.17.- *Radiometric resolution of the imaginary part of the normalized visibility.*

These plots are very well fitted by equation (8.14). Note that the error in the imaginary part of the normalized visibility is slightly smaller than that in the real part. However, to calibrate amplitude and I/Q errors, the imaginary channel must be multiplied by an 1.04 factor and, therefore, noise is amplified too.

At this point it should be remembered that these radiometric sensitivities correspond to a single baseline but, when forming synthetic radiometric images (chapter 9), uncalibrated system errors and antenna errors must be also taken into account.

8.6.5.2.- Experimental validation of the radiometric sensitivity figures

Figure 8.18 shows the test set-up used to perform sensibility measurements and to demonstrate that the instrument has the required radiometric sensitivity.

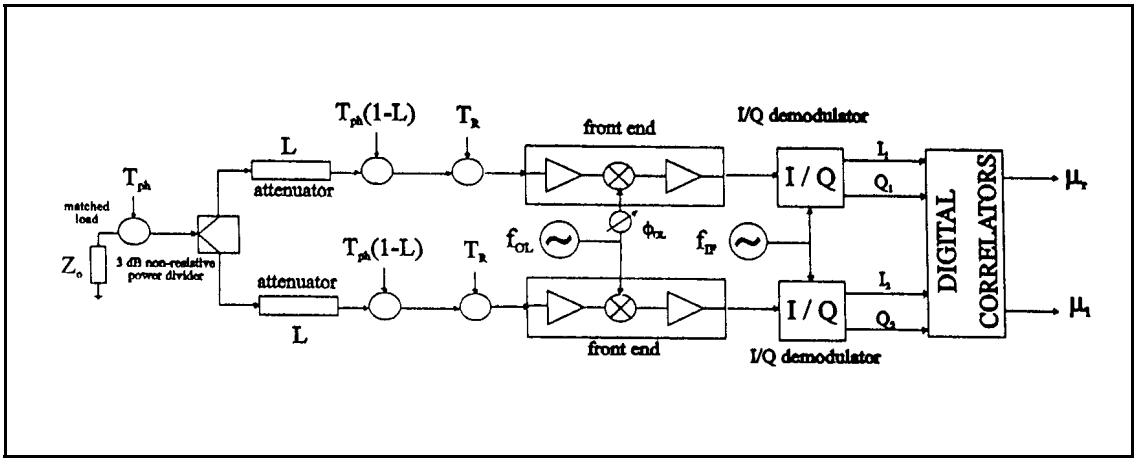

Figure 8.18.-*Sensibility measurements test set-up.*

A matched load injects correlated noise to the two channels by means of a 3 dB non-resistive power splitter. This correlated noise is further attenuated by two attenuators placed at each divider output that add their own uncorrelated noise to receivers' noise. System's output is then given by:

$$\mu_r = \frac{E[i_1 i_2]}{\sqrt{E[i_1 i_1]}\sqrt{E[i_2 i_2]}} = \frac{\frac{1}{2}T_{ph}L}{\sqrt{\frac{1}{2}T_{ph}L + T_{ph}(1-L) + T_{R_1}}\sqrt{\frac{1}{2}T_{ph}L + T_{ph}(1-L) + T_{R_2}}}\cos(N)$$

$$\mu_i = \frac{E[q_1 i_2]}{\sqrt{E[q_1 q_1]}\sqrt{E[i_2 i_2]}} = \frac{\frac{1}{2}T_{ph}L}{\sqrt{\frac{1}{2}T_{ph}L + T_{ph}(1-L) + T_{R_1}}\sqrt{\frac{1}{2}T_{ph}L + T_{ph}(1-L) + T_{R_2}}}\sin(N)$$

(8.15)

where $N = N_1 - N_2 + N_{OL}$ and N_i is the phase of the i^{th} channel and N_{OL} is the phase introduced by the phase shifter. If high values of attenuation are considered, the absolute correlate noise detected by the system is given by:

$$T_{corr} \approx \sqrt{m_r^2 + m_i^2}\ \sqrt{T_{ph} + T_{R_1}}\ \sqrt{T_{ph} + T_{R_2}} \approx \frac{1}{2} T_{ph} L \quad [K] \quad (L \gg 1) \qquad \textbf{(8.16)}$$

Figure 8.19 shows the theoretical sensitivity circles for 0, 10, 20 and 30 dB of attenuation for T_R = 100 K. For B = 30 MHz, τ = 5 s, and $T_{sys} = \sqrt{290\ \text{K} + 120\ \text{K}}\sqrt{290\ \text{K} + 90\ \text{K}} = 395\ \text{K}$, the radiometric sensitivity is given by:

$$\Delta T = \frac{T_{SYS}}{\sqrt{B\,(t\ /\ 2.41)}} = 0.05\ K \qquad \textbf{(8.17)}$$

$$|\Delta m| = \frac{\Delta T}{T_{SYS}} = 1.3\,10^{-4}$$

which sets the minimum module of the normalized visibility that can be measured.

Figure 8.20 shows the measured sensitivity circles for τ = 5 s. When the detected correlated noise is decreased the effect of radiometric resolution and system drifts are more important. System's drifts have a critical impact at 30 dB attenuation: in fact, the high eccentricity of figure 8.20d is due to an offset drift in the imaginary channel on the order of the magnitude being measured.

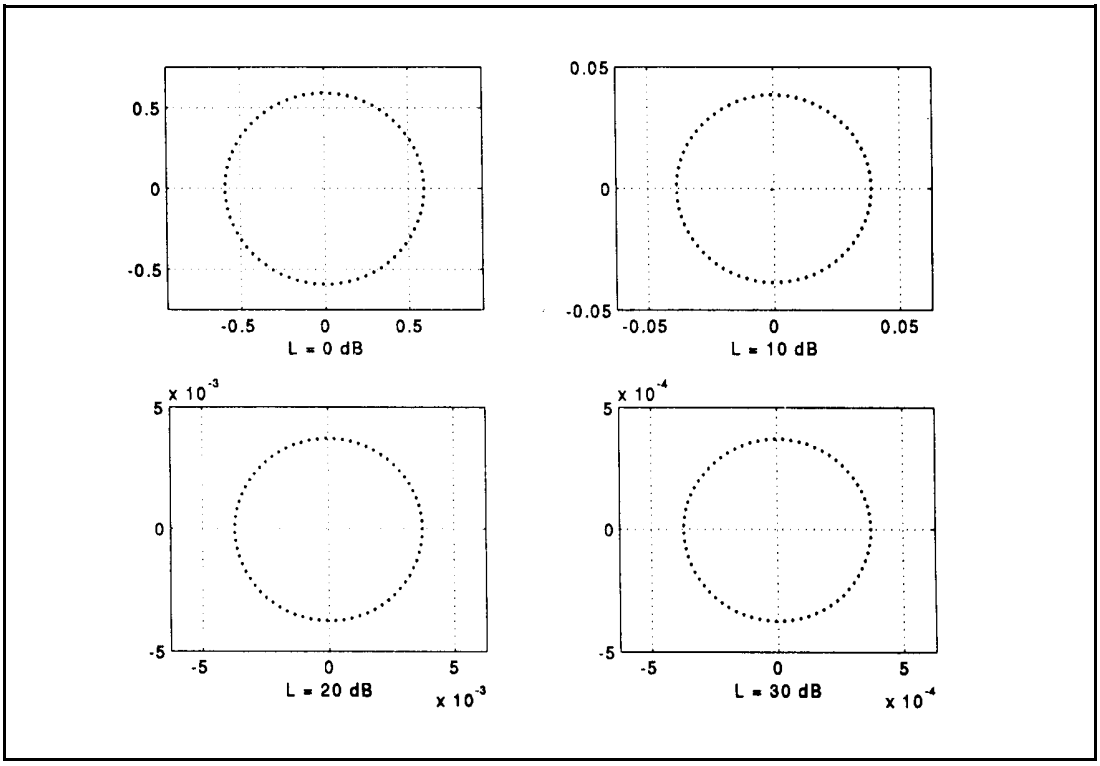

Figure 8.19.- *Theoretical sensibility circles.T_{R1}= T_{R2}=100 K, J = 4.*

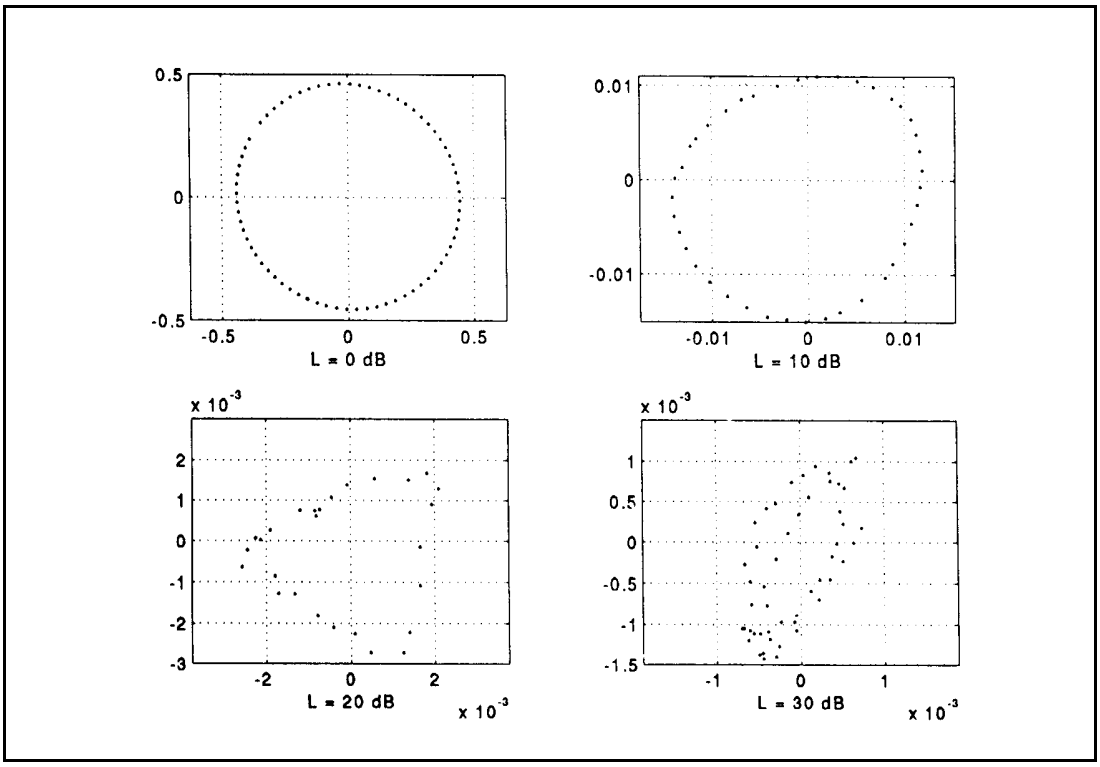

Figure 8.20.- *Measured sensibility circles.T_{R1}= 120 K, T_{R2}= 90 K, J = 5 s.*

8.7.- CONCLUSIONS

This chapter has presented a description of the basic hardware composing the interferometric radiometer. The description of some basic subsystems, such as power supplies, WR-75 to SMA and WR-75 to WR-90 transitions, or the mechanization and integration of all the subsystems in a portable instrument has been omitted.

Subsystems have been characterized pointing out the critical aspects and their influence in the overall system's performance, which has also been verified. At this point it is interesting to note that a new procedure to characterize and calibrate amplitude and phase errors in an interferometer baseline has been devised.

The result is a high sensitivity (differential) instrument:) I . 0.1 K for J = 1 s, reliable and easy to work with, as it has been demonstrated during the field measurements campaign (chapter nine), in which it has suffered from transportation shocks, long periods of continuous working and temperatures in the shade of 30 ºC. The complete integrated system is shown in figure 8.21.

Figure 8.21.- *Photograph of the complete interferometric radiometer.*

Chapter 9. EXPERIMENTAL VERIFICATION OF A 2D SYNTHETIC APERTURE INTERFEROMETRIC RADIOMETER

The first part of this chapter presents a review of the steps involved to obtain an apparent brightness temperature synthetic image: the initial hardware calibration and the calibration of phase drifts, the measurement sequence of the visibilities itself, the software calibration and the inversion of the set of visibility samples. Some of these steps have been previously explained in detail (chapter eight) or are special cases of more general calibration procedures (chapter six) and inversion algorithms (chapter five).

The second part is devoted to the measurement of the angular resolution of a 2D Synthetic Aperture Interferometric Radiometer. Experimental results are checked with the theoretical ones obtained in chapter three.

Finally the third part of this chapter presents a set of synthetic brightness temperature images of artificial and natural test scenes obtained with this hardware. One of this measurements is performed inside an anechoic chamber (constant brightness temperature). Errors in the reconstructed image agree with the radiometric accuracy budget performed in chapter four.

9.1.- OBTAINING AN APPARENT BRIGHTNESS TEMPERATURE IMAGE

9.1.1.- Calibration of the visibility samples

Offset errors are mainly generated by local oscillator leakage through the mixers and are calibrated by subtracting to each measurement the correlation obtained when the antennas are replaced by two matched loads.

$$Z_{r,i}^{(4)} = Z_{r,i\ measured}^{(5)} - Z_{r,i\ offset} \qquad \textbf{(9.1)}$$

Since peak-to-peak offset drifts are very small, on the order of 0.18 K (figure 8.11) these calibration values hold during all the measurement process.

Phase is initially hardware calibrated by injecting correlated noise generated by a matched load connected to a non-resistive power splitter whose outputs are connected instead of the antennas. Phase is adjusted by means of a phase shifter inserted between the first local oscillator and the mixer of a channel.

However, the phase drifts from the initial calibration values due to several reasons:
i) each time the "phase-stable" cables connecting the antennas to the external units are bent, phase varies several degrees,
ii) there are phase variations introduced each time cables are unplugged to replace the non-resistive power splitter by the antennas, or when the antennas are slid along the Y-arms, and
iii) by the instrumental drifts themselves (figure 8.12).

Phase drifts are calibrated by means of a "polarimetric hot point" consisting in a matched load connected to a 26 dB gain X-band amplifier connected itself to a pyramidal horn located right in front of the center of the Y-array. Once the offset is calibrated, the alignment of the "hot point" is performed by measuring the normalized correlation for two antenna positions aligned horizontally and vertically and finding its maximum. The photograph in figure 9.17 shows this configuration. Then, at each baseline a measurement with the X-band amplifier connected is performed. From this measurement the phase of the visibility sample is extracted and then subtracted from the next measurement.

When due to the geometry of the scene being imaged, it is not possible to locate the "hot point" right in the center of the field of view, the previous procedure is followed, as before, but an additional phase term $+2\pi\ (u\ \xi_o + v\ \eta_o)$ is added to the phase-calibrated visibility samples to account for the off-boresight position of the "hot point". The position (ξ_o, η_o) of the "hot point" is determined by direct hexagonal inverse Fourier Transform of the visibility samples used for calibration. The impulse response obtained in this way is blurred because of phase drift errors, but its maximum is very close its true position (section 9.2).

$$m_{r,i}^{(4)} = \sin\left(\frac{p}{2} Z_{r,i}^{(4)}\right) \qquad \textbf{(9.2)}$$

$$m^{(3)} = m^{(4)}\, e^{-j\Phi_{cal}(u,v)}\, e^{+j2p\,(ux_0 + vh_0)}$$

Amplitude mismatches and quadrature errors are calibrated according to equation (8.8):

$$m_r^{(2)} = m_r^{(3)} \qquad \textbf{(9.3)}$$

$$m_i^{(2)} = \frac{1}{g_i} \frac{m_i^{(3)} + m_r^{(3)} \sin(q_q)}{\cos(q_q)}$$

Finally, visibility samples are **denormalized** by multiplying by the channel gain factors:

$$V^{(1)} = g_1 g_2 \mu^{(1)}$$
$$g_1 = \sqrt{T_A + T_{R_1}} \; ; \quad T_{R_1} = 120K \tag{9.4}$$
$$g_2 = \sqrt{T_A + T_{R_2}} \; ; \quad T_{R_2} = 90K$$

and the zero-baseline is set as:

$$V(0,0) = T_A \tag{9.5}$$

The antenna temperature must be measured with a total power radiometer or a Dicke one, which was not available at the time these measurements were done. Except for the measurement performed inside the anechoic chamber, T_A is estimated from an image obtained for $T_A = 0$ K, depending on the portion occupied in the image by the sky and by the Earth, whose apparent brightness temperatures can be estimated. T_A usually ranges from 200 K to 300 K.

At this point, an appropriate window is computed to tapper the visibility samples. As in the error analysis and inversion methods, the Blackmann window is preferred over the rest because it is the one with the lowest secondary lobes. The rectangular one, even though has the highest spatial resolution, produces low-quality images because of the high secondary lobes that generate artifacts in the reconstructed image.

$$W^{Bl.}(u,v) = 0.42 + 0.5\cos\left(\pi \frac{D}{D_{\max}}\right) + 0.08\cos\left(2\pi \frac{D}{D_{\max}}\right) \; ; \; D = \sqrt{u^2 + v^2} \tag{9.6}$$

Finally, since fringe-washing effects are completely negligible $B/f_0 = 0.3$ % and there is only a pair of antenna patterns, visibility samples are inverted simply with the hexagonal inverse Discrete Fourier Transform explained in chapter six.

$$T_B = N_T^2 \frac{\sqrt{3}}{2} d^2 \frac{F_H^{-1}\left\{ W^{Bl.} V^{(1)} \right\}}{F_{n_1} F_{n2}} \tag{9.7}$$

9.1.2.- Measurement Sequence

Figure 9.1 shows the measured (u,v) points (asterisks) and the (u,v) samples obtained by the hermiticity of the visibility function (dots) for a Y-array of $N_{EL} = 10$ antenna positions per arm spaced $d = 0.89\,\lambda$. It also shows the set measurements used to cover the (u,v) domain with a minimum number of changes of the antennas (plugging-unplugging). The measurement sequence is summarized below. Antenna positions are counted from the center of the Y.

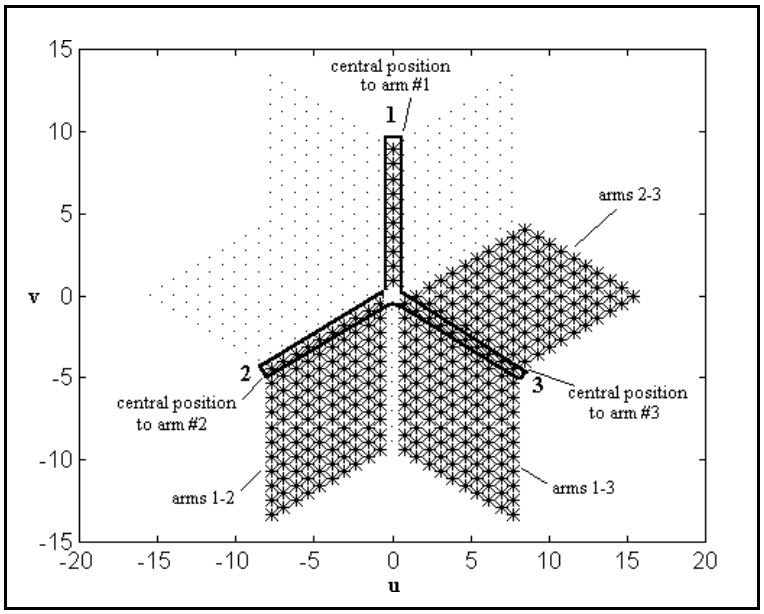

Figure 9.1.- *(*) Measured (u,v) samples and (.) (u,v) samples obtained by hermiticity for NEL=10 antennas per arm spaced d=0.898*

i) With antenna 1 in arm 1, position 1, all the correlations with antenna 2 in arm 3, positions from 1 to N_{EL}, are measured.
ii) Repeat (i) with antenna 1 in arm 1, positions 2, 3, 4... N_{EL} and antenna 2 in arm 3.
iii) Repeat steps (i) and (ii) moving antenna 1 along arm 2 instead.
iv) Repeat steps (i) and (ii) with antenna 1 slid along the first arm and antenna 2 slid along the second arm.

v) With antenna number 1 in the center and antenna number 2 in arms 1, 2 and 3 respectively measure all the possible correlations lying along the Y-arms.

For each position at least two measurements are made, the first for phase calibration by turning on the "polarimetric hot point", and the second one to measure the apparent brightness temperature distribution by turning off the "hot point". Usually a second redundant measurement is performed to check information's integrity.

9.2.- EXPERIMENTAL VERIFICATION OF INTERFEROMETER'S ANGULAR RESOLUTION

The impulse response of a Y-shaped two-dimensional interferometric radiometer is theoretically studied in chapter three. In this section the experimental results obtained by measuring noise point sources are presented and compared to the theoretical ones. As in antenna theory, the far-field condition is given by (22.5º phase error due to the spherical wave-front):

$$l \;'\; 2\frac{D^2}{8}\;13.6\;m \qquad \textbf{(9.8)}$$

where D the maximum baseline distance, D = 15.6 8, and 8 = 2.8 cm at 10.7 GHz. Since this condition can not be satisfied in laboratory conditions, one of the antennas is placed right in the center, and it is used for phase calibration as explained in section 9.1, while the other is touching the first one.

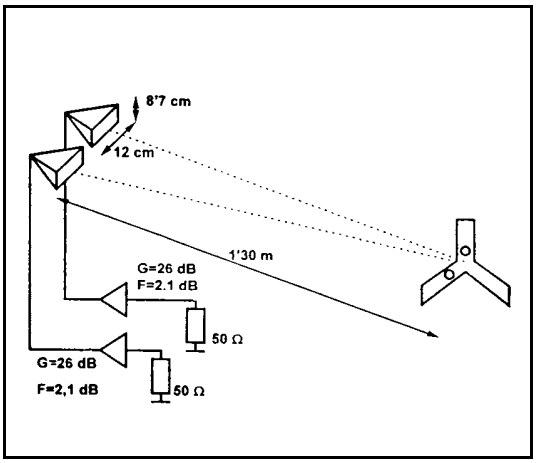

Figure 9.2.- *Near-field experimental setup for angular response measurement.*

In this way, the image is focused in the center of the field of view and signals coming from the both noise sources are focused. The experimental setup is shown in figure 9.2, for which the angular spacing between the point sources is:

$$) 2 ' \frac{12\,cm}{130\,cm} ' 5.29^{o} \qquad \textbf{(9.9)}$$

In order to distinguish both sources, their angular spacing must be larger than the interferometer's half-power synthesized beam-width. It is found that the minimum number of antenna positions per arm is N_{EL}=10 with d = 0.89 8 spacing for the Blackmann window and N_{EL} = 7 with d = 0.89 8 spacing for the rectangular window. Table 9.1 shows the main properties of the equivalent arrray factor for the rectangular and the Blackmann window.

	Rectangular window: theoretical $)2_{-3dB}$	**Rectangular window measured $)2_{-3dB}$**	**Blackmann window: theoretical $)2_{-3dB}$**	**Blackmann window: measured $)2_{-3dB}$**
N_{EL}= 10	3.21º	3.17º	4.75º	4.70º
N_{EL}= 9	3.55º	3.52º	5.27º	5.21º
N_{EL}= 8	3.99º	3.94º	5.91º	5.84º
N_{EL}= 7	4.54º	4.49º	6.73º	6.66º
N_{EL}= 6	5.20º	5.22º	7.82º	7.74º

Table 9.1.- Half-power synthesized beamwidth for different windows and different number of antenna positions per arm spaced d=0.89 8. Point sources angular spacing: 5.17º

Figures 9.3 to 9.7 show the measured response of the two-point scene. The 0 = 0 cut clearly shows the effect of beam broadening due to the smaller synthesized effective area because of the smaller number of antenna positions per arm. The agreement between theoretical and measured half-power synthesized beamwidths is shown in table 9.1. Measured Side Lobe levels also agree very well with the theoretical values: measured SLL are 7.9 dB and 15dB for the rectangular and Blackmann windows, while the corresponding theoretical values are 8.6 and 16.5 dB.

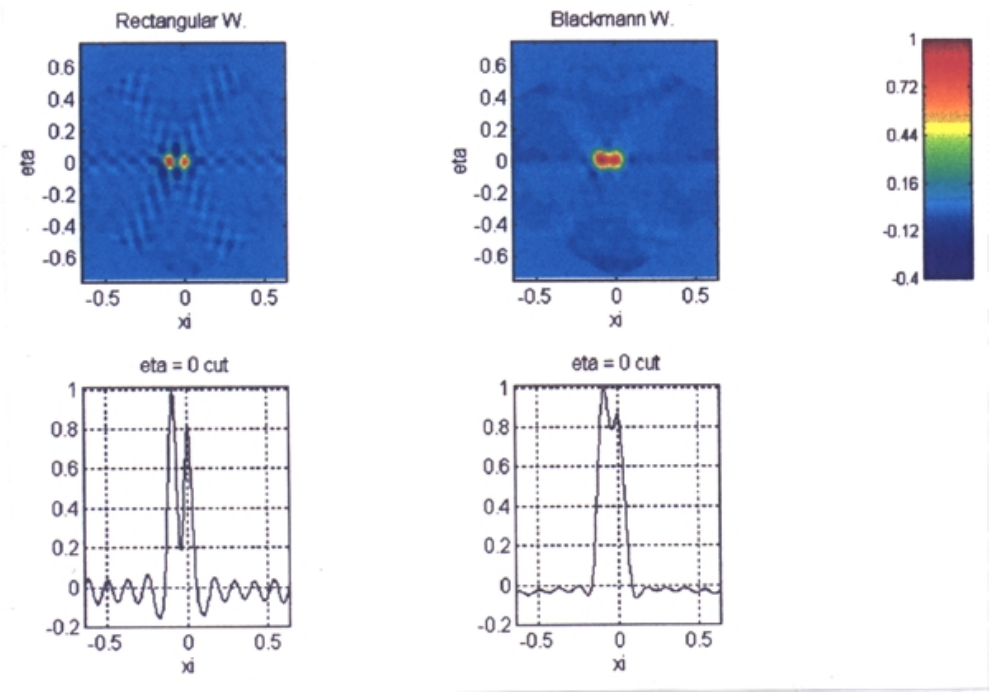

Figure 9.3.- *Measured response of two-point sources. N_{EL}=10 antenna positions per arm, d=0.89 λ spacing between antennas.*

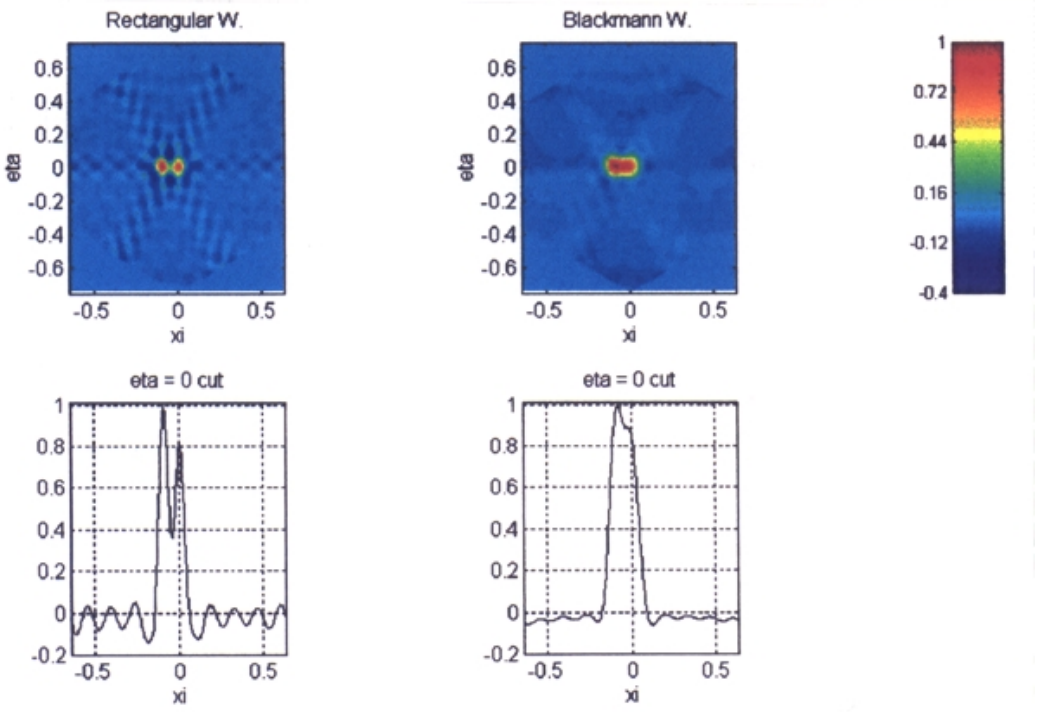

Figure 9.4.- *Measured response of two-point sources. N_{EL}=9 antenna positions per arm, d=0.89 λ spacing between antennas.*

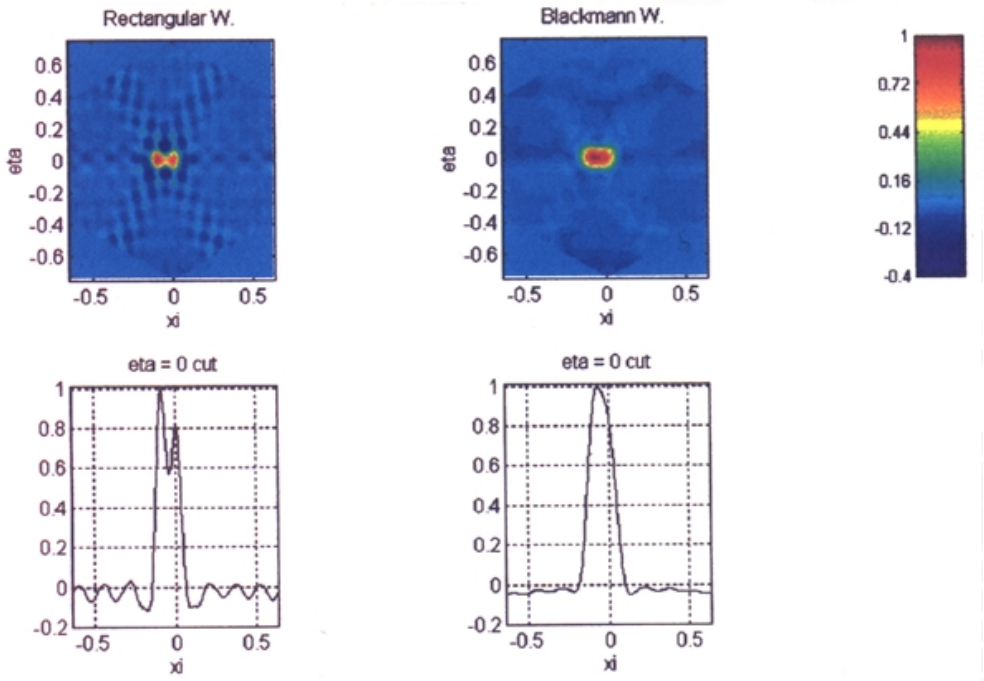

Figure 9.5.- *Measured response of two-point sources. N_{EL}=8 antenna positions per arm, d=0.89 λ spacing between antennas.*

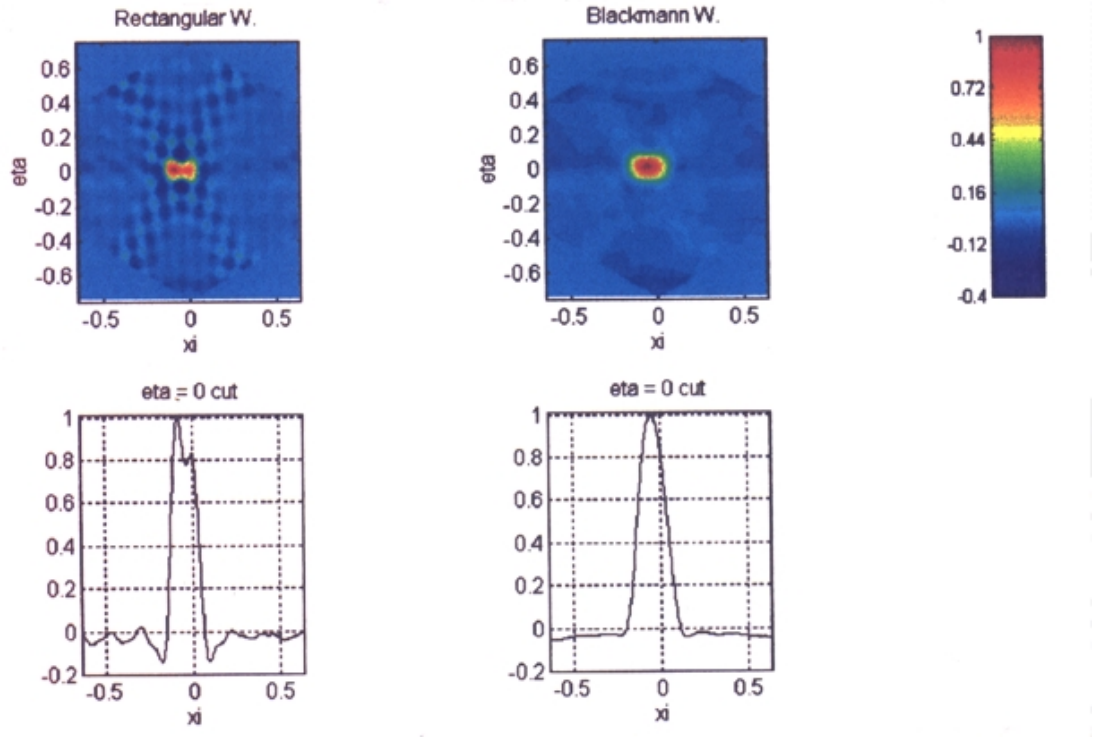

Figure 9.6.- *Measured response of two-point sources. N_{EL}=7 antenna positions per arm, d=0.89 λ spacing between antennas.*

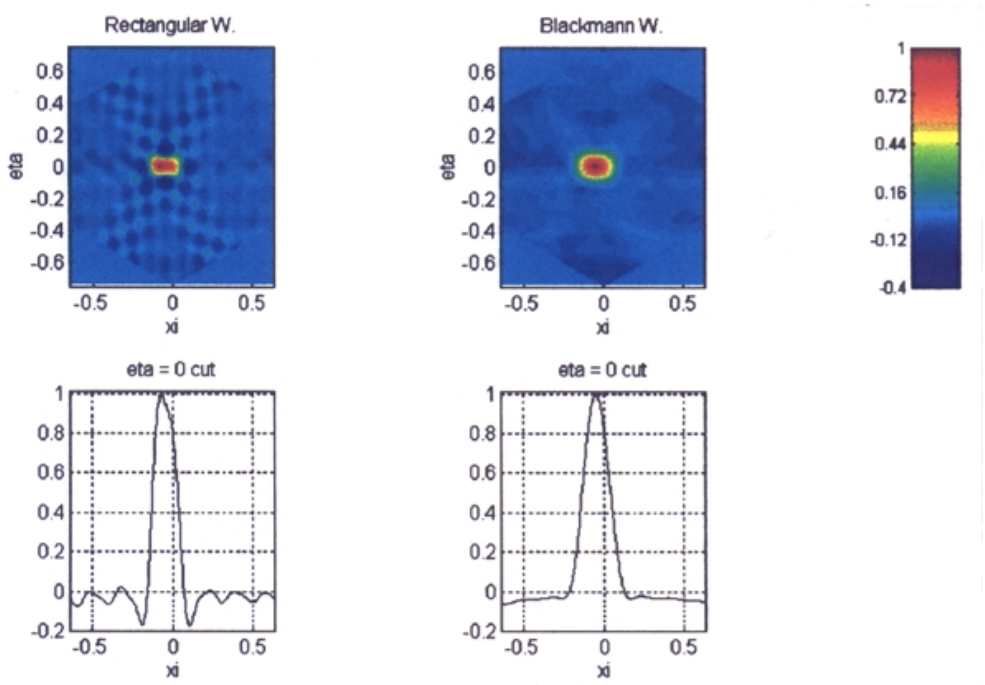

Figure 9.7.- *Measured response of two-point sources. N_{EL}=6 antenna positions per arm, d=0.89 8 spacing between antennas.*

9.3.- FIELD MEASUREMENTS CAMPAIGN

9.3.1.- Artificial Scenes

The field measurement campaign demonstrates the passive 2D-aperture synthesis concept with artificial and natural scenes with contrasts much smaller than those of the "hot points" used to measure the impulse response. Two types of artificial test scenes are shown:

i) the first one consists in the measurement inside a closed anechoic chamber of the set of visibility samples and then, the generation of the synthetic apparent brightness temperature distribution with the antenna temperature known to be the physical temperature of the anechoic chamber. This test image is used to analyze the generation of errors in the imaging process including uncalibrated errors, residual calibration errors and errors induced in discretization and inversion processes.

ii) the rest of these measurements are metallic forms over a 45º inclined plane of microwave absorbers reflecting the sky radiation plus the atmospheric downwards contribution. Metallic forms are constructed with adhesive aluminum paper glued to shaped cardboards.

9.3.1.1.- Artificial Scene No 1:
Measurement inside an Anechoic chamber: Image Error Generation

When the interferometer is put inside an anechoic chamber, microwave absorbers act as a black body: the antenna temperature is equal to the physical temperature of the absorbers and the apparent brightness temperature is constant in all directions. Consequently, all the visibilities should be zero, except for the zero baseline. However, the error sources studied in chapter four, as well as residual calibration errors in the visibilities lead to a non-constant apparent brightness temperature. This scene is then used to verify overall system's performance, including the calibration and the inversion algorithms. The radiometric accuracy budget for the interferometric radiometer can be summarized as follows:

- Discretization error:	0.13 K
- Finite integration time error:	0.61 K N_{EL} = 10, τ = 2s, Blackmann window
- Amplitude error:	1.00 K 2 % residual eccentricity
- Phase error:	0.83 K 2^{o} residual phase error
- In-plane position errors:	0.18 K 1 mm positioning error
Predicted radiometric accuracy:	**1.45 K rms**

while the **standard deviation** computed from the **reconstructed image** shown in figure 9.8 in the alias free FOV is: **1.73 K**, and peak errors are: ΔT_{max}= 4.1 K and ΔT_{min} = - 4.9K. This value agrees within a 20% with the predicted one, which does not include uncalibrated coupling effects.

9.3.1.2.- Artificial Scene No 2:
Inverted metallic "L" with small metallic square over microwave absorbers

The following results are presented showing three images: a photograph of the scene being imaged on the left side, on the upper right side the alias free field of view reconstructed image, AF-FOV $\approx \pm 17^{o}$, and the complete synthesized image including the aliased regions in the lower right side. As it is shown later, in some images the alias-free field of view can be partially extended when there are sky regions overlapping with Earth regions.

Figure 9.9 shows a metallic inverted "L" with a metallic small square underneath. The high contrast presented between the apparent brightness temperature of the microwave absorbers and the sky, on the top, or the sky radiation reflected on the metal plates is very noticeable. Note also the temperature decrease in the right side due to the edge of the absorbers, and in the center due to the small hole between them.

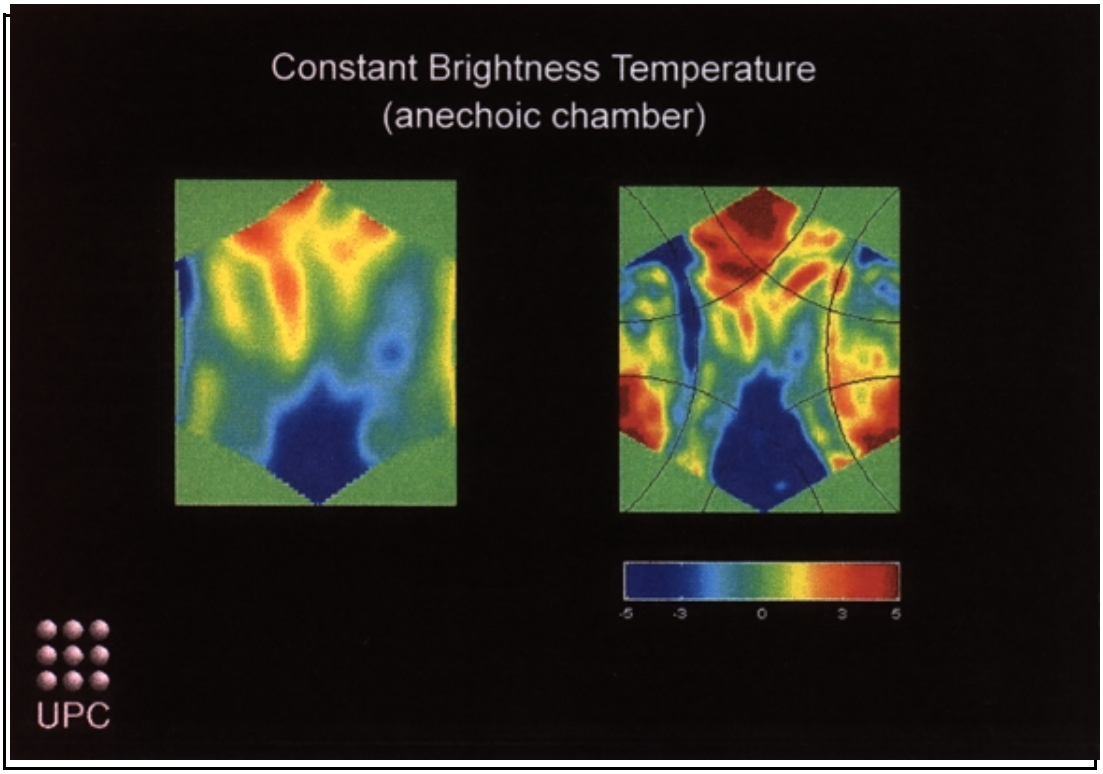

Figure 9.8.- *Artificial Scene No 1: Measurement inside an Anechoic chamber: Generation of errors. T_A=298K, N_{EL}=10, d = 0.89 λ*

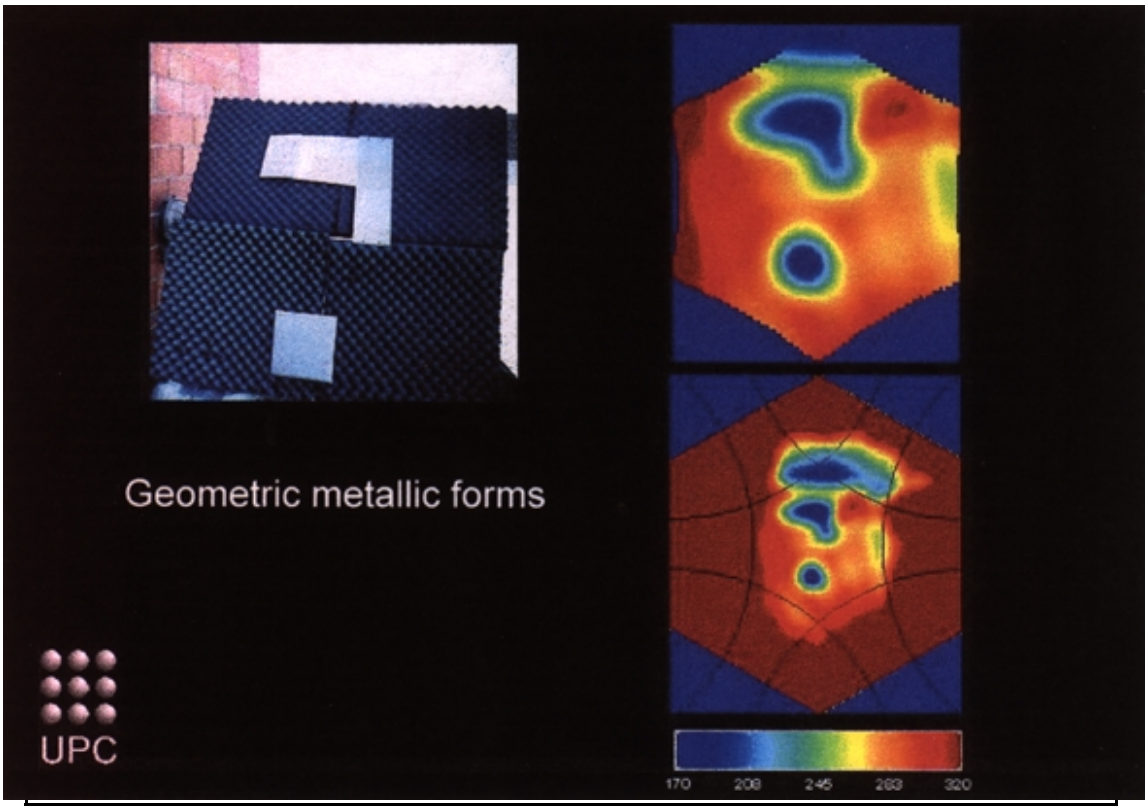

Figure 9.9.- *Artificial Scene No 2: Inverted metallic "L" with small metallic square over microwave absorbers. N_{EL} = 10, d = 0.89 λ.*

9.3.1.3.- Artificial Scene No 3:
Metallic frame over microwave absorbers

The photography of figure 9.10 shows a metallic frame over microwave absorbers. One of the Y-arms of the array can be seen on the bottom right side of photograph.

In the reconstructed brightness temperature image, in the upper side, it can be appreciated the lower temperature of the sky and also a sky reflection from a metallic hook of the wooden table used to support the microwave absorbers. Note that the apparent temperature in the aliased region under the frame is low because there are sky contributions adding, while in the left and right sides there overlapping contributions of the absorbers. In addition, note also that the "tails" of the left side alias region are more important because of the high brightness temperature of the brick wall compared to the sky temperature in the right side.

9.3.1.4.- Artificial Scene No 4:
Metallic cross over microwave absorbers

Figure 9.11 shows a photography of a metallic cross over microwave absorbers. In this scene the dimensions of the cross are much larger than the spot of the synthesized beam in order to observe the definition of contours and to test how constant is the reconstructed image inside the cross.

In the alias free reconstructed image it can be appreciated that the apparent brightness temperatures both in the metallic cross and in the absorbers is quite uniform, as expected, except for the alias tails in the left side due to the high brightness temperature of the brick wall.

In the complete reconstructed brightness temperature image, at the end of the right arm of the cross, it can be appreciated the edge of the microwave absorber, as well as in the upper side it can also be appreciated the contour formed by the contrast between the apparent brightness temperature of the microwave absorbers and that of the sky.

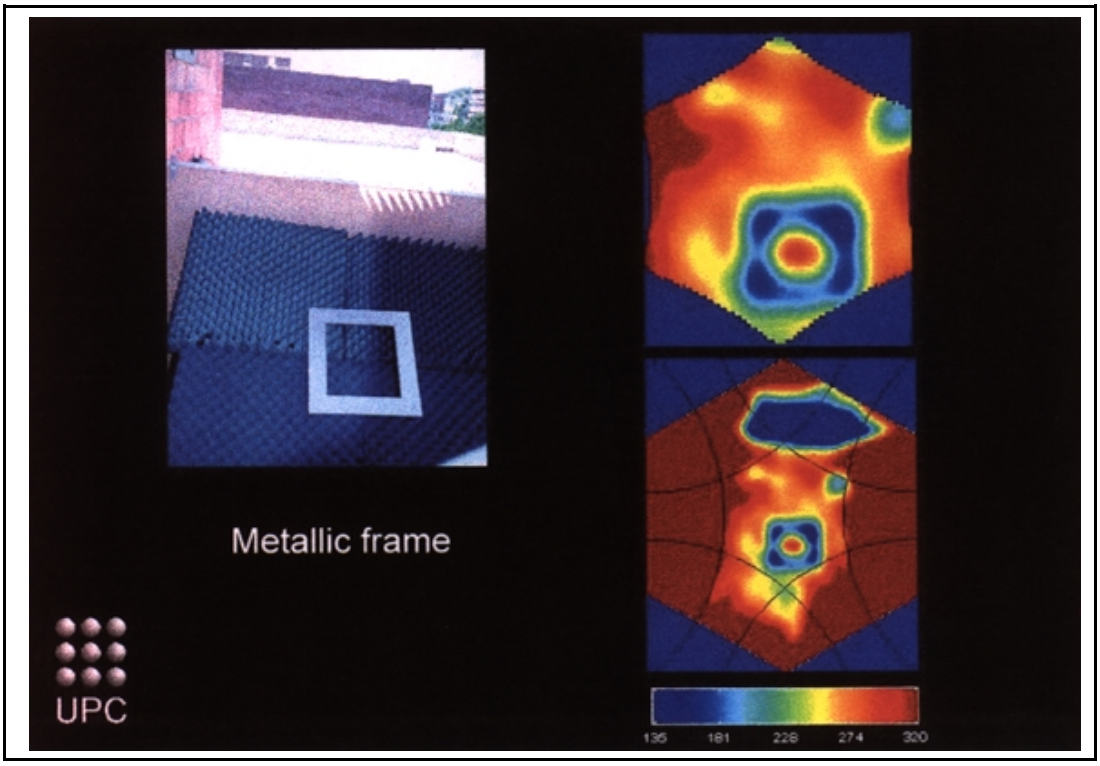

Figure 9.10.- *Artificial Scene No 3: Metallic frame over microwave absorbers.* N_{EL}*=10, d =0.898*

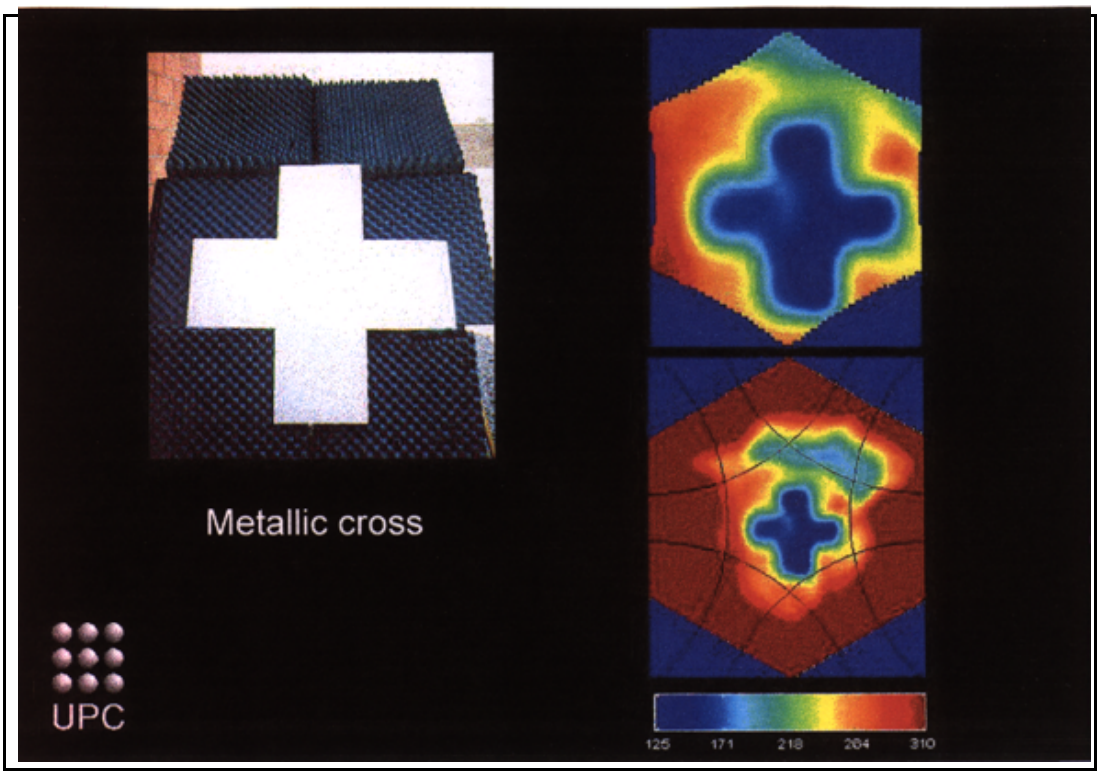

Figure 9.11.- *Artificial Scene No 4: Metallic cross over microwave absorbers* N_{EL}*= 10, d = 0.89 8*

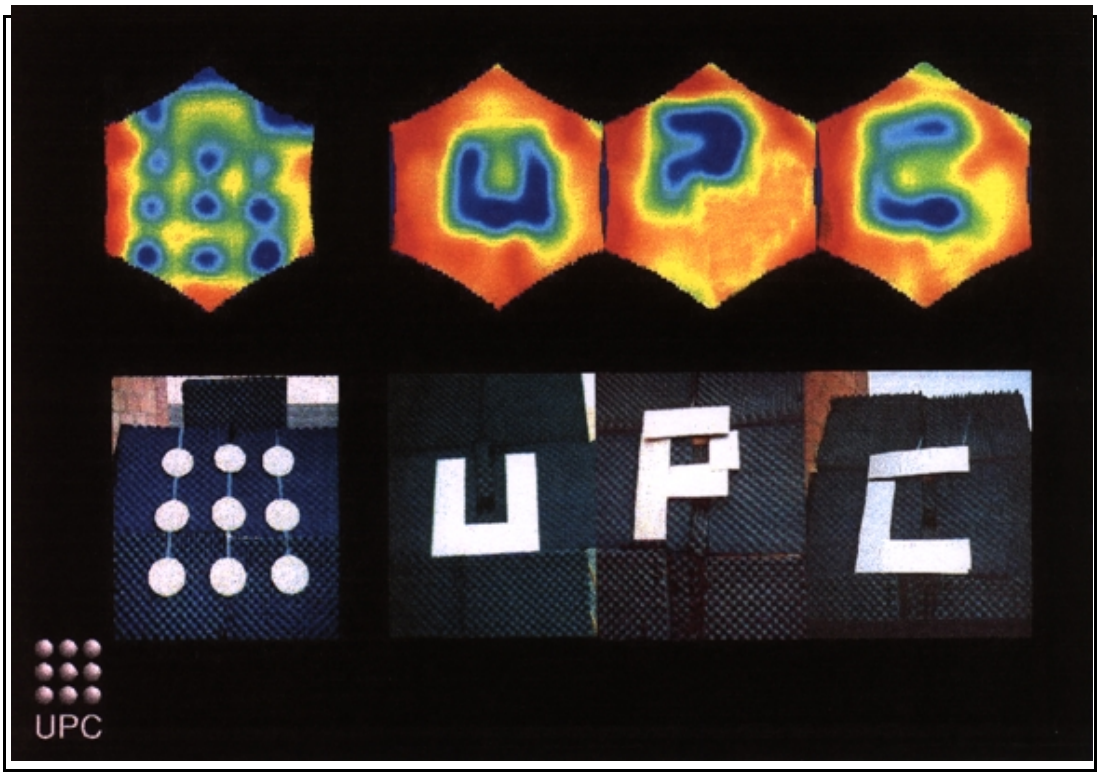

Figure 9.12.- *Artificial Scene No 5: Metallic UPC logo and acronym over microwave absorbers.* $N_{EL}=10$, $d=0.89\,\lambda$

9.3.1.5.- Artificial Scene No 5: Metallic UPC logo and acronym over microwave absorbers

The bottom side of figure 9.12 shows the logotype of the Polytechnic University of Catalonia and its acronym "UPC" formed with metallic pieces. In the upper side there are represented the four recovered brightness temperatures images. Each sign has been imaged in a single measurement since for the alias free FOV, about ±17º, and the 4.75º synthesized half-power beamwidth, alias free images are formed by about 7 x 7 independent pixels, from the N_T x N_T = 31 x 31 original ones ($N_T = 3\,N_{EL} + 1 = 31$).

The balls in the lowest side of the UPC logotype were designed to be 17 cm of diameter, just the size of the spot of the half-power synthesized beamwidth at the distance of 2 meters. The upper balls are of the same size but, as they are more distant, they are observed under a smaller angle and they are resolved more poorly. In the recovered image note the shape of the microwave absorber that is outstanding in the upper side.

As in the previous images, in the images showing the letters "U", "P" and "C" it can be observed the border between the apparent brightness temperature of the microwave absorber and that of the sky.

9.3.2.- Natural Scenes

As natural scenes we have imaged landscapes and buildings seen from the Campus Nord of Polytechnic University of Catalonia, Barcelona. In this section five successfully recovered synthetic images are presented, as well as two other ones that suffered from interferences when the interferometer was pointing to two different microwave relays.

9.3.2.1.- Natural Scene No 1: Water tank and mountain

Figure 9.13 shows a water tank over the mountain located in the right side of the photograph. On the right side of figure 9.13 it can be observed the recovered alias free FOV and the complete synthetic images corresponding to the previous photograph. It should be noted that this image has been obtained with the Y-array with 5 antenna positions per arm and the spatial resolution is poorer than before) 2^{syn}_{-3dB} = 9.35º.

This synthetic image is a clear example in which the alias free FOV can be extended beyond the strict limits imposed by the unit circle repetition. In figure 9.13c the ground-sky border can be easily appreciated. From left to right: a descent due to the brick building, an ascent due to the mountain, a hot spot in the center probably due to building, another ascent due to the mountain and, already in the aliased region, a flat summit with a small peak due to the water tank and then another ascent due to the mountain.

9.3.2.2.- Natural Scene No 2: Sta. Caterina de Siena Street and Collserola mountain range

Figure 9.14 shows a photograph of a landscape of the Collserola mountain range which limits Barcelona at the West. This image has been synthesized from the Y-array configuration with N_{EL}= 5 antenna positions per arm, spaced d=0.89 8. In the alias free synthetic image on the right side it can be appreciated how the brightness temperature map follows the mountain-sky border. Two clear spots can be appreciated in the left side. They are due to two houses with inclined slate roofs reflecting the downwards radiation from the sky. In fact, in the photograph of 9.14 only one of these two houses is shown, but they can be seen in figure 9.18. In the right side of Sta. Caterina de Siena Street (vertical in the photograph) there is another house with an inclined roof, appearing as a cold spot in the synthetic image. The vegetation in the mountains and the street appear at a higher apparent brightness temperature.

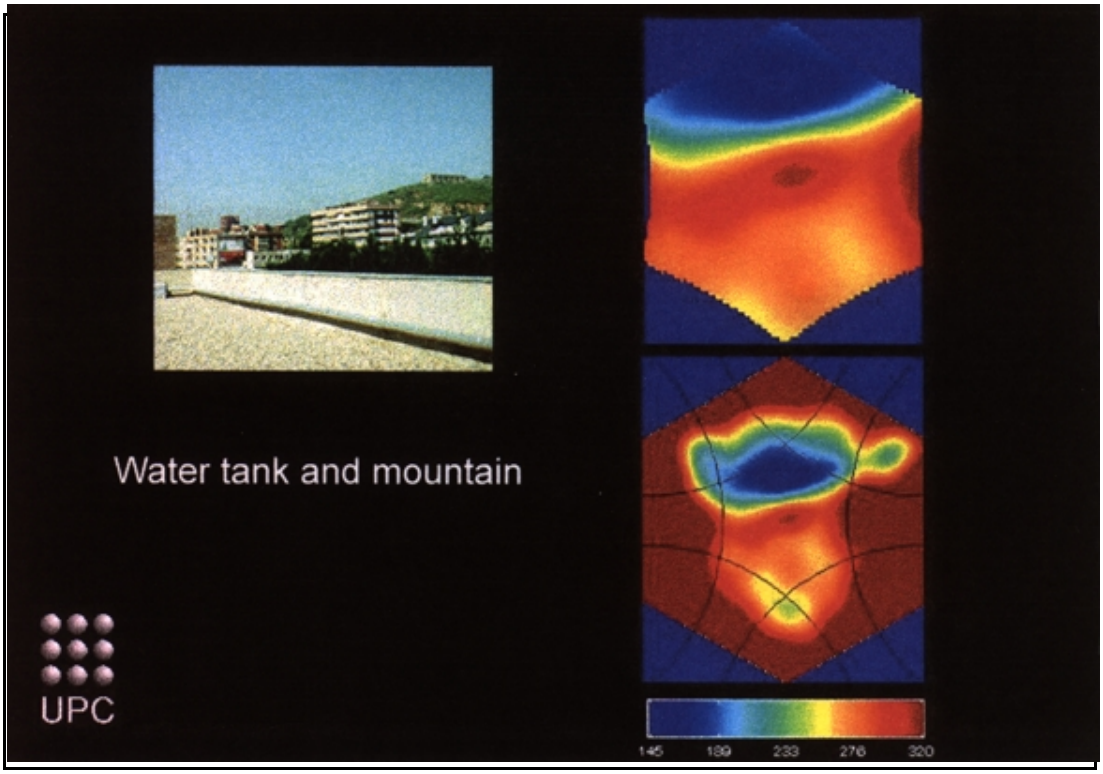

Figure 9.13.- *Natural Scene No 1: Water tank and mountain.N_{EL} = 5, d = 0.89λ*

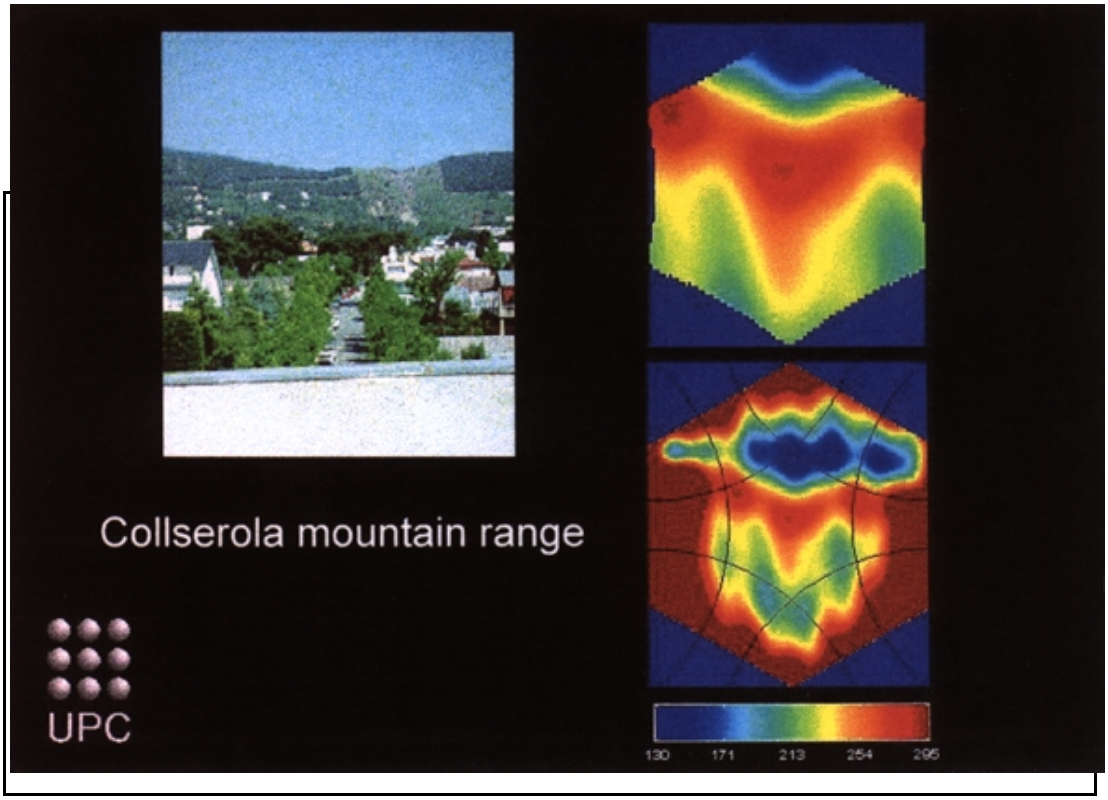

Figure 9.14.- *Natural Scene No 2: Sta. Caterina de Siena Street and Collserola mountain range N_{EL}=5, d=0.89λ*

9.3.2.3.- Natural Scene No 3:
UPC Campus Nord: roof of building D4 seen from D3's roof

Figure 9.15 shows the roof of building D4 seen from the roof of building D3. This is a quite complex image because the building-sky contour has more details and there are metallic parts over the roofs: air conditioning systems, pipes, antennas... However, in the alias-free synthetic image the building-sky contour is appreciated, from left to right: a peak due to next building's penthouse, a descent in the middle, and in the right side and ascent due to the part of D3's penthouse being imaged. Note in the upper right side the step in the brightness temperature following the step in the building.

The brightness temperature in the lower zone is not as uniform as it is in other images because the variety of materials found over the roofs: metals, woods, bricks and stones. The cold spot that is clearly appreciated in the middle is probably due to the air conditioning systems of the next building.

9.3.2.4.- Natural Scene No 4:
UPC Campus Nord: roof of buiding C3 seen from D3's roof

Figure 9.16 shows the roof of building C3 seen from the roof of building D3. In the reconstructed synthetic image there is a straight horizontal line: the building-sky contour, only interrupted by the ventilation tower on the right side. The three small chimneys on the left side occupy an angular spacing of the half-power synthesized beamwidth and are not resolved by the system, not even as a single point, because of the mixture with the sky.

This simple image clearly shows that the alias-free region can be extended, since in the left and right sides there are only sky regions overlapping with themselves. It should be pointed out that the sky apparent brightness temperature appears to be very uniform and free of artifacts, except for the alias borders.

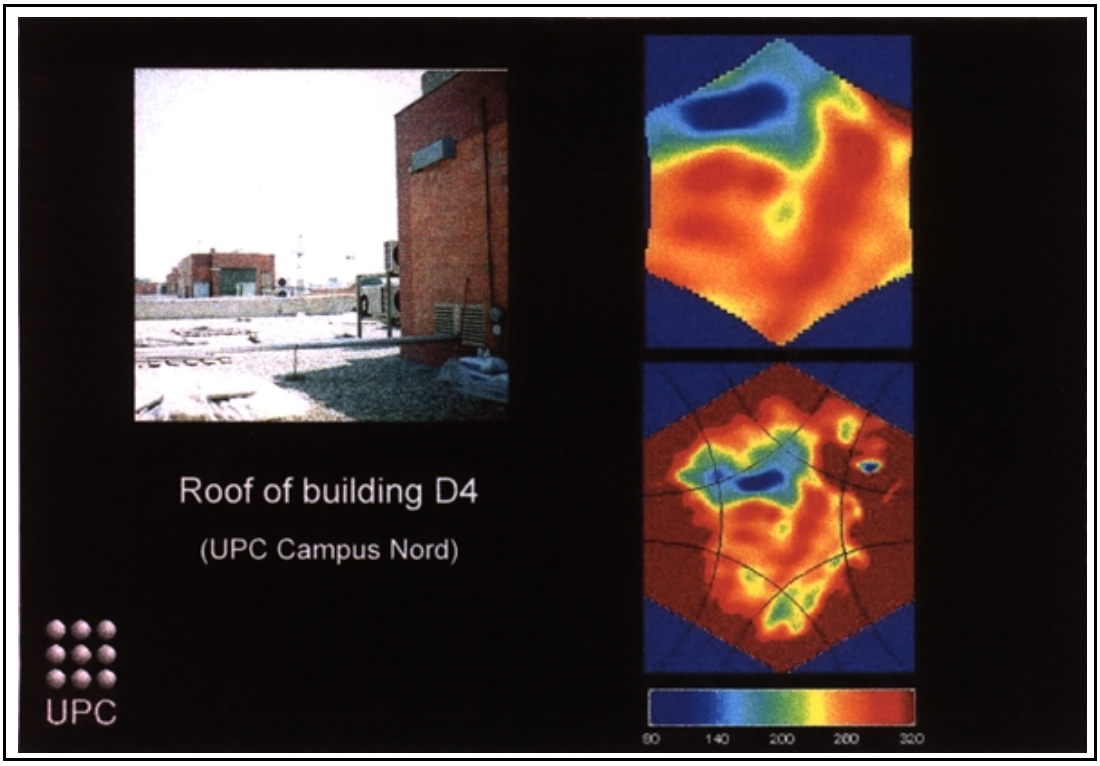

Figure 9.15.- *Natural Scene No 3: UPC Campus Nord: roof of building D4 seen from D3's roof* N_{EL}*=10, d=0.89* λ

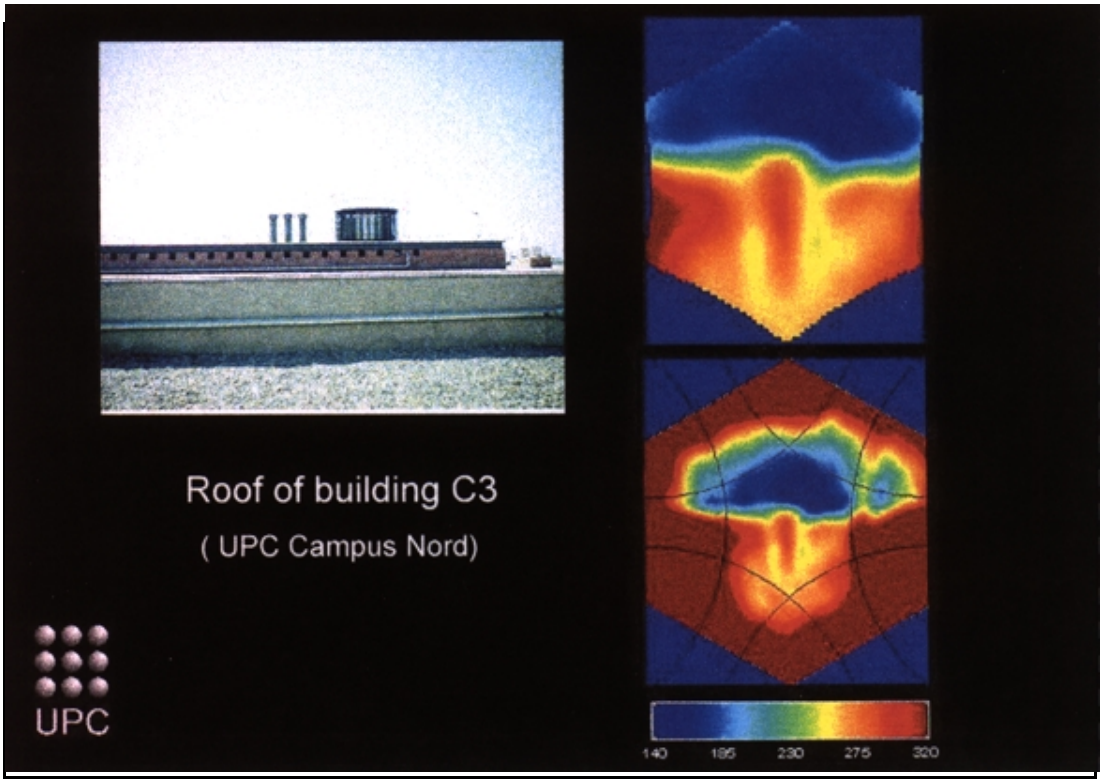

Figure 9.16.- *Natural Scene No 4: UPC Campus Nord: roof of buiding C3 seen from D3's roof* N_{EL}*=10, d= 0.89* λ

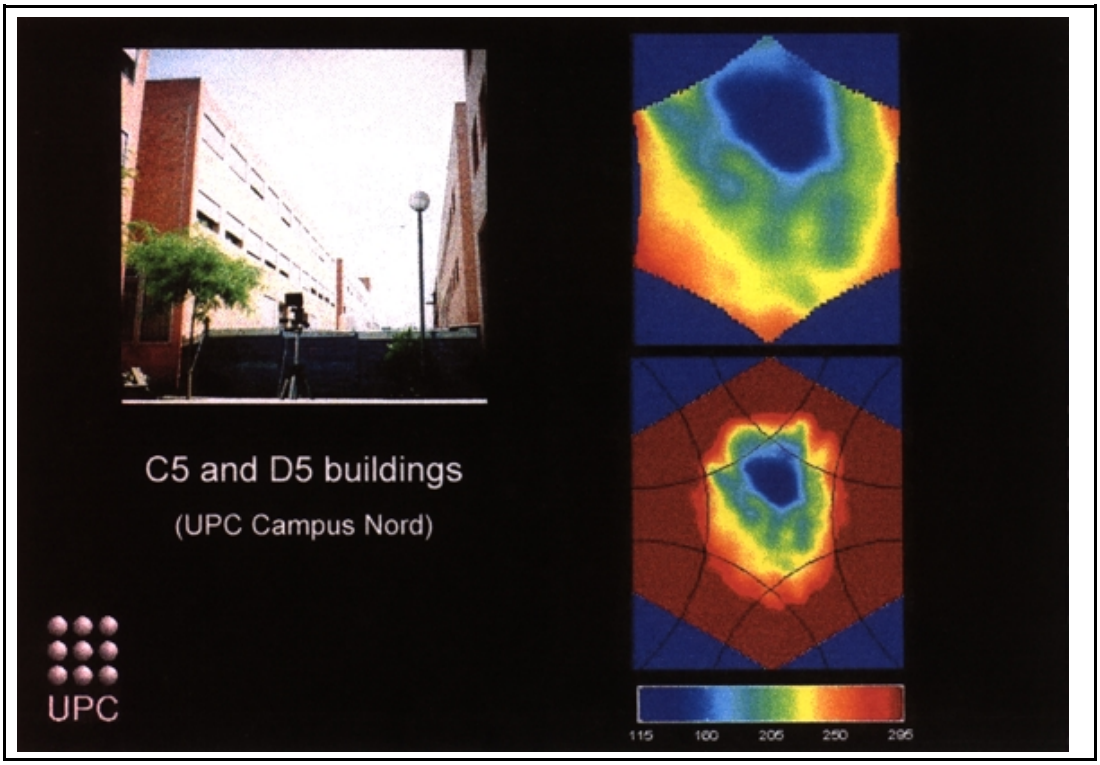

Figure 9.17.- *Natural Scene No 5: UPC Campus Nord: C5 and D5 buildings seen from the street* N_{EL}*=10, d= 0.89* λ

9.3.2.5.- Natural Scene No 5:
UPC Campus Nord: C5 and D5 buildings seen from the street

Figure 9.17 shows UPC Campus Nord C5 and D5 buildings seen from the street. In the synthetic image the brightness apparent temperature contour of the buildings can be appreciated over the cold brightness temperature of the sky. From left to right: a decreasing line due to the perspective of the buildings on the left, a flat zone in the middle with a peak at the position of the lamppost (vertical yellow line) and a vertical line for the building in the right.

Note that the alias free FOV can not be extended since most of the aliased regions are occupied by overlapping regions of high apparent brightness temperature: those of the ground and the brick buildings.

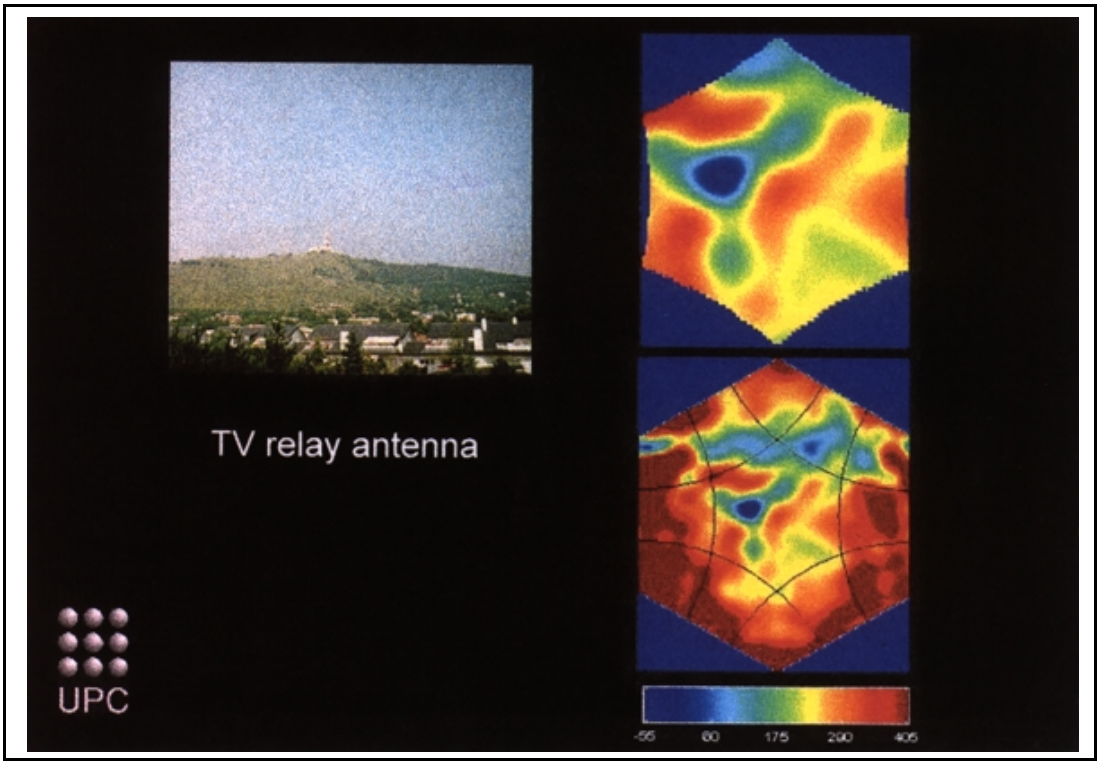

Figure 9.18.- *Natural Scene No 6: TV relay N_{EL}=10, d= 0.89 λ*

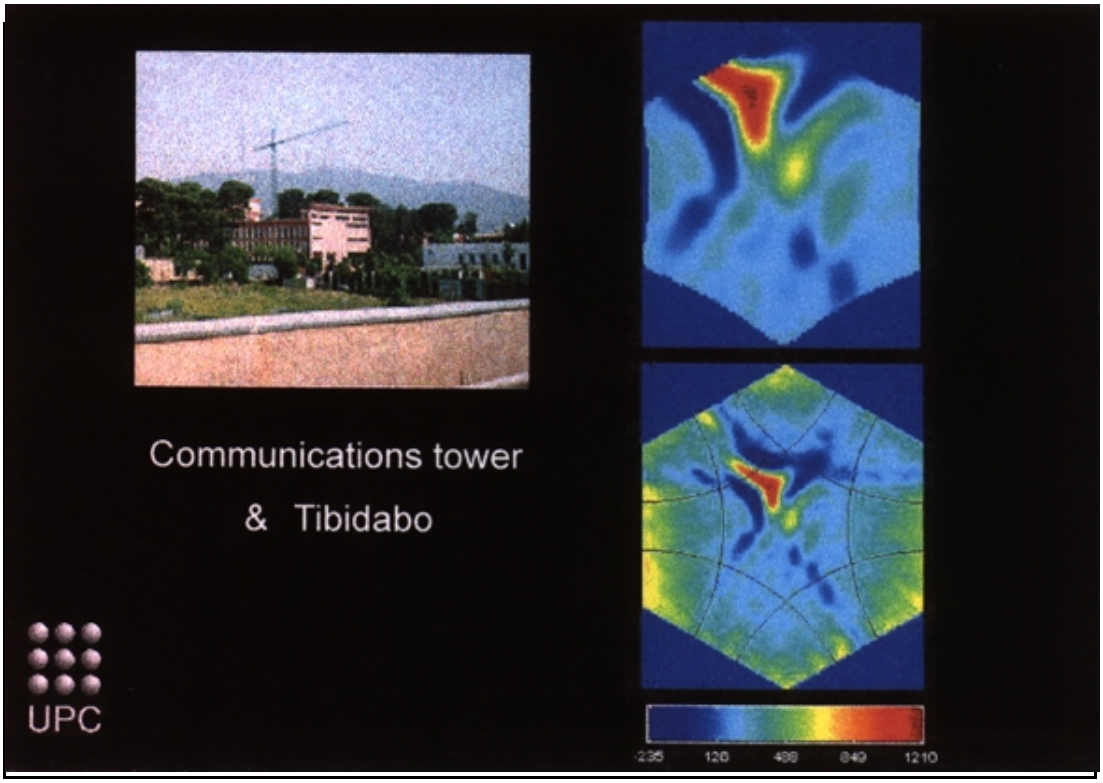

Figure 9.19.- *Natural Scene No 7: Tibidabo mountain and Norman Foster's commu nications tower N_{EL}=10, d= 0.89 λ*

9.3.2.6.- Natural Scenes No 6 and No 7:

i) TV relay ii) Tibidabo mountain and Norman Foster's Communications Tower

Figures 9.18 and 9.19 show the recovered synthetic images from a TV relay tower and the Tibidabo mountain respectively. Even though the interferometer was designed to work in the frequency band reserved for passive observations, due to radio-frequency interference from other emissions in the saturated X-band, during the measurement normalized visibilities took abnormal values and the polarimetric hot-point noise-injection calibration procedure failed.

The brilliant point in synthesized image in figure 9.19 is due to RF-interference from Norman Foster's Communications Tower. It looks like the impulse response without phase calibration.

9.4.- CONCLUSIONS

This chapter has first briefly presented the measurement technique to obtain two-dimensional synthetic aperture radiometric images: i) the calibration procedures, ii) the measurement sequence and iii) the processing of the measurements to get a synthetic brightness temperature image.

The impulse response of a Y-shaped bi-dimensional interferometric radiometer has been then measured in a phase-focused near-field set-up.

And finally, some results of a field measurement campaign have been presented:

i) a measurement inside an anechoic chamber to study error propagation and generation in the reconstructed image. Computed errors from the synthetic image agree with the radiometric accuracy budget performed, according to the error analysis developed in chapter four,

ii) a set of near-field focused artificial scenes made from metallic pieces reflecting the sky radiation, placed over inclined microwave absorbers, and

iii) a set of natural scenes of landscapes seen from the campus: mountains and buildings. At the end, two unsuccessful results have also been presented to show the sensitivity to RF-interference.

Chapter 10. CONCLUSIONS, ORIGINAL CONTRIBUTIONS AND FUTURE RESEARCH LINES.

10.1.- CONCLUSIONS

The submitted thesis is a contribution to the study of large two-dimensional synthetic aperture interferometric radiometers devoted to Earth observation, with high radiometric resolution 0.5 K, radiometric accuracy 1 K and spatial resolution 10 Km planned to monitor geophysical parameters of the Earth's surface at a global scale with 1-3 days revisit time.

To do this, the equations of interferometric radiometry were previously revised in [Bará et al 94] by Dr. I. Corbella. Previous approaches found in the literature for the computation of the angular resolution and radiometric sensitivity have been also revised and extended to the two-dimensional case and to include system imperfections and other receiver peculiarities: filter model, type of demodulation Single Side Band/Double Side Band... The trade-off between angular resolution and radiometric sensitivity is stated mathematically in the original *Interferometric Radiometer Incertitude Principle*.

A new and exhaustive analysis of system imperfections and their impact on the radiometric accuracy has been carried out, allowing to identify critical subsystems in which efforts must be focused, mainly the repeatability of the antenna voltage radiation patterns and frequency response of the channels. The improvement of system performance has also been studied by means of a space-borne Y-interferometer simulator, which includes system error models as well as the calibration and inversion algorithms described.

The calibration methods used in ESTAR, in radioastronomy and the current noise injection method proposed for the MIRAS bread-board have been revised and a new calibration method is proposed. It is a hybrid of: i) an original distributed correlated noise injection method to calibrate channel amplitude and phase errors and ii) the redundant space method, used in radioastronomy and now applied to Y-arrays, to calibrate constant antenna amplitude and phase errors.

The inversion methods used in ESTAR, in radioastronomy and some image processing techniques have been revised. Because of the difficulties encountered in these methods to deal with extended sources or to incorporate system errors, a new iterative inversion algorithm has been proposed. The method proposed in this thesis is capable to deal with system imperfections: antenna voltage pattern errors, antenna position errors and fringe-wash effects and it is based on the Hexagonal Fourier Transform proposed by the author. The HFFT processes the (u,v) hexagonally sampled visibilities by Fourier transforming them into the reciprocal (>,0) grid with standard rectangular FFT routines, preserving signal to noise ratio and avoiding interpolation artifacts.

Finally, these studies have been confirmed, as far as possible, by the development of an experimental X-band two-dimensional interferometer radiometer. Instrument's circuitry has been fully designed, implemented, characterized and calibrated with a new procedure that calibrates overall amplitude and phase errors. The instrument consists of a moving baseline formed by two antennas, two receiving channels and a 66 MHz complex 1 bit/2 level digital correlator. A measurements field campaign has been carried out to assess its performance and compare it with the theoretical predictions in terms of: radiometric sensibility and accuracy, angular resolution, calibration and synthetic image formation algorithms.

10.2.- ORIGINAL CONTRIBUTIONS

The original contributions of this thesis are listed below:

i) Generalization of the 1D ideal array factor originally described for ESTAR [Ruf et al. 88] to the two-dimensional case and to take into account system errors and decorrelation effects.

ii) Evaluation of the standard deviation of the visibility samples by taking into account the following new effects: the kind of demodulation and the shape of the receivers' frequency response.

iii) Evaluation of the average radiometric sensitivity taking into account the new formulas derived by the author for the standard deviation of the visibility samples, the hexagonal Fourier transform (viii) and the studies concerning redundancy and correlation between errors performed by Dr. J. Bará.

iv) Derivation of the new *"Interferometric Radiometer Uncertainty Principle"*, which states that the product of the angular resolution by the radiometric sensitivity is a constant that depends only on receivers' and correlators' parameters.

v) Systematic analysis and classification of interferometer errors and evaluation of their impact over the radiometric accuracy budget. The main contributions in this field are:

a) A visibility sample affected by antenna pattern errors has an error that is roughly proportional to the antenna temperature and to the same spatial frequency component of the Fourier Transform of the sum of the amplitude pattern errors added to the difference of the phase pattern errors,
b) The analysis of the impact of antenna coupling explains the shape of the experimental interference patterns found in [Ruf 91] and [Tanner and Swift 93].
c) Baseline errors, associated to the pair of antennas, receivers and the correlator establish the design tolerances if a technically feasible noise injection calibration method as proposed (iv) is to be used.

vi) Theoretical and numerical evaluation of the radiometric sensitivity and accuracy improvements by means of pixel averaging.

vii) Proposal of the distributed noise injection method originally devised by Dr. F. Torres and developed/tested by us.

viii) Proposal of a new technique to perform FFTs over hexagonal grids with standard rectangular algorithms, avoiding interpolations and preserving the signal-to-noise ratio.

ix) Proposal of a new iterative inversion algorithm that takes into account antenna voltage pattern errors and fringe-wash effects, the other errors being previously calibrated.

x) Proposal of an experimental procedure to characterize the overall performance of a baseline and calibrate it.

10.3.- FUTURE RESEARCH LINES

The future research lines opened by this thesis are:

i) a detailed analysis of channels' response, including antenna plus receiver's frequency response, in the frame of MIRAS/LICEF activities,

ii) the construction of a Dicke radiometer to complete the digital interferometer developed: providing a measurement of the antenna temperature that will enable to accurately denormalize the visibility samples and to calibrate the effect of antenna coupling.

iii) an experimental field campaign to analyze the impact of antenna coupling in the antenna radiation patterns and in the interference pattern of a baseline.

iv) the development of an integrated digital correlator to miniaturize and improve the performance of the 1 bit/2 level digital correlator unit.

v) an improvement of the 2D space-borne Y-interferometric radiometer simulator to test improved calibration methods and to analyze in more detail system's performance and its improvement by means of pixel averaging,

10.4.- ACCEPTED PAPERS ISSUED FROM THIS THESIS

At present, from the papers sent, the following papers have been published or accepted for publication:

F. Torres, A. Camps, J. Bará, I. Corbella and R. Ferrero, "On-Board Phase and Modulus Calibration of Large Aperture Synthesis Radiometers: Study Applied to MIRAS", IEEE Transactions on Geoscience and Remote Sensing, July 1996, Vol. 34, No 4, pp 1000-1009

A. Camps, J. Bará, I. Corbella, F. Torres, "The Processing of Hexagonally Sampled Signals with Standard Rectangular Techniques: Application to 2D Large Aperture Synthesis Interferometric Radiometers", accepted for publication in the IEEE Transactions on Geoscience and Remote Sensing in July 1996.

F. Torres, A. Camps, J. Bará, I. Corbella, "Impact of Receiver Errors on the Radiometric Resolution of Large 2D Aperture Synthesis Radiometers. Study Applied to MIRAS", accepted for publication in Radio Science in September 1996.

A. Camps, J. Bará, F. Torres, I. Corbella, J. Romeu, "Impact of Antenna Errors on the Radiometric Accuracy of Large Aperture Synthesis Radiometers. Study Applied to MIRAS", accepted for publication in Radio Science in October 1996.

10.5.- PUBLICATIONS IN CONFERENCES

J. Bará, A. Camps, F. Torres, I. Corbella, "Baseline Redundancy and Radiometric Sensitivity: A critical Review", SMOS Consultative Meeting on Soil Moisture and Ocean Salinity Measurements and Radiometer Techniques, ESA-ESTEC, April 20th and 21st, 1995, Noordwijk, The Netherlands, ESA document WPP 87.

A. Camps, J. Bará, I. Corbella, F. Torres, "Visibility Inversion Algorithms over Hexagonal Sampling Grids", SMOS Consultative Meeting on Soil Moisture and Ocean Salinity Measurements and Radiometer Techniques, ESA-ESTEC, April 20th and 21st, 1995, Noordwijk, The Netherlands, ESA document WPP 87.

A. Camps, J. Bará, I. Corbella, F. Torres, "Inversion Algorithms over Hexagonal Grids in Interferometric Aperture Synthesis Radiometry", Progress In Electromagnetic Research Symposium PIERS '95, University of Washington, Seattle, USA, July 1995.

M. Martín-Neira, J. M. Goutoule, A. Knight, J. Claude, J. Bará, A. Camps, F. Torres, I. Corbella, A. Lannes, E. Anterrieu, B. Laursen, N. Skou, "Integration of MIRAS Breadboard and Future Activities", International Geoscience And Remote Sensing Symposium IGARSS '96, Pasadena, USA, May 1996.

NOMENCLATURE AND BASIC CONVENTIONS

The conventions for the names and symbols of the magnitudes involved described below are used (figure N.1) :

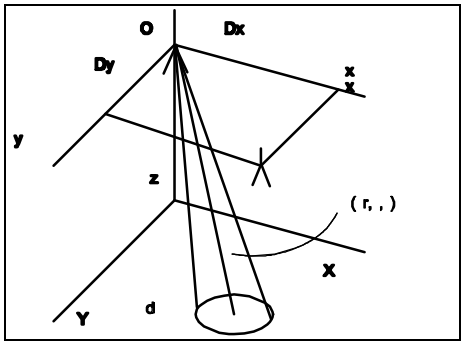

Figure N.1.- Geometry of the source (X,Y) and observation (x,y) planes.

$( )_i$		Refers to the channel number
$( )_{ij}$		Refers to the baseline formed by antennas i-j
α	[-]	Receiver voltage gain (defined below).
α_{OL}	[-]	Local oscillator ΔT factor
α_W	[-]	Windowing ΔT factor
α_F	[-]	Filter type ΔT factor
$\beta(x,y,z,f)$	[V $\Omega^{-½}$ Hz^{-1}]	Frequency domain scalar field
$(\Delta u, \Delta v, \Delta w)$	[-]	Baseline error due to antenna arm oscillations or filter mismatches
ε_{HV}	[-]	Cross-polarization ratio
$\Gamma_p(\theta,\phi)$	[-]	Fresnel reflection coefficient at *p* polarization
$\zeta = (\xi^2+\eta^2)^{1/2}$	[-]	Distance to the origin in the (ξ,η) plane
$\xi = \sin\theta\cos\phi$	[-]	Directing cosine with respect to x axis
$\eta = \sin\theta\sin\phi$	[-]	Directing cosine with respect to y axis
η_M	[-]	Antenna efficiency
η_l	[-]	Main beam efficiency
λ	[m]	Wavelength
$\rho = (u^2+v^2)^{1/2}$	[-]	Distance to the origin in the (u,v) plane
σ	[W sr^{-1} m^{-2} K^{-4}]	Stefan-Boltmann const = 5,670 10^{-8} $Wsr^{-1}m^{-2}K^{-4}$
σ^o_s	[-]	Scattering coefficient
$\mu^{(i)}(u,v)$	[-]	Normalized version of $V^{(i)}(u,v)$
Ω	[sr]	Solid angle
a	[-]	Albedo
a, b	[-]	1B/2L digital correlator's threshold error parameters

A_e	[m^2]	Antenna effective area
A_r	[m^2]	Receiving antenna effective area
$AF^o(\xi,\xi',\eta,\eta')$	[-]	Ideal array factor or impulse response to a modified temperature consisting in a delta function located at (ξ',η')
$AF^{o\varepsilon}(\xi,\xi',\eta,\eta')$	[-]	Same as $AF^o(\xi,\xi',\eta,\eta')$ for imperfect antennas, receivers or correlators without spatial decorrelation effects
$AF^f(\xi,\xi',\eta,\eta')$	[-]	Same as $AF^o(\xi,\xi',\eta,\eta')$ for with spatial decorrelation effects
b(x,y,z,t)	[$V\,\Omega^{-1/2}$]	Time domain scalar field
B	[Hz]	Bandwidth
$B(\theta,\phi)$	[$W\,sr^{-1}\,m^{-2}$]	Brightness
B_{bb}	[$W\,sr^{-1}\,m^{-2}$]	Total brightness of the blackbody
$B_f(\theta,\phi)$	[$W\,sr^{-1}\,m^{-2}\,Hz^{-1}$]	Spectral brightness density
$B_i(\theta,\phi)$	[$W\,sr^{-1}\,m^{-2}$]	Total brightness incident over an antenna
c	[$m\,s^{-1}$]	Speed of light $c = 2.998\,10^8\ m\,s^{-1}$
c_{ij}	[-]	Gain of the (ideal) correlator i-j
$d = (D_x^2+D_y^2)$	[m]	Spacing between antennas
D_x, D_y	[m]	Spacing between antennas: x- and y- component
$e(\theta,\phi)$	[-]	Emissivity
e (t)	[$V\,\Omega^{-1/2}$ or $K^{1/2}$](*)	Complex envelope of a signal
E[g]		Time average of the time variable g(t)
$E[g]_e$		Ensemble average of the random variable g
f	[Hz]	Frequency
$F(\theta,\phi)$	[-]	Antenna radiation voltage pattern Defined such that $F(\theta,\phi) = D \cdot F_n(\theta,\phi)$, where D is the directivity
$F_n(\theta,\phi)$	[-]	Normalized antenna radiation voltage pattern defined such that $\lvert F_n \rvert_{max} = 1$. It is assumed to be frequency indepdendent.
$F_t(\theta,\phi)$	[-]	Surface radiation pattern
f_o	[Hz]	Nominal center frequency of receiver i
f_i	[Hz]	Actual center frequency of receiver i
f_{OL}	[Hz]	Local oscillator frenquency
$f_{IF} = f_O - f_{OL}$	[Hz]	Nominal intermediate frequency
$f_i' = f_i - f_{OL}$	[Hz]	Intermediate frequency of receiver i
f_{ij}	[Hz]	Equivalent centerl frequency of the i-j baseline

h	[J s]	Plank's constant h = 6.626 10^{-34} J s
h_v	[m]	Vegetation cover height
h(t)		Impulse response of H(f)
H (f)	[-]	Frequency voltage transfer function of the channel, from the antenna output down to the correlator input
$H_n(f)$	[-]	Normalized ($\|H_n(f)\|_{max} = 1$) of H (f)
i (t), q(t)	[V $\Omega^{-½}$ or $K^{½}$](*)	In-phase and quadrature components of a bandpass signal
k	[rad m^{-1}]	Wavenumber
k_B	[J K^{-1}]	Boltzmann constant = 1.381 10^{-23} J K^{-1}
K_e	[m^{-1}]	Extintion coefficient of the vegetation cover
L	[-]	Mixer conversion loss
L_c	[-]	Mixer attenuation of the LO at the FI port
m_g	[g m^{-3}]	Gravimetric soil moisture
m_v	[g m^{-3}]	0-5 cm average soil moisture
N_{EL}	[-]	Number of antennas per arm in a Y-,T-, U-... array
N_T	[-]	Total number of antennas per arm in the array
N_V	[-]	Number of available different (u,v) points
P	[W]	Power
P_i	[W]	Incident power
P_r	[W]	Reflected power
r	[m]	Distance to the origin of coordinates
R, R'	[-]	Polarization coefficients
$R_a(\tau)$	[W]	Self-correlation of a(t): the analytic signal *a*(t).
$\tilde{R}_A(t)1$	[W]	Self-correlation of the complex envelope of *a*(t).
s_i	[V $\Omega^{-½}$ or $K^{½}$](*)	Analytic output of receiver i
S	[‰]	Sea salinity
$S_A(f)$	[W Hz^{-1}]	Spectral density of the complex envelope of *a*(t)
SST	[K]	Sea surface temperature
$T(x,h) = \frac{T_B(x,h)}{\sqrt{1-x^2-h^2}}\ F_{n_1}(x,h)\ F_{n_2}^{*}(x,h)$		Modified brightness temperature [K]
$T^{f}(x,h)$	[K]	Recovered T(ξ,η) from V^f(u,v)

T_A	[K]	Antenna temperature
$T_{AP}(\theta,\phi)$	[K]	Apparent brightness temperature
T_B	[K]	Brightness temperature = e T_{ph}
$T_{DN}(\theta,\phi)$	[K]	Atmospheric downward radiation
T_{lo}	[K]	Physical temperature of the local oscillator
T_{ph}	[K]	Physical temperature
T_s	[K]	Soil physical temperature
$T_{SC}(\theta,\phi)$	[K]	Scattered radiation
$T_{UP}(\theta,\phi)$	[K]	Atmospheric upward radiation
T_v	[K]	Vegetation physical temperature
T_R	[K]	Receiver's noise temperature
$T_{sys}=T_A+T_R$	[K]	System's temperature
$u = D_x/\lambda$	[-]	Normalized version of the antenna spacing: x-component
$v = D_y/\lambda$	[-]	Normalized version of the antenna spacing: y-component
$V^o(u,v)$	[K or W](*)	Ideal visibility function: $V^o(u,v) = \mathcal{F}[T(\xi,\eta)]$
$V^f(u,v)$	[K or W](*)	Same as $V^o(u,v)$ but considering spatial decorrelation effects
V_{ij}	[K or W](*)	Visibility sample measured as the correlation from signals coming from channels i and j
$V^{(1)}(u,v)$	[K or W](*)	Visibility function including antenna pattern and fringe-washing errors
$V^{(2)}(u,v)$	[K or W](*)	Same as $V^{(1)}$ but includes antenna coupling errors
$V^{(3)}(u,v)$	[K or W](*)	Same as $V^{(2)}$ but includes in-phase and quadrature errors
$V^{(4)}(u,v)$	[K or W](*)	Same as $V^{(3)}$ but includes amplitude errors
$V^{(5)}(u,v)$	[K or W](*)	Same as $V^{(4)}$ but includes offset errors
W	[-]	Relative bandwidth, B/f_o
WS	[m s^{-1}]	Wind speed
x, y, z	[m]	Coordinates in the observation plane
X, Y, Z	[m]	Coordinates of the object plane
Z_{ij}	[Ω]	Mutual impedance between antenna ports i-j

(*) Note:

If the visibility function is defined to be a power, its units are [W] and the analytic signals from which it is computed have the dimensions of [V $\Omega^{-1/2}$].

If the visibility function (2.61) is normalized by (2.62), its units are [K] and the normalized analytic signals from which it is computed have the dimensions of [$K^{1/2}$]

normalized analytic signals from which it is computed have the dimensions of [K$^{1/2}$]

* H(f) = " H_n(f) by definition.

* Ideally, all the filters should be identical and centered around f_o, where $H_n(f_o)$ should equal unity.

* Note also that the study is performed with analytic functions, whose spectra is defined only for positive frequencies. Receiver absolute and relative noise bandwidths, B and W, are defined as:

$$B = \frac{1}{"^2}\int_0^{\infty} *H(f)*^2 df = \int_0^{\infty} *H_n(f)*^2 df, \qquad W = \frac{B}{f_o} \tag{N.1}$$

* The cross-correlation function R_{ij} of the signals coming from receiving chains i and j is related to receivers' impulse responses and its normalized value r_{ij} (t) (complex degree of coherence) by the following expressions:

$$R_{ij}(t) = \int_0^{\infty} H_i(f)\, H_j^{(}(f)\, e^{j2\pi ft} df, \qquad \tilde{R}_{ij} \div R_{ij}\, e^{-j2\pi f_{ij} t}$$

$$r_{ij}(t) = \frac{R_{ij}(t)}{\left[\int_0^{\infty} *H_i(f)*^2 df \int_0^{\infty} *H_j(f)*^2 df\right]^{1/2}}, \qquad \tilde{r}_{ij} \div r_{ij}\, e^{-j2\pi f_{ij} t} \tag{N.2}$$

where $\tilde{R}_{ij}$ and $\tilde{r}_{ij}$ refer to the receiver transfer functions translated to the frequency origin and $f_{ij} \neq f_o$, but accounts for possible errors in the filter's center frequencies. It turns out that:

$$R_{ij}(t) = "_i "_j \sqrt{B_i B_j}\, r_{ij}(t) \tag{N.3}$$

* Definition of functions:

Rectangle function:

$$A\left(\frac{x}{x_o}\right) = \begin{cases} 1; & *x* \le \dfrac{*x_o*}{2} \\ 0; & *x* > \dfrac{*x_o*}{2} \end{cases} \tag{N.4}$$

Triangle function:

$$\Lambda\left(\frac{x}{x_o}\right) = \begin{cases} 1 - \left|\dfrac{x}{x_o}\right|; & *x* \le *x_o* \\ 0; & *x* > *x_o* \end{cases} \tag{N.5}$$

Step function:

$$u(x) = \begin{cases} 1; & x \ge 0 \\ 0; & x < 0 \end{cases} \tag{N.6}$$

APPENDIX 1. RADIOMETRIC SENSITIVITY COMPUTATION FOR SSB/DSB INTERFEROMETRIC RADIOMETERS USING COHERENT I/Q DEMODULATION

Let the signals at the outputs of the antennas be:

$$b_1(t) = \left[s_{i_1}(t) + n_{i_1}(t) \right]\cos(w_o t) + \left[s_{q_1}(t) + n_{q_1}(t) \right]\sin(w_o t)$$
$$b_2(t) = \left[s_{i_2}(t) + n_{i_2}(t) \right]\cos(w_o t) + \left[s_{q_2}(t) + n_{q_2}(t) \right]\sin(w_o t) \qquad \textbf{(A1.1)}$$

Subindexes "i" and "q" stand for the in-phase and quadrature components of these signals which are corrupted with receivers' thermal noise: $n_{i\,q\,1,2}(t)$. The in-phase and quadrature components of these signals, when coherently demodulated and low-pass filtered, prior to correlation, are given by:

$$\begin{aligned}
i_1(t) &= b_1(t)\cos(w_{OL} t) = \frac{1}{2}\left[s_{i_1}(t) + n_{i_1}(t) \right]\cos(\Delta w\, t) + \frac{1}{2}\left[s_{q_1}(t) + n_{q_1}(t) \right]\sin(\Delta w\, t) \\
q_1(t) &= b_1(t)\sin(w_{OL} t) = -\frac{1}{2}\left[s_{i_1}(t) + n_{i_1}(t) \right]\sin(\Delta w\, t) + \frac{1}{2}\left[s_{q_1}(t) + n_{q_1}(t) \right]\cos(\Delta w\, t) \\
i_2(t) &= b_2(t)\cos(w_{OL} t) = \frac{1}{2}\left[s_{i_2}(t) + n_{i_2}(t) \right]\cos(\Delta w\, t) + \frac{1}{2}\left[s_{q_2}(t) + n_{q_2}(t) \right]\sin(\Delta w\, t) \\
q_2(t) &= b_2(t)\sin(w_{OL} t) = -\frac{1}{2}\left[s_{i_2}(t) + n_{i_2}(t) \right]\sin(\Delta w\, t) + \frac{1}{2}\left[s_{q_2}(t) + n_{q_2}(t) \right]\cos(\Delta w\, t)
\end{aligned} \qquad \textbf{(A1.2)}$$

where: $\Delta\omega = 2\pi\,\Delta f = 2\pi\,(f_o - f_{lo})$.

Real and imaginary parts of the visibility function are computed by taking the cross-correlation between the in-phase (or quadrature components) and between the in-phase with the quadrature components of s_1' and s_2':

$$V_r(u,v) \triangleq 2\,E_t\left[i_1(t)\, i_2(t) \right]$$
$$V_i(u,v) \triangleq 2\,E_t\left[q_1(t)\, i_2(t) \right] \qquad \textbf{(A1.3)}$$

where E_τ stands for the average over τ seconds. The standard deviation of V_r and V_i are computed as the AC power of the product of those signals after low-pass filtering.

$$\begin{aligned}
p_r(t) \triangleq 2\, i_1(t)\, i_2(t) &= \frac{1}{2}\left\{ s_{i_1} s_{i_2} + s_{i_1} n_{i_2} + n_{i_1} s_{i_2} + n_{i_1} n_{i_2} + s_{q_1} s_{q_2} + s_{q_1} n_{q_2} + n_{q_1} s_{q_2} + n_{q_1} n_{q_2} \right\} = \\
&\equiv s_{i_1} s_{i_2} + s_{i_1} n_{i_2} + n_{i_1} s_{i_2} + n_{i_1} n_{i_2}
\end{aligned} \qquad \textbf{(A1.4)}$$

$$\begin{aligned}
p_i(t) \triangleq 2\, q_1(t)\, i_2(t) &= \frac{1}{2}\left\{ s_{q_1} s_{i_2} + s_{q_1} n_{i_2} + n_{q_1} s_{i_2} + n_{q_1} n_{i_2} - s_{i_1} s_{q_2} - s_{i_1} n_{q_2} - n_{i_1} s_{q_2} - n_{i_1} n_{q_2} \right\} = \\
&\equiv s_{q_1} s_{i_2} + s_{q_1} n_{i_2} + n_{q_1} s_{i_2} + n_{q_1} n_{i_2}
\end{aligned}$$

Let's first compute the auto-correlation function of $p_r(t)$:

$$
\begin{aligned}
R_{p_r p_r}(\tau) &= E\left[p_r(t)\, p_r(t+\tau) \right] = \\
&= E\left[s_{i_1}(t)\, s_{i_1}(t+\tau)\, s_{i_2}(t)\, s_{i_2}(t+\tau) \right] + \\
&+ E\left[s_{i_1}(t)\, s_{i_1}(t+\tau)\, n_{i_2}(t)\, n_{i_2}(t+\tau) \right] + \\
&+ E\left[s_{i_2}(t)\, s_{i_2}(t+\tau)\, n_{i_1}(t)\, n_{i_1}(t+\tau) \right] + \\
&+ E\left[n_{i_1}(t)\, n_{i_1}(t+\tau)\, n_{i_2}(t)\, n_{i_2}(t+\tau) \right]
\end{aligned}
\qquad \textbf{(A1.5)}
$$

Since all the signals involved in the fourth moment computation are jointly gaussian random processes:

$$
\begin{aligned}
R_{p_r p_r}(\tau) &= E\left[p_r(t)\, p_r(t+\tau) \right] = \\
&= E\left[s_{i_1}(t)\, s_{i_1}(t+\tau) \right] E\left[s_{i_2}(t)\, s_{i_2}(t+\tau) \right] + \\
&+ E\left[s_{i_1}(t)\, s_{i_2}(t) \right] E\left[s_{i_1}(t+\tau)\, s_{i_2}(t+\tau) \right] + \\
&+ E\left[s_{i_1}(t)\, s_{i_2}(t+\tau) \right] E\left[s_{i_1}(t+\tau)\, s_{i_2}(t) \right] + \\
&+ E\left[s_{i_1}(t)\, s_{i_1}(t+\tau) \right] E\left[n_{i_2}(t)\, n_{i_2}(t+\tau) \right] + \\
&+ E\left[s_{i_2}(t)\, s_{i_2}(t+\tau) \right] E\left[n_{i_1}(t)\, n_{i_1}(t+\tau) \right] + \\
&+ E\left[n_{i_1}(t)\, n_{i_1}(t+\tau) \right] E\left[n_{i_2}(t)\, n_{i_2}(t+\tau) \right]
\end{aligned}
\qquad \textbf{(A1.6)}
$$

Assuming gaussian predetection filters the following relations hold for the following second order moments:

$$
\begin{aligned}
&E\left[s_{i_{1,2}}(t)\, s_{i_{1,2}}(t+\tau) \right] = T_{A_{1,2}}\, e^{-\omega^2 B_{1,2}^2} \cos(\omega_0 \tau) \\
&E\left[s_{i_1}(t)\, s_{i_2}(t+\tau) \right] = e^{-\omega^2 B'^2} \left[V_r(u,v) \cos(\omega_0 \tau) + V_i(u,v) \sin(\omega_0 \tau) \right] \\
&E\left[s_{i_1}(t+\tau)\, s_{i_2}(t) \right] = e^{-\omega^2 B'^2} \left[V_r(u,v) \cos(\omega_0 \tau) - V_i(u,v) \sin(\omega_0 \tau) \right] \\
&E\left[n_{i_{1,2}}(t)\, n_{i_{1,2}}(t+\tau) \right] = T_{R_{1,2}}\, e^{-\omega^2 B_{1,2}^2} \cos(\omega_0 \tau) \\
&E\left[s_{i_1}(t)\, s_{i_2}(t) \right] = E\left[s_{i_1}(t+\tau)\, s_{i_2}(t+\tau) \right] = V_r(u,v) \\
&E\left[s_{i_{1,2}}(t)\, n_{i_{1,2}}(t+\tau) \right] = 0
\end{aligned}
\qquad \textbf{(A1.7)}
$$

where:

$$B^{)2} \cdot \frac{2B_1^2 B_2^2}{B_1^2 \% B_2^2} \qquad \textbf{(A1.8)}$$

When all receivers are identical equation (A1.6) reduces to:

$$\begin{aligned} & R_{p_r p_r}(\mathsf{J}) \cdot E_{\mathsf{J}}\left[\, p_r(t)\, p_r(t\%\mathsf{J}) \,\right] \cdot \\ & \cdot V_r^2(u,v) \% \frac{1}{2}\left(T_A \% T_R\right)^2 e^{\&2\mathsf{B}\mathsf{J}^2B^2}\left[\, 1 \% \cos(2)\mathsf{T}\mathsf{J}) \,\right]\% \\ & \% \frac{1}{2} e^{\&2\mathsf{B}\mathsf{J}^2B^2}\left[V_r^2(u,v)\left(1 \% \cos(2)\mathsf{T}\mathsf{J}\right) \& V_i^2(u,v)\left(1 \& \cos(2)\mathsf{T}\mathsf{J}\right)\right] \end{aligned} \qquad \textbf{(A1.9)}$$

The spectrum of $p_r(t)$ is obtained by taking the Fourier Transform in equation (A1.9):

$$\begin{aligned} & S_{p_r p_r}(f) \cdot V_r^2(u,v) *(f) \% \\ & \% \frac{1}{2}\left(T_A \% T_R\right)^2 \frac{1}{\sqrt{2}B} e^{\&\mathsf{B}\left(\frac{f}{\sqrt{2}B}\right)^2} \left(\left[*(f) \% \frac{1}{2} *(f \& 2\,)f) \% \frac{1}{2} *(f \% 2\,)f)\right] \% \right. \\ & \% \frac{1}{2\sqrt{2}B} e^{\&\mathsf{B}\left(\frac{f}{\sqrt{2}B}\right)^2} \left(\left[V_r^2(u,v) \left(*(f) \% \frac{1}{2} *(f \& 2\,)f) \% \frac{1}{2} *(f \% 2\,)f)\right) \% \right. \\ & \left. \left. \& V_i^2(u,v) \left(*(f) \% \frac{1}{2} *(f \& 2\,)f) \% \frac{1}{2} *(f \% 2\,)f)\right)\right] \right) \end{aligned} \qquad \textbf{(A1.10)}$$

where "*" stands for the convolution operator.

By passing $p_r(t)$ through a low-pass filter which integrates $p_r(t)$ over J seconds:

$$*H_{LP}(f)*^2 \cdot 1; \quad *f* < \frac{1}{2\mathsf{J}} \qquad \textbf{(A1.11)}$$

The DC component in (A1.10) gives the expected value for the visibility sample:

$$E_{\mathsf{J}}\left[\, p_r(t) \,\right] \cdot V_r(u,v) \qquad \textbf{(A1.12)}$$

The AC power will be obtained, by approximating the spectrum by its value at f=0 and multiplying by 1/2J, since 1/2J << B.

$$s^2_{p_r} = \frac{1}{2\sqrt{2}Bt}\left[(T_A + T_R)^2\left(1 + e^{-p\left(\frac{2\Delta f}{\sqrt{2}B}\right)^2}\right) + V_r^2(u,v)\left(1 + e^{-p\left(\frac{2\Delta f}{\sqrt{2}B}\right)^2}\right) - V_i^2(u,v)\left(1 - e^{-p\left(\frac{2\Delta f}{\sqrt{2}B}\right)^2}\right)\right] \quad \textbf{(A.13)}$$

Note that this expression, except for the $\sqrt{2}$ factor coming from gaussian filters, reduces to (A.II.17) of [Ruf et al. 88] when $\Delta f = 0$ (DSB receivers), but in the MIRAS case since $\Delta f > B/2$ the noise power at correlator's output is reduced by an extra factor of 2.

Proceeding in a similar way for the imaginary part of the visibility function, it can be shown that:

$$s^2_{p_i} = \frac{1}{2\sqrt{2}Bt}\left[(T_A + T_R)^2\left(1 + e^{-p\left(\frac{2\Delta f}{\sqrt{2}B}\right)^2}\right) + V_i^2(u,v)\left(1 + e^{-p\left(\frac{2\Delta f}{\sqrt{2}B}\right)^2}\right) - V_r^2(u,v)\left(1 - e^{-p\left(\frac{2\Delta f}{\sqrt{2}B}\right)^2}\right)\right] \quad \textbf{(A1.14)}$$

If digital correlators are used, the integration time τ should be replaced by an effective integration time τ_{eff} that depends on the correlator´s type. Values for τ_{eff} are shown in table 3.6 and are reproduced from [Hagen and Farley 73].

APPENDIX 2. REDUNDANCY AND CORRELATION OF ERRORS BETWEEN VISIBILITY SAMPLES

Let us consider four antennas labelled (1,2,3,4) as in figure A2.1 [Bará et al. 95B] [Bará et al. 96].

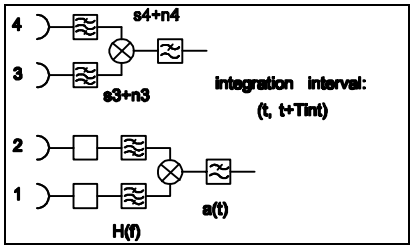

Figure A2.1.- *Two baselines measured with the same integration time T_{int}, one of them delayed τ.*

Antennas (3,4) produce the following visibility sample by integration in the time interval $(t,t+T_{int})$:

$$\hat{V}_{34}(t)=\int_{-\infty}^{\infty} a(t-r)\left[b_3(r)+n_3(r)\right]\left[b_4^*(r)+n_4^*(r)\right]dr \quad \textbf{(A2.1)}$$

where $b_i(t)$ refers to the signal from th channel in the absence of noise, $n_i(t)$ is the noise introduced by the amplifying/down-converting chain and $a(t)$ is the post-multiplication low-pass filter impulse response, which fixes the integration time T_{int}. Similarly, antennas (1,2) produce, in the delayed time interval $(t+\tau, t+\tau+T_{int})$:

$$\hat{V}_{12}(t+t)=\int_{-\infty}^{+\infty} a(t+t-s)\left[b_1(s)+n_1(s)\right]\left[b_2^*(s)+n_2^*(s)\right]ds \quad \textbf{(A2.2)}$$

Let us compute their correlation by taking ensemble averages (denoted by $E[\ ]_e$):

$$R_{\hat{V}_{12}\hat{V}_{34}}(t)=E\left[\hat{V}_{12}(t+t)\hat{V}_{34}^*(t)\right]_e=\int_{-\infty}^{+\infty}\int_{-\infty}^{+\infty} a(t-r)\,a(t+t-s)$$

$$E\left[\left(b_1(s)+n_1(s)\right)\left(b_2^*(s)+n_2^*(s)\right)\left(b_3^*(r)+n_3^*(r)\right)\left(b_4(r)+n_4(r)\right)\right]_e dr\,ds \quad \textbf{(A2.3)}$$

where both the $b_i(t)$ and the $n_i(t)$ are complex zero mean Gaussian random processes with circular joint Gaussian statistics for which [Goodmann 85]:

$$E\left[a_1 a_2 a_3^* a_4^*\right]=E\left[a_1 a_3^*\right]E\left[a_2 a_4^*\right]+E\left[a_1 a_4^*\right]E\left[a_2 a_3^*\right] \quad \textbf{(A2.4)}$$

In the integrand of (A2.3) there are 16 products of which 15 have at least one of the n_i. Since each $n_i(t)$ is uncorrelated with all the remaining processes, when taking expected values these 15 terms vanish and:

$$\begin{aligned} &E\left[b_1(s)\,b_2^*(s)\,b_3^*(r)\,b_4(r)\right]= \\ &=E\left[b_1(s)\,b_2^*(s)\right]E\left[b_3^*(r)\,b_4(r)\right]+E\left[b_1(s)\,b_3^*(r)\right]E\left[b_2^*(s)\,b_4(r)\right]= \\ &=V_{12}V_{34}^*+V_{13}(u_{13},v_{13};s-r)V_{24}^*(u_{24},v_{24};s-r)= \\ &=V_{12}V_{34}^*+V_{13}V_{24}^*\left|\tilde{r}(s-r)\right|^2 \end{aligned} \quad \textbf{(A2.5)}$$

Therefore, (A2.3) becomes:

$$R_{\hat{V}_{12}\hat{V}_{34}} = \int_{-\infty}^{+\infty}\int_{-\infty}^{+\infty} a(t-\delta)\ a(t+\tau-\delta)\left[V_{12}V_{34}^{*} + V_{13}V_{24}^{*}\tilde{r}(\delta-\tau)^{2}\right]d\delta\, d\tau \quad \text{(A2.6)}$$

Note that the low-pass filter may have an integration time of the order of 1 s, while if B = 20 MHz then $1/B = 5\times10^{-8}$ s; therefore, in (A2.6) a(t-δ)a(t+τ-δ) varies very slowly as compared to $\tilde{r}(\delta-\tau)^{2}$ and can approximated by:

$$\tilde{r}^{2}(\tau) = sinc^{2}(B\tau) \approx \frac{1}{B}\delta(\tau) \quad \text{(A2.7)}$$

If the low-pass filter has the shape:

$$A(f)^{2} = 1 \quad if \quad |f| < \frac{2}{T_{int}}, \qquad 0 \quad if \quad |f| > \frac{2}{T_{int}} \quad \text{(A2.8)}$$

then:

$$\int_{-\infty}^{+\infty} a(t-\delta)\,d\delta \int_{-\infty}^{+\infty} a(t+\tau-\delta)\,d\delta = \left[\int_{-\infty}^{+\infty} a(t)\,dt\right]^{2} = \left[A(0)\right]^{2} = 1 \quad \text{(A2.9)}$$

$$\begin{aligned} &\tilde{r}(\delta-\tau)^{2}d\delta \approx \frac{1}{B}\int_{-\infty}^{+\infty} a(t+\tau-\delta)\,a(t-\delta)\,d\delta = \\ &= \frac{1}{B}\int_{-\infty}^{+\infty} |A(f)|^{2} e^{j2\pi f\tau}\,df = \frac{1}{BT_{int}}\,sinc\left(\frac{\tau}{T_{int}}\right) \end{aligned} \quad \text{(A2.10)}$$

and (A2.6) can be written:

$$R_{\hat{V}_{12}\hat{V}_{34}} = V_{12}V_{34}^{*} + \frac{V_{13}V_{24}^{*}}{BT_{int}}\,sinc\left(\frac{\tau}{T_{int}}\right) \quad \text{(A2.11)}$$

And the cross-correlation of the errors of the two identical baselines 1-2 and 3-4 with the same integration time T_{int}, one of them delayed τ, is:

$$E\left[\Delta V_{12}(t+\tau)\,\Delta V_{34}^{*}(t)\right] = R_{\hat{V}_{12}\hat{V}_{34}}(\tau) - V_{12}V_{34}^{*} = \frac{V_{13}V_{24}^{*}}{BT_{int}}\,sinc\left(\frac{\tau}{T_{int}}\right) \quad \text{(A2.12)}$$

APPENDIX 3. REDUNDANCY IN MIRAS AND ITS IMPACT ON THE RADIOMETRIC RESOLUTION

MIRAS Y-shaped array provides a very low degree of redundancy [MMS 95], [Bará et. al 95B] [Bará et al. 96A]. If the three central elements introduced for the purpose of phase calibration are disregarded, only baselines between antennas on the same arm can be redundant. By the zero baseline it is understood that corresponding to u = v = 0, which in MIRAS is measured by a dedicated radiometer and, consequently, it is not redundant. For the Y-array with N_{EL} = 43 antennas per arm, plus a central element, there are:

-Total number of baselines: $3N_{EL}(3N_{EL}+1)/2+1 = 8386$ (the extra one corresponding to V(0,0))

-Non-redundant baselines = non-redundant (u,v)-points: $3\ N_{EL}^2 + 3\ N_{EL} + 1 = 5551$ (three are formed by the central antenna and those at the ends of the arms and one is the zero baseline)

-Redundant (u,v)-points: $3\ (N_{EL}-1) = 126$, with different degrees of redundancy.

-Total number of (u,v)-points: $3N_{EL}^2 + 4 + 3\ (N_{EL}-1) = 3N_{EL}^2+3N_{EL}+1 = 5677$

Recall that when the Hermitian property is considered every (u,v)-point is actually duplicated.

It means that 8386 - 5551 = 2709 correlations (visibilities) lead to only 126 different (u,v) points. The use of the available redundancy in a Y-array has a negligible impact over the radiometric sensitivity, less than 1% for 43 antennas per arm Y-array.

If all (u,v)-points are measured only once, the norm of the visibility error vector is:

$$<2)\ V\ 2^2> \ '\ \ j\ \ j\ \ <2)\ V(u_m,v_n)2^2> \ '\ 2\ \frac{5677}{BT_{int}}\ V^2(0,0) \qquad \textbf{(A3.1)}$$

Let us now consider redundance. For each arm let V(m) be the visibility function corresponding to the baseline formed by two antennas separated by m basic spacings (d=0.898). If all possible baselines produce a visibility sample, V(m) has a redundacy (N-m+1). Therefore, the errors of the 126 previously non-redundant (u,v)-points:

$$2\ \frac{126}{BT_{int}}\ V^2(0,0) \qquad \textbf{(A3.2)}$$

have to be replaced by (assuming uncorrelated errors):

$$2\ \frac{3V^2(0,0)}{BT_{int}}\ \sum_{m=1}^{N-1}\ \frac{1}{N-m+1}\ \cdot$$

$$\cdot\ 2\ 3[C-1+\ln(N)]\frac{V^2(0,0)}{BT_{int}}\ +\ 2\frac{10.015}{BT_{int}}V^2(0,0) \qquad \textbf{(A3.3)}$$

where C is the Euler's constant=0.5772. That is, with full redundancy in the arms of the interferometer the norm of the error vector becomes:

$$\langle 2\rangle V2^2_{red}\rangle\ =\ \sum\ \sum\ \langle 2\rangle V(u_m,v_n)2^2\rangle\ =\ \frac{5561}{BT_{int}}\ V^2(0,0) \qquad \textbf{(A3.4)}$$

and therefore, the radiometric resolution improvement is given by:

$$\frac{\Delta T(I)-\Delta T(I)_{red}}{\Delta T(I)}\ =\ 1-\left(\frac{\langle 2V2^2_{red}\rangle}{\langle 2V2^2\rangle}\right)^{1/2}\ =\ 0.0103\ =\ 1.03\% \qquad \textbf{(A3.5)}$$

That is, the average temperature resolution improvement contributed by the 2709 redundant complex correlators, from a total of 8386, is just a 1 % with the uncorrelated errors approximations, what it has seen to be somewhat higher than in the actual case due to their correlation.

APPENDIX 4. VISIBILITY ERRORS DUE TO ANTENNA PATTERN MISMATCHES

Let F_{nk} (>,0) be the normalized radiation voltage pattern of the antenna k and let $)F_{nk}$(>,0) and $)N_k$(>,0) be its amplitude and phase errors.

$$F_{n_k}(>,0) \text{ ' } F_n(>,0) \text{ [1\% })F_{n_k}(>,0)] \text{ } e^{j)N_k(>,0)} \qquad \textbf{(A4.1)}$$

Then, the product F_{nk} (>,0) F^{*}_{nl} (>,0) in (2.61) can be approximated by:

$$\begin{aligned} & F_{n_k}(>,0)\ F_{n_l}{}^{(}(>,0) \text{ .} \\ \text{. } & {}^{*}F_n(>,0)^{*2} \text{ [1\% })F_{n_k}(>,0)\%)F_{n_l}(>,0)\%j(\,)N_k(>,0)\&)N_l(>,0))]\div \\ & \div {}^{*}F_n(>,0)^{*2} \text{ [1\% },_{kl}(>,0)] \end{aligned} \qquad \textbf{(A4.2)}$$

where the term $,_{kl}$ (>,0) takes into account amplitude and phase errors and can be expanded in a Fourier series as:

$$,_{kl}(>,0) \text{ ' } \sum_{\&4\&4}^{\%4\%4} E_{kl}(u',v') \text{ } e^{j2B(u'>\%v'0)}du'dv' \qquad \textbf{(A4.3)}$$

The coefficient E_{kl} (p,q) is the (p,q) coefficient of the two-dimensional Fourier expansion of the antenna pattern error between antennas k and l.

At this point, assuming negligible decorrelation errors, equation (1) can be expressed as:

$$V_{kl}(u,v) \text{ ' } \sum_{>^2\%0^2\#1} I(>,0)[1\% ,_{kl}(>,0)]e^{\&j2B(u>\%v0)}d>d0 \text{ ' } V_{kl}^{o}(u,v)\%)V_{kl}(>,0 \qquad \textbf{(A4.4)}$$

where $V_{kl}{}^{o}$ (u,v) is the ideal visibility sample measured between antennas k and l and $)V_{kl}$(u,v) is its error due to an antenna radiation pattern mismatch. Inserting (A4.3) in (A1.4), the visibility error can be expressed as:

$$\begin{aligned})V_{kl} \text{ ' } & \sum_{\&4\&4}^{\%4\%4} E_{kl}(u',v') \sum_{>^2\%0^2\#1} I(>,0)e^{\&j2B[(u_{kl}\&u')>\%(v_{kl}\&v')0]}d>d0du'dv' \text{ ' } \\ & \text{ ' } \sum_{\&4\&4}^{\%4\%4} E_{kl}(u',v') \text{ } V_{kl}(u_{kl}\&u', v_{kl}\&v')du'dv' \end{aligned} \qquad \textbf{(A4.5)}$$

which can be approximated by:

$$) V_{kl} \cdot) S_{\&3dB} T_A E_{kl}(u_{kl}, v_{kl}) ') S_{\&3dB} T_A \iint_{>^2\%0^2\#1} , _{kl}(>, v)\, e^{\&j2B(u_{kl}>\%v_{kl}0)} d> d0 \qquad \textbf{(A4.6)}$$

where $) S_{-3dB}$ is the two-dimensional half-power band-width in (u,v) domain. Equation (A4.6) holds for low-pass visibility functions, that correspond to extended thermal sources, as the Earth seen from 800 Km height (angle of vision of 120º).

APPENDIX 5. PHASE MODULATION AND BASELINE ERROR DUE TO ANTENNA ARM OSCILLATION

Let's evaluate the visibility function when the distances from the source to the antennas (r_1 and r_2) are time dependent. Taking account the basic expressions given in [Thompson 86] [NRAO 89]:

$$\hat{V}_{12} = \frac{1}{2} E_J\left[b_1\left(t-\frac{r_1}{c} \right) b_2^{*}\left(t-\frac{r_2}{c} \right) \right] \qquad \textbf{(A5.1)}$$

This expression is also valid when $r_1 = r_1(t)$ and $r_2 = r_2(t)$. If:

$$\begin{aligned} \overline{r}_i(t) = {} & (x_{o_i} + A_{ip_i}\sin(\varphi_i)\sin(\omega_{rip} t + \theta_{ip_i}))\,\hat{x} + \\ & + (y_{o_i} + A_{ip_i}\cos(\varphi_i)\sin(\omega_{rip} t + \theta_{ip_i}))\,\hat{y} + \\ & + (z_{o_i} + A_{op_i}\sin(\omega_{rop} t + \theta_{op_i}))\,\hat{z} \\ & i = 1,2 \end{aligned} \qquad \textbf{(A5.2)}$$

Then, if $\Delta r(t) \ll r_o + \Delta r'(t)$, equation (A5.1) can be written as:

$$V_{12} = \frac{1}{2 r_1 r_2} R_A\left(\frac{\Delta r_o}{c} \right) E_J\left[e^{-jk_o \Delta r(t)} \right] \qquad \textbf{(A5.3)}$$

assuming that $R_A(t)$ is a smooth function, $\Delta r'(t) \ll \Delta r_o$, and $\Delta r'(t)/c \ll 1/B$:

$$\begin{aligned} \Delta r(t) = {} & \|\overline{r}_2 - \overline{r}_1\| - \left[(x_{o_2} - x_{o_1}) + (y_{o_2} - y_{o_1}) + (z_{o_2} - z_{o_1}) \right] + \\ & - [(A_{ip_2}\sin\varphi_2\sin(\omega_{rip} t + \theta_{ip_2} + \beta) + A_{ip_1}\sin\varphi_1\sin(\omega_{rip} t + \theta_{ip_1})) + \\ & + (A_{ip_2}\cos\varphi_2\sin(\omega_{rip} t + \theta_{ip_2}) + A_{ip_1}\cos\varphi_1\sin(\omega_{rip} t + \theta_{ip_1} + \beta)) + \\ & + (A_{op_2}\sin(\omega_{rop} t + \theta_{op_2}) + A_{op_1}\sin(\omega_{rop} t + \theta_{op_1} + \beta))] \end{aligned} \qquad \textbf{(A5.4)}$$

Defining:

$$\begin{aligned} \sigma_x^2 &= A_{ip_1}^2\sin^2\varphi_1 + A_{ip_2}^2\sin^2\varphi_2 + 2A_{ip_1}A_{ip_2}\sin\varphi_1\sin\varphi_2\cos(\theta_{ip_1} - \theta_{ip_2}) \\ \sigma_y^2 &= A_{ip_1}^2\cos^2\varphi_1 + A_{ip_2}^2\cos^2\varphi_2 + 2A_{ip_1}A_{ip_2}\cos\varphi_1\cos\varphi_2\cos(\theta_{ip_1} - \theta_{ip_2}) \\ \sigma_z^2 &= A_{op_1}^2 + A_{op_2}^2 + 2A_{op_1}A_{op_2}\cos(\theta_{op_1} - \theta_{op_2}) \end{aligned} \qquad \textbf{(A5.5)}$$

$$tg2_x = \frac{A_{ip_1}\sin\varphi_1\sin N_{ip_1} + A_{ip_2}\sin\varphi_2\sin N_{ip_2}}{A_{ip_1}\sin\varphi_1\cos N_{ip_1} + A_{ip_2}\sin\varphi_2\cos N_{ip_2}}$$

$$tg2_y = \frac{-A_{ip_1}\cos\varphi_1\sin N_{ip_1} - A_{ip_2}\cos\varphi_2\sin N_{ip_2}}{-A_{ip_1}\cos\varphi_1\cos N_{ip_1} - A_{ip_2}\cos\varphi_2\cos N_{ip_2}} \qquad \textbf{(A5.6)}$$

$$tg2_z = \frac{-A_{op_1}\sin N_{op_1} - A_{op_2}\sin N_{op_2}}{-A_{op_1}\cos N_{op_1} - A_{op_2}\cos N_{op_2}}$$

Leads to:

$$\begin{aligned} \delta r(t) &= \delta r_o(t) - \delta r^{(}t) = \\ &= -(u\cdot v\cdot w)\cdot \\ &\cdot \left[\delta_x\sin(\omega_{rip}t-\varphi_x) - \delta_y\sin(\omega_{rip}t-\varphi_y) - \delta_z\sin(\omega_{rop}t-\varphi_z)\right] \end{aligned} \qquad \textbf{(A5.7)}$$

which induces a frequency modulation:

$$\begin{aligned} E_J\left[e^{jk_o\delta r(t)}\right] &= E_J\left[e^{j2\pi\frac{\delta r(t)}{\lambda}}\right] = \\ &= e^{-j2\pi(u\cdot v\cdot w)} E_J\left[e^{-j2\pi\left(\delta_x\sin(\omega_{rip}t-\varphi_x) - \delta_y\sin(\omega_{rip}t-\varphi_y) - \delta_z\sin(\omega_{rop}t-\varphi_z)\right)}\right] \end{aligned} \qquad \textbf{(A5.8)}$$

If the displacements are small: $2\pi\delta_x/\lambda$, $2\pi\delta_y/\lambda$, $2\pi\delta_z/\lambda \ll 1$, then, the expression for the baseline error reduces to:

$$\begin{aligned} E_J\left[e^{jk_o\delta r(t)}\right] &= e^{-j2\pi(u\cdot v\cdot w)}\left[1-j2\pi\delta_x\sin\left(\frac{\omega_{rip}T}{2}-\varphi_x\right)sinc(f_{rip}T) - \right. \\ &- j2\pi\delta_y\sin\left(\frac{\omega_{rip}T}{2}-\varphi_y\right)sinc(f_{rip}T) - j2\pi\delta_z\left(\sin\left(\frac{\omega_{rop}T}{2}-\varphi_z\right)sinc(f_{rop}T)\right)\Big] \cdot \\ &\cdot e^{-j2\pi[(u\cdot\delta_x)+(v\cdot\delta_y)+(w\cdot\delta_z)]} \end{aligned} \qquad \textbf{(A5.9)}$$

Where:

$$\begin{aligned} \delta u &= \delta_x\sin\left(\frac{\omega_{rip}T}{2}-\varphi_x\right)sinc(f_{rip}T) \\ \delta v &= \delta_y\sin\left(\frac{\omega_{rip}T}{2}-\varphi_y\right)sinc(f_{rip}T) \\ \delta w &= \delta_z\sin\left(\frac{\omega_{rop}T}{2}-\varphi_z\right)sinc(f_{rop}T) \end{aligned} \qquad \textbf{(A5.10)}$$

APPENDIX 6. MODULE AND PHASE RESIDUAL ERRORS IMPACT ON RADIOMETRIC ACCURACY

6.1.- RESIDUAL MODULE CALIBRATION ERRORS

For an ideal interferometer, the expression of the expected brightness temperature can be written as:

$$\hat{I}(\gamma,\theta) = \frac{\sqrt{3}}{2} d^2 \frac{1}{|F_n(\gamma,\theta)|^2} \sum_m \sum_n W_{mn} V(u_{mn},v_{mn}) e^{j2\pi(u_{mn}\gamma+v_{mn}\theta)} \quad \textbf{(A6.1)}$$

where: $\Omega = \sqrt{3}d^2/2$ is the pixel area in the (u,v) plane,
and: d is the spacing between antennas in wavelengths.

If the module of the visibility function has an error, it translates to the recovered temperature of the scene according to equation (A6.1):

$$\hat{I}(\gamma,\theta) = \frac{\sqrt{3}}{2} d^2 \frac{1}{|F_n(\gamma,\theta)|^2} \sum_m \sum_n W_{mn} V(u_{mn},v_{mn}) (1+\varepsilon_{mn}) e^{j2\pi(u_{mn}\gamma+v_{mn}\theta)} \quad \textbf{(A6.2)}$$

If the value of the visibility function is replaced by its expression, equation (A6.2) can be re-written as:

$$\begin{aligned}\hat{I}(\gamma,\theta) = \frac{\sqrt{3}}{2} d^2 \frac{1}{|F_n(\gamma,\theta)|^2} \sum_m \sum_n W_{mn} \Big[\iint I(\gamma',\theta') |F_n(\gamma',\theta')|^2 \\ e^{-\pi\left(\frac{r_{mn}}{c}\right)^2 B^2} e^{-j2\pi(u_m\gamma'+v_n\theta')} d\gamma' d\theta' \Big] e^{j2\pi(u_{mn}\gamma+v_{mn}\theta)} + \\ + \frac{\sqrt{3}}{2} d^2 \frac{1}{|F_n(\gamma,\theta)|^2} \sum_m \sum_n W_{mn} V(u_{mn},v_{mn}) \varepsilon_{mn} e^{j2\pi(u_{mn}\gamma+v_{mn}\theta)}\end{aligned} \quad \textbf{(A6.3)}$$

Then:

$$\begin{aligned}\hat{I}(\gamma,\theta) = \frac{1}{|F_n(\gamma,\theta)|^2} \iint I(\gamma',\theta') |F_n(\gamma',\theta')|^2 AF(\gamma-\gamma',0-\theta') d\gamma' d\theta + \\ + \frac{\sqrt{3}}{2} d^2 \frac{1}{|F_n(\gamma,\theta)|^2} \sum_m \sum_n W_{mn} V(u_{mn},v_{mn}) \varepsilon_{mn} e^{j2\pi(u_{mn}\gamma+v_{mn}\theta)}\end{aligned} \quad \textbf{(A6.4)}$$

Now, the error in the expected brightness temperature distribution is:

$$\begin{aligned}\varepsilon_{\hat{I}}^2(\gamma,\theta) &= E\left[\left(\hat{I}(\gamma,\theta)-I(\gamma,\theta)\right)\left(\hat{I}(\gamma,\theta)-I(\gamma,\theta)\right)^*\right] = \\ &= E\left[\hat{I}(\gamma,\theta)\hat{I}(\gamma,\theta)^*\right] + \left\{I(\gamma,\theta)-E\left[\hat{I}(\gamma,\theta)\right]\right\}^2 - E\left[\hat{I}(\gamma,\theta)\right]^2\end{aligned} \quad \textbf{(A6.5)}$$

where:

$$\left\{ \mathrm{T}(x,h) - E\left[\hat{\mathrm{T}}(x,h) \right] \right\}^2 \qquad \textbf{(A6.6)}$$

stands for Gibbs phenomenon and aliasing effects and the term:

$$\hat{\mathrm{T}}(x,h)\,\hat{\mathrm{T}}^*(x,h) \qquad \textbf{(A6.7)}$$

can also be written as:

$$\hat{\mathrm{T}}(x,h)\,\hat{\mathrm{T}}^*(x,h) = \frac{1}{|F_n(x,h)|^4}\left[\int\int \mathrm{T}(x',h')\,|F_n(x,h)|^2\,AF(x,x',h,h')\,dx'dh' + \right. \qquad \textbf{(A6.8)}$$

$$\left. + \frac{\sqrt{3}}{2} d^2 \sum_m \sum_n W_{mn}\, V(u_{mn},v_{mn})\,\Delta v_{mn}\, e^{\,j\,2p\,(u_{mn}x + v_{mn}h)} \right]$$

Its expected value is:

$$E\left[\hat{\mathrm{T}}(x,h)\,\hat{\mathrm{T}}^*(x,h)\right] = \frac{1}{|F_n(x,h)|^4}\left[\left|\int\int \mathrm{T}_\Omega(x',h')\,|F_n(x,h)|^2\,AF(x,x',h,h')\,dx'dh'\right|^2 + \right. \qquad \textbf{(A6.9)}$$

$$\left. + \left(\frac{\sqrt{3}}{2} d^2\right)^2 \sum_m \sum_n \sum_r \sum_s W_{mn}\,W_{rs}\,V^*(u_{mn},v_{mn})\,V(u_{mn},v_{mn})\,E\left[\Delta v_{mn}\,\Delta v_{rs}\right] e^{j2p[(u_{rs}-u_{mn})x + (v_{rs}-v_{mn})h]} \right]$$

where the expectation inside the summation is different from zero only for r=m and s=n or r=-m and s=-n, since errors are assumed to be uncorrelated and the hermiticity resort is used. Moreover, in order to simplify the equations, it can be defined:

$$\mathrm{I} \triangleq \frac{1}{|F_n(x,h)|^4}\left|\int\int \mathrm{T}(x',h')\,|F_n(x,h)|^2\,AF(x,x',h,h')\,dx'\;dh\right|^2 \qquad \textbf{(A6.10)}$$

Then:

$$E\left[\hat{\mathrm{T}}(x,h)\,\hat{\mathrm{T}}^*(x,h)\right] = \mathrm{I} + \left(\frac{\sqrt{3}}{2} d^2\right)^2 \frac{1}{|F_n(x,h)|^4} \sum_m \sum_n W_{mn}^2 \left|V^*(u_{mn},v_{mn})\right|^2 s_{\Delta v}^2 + \qquad \textbf{(A6.11)}$$

$$+ \left(\frac{\sqrt{3}}{2} d^2\right)^2 \frac{1}{|F_n(x,h)|^4} \sum_m \sum_n W_{mn}^2\, V^2(u_{mn},v_{mn})\, s_{\Delta v}^2\, e^{-j\,4p\,(u_{mn}x + v_{mn}h)}$$

The first double summation accounts for m=r and n=s, and the second one for m=-r and n=-s (with m and n different from zero).

Equation (A6.11) can be re-written as:

$$E\left[\hat{T}(x,h)\,\hat{T}^{*}(x,h)\right]=1+\left(\frac{\sqrt{3}}{2}d^{2}\right)^{2}\frac{1}{\left|F_n(x,h)\right|^{4}}\,s^{2}_{\Delta v}\sum_{m}\sum_{n}W^{2}_{mn}\left|V(u_{mn},v_{mn})\right|^{2}+$$

$$+\left(\frac{\sqrt{3}}{2}d^{2}\right)^{2}\frac{1}{\left|F_n(x,h)\right|^{4}}\,s^{2}_{\Delta v}\;2\sum_{\substack{m\\ u_{mn}>0,\ v_{mn}\geq 0\\ u_{mn}\leq 0,\ v_{mn}<0}}\sum_{n}W^{2}_{mn}\,\Re\left[V^{2}(u_{mn},v_{mn})\;e^{-j4p\,(u_{mn}x+v_{mn}h)}\right] \qquad \textbf{(A6.12)}$$

Inserting this expression in equation (A6.4), the radiometric accuracy due to residual module errors is given by:

$$\Delta T^{2}(x,h)=\frac{s^{2}_{\Delta v}}{\left|F_n(x,h)\right|^{4}}\left(\frac{\sqrt{3}}{2}d^{2}\right)^{2}\left\{\sum_{m}\sum_{n}W^{2}_{mn}\;\left|V(u_{mn},v_{mn})\right|^{2}+\right.$$

$$\left.+2\sum_{\substack{m\\ u_{mn}>0,\ v_{mn}\geq 0\\ u_{mn}\leq 0,\ v_{mn}<0}}\sum_{n}W^{2}_{mn}\;\Re\left[V^{2}(u_{mn},v_{mn})\;e^{-j4p\,(u_{mn}x+v_{mn}h)}\right]\right\}+\left\{T(x,h)-E\left[\hat{T}(x,h)\right]\right\}^{2} \qquad \textbf{(A6.13)}$$

the last term in equation (A6.13) accounts for Gibbs phenomenon and aliasing effects.

6.2.- RESIDUAL PHASE CALIBRATION ERRORS

To take into account the error in the phase of the visibility function, equation (A6.1) must be replaced by:

$$\hat{T}\;(x,h)=\frac{\sqrt{3}}{2}d^{2}\frac{1}{\left|F_n(x,h)\right|^{2}}\sum_{m}\sum_{n}W_{mn}V(u_{mn},v_{mn})\;e^{j\Delta f_{mn}}\,e^{j2p(u_{mn}x+v_{mn}h)} \qquad \textbf{(A6.14)}$$

where the new exponential accounts for phase errors. When errors are small, it can be approximated by its Taylor's first degree development:

$$\hat{T}\;(x,h)=\frac{\sqrt{3}}{2}d^{2}\frac{1}{\left|F_n(x,h)\right|^{2}}\sum_{m}\sum_{n}W_{mn}V(u_{mn},v_{mn})(1+\;j\Delta f)\,e^{j2p(u_{mn}x+v_{mn}h)} \qquad \textbf{(A6.15)}$$

The development of the expressions to reach the expression of the radiometric resolution is similar as in last section.

Now:

$$E\left[\hat{\mathrm{T}}(x,h)\,\hat{\mathrm{T}}^{*}(x,h)\right]=\frac{1}{|F_n(x,h)|^4}\left[\left|\int\!\!\int \mathrm{T}(x',h')\,|F_n(x,h)|^2\,AF(x,x',h,h')\,dx'\,dh'\right|^2+\right.$$

$$\left.+\left(\frac{\sqrt{3}}{2}d^2\right)^2\sum_m\sum_n\sum_r\sum_s W_{mn}W_{rs}V^{*}(u_{mn},v_{mn})V(u_{mn},v_{mn})\,E\left[\Delta f_{mn}\Delta f_{rs}\right]e^{j\,2p\,[(u_{rs}-u_{mn})x+(v_{rs}-v_{mn})h]}\right] \tag{A6.16}$$

and:

$$E\left[\hat{\mathrm{T}}(x,h)\,\hat{\mathrm{T}}^{*}(x,h)\right]=\mathrm{I}+\left(\frac{\sqrt{3}}{2}d^2\right)^2\frac{1}{|F_n(x,h)|^4}\sum_m\sum_n W_{mn}^2\,|V^{*}(u_{mn},v_{mn})|^2\,s_{\Delta f}^2+$$

$$-\left(\frac{\sqrt{3}}{2}d^2\right)^2\frac{1}{|F_n(x,h)|^4}\sum_m\sum_n W_{mn}^2V^2(u_{mn},v_{mn})\,s_{\Delta f}^2\,e^{-j4p\,(u_{mn}x+v_{mn}h)} \tag{A6.17}$$

where the first double summation is different from zero when m = r and n = s, and the other summation is different from zero when m=-r and n=-s (m and n being different from zero).

Consequently:

$$E\left[\hat{\mathrm{T}}(x,h)\,\hat{\mathrm{T}}^{*}(x,h)\right]=\mathrm{I}+\left(\frac{\sqrt{3}}{2}d^2\right)^2\frac{1}{|F_n(x,h)|^4}\,s_{\Delta f}^2\sum_m\sum_n W_{mn}^2\,|V(u_{mn},v_{mn})|^2+$$

$$-\left(\frac{\sqrt{3}}{2}d^2\right)^2\frac{1}{|F_n(x,h)|^4}\,s_{\Delta f}^2\;2\sum_m\sum_n W_{mn}^2\,\Re e\left[V^2(u_{mn},v_{mn})\,e^{-j4p\,(u_{mn}x+v_{mn}h)}\right] \tag{A6.18}$$

And finally:

$$\Delta\mathrm{T}^2(x,h)=\left(\frac{\sqrt{3}}{2}d^2\right)^2\frac{s_{\Delta f}^2}{|F_n(x,h)|^4}\left\{\sum_m\sum_n W_{mn}^2\,|V(u_{mn},v_{mn})|^2+\right.$$

$$\left.-2\sum_{\substack{m\\ u_{mn}>0,\ u_{mn}\le 0,}}\;\sum_{\substack{n\\ v_{mn}\ge 0,\ v_{mn}<0}} W_{mn}^2\,\Re e\left[V^2(u_{mn},v_{mn})\,e^{-j4p\,(u_{mn}x+v_{mn}h)}\right]\right\}+\left\{\mathrm{T}(x,h)-E\left[\hat{\mathrm{T}}(x,h)\right]\right\}^2 \tag{A6.19}$$

Again, the last term accounts for the Gibbs phenomenon and aliasing effects.

APPENDIX 7. CONSIDERATIONS ABOUT THE ORBITAL PROPAGATOR

This appendix discusses some considerations to be taken into account in the implementation of the orbital propagator: the orbit perturbing forces for a determined accuracy, and the numerical integration of the resulting equation.

7.1.- ORBIT PERTURBING FORCES

The Keplerian satellite motion (equation (7.1)) includes only the Earth's monopole term, while equation (7.2) includes higher terms accounting for the Earth's shape and uneven mass distribution. Other relevant sources of perturbation affecting satellite's motion must be studied prior to the implementation of the orbital propagator. Table A7.1 summarizes the main perturbing forces and the acceleration experimented by the SEASAT or a ERS-1 type satellite due to the perturbing force, whose orbit is very similar to the orbit that has been proposed for MIRAS platform [MMS 95], and the acceleration uncertainty [Milani et al. 87].

Force	Acceleration (SEASAT/ERS-1)	Acceleration uncertainty
(1) Earth's monopole	790 cm/s^2	$4\ 10^{-5}$ cm/s^2
(2) Earth's oblateness	0.93 cm/s^2	$6\ 10^{-7}$ cm/s^2
(2) Low-order geopotential harmonics l=m=2	$5.4\ 10^{-3}$ cm/s^2	$5\ 10^{-6}$ cm/s^2
(2) High-order geopotential harmonics l=m=18	$3.9\ 10^{-5}$ cm/s^2	$3.9\ 10^{-5}$ cm/s^2
(3) Perturbation due to the Moon	$1.3\ 10^{-4}$ cm/s^2	$1.0\ 10^{-9}$ cm/s^2
(3) Perturbation due to the Sun	$5.6\ 10^{-5}$ cm/s^2	$2\ 10^{-10}$ cm/s^2
(3) Perturbation due to other planets (e.g. Venus)	$7.3\ 10^{-9}$ cm/s^2	-
(4) Indirect oblation	$1.4\ 10^{-9}$ cm/s^2	-
(5) Relativistic correction	$4.9\ 10^{-7}$ cm/s^2	-
(6) Atmospheric drag	$2.0\ 10^{-5}$ cm/s^2	$7\ 10^{-6}$ cm/s^2
(7) Solar radiation pressure	$9.2\ 10^{-6}$ cm/s^2	$2\ 10^{-6}$ cm/s^2
(8) Earth's albedo radiation pressure	$3.0\ 10^{-6}$ cm/s^2	$1.0\ 10^{-6}$ cm/s^2
(9) Thermal emission	$1.9\ 10^{-7}$ cm/s^2	$1.9\ 10^{-7}$ cm/s^2

Table A7.1.- *Accelerations on spacecrafts due to perturbing forces [Milani et al 87].*

Similarly, table A7.2 summarizes the equivalent accelerations and their respective uncertainties suffered by the SEASAT or a ERS-1 type satellite due to tidal effects. In the following paragraphs the perturbing forces are briefly explained:

Force	Acceleration (SEASAT/ERS-1)	Acceleration uncertainty
(10) Kinematic solid tide	$5.8\ 10^{-7}$ cm/s^2	$1.7\ 10^{-8}$ cm/s^2
(11) Kinematic oceanic tide	$1.0\ 10^{-7}$ cm/s^2	$2.0\ 10^{-8}$ cm/s^2
(12) Dynamic solid tide	$3.3\ 10^{-5}$ cm/s^2	$3.3\ 10^{-7}$ cm/s^2
(13) Dynamic oceanic tide	$3.3\ 10^{-6}$ cm/s^2	$3.3\ 10^{-7}$ cm/s^2
(14) Non-rigid Earth nutation	$2.0\ 10^{-10}$ cm/s^2	$3.0\ 10^{-11}$ cm/s^2

Table A7.2.- *Equivalent accelerations on spacecrafts due to tidal effects [Milani et al. 87]*

Therefore:
(1) Earth's monopole term μ/r^2 is the largest force influencing satellite's motion, to which other disturbing forces must be compared to evaluate the shift from the Keplerian orbit.
(2) Earth's mass distribution is not uniform nor spherical, and these departures create additional forces that are represented by the series of spherical harmonics of the gravitational Earth's potential.
(3) Gravitational perturbations due to other celestial bodies are not caused by the full gravitational attraction, but only by the tidal term: the difference between the force of the Earth and that on the satellite. The most important effects are due to the Moon and the Sun, whose effects are on the order of magnitude of the medium order geopotential harmonics. Planetary perturbations are small and do not cause any significant acceleration uncertainty.
(4) Indirect oblation force is due to Earth's oblateness that affects the motion of the Moon, and shifts the mass center of the Earth-Moon system. Its effect on the acceleration uncertainty is negligible and that of Moon's oblateness is even smaller.
(5) The relativistic correction represents the main correction to the Newtonian equations of motion introduced by the general relativity theory, but the introduced acceleration uncertainty is negligible.
(6) An exact prediction of the perturbations resulting from atmospheric drag is very complicated, because it requires a model of the upper atmosphere, the atmospheric density as a function of height, but also of time, due to solar and geomagnetic activities. In addition other parameters depending of the satellite's shape, the cross-section area perpendicular to satellite's motion and satellite's velocity relative to the atmosphere are required.

Atmospheric drag has an impact on accelerations uncertainty similar to that of high-order geopotential harmonics and must be taken into account, specially for low-orbit satellites.
(7) The magnitude of the radiation pressure acceleration depends on the satellite's ratio area-to-mass, and the solar energy flux. Time variations in the cross-sectional area, the solar activity and the eclipse events introduce further uncertainties.
(8) Earth-reflected solar radiation also introduces a perturbing acceleration proportional to the mean albedo of the Earth, which depends also on the reflecting surface of the Earth and the season. Solar radiation pressure and Earth's albedo radiation pressure have a similar impact on low-orbit satellites, which is an order of magnitude below the high-order geopotential harmonics.
(9) Thermal re-emission of the radiation absorbed by the satellite occurs usually in a anisotropic way due to emissivity, shape and satellite's surface temperature anisotropies. In addition, the radiation emitted by satellites carrying active instrumentation produces also a recoil acceleration. It has a negligible impact over accelerations' uncertainty.
(10)-(11) Moon's attraction causes periodic pulsations of the Earth, of the tracking stations and of the oceans (tides). Their impact is smaller than the higher geopotential harmonics.
(12)-(13) Dynamic solid and oceanic tides produce a geopotential time variation that affects satellite's motion. Their effects are on the order of magnitude of the higher geopotential harmonics.
(14) And tides also perturb the rotation of the Earth, affecting the reference systems used in the computation of satellite's orbit. This effect is completely negligible for our purposes.

The impact of the different forces has been studied with the aid of the "Orbital Workbench v1.1" program [Cygnus 90] by enabling or disabling different forces to act. The orbit parameters of the MIRAS' reference orbit are [MMS 95]:

	- Semi-major axis:	7159.5 Km
	- Inclination	98.549387º
	- Eccentricity	0.001165
	- Argument of perigee	90º
	- Local time descending node	10:00 h
	- Nodal crossing time (descending)	10:00 h
and:	- Mean altitude	799.8 Km

for which *disturbances due to the Moon, the Sun and the solar radiation pressure are approximately on the same order the magnitude, but their influence is negligible in front of geopotential harmonics.*

Since MIRAS' platform is not yet defined and platform parameters are missing, the effect of atmospheric drag, the dominant perturbation factor below 300 Km height and important up to 1000 Km height, has not been modeled.

7.2.- Numerical integration of the orbit

In the preceding section it was shown that the most important perturbing forces are those due to the spherical harmonics series in which the gravitational potential of the Earth is expanded and the atmospheric drag. The coefficients of the spherical harmonics are compiled in a number of texts [Lundquist and Veis 66][Michele 67][Lerch et al. 79][Lerch et al. 83][WGS-84]. As commented previously, atmospheric drag can not be at present accurately computed due to the absence of information concerning the platform.

Taking into account only the perturbations due to gravitational Earth's potential the integration of the orbit from an initial point with an initial velocity can be performed in the following way:

i) From equation (7.2), the acceleration suffered by the satellite is given by:

$$\overline{F}(\overline{r}) = m\,\overline{a}(t) = m\,\frac{d\overline{v}(t)}{dt} \tag{A7.1}$$

ii) And the velocity vector can be obtained by integrating (A7.1):

$$\int_{t_0}^{t} \frac{\overline{F}(\overline{r})}{m}\,dt = \int_{\overline{v}_0}^{\overline{v}} d\overline{v}$$

$$\frac{\overline{F}(\overline{r})}{m}\,(t-t_0) = \overline{v}-\overline{v}_0 \tag{A7.2}$$

where it has been assumed that for a small time interval ($t-t_o$) the gravitational potential of the Earth has not changed.

iii) Integrating equation (A7.2) with respect to the time, the position vector can be then computed:

$$\frac{d\overline{r}(t)}{dt} = \frac{\overline{F}(\overline{r})}{m}(t-t_0) + \overline{v}_0 = U(t-t_0) + \overline{v}_0 \tag{A7.3}$$

Finally, equation (A7.3) is a first order non-separable differential equation in $\overline{r}(t)$ that can be integrated numerically by means of a i.e. 4th order Runge-Kutta method to obtain the new position vector at the new time instant $\overline{r}(t+\Delta t)$.

When integrating equation (A7.3) some subtleties must be taken into account:

i) the numerical integration is carried in Cartesian coordinates because its simplicity,

ii) at each step, it is necessary to know the rotation rate of the Earth to decrease the longitude of the satellite's position and compute the new gravitational potential properly:

$$\theta(t) = \theta_0 - \Omega_e (t - t_0) \qquad \text{(A7.4)}$$

where Ω_e is the Earth's rotation rate, and according to WGS-84 is $\Omega_e = 7.2921151467\ 10^{-5} rad/s$ [Kaplan 95].

iii) the azimuth correction due to Earth's rotation is performed in spherical coordinates. The transformations from Cartesian-to-spherical coordinates and from spherical-to-Cartesian coordinates must be performed with the sine and cosine functions keeping the angle's quadrant to avoid errors in the satellite's position.

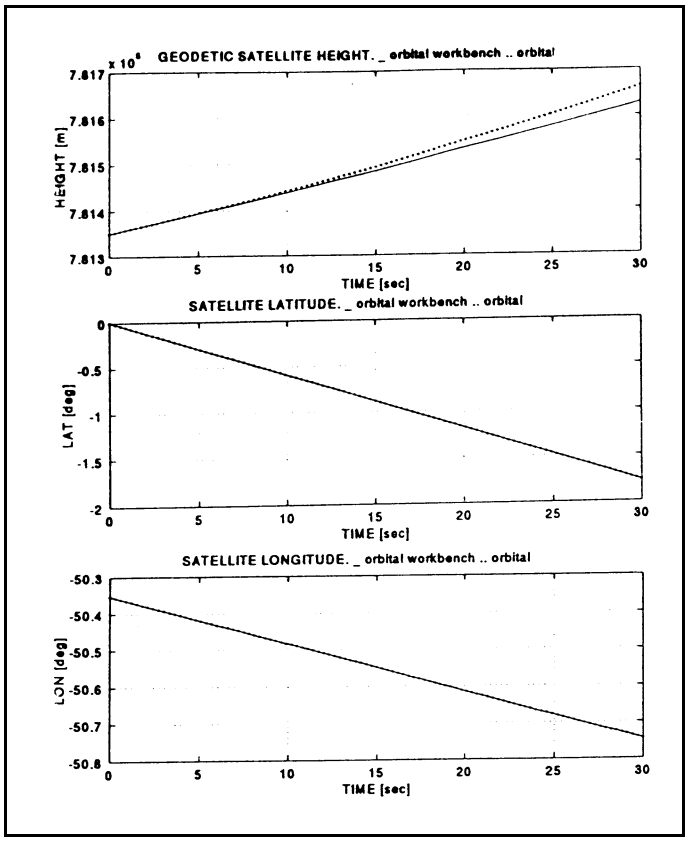

Figure A7.1.- *Orbital Workbench (-) and propagated orbit (...): i)Geodetic Height ii) Latitude and iii) Longitude.*

Figure A7.1 shows the geodetic satellite's height, the satellite's latitude and the satellite's longitude for a 30 seconds flight computed with both the Orbital Workbench (continuous line) and with our orbital propagator (dotted line). As it can be appreciated the latitude and the longitude are computed to within ±0.0005 degrees, which is the precision given by the Orbital Workbench. However, satellite's geodetic height grows initially about 30 m, but the orbit finishes closing after a complete period. This height error: 30m over 780Km geodetic height ($4\ 10^{-3}$%), has a negligible impact in the simulations because of the size of the synthesized beam's. It has been found that this error is generated in the change between spherical and cartesian coordinates due to a round-off error in the evaluation of the trigonometric functions.

APPENDIX 8. LATITUDE AND LONGITUDE CORRESPONDING TO A (ξ,η) PIXEL

The computation of the transformations between reference systems is a main concern in the simulator of a 2D space borne interferometric radiometer because the need to know exactly if a (ξ,η) pixel lies over the visible Earth's surface and, in that case, what are its coordinates over the ECEF reference system of the Earth (section 7.1) and the incidence angle in order to assign a particular value of the brightness temperature (section 7.2).

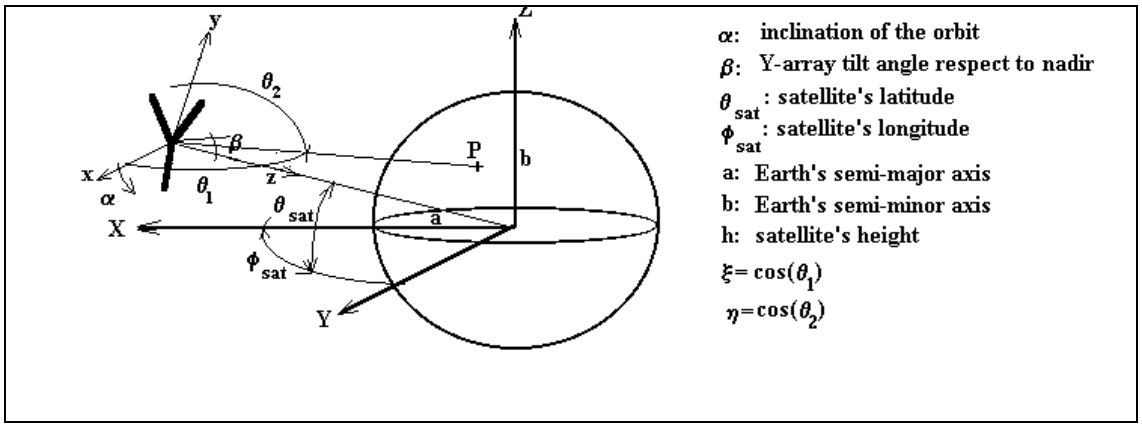

Figure A8.1.- *Geometry of the Y-array and the satellite for changing of the reference system.*

Given a (ξ,η) pixel's coordinates, its latitude and altitude can be computed according to:

i)

$$m = \sqrt{1 - x^2 - h^2} \qquad \textbf{(A8.1)}$$

ii)

$$A = \frac{\sin^2(q_{sat})}{b^2} + \frac{\cos^2(q_{sat})}{a^2}$$

$$B = \frac{1}{a^2}$$

$$C = \frac{\sin^2(q_{sat})}{a^2} + \frac{\cos^2(q_{sat})}{b^2} \qquad \textbf{(A8.2)}$$

$$D = 2\ \sin(q_{sat})\cos(q_{sat})\left[\frac{1}{b^2} - \frac{1}{a^2}\right]$$

iii)

$$
\begin{aligned}
A_1 &= B\cos^2(\varepsilon) + C\sin^2(\varepsilon) \\
B_1 &= A\sin^2(\delta) + B\sin^2(\varepsilon)\cos^2(\delta) + C\cos^2(\varepsilon)\cos^2(\delta) + D\cos(\varepsilon)\sin(\delta)\cos(\delta) \\
C_1 &= A\cos^2(\delta) + B\sin^2(\varepsilon)\sin^2(\delta) + C\cos^2(\varepsilon)\sin^2(\delta) - D\cos(\varepsilon)\sin(\delta)\cos(\delta) \\
D_1 &= -D\sin(\varepsilon) \\
E_1 &= 2A\sin(\delta) + D\cos(\varepsilon)\cos(\delta) \\
F_1 &= -2A\cos(\delta) + D\cos(\varepsilon)\sin(\delta) \\
G_1 &= 2B\sin(\varepsilon)\cos(\varepsilon)\cos(\delta) - 2C\sin(\varepsilon)\cos(\varepsilon)\cos(\delta) - D\sin(\varepsilon)\sin(\delta) \\
H_1 &= 2B\sin(\varepsilon)\cos(\varepsilon)\sin(\delta) - 2C\sin(\varepsilon)\cos(\varepsilon)\sin(\delta) + D\sin(\varepsilon)\cos(\delta) \\
I_1 &= -2A\sin(\delta)\cos(\delta) + 2B\sin^2(\varepsilon)\sin(\delta)\cos(\delta) + 2C\cos^2(\varepsilon)\sin(\delta)\cos(\delta) + \\
&\quad + D\cos(\varepsilon)\left[\sin^2(\delta) - \cos^2(\delta)\right]
\end{aligned}
\qquad \textbf{(A8.3)}
$$

iv)

$$
\begin{aligned}
A_2 &= A_1\frac{\lambda^2}{\mu^2} + B_1\frac{\theta^2}{\mu^2} + C_1 + G_1\frac{\lambda\theta}{\mu^2} + H_1\frac{\lambda}{\mu} + I_1\frac{\theta}{\mu} \\
B_2 &= \left[D_1\frac{\lambda}{\mu} + E_1\frac{\theta}{\mu} + F_1\right]R_{SAT} \\
C_2 &= A\,R_{SAT}^2 - 1 \\
R_{SAT} &= h_{SAT} + \frac{ab}{\sqrt{a^2\cos^2(\lambda_{SAT}) + b^2\sin^2(\lambda_{SAT})}}
\end{aligned}
\qquad \textbf{(A8.4)}
$$

v)

$$
\begin{aligned}
z_{p_1} &= \frac{-B_2 - \sqrt{B_2^2 - 4A_2C_2}}{2A_2} \\
x_{p_1} &= \frac{\lambda}{\mu}z_{p_1} \\
y_{p_1} &= \frac{\theta}{\mu}z_{p_1}
\end{aligned}
\qquad \textbf{(A8.5)}
$$

vi)

$$\begin{aligned} x_{11} &= (a+h_{SAT})\cos(\varphi_{SAT})\cos(\Lambda_{SAT})-x_{p_1} \\ y_{11} &= (a+h_{SAT})\cos(\varphi_{SAT})\sin(\Lambda_{SAT})-y_{p_1} \\ z_{11} &= (a+h_{SAT})\sin(\varphi_{SAT})-z_{p_1} \end{aligned} \qquad \textbf{(A8.6)}$$

vii) Select (x_{11}, y_{11}, z_{11}) pixels satisfying that:

$$B_2^2-4A_2C_2\geq 0 \quad and \quad T(\mu)=0 \qquad \textbf{(A8.7)}$$

which means that they lie over the Earth's surface.

viii)

$$\begin{aligned} x_{p_2} &= \sin(\omega)y_{11}-\cos(\omega)z_{11}+R_{SAT} \\ y_{p_2} &= -\cos(\theta)x_{11}-\sin(\theta)\cos(\omega)y_{11}-\sin(\theta)\sin(\omega)z_{11} \\ z_{p_2} &= -\sin(\theta)x_{11}+\cos(\theta)\cos(\omega)y_{11}+\cos(\theta)\sin(\omega)z_{11} \end{aligned} \qquad \textbf{(A8.8)}$$

ix)

$$\begin{aligned} x_{p_3} &= \cos(\varphi_{SAT})\cos(\Lambda_{SAT})\,x_{p_2}-\sin(\Lambda_{SAT})y_{p_2}-\cos(\Lambda_{SAT})\sin(\varphi_{SAT})z_{p_2} \\ y_{p_3} &= \cos(\varphi_{SAT})\sin(\Lambda_{SAT})\,x_{p_2}+\cos(\Lambda_{SAT})y_{p_2}-\sin(\Lambda_{SAT})\sin(\varphi_{SAT})z_{p_2} \\ z_{p_3} &= \sin(\varphi_{SAT})x_{p_2}+\cos(\varphi_{SAT})z_{p_2} \end{aligned} \qquad \textbf{(A8.9)}$$

(x_{p3}, y_{p3}, z_{p3}) are the pixels' ECEF coordinates, corresponding to a latitude and a longitude:

x)

$$\begin{aligned} latitude &= arctg\left(\frac{z_{p_3}}{\sqrt{x_{p_3}^2+y_{p_3}^2}}\right); \\ longitude &= arctg\left(\frac{y_{p_3}}{x_{p_3}}\right)+180^\circ\,u(-x_{p_3}) \end{aligned} \qquad \textbf{(A8.10)}$$

where u(x) is the step function defined as:

$$u(x)=\begin{cases} 1 & x\geq 0 \\ 0 & x<0 \end{cases} \qquad \textbf{(A8.11)}$$

APPENDIX 9. MMS CUP-DIPOLE RADIATION VOLTAGE PATTERN FIT

In the interferometric radiometer simulator described in chapter 7, antenna radiation voltage patterns have been modelled by fitting the lists of measurements provided by MATRA-MARCONI SPACE for thee cuts (0º, 45º and 90º) of nine antenna patterns: four X-polarization and five Y-polarization cup-dipoles.

It has been found that amplitudes are very well fitted, with an error smaller than 3% over the FOV |2|<60º, by the following expressions and the five parameters $"_1$, $"_2$, $"_4$, $"_5$ and $"_6$:

$$
F_{n_p}(2,N_q) \;\begin{cases} \;' \;1 \& "_{1pq} 2^{"_{2pq}}; & 2 \# 20º \\ \;' \;"_{3pq} \& \dfrac{"_{3pq} \& "_{4pq}}{50º \& 20º} (2 \& 20º); & 20º < 2 \# 50º \\ \;' \;"_{4pq}\, e^{\& "_{5pq}(50º \& 2)^{"_{6pq}}}; & 50º \# 2 \# 90º \end{cases} \qquad \textbf{(A9.1)}
$$

$$
"_{3pq} \times 1 \& "_{1pq}(20º)^{"_{2pq}}
$$

where the subscript "p" is the cup-dipole number and "q" is the cut of the antenna voltage pattern: $N_1 = 0º$, $N_2 = 45º$, $N_3 = 90º$

The following table summarizes the mean and the standard deviation of the matching parameters for the amplitude of MIRAS bread-board antenna voltage pattern:

	$"_1$	$"_2$	$"_4$	$"_5$	$"_6$	$\|F_n(0)\|$
Mean N=0º	0.0009	1.7573	0.4734	0.0176	1.1536	2.8390
Std deviation N=0º	0.0005	0.2346	0.0146	0.0065	0.0950	0.0463
Mean N=45º	0.0010	1.6841	0.4728	0.0203	1.1482	-
Std deviation N=45º	0.0004	0.1597	0.0336	0.0036	0.0661	-
Mean N=90º	0.0009	1.7012	0.5049	0.0169	1.1535	-
Std deviation N=90º	0.0005	0.2047	0.0125	0.0035	0.0562	-

Table A9.1.- *Matching parameters for MIRAS breadboard cup-dipoles antenna voltage pattern amplitude.*

Intermediate values for other azimuth angles are interpolated according to:

$$|F_n(q,f)| = |F_n(q,0^o)|\left|\frac{\sin(4f)}{4\sin f}\right| + |F_n(q,45^o)||\sin(2f)| + |F_n(q,90^o)|\left|\frac{\sin(4(f-p/2))}{4\sin(f-p/2)}\right| \quad \textbf{(A9.2)}$$

For the phase of the antenna radiation voltage pattern an eighth degree polynomial is required to fit the pattern with an error smaller than 0.5º, the limit required by the radiometric accuracy budget (chapter four).

$$\angle F_{n_p}(q,f_q) = \sum_{r=0}^{8} b_{r\,p,q}\, q^r;\ q: \text{degrees} \quad \textbf{(A9.3)}$$

where the subscript "p" is the cup-dipole number and "q" is the cut of the antenna voltage pattern: $\phi_1 = 0^o$, $\phi_2 = 45^o$, $\phi_3 = 90^o$. The following table summarizes the mean and the standard deviation of the matching parameters for the phase of MIRAS bread-board antenna voltage pattern:

	β_0	β_1	β_2	β_3	β_4	β_5	β_6	β_7	β_8
Mean $\phi=0^o$	180.6º	$-1.82\ 10^{-1}$	$5.72\ 10^{-2}$	$-6.53\ 10^{-3}$	$3.35\ 10^{-4}$	$-8.73\ 10^{-6}$	$1.25\ 10^{-7}$	$-8.81\ 10^{-10}$	$2.55\ 10^{-12}$
Std deviation $\phi=0^o$	$4.76\ 10^{-1}$	$3.29\ 10^{-1}$	$7.00\ 10^{-2}$	$6.13\ 10^{-3}$	$2.71\ 10^{-4}$	$6.59\ 10^{-6}$	$8.89\ 10^{-8}$	$6.25\ 10^{-10}$	$1.78\ 10^{-12}$
Mean $\phi=45^o$	-	$-1.53\ 10^{-1}$	$6.02\ 10^{-2}$	$-6.99\ 10^{-3}$	$3.52\ 10^{-4}$	$-8.96\ 10^{-6}$	$1.22\ 10^{-7}$	$-8.52\ 10^{-10}$	$2.38\ 10^{-12}$
Std deviation $\phi=45^o$	-	$1.58\ 10^{-1}$	$4.12\ 10^{-2}$	$3.41\ 10^{-3}$	$1.32\ 10^{-4}$	$2.85\ 10^{-6}$	$3.57\ 10^{-8}$	$2.46\ 10^{-10}$	$7.19\ 10^{-13}$
Mean $\phi=90^o$	-	$4.34\ 10^{-2}$	$1.00\ 10^{-2}$	$-1.61\ 10^{-3}$	$9.33\ 10^{-5}$	$-2.60\ 10^{-6}$	$3.81\ 10^{-8}$	$-2.85\ 10^{-10}$	$8.50\ 10^{-13}$
Std deviation $\phi=90^o$	-	$8.86\ 10^{-2}$	$3.58\ 10^{-2}$	$3.61\ 10^{-3}$	$1.67\ 10^{-4}$	$4.18\ 10^{-6}$	$5.79\ 10^{-8}$	$4.18\ 10^{-10}$	$1.23\ 10^{-12}$

Table A9.2.- *Matching parameters for MIRAS breadboard cup-dipoles antenna voltage pattern phase.*

Intermediate values for other azimuth angles are also interpolated according to (A9.2). Figures A9.1 and A9.2 show the measurements, the fitted values and the relative error committed when approximating cup-dipole #3 Y-polarization antenna voltage pattern amplitude and phase with equations (A9.1) and (A9.3) respectively. It should be noted that if antenna amplitude and phase errors were smaller, antenna voltage patterns could be fitted with less errors by simpler functions.

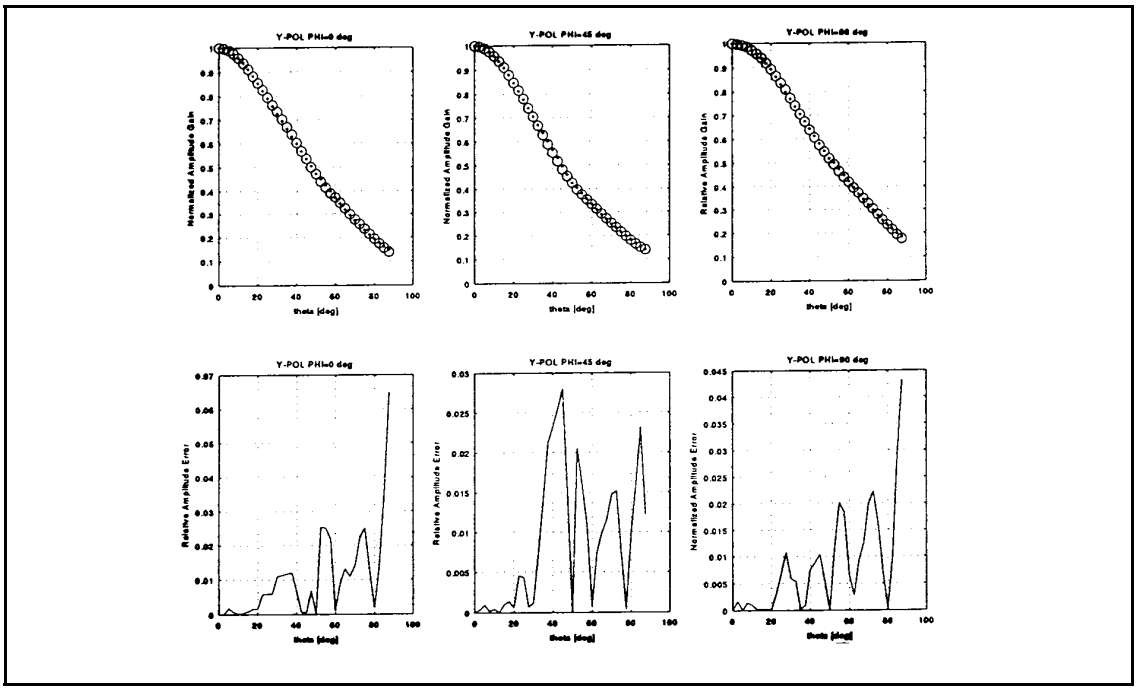

Figure A9.1.- Cup-dipole #3 Y-polarization measured amplitude pattern values (o), approximated values (.) and relative error.

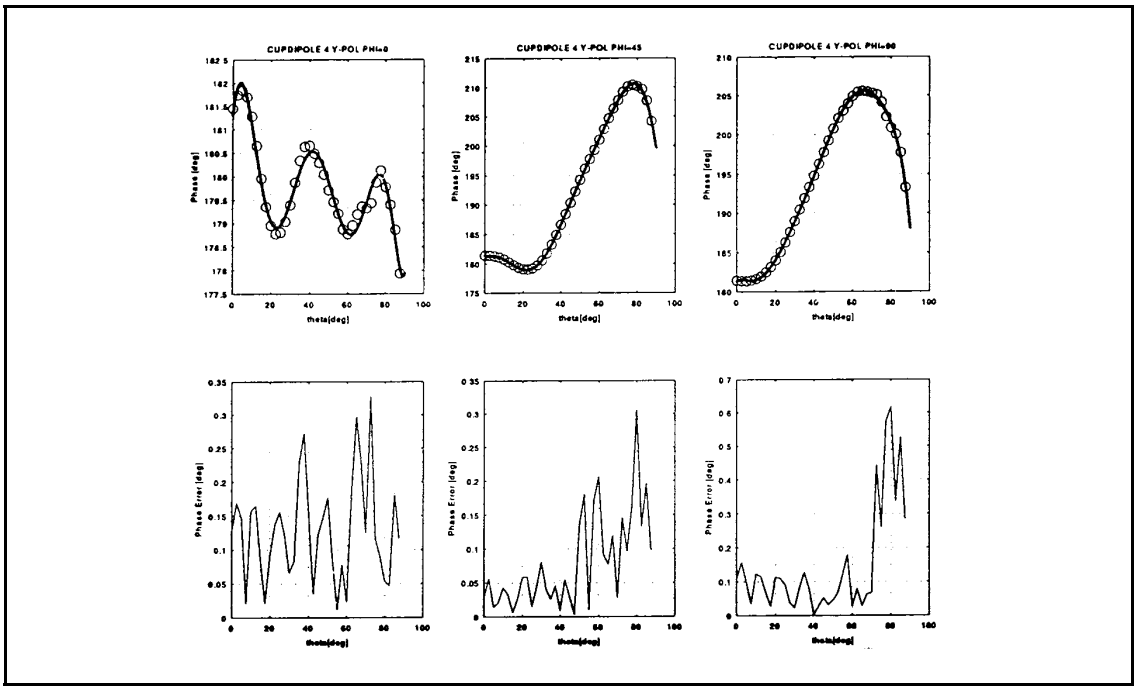

Figure A9.2.- Cup-dipole #3 Y-polarization measured phase pattern values (o), approximated values (.) and relative error.

APPENDIX 10. ANALYSIS OF CUP-DIPOLE RADIATION PATTERN

A detailed analysis of the radiation pattern of the cup-dipole is complicated because it is large to use MoM methods and small to use geometrical optics ones. The radiation problem has been analyzed as that of an aperture located at the X-Y plane illuminated with a transverse electric field of the form:

$$\overline{E} = \frac{E_o}{k_c}\{k_c\left[J_n'(K_c r)+BY_n'(k_c r)\right]\left[C\cos(n\phi)+D\sin(n\phi)\right]\sin(\beta_z z)\,\hat{\phi}+ \\ -\frac{n}{r}\left[J_n(K_c r)+BY_n(k_c r)\right]\left[-C\sin(n\phi)+D\cos(n\phi)\right]\sin(\beta_z z)\,\hat{\rho}\} \tag{A10.1}$$

satisfying the boundary conditions over the inner and external metal cylinder surfaces:

$$E_\phi(r=a,b)=0; \quad \Rightarrow J_n'(k_c a)+BY_n'(k_c a)=0 \\ J_n'(k_c b)+BY_n'(k_c b)=0 \tag{A10.2}$$

and:

$$E_r(\phi=0,B)=0; \quad \Rightarrow D=0, \quad C=1 \tag{A10.3}$$

over the dipole's arms, which are oriented along the x axis.

The solution of (A10.1) with the boundary conditions (A10.2) and (A10.3) is given by:

$$\overline{E} = \frac{E_o}{k_c}\{k_c\left[J_n'(K_c r)+BY_n'(k_c r)\right]\cos(n\phi)\,\sin(\beta_z z)\,\hat{\phi}+ \\ +\frac{n}{r}\left[J_n(K_c r)+BY_n(k_c r)\right]\sin(n\phi)\,\sin(\beta_z z)\,\hat{\rho}\} \tag{A10.4}$$

where:

$$B=-\frac{J_n'(k_{c_{np}}a)}{Y_n'(k_{c_{np}}a)} \tag{A10.5}$$

and $k_{c\,np}$ is obtained from:

$$\frac{Y_n'(k_{c_{np}}a)}{Y_n'(k_{c_{np}}b)}=-\frac{J_n'(k_{c_{np}}a)}{J_n'(k_{c_{np}}b)} \tag{A10.6}$$

that must be solved numerically. Table A10.1 summarizes the first TE modes and their cut-off wave-numbers, the B parameter and the illumination efficiency:

$kc_{n,p}$	B	0_{il}
$k_{c\ 0,1}$=271.46 rad/m	2.3716	-
$k_{c\ 1,1}$=77.52 rad/m	-0.1844	45%
$k_{c\ 1,2}$=261.78 rad/m	-0.0925	-
$k_{c\ 2,1}$=323.98 rad/m	-0.4319	-

Table A10.1.- *First modes in the cup-dipole structure and cut-off wave-numbers a=6.5 mm, b=20 mm, f=10.7 GHz, k=2B/8=226.2 rad/m*

As it can be observed, the only mode that can be excited at the frequency of 10.7 GHz is the TE_{11} one, as in a cylindrical waveguide, for which $k_{c\ 11}$=77.52 rad/m < k=226.2 rad/m and B=-0.1844. The aperture illumination efficiency computed from (A10.4) is 45% and corresponds to a directivity of 9.08 dB. Figure A10.1 shows the computed E plane cut of the radiation pattern and figure A10.2 shows the electric field components corresponding to the TE_{11} mode according to equation (A10.4).

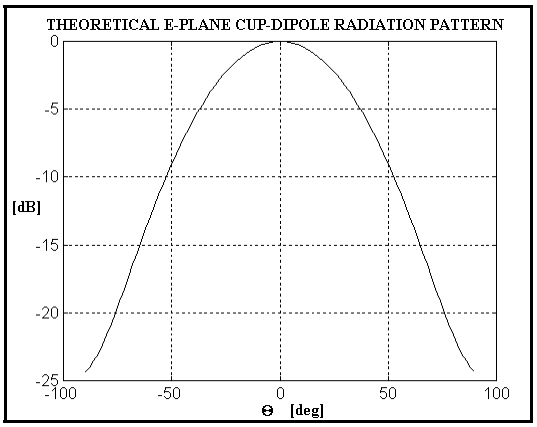

Figure A10.1.- Theoretical E-plane radiation pattern of the cup-dipole.

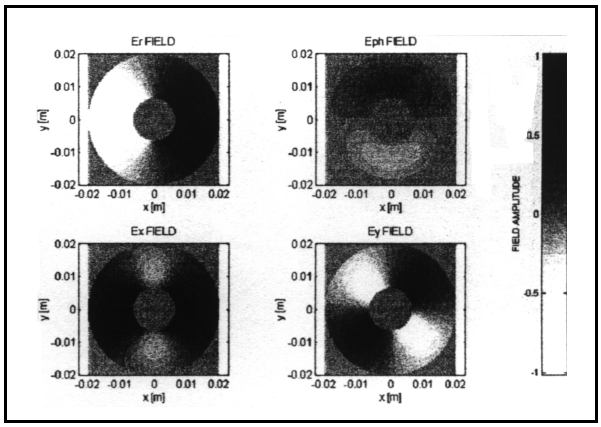

Figure A10.2.- Computed normalized amplitudes of the electric field over the aperture (cup-dipole centered and oriented along x-axis)

The cup-dipole antenna has been implemented by means of a cylindrical cavity with an open side in which a feeder has been placed. Two kind of feeders dipoles have been tested: triangular dipoles and wire dipoles. Measured antenna patterns are shown in figures 8.4 to 8.6.

APPENDIX 11. X-BAND CUP-DIPOLES MEASURED COUPLING

This appendix provides the information about the parameters of coupling between the antennas manufactured for the experimental interferometric radiometer.

The numbering of the antennas corresponds to the next illustration:

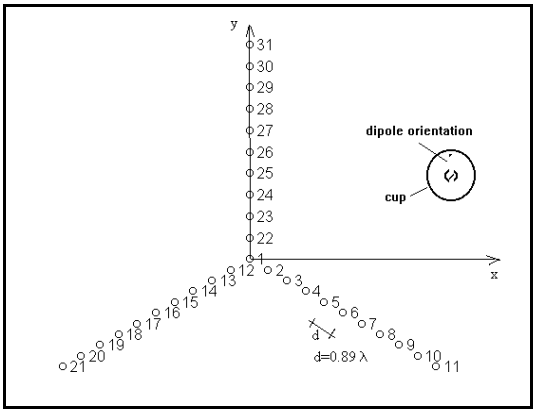

Figure A11.1.- *Antenna numbering in the Y-array*

The minimum distance between antennas is 0.898 and the central frequency 10.7GHz. The antennas are tested for vertical polarization. To achieve these results, 50 measures have been averaged. The next table presents the scattering parameters measured for several pairs of antennas according to figure A11.1. The module is given in thousandths and the phase in degrees.

POSITION	S_{11}	S_{12}	S_{21}	S_{22}
1-2	301.39 ê -80.33	31.09 ê 140.08	32.284 ê 141.07	214.48 ê -21.363
1-3	320.11 ê -34.57	10.87 ê 143.71	11.05 ê 143.2	217.1 ê -13.152
1-4	282.17 ê -46.637	6.949 ê -112.59	7.42 ê -111.79	223.27 ê -12.037
1-4 (extra antenna in between)	289.17 ê -46.50	5.5182 ê -120.45	5.28 ê -117.88	222.98 ê -13.451
1-22	323.56 ê -88.706	20.132 ê -130.19	21.146 ê -130.76	212.14 ê -20.451
1-23	322.83 ê -35.115	8.01 ê -95.258	8.476 ê -96.5	235.07 ê -17.571
1-24	317.11 ê -34.393	0.91 ê -141.23	1.205 ê -124.11	231.03 ê -17.75
1-12	302.81 ê -79.97	29.589 ê 134.6	30.294 ê 136.89	217.58 ê -15.142
1-13	319.85 ê -34.56	4.4796 ê 148.94	4.398 ê 147.62	223.75 ê -19.394
2-12	134.41 ê -14.78	16.56 ê 176.13	16.67 ê 177.17	228.04 ê 10.079
2-13	134.67 ê -14.347	2.3953 ê -151.55	2.585 ê -153.85	218.86 ê -19.979

3-12	319.89 ê -78.157	12.518 ê -92.848	13.04 ê -93.864	245.19 ê 39.678
3-13	315.54 ê -77.178	5.19 ê 4.33	5.94 ê 7.10	277.49 ê -19.223
3-14	313.1 ê -76.85	9.16 ê 118.7	9.33 ê 119.81	203.32 ê -14.726
3-15	312.1 ê -76.902	2.966 ê -172.34	3.6 ê -167.96	200.55 ê -13.612
4-12	305.95 ê -76.069	9.633 ê 63.346	9.698 ê 62.53	243.52 ê 40.261
4-13	304.93 ê -76.266	1.16 ê 165.58	1.15 ê 161.96	246.64 ê 40.802
2-22	218.44 ê -49.182	6.5 ê 46.85	6.537 ê 50.26	247.18 ê 39.93
2-23	218.73 ê -49.081	0.736 ê -38.23	0.638 ê -20.83	253.63 ê 40.873
3-22	218.03 ê -48.61	2.742 ê -56.033	2.919 ê -52.192	250.5 ê 41.3
12-22	309.13 ê 2.038	3.53 ê -44.63	3.425 ê -47.552	250.55 ê 41.25
12-23	310.75 ê 3.16	4.35 ê 115.68	4.21 ê 117.23	254.79 ê 40.953
12-24	310.2 ê 3.1242	3.14 ê -34.538	2.917 ê -22.449	253.11 ê 42.413
13-22	307.83 ê 4.06	3.037 ê 176.49	2.86 ê -170.44	253.45 ê 40.794
13-23	317.6 ê 5.05	4.22 ê -48.816	3.66 ê -42.344	247.9 ê 41.12
13-24	313.67 ê 4.52	2.83 ê 99.049	2.78 ê 114.19	254.91 ê 40.592
13-25	318.65 ê 5.81	1.979 ê 134.62	2.53 ê 135	254.23 ê 40.894

Table A11.1.- *Scattering parameters of X-band cup-dipoles.*

APPENDIX 12. RF FRONT-END DESIGN AND CHARACTERIZATION

The RF front-end is composed by two X-band TV DBS external units model TAGRA GSE-303, for the reception of the ASTRA satellites in the 10.7GHz-11.8GHz band. The performance provided by the manufacturer are listed in the table below:

Input Frequency	*10.7 GHz - 11.8 GHz*
Input connector	*Waveguide WR-75*
Noise factor	*1.0 dB*
Gain	*50 dB - 60 dB*
Output Frequency	*950 MHz - 2050 MHz*
LO Frequency	*9.750 MHz*
LO Power at the Input	*-60 dBm (max)*
Output power	*0 dBm (min)*
Output Connector	*"F" type 75Ω female*
Current consumption	*200 mA (max)*
Voltage Supply	*13 V - 24 V*
Operating Temperature Range	*-40ºC - + 60ºC*

Table 8.5.- *GSE-303 TAGRA DBS external units parameters*

Figures A12.1 and A12.2 show, respectively, the detail of the top and the bottom sides of the external units. In the top side (figure A12.1), it can be observed the three stage LNA (upper left side), the coupled line image rejection filter (upper right side) and the mixer (lower right side), as well as the quarter wavelength coupled lines for the LO (lower side). In the bottom side (figure A12.2), it can be observed the two stage wide band IF amplifier (right side), and a detail of the LO extraction and its replacement by a 50 Ω line and a SMA connector.

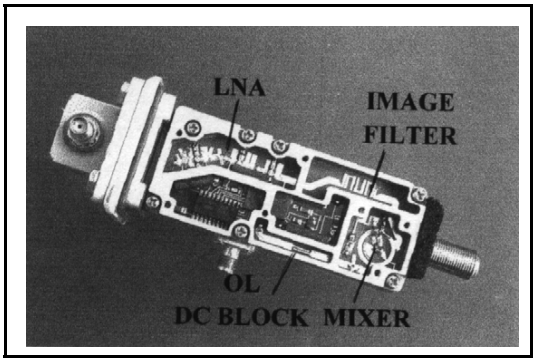

Figure A12.1.- *Upper side of the TV external units used as RF front-ends*

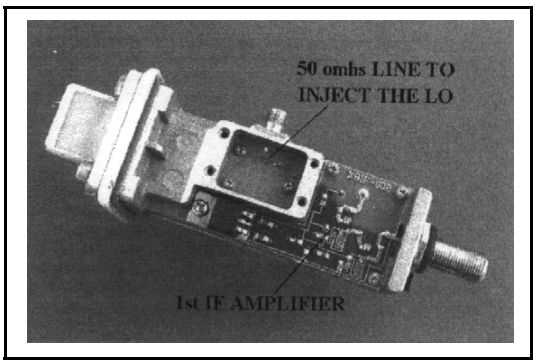

Figure A12.2.- *Bottom side of the TV external units used as RF front-ends. Note the replacement of the LO by a 50 Ω line.*

Because of the availability of commercial components at IF (filters and I/Q demodulators), the IF center frequency was fixed at 881.5 MHz, which is out of the specified output frequency band. Consequently, the LO frequency was changed accordingly and the overall gain was affected due to an increase in mixer's insertion loss. TV-DBS external units were characterized to check their output bandwidth, their gain and their noise factor.

TV-external units' frequency response was measured with a HP-70206 A spectrum analyzer. The curve in figure A12.3 shows that the half-power bandwidth cut-off frequency is 750 MHz. A similar frequency response was obtained for the other external unit with a half-power band-width cut-off frequency of 775 MHz. Ripples above 1.8 GHz are due to the cut-off frequency of the bias-T used to polarize the external units during the measurement.

Figure A12.4 shows the gain and noise factor measured with a HP 8970B Noise Figure Meter [HP B] as a function of the output frequency. Remember that the LO is extracted and replaced by a 50 S line carrying a synthesized oscillator [HP C] that allows frequency tuning. The following table summarizes the main performance of the two TV-DBS external units:

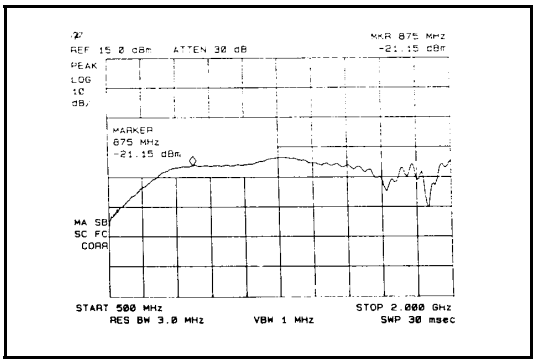

Figure A12.3.- *Output frequency response of the TV DBS external units used as a front -end.*

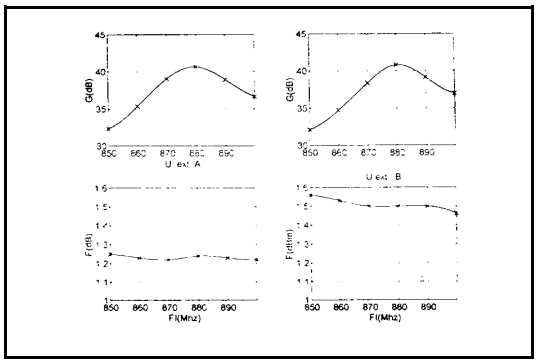

Figure A12.4.- *TV DBS external units measured gain and noise figure.*

The following table summarizes the main performance of the two TV-DBS external units:

Parameter	DBS external Unit A	DBS External Unit B
Gain	41.50 dB	42.05 dB
Noise Factor	1.22 dB	1.45 dB

Table A12.2.- *DBS external units performance for use in the experimental interferometric radiometer (f_i = 10.6895 GHz, f_o= 881.5 MHz, f_{OL}=9.808 GHz, LO power = 10 dBm).*

APPENDIX 13. IF SECTION DESIGN AND CHARACTERIZATION

The scheme of a single amplifier is shown in figure A13.1.

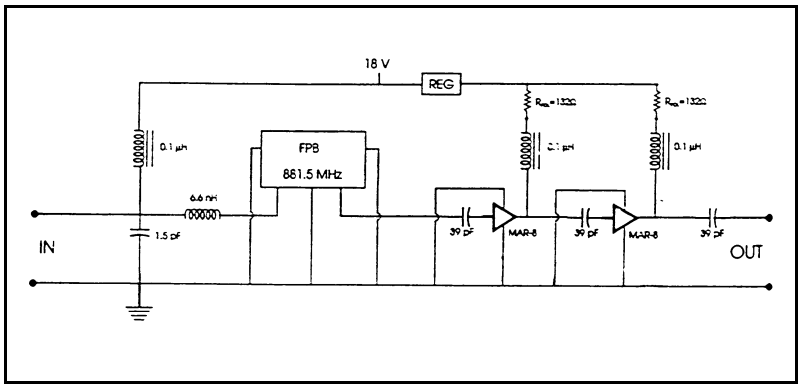

Figure A13.1.- *IF amplifier scheme: matching network, IF filter and two-stage IF amplifier*

which is shown in figure A13.2.

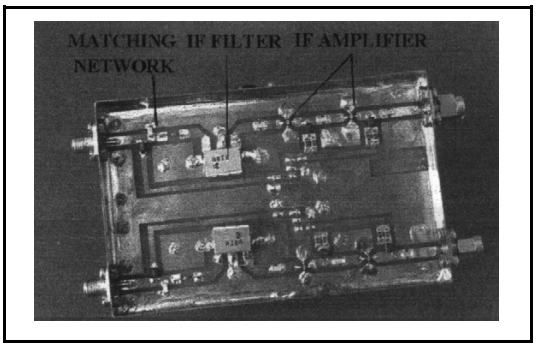

Figure A13.2.- *IF amplifiers picture*

13.1.- Impedance matching network

The impedance matching network is a simple L-circuit formed by a capacitor and an inductor, as shown in figure A13.3. Component values are computed with the Hewlett Packard's APPCAD program leading to:

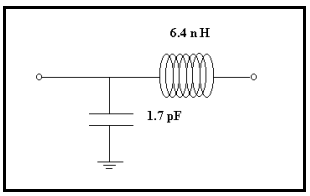

Figure A13.3.- *Impedance matching network*

$$Z_s = j35.36 \Rightarrow L_s = \frac{35.36}{2\pi 881.5\,10^6} = 6.4\,nH$$
$$Z_p = \frac{1}{j9.42} \Rightarrow C_p = \frac{9.42}{2\pi 881.5\,10^6} = 1.7\,pF \qquad \textbf{(A13.1)}$$

The matching circuit was finally built with a 1.5 pF SMD capacitor and a self-constructed three turns, 1 mm diameter inductance of 0.3 mm diameter wire. Measured matching over the IF band was better than 25 dB.

13.2.- IF Filters measurements

Figure A13.4 to A13.6 show the measured input return loss, the insertion loss and the group delay frequency response.

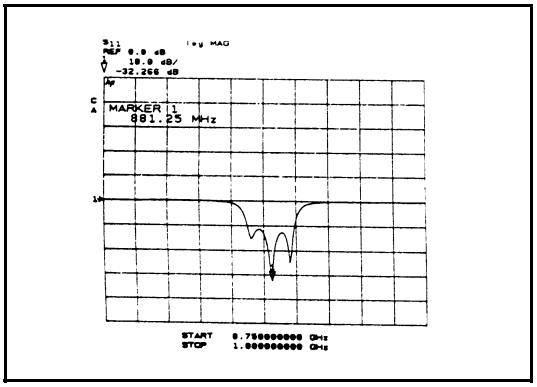

Figure A13.4.- *IF filter's input return loss.*

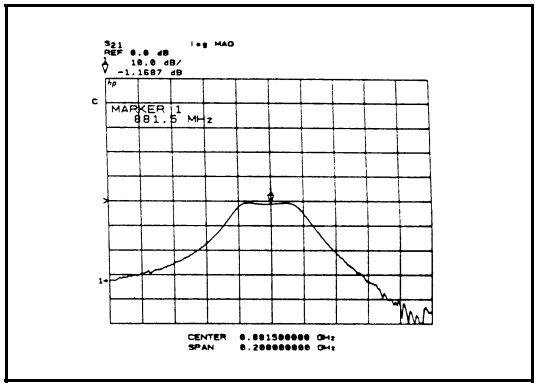

Figure A13.5.- *IF filter's insertion loss.*

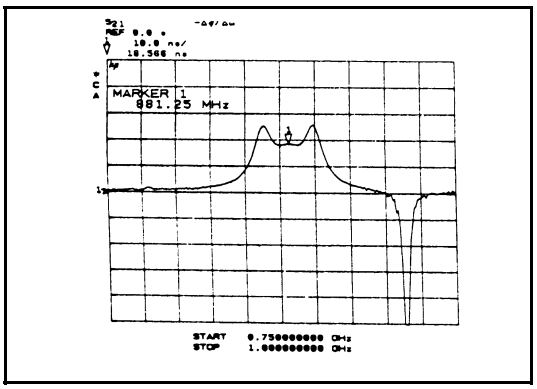

Figure A13.6.- *IF filter's group delay.*

13.3.- IF two stage amplifier

The two-stage IF amplifier is built with two MAR-8 MINICIRCUITS integrated amplifiers, each one having a maximum gain at 900 MHz of 23 dB. Chips are DC decoupled and have input/output impedances of 50 S. To avoid oscillations of the first amplifier due to the output impedance of the filter out of pass-band ground via-holes were approached to the chip and a 100 S resistance was added in parallel with the filter's output. Figures A13.7 and A13.8 show the measured gain and group delay of one channel. The main performance of the two IF amplifiers is shown in table A13.1.

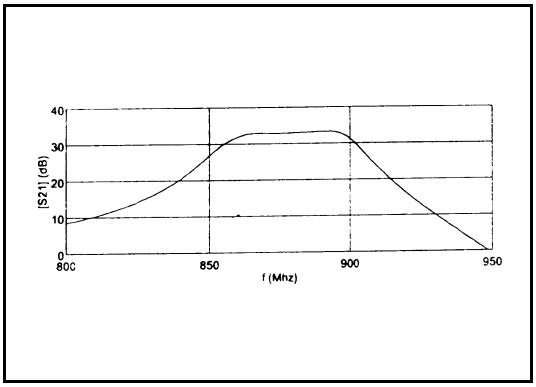

Figure A13.7.- *IF amplifiers gain frequence response.*

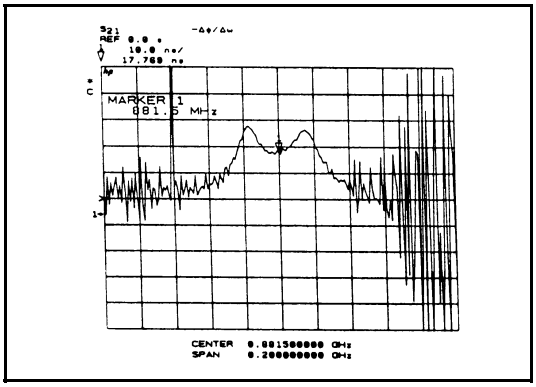

Figure A13.8.- *IF amplifiers group delay frequency response.*

Parameter	**Amplifier 1**	**Amplifier 2**
Half-power bandwidth	40 MHz	46 MHz
Gain	33 dB	36 dB
Input return loss	-17 dB	- 6.4 dB
Output return loss	-16 dB	- 7.8 dB

Table A13.1.- *Performance of IF amplifiers*

APPENDIX 14. LF SECTION DESIGN AND CHARACTERIZATION

The LF section is formed by a bank of four filters, a bank of four video amplifiers and a peak detector (figure 8.2).

14.1.- The Bank of Video Amplifiers

The bank of video amplifiers is implemented with the Linear LSI NE-592 circuit, which satisfies gain and bandwidth requirements. Its main performance are summarized in the next table.

Parameter	Value
Differential voltage gain	40 dB typ
Bandwidth	90 MHz
Input resistance	30 KS
Input capacitance	2 pF
Input bias current	5 µA
Output offset voltage	1.5 V
Output resistance	20 S

Table A14.1- *NE-592 main performance*

Since comparators' reference level is zero volts and amplifiers' output offset voltage is 1.5 V, an additional DC block is included at the output. On the other hand, to avoid oscillation problems when large gain is required, a 100 S resistance has been added in series with the 200 S gain potentiometer (not shown in figure A14.1).

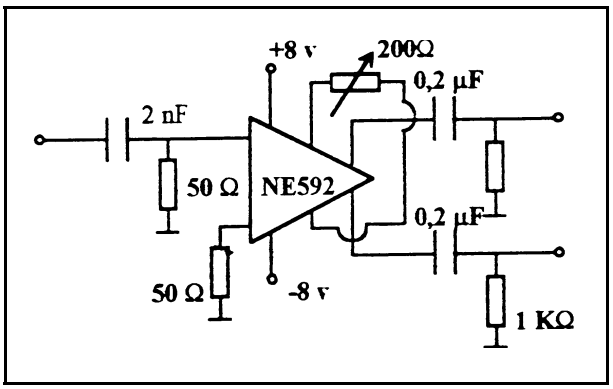

Figure A14.1 *Video amplifier scheme.*

Figure A14.1 shows the scheme of each of the four video amplifiers designed. Input/output DC blocks, as well as the gain potentiometer can be appreciated. Figure A14.2 shows the frequency response of one channel for the maximum and minimum gain.

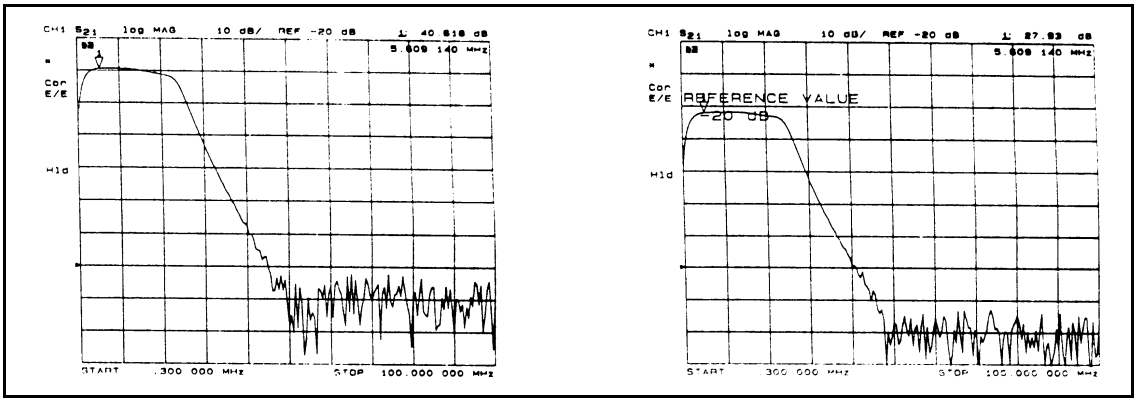

Figure A14.2.- *Video amplifier frequency response for maximum and minimum gain.*

14.2.- Peak detector and signal conditioning circuit

The peak detector scheme is shown in figure A14.3. It is composed by a 50 S parallel resistor to match input's impedance, followed by a Schottky diode and a parallel capacitor acting as a low pass filter. Figure A14.4 shows the signal conditioning circuit. It is composed by a voltage-current transducer in which R_2 is used to adjust the zero and R_4 the gain.

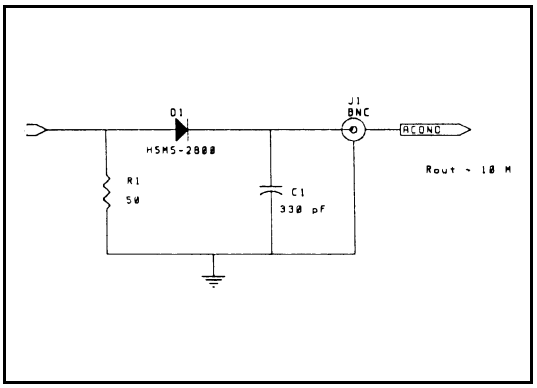

Figure A14.3.- *Peak detector scheme.*

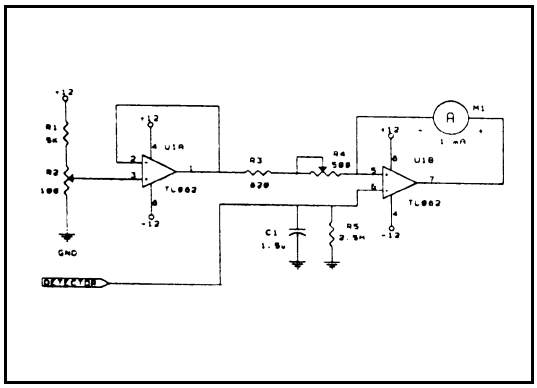

Figure A14.4.- *Scheme of the voltage-current transducer used to monitor signal's power.*

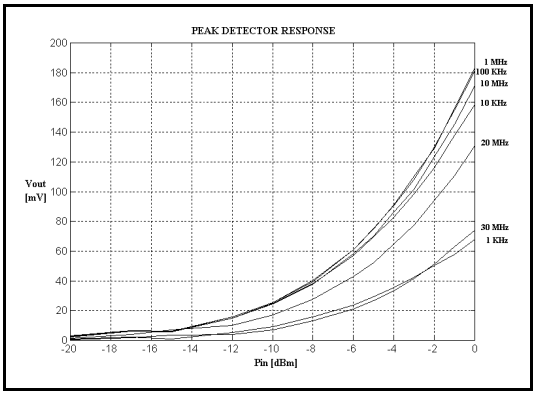

Figure A14.5.- *Peak detector transfer curve.*

Figure A14.5 shows the output voltage vs. the input power at different frequencies. As it is seen detector's bandwidth is limited from 10KHz up to 20MHz.

APPENDIX 15. DESIGN OF A 1 BIT/2 LEVEL DIGITAL CORRELATOR UNIT

15.1.- Technology and IC's selection

At the preliminary stage of the design and according to the availability of commercial components, system's bandwidth is set to 30 MHz. This requires a minimum sampling frequency of 60 MHz.

To avoid conversions between signals' levels of different technologies, i.e. ECL-TTL, the first choice is the selection of all the ICs of a single technology. On the other hand, since the available acquisition board -National Instruments' PC-LAB- uses TTL circuits, correlators' ICs are selected from the FAST TTL family for the XOR gates, the buffers and the counters, and from the LS TTL family for the shift registers that form the PISO (Parallel Input Serial Output). Available FAST TTL circuits are capable to go up to 100 MHz, above the 66 MHz clock frequency that is finally selected. LS TTL circuits are selected to minimize power consumption where speed is not required.

In the following paragraphs the function of the ICs selected is briefly described:

i) Clock: The function of the clock is to generate the signal used to control the sampling times of the comparators and to activate the counters. Kyocera´s MC68EC 66 MHz oscillator is selected because of its TTL compatible digital output and its +5V power supply. A buffer is required to improve its 10 gate fan-out.

ii) Buffer: The 74F125 FAST TTL circuit is selected because its low propagation delay, 5 ns, and its large fan-out: up to 30 gates. However, when the unit is mounted it is found that the clock does not arrive to the most distant ICs and a second buffer is connected in parallel with the first one.

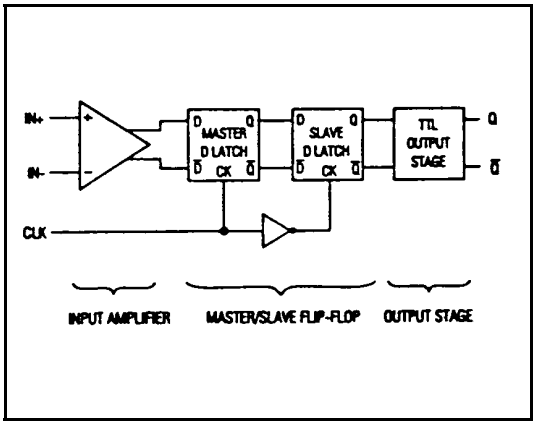

Figure A15.1.- *MAX-915 block diagram*

iii) Sampler: The MAXIM's MAX-915 high speed comparator is selected because its low propagation delay, 6 ns, its +5 V power supply, the availability of the complementary TTL output -used to simplify the multiplier circuit- and the insensitivity to oscillations provided by a Master-Slave flip-flop that isolates the input and the output, as it can be seen in figure A15.1. Its response at 66 MHz is previously tested, because the manufacturer guarantees

its performance up to 50 MHz.

iv) Multiplier: In the 1B/2L digital correlator the analog multiplier is substituted by a simple NOT-XOR gate. However, this function can be also performed if one input is negated, as indicated in table 8.11. The negated input is obtained from the complementary output of the MAX-915 comparator.

A	$\overline{A}$	B	$A \times B$	$\overline{A \times B}$	$\overline{A} \times B$
0	1	0	0	1	1
0	1	1	1	0	0
1	0	0	1	0	0
1	0	1	0	1	1

Table A15.1.- *XOR function.*

v) Counters: The 74F163 and 74F161 FAST TTL 4 bit counters are selected because they are the only ones commercially available. The 74F163 ICs have a synchronous reset, while the 74F161 have an asynchronous one.

vi) Shift registers: The 74LS166 8 bit shift registers perform the Parallel Input to Serial Output conversion. When the correlation is finished, the result is stored in the counters, it is loaded into the shift registers and then it is downloaded bit by bit to the PC-LAB acquisition board.

15.2.- Scheme of the digital correlator unit and control flow

Correlator's scheme is composed by three counter units: the first one for equalities in the i_1 and i_2 channels, leading to the real part of the visibility sample being measured, the second one for equalities in the i_2 and q_1 channels, leading to the imaginary part of the visibility sample, and the third one that counts during all the integration time. The third counter is included to improve the measurement of the integration time due to timing errors of the acquisition board. These slight errors are, however, too large to have a precise measurement of the correlation between the two signals, specially for small integration times.

The number of bits of each counter unit is determined by the maximum integration time, 64 s, and the sampling frequency: 66.666 MHz.

$$_{ants} \;'\; 66.666\,MHz\;\; 64s \;'\; 4.266.624.000 \;'\; 2^{32} \;'> 32 \qquad \textbf{(A15.1)}$$

this means: 8 x 4 bit counters and 4 x 8 bit shift registers in each counter unit.

Figure A15.2 shows the scheme of a correlator unit composed by i) the sampler and the XOR multiplier and ii) the counter unit and the control signals.

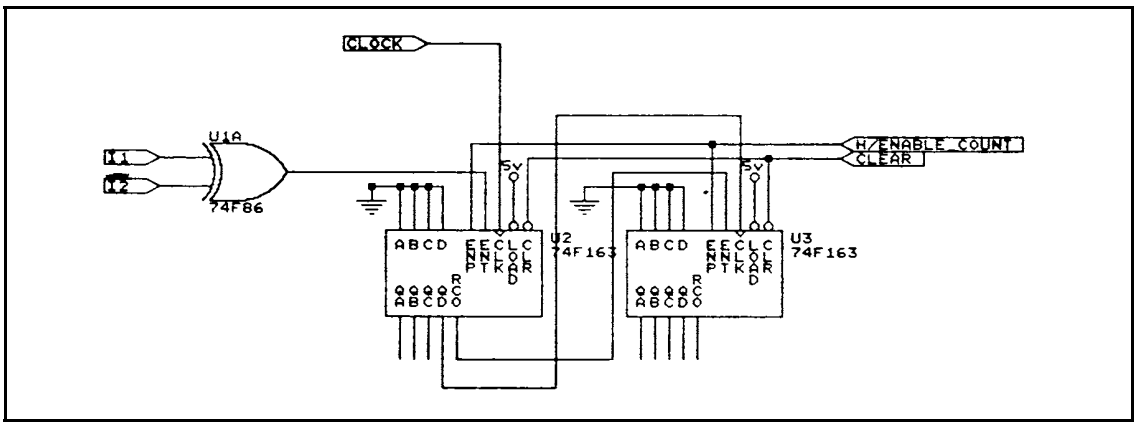

Figure A15.2..- *Scheme of a correlator: XOR (digital multiplication) and counter (digital integration).*

Figures A15.3 and A15.4 show the top and bottom views of the digital correlator unit: In the upper side the three MAX-915 comparators can be appreciated on the left, followed by the 74F86 XOR gates. The upper and lower ICs blocks are the correlators of the real and imaginary parts of the visibility sample, while the block of 12 ICs in the middle counts during the whole integration time. On the lower side the clock can be seen, as well as the two buffers in parallel with a radiator.

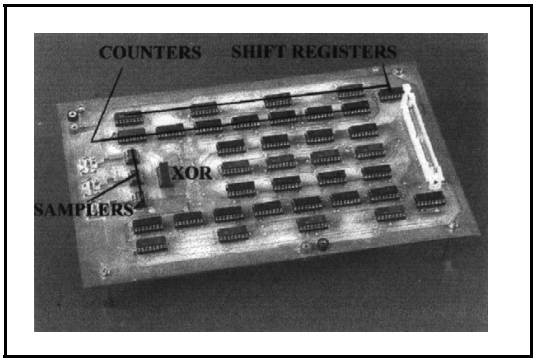

Figure A15.3.- *Digital Correlator top view.*

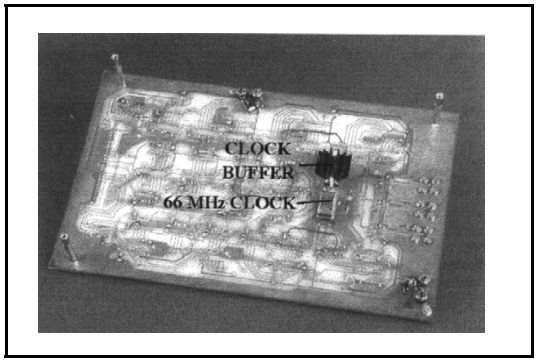

Figure A15.4.- *Digital Correlator bottom view*

As commented before, the control of the digital correlator unit is performed by a signal acquisition board by means of nine signals:

i) Signal $\overline{CLEAR}$ resets the counters before a new correlation is performed. The **H/ENABLE** signal controls the time interval in which the correlation is computed (figure A15.5) and the correlator-board **CLOCK** controls the sampling instants.

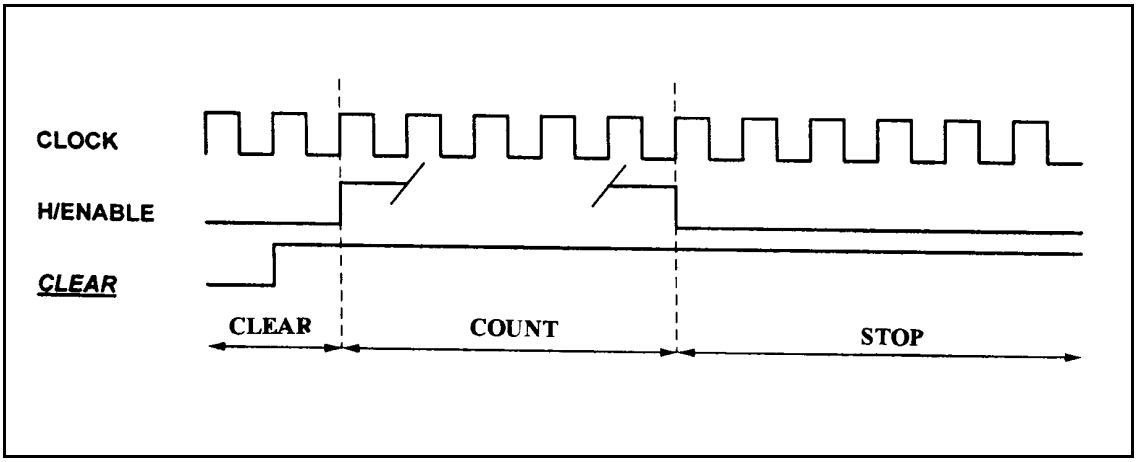

Figure A15.5.- *Control flow during the initialization and correlation intervals.*

ii) When the correlation is finished, the $\overline{LOAD}$ signal forces the shift registers to be initialized with counters' values and the **MASTER RESET** signal resets the counters for the next correlation. Then, the acquisition board sends a serial clock (**S_CLOCK**) to the three sets of shift registers and at each clock pulse, **three bits,** corresponding to the three counter units: $N_{count\ i1\text{-}i2}$, $Ncount_{\ i2\text{-}q1}$ and $N_{count\ total}$, are downloaded through independent lines to the acquisition board (figure A15.6).

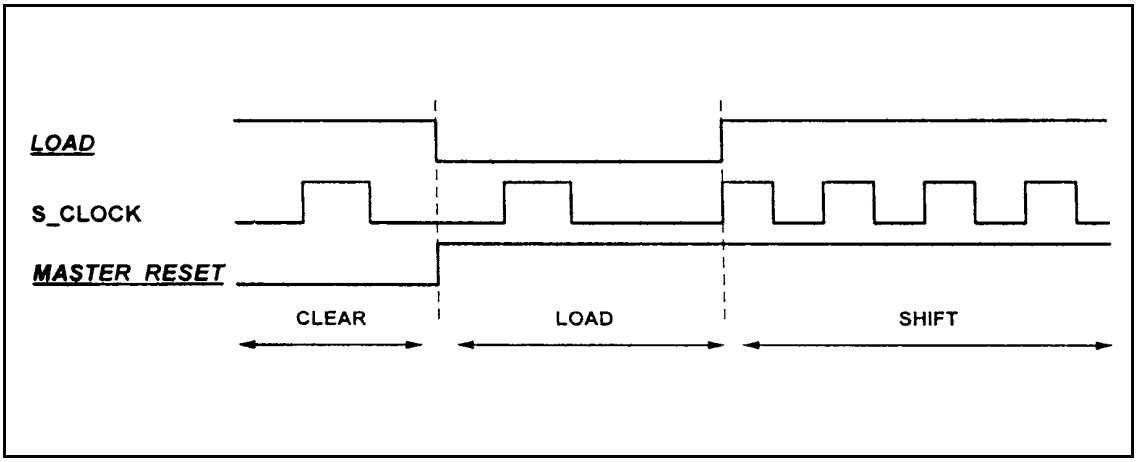

Figure A15.6.- *Control flow during the download of data to the PC-LAB adqusition board.*

References:

[Abramovitz and Stegun 63] M. Abramovitz, I. Stegun, "Handbook of Mathematical Tables", Dover Publications, N.Y. 1963.

[Andrews and Hunt 77] H. C. Andrews, B. R. Hunt, "Digital Image Restoration", Prentice-Hall Inc. 1977.

[Baker 62] H.C. Baker, A. H. La Grone, "Digital Computation of the Mutual Impedance Between Thin Dipoles", IRE Transactions on Antennas and Propagation, March 1962, pp 172-178.

[Bará et al. 94] J. Bará, A. Broquetas, A. Camps, I. Corbella, E. Daviu, S. Vilar, "Feasibility Study of a Dual Interferometer Radiometer", P.O. 132255 Final Rept. ESA-ESTEC, May 1994.

[Bará et al. 95A] J. Bará, A. Camps, F. Torres, I. Corbella, " Spatial Resolution in Bi-dmartinimensional Aperture Synthesis Radiometry", submitted for publication in IEEE Transactions on Geoscience and Remote Sensing, September 95.

[Bará et al. 95B] J. Bará, A. Camps, F. Torres, I. Corbella., "Baseline Redundancy and Radiometric Sensitivity: A critical Review", Soil Moisture and Ocean Salinity Merasurements and Radiometer Techniques. ESA-ESTEC, Noordwijk, The Netherlands, April 20-22, 1995.

[Bará 96] J. Bará, "mm-Wave Wide Band Focused Interferometry: Review of the Scientific Study", Preliminary Report, April 1996, CCN 1 to ESTEC Contract No 10590/93/NL/PV,RADET Phase 1, WP-1100

[Bará et al. 96A] J. Bará, A. Camps, I. Corbella, F. Torres, "Bi-dimensional Discrte Formulation for Aperture Synthesis Radiometers", CNN 2 to Work Order No 10 to ESTEC Contract No 9777/92/NL/PB. Final Report, January 1996.

[Bará et al. 96B] J. Bará, A. Camps, F. Torres, I. Corbella, "The Correlation of Visibility Errors and its impact on the Radiometric Resolution of an Aperture Synthesis Radiometer", submitted for publication in IEEE Transactions on Geoscience and Remote Sensing, February 96.

[Bernardini and Manduchi 94] R. Bernardini, R. Manduchi, "On the Reduction of Multidimensional DFT to Separable DFT by Smith Normal From Theorem", European Transactions on Telecommunications and Related Technologies, Vol. 5, N1 3, May-June 1994, pp 377-380.

[Born and Wolf 86] M. Born and E. Wolf, "Principles of Optics" 6th edition, ed Pergamon Press, 1986

[Bos 91] A. Bos, "A high-speed 2-bit correlator chip for Radio Astronomy", IEEE Transactions on Instrumentation and Measurement Vol 40, N1 3, June 1991, pp 591-595.

[Bracewell 61] R. N. Bracewell, "Interferometry and the Spectral Sensitivity Island Diagram", IRE Transactions on Antennas anmd Propagation, January 1961, pp 59-67.

[Brey 91] A. Brey, "Formacio d'imatges radiomètriques a frequencies de microones. Aplicacio a la teledetecció", PFC ETSETB, Universitat Politècnica de Catalunya, director PFC: A. Broquetes Ibars.

[Brown and Woodward 52] G. H. Brown, O. M. Woodward, "Experimentally Determined Radiation Characteristics of conical and Triangular Antennas", RCA Review, December 1952, pp 425-453.

[Camps et al. 95A] A. Camps, J. Bará, I. Corbella, F. Torres, "Visibility Inversion Algorithms over Hexagonal Sampling Grids", Soil Moisture and Ocean Salinity Merasurements and Radiometer Techniques. ESA-ESTEC, Noordwijk, The Netherlands, April 20-22, 1995.

[Camps et al. 95B] A. Camps, I. Corbella, J. Bará, F. Torres, "Radiometric Sensitivity Computation in Aperture Synthesis Interferometric Radiometry", submitted for publication in IEEE Transactions on Geoscience and Remote Sensing, December 95.

[Camps et al. 96A] A. Camps, J. Bará, I. Corbella, F. Torres, "The Processing of Hexagonally Sampled Signals with Standard Rectangular Techniques: Application to Aperture Synthesis Interferometric Radiometers", accepted for publication in the IEEE Transactions on Geoscience and Remote Sensing in July 1996.

[Camps et al. 96B] A. Camps, J. Bará, F. Torres, I. Corbella, "Inversion Algorithms in Aperture Synthesis Interferometric Radiometry: Application to the MIRAS Space Borne Instrument", submitted for publication in IEEE Transactions on Geoscience and Remote Sensing, February 96.

[Camps et al. 96C] A. Camps, J. Bará, F. Torres, I. Corbella, " Impact of Antenna Errors on the Radiometric Resolution of Large 2D Aperture Synthesis Radiometers. Study Applied to MIRAS", submitted for publication in Radio Science, May 96.

[Carbó and Domingo 87] R. Carbó Carré and Ll. Domingo Pascual, "Algebra Lineal y Matricial", ed. McGraw&Hill 1987. Serie Schaum.

[Cátedra et al. 95] M. F. Cátedra, R. P. Torres, J. Basterrechea, E. Gago, "The CG-FT Method. Application of Signal Processing Techniques to Electromagnetics", ed. Artech House 1995.

[Cygnus 90] Cygnus Engineering, " Orbital Workbench v 1.1. Program Description and User's Manual", Cygnus Engineering, Cupertino, California, 1990.

[Dudgeon and Mersereau 84] D. E. Dudgeon, R. M. Mersereau, "Multidimensional Digital Signal Processing", Prentice-Hall Inc. 1984

[Dugundji 57] J. Dugundji, "Envelopes and Pre-envelopes of Real Waveforms", IRE Transactions on Information Theory, 57, pp 53-57.

[Edelsohn 92] C. Edelsohn, "Synthetic Array Radiometry", Proceedings of the IGARSS 1992.

[Elachi 87] Ch. Elachi., "Introduction and Techniques of Remote Sensing", ed. John Wiley and Sons 1987.

[Evans and McLeish 77] G. Evans and C.W. McLeish, "RF Radiometer Handbook", Artech House 1977.

[Gaiser et al. 94] P. W. Gaiser, C. T. Swift, D. M. Le Vine, "L-Band Synthetic Aperture Radiometers for Earth Remote Sensing", Proceedings of the IGARSS 1994, pp 1311-1313.

[González and Wintz 77] Rafael C. González, Paul Wintz, "Digital Image Processing", Addison-Wesley 1977.

[Goodman 68] J.W. Goodman, "Introduction to Fourier Optics", ed. Mc. Graw&Hill 1968

[Goodman 85] J.W. Goodman, "Statistical Optics", Wiley Interscience, 1985.

[Goutoule et al. 94] J. M. Goutoule, U. Karft, M. Martín Neira, "MIRAS: A preliminary concept of a two dimensional L band Aperture Synthesis radiometer", Proceedings of the Specialist Meeting on Microwave Radiometry and Remote Sensing of the Environment, Roma, February 1994, VSP Publishers.

[Guessoum and Mersereau 86] A. Guessoum, R. M. Mersereau, "Fast algorithms for the Multidimensional Discrete Fourier Transform", IEEE Transactions on Acoustics, Speech and Signal Processing, Vol. ASSP-34, N1 4, August 1986, pp 937-943.

[Gündüzhan et al. 94] E. Gündüzhan, A. E. Çetin, A. M. Tekalp, "DCT Coding of Nonrectangulary Sampled Images", IEEE Signal Processing Letters, Vol. 1, N1 9, September 1994, pp 131-133.

[Hagen and Farley 73] J. B. Hagen, D. T. Farley, "Digital-Correlation Techniques in Radio Science", Radio Science, Vol. 8, N1 8-9, pp 775-784, August-September 1973.

[Hamaker et al. 77] J. P. Hamaker, J. D. O'Sullivan, J. E. Noordam, "Image sharpness, Fourier Optics and Redundant-Spacing Interferometry", Journal of the Optical Society of America, Vol 67, No 8, August 1977, pp 1122-1123

[HP A] "HP 346 A/B/C Noise Sources", Hewlett Packard.

[HP B] "HP 8970B Noise Figure Meter", Hewlett Packard.

[HP C] "HP 83752A Synthesized Sweeper", Hewlett Packard.

[HP D] "HP 8656B Synthesized Signal Generator", Hewlett Packard.

[HP E] Vector Modulation Measurements. Coherent pulsed test of radar and electronic warfare systems. Application Note 343-3.

[Ishiguro 80] M. Ishiguro, "Minimum Redundancy Linear Arrays for a Large Number of Antennas", Radio Science, Vol 15, N1 6, pp 1163-1170, November-December 1980.

[Jackson et al. 93] T. J. Jackson, D. M. LeVine, A. J.Griffis, D. C. Goodrich, T, J, Schmugge, C. T Swift, P. E. O'Neill, "Soil Moisture and Rainfall Estimation over a Semiarid Environment with the ESTAR Microwave Radiometer", IEEE Transactions on Geoscience and Remote Sensing, Vol. 31, N1 4, July 1993, pp 836-841.

[Jackson and LeVine 92] T.J. Jackson, D.M. Le Vine et al., "Soil Moisture Verification Study of the ESTAR Microwave Radiometer Walnut Gulch AZ 1991", Proc. IGARSS'92, pp. 486-488, May, 1992.

[Jain 89] Anil K. Jain, "Fundamentals of Digital Image Processing", Prentice-Hall Inc.. 1989

[Jain and Ranganath 81] A. K. Jain, S. Ranganath, "Extrapolation Algorithms for Discrete Signal with Application in Spectral Estimation", IEEE Transactions on Acoustics, Speech and Signal Processing, Vol. ASSP-29, N1 4, August 1981, pp 830-845.

[Jennison 58] R. C. Jennison, "A phase sensitive interferometer technique for the measurement of Fourier transforms of spatial brightness distributions of small extent", Mon. Not. Roy. Astron. Soc. 118, pp 276-284, 1958

[Johnson 93] R. C. Johnson, "Antenna Engineering Handbook", 3rd edition, Mc Graw-Hill 1993

[Kaplan 95] E.D. Kaplan, "Understanding GPS. Principles and Applications", ed. Artech House, 1995.

[King 57] H. E. King, "Mutual Impedance of Unequal Length Antennas in Echelon", IRE Trasactions on Antennas and Propagation, July 1957, pp 306-313.

[Komiyama 91] K. Komiyama, "High-Resolution Imaging by Supersynthesis Radiometers (SSR) for the passive microwave remote sensing of the Earth", Electronic Letters, 14th February 1991, Vol 27, N1 4, pp 389-390.

[Komiyama 92] K. Komiyama, "Supersynthesis Radiometer for Passive Microwave Imaging", Proceedings of the IGARSS 1992.

[Kraft 91A] U. R. Kraft, "Space-borne Synthetic Aperture Interferometric Radiometer for Global Monitoring of the Earth", Proceedings of the IGARSS 1991, pp 50-53.

[Kraft 91B] U. R. Kraft, "Pattern Characteristics and Beamforming for Synthetic Aperture Interferometric Radiometer Antennas", ICAP 1991.

[Lang and McClellan 80] S. W. Lang, J. H. McClellan, "Frequency Estimation with Maximum Entropy Spectral Estimators", IEEE Transactions on Acoustics, Speech and Signal Processing, Vol. ASSP-28, N1 6, December 1980.

[Lang and McClellan 82] S. W. Lang, J. H. McClellan, "Multidimensional MEM Spectral Estimation", IEEE Transactions on Acoustics, Speech and Signal Processing, Vol. ASSP-30, N1 6, December 1982, pp 880-886.

[Lannes and Anterrieu 94] A. Lannes, E. Anterrieu, "Image Reconstruction Methods for Remote Sensing by Aperture Synthesis", IGARSS 1994, Pasadena Symposium.

[Lannes 90] A. Lannes, "Remarcable algebraic structures of phase-closure imaging and their algorithmic implications in aperture synthesis", Journal Optics Society of America, Vol. 7, N1 3, March 1990.

[Laursen 95] B. Laursen, "Calibration of a Synthetic Aperture Radiometer", ESTEC P.O. No 141285, October 1995, R 624.

[Laursen and Skou 94] B. Laursen, Niels Skou, "A Space-Borne Synthetic Aperture Radiometer Simulated by the TUD Demostration Model", Proceedings of the IGARSS 1994, pp 1314-1316.

[Laursen and Skou 95], B. Laursen, N. Skou, "Calibration of the TUD Ku-Band Synthetic Aperture Radiometer", Proceedings of the IGARSS 1995, pp 812-814.

[LeVine et al. 83] D. M. LeVine, J. C. Good, "Aperture Synthesis for Microwave Radiometry in Space", NASA Technical Memorandum 85033, August 1983.

[LeVine et al. 89] D. M. LeVine, T. T. Wilheit, R. E. Murphy, C. T Swift, "A Multifrequency Microwave Radiometer of the Future", IEEE Transactions on Geoscience and Remote Sensing. Vol 27, N1 2, March 1989, pp 193-199.

[LeVine et al. 90] D. Le Vine, M. Kao, A. Tanner, C. Swift, A. Griffs: 'Initial Results in the Development of a Synthetic Aperture Microwave Radiometer', IEEE Trans. on Geoscience and Remote Sensing, Vol. 28, N1 4, pp 614-619, July 1990.

[LeVine 90] D. M. LeVine, "The Sensitivity of Synthetic Aperture Radiometers for Remote Sensing from Space", Radio Science, Vol. 25, N1 4, pp 441-453, July.August 1990.

[LeVine et al. 92] D. M. LeVine, A. J. Griffis, C. T. Swift, T. J. Jackson, "ESTAR: A Synthetic Aperture Microwave Radiometer for remote Sensing Applications", Proceedings of the IEEE, Vol. 82, N1 12, december 1992.

[Lim and Malik 81] J. S. Lim, N. A. Malik, "A New Algorithm for Two-Dimesional Maximum Entropy Power Spectrum Estimation", IEEE Transactions on Acoustics, Speech and Signal Processing, Vol. ASSP-29, N1 3, June 1981, pp 401-413.

[Lim 90] J. S. Lim, "Two-dimensional Signal and Image Processing", Prentice-Hall 1990.

[Malik and Lim 82] N. A. Malik, J. S. Lim, "Properties of Two-Dimesional Maximum Entropy Power Spectrum Estimates", IEEE Transactions on Acoustics, Speech and Signal Processing, Vol. ASSP-30, N1 5, October 1982, pp 762-798.

[Malliot 93] H. A. Malliot, "A Cross-beam Interferometer Radiometer for High Resolution Microwave Sensing", IEEE Aerospace Applications Conference Digest 1993, pp 77-86.

[Martín 90] F. Martín Asín, "Geodesia y Cartografía Matemática", ed. Paraninfo, 1990.

[Martín-Neira et al. 94] M. Martín-Neira, Y. Menard, J. M. Goutoule, U. Kraft, "MIRAS, a Two-Dimensional Aperture Synthesis Radiometer", Proceedings of the IGARSS 1994, pp 1323-1325.

[Martín-Neira 95] M. Martín-Neira, "Technical Note. WINTER-F: mm-Wave Wide Band Focused Interferometry", XRI/134.MMN/95, ESA-ESTEC

[Mc Donough 74] R. N. Mc Donough, "Maximum Entropy Spatial Processing of Array Data", Geophysics, Vol 39, December 1974, pp 843-851.

[Mersereau 79] R. M. Mersereau, "The Processing of Hexagonally Sampled Signals", Proceedings of the IEEE, Vol 67, N1 6, June 1979, pp 930-949.

[Mersereau and Dudgeon 74] R. M. Mersereau, D. E. Dudgeon, "The Representation of Two-Dimensional Sequences as One-Dimensional Sequences", IEEE Transactions on Acoustics, Speech and Signal Proocessing, Vol. ASSP-22, N1 5, October 1974, pp 320-325.

[Mersereau and Speake 81] R. M. Mersereau, T. C. Speake, "A Unified Treatment of Cooley-Tukey Algorithms for the Evaluation of the Multidimensional DFT", IEEE Transactions on Acoustics, Speech and Signal Processing, Vol. ASSP-29, N1 5, October 1981, pp 1011-1018.

[Milman 88] A. S. Milman, "Sparse-aperture Microwave Radiometers for Earth Remote Sensing", Radio Science, Vol 23, N1 2, March-April 1988, pp 193-205.

[MMS 95] Matra Marconi Space, "MIRAS: Microwave Imaging Radiometer with Aperture Synthesis. Microwave Radiometry Critical Technical Development", ESA-ESTEC, Mid Term Rept., January 1995. ESTEC Contract 9777/92/NL/PB.

[Moffet 63] A. T Moffet, "Minimum Redundancy Linear Arrays", IEEE Transactions on Antennas and Propagation, Vol AP16, N1 2, March 1963.

[NASA 95 A] Meeson, B. W., F. E. Corprew, J.M.P. McManus, D.M. Myers, J.W. Closs, K.J. Sun, D.J. Sunday, P. J. Sellers. 1995 ISLSCP Initiative I-Global Data Sets for Land-Atmosphere Models, 1987-1988. Volumes 1-5. Published on CD by NASA (USA_NASA_GDAAC_ISLSCP_001-USA_NASA_GDAAC_ISLSCP_005).

[NASA 95 B] Sellers, P.J., B.W. Meeson, J. Closs, J. Collatz, F. Corprew, D. Dazlich, F.G. Hall, Y. Kerr, R. Koster, S. Los, K. Mitchell, J. McManus, D. Myers, K.J. Sun, P. Try. 1995. An Overview of the ISLSCP Initiative I Global Data Sets. On: ISLSCP Initiative I-Global Data Sets for Land-Atmosphere Models, 1987-1988. Volume 1-5. Published on CD by NASA. Volume 1: USA_NASA_GDAAC_ISLSCP_001, OVERVIEW.DOC

[NRAO 89] "Synthesis Imaging in Radio Astronomy". Vol 6. NRAO Synthesis Imaging Summer School. Astronomical Society of the Pacific 1989.

[Nussbamer 81] H. Nussbamer, "New Polynomial Transform Algorithms for Multidimensional DFTs and Convolutions", IEEE Transactions on Acoustics, Speech and Signal Processing, Vol. ASSP 29, N1 1, February 1981, pp 74-83.

[Papoulis 75] A. Papoulis, "A New Algorithm in Spectral Analysis and Band-Limited Extrapolation", IEEE Transactions on Circuits and Systems, Vol CAS-22, N1 9, September 1975, pp 735-742.

[Peake 59] W. H. Peake, "Interaction of Electromagnetic Waves with some Natural Surfaces", IRE Transactions on Antennas and Propagation, December 1959, pp 324-329.

[Peichl and Süb 94]] M. Peichl, H. Süb, "Theory and Design of an Experimental Aperture Synthesis Radiometer", PIERS 94, Noordwijk, The Netherlands, July 1994.

[Phipp Jr. 86] T. E. Phipp Jr., "The Inversion of Large Matrices", BYTE April 1986, pp 181-188

[Pospelev 95] M. N. Pospelov, "Surface Wind Speed Retrieval Using Passive Microwave Polarinetry: The Dependence on Atmospheric Stability", IGARSS 95 (?):

[Press 86] W. H. Press, "Numerical Recipies in C: The art of Scientific Computation", Cambridge University Press, 1986.

[Proakis and Manolakis 88] J. G. Proakis, D. G. Manolakis, "Introduction to Digital Signal Processing", Mc. Millan Publishing Company 1988.

[Read 61] R. B. Read, "Two-element Interferometer for Accurate Position Determinations at 960Mc", IRE Transactions on Antennas and Propagation, Janaury 1961, pp 31-35.

[Richmond and Geary 70] J. H. Richmond, N.H. Geary, "Mutual Impedance Between Coplanar-Skew Dipoles", Proceedings of the IEEE, 1970, pp 130-132.

[Rogers et al. 74] A. E. E. Rogers, H. F. Hinteregger, A. R. Whitney, C.C. Counselman, I.I. Shapiro, J.J. Wittels, W. K. Klemperer, W. W. Warnock, T. A. Clark, L. K. Hutton, G. E. Marandino, B. O. Ronnang, O. E. H. Rydbeck, A. E. Niell, "The Structure of Radio Sources 3C 273B and 3C 84 Deduced from the "Closure" Phases and Visibility Amplitudes Observed with Three-Element Interferometers", The Astrophysical Journal, 193, pp 293-301, October 1974.

[Rogstad 68] D. H. Rogstad, " A Technique for Measuring Visibility Phase with an Optical Interferometer in the Presence of Atmospheric Seeing", Applied Optics, Vol 7, No 4, April 1968, pp 585-588.

[Rozario and Papoulis 87] N. Rozario, A. Papoulis, "Spectral Estimation from Nonconsecutive Data", IEEE Transactions on Information Theory, Vol. IT-33, N1 6, November 1987, pp 889-894.

[Ruf et al. 88] C. S. Ruf, C. T Swift, A. B. Tanner, D. M. LeVine, "Interferometric Synthetic Aperture Radiometry for the Remote Sensing of the Earth", IEEE Transactions on Geoscience and Remote Sensing, Vol. 26, N1 5, September 1988, pp 597-611.

[Ruf 91] C. S. Ruf, "Error Analysis of Image Reconstruction by a Synthetic Aperture Interferometric Radiometer", Radio Science, Vol. 26, No 6, pp 1419-1434, November-December 1991.

[Schafer et al. 81] R. W. Schafer, R. M. Mersereau, M. A. Richards, "Constrained Iterative Restoration Algorithms", Proceedings of the IEEE, Vol 69, N1 4, April 1981, pp 432-450.

[Skolnik 81] M. I. Skolnik, "Introduction to Radar Systems", Mc Graw&Hill 1981.

[Skou 89] N. Skou, "Microwave Radiometer Systems: Design and Analysis", Artech House 1989.

[SMOS 95] Consultative Meeting on Soil Moisture and Ocean Salinity: Measurement Requirements and Radiometer Techniques, ESTEC, Noordwijk, The Netherlands, 21-21 April 1995, ESA WPP-87.

[Steinberg and Subbaram 91] B.D. Steinberg, H. M. Subbaram, "Microwave Imaging Techniques", John Wiley and Sons 1991.

[Stogryn 67] A. Stogryn, "The Aparent temperature of the Sea at Microwave Frequencies", IEEE Transactions on Antenas and Propagation, Vol. 15, No 2, March 1967, pp 278-286.

[Süss et al. 89] H. Süss, K. Grüner, W. J. Wilson, "Passive Millimiter-Wave Imaging: A Tool for Remote Sensing", Ala Frequenza, n1 5-6, Vol LVII, 1989, pp 457-465.

[Swenson and Mathur 68] G. W. Swenson, N. C. Mathur, "The Interferometer in Radio Astronomy", Proceedings of the IEEE, Vol. 56, N1 12, December 1968, pp 2.114-2.130.

[Swift and Hevisi 95] C. T. Swift, L. Hevisi, "Design of a Ka Band Polarimetric Radiometer", Proceedings of the IGARSS 95, pp 2419-2420.

[Swift et al. 91] C. T. Swift, D. M. LeVine, C.S. Ruf, "Aperture Synthesis Concepts in Microwave Remote Sensing of the Earth", IEEE Transactions on Microwave Theory and Techniques, Vol. 39, No 12, December 1991, pp 1931-1935.

[Swift 93] C. T Swift, "ESTAR: The Electronically Scanned Thinned Array Radiometer for Remote Sensing Measurement of Soil Mositure and Ocean Salinity", NASA Technical Memorandum 4523, 1993

[Tanner and Swift 93] A. B. Tanner, C. T Swift, "Calibration of a Synthetic Aperture Radiometer", IEEE Transactions on Geoscience and Remote Sensing, Vol 31, N1 1, January 1993., pp 257-267.

[Thompson and d'Addario 82] A. R. Thompson, L. R. d'Addario, "Frequency Response of a Synthesis Array: Performance Limitations and Design Tolerances", Radio Science, Vol 17, N1 2, March-April 1982, pp 357-369.

[Thompson et al. 86] A. R. Thompson, J. M. Moran, G. W. Swenson, "Interferometry and Synthesis in Radio Astronomy", John Wiley and Sons 1986.

[Tiuri 64] M. E. Tiuri, "Radio Astronomy Receivers", IEEE Transactions on Antennas and Propagation, December 1964, pp 930-938.

[Torres et al. 96A] F. Torres, A. Camps, J. Bará, I. Corbella, " Impact of Receiver Errors on the Radiometric Resolution of Large 2D Aperture Synthesis Radiometers. Study Applied to MIRAS", accepted for publication in Radio Science, September 96.

[Torres et al. 96B] F. Torres, A. Camps, J. Bará, I. Corbella, R. Ferrero, " On-board Phase and Module Calibration of Large Aperture Synthesis Radiometers. Study Applied to MIRAS", IEEE Transactions on Geoscience and Remote Sensing, July 96, Vol 34, No 4, pp 1000-1009.

[Trussel 83] H. J. Trussell, "Convergence Criteria for Iterative Restoration Methods", IEEE Transactions on Acoustics, Speech and Signal Processing, Vol. ASSP-31, N1 1, February 1983, pp. 129-136.

[Trussell 80] H. J. Trussell, "The Relation Between Image Restoration by the Maximum A Posteriori Method and a Maximum Entropy Method", IEEE Transactions on Acoustics, Speech and Signal Processing, Vol. ASSP-28, N1 1, February 1980, pp 114-117.

[Ulaby et al. 81] Fawwaz T. Ulaby, Richard. K. Moore and Adrian K. Fung, "Microwave Remote Sensing. Active and Passive Vol. I. Fundamentals and Radiometry", Artech House 1981.

[Ulaby et al 82] Fawwaz T. Ulaby, Richard. K. Moore and Adrian K. Fung, "Microwave Remote Sensing. Active and Passive Vol II. Radar Remote Sensing and Surface Scattering and Emission Theory", Artech House 1982.

[Ulaby et al. 86] Fawwaz T. Ulaby, Richard. K. Moore and Adrian K. Fung, "Microwave Remote Sensing. Active and Passive Vol III. From Theory to Applications", Artech House 1986.

[Wahl 87] F. M. Wahl, "Digital Image Processing", Artech House 1987.

[Wentz 95] F. J. Wentz, "Wind-Vector Satellite Radiometer", Proceedings of the IGARSS 95, pp 2405-2406.

[Wernecke and d'Addario 77] S. J. Wernecke, L. R. d'Addario, "Maximun Entropy Image Reconstruction", IEEE Transactions on Computers, April 1977, pp 287-300.

Tesis Doctoral

APPLICATION OF INTERFEROMETRIC RADIOMETRY TO EARTH OBSERVATION

Adriano José CAMPS CARMONA
Department of Signal Theory and Communications, Polytechnic University of Catalonia, Barcelona, SPAIN, 1996

Rev: January 2000 (electronic version)

page	**line**	**It says**	**It should say**
20	eqn (2.14)	$R_A(\boldsymbol{t}) = \ldots$	$\tilde{R}_A(\boldsymbol{t}) = \ldots$
22	eqn (2.29)	$\operatorname{sinc}\left(\frac{u\boldsymbol{x}_0 + v\boldsymbol{h}_0}{W}\right)$	$\operatorname{sinc}\left(\frac{u\boldsymbol{x}_0 + v\boldsymbol{h}_0}{W^{-1}}\right)$
	-1	... in figure 2.4.	... in figure 2.3.
29	eqn. (2.59)	A_1A_2	$A_{e1}A_{e2}$
37	eqn. (3.10)	K	(nothing)
38	-2	...on those...	...in those...
	-1	...and (3.8)	...and (3.7)
52	+2	... (3.63) and (3.65)...	... (3.53) and (3.55)...
64	eqn. (3.90) 2nd line	-	a d factor is missing
169	+10	hole	whole
224	eqn. (8.1)	$V(u,v) = R_{i_\parallel i_\parallel}(0) + j\,R_{q_\parallel i_\parallel}(0)$	$V(u,v) = R_{i_1 i_2}(0) + j\,R_{q_1 i_2}(0)$
238	-3	from 1.13 down to 1.02	from 0.13 down to 0.02
242	eqn (8.15)	$\frac{\frac{1}{2}T_{ph}L}{\sqrt{\frac{1}{2}T_{ph} + T_{ph}(1-L) + T_{R_\parallel}}\sqrt{\frac{1}{2}T_{ph} + T_{ph}(1-L) + T_{R_\parallel}}}$	$\frac{\frac{1}{2}T_{ph}L}{\sqrt{\frac{1}{2}T_{ph} + T_{ph}(1-L) + T_{R_1}}\sqrt{\frac{1}{2}T_{ph} + T_{ph}(1-L) + T_{R_2}}}$
289	eqn (A5.8)	$\ldots E_t\left[e^{-j2p(\Delta_{xsin}(w_{rip}t+q_x)x + \Delta_{ysin}(w_{rip}t+q_y)h + \Delta_{zsin}(w_{rop}t+q_z)g)}\right]$	$\ldots E_t\left[e^{-j2p(\Delta_x\sin(w_{rip}t+q_x)x + \Delta_y\sin(w_{rip}t+q_y)h + \Delta_z\sin(w_{rop}t+q_z)g)}\right]$
298	+1	... because its ...	... because of its ...
318	eqn (A15.1)	left side truncated	N_{counts}

In creating the pdf files some double overlines (notation for matrices) appear a a single overline. (e.g. $\overline{C}$).

PAPERS RELATED TO THIS WORK PUBLISHED OR UNDER REVISION PROCESS:

PUBLICACIONS

KEY:L=full book, CL= book chapter, A= paper, R="review", E=editor

Authors (by order): *F. Torres, A. Camps*, J. Bará, I. Corbella, R. Ferrero

TITLE: **"On-Board Phase and Modulus Calibration of Large Aperture Synthesis Radiometers: Study Applied to MIRAS"**

REF. MAGAZINE/BOOK: *IEEE Transactions on Geoscience and Remote Sensing. GRS-34, No 4, pp 1000-1009, July 1996.*

KEY:*A*

Authors (by order): *A. Camps, J. Bará, I. Corbella, F. Torres*

TITLE: **"The Processing of Hexagonally Sampled Signals with Standard Rectangular Techniques: Application to 2D Large Aperture Synthesis Interferometric Radiometers"**

REF. MAGAZINE/BOOK: *IEEE Transactions on Geoscience and Remote Sensing, GRS-35, No 1, pp 183-190 January 1997.*

KEY:*A*

Authors (by order): *F. Torres, A. Camps, J. Bará, I. Corbella*

TITLE: **"Impact of Receiver Errors on the Radiometric Resolution of Large 2D Aperture Synthesis Radiometers. Study Applied to MIRAS"**

REF. MAGAZINE/BOOK: *Radio Science, Vol 32, N 2, pp 629-642, March-April 1997.*

KEY:*A*

Authors (by order): *A. Camps, J. Bará, F. Torres, I. Corbella, J. Romeu*

TITLE: **"Impact of Antenna Errors on the Radiometric Accuracy of Large Aperture Synthesis radiometers. Study Applied to MIRAS"**

REF. MAGAZINE/BOOK: *Radio Science, Vol. 32, N 2, pp 657-668, March-April 1997.*

KEY:*A*

Authors (by order): *A. Camps, F. Torres, I. Corbella, J. Bará, , J. A. Lluch*

TITLE: **"Threshold and Timing Errors of 1 bit/2 level Digital Correlators in Earth Observation Synthetic Aperture Radiometry"**

REF. MAGAZINE/BOOK: *Electronics Letters, Vol 33, No 9, pp 821-813, 24th April 1997.*

KEY:*A*

Authors (by order): *A. Camps, F. Torres, I. Corbella, J. Bará, X. Soler.*

TITLE: **"Calibration and experimental results of a two-dimensional interferometric radiometer laboratory prototype"**

REF. MAGAZINE/BOOK: *Radio Science, Vol. 32,* Nº 5, pp 1821-1832, *September-October 1997.*

KEY:*A*

Authors (by order): *A. Camps, J. Bará, F. Torres, I. Corbella.*

TITLE: **"Extension of the CLEAN Technique to the Microwave Imaging of Continuous Thermal Sources by Means of Aperture Synthesis Radiometers"**

REF. MAGAZINE/BOOK: *Progress In Electromagnetics Research*, PIER 18, pp 67-83, *January 1998.*

KEY:*A*

Authors (by order): *A. Camps, I. Corbella, J. Bará, F. Torres.*

TITLE: **"Radiometric Sensitivity Computation in Aperture Synthesis Interferometric Radiometry".**

REF. MAGAZINE/BOOK: *IEEE Transactions on Geoscience and Remote Sensing, GRS-35, No 2, pp 680-685, , March 1998*

KEY:*A*

Authors (by *order): J. Bará, A. Camps, F. Torres, I. Corbella.*

TITLE: **"Angular Resolution of two-dimensional hexagonally sampled interferometric radiometer"**

REF. MAGAZINE/BOOK*: Radio Science, Vol 33, No 5, pp 1459-1473, September-October 1998.*

KEY:*A*

Authors (by *order): A. Camps, A., F. Torres, I. Corbella, J. Bará, P. de Paco.*

TITLE: **"Mutual Coupling Effects on Antenna Radiation Pattern : An Experimental Study Applied to Interferometric Radiometers"**

REF. MAGAZINE/BOOK*: Radio Science, Vol 33, No 6, pp 1543-1552, November-December 1998.*

KEY:*A*

Authors (by *order): A. Camps, J. Bará, F. Torres, I. Corbella, F. Monzón*

TITLE: **"Experimental Validation of radiometric sensitivity in correlation radiometer"**

REF. MAGAZINE/BOOK*: Electronics Letters, December 1998, Vol. 34, No 25, pag. 2377-2379.*

KEY:*A*

Authors (by *order): A. Camps, F. Torres, J. Bará, I. Corbella, F. Monzón.*

TITLE: **"Automatic calibration of channels frequency response in interferometric Radiometers"**

REF. MAGAZINE/BOOK*: Electronics Letters, 21st January 1999, Vol 35, No 2, pp 115-116.*

KEY:*A*

Authors (by *order): A. Camps, I. Corbella, F. Torres, J. Bará, J. Capdevila.*

TITLE: **"RF Interference Analysis in Aperture Synthesis Interferometric Radiometers: Application to L-band MIRAS instrument"**

REF. MAGAZINE/BOOK*: Accepted for publication, IEEE Trans on Geoscience and Remote Sensing, July 1999.*

KEY:*A*

Authors (by *order): I. Corbella, I., A. Camps, F. Torres, J. Bará.*

TITLE: **"Analysis of noise injection networks for interferometric radiometer calibration"**

REF. MAGAZINE/BOOK*: Accepted for publication, IEEE Trans on Microwave Theory and Techniques, July 1999.*

KEY:*A*

Authors (by *order): F. Torres, A. Camps, I. Corbella, J. Barà, N. Duffo, M. Vall.llossera.*

TITLE: **"Calibration trade-off in large interferometric radiometers devoted to Earth Observation"**

REF. MAGAZINE/BOOK*: 6th Specialist Meeting on Microwaves Radiometry*, VSP, Zeist, The Netherlands, in press, 1999

KEY:*CL*

Authors (by *order): J. Bará, A. Camps, F. Torres, I. Corbella.*

TITLE: **"The correlation of visibility errors and its impact on the radiometric resolution of an aperture synthesis radiometer"**

REF. MAGAZINE/BOOK*: submitted for publication.*

KEY:*A*

Authors (by *order): A. Camps, A. Cardama, D. Infantes*

TITLE: **"Genetic Pattern Synthesis of Large linear thinned arrays"**

REF. MAGAZINE/BOOK*: submitted for publication.*

KEY:*A*

Authors (by *order): J. Bará, I. Corbella, F. Torres, A. Camps, M. Martín-Neira, G. Nesti, E. Olhmer*
TITLE: **" Remote Sensing of Hydrometeors by means of interferometric radiometry: theory and experimental results"**
REF. MAGAZINE/BOOK*: accepted for publication iin Radio Science, January 2000.*

KEY:*A*

Authors (by *order): J. Bará, A. Camps, I. Corbella, F. Torres*
TITLE: **"The specification of channel filters for an interferometric radiometer"**
REF. MAGAZINE/BOOK*: submitted for publication.*

KEY:*A*

Authors (by *order): A. Camps, F. Torres, I. Corbella, J. Barà, M. Martín-Neira, N. Duffo, M. Vall.llossera*
TITLE: **"2D Synthetic Aperture Imaging Radiometers for Earth Observation: the SMOS mission"**
REF. MAGAZINE/BOOK*: submitted for publication.*

KEY:*A*

Authors (by *order): A. Camps, F. Torres, S.J. Frasier.*
TITLE: **"Redundant Space Calibration of Hexagonal and Y-shaped Radars and Interferometric Radiometers "**
REF. MAGAZINE/BOOK*: submitted for publication.*

KEY:*A*

OTHER PUBLICATIONS

Authors (by order): *A. Camps, E. Ohlmer.*
TITLE: ***"The RADET Experiments concluded at the EMSL"***
REF. MAGAZINE/BOOK: *European Microwave Signature Laboratory Newsletter*, N 12, pp 1-3, *December* 1997.

KEY:*A*

A

CONFERENCE PAPERS

AUTHORS:	*J. Bará, A. Camps, F. Torres, I. Corbella.*
TITLE:	**"Baseline Redundancy and Radiometric Sensitivity: A Critical Review"**
PARTICIPATION:	*Invited Presentation*
CONFERENCE:	*Soil Moisture and Ocean Salinity (SMOS) Consultative Meeting*
PUBLICATION:	*ESA WPP-87, 1995*
PLACE:	*ESA-ESTEC, Noordwijk, Holanda*
DATE:	*April, 1995*

AUTHORS:	*A. Camps, J. Bará, I. Corbella, F. Torres.*
TITLE:	**"Visibility Inversion Algorithms Over Hexagonal Sampling Grids"**
PARTICIPATION:	*Invited Presentation*
CONFERENCE:	*Soil Moisture and Ocean Salinity (SMOS) Consultative Meeting*
PUBLICATION:	*ESA WPP-87, 1995*
PLACE:	*ESA-ESTEC, Noordwijk, Holanda*
DATE:	*April, 1995*

AUTHORS:	*A. Camps, J. Bará, I. Corbella, F. Torres.*
TITLE:	**"Inversion Algorithms Over Hexagonal Grids in Interferometric Aperture Synthesis Radiometry"**
PARTICIPATION:	*Presentation*
CONFERENCE:	*Progress In Electromagnetic Research Symposium, PIERS 1995*
PUBLICATION:	*Proceedings PIERS 95*
PLACE :	*University of Washington, Seattle (USA)*
DATE:	*July, 1995*

AUTHORS:	*M. Martín-Neira, J. M. Goutoule, A. Knight, J. Claude, J. Bará, A. Camps, F. Torres, I. Corbella, A. Lannes, E. Anterrieu, B. Laursen, N. Skou*
TITLE:	**"Integration of MIRAS Breadboard and Future Activities"**
PARTICIPATION:	*Presentation*
CONFERENCE:	International Geoscience and Remote Sensing Symposium IGARSS '96
PUBLICATION:	*Proceedings IGARSS 96*
PLACE:	Pasadena, USA
DATE:	*May, 1996*

AUTHORS:	*M. Martín-Neira, J. Bará, A. Camps, F. Torres, I. Corbella, O. Gasparini, M. V. Arbolino*
TITLE:	**"Theoretical Research on New Concepts for the Remote Sensing of Hydrometeors"**
PARTICIPATION:	*Presentation*
CONFERENCE:	International Geoscience and Remote Sensing Symposium IGARSS '96
PUBLICATION:	*Proceedings IGARSS 96*
PLACE:	Pasadena, USA
DATE:	*May, 1996*

AUTHORS:	*A. Camps, F. Torres, J. Bará, I. Corbella, M. Pino, M. Martín Neira.*
TITLE:	**"Evaluation of MIRAS spaceborne instrument performance: snap shot radiometric accuracy and its improvement by means of pixel averaging"**
PARTICIPATION:	*Presentation*
CONFERENCE:	The European Symposium on Aerospace Remote Sensing, Conference on Sensors, Systems and Next Generation Satellites III.
PUBLICATION:	*Proceedings of the Europto 1997.*
PLACE:	London, UK.
DATE:	*September, 1997.*

AUTHORS:	*A. Camps, F. Torres, I. Corbella, J. Bará, A. Abad.*
TITLE:	**" Modeling the radiometric signatures of the earth from space: a tool to study the performance of new radiometers"**
PARTICIPATION:	*Presentation*
CONFERENCE:	The European Symposium on Aerospace Remote Sensing, Conference on Sensors, Systems and Next Generation Satellites IV.
PUBLICATION:	*Proceedings of the Europto 1998.*
PLACE:	Barcelona, Spain.
DATE:	*September, 1998.*

AUTHORS:	*I. Corbella, F. Torres, A. Camps, J. Bará..*
TITLE:	**"A new calibration technique for interferometric radiometers"**
PARTICIPATION:	*Presentation*
CONFERENCE:	The European Symposium on Aerospace Remote Sensing, Conference on Sensors, Systems and Next Generation Satellites IV.
PUBLICATION:	*Proceedings of the Europto 1998.*
PLACE:	Barcelona, Spain.
DATE:	*September, 1998.*

AUTHORS:	*Harvey, A.R., A. H. Greenaway, A. Camps, I. Corbella, F. Torres, J. Bará, M. Martin-Neira*
TITLE:	**" Millimetre-Wave Aperture Synthesis Radiometry for Snow and Ice Mapping**
PARTICIPATION:	*Presentation*
CONFERENCE:	International Geoscience and Remote Sensing Symposium IGARSS '99
PUBLICATION:	*Proceedings IGARSS 96*
PLACE:	Hamburg, Germany
DATE:	*June, 1999.*

AUTHORS:	*Y. Kerr, J. Font, P. Wadteufel, A. Camps, J. Barà, I. Corbella, F. Torres, N. Duffo, M. Vall.llossera, G. Caudal*
TITLE:	**" Next Generation Radiometers: SMOS. A Dual Pol L-band 2D Apertures Synthesis Radiometers "**
PARTICIPATION:	*Invited Presentation*
CONFERENCE:	2000 IEEE Aerospace Conference
PUBLICATION:	-
PLACE:	Montana, USA
DATE:	*March, 2000.*